

**Faculty of Science and Engineering**

**Department of Chemistry**

**An Exploratory Investigation of the Photophysical and Photochemical  
Properties of Rhenium(I) N-Heterocyclic Carbene Tricarbonyl Complexes**

**Jamila Glorian Vaughan**

**This thesis is presented for the Degree of**

**Doctor of Philosophy**

**of**

**Curtin University**

**October, 2017**

**Declaration**

**To the best of my knowledge and belief this thesis contains no material previously published by any other person except where due acknowledgment has been made.**

**This thesis contains no material which has been accepted for the award of any other degree or diploma in any university. Signature:.....**



**Date:.....** 31/04/2017





# Contents

<b>1</b>	<b>Introduction</b>	<b>25</b>
1.1	Rhenium(I) Coordination Complexes . . . . .	25
1.2	Rhenium(I) Diimine Complexes . . . . .	26
1.3	The N-Heterocyclic Carbene . . . . .	27
1.3.1	Donor Properties of N-Heterocyclic Carbenes . . . . .	29
1.4	Rhenium N-Heterocyclic Carbene Complexes . . . . .	30
1.5	An Introduction To the Photophysical Properties of Transition Metal Complexes . . . . .	33
1.5.1	Specific Types of Electronic Transitions . . . . .	35
1.5.2	Metal-Metal or d-d Transitions . . . . .	36
1.5.3	Charge Transfer Transitions . . . . .	36
1.5.4	Ligand-Centred Transitions . . . . .	37
1.5.5	Excited State Lifetime . . . . .	38
1.5.6	Quantum Yield . . . . .	38
1.5.7	Energy Gap Law . . . . .	39
1.5.8	Tuning the Emission Properties . . . . .	40
1.5.9	Rigidochromic Effect . . . . .	41
1.5.10	Quenchers of Phosphorescence . . . . .	43
1.6	Luminescent Rhenium(I)-NHC Carbonyl Complexes . . . . .	43
1.7	Aims . . . . .	46
<b>2</b>	<b>Synthesis and Characterisation of NHC Ligands and their Re Complexes</b>	<b>47</b>
2.1	Overview . . . . .	47

2.2	Rationale . . . . .	48
2.3	Synthesis of N-Substituted Imidazoles . . . . .	49
2.3.1	Synthetic Strategy . . . . .	49
2.4	Synthesis of N-Heterocyclic Carbene Ligand Precursors . . . . .	52
2.4.1	Synthetic Strategy . . . . .	52
2.5	Synthesis of Rhenium(I)-NHC Tricarbonyl Complexes . . . . .	60
2.5.1	Target Compounds . . . . .	60
2.5.2	Synthetic Strategy . . . . .	62
2.5.3	Rhenium(I)-1-(2-pyridyl)imidazol-2-ylidene Tricarbonyl Series	64
2.5.4	Rhenium(I)-1-(2-pyrimidyl)imidazol-2-ylidene Tricarbonyl Series . . . . .	67
2.5.5	Rhenium(I)-1-(2-quinoyl)imidazol-2-ylidene and Rhenium(I)-1-(2-quinoxyl)imidazol-2-ylidene Tricarbonyl Series . . . . .	67
2.5.6	<sup>1</sup> H and <sup>13</sup> C Nuclear Magnetic Resonance Spectroscopy Studies	68
2.5.7	Infrared Spectroscopy . . . . .	71
2.5.8	X-Ray Crystal Structures . . . . .	72
2.6	Summary and Concluding Remarks . . . . .	78
<b>3</b>	<b>Photophysical Investigation of Re(I)-NHC Tricarbonyl Compounds</b>	<b>79</b>
3.1	Overview . . . . .	79
3.2	Rationale . . . . .	79
3.3	Absorption Profiles . . . . .	80
3.3.1	Absorption Profiles of the Azolium Salts . . . . .	80
3.3.2	Absorption Profiles of the Re(I)-NHC Tricarbonyl Compounds	85
3.3.3	Absorption Profiles of the 1-(2-Pyridyl)-imidazol-2-ylidene Series . . . . .	86
3.3.4	Absorption Profiles of the 1-(2-Pyrimidyl)-imidazol-2-ylidene Series . . . . .	88
3.3.5	Absorption Profiles of the 1-(2-Quinoyl)-imidazol-2-ylidene Series . . . . .	91

3.3.6	Absorption Profiles of the 1-(2-Quinoxyl)-imidazol-2-ylidene Series . . . . .	92
3.4	Time Dependent- Density Functional Theory . . . . .	93
3.5	Excitation and Emission Profiles . . . . .	96
3.5.1	The 1-(2-Pyridyl)-imidazol-2-ylidene Series . . . . .	96
3.5.2	The 1-(2-Pyrimidyl)-imidazol-2-ylidene Series . . . . .	99
3.5.3	The 1-(2-Quinoxyl)-imidazol-2-ylidene Series . . . . .	100
3.5.4	The 1-(2-Quinoxyl)-imidazol-2-ylidene Series . . . . .	101
3.5.5	Photophysical Properties at 77 K . . . . .	102
3.6	Singlet Oxygen Phosphorescence . . . . .	107
3.7	Summary and Concluding Remarks . . . . .	108
<b>4</b>	<b>Literature Overview of Photochemically Active Rhenium(I) Complexes</b>	<b>111</b>
4.1	Introduction . . . . .	111
4.2	Photochemical Ligand Substitution Reactions of Rhenium(I) Pentacarbonyl Complexes . . . . .	111
4.2.1	Electron Transfer Assisted Photochemical Ligand Substitution Reactions of Rhenium(I)-Diimine Complexes . . . . .	116
4.2.2	Photochemical Ligand Substitution Reactions of Rhenium(I)-Diimine Tricarbonyl Complexes from the <sup>3</sup> LF State . . . . .	118
4.2.3	Photochemical Ligand Substitution Reactions of Rhenium(I)-Diimine Complexes involving Higher Excited States (HES) . . . . .	122
4.3	Summary and Concluding Remarks . . . . .	127
<b>5</b>	<b>Photochemical Investigation of Re(I)-NHC Tricarbonyl Compounds</b>	<b>129</b>
5.1	Overview . . . . .	129
5.2	Previously Studied Benzimidazol-2-ylidene Systems . . . . .	130
5.3	1-(2-Pyridyl)-imidazol-2-ylidene Series . . . . .	131
5.3.1	Investigation of the Photostability of 3Br and 3Cl . . . . .	132
5.3.2	Investigation of the Photochemical Properties of <i>fac</i> -[Re(PyImPh)-(CO) <sub>3</sub> (NCCH <sub>3</sub> )] <sup>+</sup> . . . . .	139

5.3.3	Proposed Photochemical Mechanism . . . . .	142
5.3.4	Solvent Dependence . . . . .	146
5.4	The Photochemical Activity of the Remainder of the Pyridyl NHC Series	151
5.5	Photochemical Investigation of the Pyrimidyl, Quinoyl and Quinoxyl NHC Compounds . . . . .	153
5.6	Summary and Concluding Remarks . . . . .	159
<b>6</b>	<b>Photochemical Investigation of Re(I)-NHC Tricarbonyl Compounds with Organophosphorous Ligands</b>	<b>161</b>
6.1	Overview . . . . .	161
6.2	Characterisation of Rhenium(I) Complexes with L <sup>P</sup> Ligands by <sup>31</sup> P NMR	162
6.3	Bifurcated Mechanistic Studies of Rhenium(I)-Diimine Tricarbonyl Compounds with L <sup>P</sup> Ligands . . . . .	165
6.4	Stability of 3Br in the Presence of L <sup>P</sup> Ligands . . . . .	166
6.5	Photochemical Activity of 3Br with Triethylphosphite in Acetone . . .	171
6.5.1	Proposed Mechanism for the PLSRs of 3Br in the Presence of Triethylphosphite . . . . .	176
6.5.2	Characterisation of the <i>cis,trans</i> - and <i>cis,cis</i> - [Re(PyImPh)- (CO) <sub>2</sub> (P(OEt) <sub>3</sub> )Br] Photoproducts . . . . .	178
6.6	Photochemical Activity of 3Br with Triphenylphosphine . . . . .	179
6.6.1	Proposed Mechanism for the PLSRs of <i>fac</i> -[Re(PyImPh)(CO) <sub>3</sub> Br] (3Br) in the Presence of Triphenylphosphine . . . . .	188
6.7	Summary and Concluding Remarks . . . . .	189
<b>7</b>	<b>Summary, Conclusions and Future Work</b>	<b>191</b>
7.1	Summary and Conclusions . . . . .	191
7.2	Future Work . . . . .	194
<b>8</b>	<b>Experimental</b>	<b>197</b>
8.1	General Considerations . . . . .	197
8.2	Synthesis of N-Substituted Imidazoles . . . . .	198

8.2.1	1-Phenylimidazole . . . . .	198
8.2.2	1-(2-Pyridyl)imidazole . . . . .	199
8.3	Synthesis of N-Heterocyclic Carbene Ligand Precursors . . . . .	199
8.3.1	1-(2-Pyridyl)-3-butylimidazolium Bromide (PyImBuH.Br) . .	199
8.3.2	1-(2-Pyridyl)-3-butylimidazolium Hexafluorophosphate (PyImBuH.PF <sub>6</sub> ) . . . . .	200
8.3.3	1-(2-Pyridyl)-3-(2,4,6-trimethylphenyl)imidazolium Bromide (Py- ImMsH.Br) . . . . .	201
8.3.4	1-(2-Pyridyl)-3-(2,4,6-trimethylphenyl)imidazolium Chloride (Py- ImMsH.Cl) . . . . .	201
8.3.5	1-(2-Pyridyl)-3-phenylimidazolium Chloride (PyImPhH.Cl) .	202
8.3.6	1-(2-Pyridyl)-3-phenylimidazolium Bromide (PyImPhH.Br) .	203
8.3.7	1-(2-Pyrimidyl)-3-(2,4,6-trimethylphenyl)-imidazolium Chlo- ride (PmImMsH.Cl) . . . . .	204
8.3.8	1-(2-Pyrimidyl)-3-(2,4,6-trimethylphenyl)-imidazolium Hex- afluorophosphate (PmImMsH.PF <sub>6</sub> ) . . . . .	205
8.3.9	1-(2-Pyrimidyl)-3-phenylimidazolium Chloride (PmImPhH.Cl)	206
8.3.10	1-(2-Pyrimidyl)-3-phenylimidazolium Hexafluorophosphate	207
8.3.11	1-(2-Quinoyl)-3-phenylimidazolium Chloride (QuImPhH.Cl)	208
8.3.12	1-(2-Quinoyl)-3-phenylimidazolium Hexafluorophosphate (QuImPhH.PF <sub>6</sub> ) . . . . .	209
8.3.13	1-(2-Quinoxyl)-3-phenylimidazolium Chloride (QxImPhH.Cl) . . . . .	209
8.3.14	1-(2-Quinoxyl)-3-phenylimidazolium Hexafluorophosphate	210
8.4	Synthesis of Rhenium(I)-NHC Tricarbonyl Complexes . . . . .	211
8.4.1	<i>rac-fac</i> -Chlorotricarbonyl[1-(2-pyridyl)-3-butylimidazol-2-ylidene]- rhenium(I) (1Cl) . . . . .	211
8.4.2	<i>rac-fac</i> -Bromotricarbonyl[1-(2-pyridyl)-3-butylimidazol-2-ylidene]- rhenium(I) (1Br) . . . . .	212

8.4.3	<i>rac-fac</i> -Chlorotricarbonyl[1-(2-pyridyl)-3-(2,4,6-trimethylphenyl)-imidazol-2-ylidene]rhenium(I) (2Cl) . . . . .	213
8.4.4	<i>rac-fac</i> -Bromotricarbonyl[1-(2-pyridyl)-3-(2,4,6-trimethylphenyl)-imidazol-2-ylidene]rhenium(I) (2Br) . . . . .	214
8.4.5	<i>rac-fac</i> -Chlorotricarbonyl[1-(2-pyridyl)-3-(phenyl)imidazol-2-ylidene]rhenium(I) (3Cl) . . . . .	215
8.4.6	<i>rac-fac</i> -Bromotricarbonyl[1-(2-pyridyl)-3-(phenyl)imidazol-2-ylidene]rhenium(I) (3Br) . . . . .	216
8.4.7	<i>rac-fac</i> -Chlorotricarbonyl[1-(2-pyrimidyl)-3-mesitylimidazol-2-ylidene]rhenium(I) (4Cl) . . . . .	218
8.4.8	<i>rac-fac</i> -Bromotricarbonyl[1-(2-pyrimidyl)-3-mesitylimidazol-2-ylidene]rhenium(I) (4Br) . . . . .	219
8.4.9	<i>rac-fac</i> -Chlorotricarbonyl[1-(2-pyrimidyl)-3-phenylimidazol-2-ylidene]rhenium(I) (5Cl) . . . . .	220
8.4.10	<i>rac-fac</i> -Bromotricarbonyl[1-(2-pyrimidyl)-3-phenylimidazol-2-ylidene]rhenium(I) (5Br) . . . . .	221
8.4.11	<i>rac-fac</i> -Chlorotricarbonyl[1-(2-quinoliny)l)-3-phenylimidazol-2-ylidene]rhenium(I) (6Cl) . . . . .	222
8.4.12	<i>rac-fac</i> -Bromotricarbonyl[1-(2-quinoliny)l)-3-phenylimidazol-2-ylidene]rhenium(I) (6Br) . . . . .	223
8.4.13	<i>rac-fac</i> -Chlorotricarbonyl[1-(2-quinoxaliny)l)-3-phenylimidazol-2-ylidene]rhenium(I) (7Cl) . . . . .	224
8.4.14	<i>rac-fac</i> -Bromotricarbonyl[1-(2-quinoxaliny)l)-3-phenylimidazol-2-ylidene]rhenium(I) (7Br) . . . . .	225
8.5	Photophysical Measurements . . . . .	226
8.6	Computational Calculations . . . . .	227
8.7	Photochemistry Experimental Details . . . . .	228
8.7.1	Thermal Stability Measurements with CD <sub>3</sub> CN . . . . .	228
8.7.2	Thermal Stability Measurements with L <sup>P</sup> Ligands . . . . .	228
8.7.3	Photolysis Monitored by Absorption and Emission Spectroscopy . . . . .	228

8.7.4	Photolysis Monitored by $^1\text{H}$ NMR and Infrared Spectroscopy	229
8.7.5	Lamp Photolysis	229
8.7.6	Photostable Control	230
8.7.7	Temperature Controlled Photolysis	231
8.7.8	Temperature Controlled Excited State Lifetime Measurements	232
8.8	Synthesis and Characterisation of Solvates and Photochemical Products	232
8.8.1	Acetonitrile Solvate <i>fac</i> -[Re(PyImPh)(CO) <sub>3</sub> (NCCH <sub>3</sub> )] <sup>+</sup>	232
8.8.2	Acetonitrile Solvate; <i>fac</i> -[Re(QuImPh)(CO) <sub>3</sub> (NCCH <sub>3</sub> )] <sup>+</sup> tetrafluoroborate	233
8.8.3	<i>cis,trans</i> - and <i>cis,cis</i> -[Re(CO) <sub>2</sub> (PyImPh)(P(OEt) <sub>3</sub> )Br]	234
<b>9</b>	<b>Appendix</b>	<b>237</b>
9.1	Selected Bond Lengths and Angles Tables	237
9.1.1	X-Ray Crystallographic Data for 1Cl	237
9.1.2	X-Ray Crystallographic Data for 2Cl	239
9.1.3	X-Ray Crystallographic Data for 2Br	241
9.1.4	X-Ray Crystallographic Data for 3Cl	243
9.1.5	X-Ray Crystallographic Data for 3Br	245
9.1.6	X-Ray Crystallographic Data for 5Cl	247
9.1.7	X-Ray Crystallographic Data for 5Br	249
9.1.8	X-Ray Crystallographic Data for 6Cl	251
9.1.9	X-Ray Crystallographic Data for 6Br	253
9.1.10	X-Ray Crystallographic Data for 7Br	255
9.1.11	X-Ray Crystallographic Data for <i>cis,cis</i> -[Re(PyImPh)(CO) <sub>2</sub> (NCCH <sub>3</sub> )Cl]	258
9.1.12	X-Ray Crystallographic Data for <i>cis,cis</i> -[Re(PyImPh)(CO) <sub>2</sub> (P(OEt) <sub>3</sub> )Br]	260
9.1.13	X-Ray Crystallographic Data for <i>cis,trans</i> -[Re(PyImPh)-(CO) <sub>2</sub> (P(OEt) <sub>3</sub> )Br]	262

9.1.14	X-Ray Crystallographic Data for <i>cis,trans</i> -[Re(PyImPh)(PPh <sub>3</sub> ) <sub>2</sub> (CO)Cl/Br]	264
9.2	Emission and Excitation Spectra . . . . .	266
9.3	Predicted Absorption Profiles . . . . .	267
9.4	Calculated Transitions . . . . .	275
9.5	Calculated Orbital Contours . . . . .	306

# Acknowledgments

First and foremost, sincere thanks to my supervisor Max Massi for his help, guidance and patience over of the course of this very long journey.

Thank you to my original co-supervisor David Brown for starting this journey with me and to my associate supervisor Mark Ogden for being there at the end.

Thank you to the staff members of the Curtin Chemistry synthesis group especially Mauro Mocerino for all your advice and encouragement.

Thank you to Brian Skelton for his fabulous X-ray crystals structures.

Thank you to Paolo Raiteri and Phil Wright for all the amazing computational work.

Thank you to all my fellow PhD cohort who have who I have shared the laughter and the tears with. Mel, Guy, Eva, Dan, Nursha, Phil, Brodie, Karen, Erin, Krish, Danica, Rhys, Cal, Matt and everyone else along the way; this journey was long and arduous but sharing it with all of you made it worthwhile. You've all inspired me in different ways; I'm so proud of you all and can't wait to see what you all do with the next chapter of your lives.

Thank you to my family; Gloria, Michael and Amira for their unconditional love and support.

And last but not least, thank you Shane O Sullivan. I honestly could not have done this without you. Thank you for never giving up on me.



# List of Abbreviations

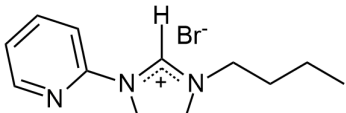
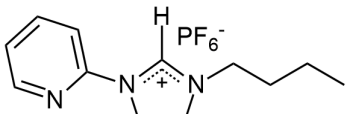
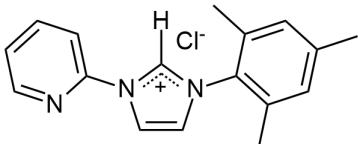
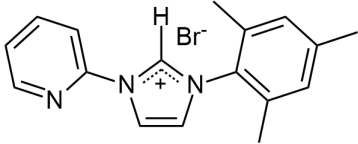
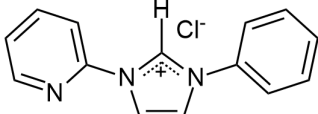
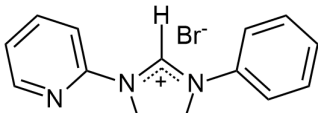
<b>Abbreviation</b>	<b>Full Phrase</b>
$^{13}\text{C}$ NMR	Carbon-13 Nuclear Magnetic Resonance Spectroscopy
$^1\text{H}$ NMR	Proton Nuclear Magnetic Resonance Spectroscopy
$^{31}\text{P}$ NMR	Phosphorous-31 Nuclear Magnetic Resonance Spectroscopy
A	Absorbance
ATR-IR	Attenuated Total Reflectance - Infrared
bpy	2,2'-Bipyridine
CNR or CN-R	Isocyanate ligand
D	Integrated intensity of luminescence
d	Day
DCM	Dichloromethane
DMSO	Dimethylsulfoxide
DMSO- $\text{d}_6$	Deuterated dimethylsulfoxide
<i>fac</i>	Facial isomer
FT-IR	Fourier Transform Infrared
HES	Higher Excited State
HMBC 2D NMR	Heteronuclear Multiple Bond Correlation Two Dimensional Nuclear Magnetic Resonance Spectroscopy
HOMO	Highest occupied molecular orbital
hr	Hour
HV	Hot/higher Vibrational
I	Intensity
IL	Intraligand
IR	Infrared

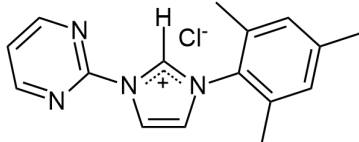
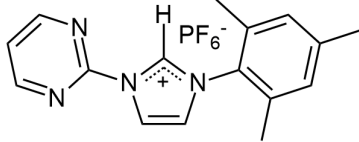
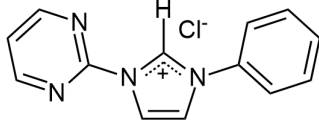
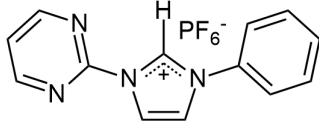
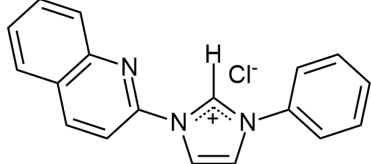
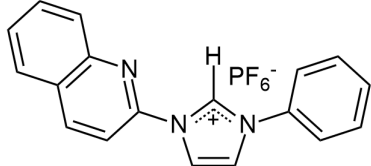
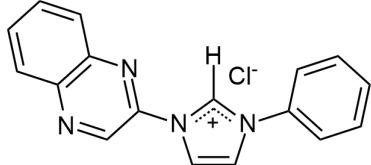
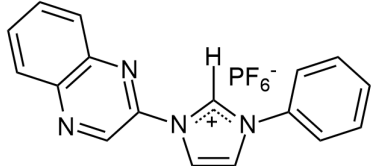
<b>Abbreviation</b>	<b>Full Phrase</b>
$k_{nr}$	Non-radiative decay constant
$k_r$	Radiative decay constant
L	Ligand
$L^P$	Organophosphorous Ligand
LC	Ligand Centred
LED	Light Emitting Device
LF	Ligand Field
LLCT	Ligand to Ligand Charge Transfer
LMCT	Ligand to Metal Charge Transfer
LUMO	Lowest Unoccupied Molecular Orbital
LV	Lowest Vibrational
MC	Metal Centred
MeCN-d <sub>3</sub> or CH <sub>3</sub> CN-d <sub>3</sub>	Deuterated acetonitrile
<i>mer</i>	Meridional isomer
MLCT	Metal to Ligand Charge Transfer
MLCT(HV)	Metal to Ligand Charge Transfer (Hot/Higher Vibrational)
MLCT(LV)	Metal to Ligand Charge Transfer (Lower Vibrational)
MLLCT	Metal to Ligand to Ligand Charge Transfer
n	Non-bonding electrons
N <sup>^</sup> C	Bidentate ligand with C and N donor atoms
NAS	Nucleophilic Aromatic Substitution
NHC	N-Heterocyclic Carbene
NMR	Nuclear Magnetic Resonance Spectroscopy
OD	Optical Density
phen	1,10-Phenanthroline
PLSR	Photochemical Ligand Substitution Reaction
py	Pyridine
Q	Quencher
R	Carbon based substituent
S <sub>N</sub> 1	Unimolecular Nucleophilic Substitution
S <sub>N</sub> 2	Bimolecular Nucleophilic Substitution
TCSPC	Time Correlated Single Photon Counting

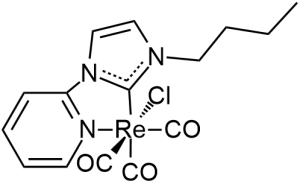
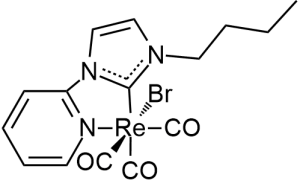
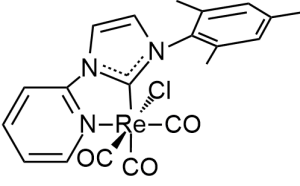
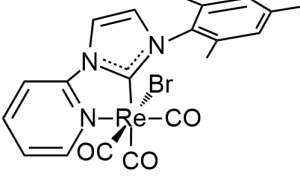
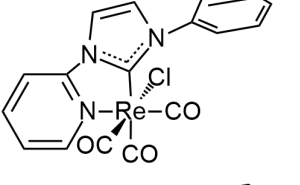
<b>Abbreviation</b>	<b>Full Phrase</b>
TDDFT	Time Dependent Density Functional Theory
TEP	Triethynylphosphine
<i>tert</i>	Tertiary
THF	Tetrahydrofuran
TR	Time Resolved
TRIR	Time Resolved Infrared
UV	Ultraviolet
UV-Vis	Ultraviolet-Visible
X	Halogen based substituent



# List of Compounds

Structure	Abbreviation	Number
	PyImBuH.Br	1
	PyImBuH.PF <sub>6</sub>	2
	PyImMsH.Cl	3
	PyImMsH.Br	4
	PyImPhH.Cl	5
	PyImPhH.Br	6

Structure	Abbreviation	Number
	PmImMsH.Cl	7
	PmImMsH.PF <sub>6</sub>	8
	PmImPhH.Cl	9
	PmImPhH.PF <sub>6</sub>	10
	QuImPhH.Cl	11
	QuImPhH.PF <sub>6</sub>	12
	QxImPhH.Cl	13
	QxImPhH.PF <sub>6</sub>	14

Structure	Abbreviation	Number
	<i>fac</i> -[Re(PyImBu)(CO) <sub>3</sub> Cl]	<b>1Cl</b>
	<i>fac</i> -[Re(PyImBu)(CO) <sub>3</sub> Br]	<b>1Br</b>
	<i>fac</i> -[Re(PyImMs)(CO) <sub>3</sub> Br]	<b>2Cl</b>
	<i>fac</i> -[Re(PyImMs)(CO) <sub>3</sub> Br]	<b>2Br</b>
	<i>fac</i> -[Re(PyImPh)(CO) <sub>3</sub> Cl]	<b>3Cl</b>
	<i>fac</i> -[Re(PyImPh)(CO) <sub>3</sub> Br]	<b>3Br</b>

Structure	Abbreviation	Number
	<i>fac</i> -[Re(PmImMs)(CO) <sub>3</sub> Cl]	<b>4Cl</b>
	<i>fac</i> -[Re(PmImMs)(CO) <sub>3</sub> Br]	<b>4Br</b>
	<i>fac</i> -[Re(PmImPh)(CO) <sub>3</sub> Cl]	<b>5Cl</b>
	<i>fac</i> -[Re(PmImPh)(CO) <sub>3</sub> Br]	<b>5Br</b>
	<i>fac</i> -[Re(QuImPh)(CO) <sub>3</sub> Cl]	<b>6Cl</b>
	<i>fac</i> -[Re(QuImPh)(CO) <sub>3</sub> Br]	<b>6Br</b>
	<i>fac</i> -[Re(QxImPh)(CO) <sub>3</sub> Cl]	<b>7Cl</b>
	<i>fac</i> -[Re(QxImPh)(CO) <sub>3</sub> Br]	<b>7Br</b>





# Chapter 1

## Introduction

### 1.1 Rhenium(I) Coordination Complexes

The discovery of rhenium in 1925 by Ida Tacke, Walter Noddack and Otto Berg marked the beginning of the exploration into the chemical properties of the last stable non-radioactive element currently known.<sup>1</sup> The chemistry of rhenium has opened up interesting avenues in coordination chemistry due in part to the wide range of available oxidation states (-1, 0, +1...+7), as shown in **Figure 1.1**. Rhenium is also a useful comparison to <sup>99m</sup>Tc, which has nuclear imaging properties for medical applications but can be challenging to work with on a macroscale due its radioactivity and short half-life.<sup>2-5</sup> The most widely reported rhenium coordination complexes feature rhenium(V), due to the stability of the rhenium(V) oxo, imido, sulfido or nitrido core.<sup>2,6</sup> Despite the focus on rhenium(V) cores, it has been determined that when used in conjunction with the correct ligands, rhenium(I) exhibits favourable luminescent properties with applications in light emitting devices and biological imaging.<sup>7,8</sup>

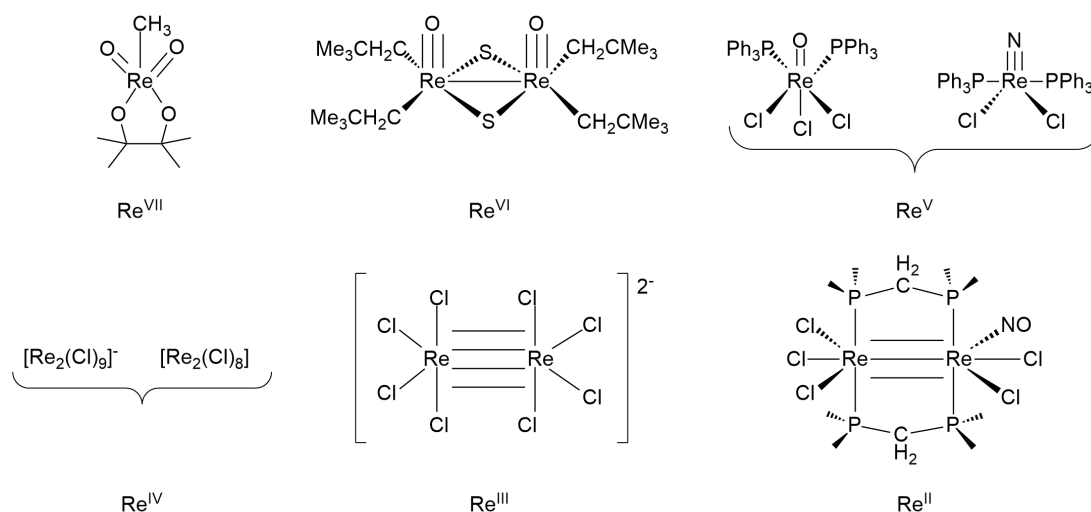
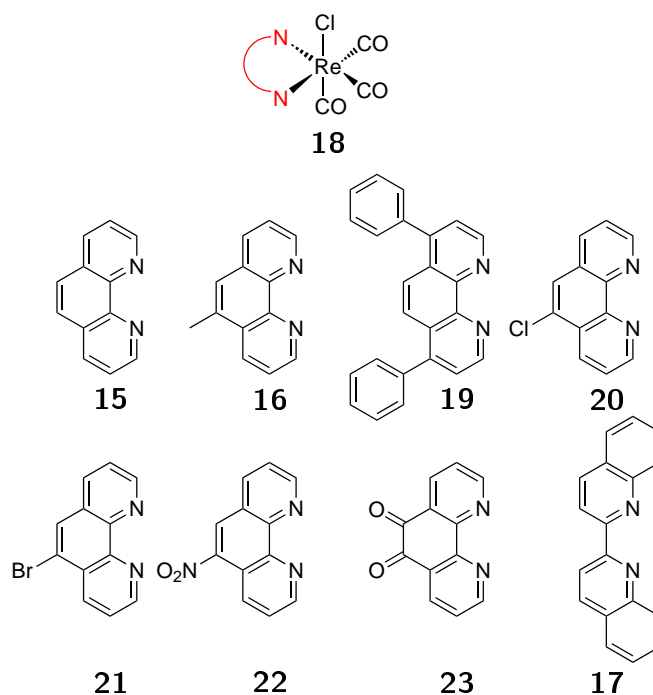


Figure 1.1: Rhenium complexes depicting the variable oxidation states and binding modes of rhenium (Adapted from Vites, 1994).<sup>9</sup>

## 1.2 Rhenium(I) Diimine Complexes

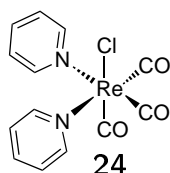
Diimine ligands such as 1,10-phenanthroline (phen) (**15**) and its derivatives (**16-17** **Scheme 1.1**) have been the conventional ligands of choice for the synthesis of luminescent rhenium(I) complexes since Wrighton and Morse's inaugural findings in 1974.<sup>7</sup> Wrighton and Morse discovered that the diimine tricarbonyl rhenium(I) compounds, based on the formula of **18**, underwent radiative decay from a triplet excited state. The radiative decay was measured at 77 K in frozen media and at 298 K in fluid solutions. The authors observed a novel phenomenon coined "luminescence rigidochromism," where the shape of the emission profile was drastically different in the frozen medium compared to the fluid solution. The authors also noted that the emission maximum shifted upon freezing the solvent.

The authors then investigated Mn(I) complexes with the same ligands in **Scheme 1.1** and found the complexes did not exhibit any detectable luminescence. Additionally, the compound *fac*-[Re(py)<sub>2</sub>(CO)<sub>3</sub>Cl] (**24**) was not measurably luminescent under any conditions, implying that the optical properties were intrinsic to the rhenium(I)-diimine tricarbonyl system. Since the work of Wrighton and Morse, over 150 different rhenium(I)-diimine tricarbonyl coordination complexes have been reported.<sup>8</sup>



Scheme 1.1: The first reported luminescent rhenium(I)-diimine tricarbonyl complexes (Adapted from Wrigton, 1974).<sup>7</sup>

Whilst the chemistry of rhenium(I) with diimine ligand systems have been heavily investigated, ligands with similar charge, aromaticity and binding modes such as the N-heterocyclic carbene ligand have been largely overlooked.



Scheme 1.2: The rhenium(I)-dipyridine tricarbonyl compound was determined to not be measurably luminescent under any conditions (Adapted from Wrigton, 1974).<sup>7</sup>

### 1.3 The N-Heterocyclic Carbene

A singlet carbene is a formally neutral divalent  $sp^2$  hybridised carbon with two single bonds, a lone pair of electrons in a  $sp^2$  orbital and an empty 2p orbital as shown in **Figure 1.2**. Whilst there are other types of carbenes with geometry and bonding not described below, such a linear and triplet, the contents of this thesis focuses on carbenes with the following bonding.

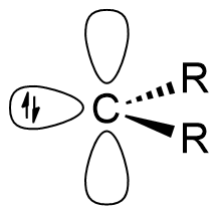


Figure 1.2: A simplified schematic of a singlet carbene.

Traditional carbenes, such as the one in **Figure 1.2**, are highly reactive with a propensity to dimerise and are therefore difficult to isolate.<sup>10</sup> In 1968 Wanzlick and co-workers discovered that carbenes adjacent to heteroatoms, particularly nitrogen (**Scheme 1.3**), were considerably more stable than traditional carbenes.<sup>11</sup> The stabilisation was attributed to electron donation into the 2p orbital of the carbon atom by the adjacent nitrogen atoms as shown in **Figure 1.3**. Furthermore, the four  $\pi$  electrons of the two nitrogen atoms are shared between the carbon and the nitrogen atoms to result in the overall resonance stabilisation of the carbene.

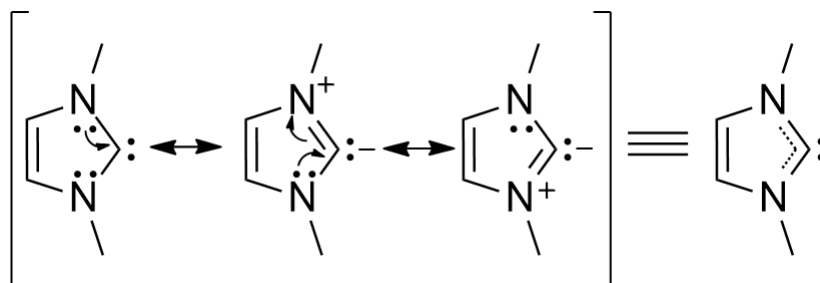
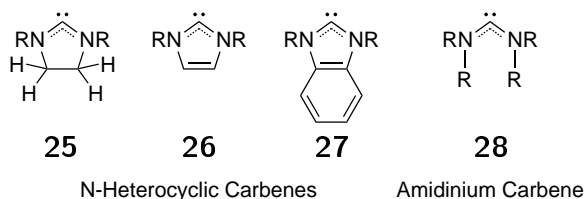


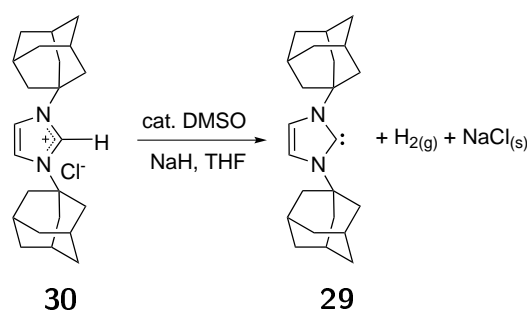
Figure 1.3: Stabilisation of the carbene carbon atom *via* electron donation from the two adjacent nitrogen atom in the NHC framework.

Carbenes adjacent to heteroatoms are classed as persistent carbenes as they are more stable than the hydrocarbon based carbene depicted in **Figure 1.2**. There are several examples of persistent carbenes with stabilising heteroatoms such as oxygen and sulfur however the field is dominated by the diamino type species depicted in **Scheme 1.3**. Of the diaminocarbenes, the most renowned are the N-heterocyclic carbenes (NHCs) (**25**, **26**, **27**), which are the cyclic variation of amidinium species.



Scheme 1.3: Types of persistent carbenes.

The first report of a free carbene in the solid state was in 1991, where Arduengo and co-workers successfully isolated crystalline 1,3-di(adamantyl)imidazolin-2-ylidene (**29**), a NHC stabilised by bulky adamantyl groups on the N1 and N3 positions shown in **Scheme 1.4**.<sup>12</sup> Since Arduengo's achievement, research in the field of N-heterocyclic carbenes has flourished and the chemistry of free NHCs as well as a variety of NHC-metal complexes has become an area of extensive investigation with catalytic, medicinal and optical applications.<sup>3,13–21</sup>



Scheme 1.4: Synthesis of the first crystalline carbene (Adapted from Arduengo, 1991).<sup>12</sup>

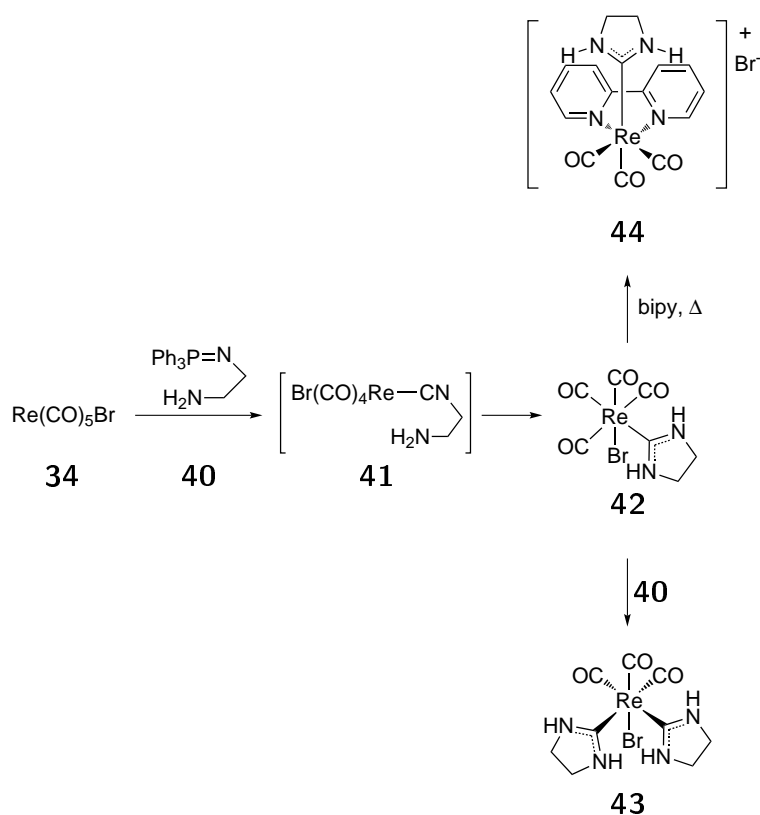
### 1.3.1 Donor Properties of N-Heterocyclic Carbenes

N-Heterocyclic carbene ligands are strong  $\sigma$  donors and are poor  $\pi$  acceptors like the phosphine ligands, and as such are considered “phosphine mimics”.<sup>13</sup> NHCs are useful alternatives to phosphines as they are generally easier to synthesise and functionalise. A number of NHC-metal complexes, specifically complexes of palladium, ruthenium and iridium are known to exhibit greater catalytic activity than their phosphine analogues.<sup>16–18,22–24</sup> NHC ligands can also have versatile binding modes, can act as bis- and tris-chelators and can also be utilised in pincer, tripodal and bridging motifs.<sup>18,25</sup> This synthetic versatility allows NHCs to participate in varied coordination geometries and therefore be applied to numerous metal centres.



The isopropyl amidinium carbene analogue (**38**) was further reacted with triphenylphosphine in THF at reflux and the triphenylphosphine was observed to displace the carbonyl ligand *cis* to both the amidinium carbene and the bromo ligands to form a neutral *fac*-tricarbonyl species (**39**).

The authors speculated that this configuration should not be sterically favoured due to the bulkiness of the phenyl rings of the phosphine in close proximity to the bulky amidinium carbene. They concluded that the carbonyl ligand was displaced due to labilising effect of the bromo and carbene ligands *cis* to the carbonyl.<sup>28</sup>



Scheme 1.7: Rhenium(I)-imidazoline N-Heterocyclic Carbene Complexes reported by Liu et al. (1996) and Chen et al. (2012).<sup>29,30</sup>

Liu and co-workers advanced the findings of Lu and were able to synthesise two rhenium(I)-N-heterocyclic-imidazolidin-2-ylidene compounds.<sup>29</sup> They found that if the phosphinimine was functionalised with an amine to form an aminophosphinimine, then the resulting ligand (**40**) could coordinate to the rhenium(I) to form a rhenium(I)-isocyanide intermediate (**41**). This complex then underwent intramolecular cyclisation to form rhenium(I)-N-heterocyclic carbene species (**42**) in one step as shown in **Scheme 1.7**.

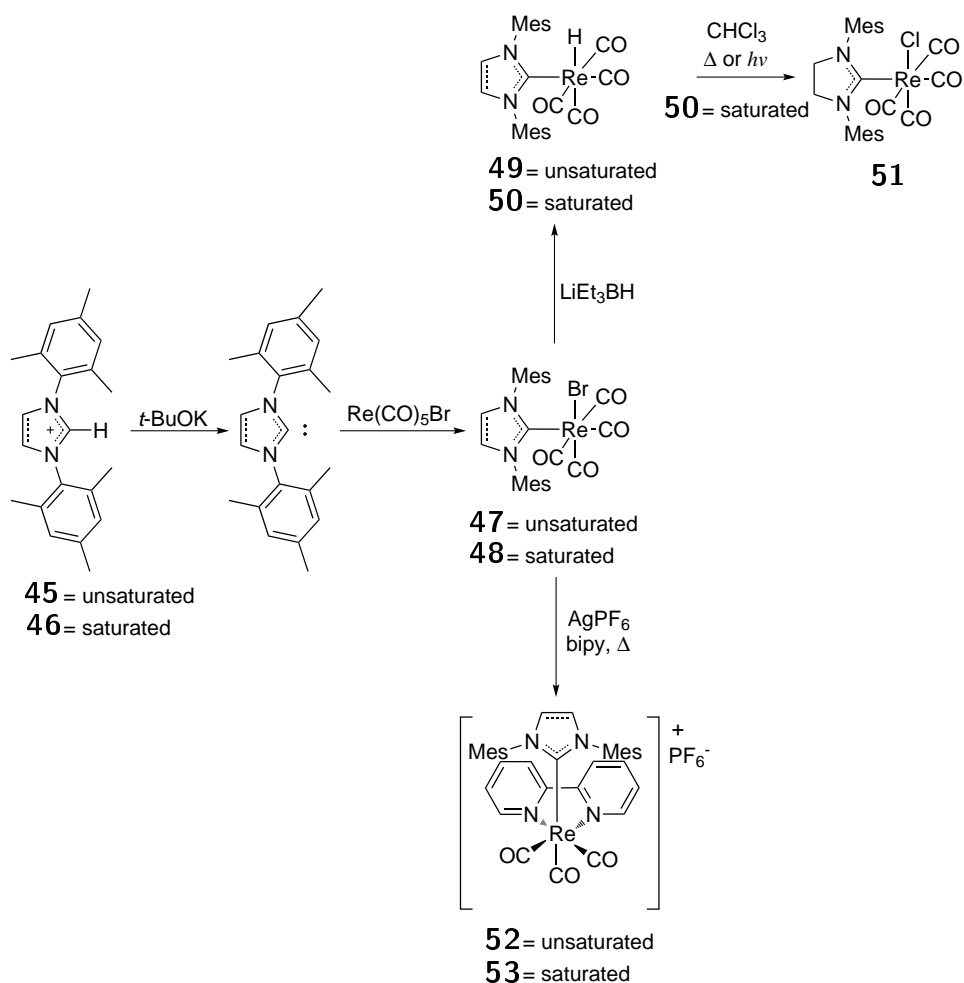
If treated with two equivalents of the aminophosphinimine ligand (**40**), a bis-substituted bromo tricarbonyl imidazolidin-2-ylidene rhenium(I) species (**43**) was formed. X-Ray crystal structure analysis confirmed that the configuration was *facial*. The authors noted that the Re-C bond of the carbonyl in *trans* to the bromo ligand was reduced in length due in comparison to the two carbonyls in *trans* to the carbene ligands due to the enhanced *trans* effect of the carbene ligand.

In 2012 Liu and Chen reported the synthesis of rhenium(I) carbonyl complexes with unsaturated 1,3-di-mesitylimidazol-2-ylidene (**45**) and saturated 1,3-dimesityl-4,5-imidazolin-2-ylidene (**46**) “IMes<sub>2</sub>” ligands via the free carbene method, as shown in **Scheme 1.8**.<sup>30</sup>

The authors found the chemical shift of the NCN carbene carbon to differ in the <sup>13</sup>C NMR for the unsaturated compound (**47**, 177.4 ppm) vs the saturated compound (**48**, 203.9 ppm). This in accordance with many reports that state that the electron density distribution is different for the imidazol-ylidene vs the saturated imidazolidin-ylidene due to the aromaticity of the former type of complexes.<sup>10,31,32</sup> Interestingly, no discernible difference in the CO stretching frequencies of **47** and **48** was observed therefore it was concluded that donor strength of the two IMes<sub>2</sub> ligands (**45** and **46**) was the same despite the difference in aromaticity.

In the presence of LiEt<sub>3</sub>BH, **47** and **48** formed their hydrido complexes; **49** and **50**. Both hydrido compounds were isolated as air stable solids, however, when dissolved in chlorinated solvents they underwent ligand exchange to form the chloro species **51**. Whilst it was noted that the process required activation, either thermally or photochemically, the mechanism was never determined.

Although the synthesis of **44**, shown in **Scheme 1.8**, was found to occur by heating **42** in the presence of bipy the authors found that AgPF<sub>6</sub> was necessary to facilitate the formation of **52** and **53** via the silver halide abstraction method as shown in **Scheme 1.8**. The UV-vis absorption spectra of **52** and **53** were collected and no discernible difference between the two absorption profiles was noted. No further photophysical investigation into the potential emissive properties of either complex was performed.



Scheme 1.8: Rhenium(I) carbonyl complexes with a bulky NHC ligand (Chen, 2012).<sup>30</sup>

## 1.5 An Introduction To the Photophysical Properties of Transition Metal Complexes

The optical or “photophysical” properties of rhenium(I) coordination complexes and other transition metal complexes are caused by the absorption of photons. When a molecule is excited by a photon, the photon is absorbed by the electronic configuration of the ground state of the molecule, or “ $S_0$ ”, and this energy promotes an electron in the highest occupied molecular orbital (HOMO) to a higher energy unoccupied molecular orbital to form the electronic configuration of an excited state,  $S_n$  (**Figure 1.4**). The excited electronic configuration  $S_n$  will undergo internal conversion (IC) and the molecule will vibrationally relax to the lowest energy excited configuration,  $S_1$ , where the excited electron will reside in the lowest unoccupied molecular orbital (LUMO). Internal conversion is a rapid process and will generally occur within picoseconds ( $10^{-12}$

s). This process is non-radiative and as such no light is emitted during the rapid relaxation from  $S_n$  to  $S_1$ . The vibrational energy consumed by this process is transferred as heat to the surrounding medium.

Singlet multiplicity is where all the electrons are paired with opposite spins. If the electron in the higher energy orbital has not changed spin and is still paired with an electron in the HOMO of the opposite spin, this is known as the singlet excited state,  $S_1$ . When an electron relaxes from a higher energy orbital of  $S_1$  configuration back to its ground state of  $S_0$  configuration, the remaining energy from the absorbed photon is released by the molecule *via* radiative decay or consumed vibrationally *via* non-radiative decay. The radiative decay process is known as fluorescence. Fluorescence is short lived and has a short emissive lifetime as the  $S_1$  to  $S_0$  transition is spin allowed and therefore occurs rapidly.<sup>33</sup> Typical fluorescent lifetimes are in the tens of nanoseconds.<sup>33</sup> As internal conversion takes place in the picosecond time range it can be inferred to be fully complete by the time the fluorescent decay begins, therefore fluorescence should be occurring from the lowest vibrational level of  $S_1$ .<sup>33</sup>

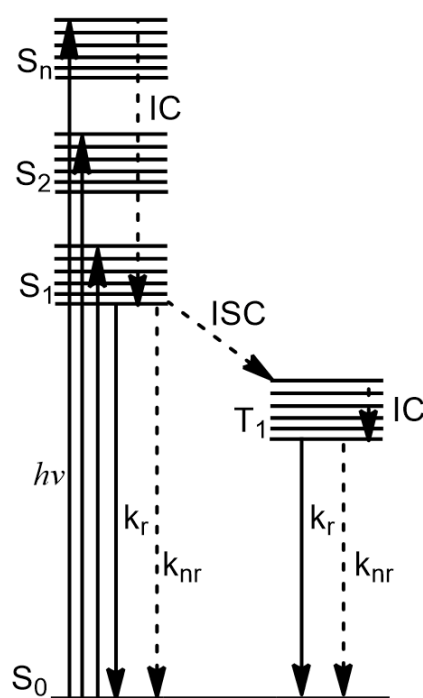


Figure 1.4: Jablonski diagram of general electronic transitions.

In the case of rhenium(I) metal complexes, the spin-orbit coupling property allows

for the mixing of the spin character of the singlet excited state and that of the triplet excited state. This allows for intersystem crossing (ISC) to occur which is when the electron in the higher energy orbital changes spin such that it has the same spin orientation as the unpaired electron in the HOMO which results in a triplet excited state configuration,  $T_1$ . A triplet state has an elongated excited state lifetime as the  $T_1$  to  $S_0$  transition is spin forbidden. When an electron relaxes from a higher energy orbital of  $T_1$  configuration back to the ground state  $S_0$  configuration, the remaining energy from the absorbed photon is released by the molecule as radiative decay or consumed vibrationally as non-radiative decay. The radiative decay process is known as phosphorescence. Fluorescence and phosphorescence are collectively known as luminescence. The term luminescence should be used when the origin of the emission is unknown. Radiative transitions have the decay constant  $k_r$  and non-radiative transitions have the decay constant  $k_{nr}$ .

### 1.5.1 Specific Types of Electronic Transitions

Without an external field applied, the five  $d$  orbitals of a transition metal are degenerate (are of the same energy). When an octahedral field is applied, the energy levels split into three lower ( $t_{2g}$ ) energy levels and two higher ( $e_g$ ). An example of a low spin  $d^6$  metal complex with six equivalent ligands is shown in **Figure 1.5**. The molecular orbital diagram in **Figure 1.5** is only valid for complexes with strong  $t_{2g}$ - $e_g$  splitting and  $\pi^*$ -accepting ligands.

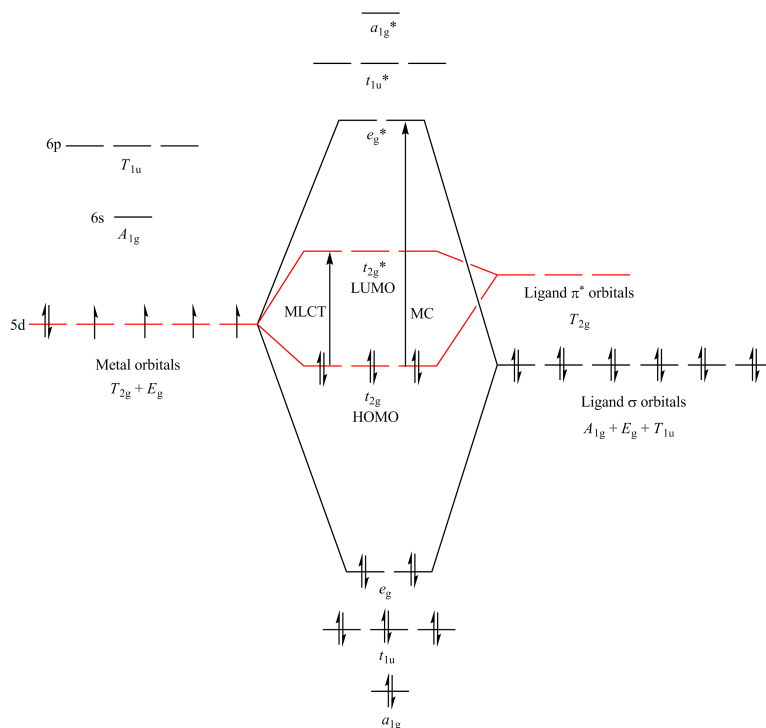


Figure 1.5: Diagram representing the splitting of the molecular orbitals when an octahedral field is applied by six equivalent to form a low spin  $d^6$  metal complex. Only the  $t_{2g}$  combinations are considered for clarity.

There are three types of electronic transitions that can arise within a  $d^6$  transition metal complex being metal-metal, ligand-ligand or mixed metal-ligand.

### 1.5.2 Metal-Metal or d-d Transitions

Ligand field (LF) or metal centred (MC) transitions are  $d-d$  transitions. A  $d-d$  transition occurs when an electron is promoted from the  $t_{2g}$  orbital to the empty  $e_g^*$  of the metal by the energy of an absorbed photo as shown in **Figure 1.5**. Pure  $d-d$  transitions are Laporte forbidden as there is no change in parity.<sup>34</sup>

### 1.5.3 Charge Transfer Transitions

Charge transfer transitions are another type of transition possible in  $d^6$  metal complexes and are the most utilised for light emitting applications if one of the ligands has  $\pi^*$  acceptor orbitals available. A charge transfer is a process where an electron is excited

by a photon from a donor portion of the complex to an acceptor portion of the complex to form an excited state. Charge transfer transitions can be a metal-to-ligand charge transfer (MLCT), ligand-to-metal charge transfer (LMCT) or ligand-to-ligand charge transfer (LLCT).

A ligand to metal charge transfer typically occurs in metal complexes where the metal is in a high oxidation state and the ligand contains non-bonding (n) electrons.<sup>35</sup> The ligand is electron rich and easily oxidised whilst the metal centre is electron poor and readily reduced. A metal to ligand charge transfer is commonly observed when the metal is in low oxidation state and the ligand has low lying acceptor  $\pi^*$  orbitals. In this case the metal is easily oxidised and the ligand is readily reduced.<sup>35</sup> The most common ligand favoured for inducing MLCT transitions in low oxidation state metals are the diimine ligands such as bipyridine and phenanthroline.<sup>35</sup> The lowest energy rhenium(I)-diimine transitions typically consist of a combination of metal-to-ligand and ligand-ligand charge transfers known as a metal-to-ligand-ligand charge transfer (MLLCT).

Charge transfer bands are sensitive to solvent polarity due to large dipole change between the ground state and excited state. This sensitivity to solvent polarity is known as solvatochromism.<sup>35</sup> The identity of charge transfer bands can therefore be confirmed by changing the polarity of the solvent and if the absorption and/or emission maximum of the band shifts, this is indicative of a charge transfer state. If the absorption maximum undergoes a bathochromic shift (redshift) when increasing the polarity of the solvent then the excited state is more polar than the ground state. If the absorption maximum undergoes a hypsochromic shift (blueshift) upon increasing the polarity of the solvent then the polarity of the excited state is less than the polarity of the ground state.<sup>35</sup>

#### 1.5.4 Ligand-Centred Transitions

Ligand centred (LC) or intraligand (IL) transitions are typical in coordination complexes that utilise aromatic ligands with extended  $\pi$  and  $\pi^*$  orbitals.<sup>35</sup> LC transitions involve the promotion of an electron from a  $\pi$  orbital based on the ligand to an empty  $\pi^*$  based on either the same or a neighbouring ligand. Ligand to ligand charge transfers (LLCT) can also occur in systems with non-equivalent ligands where one ligand

is readily reduced and the other is readily oxidised.

### 1.5.5 Excited State Lifetime

There are two key ways of quantifying the luminescent qualities of a molecule; lifetime and quantum yield. Observed excited state lifetime is calculated by the following equation:

$$\tau_{(\text{obs})} = \frac{1}{k_r + k_{nr}}$$

where  $k_r$  is the rate constant for radiative decay and  $k_{nr}$  is the rate constant for non-radiative decay.<sup>33</sup>

The natural lifetime ( $\tau_{(n)}$ ) is the radiative lifetime of the excited state species in the absence of any non-radiative decay and can be calculated by either of the following equations:

$$\tau_{(n)} = \frac{1}{k_r} \quad \tau_{(n)} = \frac{\tau_{(\text{obs})}}{\Phi}$$

The natural lifetime can be considered the optimal lifetime however the value can be misleading to the achievable performance of the emissive species as it does not take into account the non-radiative decay caused by solvent interactions, quenchers, photochemical reactions, geometric distortions and vibrations. Therefore all lifetime values report herein are in terms of the observed excited state lifetime unless otherwise stated.

### 1.5.6 Quantum Yield

The quantum yield ( $\Phi$ ) is the ratio of the number of photons emitted by the molecule relative to the number of photons absorbed by the molecule.<sup>33</sup> It is calculated by the following equation:

$$\Phi = \frac{k_r}{k_r + k_{nr}}$$

Quantum yields are measured in absorbance and emission spectroscopy using the following equation:

$$\Phi_x = \Phi_r \left[ \frac{A_r(\lambda_r)}{A_x(\lambda_x)} \right] \left[ \frac{I_r(\lambda_r)}{I_x(\lambda_x)} \right] \left[ \frac{n_x^2}{n_r^2} \right] \left[ \frac{D_x}{D_r} \right]$$

Figure 1.6: Equation for the determination of quantum yield ( $\Phi_x$ ) (Adapted from Eaton, 1988).<sup>36</sup>

where  $A$  is the absorbance at the excitation wavelength ( $\lambda$ ),  $I$  is the intensity of the excitation light at the excitation wavelength ( $\lambda$ ),  $n$  is the refractive index of the solvent,  $D$  is the integrated intensity of the luminescence, and  $\Phi$  is the quantum yield.<sup>36</sup> The subscripts  $r$  and  $x$  refer to the reference and the sample, respectively.

The quantum yield value is a good measure of the efficiency of the radiative decay as the higher the ratio, the more photons emitted per number of photons absorbed. The higher the quantum yield of a compound, the brighter the emission. An ideal candidate for optical applications will have a long lifetime and high quantum yield value.

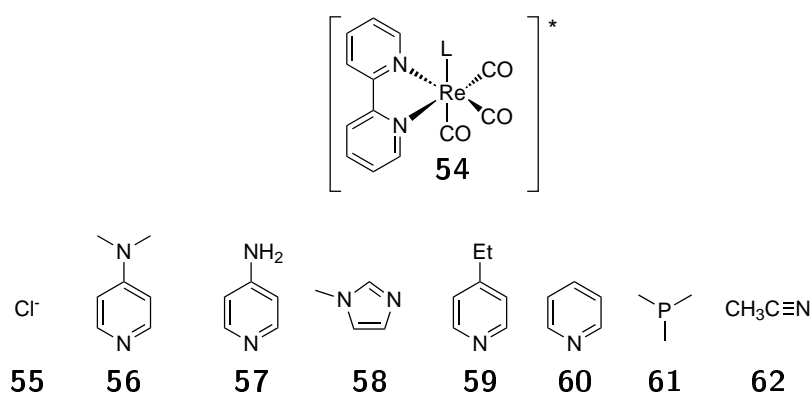
### 1.5.7 Energy Gap Law

The energy gap law states that as the gap between the emissive state and the ground state decreases (demonstrated by **Figure 1.7**),  $k_{nr}$  increases exponentially.<sup>33,37</sup>

Table 1.1: Photophysical properties for a series of *fac*-[Re(bpy)(CO)<sub>3</sub>L] (**54**) complexes that demonstrate the energy gap law. Measurements were performed in deoxygenated dichloromethane solutions at ambient temperature.<sup>38</sup>

Ligand	$\lambda_{em}$ (nm)	$\Phi$	$\tau_{obs}$ (ns)	$k_r$ (s <sup>-1</sup> )	$k_{nr}$ (s <sup>-1</sup> )
Cl <sup>-</sup> ( <b>55</b> )	622	0.005	51	9.79x10 <sup>4</sup>	1.95x10 <sup>7</sup>
4-( <i>N,N</i> -Dimethylamino)-pyridine ( <b>56</b> )	610	0.017	95	1.78x10 <sup>5</sup>	1.03x10 <sup>7</sup>
4-Aminopyridine ( <b>57</b> )	597	0.052	129	4.06x10 <sup>5</sup>	7.34x10 <sup>6</sup>
<i>N</i> -Methylimidazole ( <b>58</b> )	597	0.058	161	3.59x10 <sup>5</sup>	5.85x10 <sup>6</sup>
4-Ethylpyridine ( <b>59</b> )	589	0.18	604	2.96x10 <sup>5</sup>	1.36x10 <sup>6</sup>
Pyridine ( <b>60</b> )	558	0.16	669	2.36x10 <sup>5</sup>	1.26x10 <sup>6</sup>
P(CH <sub>3</sub> ) <sub>3</sub> ( <b>61</b> )	544	0.27	1169	2.32x10 <sup>5</sup>	6.23x10 <sup>5</sup>
CH <sub>3</sub> CN ( <b>62</b> )	536	0.41	1201	3.43x10 <sup>5</sup>	4.90x10 <sup>5</sup>

This trend was confirmed by a series of rhenium(I) complexes reported by Caspar and co-authors shown in **Table 1.1** with the structures shown in **Scheme 1.9**.<sup>39</sup> Caspar confirmed that as the energy gap decreases,  $k_{nr}$  increases.



Scheme 1.9: Rhenium(I)-diimine tricarbonyl complexes investigated by Caspar (1982).<sup>39</sup>

### 1.5.8 Tuning the Emission Properties

The energy gap can be effectively “tuned” by changing the donor strength and conjugation of the ligands. For a MLCT transition, highly conjugated ligands should lower the energy of the LUMO acceptor orbitals and decrease the energy gap. Increasing the  $\sigma$  donor strength of the ligands should increase the electron density around the metal centre and reduce the energy required to populate the lowest excited state which also decreases the energy gap by destabilisation of the 5d orbitals. Reducing the electron density of the metal centre, by replacing anionic ligands with neutral ligands or weaker  $\sigma$  donors, results in a cationic complex which increases the energy required to promote an electron to higher energy orbital and increases the energy gap as demonstrated in **Figure 1.7**.

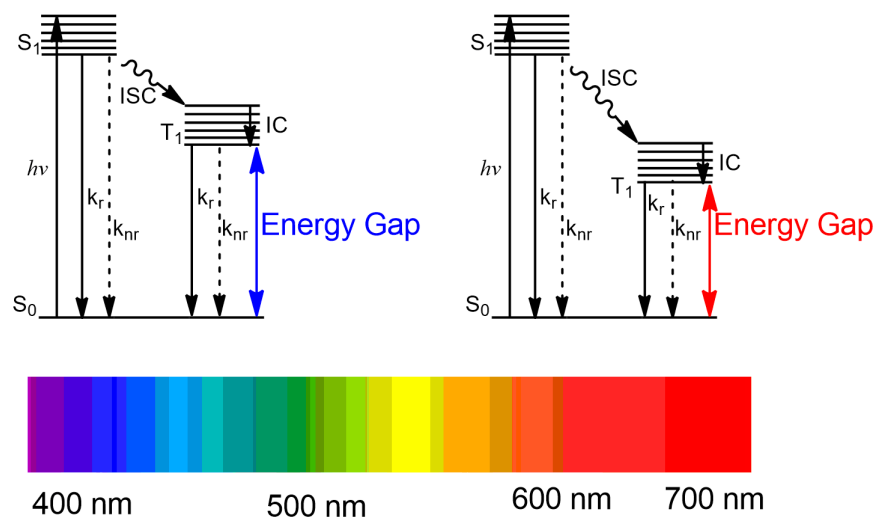


Figure 1.7: Simplified Jablonski diagram demonstrating the energy gap between the lowest excited state and the ground state ( $S_0$ ) and the relationship to the wavelength of the emitted energy.

The ability to tune the emission of metal complexes is useful for tailoring the complexes to specific applications. For example, red emitting compounds are useful for biological imaging agents as red light penetrates deeper into tissue.<sup>40,41</sup> White light is highly coveted by the LED industry and can be produced by combining the emissions profiles of blue, yellow-green and red emitters or by combining a blue emitter with a yellow phosphor.<sup>42</sup> Additionally, triplet state emitters, such as phosphorescent rhenium(I) complexes, are highly desirable as they are more efficient than singlet state emitters such as organic dyes for light emitting devices.<sup>43</sup> Therefore a rhenium(I)-NHC complex with a highly tuneable phosphorescent emission can potentially have several applications in a variety of industries.

### 1.5.9 Rigidochromic Effect

The rigidochromic effect was first observed by Wrighton and Morse in 1974 who found that at lower temperatures the emission spectrum of their rhenium(I) species became more structured and blueshifted compared to the room temperature measurements.<sup>7</sup> The solvent molecules are frozen, therefore they can no longer rearrange their dipoles to stabilise the excited state. Therefore the excited state is destabilised which raises

the energy level of the  $^3\text{MLCT}$ , increases the energy gap and hence results in a hypsochromic shift in the emission maximum as shown in **Figure 1.8a**.<sup>44,45</sup>

At 77 K the solution is frozen, therefore collisions with the solvent are avoided and vibrations within the complex itself are significantly reduced. The solvent cannot re-arrange to stabilise the excited states which results in energy of charge transfer states being affected whilst less polar transition such as  $\pi \rightarrow \pi^*$  transitions remain relatively unaffected.<sup>45</sup> The emission profile of pure charge transfer states should remain quite unstructured upon freezing whilst ligand centred or intraligand  $\pi \rightarrow \pi^*$  transitions should become highly structured.<sup>44</sup> For some systems the energy of the  $^3\text{MLCT}$  is raised higher than the energy of the  $^3\text{IL}$  as shown by **Figure 1.8b**. This means that in frozen matrix the lowest excited state is no longer purely a  $^3\text{MLCT}$  but has predominant  $^3\text{IL}$  character, which results in the increased vibronic nature of the emission profile.<sup>44,45</sup>

The excited state lifetime values are also much longer when recorded in the frozen matrix as there is less quenching of the excited by bimolecular deactivation processes.<sup>34</sup> Non-radiative decay *via* vibrational relaxation is also reduced due to the rigidity of the system which also increases the observed excited state lifetime.

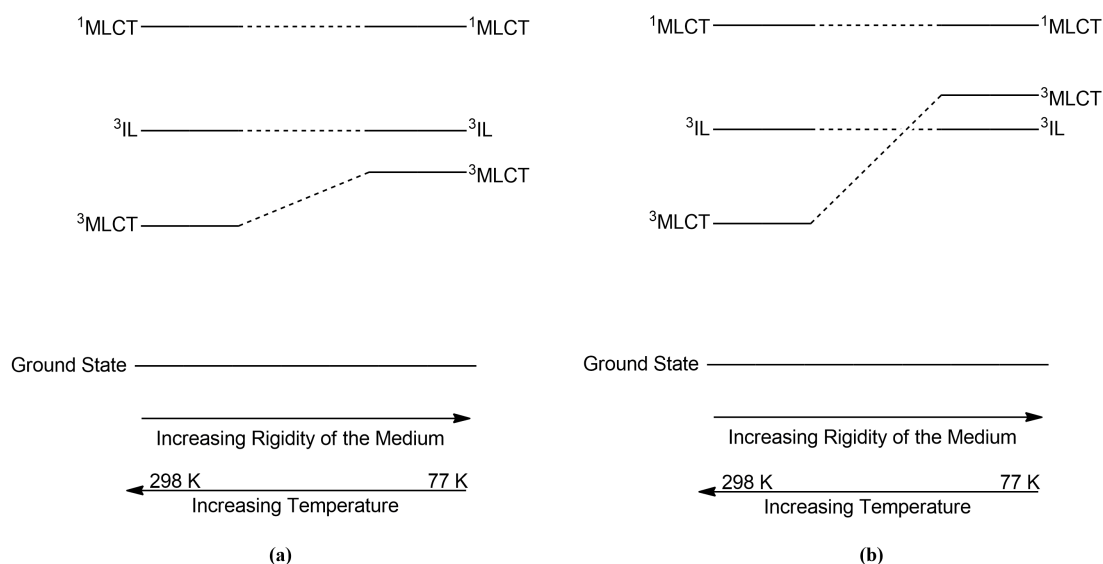


Figure 1.8: The rigidochromic effect on the  $^3\text{MLCT}$  excited state (Adapted from Sacksteder, 1990).<sup>44</sup>

### 1.5.10 Quenchers of Phosphorescence

Molecular oxygen is a quencher of triplet excited states. This arises as the ground state of molecular oxygen is triplet in character and overlaps well with the excited triplet state of an excited transition metal complex as shown in **Figure 1.9**. This sensitivity to oxygen can be used to infer the multiplicity of excited states when the multiplicity is unknown. The excited

state lifetime of a triplet state will notably increase when oxygen is removed from the system whilst a singlet state will be unaffected. The removal of oxygen is accomplished by purging the solution with another gas, typically nitrogen or argon, or undergoing freeze-pump-thaw cycles. The sensitivity of triplet emitters to oxygen quenching is known as oxygen sensitisation.

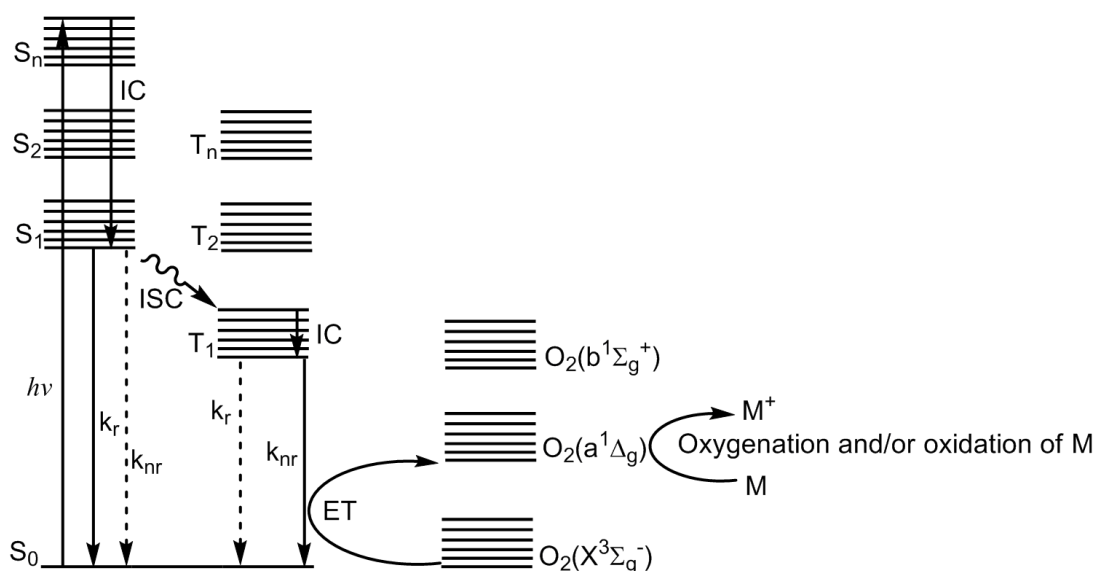
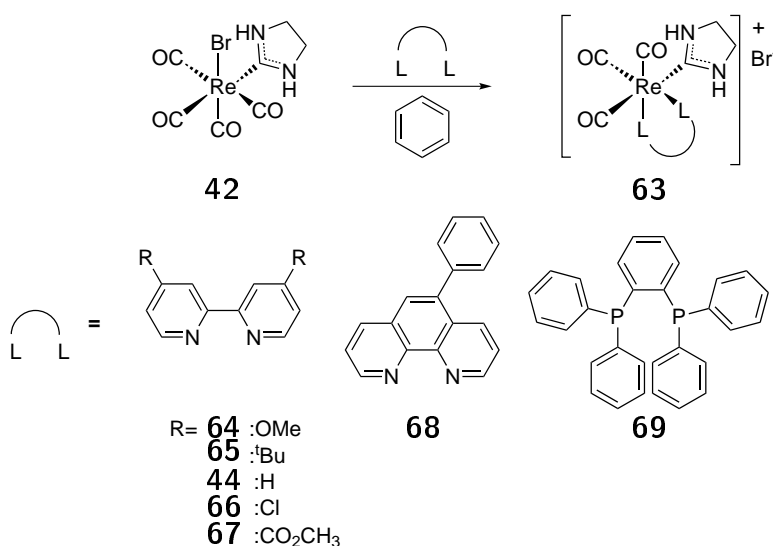


Figure 1.9: Jablonski diagram illustrating energy transfer (ET) from the excited triplet state of a molecule to the ground triplet state of molecular oxygen (Adapted from Ogilby, 2010).<sup>46</sup>

## 1.6 Luminescent Rhenium(I)-NHC Carbonyl Complexes

In 1998 Xue and co-workers realised the luminescent properties of NHC rhenium(I) complexes and their potential for applications in light emitting devices and optical



Scheme 1.10: First Luminescent Rhenium(I)-N-heterocyclic Carbene Complexes (Xue, 1998).<sup>47</sup>

imaging.<sup>47</sup> Interestingly the inaugural report of a luminescent carbene complex, being a platinum(II) macrocycle bearing dicarbene ligands, had occurred merely months beforehand.<sup>48</sup> Xue et al. synthesised the neutral bromo tetracarbonyl rhenium(I) complex (**42**) with an imidazoline based N-heterocyclic ligand using the aminophosphinimine cyclisation method reported by Liu et al.<sup>29</sup> Various diimine and diphosphine ligands (**Scheme 1.10**) were then coordinated by refluxing **42** in benzene affording the cationic rhenium(I)-NHC tricarbonyl (**63**) species.

The photophysical data for Xue's compounds is summarised in **Table 1.2**. All the compounds were emissive at room temperature bar the complex involving the diphosphine ligand (**70**). The complexes exhibited broad emission bands at room temperature in both dichloromethane and acetonitrile solutions. The emission maxima exhibited a hypsochromic shift upon increasing the solvent polarity indicating a polar ground state and non-polar excited state.

The room temperature emission maxima for the bipyridine compounds (**64-67**) were centred around 565 nm and blueshifted as the R substituent on the bipyridine ligand was made more electron donating (**64** and **65**) and redshifted as the R group became more electron withdrawing (**67**).

Whilst molecular orbital calculations showed minimal contribution (6.5%) from the  $p_z$  orbital of the carbene to the LUMO, the lowest excited state was still ascribed to a

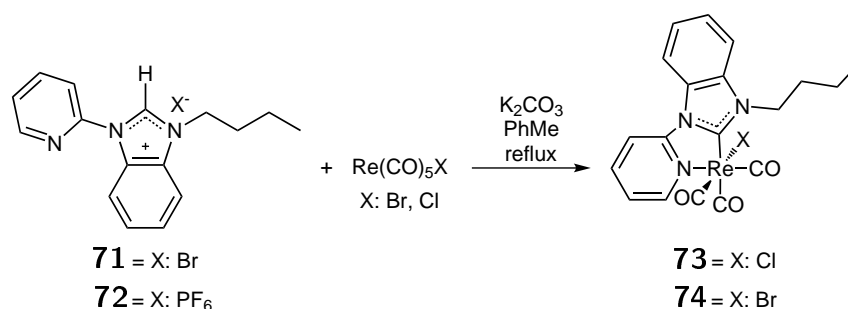
Table 1.2: Room temperature photophysical data for the first reported luminescent Rhenium(I)-N-Heterocyclic Carbene Complexes (Xue, 1998).<sup>47</sup>

Compound	CH <sub>2</sub> Cl <sub>2</sub>			CH <sub>3</sub> CN		
	$\lambda_{max}$ nm	$\phi_{em}$	$\tau$ ns	$\lambda_{max}$ nm	$\phi_{em}$	$\tau$ ns
<b>64</b>	558	0.04	194	570	0.012	64
<b>65</b>	553	0.088	330	565	0.038	150
<b>44</b>	565	0.068	230	577	0.021	97
<b>66</b>	603	0.0075	45	615	0.002	20
<b>67</b>	620	0.015	97	635	0.0039	40
<b>68</b>	555	0.3	2520	565	0.11	932
<b>69</b>	Not luminescent					

Re $\rightarrow\pi^*$ (diimine) with partial Re $\rightarrow\sigma^*$ (carbene) character. The room temperature emission was assigned to decay from an triplet metal to ligand charge transfer (<sup>3</sup>MLCT) state.

At 77 K the emission of **68** became more structured and characteristic of emission from an intraligand (IL) state. Despite not being emissive at room temperature, **69** was emissive at 77 K with the emission also being characteristic of an IL state.

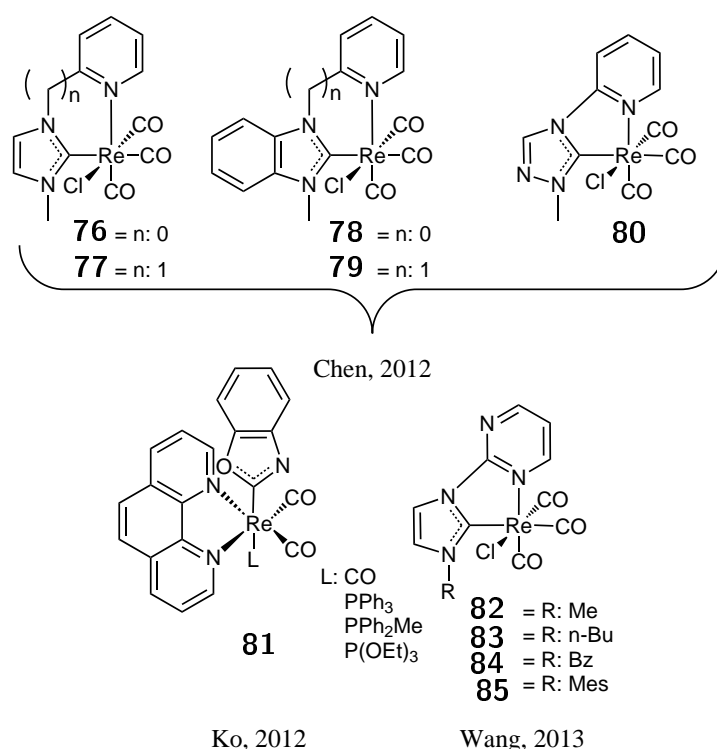
The first report of luminescent rhenium(I)-N-heterocyclic carbene complex where the carbene ligand acted as the major  $\pi^*$  acceptor in the lowest excited state was by Massi and co-workers in 2011, who reported the synthesis of two 1-(2-pyridyl)-benzimidazol-2-ylidene rhenium(I) tricarbonyl complexes as shown in **Scheme 1.11**.<sup>49</sup>



Scheme 1.11: Second Reported Luminescent Rhenium(I)-N-heterocyclic Carbene Complexes (Massi, 2011).<sup>49</sup>

It was found that both the bromo and chloro analogues of **75** were luminescent in acetonitrile and dichloromethane solutions and said emission was characterised as being largely <sup>3</sup>MLCT in character with partial <sup>3</sup>LLCT contribution. Time-Dependent Density Functional Theory (TDDFT) calculations concluded that the largest contributor to the lower energy absorption was the HOMO-1 $\rightarrow$ LUMO transition for both **74** (95%)

and **73** (94%). The frontier orbital distribution of the LUMO for **73** and **74** showed that the orbital density was localised on the nitrogen and carbon atoms of the benzimidazol-2-ylidene NHC ligand as well as all the atoms of the adjoining pyridyl ring. The orbital distribution of the HOMO-1 of **73** and **74** was largely localised on the rhenium metal centre and the halogen ligand. Therefore the distribution of the orbitals involved in the HOMO-1 → LUMO transition are in accordance with an <sup>1</sup>MLLCT absorption from where <sup>3</sup>MLLCT decay can occur. Since 2011 there have been several more reports of luminescent rhenium(I)-NHC tricarbonyl compounds as shown in **Scheme 1.12**.<sup>30,50,51</sup>



Scheme 1.12: Luminescent Rhenium(I)-N-heterocyclic Carbene Tricarbonyl Complexes.<sup>30,50,51</sup>

## 1.7 Aims

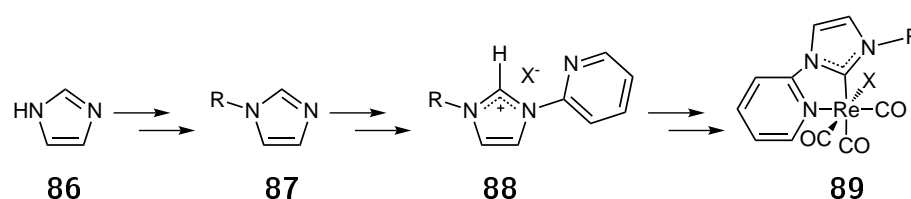
This research will endeavour to expand upon the current knowledge of the photophysical and photochemical properties of rhenium(I) when paired with N-heterocyclic carbene ligands. Specific focus will be placed on developing and characterising new ligand systems based on the pyridyl type NHC ligands. The robustness of these types rhenium(I) NHC complexes will be assessed with the aim of utilising these complexes for light emitting purposes.

## Chapter 2

# Synthesis and Characterisation of NHC Ligands and their Re Complexes

### 2.1 Overview

The synthetic pathways utilised as well as the full characterisation of all novel compounds will be discussed herein. Imidazole (**86**) is initially used to synthesise the building blocks of the ligands, the N-substituted imidazoles (**87**). This is followed by the synthesis of the ligand precursors, the azolium salts (**88**), and finally the synthesis of the target rhenium(I)-NHC tricarbonyl complexes (**89**).



Scheme 2.1: Overview of general synthesis of rhenium(I)-NHC tricarbonyl complexes.

This research focuses on four modification sites; the N-heterocyclic carbene of the bidentate ligand (**Figure 2.1** in green), the N-donor ring on the N3 position of the NHC (**Figure 2.1** in blue), the R substituent on the N1 position of the NHC (**Figure 2.1** in orange) and the ancillary ligand “X” (**Figure 2.1**, in red).

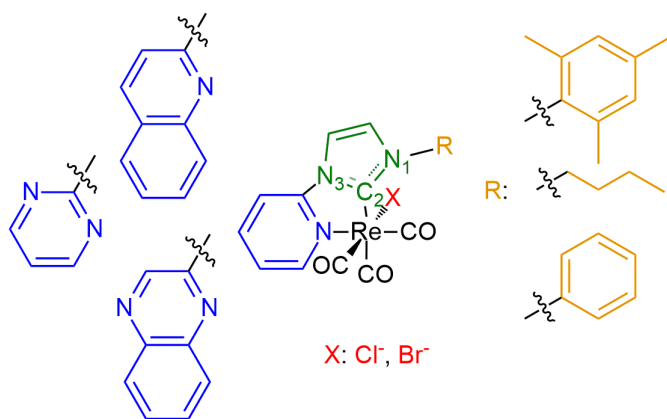
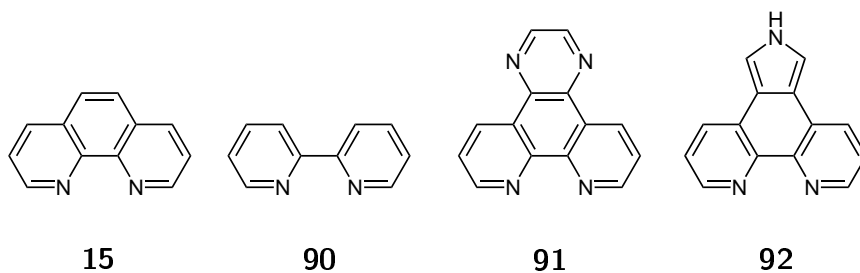


Figure 2.1: The basic tricarbonyl[1-(2-pyridyl)-imidazol-2-ylidene]rhenium(I) motif depicting the various functionalisation sites.

## 2.2 Rationale

There are several advantages of using the N-heterocyclic carbene (NHC) framework as opposed to the traditional diimine/polypyridine ligands such as those shown in **Scheme 2.2**. The NHC ligand motif, (**Figure 2.1**), investigated in this research has three different sites which can be independently modified. Not only can these sites be used to tune the output of the emission, which will be more thoroughly discussed in **Chapter 3**, they can also be modified to increase solubility and improve photostability for various applications.<sup>8,52,53</sup>

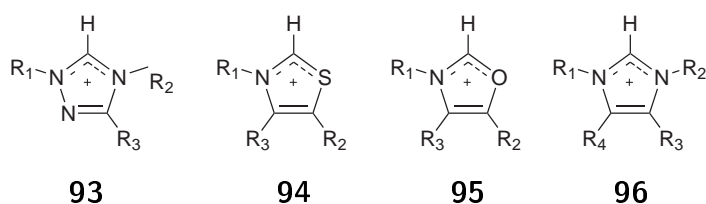


Scheme 2.2: Polypyridine (diimine) ligands typically coordinated to rhenium(I).

## 2.3 Synthesis of N-Substituted Imidazoles

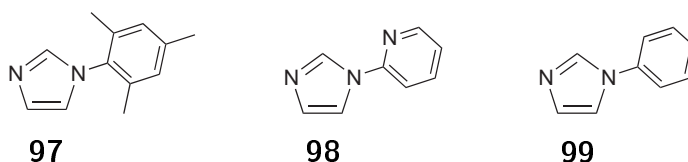
### 2.3.1 Synthetic Strategy

N-Heterocyclic carbenes are commonly formed by the deprotonation of the C2 carbon of 1,3-diheteroatomic azolium salts such as triazoles (**93**), thiazoles (**94**), oxazoles (**95**) and imidazoles (**96**).



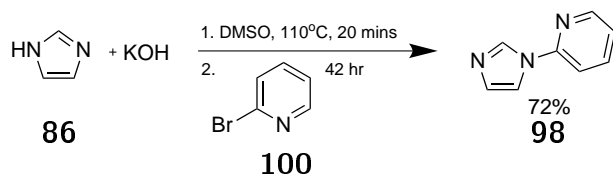
Scheme 2.3: Common azolium salt based precursors for carbene ligand formation.

For this study, imidazol-ylidene type carbenes were required, therefore N-substituted imidazoles needed to be prepared as building blocks for the NHC ligands. Three different N-substituted imidazoles had to be synthesised; 1-mesitylimidazole (**97**), 1-(2-pyridyl)imidazole (**98**) and 1-phenylimidazole (**99**).



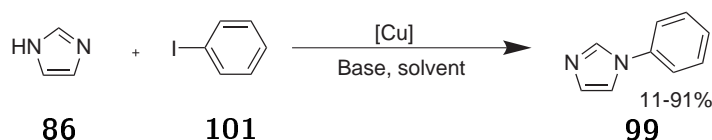
Scheme 2.4: Target N-substituted imidazoles.

1-Mesitylimidazole (**97**) was previously synthesised in house in large quantities using the method outlined by Gardiner and co-workers and did not need to be re-synthesised for this research project.<sup>54</sup> 1-(2-Pyridyl)imidazole (**98**) was prepared *via* a nucleophilic aromatic substitution between 2-bromopyridine (**100**) and imidazole (**86**) in good yield utilising a procedure outline by Yuan and co-workers as shown in **Scheme 2.5**.<sup>55</sup>



Scheme 2.5: Synthesis of 1-(2-pyridyl)imidazole.

1-Phenylimidazole (**99**) was synthesised *via* a copper catalysed Ullmann coupling reaction of iodobenzene (**101**) with imidazole (**86**). Ullmann coupling reactions can be used to couple two aryl groups or an aryl group and a nucleophile.<sup>56</sup> As benzene rings are more reactive towards electrophilic aromatic substitution rather than nucleophilic aromatic substitution, a copper catalyst is needed to facilitate the reaction.



Scheme 2.6: General scheme for the synthesis of 1-phenylimidazole.

There are several proposed mechanisms for this reaction however the catalytically active species is widely accepted as being Cu(I).<sup>56</sup> Some mechanisms propose the existence of a Cu(III) intermediate, however for this work it was assumed that the active catalyst was Cu(I) acting through either a  $\sigma$ -bond intermediate or a  $\pi$ -bond intermediate.<sup>56</sup>

The Ullmann coupling reaction did not prove to be readily re-producible. For the initial synthesis a set of conditions outlined by Xu and co-workers using a copper(II) acetate catalyst were trialled and produced the expected product in high yield as shown in **Table 2.1**.<sup>57</sup>

The second time the copper(II) acetate catalyst was utilised the peaks of the aromatic hydrogens in the <sup>1</sup>H NMR spectrum were very broad as depicted by the top trace in **Figure 2.2** which was indicative of residual copper coordinating with the 1-phenylimidazole. The presence of copper was confirmed by the appearance of blue crystals in the oily product after being stored in a sample vial for 24 hours.

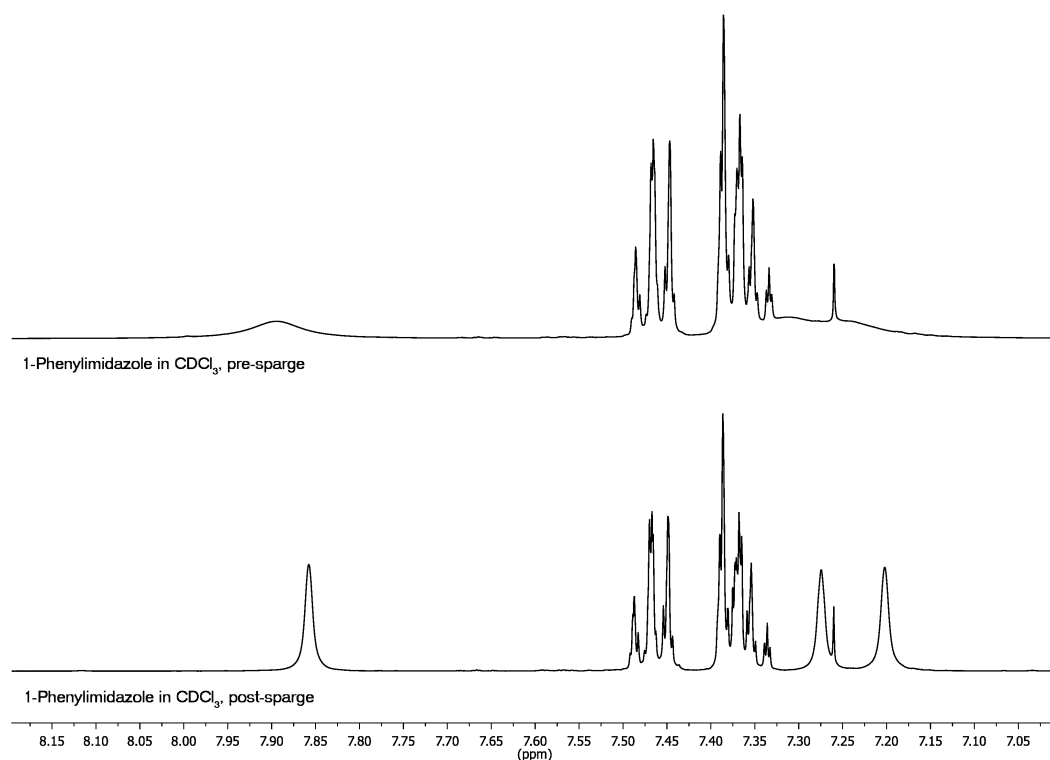


Figure 2.2:  $^1\text{H}$  NMR spectra of 1-phenylimidazole in  $\text{CDCl}_3$  before and after sparging with concentrated  $\text{HCl}$ .

In an attempt to remove the residual copper species, the oily product was sparged with air in the presence of concentrated hydrochloric acid to oxidise the copper(I) to copper (II) and provide a chloride source that the copper(II) should preferentially bind to. The solution was then neutralised with aqueous sodium hydroxide and re-extracted with ethyl acetate. This improved the appearance of the  $^1\text{H}$  NMR spectrum as shown by the bottom trace in **Figure 2.2** and the 1-phenylimidazole was subsequently used to synthesise batches of the  $\text{PyImPhH.Cl}$  (**5**) and  $\text{PyImPhH.Br}$  (**6**) azolium salts.

Unfortunately, it later became apparent that the second batch of 1-phenylimidazole had become contaminated with chloride after crystal structures using the  $\text{PyImPhH.Br}$  precursor ligand were obtained with mixed chloro/bromo halide even though no chloride source was present in the crystallisation mixture. The chloride source was traced back to the oxidative step and the chloride contaminated 1-phenylimidazole and  $\text{PyImPhH.Br}$  (**6**) were subsequently discarded.

A procedure outlined by Huang and co-workers using copper(I) iodide as the catalyst was then investigated as an alternative as it was inferred that the copper(I) iodide should

be a more effective catalyst as it was already in the optimum oxidation state.<sup>58</sup> The oily product was again sparged with air to oxidise any Cu(I) but this time 85% phosphoric acid in water (5 mL) was utilised to avoid chloride contamination.

Table 2.1: Comparative yields of 1-phenylimidazole.

Copper Catalyst	Base	Solvent	Reaction Time	Yield
Cu(OAc) <sub>2</sub> <sup>57</sup>	CsCO <sub>3</sub>	DMF	3 d	91%
Cu(OAc) <sub>2</sub> * <sup>57</sup>	CsCO <sub>3</sub>	DMF	3 d	55%
CuI <sup>58</sup>	KOH	DMSO	24 hr	72%
Cu <sub>2</sub> O <sup>58</sup>	KOH	DMSO	24 hr	11%

\*Contaminated with chloride

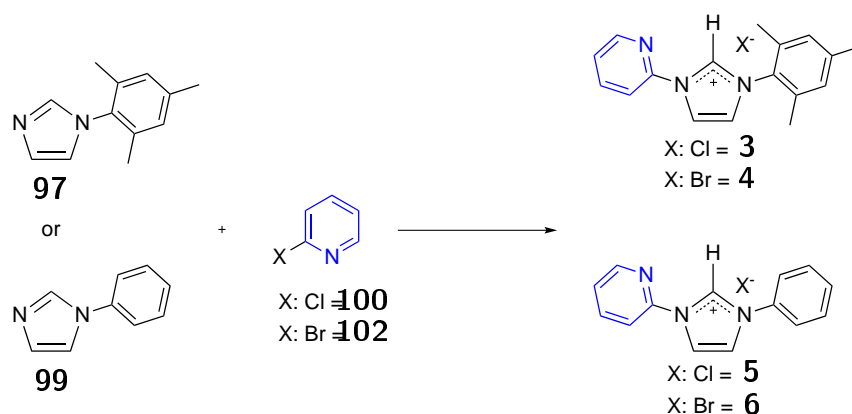
Copper(I) oxide was then trialled as the copper catalyst as Huang and co-workers reported it was easily recycled for further reactions.<sup>58</sup> This resulted in a decreased yield which was again attributed to copper strongly coordinating with the 1-phenylimidazole. Overall the original method using copper(II) acetate was found to be preferable as not only is copper(II) acetate cheaper than copper(I) oxide, according to the current Sigma Aldrich catalogue, and less harmful to the environment than copper(I) iodide but it also produced better yields in general.

## 2.4 Synthesis of N-Heterocyclic Carbene Ligand Precursors

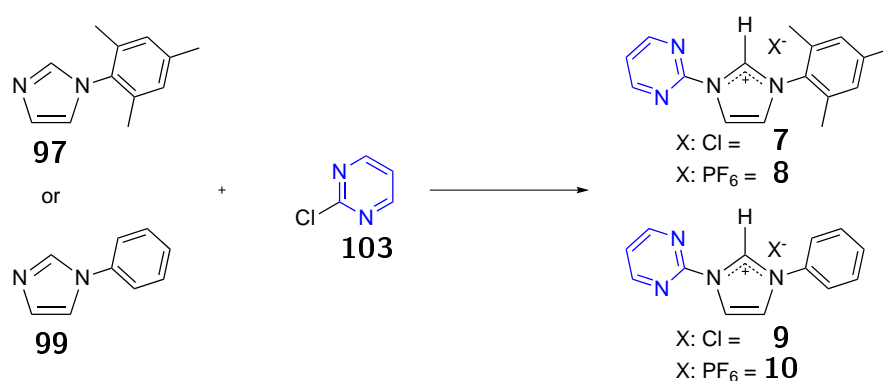
### 2.4.1 Synthetic Strategy

As previously mentioned in **Section 1.3**, N-heterocyclic carbenes are highly reactive in their free carbene state therefore they are generally synthesised and stored as stable azolium salt precursors which can be subsequently deprotonated to form the free carbene when required.

The next step after forming the N-substituted imidazole was to functionalise compounds **97**, **98** and **99** at the N3 position to form the desired azolium salts. 1-Phenylimidazole



Scheme 2.7: Generic scheme for the synthesis of the pyridyl series of azolium salt NHC precursors.

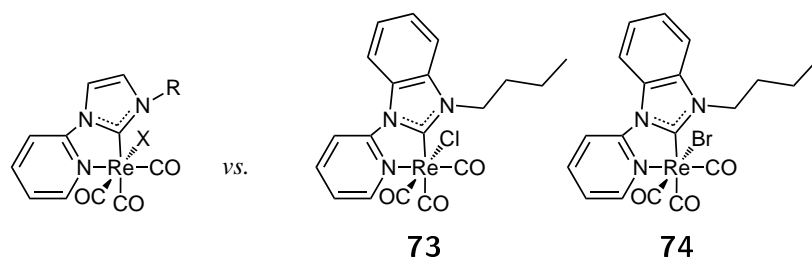


Scheme 2.8: Generic scheme for the synthesis of the pyrimidyl series of azolium salt NHC precursors. As bromide derivatives were used to synthesise all ligands, a salt metathesis with potassium hexafluorophosphate was performed to remove the bromide anion and avoid halide contamination when synthesising the corresponding chloro rhenium complexes.

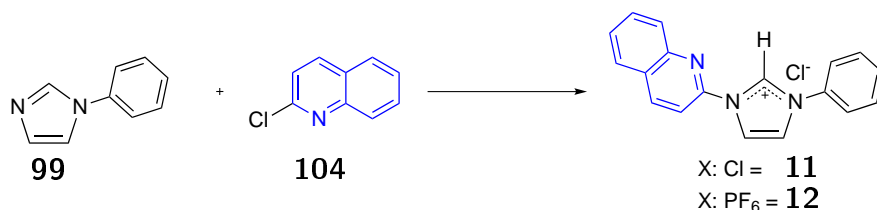
(99) and 1-mesitylimidazole (97) needed to be substituted with a heterocyclic ring on the N3 position to form the required bidentate N<sup>+</sup>C type ligand. The first types of heterocycle utilised in this research were the 2-halopyridines in the form of 2-chloropyridine (102) and 2-bromopyridine (100) to form the pyridyl azolium salt series as shown in **Scheme 2.7**.

The pyridyl azolium salt series would be used as a direct comparison to the rhenium(I)-1-(2-pyridyl)benzimidazol-2-ylidene compounds (73 and 74) previously investigated (**Scheme 2.9**).<sup>49</sup> It will be assessed in **Chapter 3** whether reducing the conjugation of the NHC ligand system by the removal of the fused benzene ring on the backbone of the imidazole affects the properties of the resulting rhenium(I)-NHC tricarbonyl complex.<sup>49</sup>

To assess the impact of increasing the electron deficiency of the N-donor ring, 2-

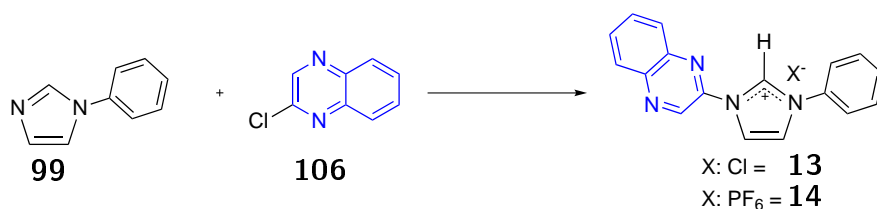


Scheme 2.9: 1-(2-pyridyl)imidazol-2-ylidene series vs. 1-(2-pyridyl)benzimidazol-2-ylidene series.



Scheme 2.10: Generic scheme for the synthesis of the quinoyl series of azolium salt NHC precursors.

chloropyrimidine (**103**) was used to form the pyrimidyl azolium salt series as shown in **Scheme 2.8**. The effect of increasing the conjugation of the N-donor ring would then be investigated by reacting 2-chloroquinoline (**104**) with 1-phenylimidazole (**105**) to form the quinoyl series as shown in **Scheme 2.10**.

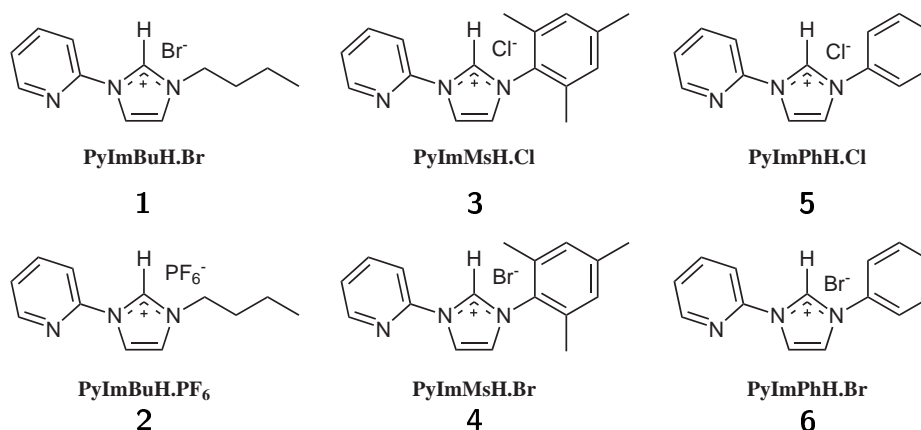


Scheme 2.11: Generic scheme for the synthesis of the quinoxyl series of azolium salt NHC precursors.

Finally, to evaluate the impact of increasing the conjugation and increasing the electron deficiency of the N-donor ring, 2-chloroquinoxaline (**106**) would be reacted with 1-phenylimidazole (**99**) to form the quinoxyl series as shown in **Scheme 2.11**.

The synthesis of pyridyl functionalised azolium salts (**Scheme 2.12**) is well established and typically occurs *via* a nucleophilic aromatic substitution (NAS) between a 2-halopyridine and a N1 substituted imidazole. Synthesis of the literature compounds PyImMsH.Br (**4**) and PyImMsH.Cl (**3**) proceeded *via* a NAS between the appropriate 2-halopyridine and 1-mesitylimidazole in a pressure tube as shown in **Scheme 2.13**.<sup>59,60</sup> This method was utilised for the synthesis of all of the studied halide azolium

salts except for PyImBuH.Br (**1**).

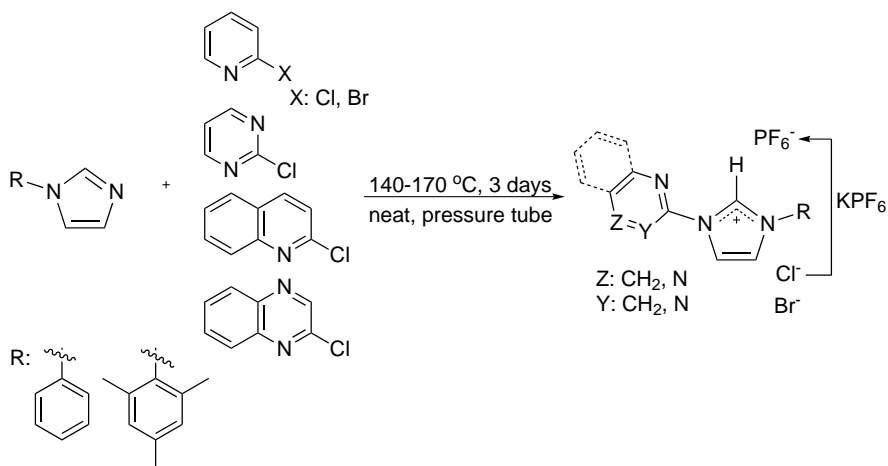


Scheme 2.12: The pyridyl series of azolium salts.

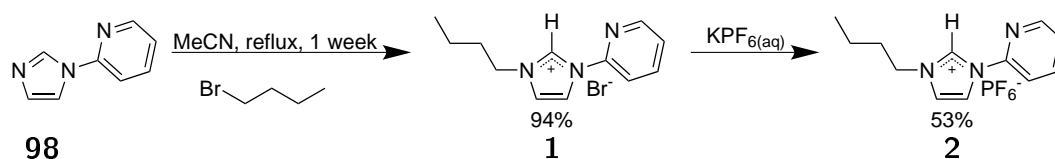
Whilst in the literature PyImBuH.Br (**1**) can be synthesised *via* a NAS reaction between 2-bromopyridine and 1-butylimidazole, as first outlined by Albrecht and co-workers, this research utilised a different approach.<sup>61</sup> 1-(2-Pyridyl)imidazole (**98**) was first synthesised and then reacted with 1-bromobutane in acetonitrile in a S<sub>N</sub>2 substitution to form the desired azolium salt as shown in **Scheme 2.17**.

The chloro group of 1-chlorobutane was previously found to be a poor leaving group to undergo the same reaction to form the chloro derivative. Therefore, a salt metathesis with the bromo derivative, **1**, and potassium hexafluorophosphate was performed to synthesise PyImBuH.PF<sub>6</sub> (**2**, **Scheme 2.12**). This resulted in an azolium salt with a poorly coordinating anion that could be used to synthesise the required rhenium compound (**1Cl**) without halide contamination.<sup>62</sup>

The pyrimidyl azolium salts (**Scheme 2.15**) were also synthesised *via* the same method outlined in **Scheme 2.13**. The chloro azolium salts then underwent a salt metathesis with potassium hexafluorophosphate to make the non-chloro derivative for the following reaction with [Re(CO)<sub>5</sub>Br]. The chloro pyrimidyl azolium salts, **7** and **9**, were found to be extremely hygroscopic and very difficult to isolate as they would rapidly absorb water and liquefy making isolation *via* vacuum filtration difficult.



Scheme 2.13: Synthetic pathway for the synthesis of the azolium salt NHC precursors.

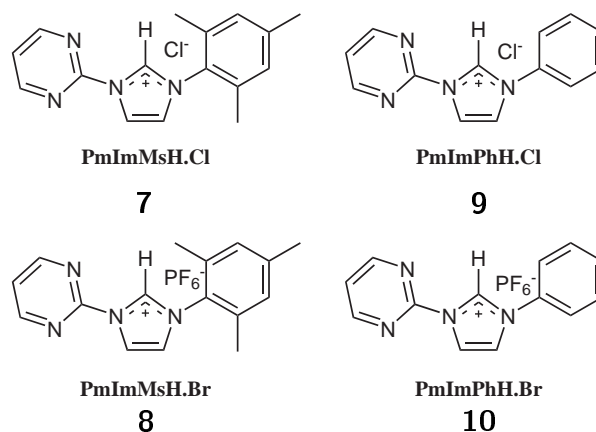


Scheme 2.14: Synthesis of 1-butyl-3-(2-pyridyl)imidazolium bromide.

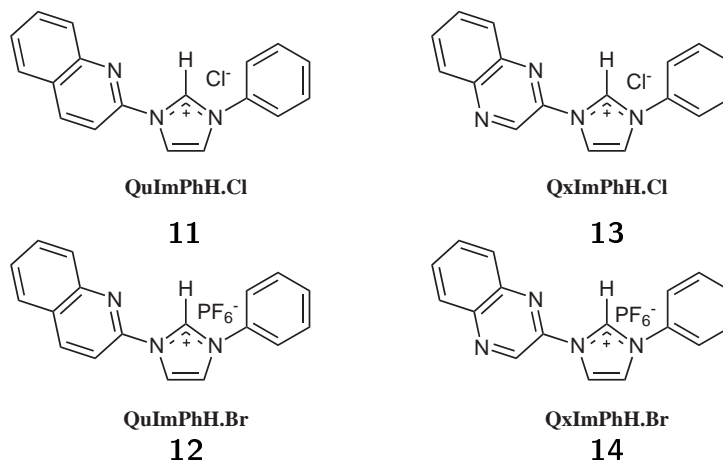
Previous work by Strassner and co-workers found that sonicating the azolium salt in tetrahydrofuran instead of diethyl ether produced a drier, more manageable product.<sup>63</sup> This technique was therefore adopted for the purification of all azolium salts. It was also noted that upon anion exchange from chloride to hexafluorophosphate, the azolium salts became less hygroscopic hence easier to work with.

As per the pyrimidyl azolium salts, only the chloride analogue of the quinoline and quinoxaline azolium salts (**Scheme 2.16**) were synthesised and then underwent salt metathesis with  $\text{KPF}_6$ .

The elemental analysis of all the fourteen azolium salts, bar PmImPhH. $\text{PF}_6$  (**10**), matched well with some reasonable fitting for water molecules required due to the hygroscopic nature of the salts. An elementally pure sample of PmImPhH. $\text{PF}_6$  (**10**) was difficult to obtain. Further experimental details pertaining to the synthesis and characterisation of the azolium salts is detailed in **Experimental Sections 8.3.1-8.3.14**.



Scheme 2.15: The pyrimidyl series of azolium salts.



Scheme 2.16: The quinoyl and quinoxyl series of azolium salts.

The successful synthesis of the azolium salts was implied by the appearance of the downfield peak in the  $^1\text{H}$  NMR spectrum attributed to the H2 proton of the NCHN “carbene” carbon as shown in **Figure 2.3**.

It was noted in the  $^1\text{H}$  NMR of the compounds with mesityl substituents (**3**, **4**, **7** and **8**) that there appeared to be free rotation about the N1-C bond as there were two singlets visible in the  $^1\text{H}$  NMR spectrum at 2.35 and 2.11 ppm integrating for 3 and 6 protons respectively as depicted in **Figure 2.4**. As there are two singlets, opposed to three, this indicates that the two ortho methyl groups (**Figure 2.4**, depicted in blue) are equivalent due to free rotation of the ring. If the mesityl moiety was restricted in rotation then three singlets should be observed in that region.

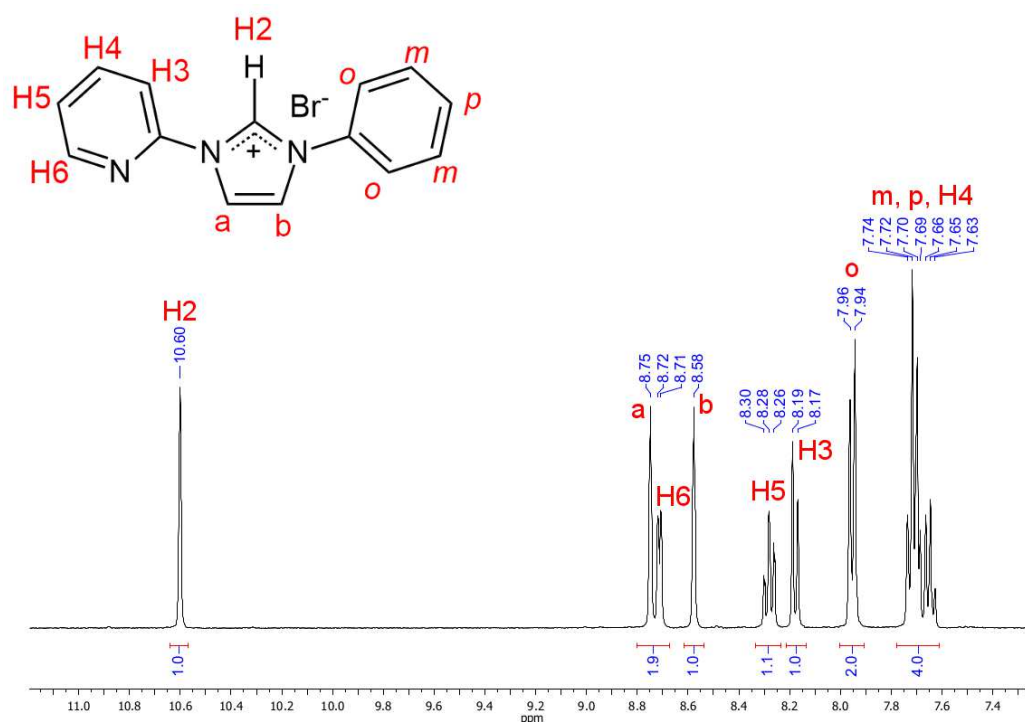


Figure 2.3: <sup>1</sup>H NMR of PyImPhH.Br (**6**) in DMSO-d<sub>6</sub> with proton assignments.

In general, it was found that alternating the anion between bromide, chloride and hexafluorophosphate had a slight observable effect on the proton NMR of the azolium salt. As shown in **Figure 2.5** the singlet of the H2 proton of the chloride analogue, QuImPhH.Cl (**11**) is shifted slightly downfield to that of the PF<sub>6</sub><sup>-</sup> analogue, QuImPhH.PF<sub>6</sub> (**12**). The slight downfield shift exhibited by the H2 proton in the bottom trace is attributed to the strong hydrogen bond interaction between the H2 proton and the Cl<sup>-</sup> anion which known to occur for halide azolium salts.<sup>64</sup>

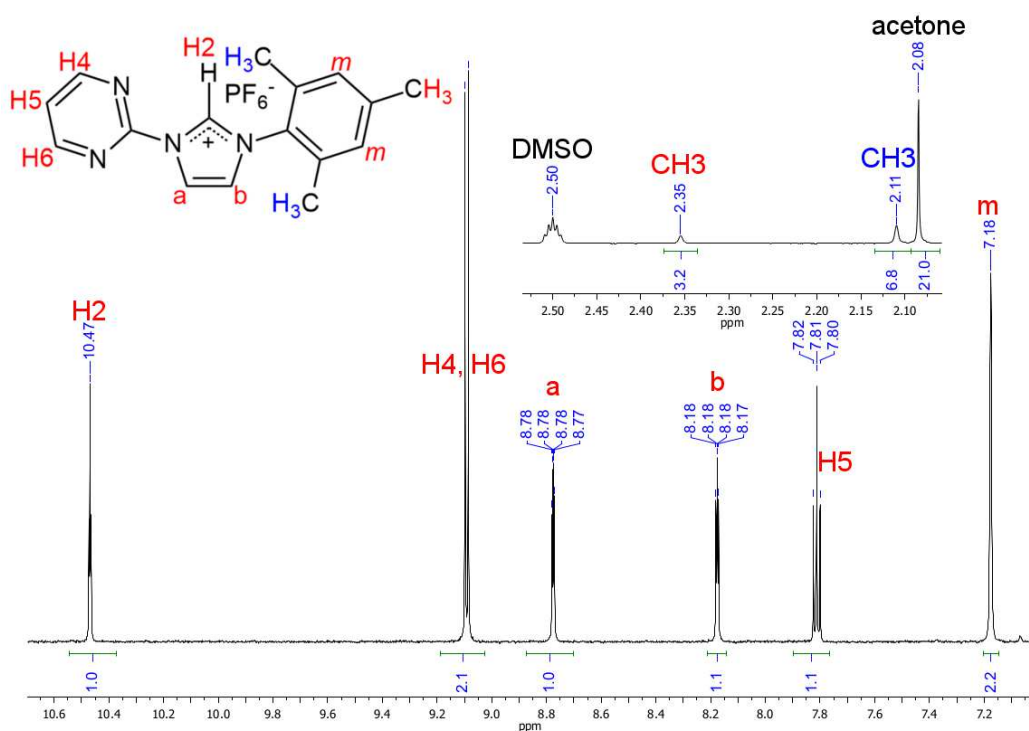


Figure 2.4:  $^1\text{H}$  NMR spectrum of PyImMsH.Br (**4**) in DMSO- $d_6$  demonstrating free rotation about the N1-C bond.

The hexafluorophosphate anion is known as a poor acceptor of hydrogen bonds therefore the resonance for the H2 proton of QuImPhH.PF<sub>6</sub> is slightly upfield to that of QuImPhH.Cl.<sup>65</sup> The bromide anion is also considered a strong hydrogen bond acceptor therefore no discernible difference was observed between the H2 proton signal shifts between the bromo and chloro azolium salt analogues.<sup>64</sup>

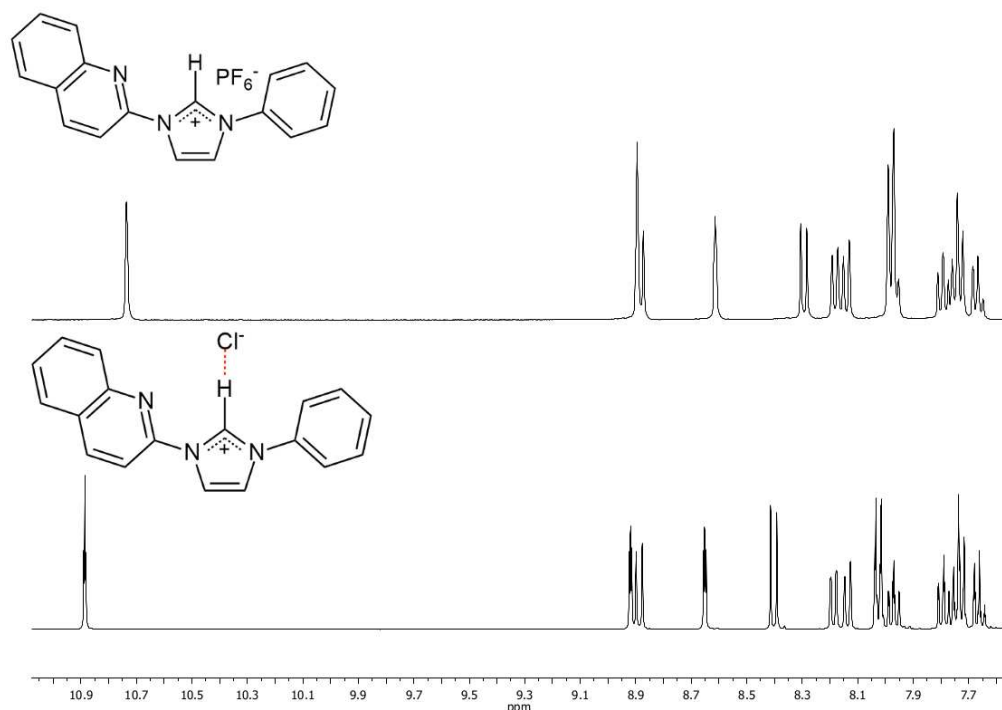


Figure 2.5:  $^1\text{H}$  NMR of the chloride salt (bottom trace) QuImPhH.Cl (**11**) vs. the potassium hexafluorophosphate salt QuImPhH.PF<sub>6</sub> (**12**) (top trace).

## 2.5 Synthesis of Rhenium(I)-NHC Tricarbonyl Complexes

### 2.5.1 Target Compounds

This research was focused on four series of rhenium(I)-NHC tricarbonyl complexes shown in **Figures 2.6-2.8**. The initial synthetic targets were the six compounds of the rhenium(I)-1-(2-pyridyl)imidazol-2-ylidene series (**Figure 2.6**). Once this series was complete the impact of modifying the “R” substituent between alkyl, aromatic and bulky aromatic and interchanging the ancillary ligand between the chloro to bromo could be fully assessed.

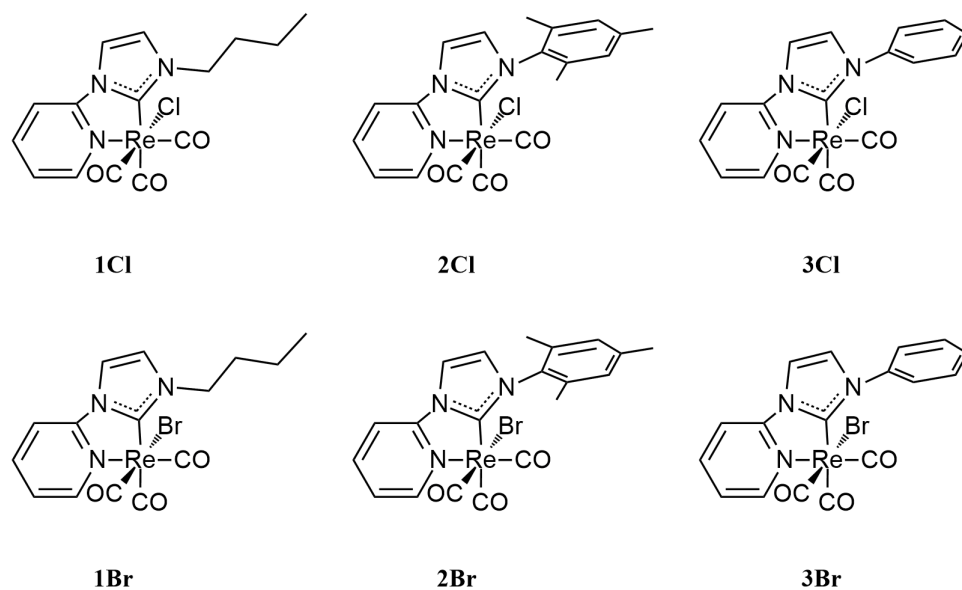


Figure 2.6: Target compounds of the rhenium(I)-1-(2-pyridyl)imidazol-2-ylidene series.

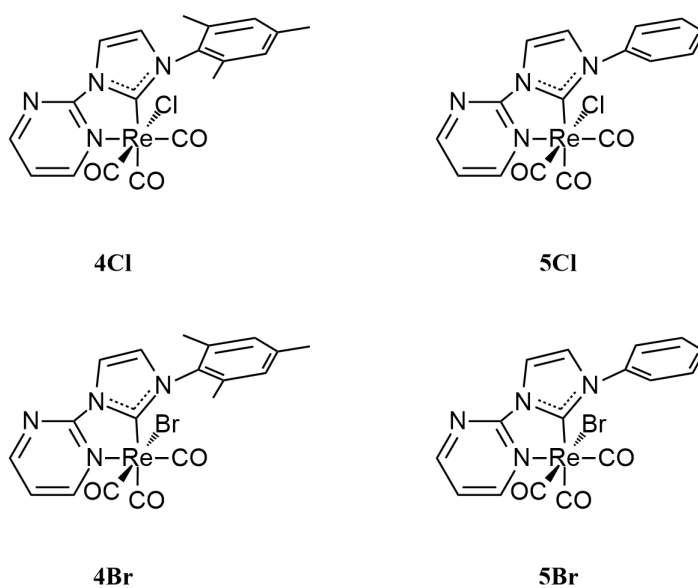


Figure 2.7: Target compounds of the rhenium(I)-1-(2-pyrimidyl)imidazol-2-ylidene series.

The next synthetic target was to create a second series of compounds based on a pyrimidyl N-donor ring being the 1-(2-pyrimidyl)imidazol-2-ylidene series as depicted in **Figure 2.7** and series based on 1-(2-quinoyl)imidazol-2-ylidene (**Figure 2.8**) to assess

the effect of increasing the conjugation of the N-donor heterocycle. The final synthetic target was the 1-(2-quinoyl)imidazol-2-ylidene series where both the effect of increased electron deficiency and increased conjugation could be assessed. For these two series the R substituent would consistently be the phenyl ring however the ancillary ligand would continue to be varied between the chloro and the bromo. Once the synthesis of these four series was complete, then the impact of making modulations to the NHC ligand structure could be assessed and structure-activity relationships could be developed.

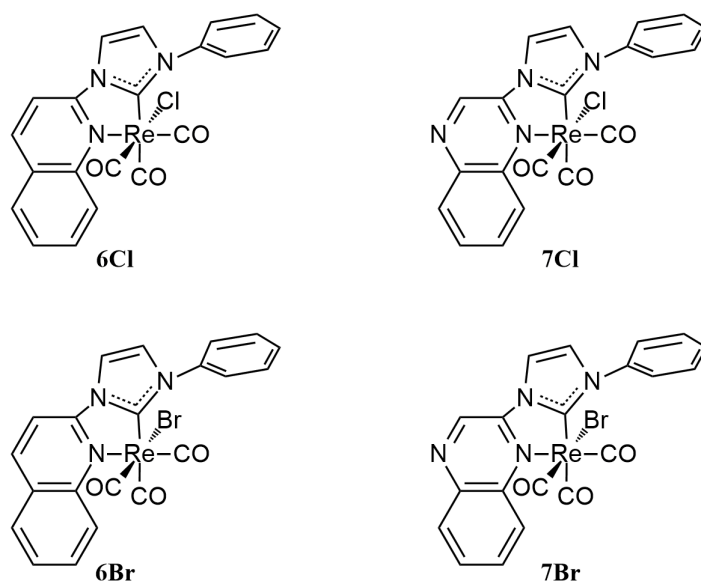


Figure 2.8: Target compounds of the rhenium(I)-1-(2-quinoyl)imidazol-2-ylidene and rhenium(I)-1-(2-quinoxyl)imidazol-2-ylidene series.

## 2.5.2 Synthetic Strategy

In literature there are three major preparative routes utilised to synthesise NHC transition metal complexes as depicted in **Figures 2.9, 2.10** and **2.11**. The first is the free carbene method which involves first deprotonating the NHC precursor, the azolium salt, with a strong base to form the free carbene (**Figure 2.9**).

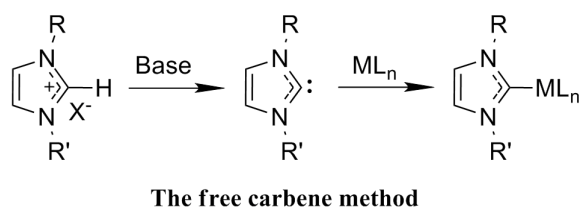


Figure 2.9: The generic scheme of the free carbene method for the synthesis of metal-NHC complexes.

The free carbene is then isolated *via* filtration and a solution of the metal source is added. This method is highly water and air sensitive as the free carbene is prone to decomposition in the presence of either and must be performed under strict anhydrous conditions using Schlenk techniques. This method is not suitable for hygroscopic NHC precursor azolium salts as they are extremely difficult to dry effectively.

The second and more robust method is the *in situ* method which involves deprotonating the NHC precursor with a weak base to generate the free carbene in the presence of the metal source allowing for immediate coordination as shown in **Figure 2.10**. This method is more resistant to water contamination however degassing *via* the freeze pump thaw method is recommended to remove any oxygen present.

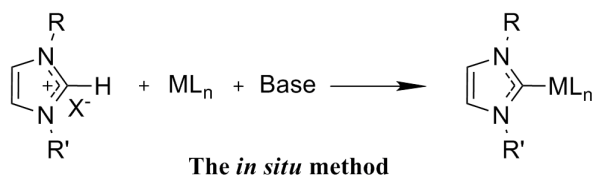
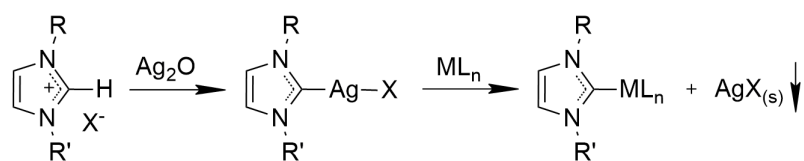


Figure 2.10: The generic scheme of the *in situ* method for the synthesis of metal-NHC complexes.

The third method is the silver transfer method developed by Wang and Lin in 1998 as a facile way to synthesise gold(I) and palladium(II) NHC complexes from a silver precursor.<sup>66</sup> This method involves reacting the azolium salt with a basic silver source, typically silver(I) oxide, to form a silver(I)-NHC complex as depicted in **Figure 2.11**. The silver(I)-NHC complex is then further reacted with the desired metal source bound

to any ligand. The NHC ligand should preferentially coordinate to the metal source as the silver precipitates as an insoluble silver halide salt.



**The silver transfer method**

Figure 2.11: The generic scheme of the silver transfer method for the synthesis of metal-NHC complexes.

This last method has several advantages with respect to the free carbene and *in situ* method, as it can be performed at lower temperatures and it was found to be largely air and water insensitive for Wang and Lin's systems.<sup>66</sup> Wang and co-workers reported that the reaction should proceed at no higher than 50 °C to prevent formation of unidentifiable side products.<sup>51</sup>

Brown and co-workers previously found the silver transfer method to work well for the synthesis of NHC pincer ligand complexes of silver(I) and palladium(II), however, when water was present the azolium salt hydrolysed to form the formamide decomposition product.<sup>25</sup> This was avoided by the addition of 3Å molecular sieves to the reaction mixture. The silver transfer method must also be performed in the absence of light as silver salts are photosensitive. The aforementioned methods would be utilised to synthesise the four series of rhenium(I)-NHC tricarbonyl complexes.

### 2.5.3 Rhenium(I)-1-(2-pyridyl)imidazol-2-ylidene Tricarbonyl Series

For the synthesis of **1Br**, **2-3Cl/Br** the *in situ* method was utilised in favour of the free carbene method which was found to be low yielding. This was attributed to the hygroscopic nature of azolium salts. Within this research, a previous work up procedure for the *in situ* method was optimised.<sup>62</sup> Previously the complexes were purified *via* flash chromatography on a short plug of silica with acetonitrile/acetone/triethylamine as the

eluting solvent. It was determined herein that Brockmann II acidic alumina was a better stationary phase when used with dichloromethane as the eluting solvent. Using this alternative work up procedure significantly improved the yields and the feasible scale of **1Br**, **2-3Cl/Br**.<sup>62</sup>



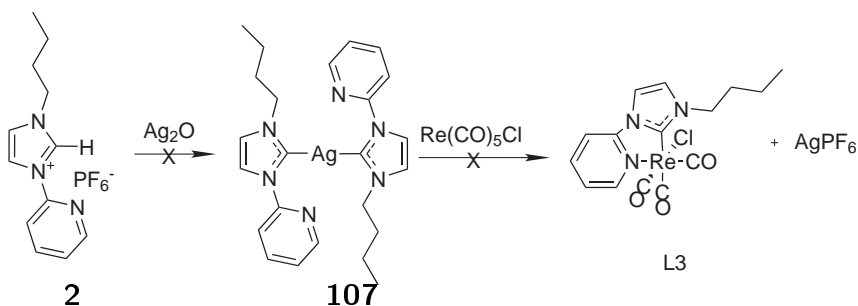
Scheme 2.17: Ligands used for the attempted synthesis of **1Cl**.

Table 2.2: Attempted reaction conditions for the synthesis of **1Cl**.

Method	Conditions	Outcome
<b><i>In situ</i></b>		
	PF <sub>6</sub> <sup>-</sup> salt ( <b>2</b> ), toluene, K <sub>2</sub> CO <sub>3</sub> as base, reflux	No product isolated
	PF <sub>6</sub> <sup>-</sup> salt ( <b>2</b> ), toluene K <sub>2</sub> CO <sub>3</sub> :NEt <sub>3</sub> as dual base system, reflux	No product isolated
<b>Silver transfer</b>		
	PF <sub>6</sub> <sup>-</sup> salt ( <b>2</b> ), CH <sub>3</sub> Cl, Ag <sub>2</sub> O, reflux	No product isolated
	PF <sub>6</sub> <sup>-</sup> salt ( <b>2</b> ), CH <sub>3</sub> Cl, Ag <sub>2</sub> O, reflux	<sup>1</sup> H NMR of intermediate looked promising, no product isolated
	Br <sup>-</sup> salt ( <b>1</b> ), CH <sub>3</sub> Cl, Ag <sub>2</sub> O, reflux	No pure product isolated, IR indicated mainly starting material (ReCO <sub>5</sub> Cl) present
	PF <sub>6</sub> <sup>-</sup> salt ( <b>2</b> ), CH <sub>3</sub> Cl, Ag <sub>2</sub> O, room temp. Increased temp to reflux after addition of ReCO <sub>5</sub> Cl	No product isolated
<b>Silver transfer</b>		
	Br <sup>-</sup> salt ( <b>1</b> ), CH <sub>2</sub> Cl <sub>2</sub> , Ag <sub>2</sub> O, room temp. Increased temp to reflux after addition of ReCO <sub>5</sub> Cl	Pure by elemental and X-Ray crystal structure, 29%.

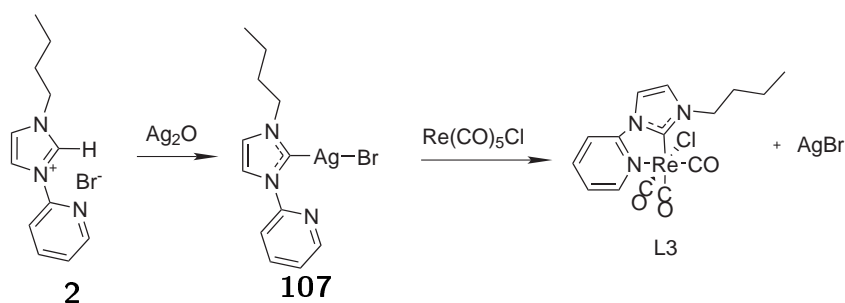
The synthesis of **1Cl** proved more difficult than of **1Br**, **2-3Cl/Br** and several different conditions were trialled (Table 2.2). The *in situ* method was quickly abandoned in favour of the silver method. The silver method (Figure 2.11) was initially trialled

using the potassium hexafluorophosphate salt; PyImBuH.PF<sub>6</sub> (**2**) to prevent halide contamination. As the PF<sub>6</sub><sup>-</sup> anion is such a weakly coordinating anion the proposed intermediate is that of **107** as shown in **Scheme 2.18**. Once the successful formation of the silver complex intermediate could be inferred by the disappearance of the H2 proton in the <sup>1</sup>H NMR spectrum then [Re(CO)<sub>5</sub>Cl] was added to the reaction mixture.



Scheme 2.18: Synthesis of 1Cl

It was found that the reaction only proceeded when dichloromethane was utilised in conjunction with PyImBuH.Br (**1**) and the silver complex formation step was allowed to proceed at room temperature as demonstrated in **Scheme 2.19**. Subsequent reports have confirmed that the silver complex intermediate is in fact quite temperature sensitive and the reaction will not afford product if heated too strongly.<sup>51</sup>



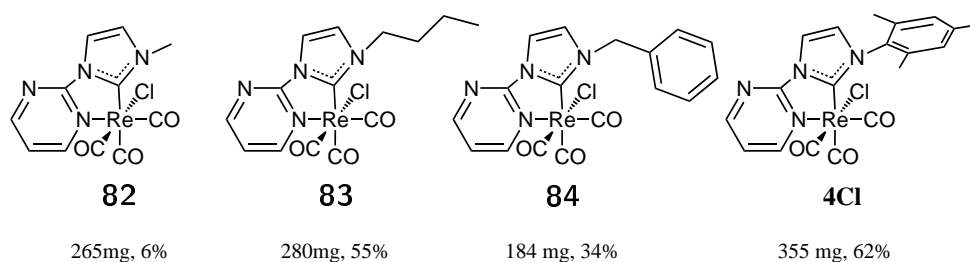
Scheme 2.19: Attempted synthesis of 1Cl

Even though the bromide azolium salt was utilised, the end product was found to only contain the chloro ligand which was evidenced by elemental and X-ray crystal structure analysis. Rhenium(I) has previously shown a preference for the chloride halogen over the bromide when both are present. This is attributed to the increased lability of the bromide versus the chloride ligand and that the chloro is a stronger  $\sigma$  donor.<sup>35,67</sup>

## 2.5.4 Rhenium(I)-1-(2-pyrimidyl)imidazol-2-ylidene Tricarbonyl Series

The successful synthesis of the 1-(2-pyridyl)imidazol-2-ylidene series allowed for the synthesis of other analogues. The 1-(2-pyrimidyl)imidazol-2-ylidene series was synthesised by the *in situ* method in moderate yields and X-ray quality crystals of **5Cl** and **5Br** were obtained. The bromo complexes (**4Br** and **5Br**) were synthesised starting from the PF<sub>6</sub><sup>-</sup> azolium salts, (**8** and **10**).

During the course of this work the synthesis of **4Cl** was reported by Wang and co-workers who synthesised a suite of rhenium(I)-1-(2-pyrimidyl)imidazol-2-ylidene tricarbonyl compounds *via* the silver transfer method as shown in **Scheme 2.20**.<sup>51</sup> Their reported work-up procedure involved a column on silica gel with an eluting solvent of CH<sub>2</sub>Cl<sub>2</sub>-MeOH (40:1). The scale and yields reported by Wang vary to those described within.<sup>51</sup>



Scheme 2.20: Synthetic yields of a series of rhenium(I)-1-(2-pyrimidyl)-2-ylidene tricarbonyl compounds (Wang, 2013).

## 2.5.5 Rhenium(I)-1-(2-quinoyl)imidazol-2-ylidene and Rhenium(I)-1-(2-quinoxyl)imidazol-2-ylidene Tricarbonyl Series

The 1-(2-quinoyl)imidazol-2-ylidene and 1-(2-quinoyl)imidazol-2-ylidene series were synthesised utilising the *in situ* method. Within this research a previous purification for the *in situ* method was optimised.<sup>68</sup> Previously the toluene reaction mixture was dissolved in hexanes and extracted with acetonitrile. This method was improved by adding water to the toluene/hexanes layer which forced the rhenium complex to precipitate. The toluene/hexanes layer was then removed and the water was extracted with

dichloromethane which was then purified by column chromatography on Brockmann II acidic alumina. This modified procedure significantly improved the yields and the feasible scale of **6-7Cl/Br**.<sup>68</sup>

All fourteen target rhenium compounds were found to be pure by elemental analysis with some fitting required for dichloromethane, which was often seen in the <sup>1</sup>H NMR spectrum post column chromatography. Further experimental details pertaining to the synthesis and characterisation of **1-7Cl/Br** is detailed in **Experimental Sections 8.4.1-8.4.14**.

## 2.5.6 <sup>1</sup>H and <sup>13</sup>C Nuclear Magnetic Resonance Spectroscopy Studies

The successful synthesis of the Re(I)-NHC complexes was initially supported by the disappearance of the H2 proton of the azolium salt situated in the <sup>1</sup>H NMR spectrum of the azolium reagents around 10.5 ppm in DMSO-*d*<sub>6</sub>. The alkyl protons of the butyl substituted compounds **1Cl/Br** showed no change upon coordination as expected.

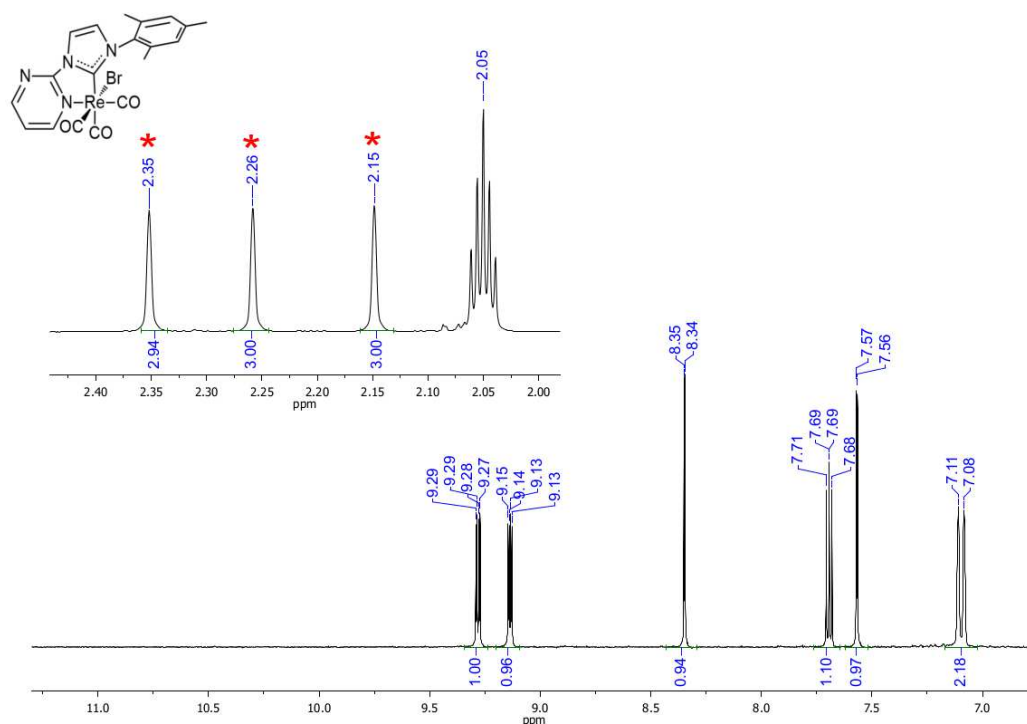


Figure 2.12: <sup>1</sup>H NMR of **4Br** in acetone-*d*<sub>6</sub> showing three unique proton environments for each of the three methyl groups of the mesityl substituent (red asterisks).

It was also noted that in the proton NMR of the mesityl substituted compounds (**2Cl/Br** and **4Cl/Br**) that unlike the azolium salt starting material (**Figure 2.4**) there were three distinct proton environments each integrating for three hydrogens as shown for **4Br** in **Figure 2.12**. This indicated that there was restricted rotation about the N1-C bond once the ligand was coordinated to the rhenium metal centre as anticipated. This was attributed to the increased steric hindrance caused by the methyl substituents as opposed to the less bulky hydrogens of the simpler phenyl substituent.

Table 2.3: Selected  $^{13}\text{C}$  NMR chemical shifts of the rhenium(I)-NHC tricarbonyl complexes.

Compound	Solvent	Chemical shift (ppm)			
<b>1Cl</b>	DMSO-d <sub>6</sub>	198.93 (CO)	197.98 (CO)	190.05 (NCN)	189.20 (CO)
<b>1Br</b>	CDCl <sub>3</sub>	197.32 (CO)	196.75 (CO)	192.97 (NCN)	187.96 (CO)
<b>2Cl</b>	CDCl <sub>3</sub>	197.71 (CO)	196.82 (CO)	194.69 (CO)	188.74 (NCN)
<b>2Br</b>	CDCl <sub>3</sub>	196.89 (CO)	195.93 (CO)	194.20 (CO)	188.22 (NCN)
<b>3Cl</b>	DMSO-d <sub>6</sub>	197.9 (CO)	196.8 (CO)	190.9 (NCN)	189.2 (CO)
<b>3Br</b>	DMSO-d <sub>6</sub>	197.3 (CO)	196.2 (CO)	190.0 (NCN)	188.7 (CO)
<b>4Cl</b>	DMSO-d <sub>6</sub>	197.6 (CO)	195.5 (CO)	192.4 (NCN)	188.6 (CO)
<b>4Br</b>	DMSO-d <sub>6</sub>	196.7 (CO)	194.9 (CO)	191.2 (NCN)	188.1 (CO)
<b>5Cl</b>	DMSO-d <sub>6</sub>	197.3 (CO)	196.5 (CO)	190.4 (NCN)	188.6 (CO)
<b>5Br</b>	DMSO-d <sub>6</sub>	196.6 (CO)	195.9 (CO)	189.4 (NCN)	188.1 (CO)
<b>6Cl</b>	DMSO-d <sub>6</sub>	198.4 (CO)	195.2 (CO)	192.8 (NCN)	189.5 (CO)
<b>6Br</b>	DMSO-d <sub>6</sub>	197.7 (CO)	194.6 (CO)	191.8 (NCN)	188.9 (CO)
<b>7Cl</b>	DMSO-d <sub>6</sub>	197.9 (CO)	194.9 (CO)	194.0 (NCN)	188.1 (CO)
<b>7Br</b>	CDCl <sub>3</sub>	197.2 (CO)	196.4 (CO)	193.2 (NCN)	186.8 (CO)
<b>4Cl</b> <sup>51</sup>	DMSO-d <sub>6</sub>	198.0 (NCN)	195.9 (CO)	192.7 (CO)	189.0 (CO)

The  $^{13}\text{C}$  spectra for all fourteen compounds exhibit four downfield signals in the region of 197-188 ppm in  $\text{DMSO-}d_6$  or  $\text{CDCl}_3$  characteristic of the three carbonyls groups and NCN carbene carbon as demonstrated in **Table 2.3**. The presence of these signals is also indicative of successful formation of the the rhenium(I)-NHC tricarbonyl complex.

Unlike Wang and co-workers who assigned the NCN carbene carbon of **4Cl** to the most downfield resonance at 198.0 ppm in  $\text{DMSO-}d_6$ , this research has assigned the NCN carbon of **4Cl** to the less downfield resonance occurring at 192.4 ppm.<sup>51</sup> This is due to the correlation in the HMBC 2D NMR spectrum between the carbon resonance at 192.4 ppm and the protons of imidazolium backbone as shown in **Figure 2.13**. This technique was used for the assignment of all NCN resonances.

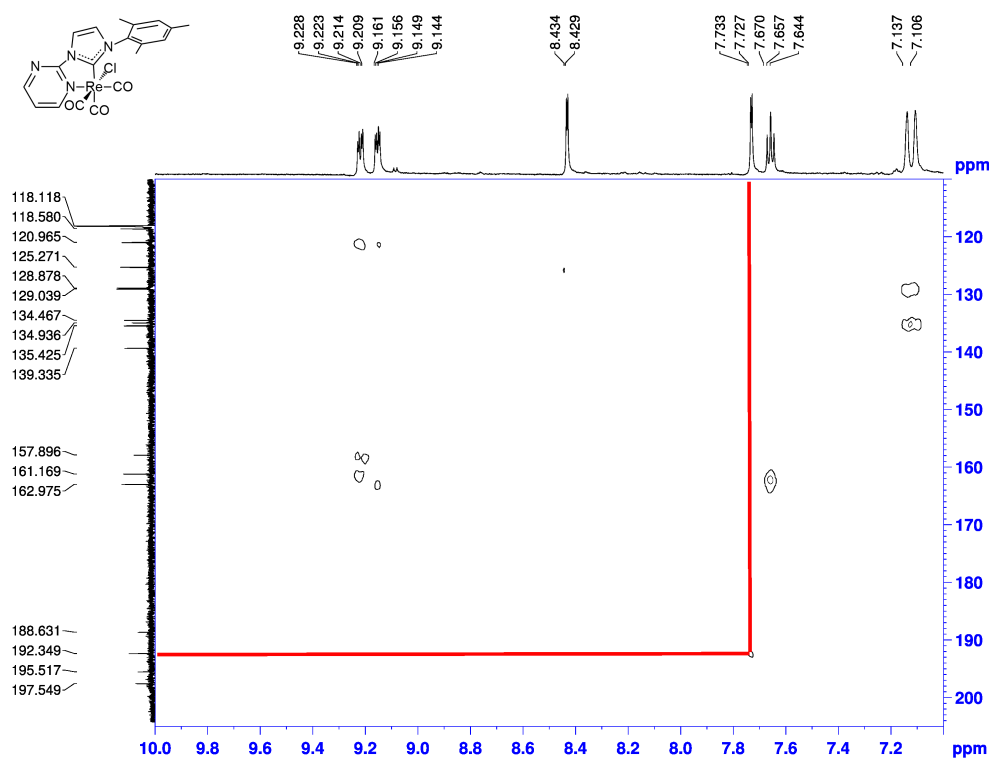


Figure 2.13: HMBC 2D NMR of **4Cl** demonstrating the assignment of the NCN signal *via* the correlation of the imidazolyl proton with the downfield signal at 192.3 ppm.

## 2.5.7 Infrared Spectroscopy

All the compounds displayed three independent CO stretches which is typical of  $C_1$  *fac*-tricarbonyl complexes (Table 2.4). The stretching frequencies are typical of neutral rhenium(I)-diimine tricarbonyl analogues.<sup>8</sup> The stretching peaks of **1-3Cl/Br** are very similar indicating that modification of the imidazole N1 side chain does not significantly affect the electron density around the rhenium metal centre.

Table 2.4: Stretching frequency values ( $\text{cm}^{-1}$ ) for the carbonyl bands of compounds **1-7Cl/Br** in DMSO solutions and literature rhenium(I)-NHC tricarbonyl compounds in various media.

Compound	$\nu_1$	$\nu_2$	$\nu_3$	
<b>1Cl</b>	2017	1911	1887	
<b>1Br</b>	2014	1915	1885	
<b>2Cl</b>	2015	1918	1882	
<b>2Br</b>	2016	1920	1885	
<b>3Cl</b>	2014	1913	1886	
<b>3Br</b>	2016	1919	1888	
<b>4Cl</b>	2018	1921	1887	
<b>4Br</b>	2018	1923	1889	
<b>5Cl</b>	2018	1919	1889	
<b>5Br</b>	2019	1922	1892	
<b>6Cl</b>	2014	1919	1886	
<b>6Br</b>	2015	1918	1889	
<b>7Cl</b>	2017	1921	1893	
<b>7Br</b>	2018	1921	1896	
<i>fac</i> -[Re(PyBzBu)(CO) <sub>3</sub> Cl] ( <b>73</b> ) <sup>a</sup>	2016	1919	1898	1870
<i>fac</i> -[Re(PyBzBu)(CO) <sub>3</sub> Br] ( <b>74</b> ) <sup>a</sup>	2018	1928	1906	1872
<i>fac</i> -[Re(PyBzMe)(CO) <sub>3</sub> Cl] ( <b>78a</b> ) <sup>b</sup>	2016	1924	1878	
<i>fac</i> -[Re(PyImMe)(CO) <sub>3</sub> Cl] ( <b>76a</b> ) <sup>b</sup>	2019	1920	1860	
<b>4Cl</b> <sup>c</sup>	2017	1922	1891	

<sup>a</sup> KBr disc, four stretches present due to solid state effects,<sup>49</sup> <sup>b</sup>KBr disc,<sup>69</sup> <sup>c</sup> synthesised by Chen and co-authors, recorded in a KBr disc.<sup>51</sup>

There is also no discernible difference upon changing the halogen from chloride to bromide. This is consistent with the literature examples of **73** vs. **74**.<sup>49</sup> Notably alternating the N-donor ring between the pyridyl, pyrimidyl, quinoyl and quinoxyl moieties also does not have a discernible effect on the CO stretching frequencies. This implies that the electron density around the rhenium metal centre and the back-bonding to

the carbonyl ligands is not significantly altered by making these modifications to the N-donor heterocycle.

## 2.5.8 X-Ray Crystal Structures

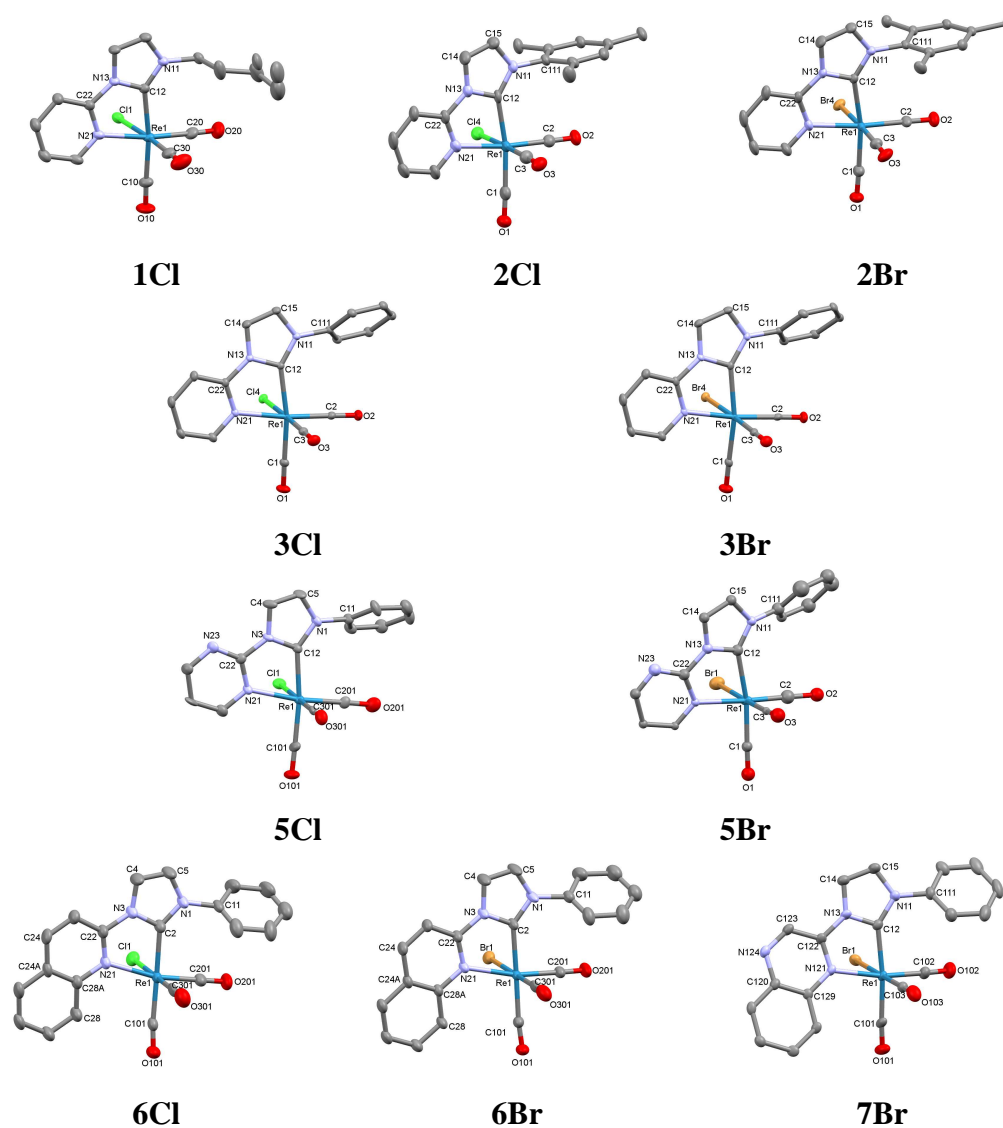


Figure 2.14: Molecular structures of **1Cl**, **2Cl**, **2Br**, **3Cl**, **3Br**, **5Cl**, **5Br**, **6Cl**, **6Br** and **7Br** with ellipsoids drawn at the 50% probability level. The hydrogens have been omitted for clarity.

X-Ray structural characterisation was obtained for ten of the fourteen rhenium complexes and selected bond lengths and angles are detailed in **Tables 2.5-2.6**. The X-ray

structures were solved by Associate Professor Brian Skelton of the Centre for Microscopy, Characterisation and Analysis at the University of Western Australia. The results were given to the author and are discussed herein. The molecular structures are depicted in **Figure 2.14**. Full crystallographic parameters, bond lengths and angles are in **Appendix 9.1**.

Table 2.5: Selected bond lengths (Å).

<b>Bond Length (Å)</b>			
<b>Compound</b>	<b>Re-C(20) CO <i>trans</i> to N atom</b>	<b>Re-C(10) CO <i>trans</i> to C atom</b>	<b>Re-C(30) CO <i>trans</i> to halogen</b>
<b>1Cl</b>	1.910(3)	1.957(2)	1.913(3)
<b>2Cl</b>	1.917(6)	1.942(5)	1.953(9)
<b>2Br</b>	1.921(4)	1.952(4)	2.002(8)
<b>3Cl</b>	1.9169(11)	1.9552(11)	1.9123(10)
<b>3Br</b>	1.923(4)	1.957(3)	1.917(4)
<b>5Cl</b>	1.907(10)	1.946(10)	1.969(14)
<b>5Br</b>	1.77(3)	1.92(2)	1.99(3)
<b>6Cl</b>	1.908(4)	1.949(5)	1.977(6)
<b>6Br</b>	1.913(4)	1.955(4)	2.058(5)
<b>7Br</b>	1.906(6)	1.964(6)	2.000(7)

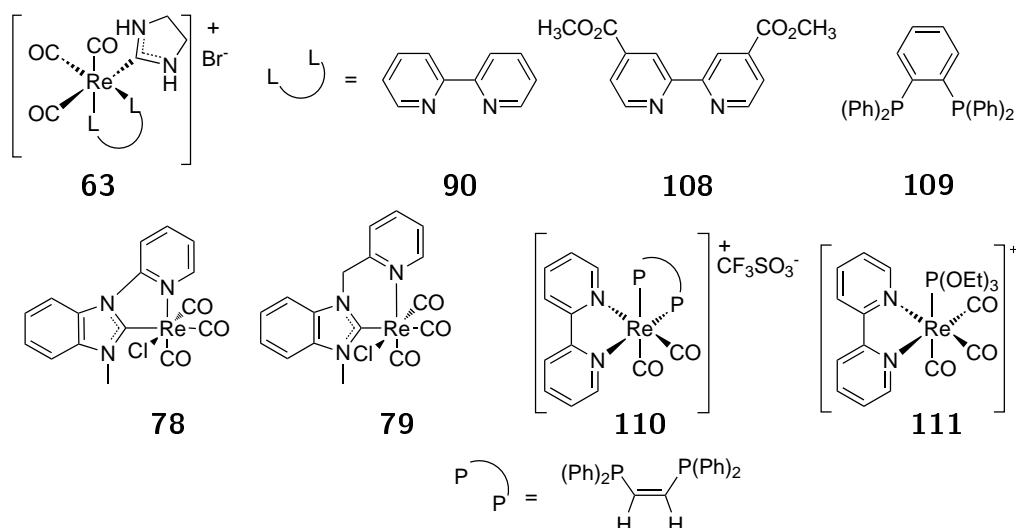
Table 2.6: Selected bond lengths (Å) and bond angles (°) continued.

Bond Length (Å) and Bond Angles (°)				
Compound	Re-C(12)	Re-N(21)	Re-X(1)	C(12)-Re-N(21); Bite angle of N <sup>^</sup> C ligand
<b>1Cl</b>	2.133(2)	2.2083(19)	2.5080(6)	74.41(7)
<b>2Cl</b>	2.08(4) and 2.123(5)	2.199(4)	2.321(6) and 2.434(3)	74.38(3)
<b>2Br</b>	2.113(15) and 2.125(4)	2.197(3)	2.4097(13) and 2.5102(9)	74.70(12)
<b>3Cl</b>	2.1488(10)	2.2117(8)	2.4956(2)	74.67(17)
<b>3Br</b>	2.145(3)	2.210(3)	2.6255(4)	74.60(13)
<b>5Cl</b>	2.136(9)	2.211(8)	2.494(3)	73.5(3)
<b>5Br</b>	2.19(2)	2.20(2)	2.621(3)	75.8(8)
<b>6Cl</b>	2.119(4)	2.277(3)	2.4799(13)	73.84(14)
<b>6Br</b>	2.114(4)	2.275(3)	2.6243(5)	74.10(11)
<b>7Br</b>	2.112(6)	2.227(5)	2.6272(7)	74.8(2)

The *facial* arrangement of the three carbonyl ligands was confirmed for all the species. The halogen of **2Cl/Br** was positionally disordered with respect to the carbonyl group in the *trans* position whilst **1Cl** showed disorder over the two terminal carbon atoms of the butyl chain. In all cases the structures showed that the N-donor ring and imidazole ring are virtually co-planar as depicted in **Figure 2.14**.

The mesityl-substituted complexes **2Cl/Br** and **4Br** show that the mesityl ring is almost perpendicular to the imidazole ring when coordinated to the rhenium centre, whilst the phenyl ring of the phenyl analogues shows the aromatic ring to be oriented *ca.* 40° to the imidazole ring. This further confirms that the mesityl ring is more restricted in its rotation in comparison to the phenyl ring derivative which was previously inferred from the <sup>1</sup>H NMR spectra (**Figure 2.12**). As the mesityl and phenyl rings are not co-planar with the imidazole and N-donor ring they can be considered to be a separate aromatic system to the heterocyclic ring system which could potentially effect the photophysical properties.

The Re-C(12), Re-N(21) and Re-X(1) bond lengths are consistent with literature rhenium(I)-NHC tricarbonyl complexes.<sup>47,49,51,69</sup> The Re-CO bond lengths are also consistent



Scheme 2.21: Structures of literature rhenium(I) compounds with NHC and organophosphorous ligands.

with lengths for other rhenium(I) complexes with NHC and organophosphorous ligands as shown in **Tables 2.7-2.10**. Overall this there is not much discrepancy between the Re-CO bond lengths with all values ranging between 1.906-2.058 Å. The only exception is **5Br** where the length of the Re-CO bond of the CO in *trans* to the pyridyl ring is 1.77 Å. This is attributed to desolvation of the crystal which gave a poorly resolved fit due to the low precision structure.

Table 2.7: Selected bond lengths (Å) and angles (°) of literature rhenium(I) compounds with NHC and organophosphorous ligands.

Compound	Ligand (where applicable)	Bond Length (Å)		
		Re-C(20) CO <i>trans</i> to N atom	Re-C(10) CO <i>trans</i> to C atom	Re-C(30) CO <i>trans</i> to halogen
<b>63</b> <sup>47</sup>	<b>90</b>	1.917(9) (diimine) and 1.924(9) (diimine)	1.965(9)	-
<b>63</b> <sup>47</sup>	<b>108</b>	1.908(5) (diimine) and 1.928(5) (diimine)	1.966(5)	-
<b>74</b> <sup>49</sup>		1.915(3)	1.969(3)	1.938(3)
<b>78</b> <sup>69</sup>		1.925(8)	1.949(8)	1.954(10)
<b>79</b> <sup>69</sup>		1.907(8)	1.954(8)	1.883(8)
<b>83</b> <sup>51</sup>		1.906(4)	1.956(4)	1.903(4)
<b>4Cl</b> <sup>51</sup>		1.945(8)	1.969(7)	1.906(8)

Table 2.8: Selected bond lengths (Å) and angles (°) of literature rhenium(I) compounds with NHC and organophosphorous ligands continued.

Compound	Ligand (where applicable)	Bond Length (Å)			Bond Angle (°)
		Re-C(12)	Re-N(21)	Re-X(1)	C(12)-Re-N(21); Bite angle of N^C ligand
<b>63</b> <sup>47</sup>	<b>90</b>	2.171(7)	2.178(6) (diimine) and 2.175(6) (diimine)	-	-
<b>63</b> <sup>47</sup>	<b>108</b>	2.163(4)	2.178(3) (diimine) and 2.172(3) (diimine)	-	-
<b>74</b> <sup>49</sup>		2.114(3)	2.198(2)	2.6436(3)	73.97(9)
<b>78</b> <sup>69</sup>		2.127(7)	2.194(6)	2.489(2)	74.2(3)
<b>79</b> <sup>69</sup>		2.148(8)	2.191(6)	2.5156(19)	81.3(3)
<b>83</b> <sup>51</sup>		2.146(3)	2.211(2)	2.5016(9)	73.94(11)
<b>4Cl</b> <sup>51</sup>		2.133(7)	2.186(7)	2.484(3)	73.9(3)

The Re-CO bond lengths are very similar regardless of the ligand in *trans*. It would be expected when a strong donor ligand is *trans* to a carbonyl that the Re-CO bond would be weakened and the Re-C bond length would increase. As the carbene ligand is a stronger  $\sigma$  donor ligand, it is expected that the longest Re-CO bond of the three CO ligands would be observed for the carbonyl ligand in *trans* to the NHC carbon. However this trend is not observed for this data set and the longest Re-CO bond varies between the CO in *trans* to the halogen and the CO in *trans* to the carbene.

Table 2.9: Selected bond lengths (Å) of literature rhenium(I) compounds with NHC and organophosphorous ligands continued.

Bond Length (Å)				
Compound	Ligand (where applicable)	CO trans to N atom (diimine)	CO trans to P atom	CO trans to Cl atom
<b>63</b> <sup>47</sup>	<b>109</b>	-	1.963(6) and 1.950(6)	-
<b>112</b> <sup>70</sup>		Not stated	1.93	-
<b>110</b> <sup>71</sup>		1.895(5)	1.931(5)	-

This discrepancy is also seen in the literature and is exemplified by **78** where the longest Re-C bond belongs to the CO in *trans* to the chloro ligand.<sup>69</sup> This disparity is attributed to the geometry of these types of compounds being distorted octahedron. The distortion of the geometry is due to the bite angle of the NHC ligand being less than ideal (90 °) for octahedral geometry. The C(12)-Re-N(21) bite angle is consistently 73-74 ° as shown in **Table 2.6** which means the carbon atom of the carbene is not in the ideal position for favourable orbital overlap which could account for the inconsistent trend in Re-CO bond length. The *trans* groupings (**Appendix 9.1**) are also less than 180 ° which is also indicative of a distorted octahedron.

Table 2.10: Selected bond lengths (Å) of literature rhenium(I) compounds with NHC and organophosphorous ligands continued.

Bond Length (Å)				
Compound	Ligand (where applicable)	CO trans to C atom (carbene)	Re-P	Re-C (carbene)
<b>63</b> <sup>47</sup>	<b>109</b>	1.928(7)	2.437(1) and 2.444(1)	2.199(6)
<b>112</b> <sup>70</sup>		-	Not stated	-
<b>110</b> <sup>71</sup>		-	2.3647(13)	-

## 2.6 Summary and Concluding Remarks

Ten new azolium salts, in addition to four previously reported azolium salts, were synthesised and fully characterised by  $^1\text{H}$  and  $^{13}\text{C}$  NMR spectroscopy. The hexafluorophosphate salts, **QuImPhH.PF<sub>6</sub>** and **QxImPhH.PF<sub>6</sub>**, were used “as is” without further characterisation. The remaining novel azolium salts were found to pure by elemental analysis. These salts were then subsequently used to synthesise thirteen novel rhenium(I)-NHC tricarbonyl complexes in addition to one previously reported compound *via* the *in situ* method. **1Cl** proved to be the most difficult to synthesise and was successfully formed *via* the silver transfer method. The rhenium(I)-NHC tricarbonyl complexes were found to be pure by elemental analysis and were fully characterised by  $^1\text{H}$  and  $^{13}\text{C}$  NMR spectroscopy and infrared spectroscopy.  $^1\text{H}$  NMR confirmed that the mesityl moieties of **2Cl/Br** and **4Cl/Br** were restricted in rotation compared to the freely rotating phenyl substituents of **3Cl/Br** and **5-7Cl/Br**. IR spectroscopy confirmed that the strength of the CO backbonding was similar for all fourteen complexes. Crystals of X-ray quality were obtained for ten of the compounds which confirmed the *facial* configuration of the carbonyl ligands and established that the complexes exhibited a distorted octahedral geometry which is typical of bidentate NHC ligands with reduced bite angles.

# Chapter 3

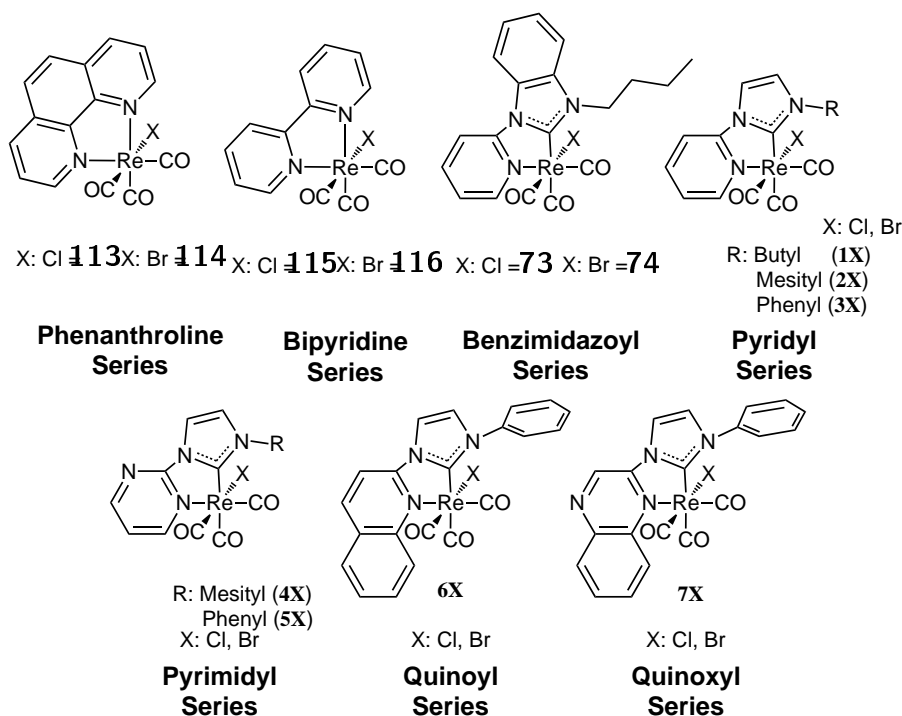
## Photophysical Investigation of Re(I)-NHC Tricarbonyl Compounds

### 3.1 Overview

The photophysical properties of rhenium(I)-diimine tricarbonyl type compounds such as *fac*-[Re(phen)(CO)<sub>3</sub>Br] (**113**) and their applications have been thoroughly scrutinised since the inaugural work of Wrighton and Morse.<sup>7</sup> Substituting the traditional diimine framework for a N-heterocyclic carbene ligand, specifically the 1-(2-pyridyl)-imidazol-2-ylidene archetype, provides a new alternative avenue for functionalisation and tuning of optical properties. The photophysical properties, specifically the absorption, excitation and emission profiles, observed excited state lifetime and quantum yield of the rhenium(I)-NHC tricarbonyl compounds synthesised in **Chapter 2** will be investigated and characterised herein.

### 3.2 Rationale

Previous work on the benzimidazol-2-ylidene series, (compounds **73** and **74**, **Scheme 3.1**), has shown that the pyridine is heavily involved in the relative energy of MLCT.<sup>49</sup> Therefore modifications at this site should have a pronounced effect on the photo-physics of the compounds allow for “tuning” of the optical output.



Scheme 3.1: Rhenium(I) tricarbonyl compounds discussed in this chapter.

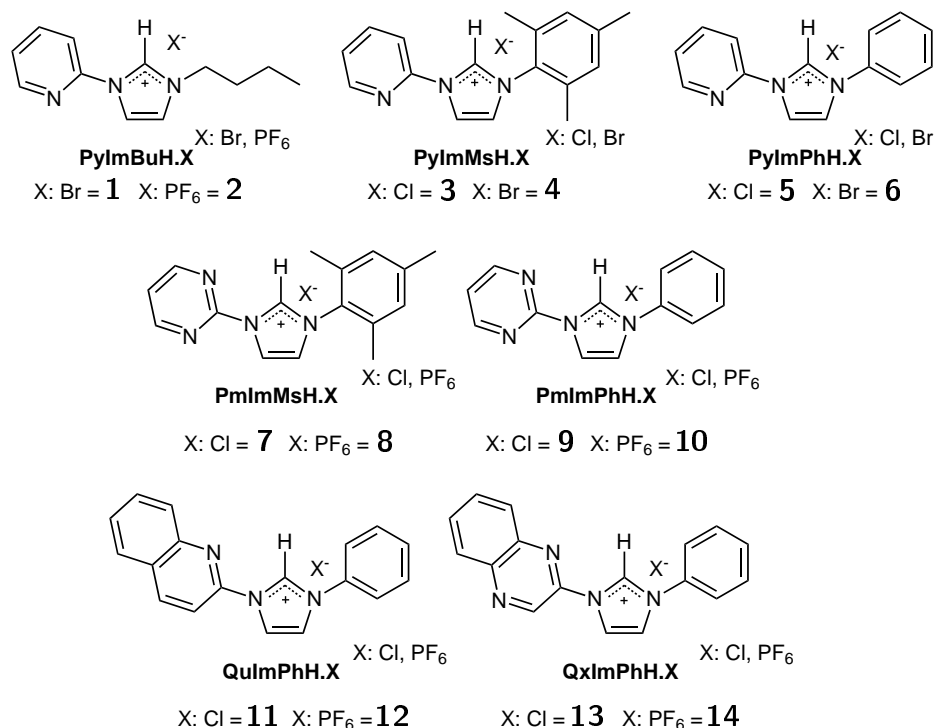
By varying the N-donor ring from a pyridyl ring to a pyrimidyl the LUMO should be stabilised. The more electron deficient pyrimidyl ring should make the promotion of an electron from the metal 5d orbital to the ligand  $\pi^*$  acceptor orbital more favourable, hence reducing the energy of the HOMO-LUMO transition and red-shifting the emission. By increasing the conjugation of the N-donor ring by using a quinoline ring, the energy of the LUMO should be lowered. This modification should also red-shift the emission. Both modifications will be simultaneously employed by using a quinoxaline ring as the N-donor ring.

## 3.3 Absorption Profiles

### 3.3.1 Absorption Profiles of the Azolium Salts

The absorption profiles of the azolium salts are shown in **Figures 3.1, 3.2, and 3.3**, and their chemical structure are reiterated in **Scheme 3.2**. The absorption maxima of the major bands are summarised in **Table 3.1**.

The absorption profiles of the pyridyl series and pyrimidyl series are very similar and consist of one major band centred around 270 nm for **1-3Cl/Br**, 235 nm for **4Cl/Br**



Scheme 3.2: Chemical structure of the azolium salt ligand precursors where X depicts the various anions used.

and 250 for **5Cl/Br**. For several of the pyridyl compounds there is also a high energy shoulder ( $>250$  nm). For electron deficient heterocyclic rings with two or less nitrogens, such as pyridine and pyrimidine, the  $n \rightarrow \pi^*$  transitions are not very prominent therefore the bands can be assigned to  $\pi \rightarrow \pi^*$  transitions.<sup>72</sup> The absorption maxima of the pyrimidyl series are slightly red-shifted to that of the pyridyl series and this is attributed to the increased electron deficiency of the pyrimidyl ring. There is no remarkable difference between the absorption profiles based on the changing identity of the R substituent or halide counter anion.

Table 3.1: Absorption maxima of azolium salts in *ca.*  $10^{-5}$  M dichloromethane solutions

Compound	$\lambda_{\text{abs}}$ [nm] ( $10^4 \epsilon$ [ $\text{M}^{-1}\text{cm}^{-1}$ ])
<b>PyImBuH.Br (1)</b>	235.8 (0.69), 268 (0.62).
<b>PyImBuH.PF<sub>6</sub> (2)</b>	237 (0.81), 267 (0.65).
<b>PyImMsH.Cl (3)</b>	240 (0.96), 269 (0.90).
<b>PyImMsH.Br (4)</b>	268 (0.87).
<b>PyImPhH.Cl (5)</b>	251 (1.08), 272 (1.17).
<b>PyImPhH.Br (6)</b>	271 (1.28).
<b>PmImMsH.Cl (7)</b>	238 (0.78).
<b>PmImMsH.PF<sub>6</sub> (8)</b>	236 (1.26).
<b>PmImPhH.Cl (9)</b>	250 (1.00).
<b>PmImPhH.PF<sub>6</sub> (10)</b>	251 (2.05).
<b>QuImPhH.Cl (11)</b>	253 (2.81), 300 (0.91), 312 (0.76), 326 (0.51).
<b>QuImPhH.PF<sub>6</sub> (12)</b>	256 (3.64), 301 (0.94), 312 (0.89), 327 (0.63).
<b>QxImPhH.Cl (13)</b>	255 (2.84), 325 (1.01), 339 (0.81).
<b>QxImPhH.PF<sub>6</sub> (14)</b>	257 (2.90), 328 (1.04).

The absorption profiles of the quinoyl and quinoxyl azolium salts exhibit a more structured emission profile than the previous azolium salts. For the quinoyl series, compounds QuImPhH.Cl (**11**) and QuImPhH.PF<sub>6</sub> (**12**), there are four distinct bands; a high intensity band at ~255 ( $>28000 \text{ cm}^{-1}\text{M}^{-1}$ ) which tails off into a structured band with three notable peaks at ~302 nm ( $>9000 \text{ cm}^{-1}\text{M}^{-1}$ ), ~313 nm ( $>7600 \text{ cm}^{-1}\text{M}^{-1}$ ) and ~327 nm ( $>5100 \text{ cm}^{-1}\text{M}^{-1}$ ). The high intensity band at ~255 nm is attributed to an allowed  $\pi \rightarrow \pi^*$  transition. The lower energy bands are tentatively assigned to  $\pi \rightarrow \pi^*$  transitions with  $n \rightarrow \pi^*$  character due to their decreased molar absorptivity.

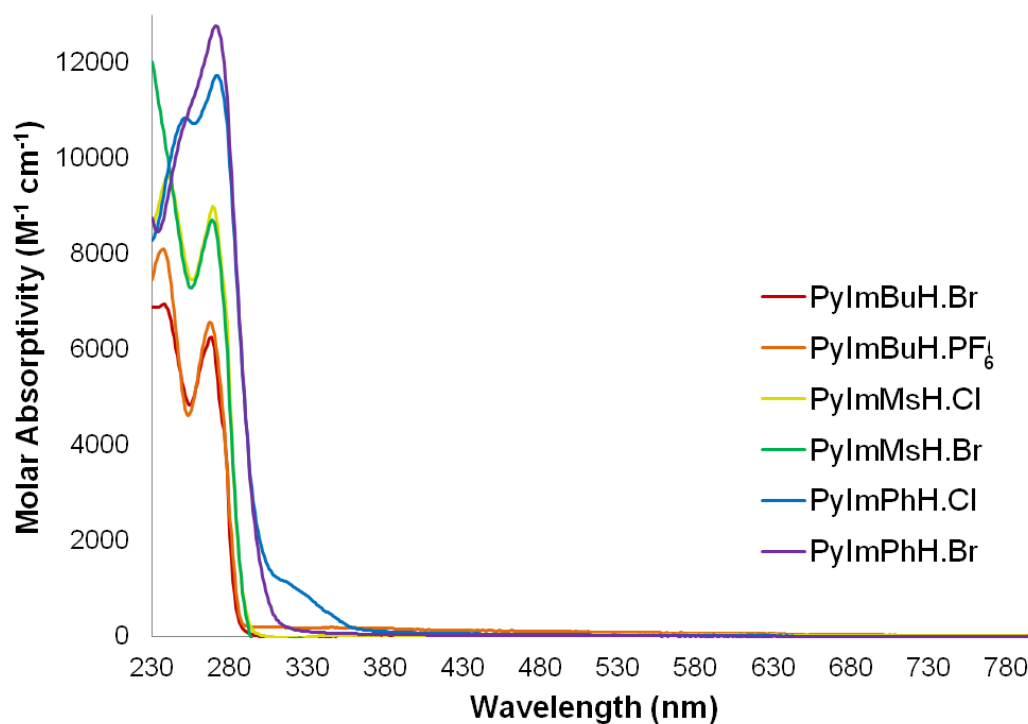


Figure 3.1: Absorption profiles of the pyridyl azolium salts, compounds **1-6**, in *ca.*  $10^{-5}$  M dichloromethane solutions.

The absorption spectra of the quinoxaline azolium salts, QxImPhH.Cl (**13**) and QxImPhH.PF<sub>6</sub> (**14**) display one high intensity band at  $\sim 256$  nm ( $>28400$   $\text{cm}^{-1}\text{M}^{-1}$ ) and then a smaller, less intense band at  $\sim 326$  nm ( $>10000$   $\text{cm}^{-1}\text{M}^{-1}$ ). The absorption profile of the chloro salt, QxImPhH.Cl (**13**), is slightly more structured and convoluted than that of QxImPhH.PF<sub>6</sub> (**14**) and an additional peak is seen at 339 nm ( $8100$   $\text{cm}^{-1}\text{M}^{-1}$ ).

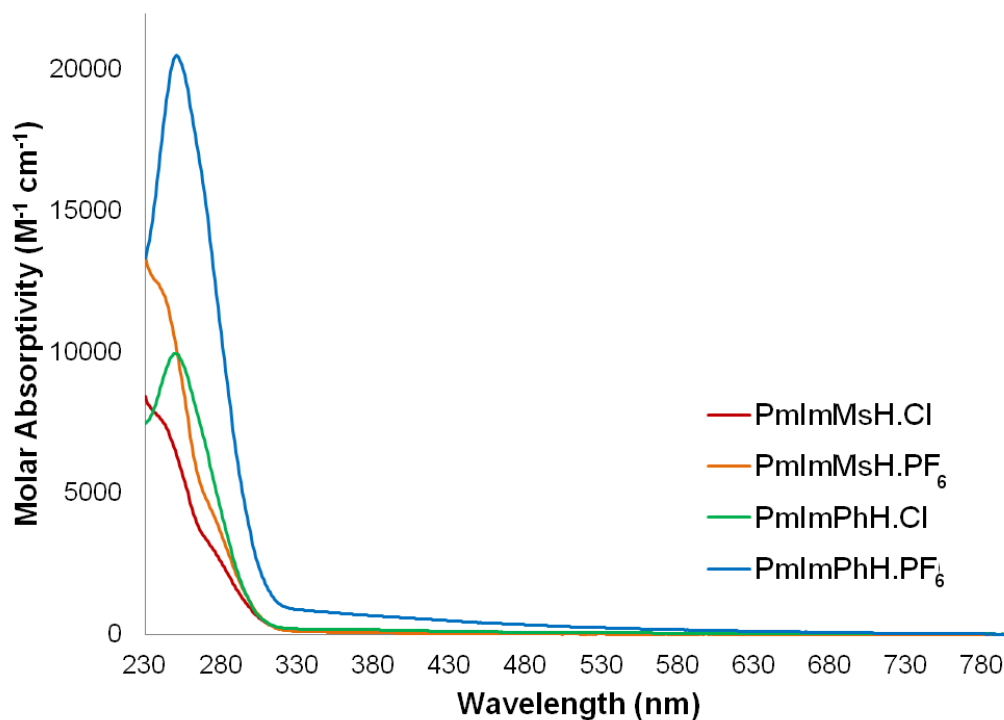


Figure 3.2: Absorption profiles of the pyrimidyl azolium salts, compounds **7-10**, in *ca.*  $10^{-5}$ M dichloromethane solutions.

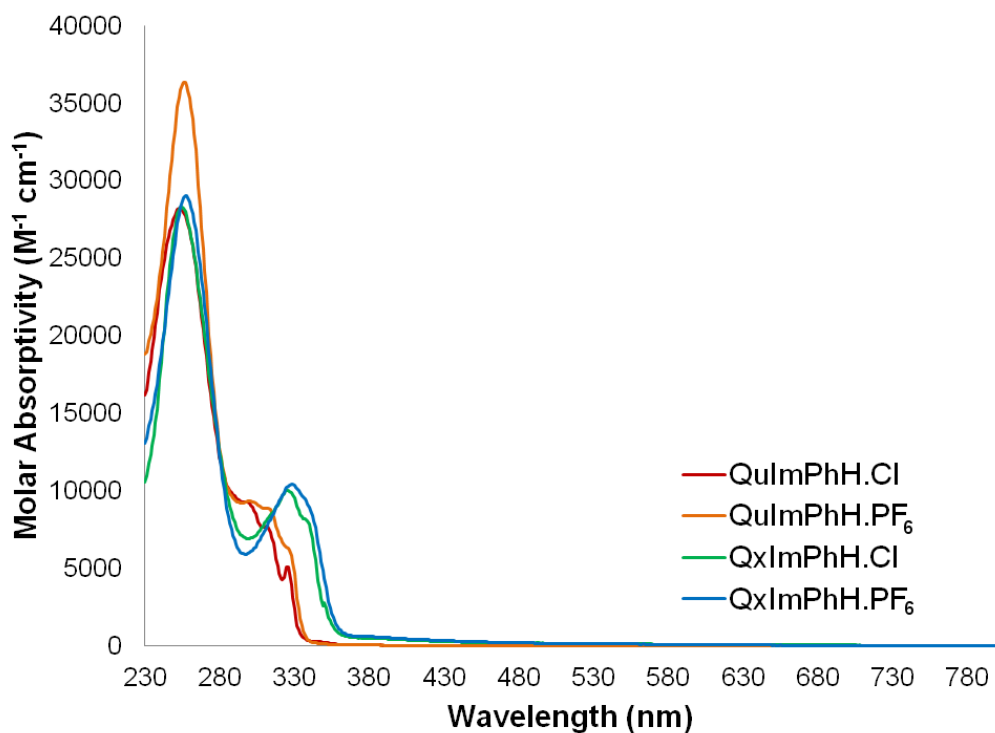


Figure 3.3: Absorption profiles of the azolium salts of the quinoyl and quinoxyl series, compounds **11-14**, *ca.*  $10^{-5}$  M in dichloromethane.

The absorption bands, particularly the lower energy band at ~326 nm, are redshifted in comparison to the quinoyl series as the quinoxyl system is more electron deficient, as expected. The high energy band at ~256 nm is attributed to a  $\pi \rightarrow \pi^*$  transition whilst the other, lower energy bands are attributed to  $\pi \rightarrow \pi^*$  transitions with  $n \rightarrow \pi^*$  character.

### 3.3.2 Absorption Profiles of the Re(I)-NHC Tricarbonyl Compounds

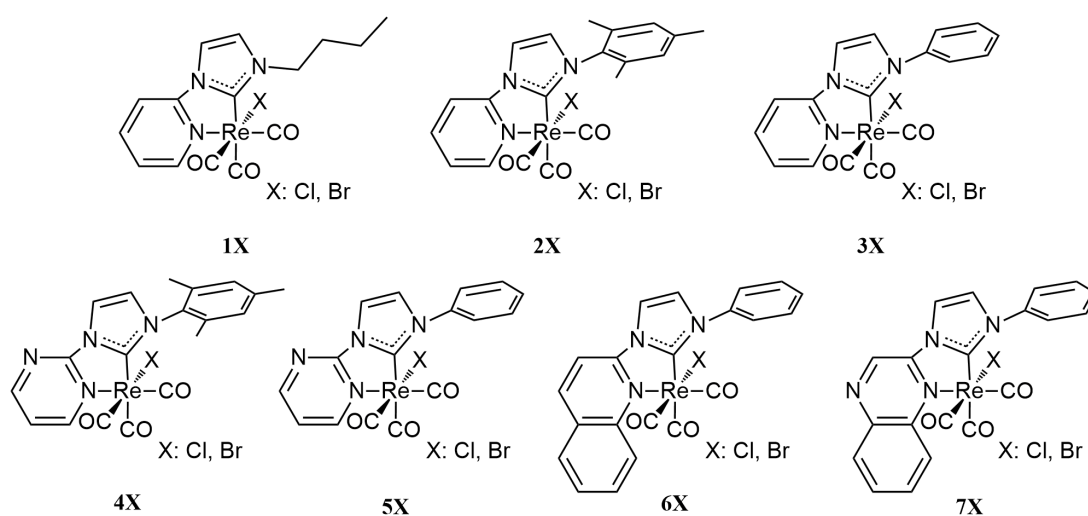


Figure 3.4: Chemical structure of the rhenium(I)-NHC tricarbonyl complexes.

The absorption maxima of compounds **1-7Cl/Br** in dilute (*ca.*  $10^{-5}$  M) dichloromethane and acetonitrile solutions are summarised in **Table 3.2** and their chemical structures are reiterated in **Figure 3.4**.

Table 3.2: Absorption maxima of compounds **1-7Cl/Br** and comparison Re(I) tricarbonyl compounds in *ca.* 10<sup>-5</sup> M dichloromethane and acetonitrile solutions.

Compound	$\lambda_{\text{abs}}$ [nm] ( $10^4 \epsilon$ [ $\text{M}^{-1}\text{cm}^{-1}$ ])	
	Dichloromethane	Acetonitrile
<b>1Cl</b>	268 (0.92), 354 (0.41).	273 (0.87), 341 (0.53).
<b>1Br</b>	278 (0.65), 357 (0.39).	281 (0.73), 343 (0.44).
<b>2Cl</b>	277 (0.95), 360 (0.40).	273 (1.69), 344 (0.61).
<b>2Br</b>	277 (0.83), 363 (0.43).	275 (0.47), 349 (0.34).
<b>3Cl</b>	276 (1.00), 359 (0.41).	276 (0.99), 350 (0.44).
<b>3Br</b>	276 (1.00), 362 (0.35).	280 (0.81), 350 (0.37).
<b>4Cl</b>	245 (3.01), 362 (0.82).	247 (1.73), 348 (0.76).
<b>4Br</b>	250 (2.05), 366 (0.61).	251 (1.38), 358 (0.28).
<b>5Cl</b>	246 (3.13), 362 (0.68).	257 (1.75), 351 (0.45).
<b>5Br</b>	248 (3.33), 366 (0.69).	258 (1.50), 353 (0.44).
<b>6Cl</b>	237 (1.92), 257 (1.66), 325 (0.56), 392 (0.38).	242 (2.71), 253 (2.94), 325 (0.88), 370 (0.41).
<b>6Br</b>	255 (3.15), 324 (1.00), 382 (0.36).	254 (3.62), 324 (1.04), 376 (0.36).
<b>7Cl</b>	252 (2.54), 344 (0.90), 415 (0.36).	250 (2.22), 341 (0.84), 407 (0.27).
<b>7Br</b>	255 (3.27), 344 (1.13), 427 (0.41).	254 (4.94), 341 (1.82), 409 (0.64).
<i>fac</i> - [Re(PyBzBu)(CO) <sub>3</sub> Cl] (73) <sup>49</sup>	275 (8.2), 358 (0.45).	261 (1.31), 280 (1.30), 350 (0.51).
<i>fac</i> - [Re(PyBzBu)(CO) <sub>3</sub> Br] (74) <sup>49</sup>	277 (4.8), 357 (0.56).	265 (1.73), 279 (1.76), 351 (0.58).
<i>fac</i> -[Re(phen)(CO) <sub>3</sub> Cl] (113) <sup>73</sup>	374.	364.

### 3.3.3 Absorption Profiles of the 1-(2-Pyridyl)-imidazol-2-ylidene Series

The absorption profiles of the 1-(2-pyridyl)-imidazol-2-ylidene series, compounds **1-3Cl/Br**, in dichloromethane are shown in **Figure 3.5** and the absorption profiles in acetonitrile are shown in **Figure 3.6**. Throughout the series the absorption profiles are very similar despite changes in the halide ancillary ligand and the R substituent. All six compounds exhibit a low intensity, broad, absorption band centred around 360 nm ( $\sim 3500 \text{ M}^{-1}\text{cm}^{-1}$ ) and a small shoulder around 277 nm ( $>6500 \text{ M}^{-1}\text{cm}^{-1}$ ). The high

intensity shoulder at 277 nm is similar to that observed in the absorption profiles of the precursor azolium salts shown in **Figure 3.1** and is therefore tentatively assigned to an intraligand (IL)  $\pi \rightarrow \pi^*$  transition involving the NHC ligand. The broad band at  $\sim 360$  nm is not present in the absorption spectra of the precursor azolium salts and is therefore attributed to a transition involving the metal centre.

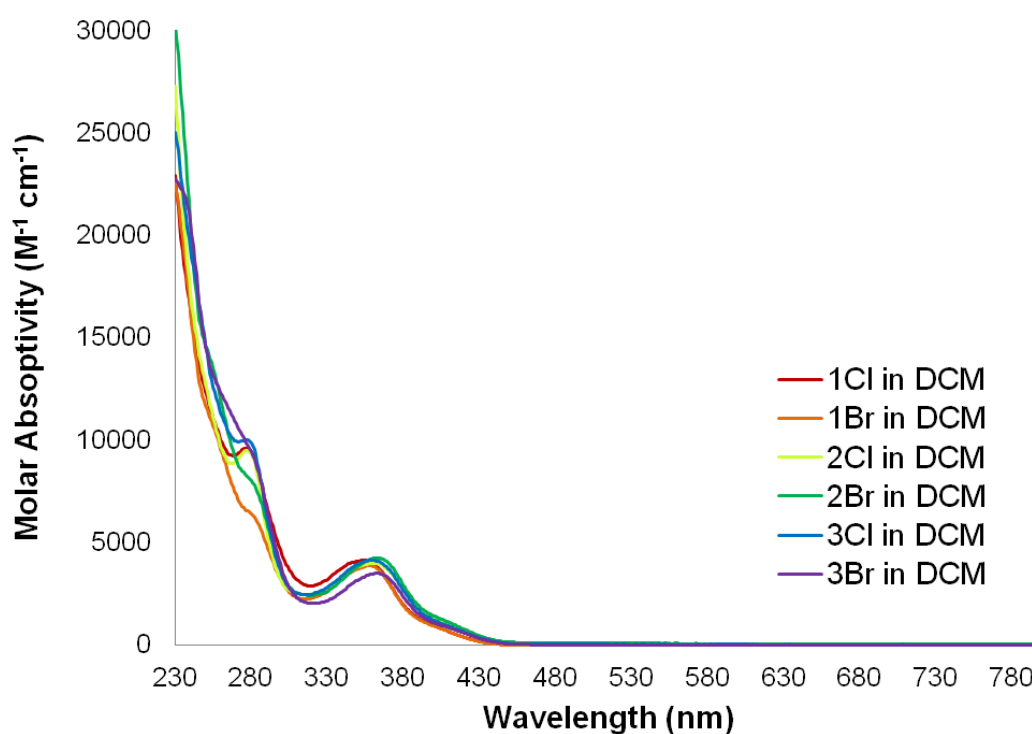


Figure 3.5: Absorption profile of **1-3Cl/Br** in *ca.*  $10^{-5}$  M dichloromethane solutions

The broad band slightly blueshifts ( $\sim 10$  nm) for each compound upon changing the solvent from dichloromethane to the more polar acetonitrile as demonstrated in **Figure 3.8**. This solvatochromic behaviour is indicative of a charge transfer state.<sup>35</sup>

Based on the solvatochromic behaviour, low molar extinction coefficient, broad, structureless shape and absence in the absorption spectra of the ligand precursors this band is attributed to a MLCT transition from the rhenium metal centre to the NHC ligand. MLCT transition bands typically exhibit a molar extinction coefficient of about 1000 to 50,000  $M^{-1}cm^{-1}$  which fits with the transition in question.<sup>33,35</sup>

As predicted, the MLCT absorption is blueshifted compared to the rhenium(I)-diimine analogue *fac*-[Re(phen)(CO)<sub>3</sub>Cl] (**113**) which is reported as 374 nm in dilute dichloromethane

solutions.<sup>73</sup> The blueshift is attributed to the decreased conjugation of the NHC ligand system in comparison to the phenanthroline ligand system which should raise the energy of the LUMO and subsequently blueshift the absorption energy.

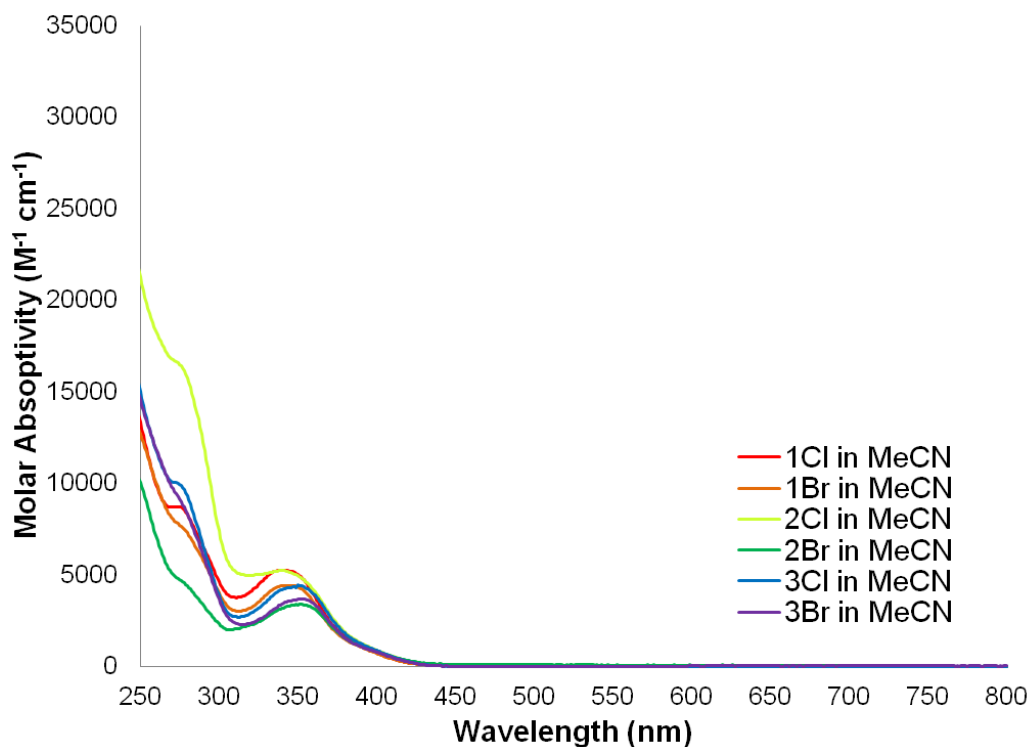


Figure 3.6: Absorption profile of **1-3Cl/Br** in *ca.*  $10^{-5}$  M acetonitrile solutions

The absorption profiles **1-3Cl/Br** are very similar to that observed for the 1-(2-pyridyl)-benzimidazol-2-ylidene compounds, **73** and **74**. This would indicate that modifying the backbone of the NHC ligand from a benzimidazole to an imidazole does not greatly effect the absorption of the lower energy transitions. In fact, computational calculations of the MLCT transition of **73** and **74** showed that the orbitals of the phenyl ring of the benzimidazole were not involved in the lowest energy transition.<sup>49</sup>

### 3.3.4 Absorption Profiles of the 1-(2-Pyrimidyl)-imidazol-2-ylidene Series

The absorption profiles of the 1-(2-pyrimidyl)-imidazol-2-ylidene series, compounds **4-5Cl/Br**, in dichloromethane and in acetonitrile solutions are depicted in **Figures 3.7** and **3.8** respectively.

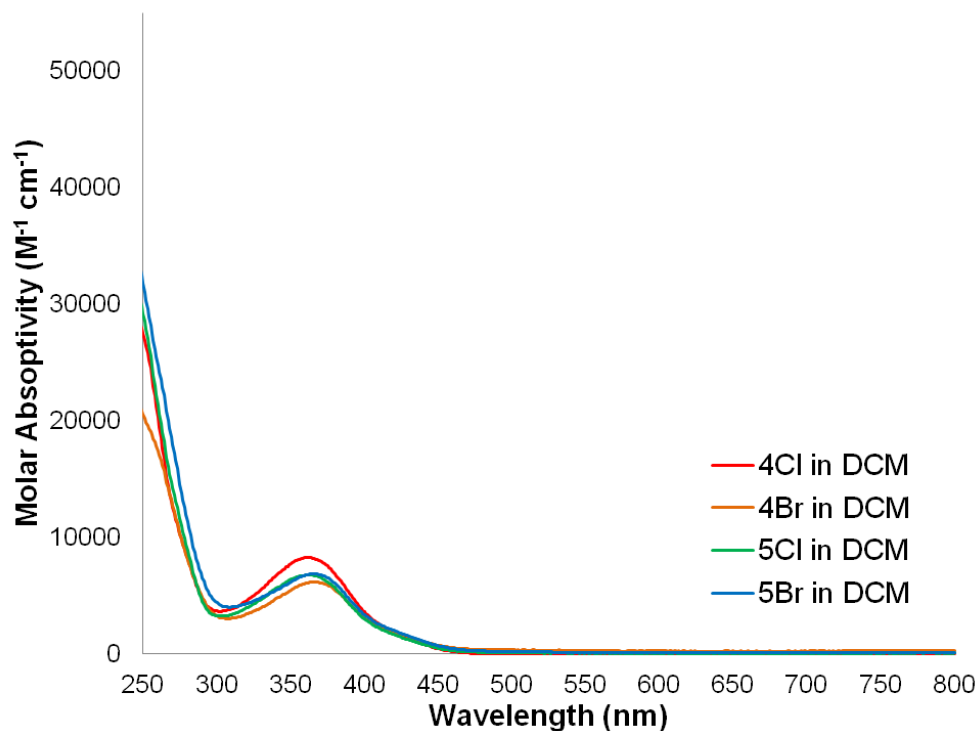


Figure 3.7: Absorption profile of **4-5Cl/Br** in *ca.*  $10^{-5}$  M dichloromethane solutions

Like the 1-(2-pyridyl)-imidazol-2-ylidene series the absorption profiles of the 1-(2-pyrimidyl)-imidazol-2-ylidene series compounds are very similar to each other despite changes in the halide ancillary ligand and the R substituent. Additionally the shape of the absorption profiles of the 1-(2-pyrimidyl)-imidazol-2-ylidene series are similar to that observed for the 1-(2-pyridyl)-imidazol-2-ylidene series however the molar extinction coefficients values are greater for the former. As with the preceding series, 1-(2-pyrimidyl)-imidazol-2-ylidene series display two distinct bands one broad, low intensity band at  $\sim 365$  nm ( $>3000$   $M^{-1}cm^{-1}$ ) and a higher intensity band at  $\sim 245$  nm ( $>16000$   $M^{-1}cm^{-1}$ ).

The high intensity band at  $\sim 245$  nm is again assigned to a intraligand (IL)  $\pi \rightarrow \pi^*$  transition involving the  $\pi$  system of the NHC ligand. The broad band is assigned to an MLCT transition due to its non-appearance in the absorption profile of the ligand precursors, the hypsochromic shift upon ( $>8$  nm) changing the solvent from dichloromethane to acetonitrile as shown in **Figure 3.8** and the low molar extinction coefficient.

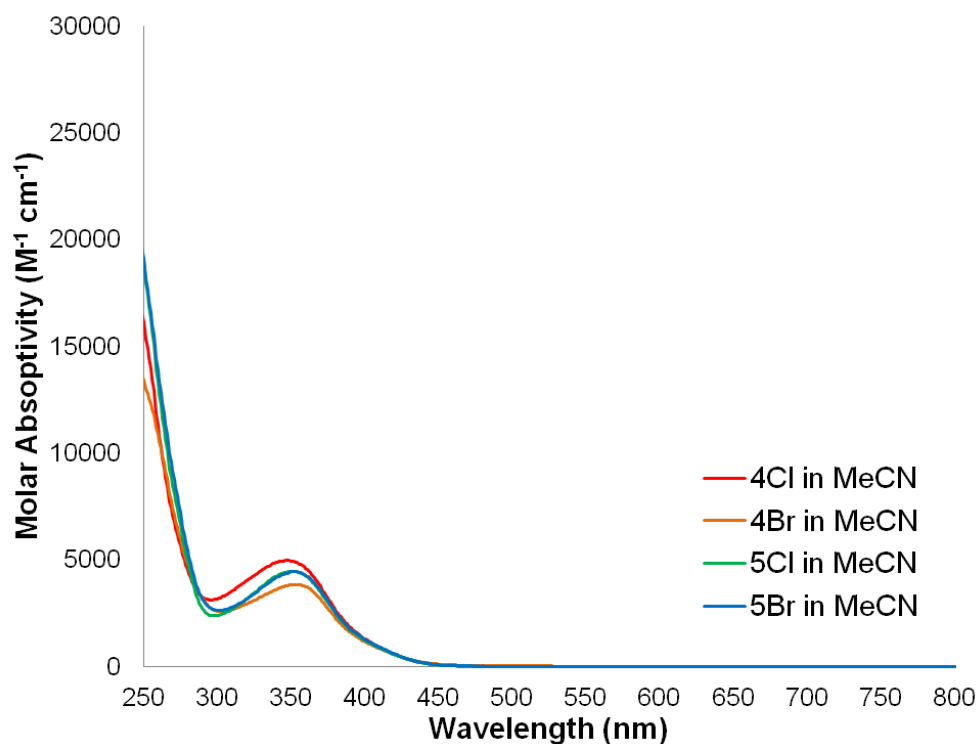


Figure 3.8: Absorption profile of **4-5Cl/Br** in *ca.*  $10^{-5}$  M acetonitrile solutions

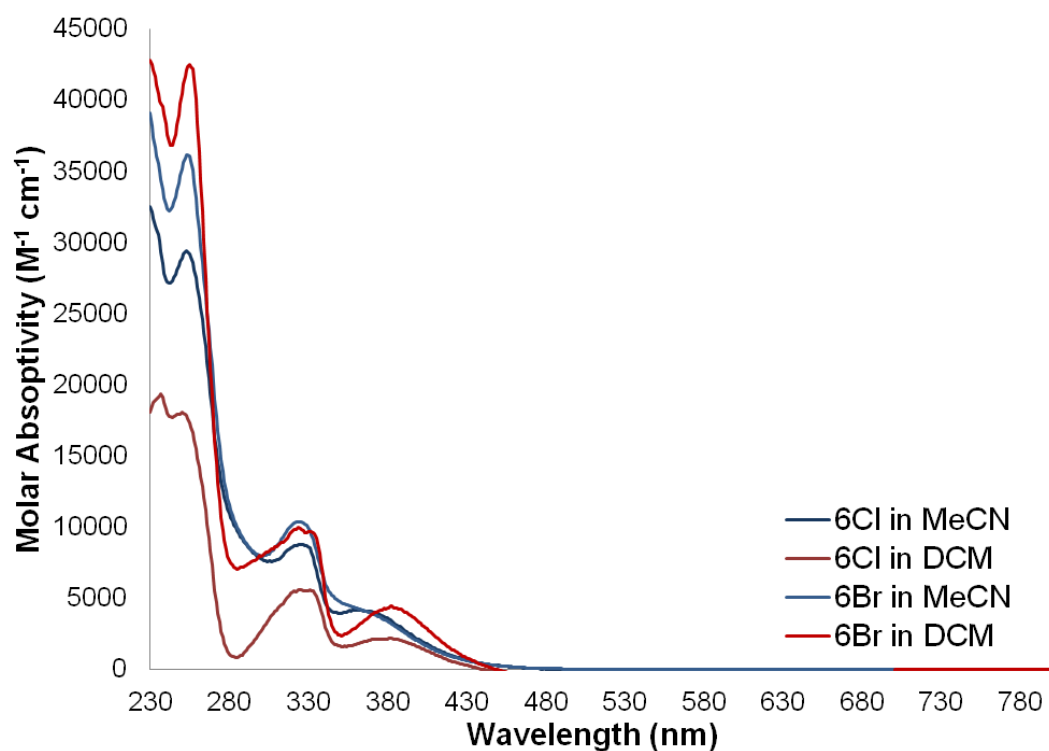


Figure 3.9: Absorption profile of **6Cl** and **6Br** in acetonitrile and dichloromethane (*ca.*  $10^{-5}$ M) solutions.

### 3.3.5 Absorption Profiles of the 1-(2-Quinoyl)-imidazol-2-ylidene Series

The absorption profiles of the 1-(2-quinoyl)-imidazol-2-ylidene series, compounds **6Cl** and **6Br**, in dichloromethane and in acetonitrile are depicted in **Figure 3.9**.

Unlike the **1-5Cl/Br**, **6Cl** and **6Br** exhibit a more structured absorption profile in dichloromethane with three distinct bands centred around 255 nm ( $>17000 \text{ M}^{-1}\text{cm}^{-1}$ ), 325 nm ( $>5000 \text{ M}^{-1}\text{cm}^{-1}$ ) and 385 nm ( $>2000 \text{ M}^{-1}\text{cm}^{-1}$ ). **6Cl** has an additional fourth, higher energy band at 237 nm in dichloromethane solutions. This band is less visible in acetonitrile solutions and appears as a small shoulder at 242 nm.

In acetonitrile solutions of **6Cl/Br**, the lowest energy band at  $\sim 385$  nm observed in dichloromethane, blueshifts to  $\sim 375$  nm. This broad band is therefore attributed to a charge transfer, in all likelihood an MLCT transition, due to its broad, structureless shape, solvatochromic nature and non-appearance in the absorption profile of the precursor salts.

The charge transfer band is quite red-shifted in comparison to the same band in the absorption profiles of **1-5Cl/Br** and this is attributed to the additional six-membered ring of the quinoxyl ring compared to the pyridyl and pyrimidyl rings. This increase in conjugation should theoretically lower the energy level of the LUMO and red-shift the absorption energy as was observed experimentally.

The band at 325 nm does not exhibit any solvatochromic behaviour upon changing the solvent from dichloromethane to acetonitrile. The band is therefore tentatively assigned to a  $\pi \rightarrow \pi^*$  transition with possible  $n \rightarrow \pi^*$  character. The high energy band at  $\sim 255$  nm and the band exhibited by **6Cl** at 237 nm are assigned to an intraligand (IL)  $\pi \rightarrow \pi^*$  transition involving the NHC ligand as they do not display any solvatochromic behaviour, have a high extinction coefficient and are similar to the high energy bands observed in the absorption profile of the precursor azolium salts as shown in **Figure 3.3**.

### 3.3.6 Absorption Profiles of the 1-(2-Quinoxyl)-imidazol-2-ylidene Series

The absorption profiles of the 1-(2-quinoxyl)-imidazol-2-ylidene series, compounds **7Cl** and **7Br**, in dichloromethane and in acetonitrile are depicted in **Figure 3.10**.

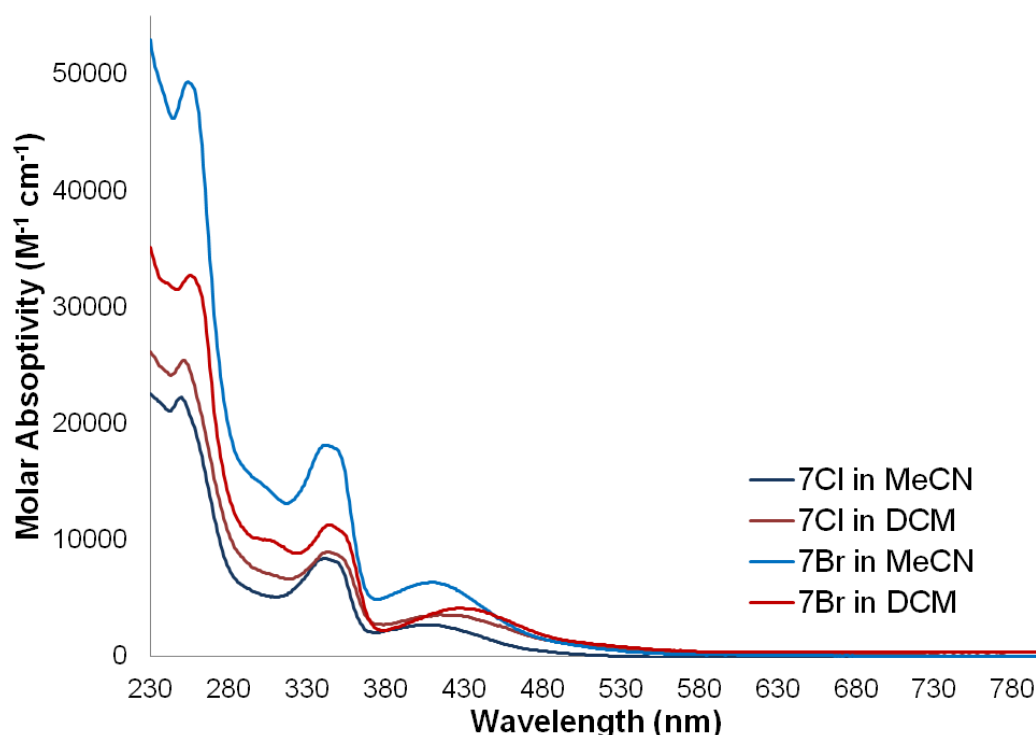


Figure 3.10: Absorption profile of **7Cl** and **7Br** in acetonitrile and dichloromethane (*ca.*  $10^{-5}$  M) solutions.

Much the same as the previous series, the absorption profiles of **7Cl** and **7Br** are more structured than that of **1-5Cl/Br**. The shape of the bands of the absorption spectra of **7Cl** and **7Br** are very similar to that observed for the **6Cl** and **6Br** however all of the absorption maxima are red-shifted.

There are three absorption bands at  $\sim 255$  nm ( $>25000$   $M^{-1}cm^{-1}$ ),  $\sim 344$  nm ( $>9000$   $M^{-1}cm^{-1}$ ) and  $\sim 425$  nm ( $>3600$   $M^{-1}cm^{-1}$ ). The high energy band at 255 nm is again assigned to a  $\pi \rightarrow \pi^*$  transition involving the  $\pi$  system of the NHC ligand due to its sharp profile, lack of solvatochromism and similarity to the high energy absorption band in the absorption profile of the precursor azolium salts.

The band at 344 nm is red-shifted compared to the same band for **6Cl** and **6Br** (~325 nm). The conjugation and overall aromaticity of the ligand systems are the same between the two series therefore the red-shift is attributed to increased electron deficiency of the quinoxaline ring compared to the quinoline ring. It is noteworthy that increasing the electron deficiency by changing the quinoline ring to the quinoxaline ring had a more pronounced effect on the absorption spectrum than that observed for changing the pyridine ring to the pyrimidine ring.

The lowest energy band at ~425 nm is significantly red-shifted compared to the lowest energy band of the preceding series. The band exhibits solvatochromic behaviour and blueshifts in acetonitrile. Based on this solvatochromic behaviour and broad, structureless shape this band is attributed to a MLCT transition.

### 3.4 Time Dependent- Density Functional Theory

Time Dependent- Density Functional Theory (TDDFT) calculations were performed to investigate the electron density distribution of the rhenium(I)-NHC tricarbonyl compounds to validate the interpretation of the experimental photophysical data *via* analysis of the simulated absorption spectra and HOMO-LUMO orbital contour diagrams. The simulated absorption spectra, calculated transitions and orbital contours are available in **Appendix 9.4** and **9.5**, the experimental parameters are defined in **Experimental Section 8.6** and the key data points are reiterated in **Table 3.3** and **Figure 3.11**. The calculations were performed using GAUSSIAN 09 in order to calculate the absorption spectra for synthesised complexes.<sup>74</sup> Prior to these calculations, the structures were relaxed at the B3LYP level of theory in the presence of an implicit solvent (dichloromethane). The Re atoms were treated with the Stuttgart–Dresden (SDD) effective core potential;<sup>75</sup> the Pople 6-311++G\*\* basis set was used for C, H, N, O, Cl, and Br atoms, and in all calculations the effect of the solvent was mimicked with the PCM solvation model,<sup>76</sup> with parameters adequate for dichloromethane. The low-lying singlet–singlet excitation energies were calculated at the same level of theory, and the spectra were reproduced as the superposition of functions with heights proportional to calculated intensities and a variance of 11 nm.

The predicted absorption spectra of compounds **1-7Cl/Br** are well aligned with the

experimental data previously discussed in **Section 3.3.2**. All fourteen compounds show two major transitions in the predicted absorption spectra, a lower energy transition around 370-470 nm and a higher energy transition around 260-320 nm.

Table 3.3: Selected highest intensity calculated transitions for compounds **1-7Cl/Br**.

Compound	Wavelength	Intensity	Levels	Character
<b>1Cl</b>	370.78 nm	0.1111	HOMO-1 -> LUMO	95.2 %
	260.23 nm	0.1771	HOMO-5 -> LUMO	51.8 %
<b>1Br</b>	378.37 nm	0.0821	HOMO-1 -> LUMO	95.8 %
	248.23 nm	0.1258	HOMO-6 -> LUMO	41.2 %
<b>2Cl</b>	374.46 nm	0.1068	HOMO-1 -> LUMO	94.3 %
	258.49 nm	0.1255	HOMO-6 -> LUMO	63.7 %
<b>2Br</b>	382.62 nm	0.0805	HOMO-1 -> LUMO	94.9 %
	261.83 nm	0.1319	HOMO-7 -> LUMO	65.5 %
<b>3Cl</b>	376.08 nm	0.1112	HOMO-1 -> LUMO	95.0 %
	265.94 nm	0.2067	HOMO-4 -> LUMO	77.7 %
<b>3Br</b>	384.74 nm	0.0774	HOMO-1 -> LUMO	96.1 %
	270.80 nm	0.1328	HOMO-5 -> LUMO	53.1 %
<b>4Cl</b>	390.44 nm	0.0825	HOMO-1 -> LUMO	91.3 %
	273.00 nm	0.0980	HOMO-5 -> LUMO+1	72.0 %
<b>4Br</b>	390.44 nm	0.0825	HOMO-1 -> LUMO	91.3 %
	273.00 nm	0.0980	HOMO-5 -> LUMO+1	72.0 %
<b>5Cl</b>	391.58 nm	0.0863	HOMO-1 -> LUMO	91.6 %
	271.84 nm	0.0943	HOMO-4 -> LUMO	51.5 %
<b>5Br</b>	401.64 nm	0.0651	HOMO-1 -> LUMO	94.3 %
	273.97 nm	0.0998	HOMO-5 -> LUMO	60.4 %
<b>6Cl</b>	410.61 nm	0.0984	HOMO-1 -> LUMO	97.5 %
	298.08 nm	0.1358	HOMO-2 -> LUMO+1	33.3 %
<b>6Br</b>	420.40 nm	0.0758	HOMO-1 -> LUMO	97.8 %
	298.90 nm	0.1038	HOMO-6 -> LUMO	49.9 %
<b>7Cl</b>	462.54 nm	0.0955	HOMO-1 -> LUMO	98.4 %
	320.22 nm	0.1113	HOMO-5 -> LUMO	25.8 %
<b>7Br</b>	477.66 nm	0.0714	HOMO-1 -> LUMO	98.7 %
	318.47 nm	0.2730	HOMO-7 -> LUMO	28.3 %

The TDDFT calculations predict that for all of the rhenium(I)-NHC tricarbonyl complexes the lower energy transition has high (>91%) HOMO-1→LUMO character as shown in **Table 3.3**. The calculated orbital contours of the HOMO-1 and LUMO for a representative selection of the compounds from each of the four series is shown in **Figure 3.11**. For all fourteen compounds the HOMO-1 is largely comprised of the 5d orbitals of the rhenium metal centre and the 3p or 4p orbitals of the halide ligand.

The LUMO can be seen to be localised largely on the  $\pi^*$  orbitals of the N-donor ring of the NHC ligand and the  $\pi^*$  orbital of the carbene carbon as shown in **Figure 3.11**. For the more conjugated 1-(2-quinoyl)-imidazol-2-ylidene and 1-(2-quinoxyl)-imidazol-2-ylidene ligand systems the LUMO can be seen to extend over the whole  $\pi^*$  system of the fused rings.

Based on these calculations, the lower energy transition at ~370-470 nm can be more accurately characterised as a metal-ligand to ligand charge transfer (MLLCT) transition rather than a pure metal to ligand charge transfer (MLCT) transition due to the participation of the halide ligand in the HOMO-1. It is noteworthy that the orbitals of the R substituent are not involved in the MLLCT transition which further indicates that modifications at this site will not impact on the optical properties as strongly as modification to the N-donor ring.

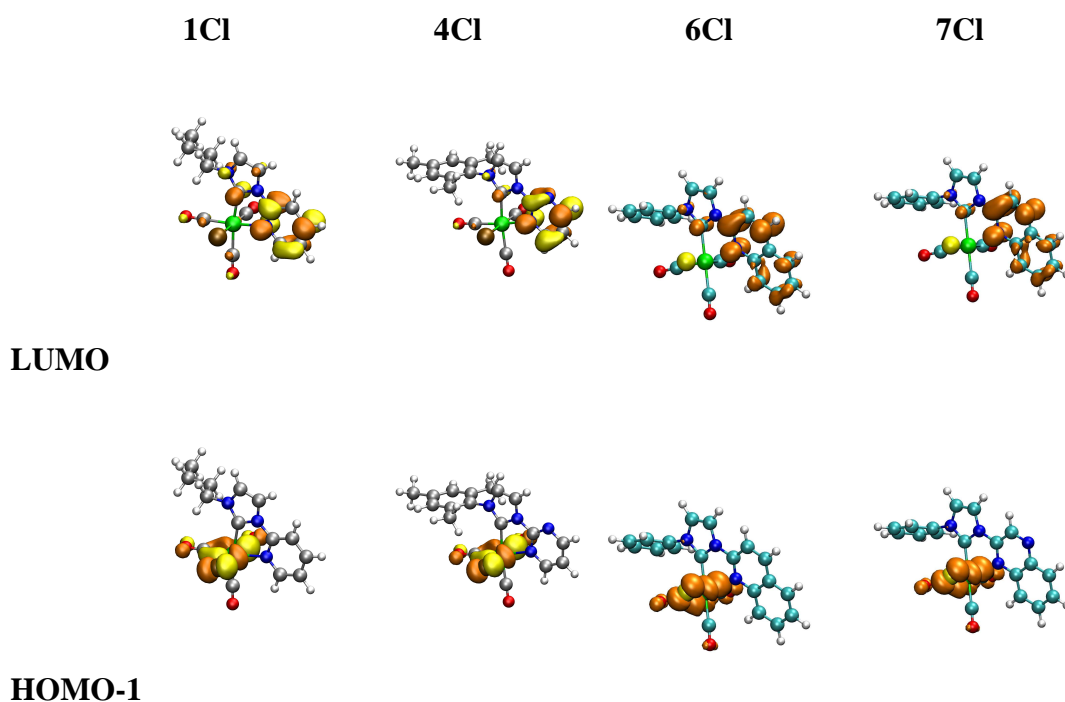


Figure 3.11: Calculated orbital contours of the LUMO and HOMO-1 of exemplar compounds **1Cl**, **4Cl**, **6Cl** and **7Cl**.

The higher energy transition at ~260-320 nm was experimentally assigned to an intraligand (IL)  $\pi \rightarrow \pi^*$  transition in **Section 3.3.2**. Unlike the lower energy MLLCT transition, the levels involved in the higher energy transition differ for each of the

compounds. The acceptor orbitals are comprised of either the LUMO or the LUMO+1 for compounds **4Cl/Br** and **6Cl**. The donor orbitals vary from the HOMO-2 all the way to the HOMO-7. Analysis of the orbital contours of the LUMO+1 depicted **Appendix 9.5** for compounds **4Cl/Br** and **6Cl** show that the LUMO+1 is largely comprised of the  $\pi^*$  orbitals of the imidazole ring and the N-donor ring. The lower HOMO orbitals involved in the higher energy transition in **Table 3.3** were analysed. Whilst the transitions were largely IL in nature, for several of the rhenium(I)-NHC complexes the orbitals involved contained small contributions from the rhenium metal centre. Therefore the higher energy transition around ~260-320 nm can be better characterised as intraligand  $\pi \rightarrow \pi^*$  transition with slight MLCT character.

## 3.5 Excitation and Emission Profiles

### 3.5.1 The 1-(2-Pyridyl)-imidazol-2-ylidene Series

The emission maxima, lifetime and quantum yield values of compounds **1-7Cl/Br** in air equilibrated and degassed dichloromethane solutions are summarised in **Table 3.4**. The normalised excitation and emission spectra of the 1-(2-pyridyl)-imidazol-2-ylidene series, compounds **1-3Cl/Br**, in dichloromethane solutions are shown in **Figure 3.12**. All six compounds show very similar, broad, structureless emission centred around 520 nm. This is typical of emission from a charge transfer state such as an MLLCT. The emission maxima is consistent between the chloro and bromo analogues of the series.

This result is similar to the Re(I)-benzimidazol-2-ylidene systems; **73** and **74**. As expected, the emission of the series is blueshifted from that of a standard Re(I)-diimine systems such as *fac*-[Re(phen)CO<sub>3</sub>Cl] (**113**). This is attributed to the reduced conjugation of the imidazol-2-ylidene system NHC system versus the diimine systems.

Table 3.4: Photophysical properties of compounds **1-7Cl/Br** at room temperature in *ca.* 10<sup>-5</sup> M dichloromethane solutions.

Compound	$\lambda_{em}$ (nm)	$\tau^a$ (ns)	$\tau^b$ (ns)	$\Phi^a$	$\Phi^b$
<b>1Cl</b>	514	32	43	0.007 <sup>c</sup>	0.012 <sup>c</sup>
<b>1Br</b>	520	9 (73%), 36 (27%)	10 (65%), 48 (35%)	0.006 <sup>c</sup>	0.043 <sup>c</sup>
<b>2Cl</b>	520	50	80	0.008 <sup>d</sup>	0.014 <sup>d</sup>
<b>2Br</b>	510	19	24	0.001 <sup>d</sup>	0.002 <sup>d</sup>
<b>3Cl</b>	522	60	140	0.03 <sup>d</sup>	0.09 <sup>d</sup>
<b>3Br</b>	516	19	23	0.02 <sup>d</sup>	0.03 <sup>d</sup>
<b>4Cl<sup>f</sup></b>	582	99	300	0.013 <sup>d</sup>	0.027 <sup>d</sup>
<b>4Br</b>	577	106	373	0.013 <sup>d</sup>	0.033 <sup>d</sup>
<b>5Cl</b>	583	98	211	0.016 <sup>d</sup>	0.024 <sup>d</sup>
<b>5Br</b>	575	109	397	0.019 <sup>d</sup>	0.060 <sup>d</sup>
<b>6Cl</b>	626	240	1065	0.03 <sup>d</sup>	0.13 <sup>d</sup>
<b>6Br</b>	622	263	993	0.03 <sup>d</sup>	0.10 <sup>d</sup>
<b>7Cl</b>	494	5	5	0.039 <sup>d</sup>	0.052 <sup>d</sup>
<b>7Br</b>	432	2	2	<0.001 <sup>d</sup>	<0.001 <sup>d</sup>
<i>fac</i> -[Re(PyBzBu)(CO) <sub>3</sub> Cl] (73) <sup>49</sup>	510	52	89	-	0.010 <sup>d</sup>
<i>fac</i> -[Re(PyBzBu)(CO) <sub>3</sub> Br] (74) <sup>49</sup>	503	15	16	-	0.002 <sup>d</sup>
<i>fac</i> -[Re(phen)(CO) <sub>3</sub> Cl] (113) <sup>7,73</sup>	602 <sup>73</sup>	173 <sup>73</sup>	288 <sup>73</sup>	0.0363 <sup>e</sup>	
<i>fac</i> -[Re(bpy)(CO) <sub>3</sub> Cl] (117)	622 <sup>38</sup>		51 <sup>38</sup>		0.005 <sup>38</sup>

<sup>a</sup>air-equilibrated solution, <sup>b</sup>degassed solution, <sup>c</sup>rhodamine 101 in air-equilibrated ethanol used as the reference, <sup>d</sup>[Ru(bpy)<sub>3</sub>]Cl<sub>2</sub> in air-equilibrated water used as the reference, <sup>e</sup>RCA 7102 PMT detector, quantum yields in 298 K solutions measured in benzene solvent, the author did not state if the solution was degassed,<sup>7</sup> <sup>f</sup> previously reported by Chen et al. however different values were obtained.<sup>51</sup>

Additionally, the emission maxima do not significantly alter upon changing the R-substituent from the butyl to mesityl to phenyl. This is attributed to the phenyl and mesityl rings not lying completely co-planar with the imidazol-pyridyl system.

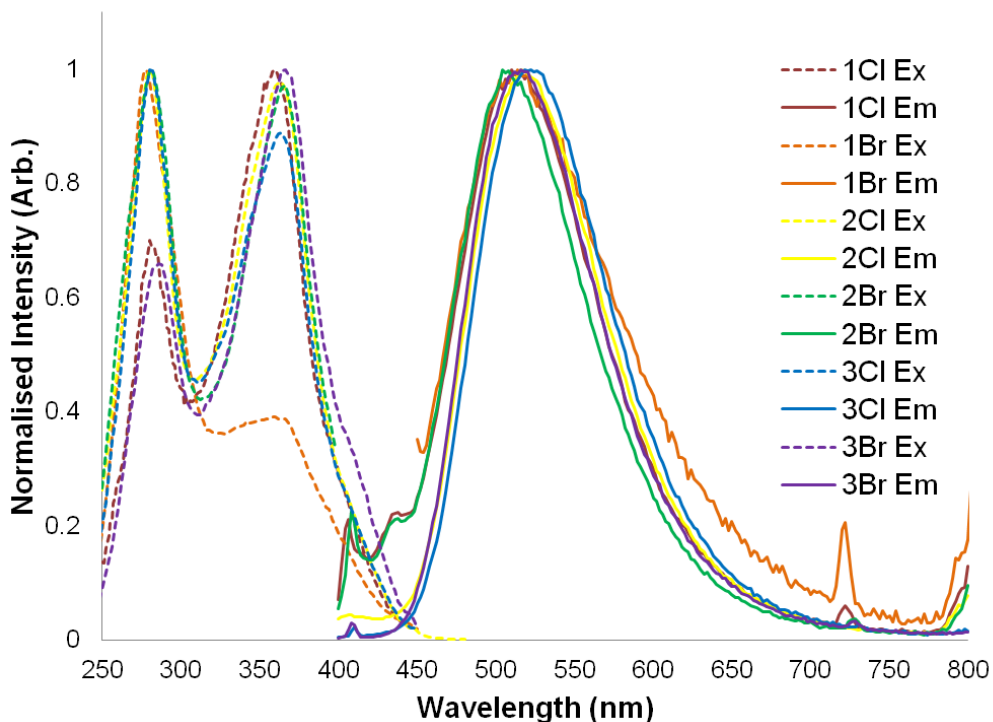
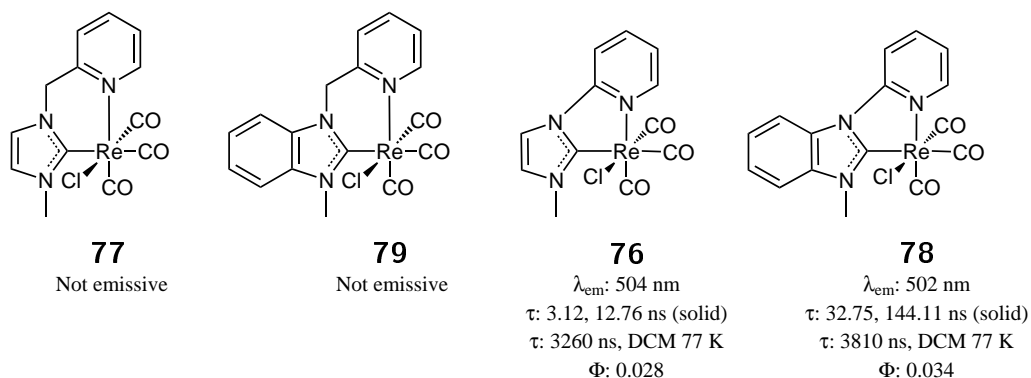


Figure 3.12: Normalised excitation (dashed line) and emission (bold line) spectra of **1-3Cl/Br**, in dichloromethane (*ca.*  $10^{-5}$  M).

The observed excited state lifetime values ( $\tau_{(obs)}$ ) increase upon degassing which is indicative of emission from a triplet state. As discussed in **Section 1.5.10**, triplet excited states can be easily quenched by the presence of ground state triplet oxygen *via* singlet oxygen sensitisation. Therefore, when oxygen is removed from the system, this quenching pathway is eliminated. The excited state lifetimes of compounds **1-3Cl/Br** are consistent with previously reported Re(I)-NHC tricarbonyl systems but are slightly lower than other solution state measurements for Re(I)-diimine complexes.<sup>8,69</sup>

Previous studies on the Re(I)-benzimidazol-2-ylidene systems, **73** and **74** found the bromo analogue to have a significantly reduced lifetime in comparison to the chloro compound. This was attributed to the higher lability of the bromo ligand.<sup>49,67</sup> A similar trend is observed herein where **2Cl** (50 ns, air equil) and **3Cl** (60 ns, air equil) have slightly longer lifetimes than their bromo counterparts **2Br** (19 ns, air equil) and **3Br** (19 ns, air equil) in both degassed and air-equilibrated environments. Furthermore, **2Br** and **3Br** have slightly lower quantum yield values when compared to their chloro analogues **2Cl** and **3Cl** which is also attributed to the increased lability of the

bromo ligand versus the chloro ligand. As the lifetime of **1Br** was found to be bi-exponential this trend cannot be extended to the butyl chain series; compounds **1Cl** and **1Br**. The biexponential behaviour for **1Br** is tentatively assigned to contribution from a  $^1\text{LC}$  and/or  $^1\text{MLLCT}$  states similar to the biexponential behaviour observed for *fac*-[Re(PyBzBu)(CO)<sub>3</sub>Br] (**74**) which is discussed further in the next chapter.<sup>49</sup>



Scheme 3.3: Photophysical properties of a series Re-pyridyl-NHC compounds in degassed dichloromethane solutions. Lifetime values were calculated from solid state samples and DCM solutions at 77 K (Adapted from Li, 2012).<sup>69</sup>

The quantum yield of the 1-(2-pyridyl)-imidazol-2-ylidene series could be considered low in comparison to the more efficient Re(I)-diimine systems discussed in **Section 1.2** however the values are comparable to similar Re(I)-NHC tricarbonyl systems. The 1-(2-pyridyl)-benzimidazol-2-ylidene compounds, **73** and **74**, had quantum yields of 0.010 and 0.002 respectively whilst Chen, Zheng and co-workers have reported quantum yield values for **76** and **78** of 0.028 and 0.034 respectively in degassed solutions.<sup>49,69</sup>

### 3.5.2 The 1-(2-Pyrimidyl)-imidazol-2-ylidene Series

The normalised excitation and emission spectra of **4-5Cl/Br** in dichloromethane are shown in **Figure 3.13**. As per the previous series, **4-5Cl/Br** also display broad, structureless emission typical of emission from a charge transfer, specifically MLLCT, excited state.

The emission maxima for **4-5Cl/Br** are centred around 580 nm, which is bathochromically shifted by 60 nm in comparison to the **1-3Cl/Br**. This demonstrates that the

tunability of the photophysical properties of these rhenium(I)-NHC tricarbonyl compounds can be shifted from the green region to the yellow region by making a simple structural change to the compound. The red-shift upon going from the 1-(2-pyridyl)-imidazol-2-ylidene series to the 1-(2-pyrimidyl)-imidazol-2-ylidene series is expected and is attributed to the increased electron deficiency of the pyrimidyl ring and consequent lowering of the energy level of the LUMO.

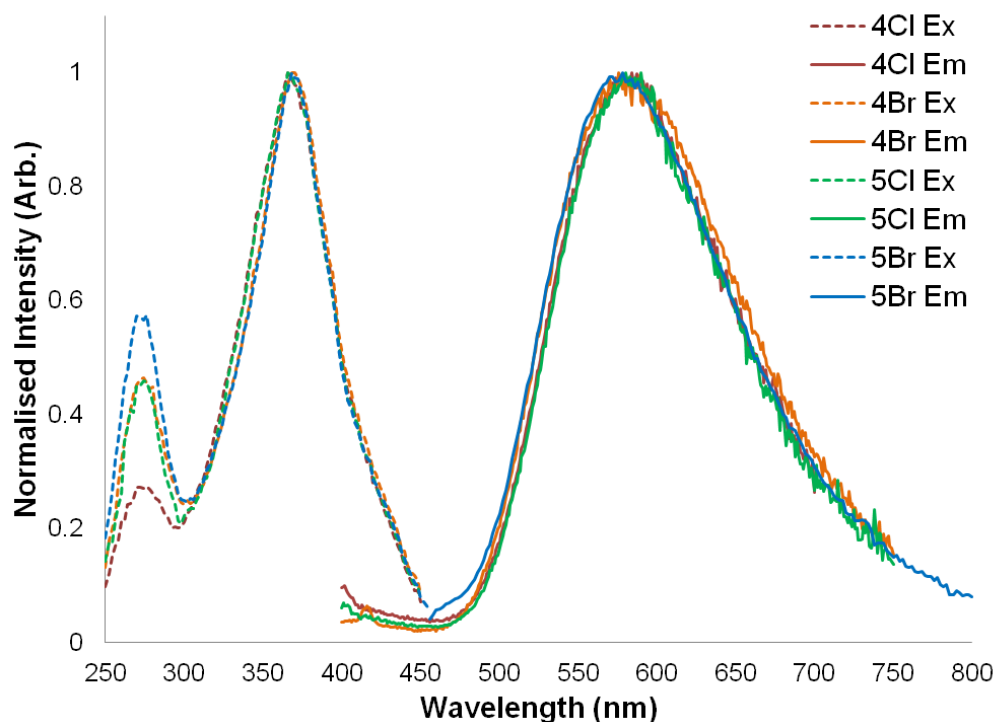


Figure 3.13: Normalised excitation (dashed line) and emission (bold line) spectra of **4-5Cl/Br** in dichloromethane (*ca.*  $10^{-5}$  M).

### 3.5.3 The 1-(2-Quinoyl)-imidazol-2-ylidene Series

The normalised excitation and emission spectra of the compounds in dichloromethane are shown in **Figure 3.14**. Compounds **6Cl** and **6Br** display a broad, structureless emission, indicative of emission from a charge transfer state. As expected, the emission maxima of the 1-(2-quinoyl)-imidazol-2-ylidene series is significantly red-shifted (100 nm) compared to the parent 1-(2-pyridyl)-imidazol-2-ylidene series. This bathochromic shift is attributed to the increased conjugation of the N-donor ring which lowers the energy of the LUMO. The magnitude of the redshift is much greater than that achieved

by merely increasing the electron deficiency upon changing the pyridyl ring to the pyrimidyl ring.

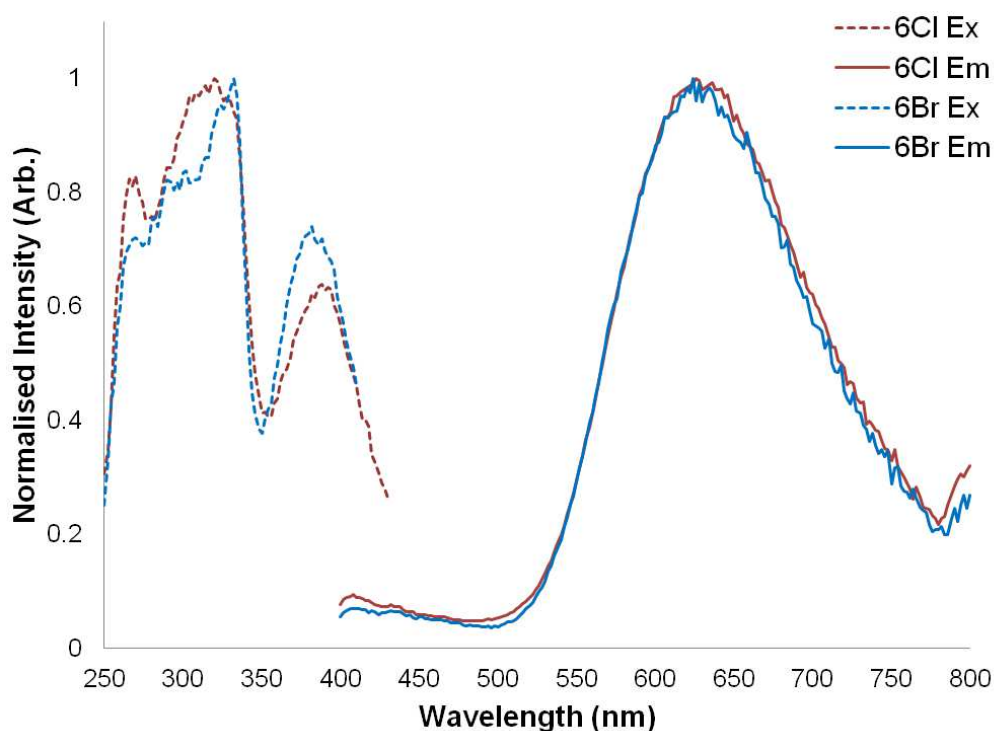


Figure 3.14: Normalised excitation (dashed line) and emission (bold line) spectra of **6Cl/Br** in dichloromethane (*ca.*  $10^{-5}$  M).

As per compounds **1-5Cl/Br**, the excited state lifetime values of **6Cl** and **6Br** lengthen upon degassing. As previously stated this is indicative of a triplet excited state. The lifetime values for the 1-(2-quinoyl)-imidazol-2-ylidene series are much longer than of compounds **1-5Cl/Br**. The quantum yield values are also greater than the values of compounds **1-5Cl/Br** by one order of magnitude. This is attributed to potential mixing with LC states.

### 3.5.4 The 1-(2-Quinoxyl)-imidazol-2-ylidene Series

The normalised excitation and emission spectra for **7Cl** in dichloromethane is shown in **Figure 3.15**. The emission of **7Br** is so weak it could be considered non-emissive for practical purposes and is shown in **Figure A1.1** in **Appendix 9.2**.

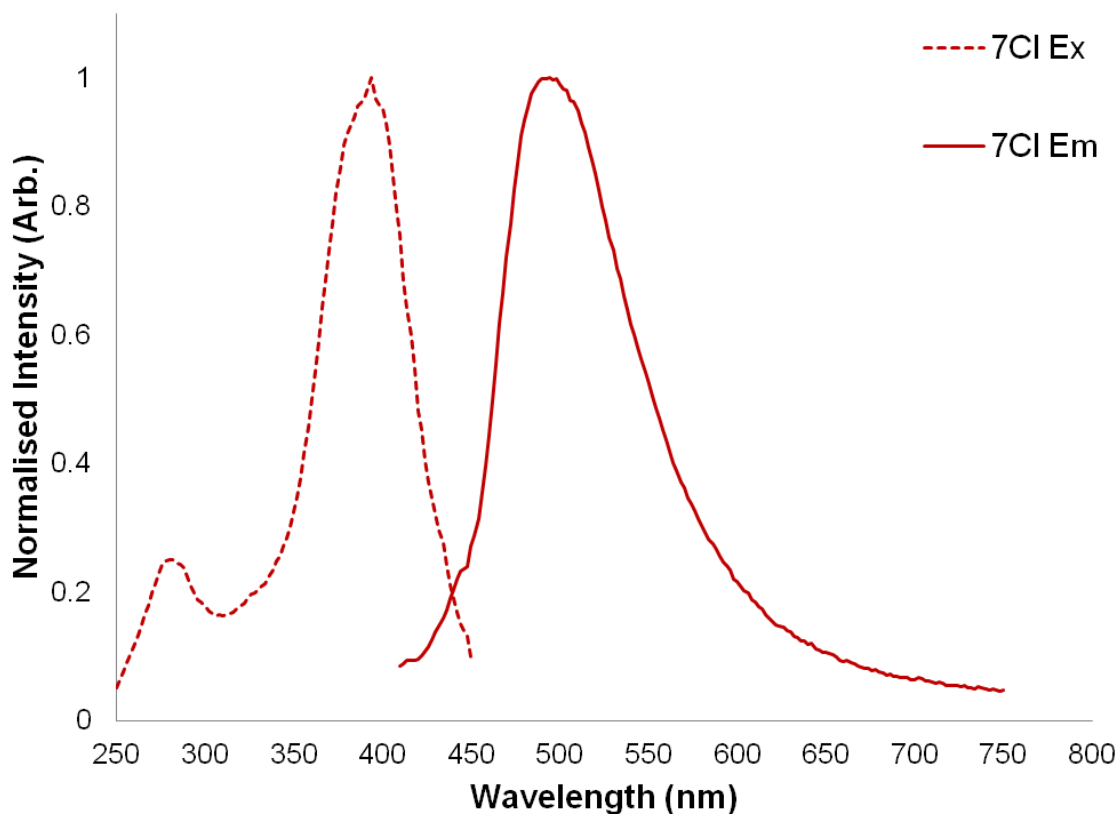


Figure 3.15: Normalised excitation (dashed line) and emission (bold line) spectra of **7Cl** in dichloromethane (*ca.*  $10^{-5}$  M).

The emission maximum of **7Cl** is centred at 494 nm which is also very blueshifted in comparison to the preceding series. The blueshift in the emission maximum of **7Cl** is unexpected as the increased the conjugation and electron deficiency of the ligand should theoretically red-shift the emission however the significant blueshift is observed experimentally. The excited state lifetime of **7Cl** is also very short being 5 ns. This is relatively short lived not only in comparison to compounds **1-6Cl/Br** but for rhenium(I) complexes in general.<sup>8</sup>

### 3.5.5 Photophysical Properties at 77 K

The emission maxima and excited state lifetimes values from frozen matrices of compounds **1-7Cl/Br** are compiled in **Table 3.5**. The emission profiles of compounds **1-3Cl/Br** in frozen dichloromethane solutions are shown in **Figure 3.16**.

Table 3.5: Emission maxima and observed excited state lifetime of compounds **1-7Cl/Br** in a dichloromethane frozen matrix (77 K).

Emission (77 K)		
Compound	$\lambda_{em}$ (nm)	$\tau$ ( $\mu$ s)
<b>1Cl</b>	462	5.7
<b>1Br</b>	464	1.9 (14%) 6.9 (86%)
<b>2Cl</b>	470	4.9 (27%) 9.3 (73%)
<b>2Br</b>	470	2.6 (17%) 7.9 (83%)
<b>3Cl</b>	482	5.2
<b>3Br</b>	474	5.6
<b>4Cl</b>	508	10.3
<b>4Br</b>	510	8.5
<b>5Cl</b>	504	7.6
<b>5Br</b>	512	6.0
<b>6Cl</b>	552	14.4
<b>6Br</b>	562	15.0
<b>7Cl</b>	610	3.6
<b>7Br</b>	610	5.3

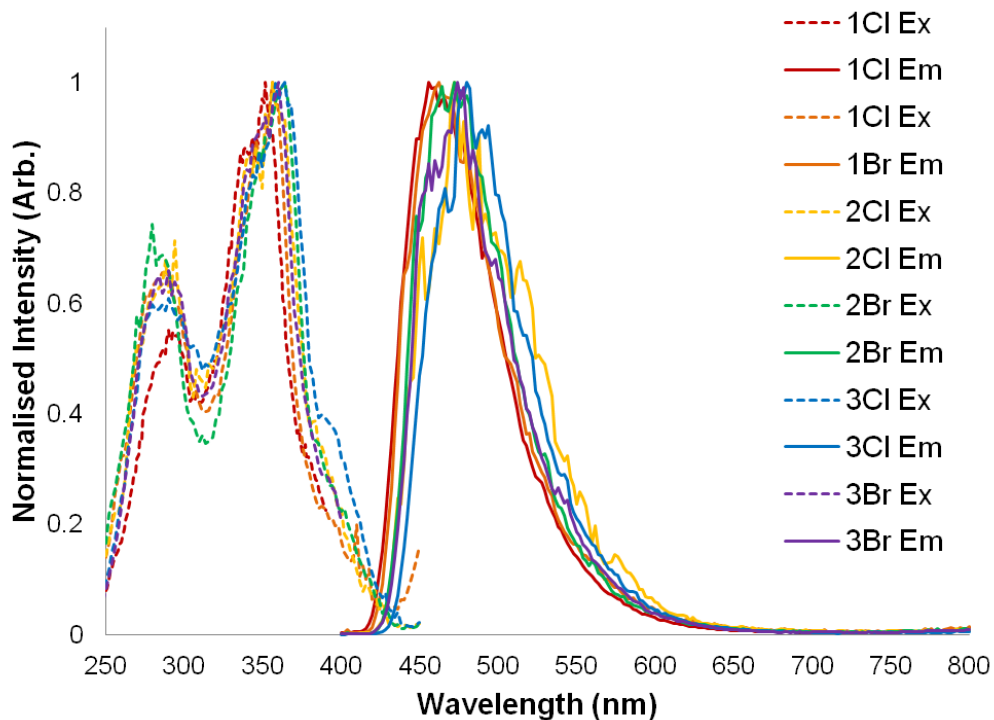


Figure 3.16: Excitation and emission spectra of **1-3Cl/Br** in a frozen *ca.*  $10^{-5}$  M dichloromethane matrix at 77 K.

The structure of the emission profile for compounds **1-3Cl/Br** is still quite broad and however there is a small amount of fine structure apparent. This fine structure could be caused by ligand centred (LC) transitions indicating that at 77 K that compounds **1-3Cl/Br** are emissive from a mixed  $^3\text{LC}$ - $^3\text{MLLCT}$  state rather than a pure  $^3\text{MLLCT}$ . The LC transitions are more prominent in a rigid matrix due to the rigidochromic effect previously explained in **Section 1.5.9**. The emission maxima are blueshifted compared to the room temperature values which is also attributed to the rigidochromic effect.

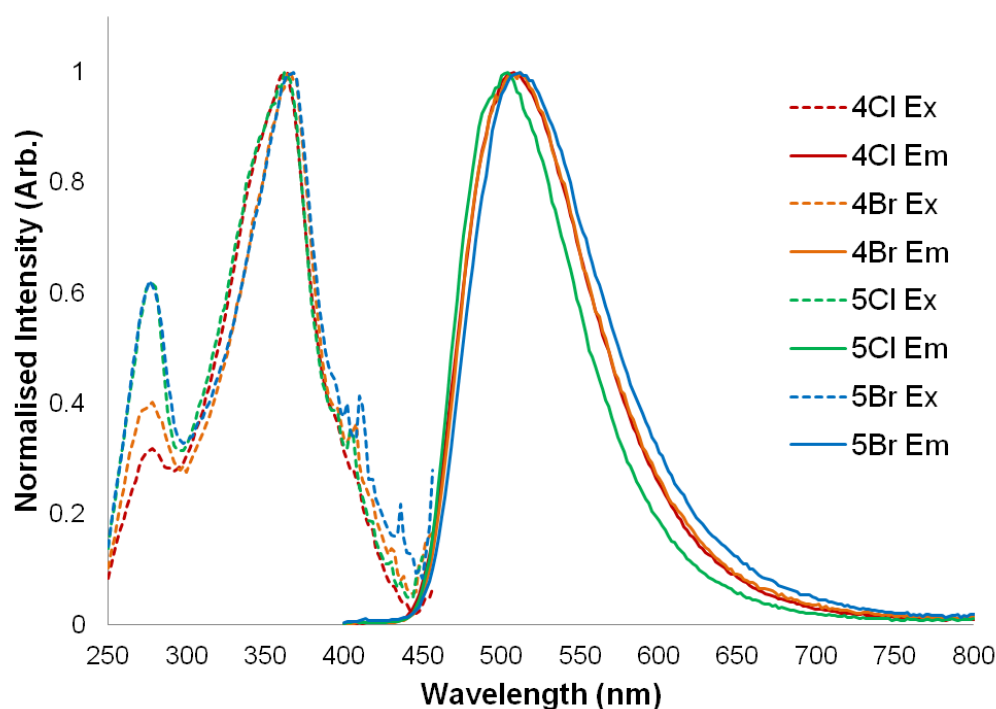


Figure 3.17: Normalised excitation and emission spectra of **4-5Cl/Br** in a frozen *ca.*  $10^{-5}$  M dichloromethane matrix at 77 K.

The 77 K emission profiles of compounds **4-5Cl/Br**, are displayed in **Figure 3.17**. The emission profiles of the 1-(2-pyrimidyl)-imidazol-2-ylidene series have retained their shape upon cooling to 77 K. There is a small amount of fine structure apparent however it is not as prominent as that observed for compounds **1-3Cl/Br**. Therefore the emission of compounds **4-5Cl/Br** at 77 K is still characterised as occurring from an  $^3\text{MLLCT}$  state. The emission maxima is blueshifted compared to the room temperature measurements further confirming the identity of the emissive state as MLLCT. As

expected the frozen matrix excited state lifetime values are elongated compared to the ambient temperature measurements.

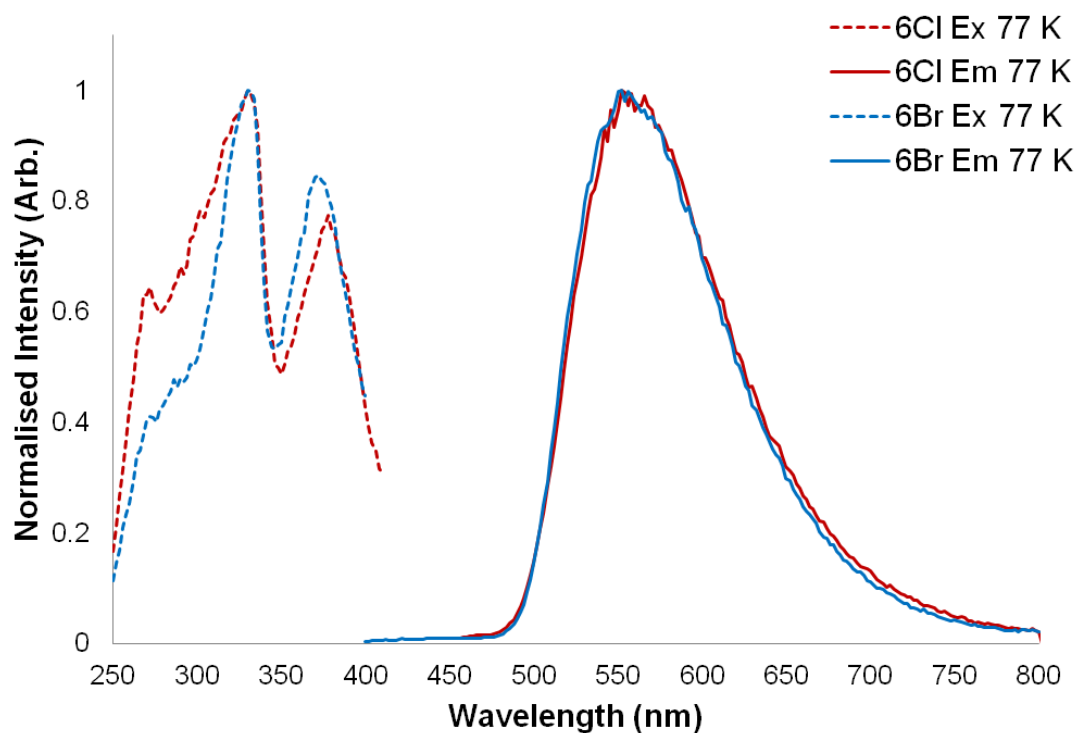


Figure 3.18: Normalised excitation and emission spectra of **6Cl** and **6Br** in a frozen *ca.*  $10^{-5}$  M dichloromethane matrix at 77 K.

The 77 K emission profiles of compounds **6Cl/Br** are depicted in **Figure 3.18**. Examination of the emission profiles at 77 K of **6Cl/Br** show that the emission profiles retain their broad, structureless shape. Additionally, the emission has blueshifted as would be expected from emission occurring from a  $^3\text{MLLCT}$  state. As both of the emission profiles exhibit no fine structure and hypsochromically shift it would seem that at 77 K the emissive state is predominantly  $^3\text{MLLCT}$  in character.

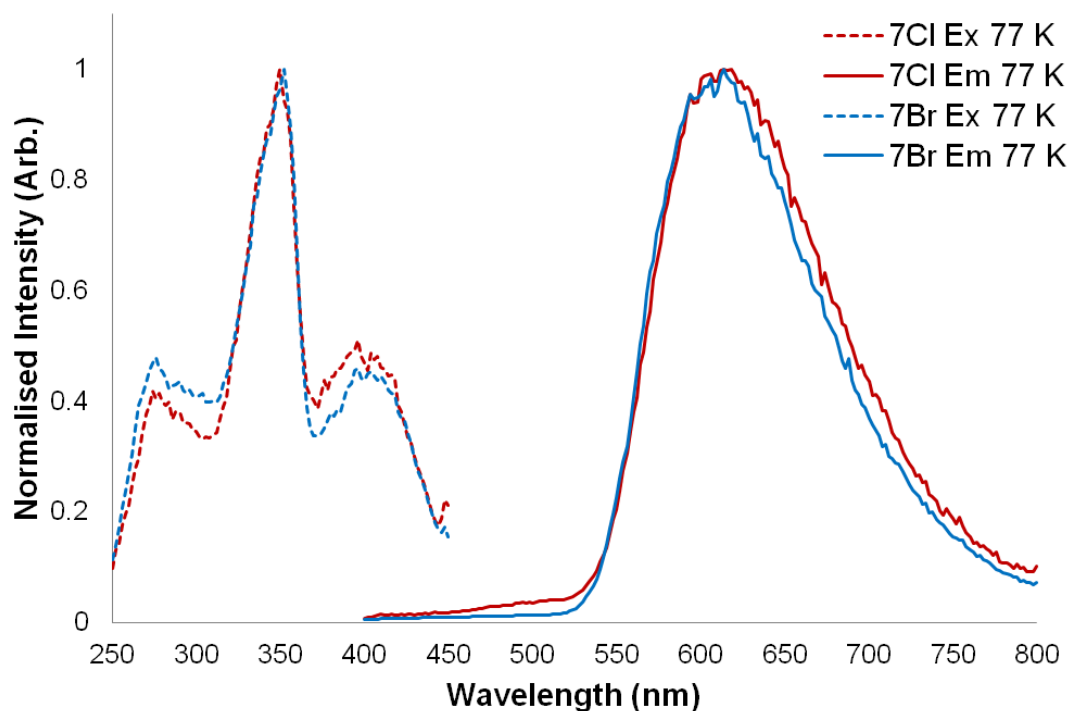


Figure 3.19: Normalised excitation and emission spectra of **7Cl** and **7Br** in a frozen *ca.*  $10^{-5}$  M dichloromethane matrix at 77 K.

The 77 K emission profiles of compounds **7Cl/Br** are depicted in **Figure 3.18**. It is noteworthy that at 77 K **7Br** exhibits a detectable emission unlike at room temperature where it was considered non-emissive. As per the preceding series, the excited state lifetime values of compounds **7Cl** and **7Br** at 77 K have significantly lengthened compared to the 298 K measurements. However, unlike the compounds **1-6Cl/Br**, the emission maxima at 77 K for **7Cl** and **7Br** is red-shifted in comparison to the room temperature measurements. The temperature dependency of the emission can be seen in **Figure 3.20** which depicts how the red-shifted emission at 77 K hypsochromically shifts upon allowing the frozen matrix to melt to 298 K. The largest temperature shift, denoted by the arrow, occurs at 47 K. This data indicates that at ambient conditions, the  $^3\text{MLLCT}$  emission is quenched.

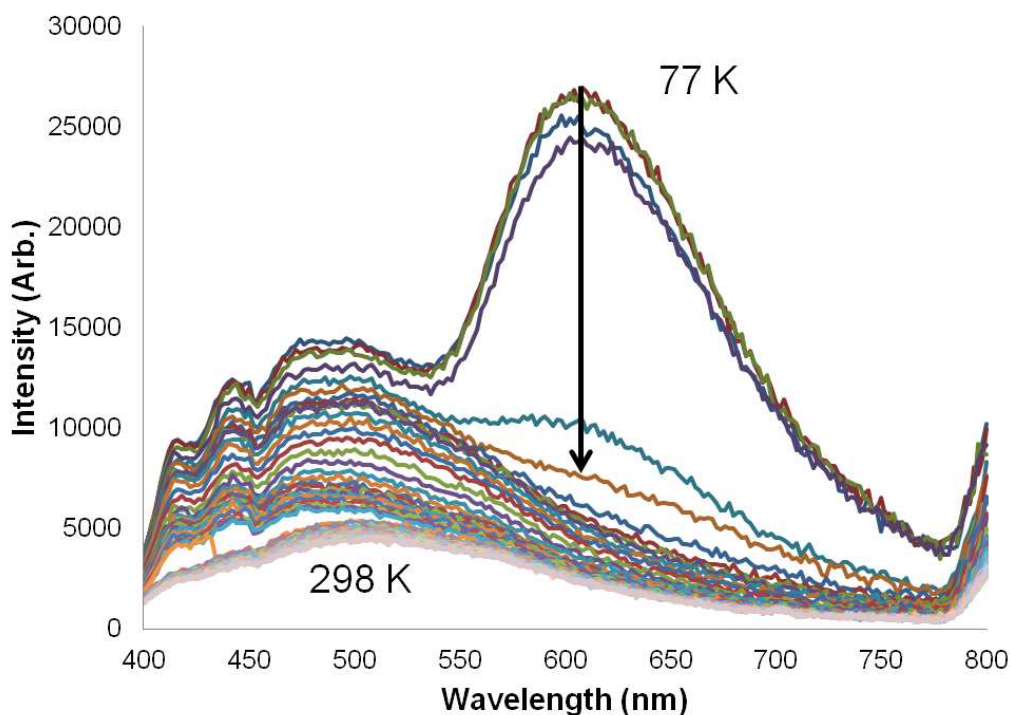


Figure 3.20: Temperature emission map of **7Cl** in a *ca.*  $10^{-5}$  M DCM solution excited at  $\lambda_{\text{ex}}$  350 nm for 50 consecutive scans at successively increasing temperature increments.

### 3.6 Singlet Oxygen Phosphorescence

Emission from triplet excited states is greatly effected by the presence of oxygen due to singlet oxygen sensitisation as previously described in **Section 1.5.10**. Detecting the presence of singlet oxygen is therefore one way to confirm that the emissive state of a molecule is triplet in multiplicity. The most definitive way to detect singlet oxygen is by detecting the characteristic line-like phosphorescence of singlet oxygen at 1270-1275 nm.<sup>46</sup> The phosphorescence of singlet oxygen is more visible in non-protic solvents such as dichloromethane as it efficiently quenched by the O-H vibrations of protic solvents.

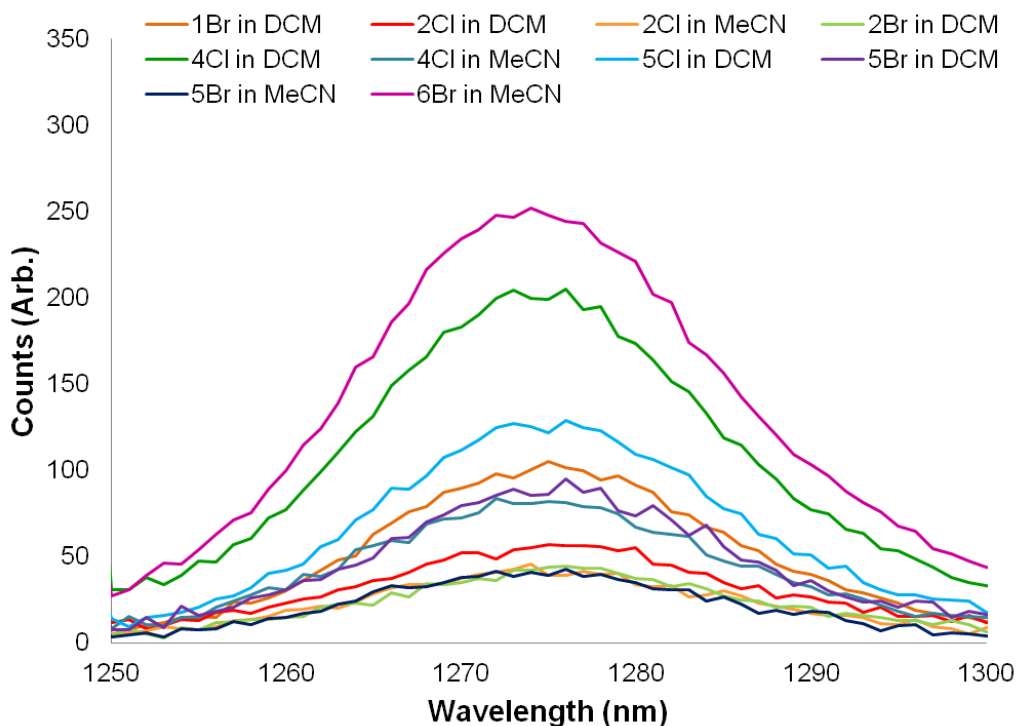


Figure 3.21: Non-normalised emission spectra showing the phosphorescence of  $^1\text{O}_2$  sensitised by various rhenium(I)-NHC tricarbonyl compounds and  $\text{Ru}(\text{bpy})_3\text{Cl}_2$  in ca.  $10^{-5}$  M dichloromethane or acetonitrile solutions.

By exciting to the lowest excited state, the phosphorescence of singlet oxygen at 1275 nm was visible in the following trialled compounds **1Br**, **2Cl**, **2Br**, **4Cl**, **5Cl**, **5Br** and **6Br** at room temperature as demonstrated in **Figure 3.21**. Measurements for **2Cl**, **4Cl** and **5Br** were performed in both acetonitrile and dichloromethane solutions and singlet oxygen phosphorescence was observed for both. The detected presence of singlet oxygen is further evidence that compounds **1-6Cl/Br** are emissive from triplet states. No detectable singlet oxygen phosphorescence was observed for compounds **7Cl** and **7Br** in either dichloromethane or acetonitrile solution. As **7Cl** and **7Br** has significantly shorter emissive state lifetimes than the other compounds the potential for oxygen sensitisation is reduced.

### 3.7 Summary and Concluding Remarks

The photophysical properties of fourteen rhenium(I)-NHC tricarbonyl compounds were investigated and they were found to perform as well as similar rhenium(I)-NHC sys-

tems. The observed excited state lifetime and quantum yield of the 1-(2-pyridyl)-imidazol-2-ylidene compounds, **1-3Cl/Br**, was less than expected indicating that some non-radiative channel may be active in these compounds. Compounds **1-6Cl/Br** were found to be emissive at room temperature in dichloromethane solutions from an <sup>3</sup>MLLCT state. The emission maximum was observed to red-shift as the N-donor ring was made more electron deficient and more conjugated proving that the optical output can be tuned by modifying the N-donor ring. Modifications to the halide ancillary ligand and R substituent did not effect the optical output of the compounds. The emission of **7Br** was extremely weak and the compound was considered non-emissive at room temperature for practical purposes. At ambient conditions the emission from **7Cl** was significantly blueshifted and the observed lifetime was extremely short indicating that the the triplet state is thermally suppressed. At 77 K in a frozen matrix the emission of **7Cl** was seen to red-shift indicating that emission from the triplet state was possible. **7Br** was also emissive at 610 nm from an apparent triplet state at 77 K.



# Chapter 4

## Literature Overview of Photochemically Active Rhenium(I) Complexes

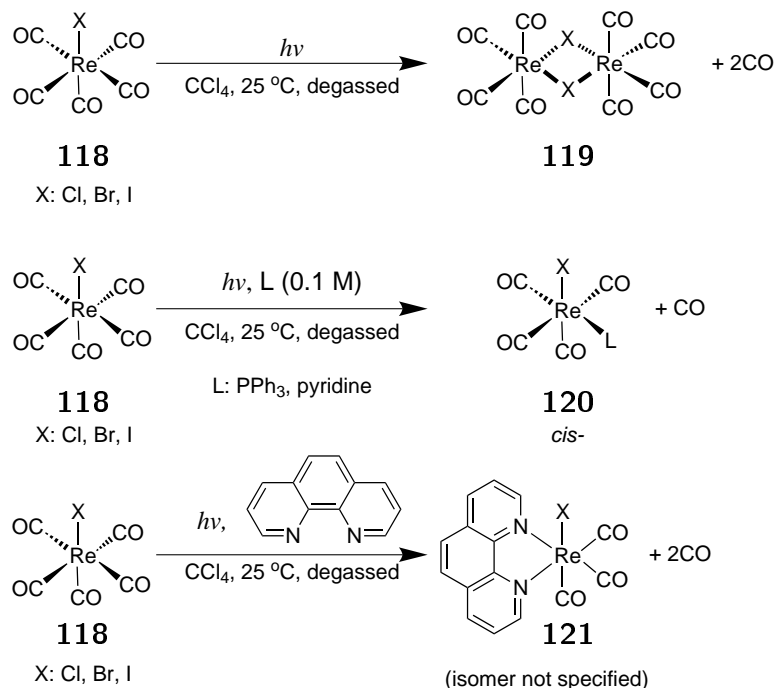
### 4.1 Introduction

Rhenium(I)-diimine complexes are coveted for their photophysical properties which can be utilised in applications such as light emitting devices, biological imaging, photocatalysis and photovoltaic devices.<sup>8</sup> The success of these applications is reliant on the stability of the compounds in the excited state. However since the 1970's rhenium(I) compounds have been known to participate in light induced chemical reactions, specifically photochemical ligand substitution reactions (PLSRs).<sup>77</sup> Although other electrochemical ligand substitution reactions are known to occur, this overview is focused solely on photoactivated processes and the techniques used to elucidate the mechanisms of these types of reactions.

### 4.2 Photochemical Ligand Substitution Reactions of Rhenium(I) Pentacarbonyl Complexes

The photochemical properties of rhenium complexes have been of great interest since the 1970's where Wrighton and Morse conducted a photochemical investigation of

the ligand substitution reactions of rhenium(I) pentacarbonyl halide type compounds, **118**, as shown in **Scheme 4.1**.<sup>77</sup> When excited with ultraviolet radiation the rhenium pentacarbonyl compounds (**118**) dimerised to form **119** and released two molecules of carbon monoxide.



Scheme 4.1: Photochemical investigation of rhenium(I) pentacarbonyl halide complexes (Adapted from Wrighton, 1976).<sup>77</sup>

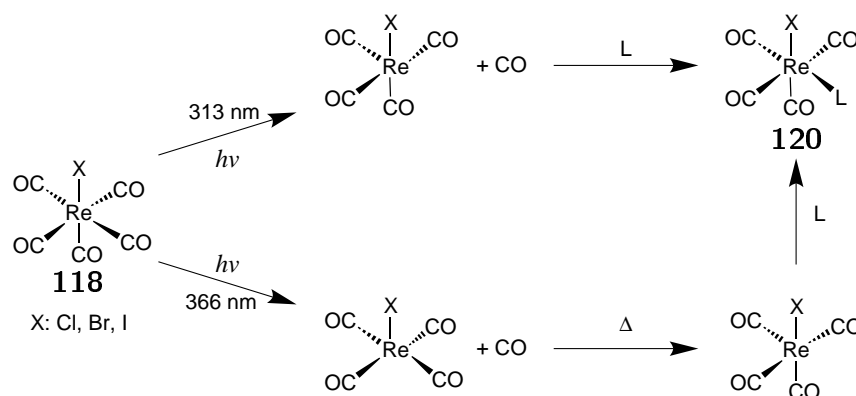
When mono- and bidentate ligands were present in solution, ligand substitution occurred. The monodentate ligands, triphenylphosphine and pyridine, were only substituted once affording the release of one molecule of carbon monoxide even though they were present in a stoichiometric excess to **118**. The photoproducts of these reactions were found to be exclusively the *cis* isomer (**120**). When **118** was photolysed in the presence of 1,10-phenanthroline, the diimine ligand was substituted once affording two molecules of carbon monoxide. The isomerism of the resulting compound, be it *fac* or *mer*, was not stated. Little difference was seen in the photochemical quantum yields of the different ligand solutions implying a dissociative mechanism. The identity of the photo products were confirmed by comparing the IR bands to that of known compounds.

Wrighton and Morse monitored two excitation wavelengths; 366 nm and 313 nm. They determined that at 366 nm they were exciting the  $d_z^2(a_1)$  orbital and 313 nm corresponded to excitation of the  $d_{x^2-y^2}(b_1)$  orbital. The photochemical quantum yield was

reduced when exciting at 366 nm. It was therefore inferred that the  $d_{x^2-y^2}$  orbital was more photochemically active than the  $d_z^2$  orbital.

Excitation of the  $d_z^2$  orbital should labilise the CO in *trans* to the halide whereas excitation  $d_{x^2-y^2}$  should labilise one of the CO ligands in *cis* to the halide. As the *cis* CO ligands are known to be more labile, it is acceptable that these ligands would more readily labilise in the excited state.

No *trans* product was ever identified, however photochemistry was occurring from excitation of the  $d_z^2$  orbital therefore the authors speculated the existence of the photochemical mechanism shown in **Scheme 4.2** where any *trans* photoproduct irreversibly rearranged to give the *cis* product.



Scheme 4.2: Mechanism of the photochemical ligand substitution reactions of rhenium(I) pentacarbonyl halide complexes proposed by Wrighton and Morse (Adapted from Wrighton, 1976).<sup>77</sup>

It is also noteworthy that photochemistry was seen to occur in the presence of other donor molecules such as ethanol, acetonitrile and 4-styrylpyridine and although these observations were purely qualitative, the authors speculated that CO release did occur. In a rigid matrix at 77 K no photochemistry was observed however it was still apparent at 200 K where the solutions were still fluid.

Interestingly Wrighton found the bromo compounds to be more photochemically active than both the chloro and the iodo compounds. The photoactivity order of the halide ligands was determined to be bromo>chloro>iodo. No halide exchange was ever observed and this was rationalised by the fact that the halide ligands are good  $\pi$  donors compared to the CO ligands.

A report by Treichel and co-authors in 1977 showcased how various substitution patterns can be formed from the photolysis of  $[\text{Re}(\text{CO})_5\text{Br}]$  (**34**) in the presence of a



methyl isocyanide ligand as shown in **Scheme 4.3**.<sup>78</sup>

For their photolysis reactions the authors used a mercury lamp of unspecified spectral output. The primary compound formed was the di-substituted tricarbonyl compound, *fac*-[Re(CNMe)<sub>2</sub>(CO)<sub>3</sub>Br] (**123**). The disappearance of this initial photoproduct was monitored by infrared spectroscopy and was found to further react to form seven additional photoproducts being the second di-substituted isomer; *mer,cis*-[Re(CNMe)<sub>2</sub>(CO)<sub>3</sub>Br] (**125**) three tri-substituted isomers; *mer,cis*-[Re(CNMe)<sub>3</sub>(CO)<sub>2</sub>Br] (**126**),

*fac*-[Re(CNMe)<sub>3</sub>(CO)<sub>2</sub>Br] (**127**) and *mer,trans*-[Re(CNMe)<sub>3</sub>(CO)<sub>2</sub>Br] (**128**), the tetra-substituted monocarbonyl compound *trans*-[Re(CNMe)<sub>4</sub>(CO)Br] (**124**) and the penta-substituted monocarbonyl salt [Re(CNMe)<sub>5</sub>(CO)]Br (**130**). If the reaction was stopped sooner then a small amount of the monosubstituted [Re(CNMe)(CO)<sub>4</sub>Br] (**129**) was also found to present.

By varying the equivalents of methyl isocyanide, the photolysis time and the work up procedure the authors were able to identify all seven photoproducts and isolate all but **128** and **129** as elementally pure substances. A pure sample of [Re(CNMe)(CO)<sub>4</sub>Br] (**129**) was obtained from a thermal reaction.

Interestingly, whilst the *mer,cis*- and *fac*- isomers (**126** and **127**) were observed to form under thermal conditions, the *mer,trans*- isomer, **128**, was only observed to form under photolytic conditions. The same was found for the isomer, *mer,cis*-[Re(CNMe)<sub>2</sub>(CO)<sub>3</sub>Br] (**125**), which could not be synthesised thermally.

All the isolated compounds were found to be stable towards rearrangement except for the *facial* isomer, **127**, which was observed to melt at 176 °C and then solidified as the *mer,cis*- isomer, **126**, which then re-melted at 220 °C.

The authors used the results of their thermal reactions to elucidate the thermal substitution mechanism of rhenium(I)-pentacarbonyl compounds with isocyanide ligands as shown in **Figure 4.1**. Whilst a photochemical mechanism was not determined, the authors demonstrated how more varied isomeric configurations can be achieved photochemically rather than thermally.

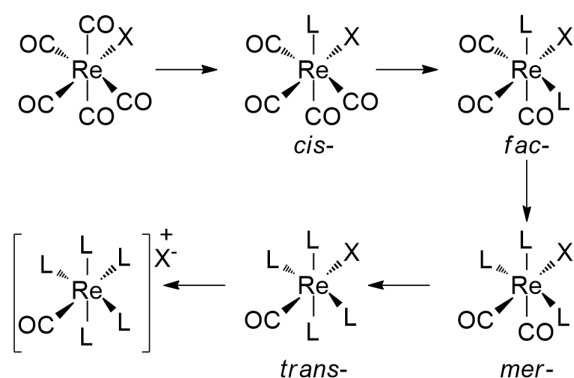
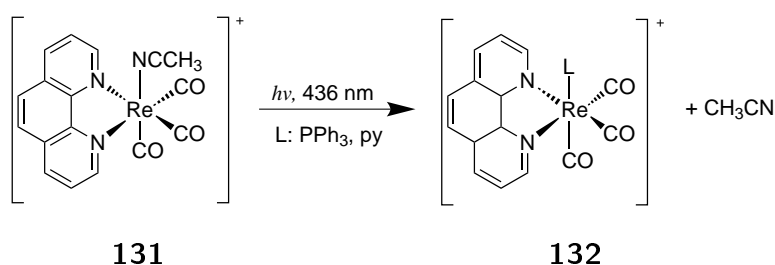


Figure 4.1: Proposed mechanism for the thermal substitution of  $[\text{Re}(\text{CO})_5\text{Br}]$  (**34**) by methyl isocyanide (Adapted from Treichel, 1977).<sup>78</sup>

#### 4.2.1 Electron Transfer Assisted Photochemical Ligand Substitution Reactions of Rhenium(I)-Diimine Complexes

The photochemical properties of rhenium(I)-diimine tricarbonyl complexes have been also been intensely investigated as the excited state of such complexes was found to partake as a photocatalyst for a number of redox reductions such as reduction of ketones and the reduction of carbon dioxide.<sup>79,80</sup>

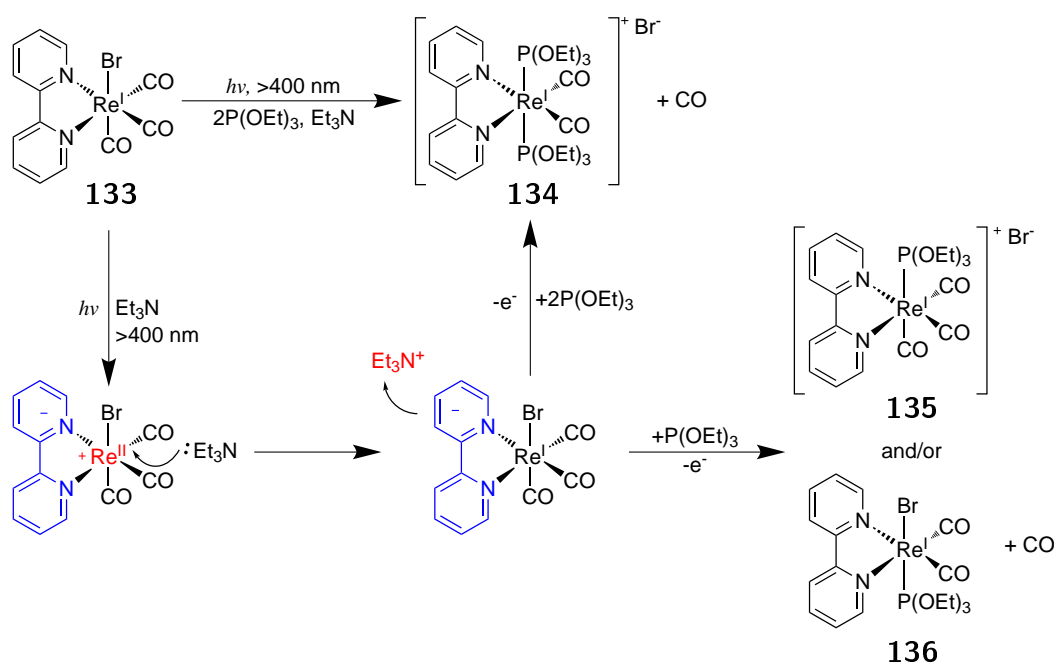


Scheme 4.4: The first report of a photoactivated ligand substitution reaction with a rhenium(I)-diimine complex (Adapted from Summers, 1981).<sup>81</sup>

The first known report of a photoactivated reaction of a rhenium(I) diimine tricarbonyl complex, where the product was actually a photochemical ligand substitution reaction product and not a redox product, was by Summers and co-workers in 1981. They found that the acetonitrile solvate  $\text{fac-}[\text{Re}(\text{phen})(\text{CO})_3(\text{NCCH}_3)]^+$  (**131**), was photochemically active in PLSRs.<sup>81</sup> The solvate itself, **131**, was synthesised *via* a silver halide extraction and was found to be thermally inert.<sup>82</sup>

The photochemical reaction, as shown in **Scheme 4.4**, only proceeded when the solution was irradiated with 436 nm light and when a quencher (Q) was present. The reaction was proposed to proceed by an electron transfer process which is known to quench the radiative decay from the excited state.

When the secondary ligand (L) was triphenylphosphine, the triphenylphosphine itself was the quencher however when L was pyridine then *N,N'*-dimethyl-*p*-toluidine was used as the electron transfer quencher. The quenched excited state complex was presumed to initiate the chain reaction which resulted in the photo product.



Scheme 4.5: The second report of the photoactivated ligand substitution reactions of rhenium(I)-diimine complexes (Adapted from Pac, 1991).<sup>83</sup>

A similar type of light activated ligand substitution reactions utilising a rhenium(I)-diimine tricarbonyl complex was reported in 1991 by Pac and co-workers who found that *fac*- $[\text{Re}(\text{bpy})(\text{CO})_3\text{Br}]$ , (**133**) participated in PLSRs with triethylphosphite to form three possible photoproducts.<sup>83</sup>

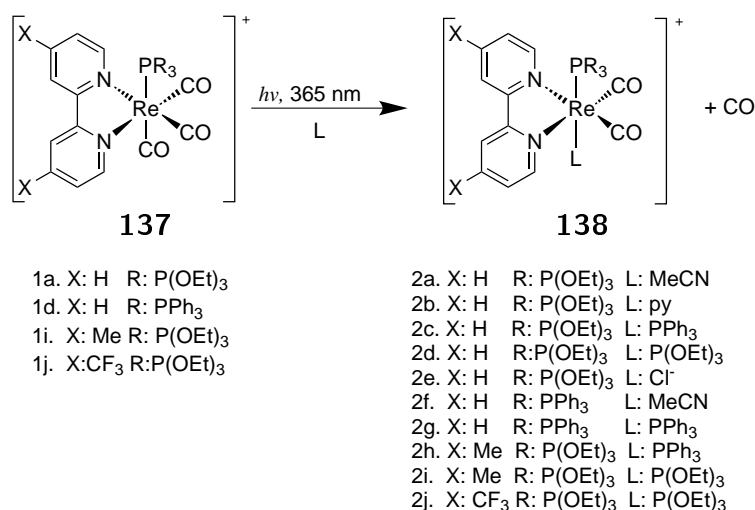
Using  $^1\text{H}$  NMR and other spectroscopic techniques, the identity of three photoproducts were determined. The first was **136** where a CO ligand has been exchanged for a  $\text{P}(\text{OEt})_3$  ligand, the second was **135** where the bromo ligand has been exchanged for  $\text{P}(\text{OEt})_3$  and the third was **134** where both the bromo and a CO ligand have been exchanged for two equivalents of  $\text{P}(\text{OEt})_3$ .

The photochemical reaction occurred when the reaction mixture was irradiated at  $>400$

nm and in the presence of triethylamine. The photochemical mechanism was proposed to be similar to that determined by Summers and co-workers ten years earlier where an electron transfer agent, in this case triethylamine, acted as quencher that quenched the excited state which then initiated the ligand exchange as shown in **Scheme 4.5**.

#### 4.2.2 Photochemical Ligand Substitution Reactions of Rhenium(I)-Diimine Tricarbonyl Complexes from the $^3\text{LF}$ State

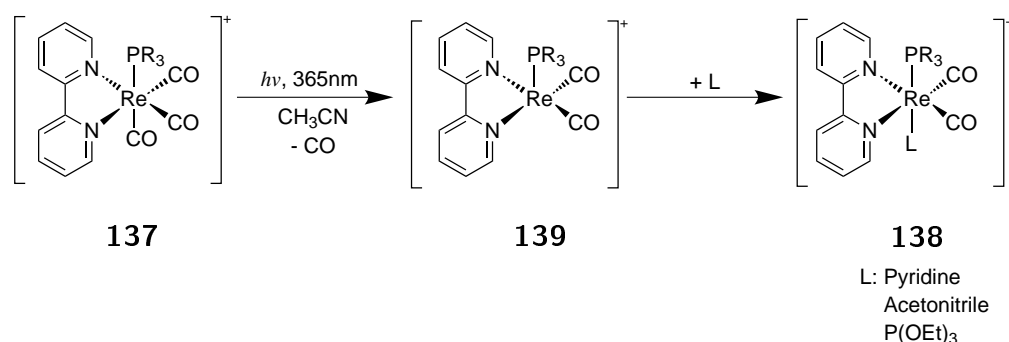
The first report of photochemical ligand substitution reaction with a rhenium(I)-diimine tricarbonyl complex occurring without an electron transfer donor agent was in 2000 by Ishitani and co-workers. They found that when strong field organophosphorous ligands ( $L^P$ ), specifically triethylphosphite and triphenylphosphine, were bound to rhenium(I), the carbonyl ligand in *trans* to the organophosphorous ligand could be photochemically displaced. This photochemical displacement reaction was found to occur when the rhenium(I)-diimine tricarbonyl complexes were excited at  $\lambda_{ex}$  365 nm and it was used to synthesise a suite of dicarbonyl rhenium(I) complexes as shown in **Scheme 4.6**.<sup>84</sup>



Scheme 4.6: The first report of photoactivated ligand substitution reaction of rhenium(I)-diimine type complexes occurring without an electron transfer agent (Adapted from Koike, 2000).<sup>84</sup>

This reaction is very similar to that investigated by Pac and co-workers, however, instead of forming the rhenium(I)-diimine phosphite tricarbonyl complex *via* photochemical ligand substitution Ishitani pre-synthesised the photoactive species, com-

pound **137**, by the silver halide extraction method to form an acetonitrile solvate, which could then be exchanged for various organophosphorous ligands ( $L^P$ ).<sup>85</sup>



Scheme 4.7: Proposed mechanism of the photochemical ligand substitution reaction (Adapted from Koike, 2002).<sup>70</sup>

Two years later, the same group proposed a mechanism for the PLSR of this class of rhenium(I) compounds (**137**).<sup>70</sup> By monitoring the displacement of <sup>13</sup>C-labelled carbon monoxide by <sup>13</sup>C NMR, they determined the reaction proceeded by the “site-specific” labilisation of the CO in *trans* to the phosphorous ligand and that the remaining CO ligands did not rearrange post-photolysis. The mechanism was determined to be dissociative, as shown in **Scheme 4.7**, as the quantum yield of the formation of the products was not affected by the concentration or nucleophilicity of the entering ligand. The authors rationalised that the photoproducts were photostable as the secondary ligands, pyridine and chloride, had a weaker *trans* effect than the  $L^P$  type ligands.

This labilisation was hypothesised to occur from the triplet ligand field (<sup>3</sup>LF) excited state which was thermally accessible from the <sup>3</sup>MLCT of  $[\text{Re}(\text{diimine})(L^P)(\text{CO})_3]^+$  type compounds such as **137**, as illustrated by the Jablonski diagram in **Figure 4.2**.

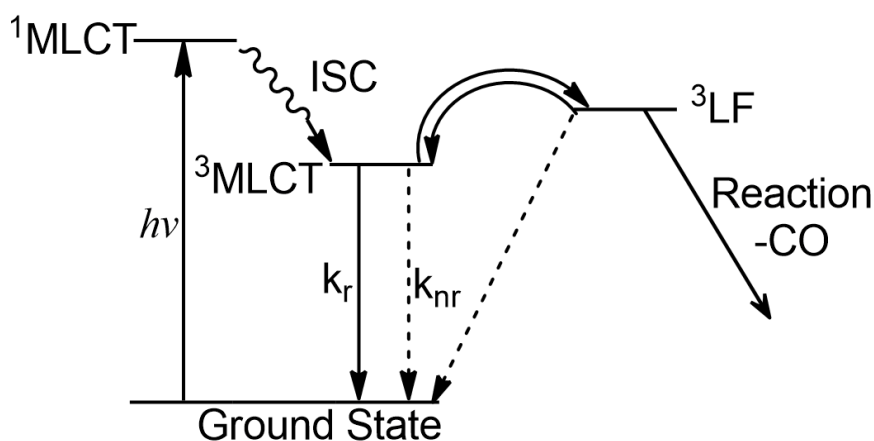


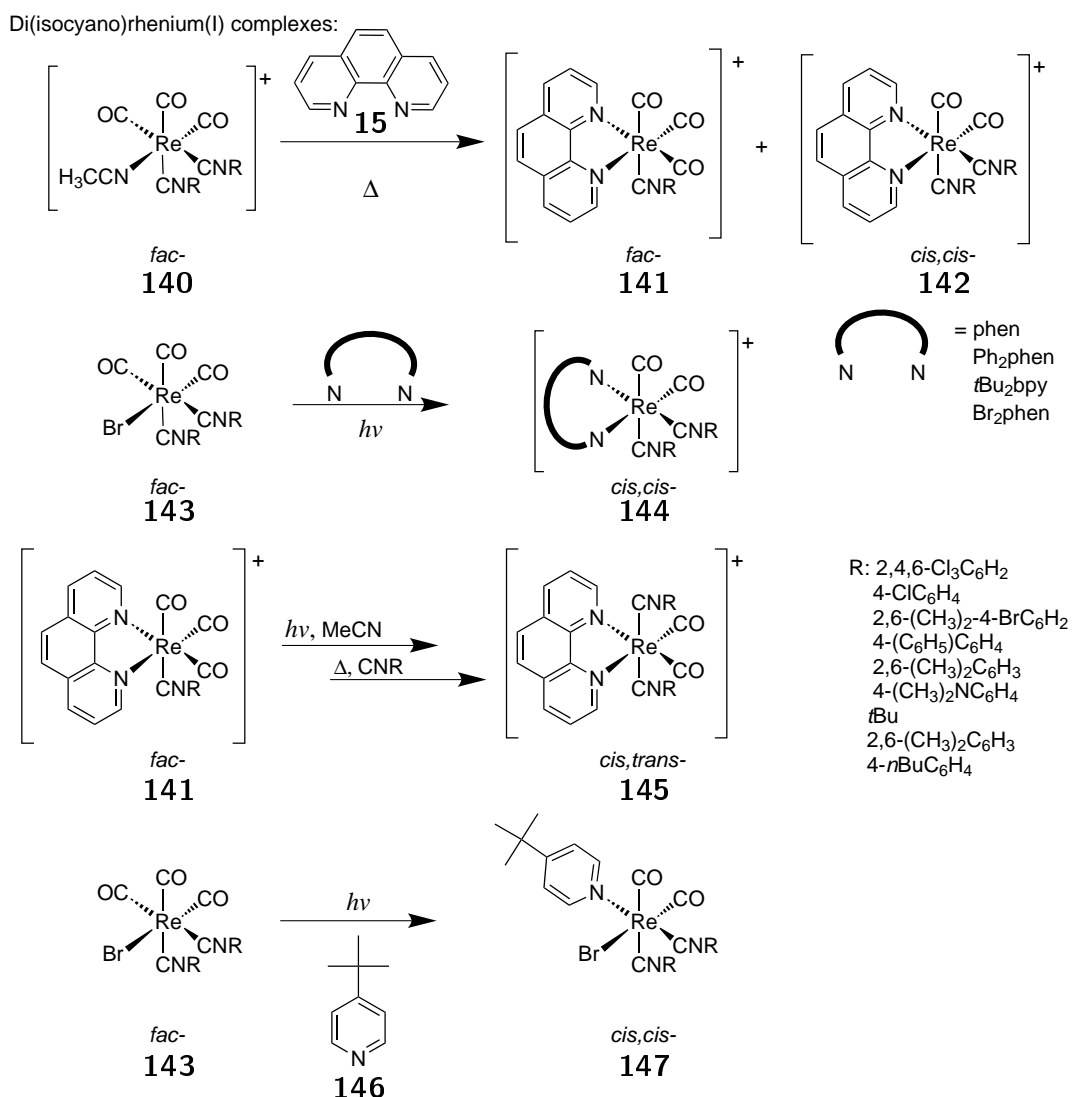
Figure 4.2: Simplified Jablonski diagram showing photochemistry occurring from the  $^3\text{LF}$  state (Adapted from Koike 2002)<sup>70</sup>

They concluded that whilst the  $^3\text{LF}$  state of other rhenium(I) compounds such as (**117**) and (**138**, where L: py) was presumably thermally accessible at room temperature from their  $^3\text{MLCT}$ , based on the temperature dependence of their excited state lifetimes, the lack of PLSRs of such compounds was attributed to the weaker *trans* effect of the pyridyl and chloro ligands compared to the organophosphorous ligands.

A similar PLSR was observed for rhenium(I)-diimine -di(isocyano) and -tri(isocyano) complexes by Ko et al. in 2010 and 2012.<sup>86,87</sup> Ko found that when benzene solutions of the respective precursor, **143**, was photolysed with broadband UV light in the presence of four equivalents of the required diimine, that the *cis,cis*- isomer, **144**, was the primary photo product as shown in **Scheme 4.8**. This photolysis method was preferred over the thermal synthetic method which involved using the acetonitrile solvate, compound **140**, as this method resulted in a difficult to separate mixture of the *fac*- (**141**) and *cis,cis*- isomers (**142**).

It was also found that the *cis,trans*- isomer, **145**, could be synthesised *via* the stereo selective substitution of the facial compound, **141**. The facial compound (**141**) was first photolysed in acetonitrile to form an intermediate photo product which was then subsequently thermally reacted with the appropriate isocyanate ligand (CNR) to give the desired *cis,trans*- isomer, **145**.

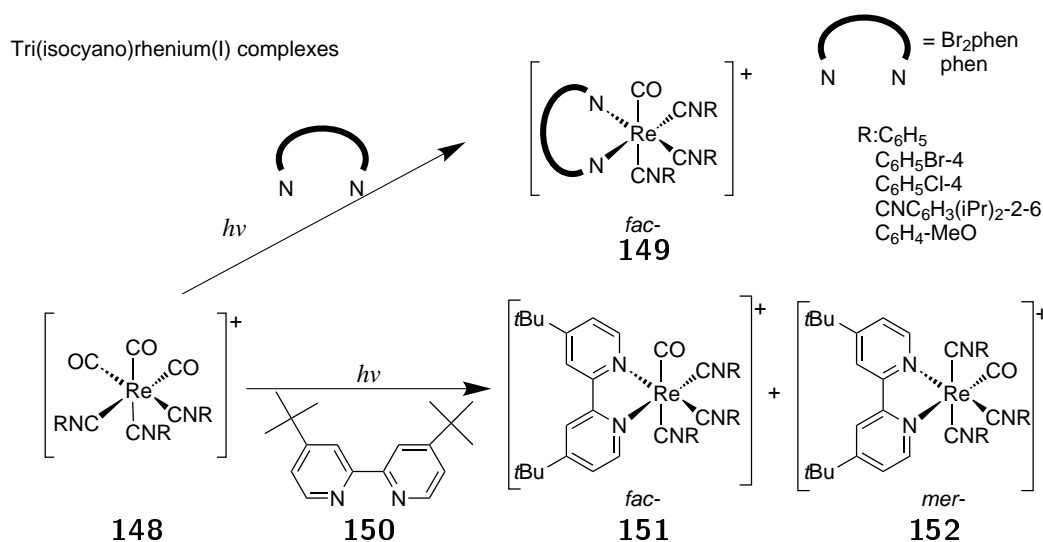
In order to elucidate the photochemical mechanism of these substitution reactions Ko et al. photolysed a solution of **143** in the presence of 4-*tert*-butylpyridine (**146**) and



Scheme 4.8: Photochemical ligand substitution reactions with isocyanate ligands (Adapted from Ko, 2010).<sup>86</sup>

monitored the reaction by TRIR in an attempt to mimic the investigation performed by Wrighton and Morse on [Re(CO)<sub>5</sub>X] (**118**) type compounds in 1976. Ko determined that as only one substitution of CO for 4-*tert*-butylpyridine occurred and that because the photo product was exclusively the *cis,cis*- isomer (**147**) the mechanism of this reaction must be similar to the dissociative mechanism determined by Wrighton and Morse as previously shown in **Scheme 4.2**.

The tri(isocyano) compounds, such as **148**, were also found to be photoactive as shown in **Scheme 4.9**. Unlike the previous ligand substitution reactions, Ko found the PLSRs of the tri(isocyano) compounds were not as stereo selective as those of the di(isocyano) complexes. When 1,10-phenanthroline and 5,6-dibromo-1,10-phenanthroline were used as the diimine, the reaction was stereo selective for the *fac*- isomer (**149**) exclusively.



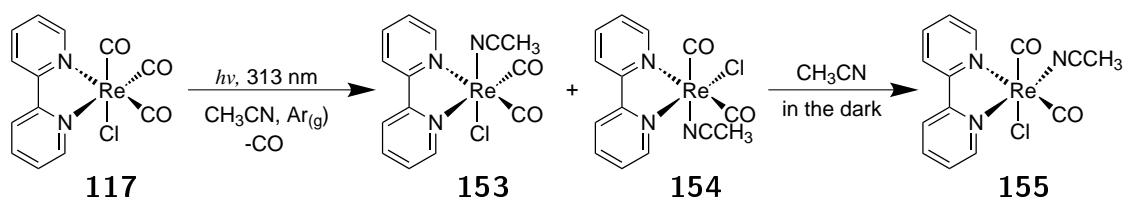
Scheme 4.9: Photochemistry of rhenium(I) tri(isocyano) compounds (Adapted from Ko, 2012).<sup>87</sup>

However when a bulkier, more electron releasing diimines such as 4,4'-di-*tert*-butyl-2,2'-bipyridine (**150**) were used the stereo selectivity was lost resulting in both the *fac*- (**151**) and *mer*- (**152**) isomers.

#### 4.2.3 Photochemical Ligand Substitution Reactions of Rhenium(I)-Diimine Complexes involving Higher Excited States (HES)

In 2007, Ishitani and co-workers reported the first observations of PLSRs involving a rhenium(I)-diimine tricarbonyl compound without the aid of strong field ligands such the organophosphorous and isocyano ligands or an electron transfer agent as previously discussed. The rhenium-diimine compound, *fac*-[Re(bpy)(CO)<sub>3</sub>Cl] (**117**) is known to be photostable when excited with 365 nm light. This excitation corresponds to population of the <sup>1</sup>MLCT manifold.

However, Ishitani and co-workers found that when **117** was photolysed with a shorter wavelength, <313 nm, a photochemical ligand substitution reaction occurred.<sup>88</sup> When photolysed with 313 nm light in acetonitrile under an argon atmosphere, **117** underwent CO dissociation to form two initial dicarbonyl photoproducts; *cis,trans*-[Re(bpy)-(NCCH<sub>3</sub>)(CO)<sub>2</sub>Cl] (**153**) and *cis,cis*-[Re(bpy)(NCCH<sub>3</sub>)(CO)<sub>2</sub>Cl] (**154**) as shown in **Scheme 4.10**. The *cis,cis*- compound (**154**) then underwent further isomerisation in acetonitrile to form compound **155**. The authors speculated that these photochemical reactions were occurring from higher excited states of MLCT character.



Scheme 4.10: Photochemical ligand substitution reactions of rhenium(I)-bipyridine tricarbonyl chloride in acetonitrile (Adapted from Sato, 2007).<sup>88</sup>

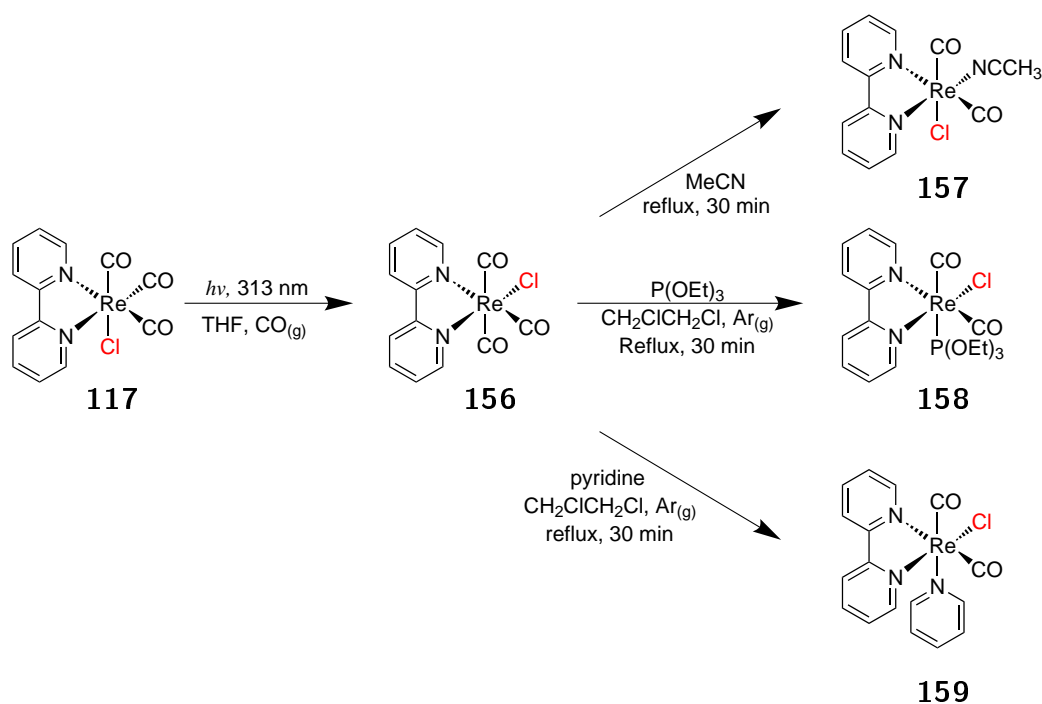
The reactions were found to be analogous for several derivatives of **117** allowing for the synthesis of a suite rhenium(I)-bipyridine dicarbonyl complexes.<sup>88</sup>

Following this report, the same group found that when **117** was photolysed with 313 nm in tetrahydrofuran under a carbon monoxide atmosphere, CO loss did not occur. In fact **117** was found to photochemically rearrange to form its isomer *mer*-[Re(bpy)(CO)<sub>3</sub>Cl] (**156**) as shown in **Scheme 4.10**.<sup>89</sup>

This compound could then be further thermally reacted with other ligands such as acetonitrile, triethylphosphite and pyridine to displace a CO ligand and form *cis,trans*-rhenium(I)-diimine dicarbonyl chloride compounds as exemplified by **157**, **158** and **159**. Interestingly in the case of **157** it is the chloro ligand in the *trans* position and not the acetonitrile ligand as predicted indicating that some spatial rearrangement of the ligands has occurred.

A thorough investigation of the photochemical mechanism of the PLSRs *fac*-[Re(bpy)-(CO)<sub>3</sub>Cl] (**117**) followed and five years later the authors published the proposed photochemical mechanism.<sup>90</sup> Using time resolved (TR) infrared-, UV-visible- and emission-spectroscopy techniques the authors were able to elucidate that the PLSRs were occurring from the population of higher excited states (HES). Depending on the solvent there were three mechanistic pathways proposed as illustrated by Scheme 4.12.

When photolysed with 313 nm light in a poorly coordinating solvent such as THF the authors proposed that the <sup>1</sup>HES was populated which rapidly underwent intersystem crossing to the <sup>3</sup>HES, avoiding population of the <sup>1</sup>MLCT as shown in **Scheme 4.13**. The <sup>3</sup>HES could then internally convert and populate the lower lying excited states such as the <sup>3</sup>LF and hot vibrational <sup>3</sup>MLCT states otherwise known as the <sup>3</sup>MLCT(HV).

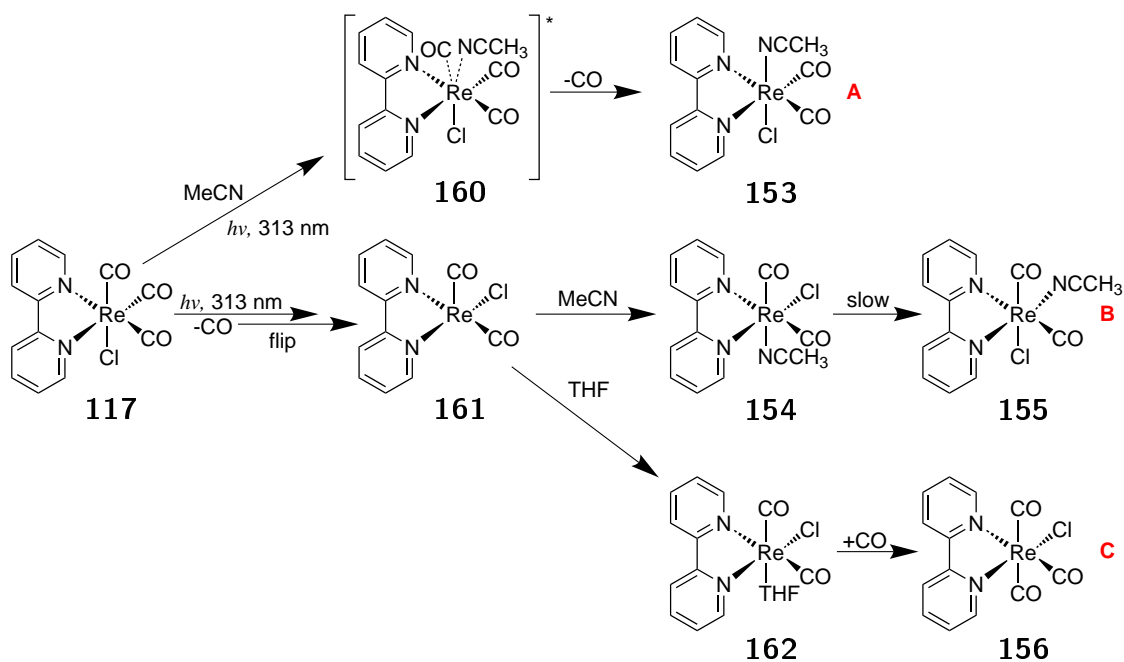


Scheme 4.11: Further photochemical reactions of rhenium(I)-bipyridine tricarbonyl chloride (Adapted from Sato, 2007).<sup>89</sup>

The  $^3\text{LF}$  is a known reactive state and population of this state allows for dissociation of the CO ligand in *trans* to the chloro ligand resulting in the five coordinate intermediate.<sup>70</sup> The unsaturated intermediate, is then thought to undergo an irreversible rearrangement, comparable to that proposed by Wrighton and Morse, to form **161**.<sup>77</sup> From the hot vibrational  $^3\text{MLCT}$  levels the molecule can relax to the lowest vibrational levels (LV) of the  $^3\text{MLCT}$  and from there relax by radiative decay to the ground state. A THF molecule can coordinate in the vacant site of **161** to form **162** as shown by pathway C in **Schemes 4.12** and **4.13**. In a CO rich environment a CO ligand can then displace the THF and re-coordinate to the rhenium resulting in the *mer*- isomer (**156**) of the *fac*- starting material (**117**).

In acetonitrile solutions there are two competing pathways. The first pathway is pathway A in **Scheme 4.12** which involves the formation of a seven-coordinate intermediate (**160**) *via* an associative pathway as opposed to a dissociative pathway. The seven coordinate intermediate (**160**) is short lived and rapidly converts to the final photo product, the acetonitrile solvate (**153**), within 100 ps.

This associative pathway was thought to occur through population of hot vibrational level of the MLCT state rather than the  $^3\text{LF}$  state as the latter favours a dissociative

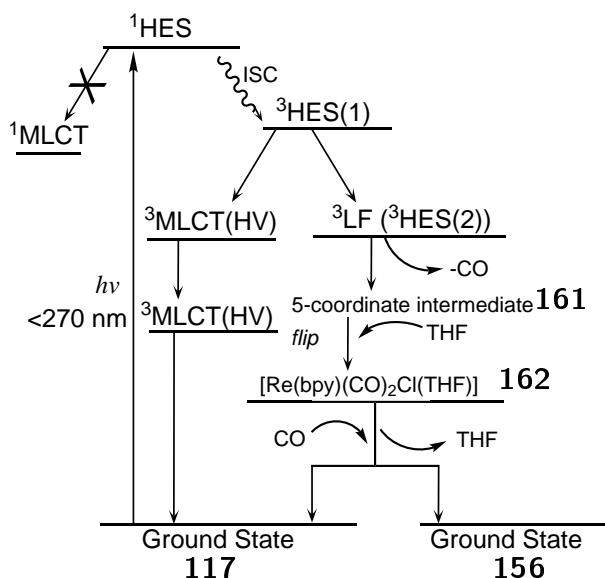


Scheme 4.12: Photochemical mechanism of the PLSRs of rhenium(I)-bipyridine tricarbonyl chloride (Adapted from Sato, 2012).<sup>90</sup>

pathway as previously discussed.<sup>70,91</sup> In an MLCT state, the electron density of the rhenium metal centre is reduced compared to the ground state. Population of an MLCT also has reduced electron density of the rhenium centre when compared to population of a LF or LC state.

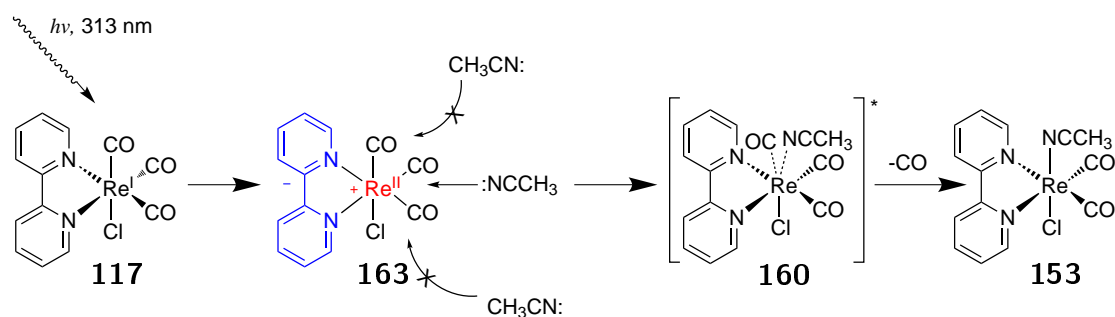
The second is pathway B in **Scheme 4.12**, which is very similar to pathway C, and involves the dissociation of the CO in *trans* to the chloro and subsequent rearrangement to form the five coordinate intermediate (**161**). This process was found to require thermal activation which was attributed to the energy needed for the ligand rearrangement. Once the intermediate has rearranged then a molecule of acetonitrile can coordinate in the vacant site to form **154**. As previously mentioned this compound was found to not be thermally stable and slowly isomerises to form **155** when left in the dark.

The reduced electron density around the metal centre makes nucleophilic attack from an appropriately orientated acetonitrile molecule in close proximity more favourable leading to the seven coordinate intermediate as demonstrated by compound **163** in **Scheme 4.14**. This type of intermediate is unlikely to form from population of an <sup>3</sup>LF state and is evidence that photochemical ligand substitution is possible from an excited state of MLCT character rather than of LF character.



Scheme 4.13: Photochemical mechanism of the PLSR of rhenium(I)-bipyridine tricarbonyl chloride in tetrahydrofuran (Adapted from Sato, 2012).<sup>90</sup>

The authors rationalised that dissociation of a CO molecule from the seven coordinate intermediate (**160**) to form **153** required additional energy as this final photo product did not occur when photolysing at lower energy wavelengths (>313 nm) that are known to populate the lower vibrational levels of the <sup>1</sup>MLCT. Therefore energy sufficient enough to populate the MLCT is not necessarily enough energy to allow photochemistry to occur.



Scheme 4.14: Photochemical mechanism of formation of the seven-coordinate intermediate (Adapted from Sato 2012).<sup>90</sup>

To summarise, in the case of *fac*-[Re(bpy)(CO)<sub>3</sub>Cl] (**117**), higher energy excitation wavelengths (<313 nm) are needed to populate the higher excited states from which the <sup>3</sup>LF can be populated (pathway B and C) as well as populate the MLCT and provide the required energy for dissociation and photochemistry to occur (pathway A). From this study it can be concluded that PLSRs and CO loss can occur from both the <sup>3</sup>LF and

$^3\text{MLCT}$  states if there is sufficient energy available and also that from these respective energy levels, CO loss follows different mechanistic pathways.

### 4.3 Summary and Concluding Remarks

Rhenium(I)-diimine tricarbonyl complexes have been observed to participate in an array of photochemical ligand substitution reactions (PLSRs). Initial reports by Wrighton found the rhenium(I)-bromo compounds to be more photochemically active than their chloro and iodo analogues. When strong field ligands, such as organophosphorous ligands or isocyano ligands are present the photochemistry typically occurs from the thermally accessible  $^3\text{LF}$  otherwise known as the  $^3\text{MC}$  state by way of a dissociative mechanism which forms a five coordinate intermediate. The CO dissociated from the rhenium metal centre is typically the CO ligand in *trans* to the strong field ligand.

In the absence of strong field ligands photochemistry can still occur however higher energy excitation wavelengths  $<313$  nm are necessary to populate the higher excited states (HES). This type of photochemistry can occur *via* several competing pathways; either from the thermally accessible  $^3\text{LF}$  by way of a dissociative mechanism which involves a spatial rearrangement of the ligands or from the hot vibrational levels of the  $^3\text{MLCT}$  ( $^3\text{MLCT}(\text{HV})$ ) *via* an associative mechanism which involves the formation of a seven coordinate species. Both pathways require energy greater than 313 nm to occur and result in CO release.

In all cases acetonitrile is the most common solvent utilised in these types of PLSRs as it is strongly coordinating solvent which can participate in the PLSR as the replacement ligand and it is photochemically stable. Other ligands commonly investigated were pyridine and organophosphorous based ligands, specifically triethylphosphite.

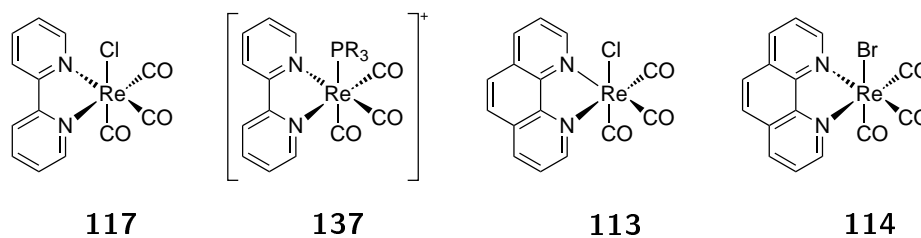


# Chapter 5

## Photochemical Investigation of Re(I)-NHC Tricarbonyl Compounds

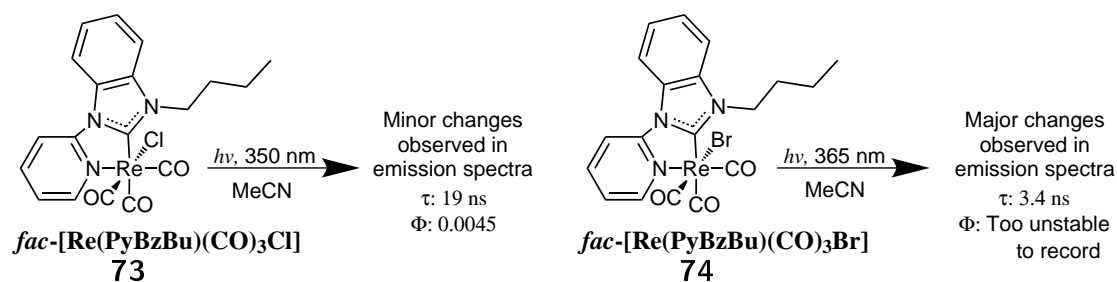
### 5.1 Overview

Whilst the photochemical ligand substitution reactions (PLSRs) of rhenium(I)-diimine tricarbonyl complexes have been scrutinised, the photochemical properties of their rhenium(I)-N-heterocyclic carbene tricarbonyl analogues have scarcely been investigated.<sup>70,77,78,81,84–91</sup>



Scheme 5.1: Structures of rhenium(I)-diimine tricarbonyl compounds discussed in this chapter.

In this investigation, standard synthetic analytical techniques such as NMR and infrared (IR) spectroscopy as well as synthetic strategies will be utilised with the aim of highlighting possible photochemical mechanisms and related photoproducts.



Scheme 5.2: Previously investigated rhenium(I)-NHC complexes and their photophysical properties in degassed MeCN solutions.

## 5.2 Previously Studied Benzimidazol-2-ylidene Systems

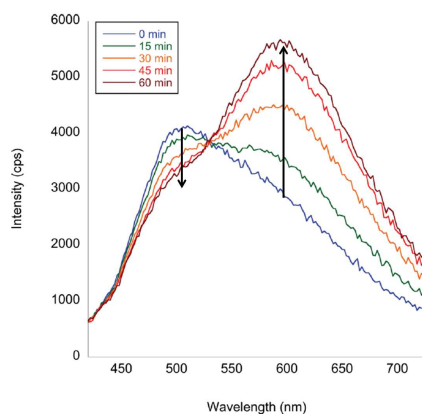
Previous studies on benzimidazol-2-ylidene based Re(I)-NHC tricarbonyl systems indicated that the bromo compound,  $fac-[Re(PyBzBu)(CO)_3Br]$  (**74**), was less stable than the chloro analogue  $fac-[Re(PyBzBu)(CO)_3Cl]$  (**73**) in acetonitrile solutions as shown in **Scheme 5.2**.

Additionally,  $fac-[Re(PyBzBu)(CO)_3Br]$  (**74**) had shorter excited state lifetime and lower quantum yield values than  $fac-[Re(PyBzBu)(CO)_3Cl]$  (**73**) in both dilute dichloromethane and acetonitrile solutions. The difference in photophysical properties between the two seemingly similar compounds was attributed to the increased lability of the bromo compared to the chloro ligand.<sup>49,67</sup>

This was further investigated by taking subsequent emission spectra of a dilute *ca.*  $10^{-4}$  M acetonitrile solution of  $fac-[Re(PyBzBu)(CO)_3Br]$  (**74**) every 15 minutes for the period of 1 hour with an excitation wavelength of 365 nm. This wavelength corresponded to excitation to the <sup>1</sup>MLCT manifold and was the excitation wavelength used to determine the emissive state lifetime. In the 1 hour time frame the original emission maximum centred at around 506 nm decreased in intensity and a second, more intense, red-shifted emission maximum centred around 596 nm started to appear as depicted in **Figure 5.1**.

The excited state lifetime of  $fac-[Re(PyBzBu)(CO)_3Br]$  (**74**) was re-recorded after the 1 hour photolysis and the previously monoexponential lifetime had become biexponential with a new longer component of 24 ns (88%) and the previously measured shorter component of 3.4 ns (11%).

*fac*-[Re(PyBzBu)(CO)<sub>3</sub>Br] (**74**)



*fac*-[Re(PyBzBu)(CO)<sub>3</sub>Cl] (**73**)

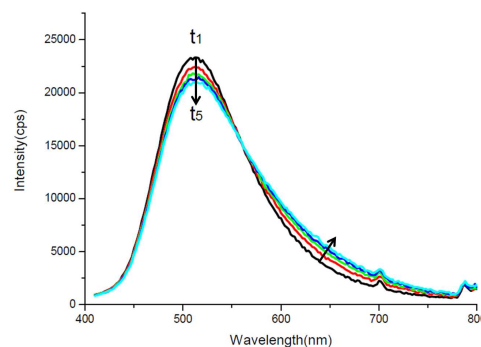


Figure 5.1: Multiple emission spectra of air-equilibrated *ca.* 10<sup>-4</sup> M acetonitrile solutions of *fac*-[Re(PyBzBu)(CO)<sub>3</sub>Br] ( $\lambda_{\text{ex}} = 365$  nm) and *fac*-[Re(PyBzBu)(CO)<sub>3</sub>Cl] ( $\lambda_{\text{ex}} = 350$  nm) showing the change in the emission spectrum over the period of 1 hour (Adapted from: Casson, 2011).<sup>49</sup>

The same experiment was performed with more dilute solutions, *ca.* 10<sup>-5</sup> M and 10<sup>-6</sup> M, of *fac*-[Re(PyBzBu)(CO)<sub>3</sub>Br] (**74**) and the results were found to be reproducible. In the case of the *fac*-[Re(PyBzBu)(CO)<sub>3</sub>Cl] (**73**) there is a slight decrease in the intensity of the original emission maximum and the hint of the appearance of a new red-shifted band as indicated by the arrows in **Figure 5.1**. At the time the authors believed this new red-shifted band denoted the transformation of *fac*-[Re(PyBzBu)(CO)<sub>3</sub>Cl] into a different species during photolysis.

### 5.3 1-(2-Pyridyl)-imidazol-2-ylidene Series

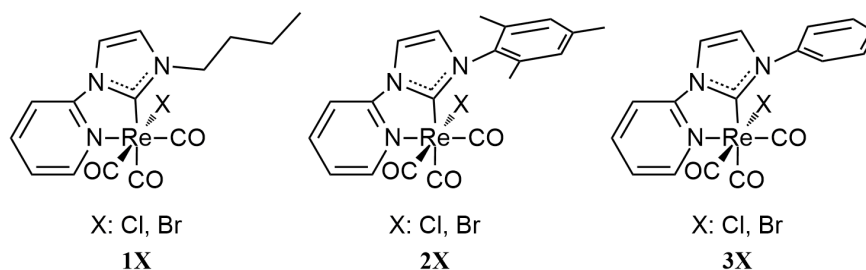


Figure 5.2: The 1-(2-pyridyl)-imidazol-2-ylidene series, compounds **1-3Cl/Br**.

As discussed in **Chapter 3**, the 1-(2-pyridyl)-imidazol-2-ylidene series, compounds **1-3Cl/Br** as shown in **Figure 5.2**, had shorter excited state lifetimes and smaller quantum yields compared to the 1-(2-pyrimidyl)- and 1-(2-quinoyl)-imidazol-2-ylidene series.

As **73** and **74** had demonstrated halide ligand lability in acetonitrile solutions, a photochemical investigation of **1-3Cl/Br** was conducted to deduce whether the poor performing lifetime and quantum yield values reported in **Table 3.4** were attributable to photochemical ligand substitution reactions.

The first compounds to be analysed were the 1-(2-pyridyl)-3-(phenyl)imidazol-2-ylidene (PyImPh) derivatives; **3Br** and **3Cl**.

### 5.3.1 Investigation of the Photostability of **3Br** and **3Cl**

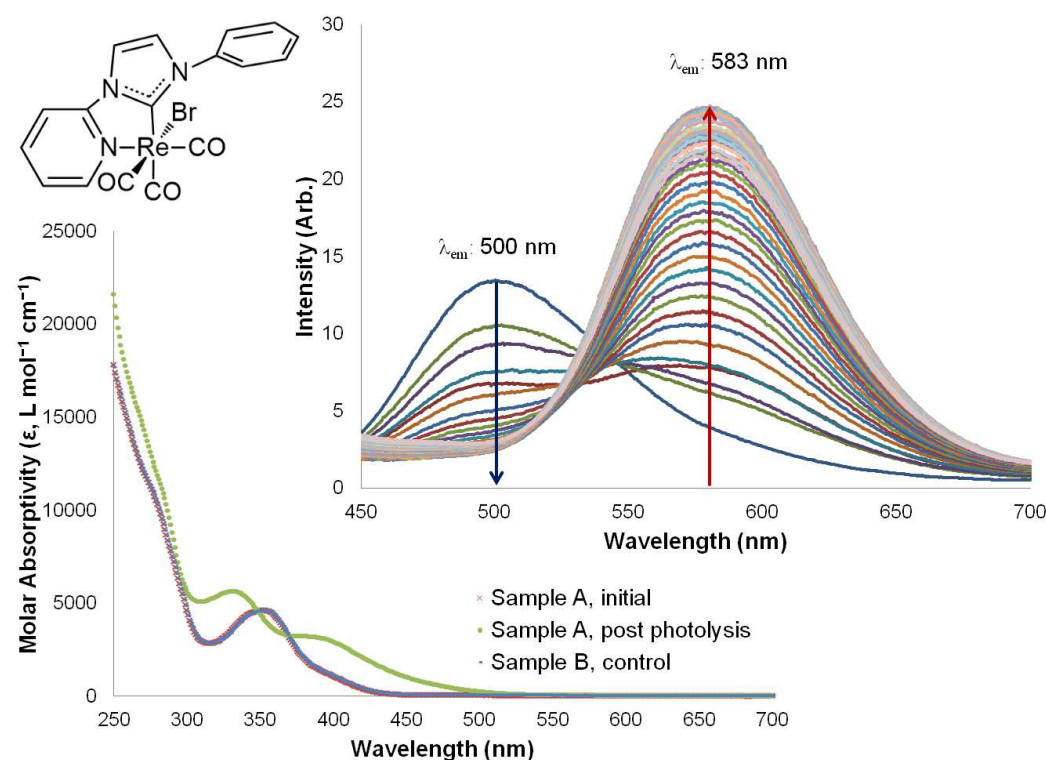


Figure 5.3: UV-Vis absorption and emission spectra of **3Br** in acetonitrile showing the spectral changes of the photolysed sample (A) vs. the control sample kept in the dark (B).

A parallel experiment was developed where a *ca.*  $10^{-5}$  M stock solution of **3Br** in acetonitrile was prepared and two aliquots (sample A and sample B) were taken. The

UV-vis absorption spectra of the first aliquot, sample A, was recorded and kept as the initial reference spectrum. Sample A was then photolysed at 370 nm for 99 consecutive scans in accordance with the parameters outlined in **Experimental Section 8.7.3**.

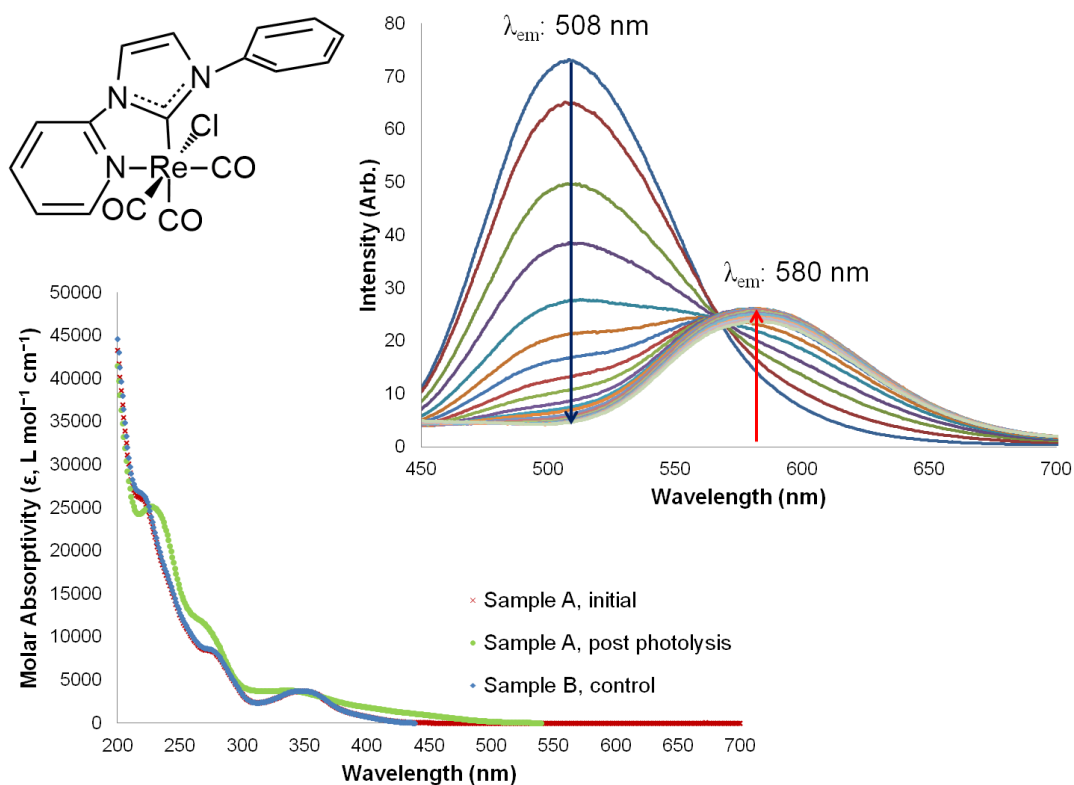


Figure 5.4: UV-Vis absorption and emission spectra of **3Cl** in acetonitrile showing the spectral changes of the photolysed sample (A) vs. the control sample kept in the dark (B).

Whilst this experiment was being performed, sample B was being kept in the dark. At the end of the 4 hour photolysis, the absorption spectrum of sample A was run and was found to be different to the initial spectrum as shown in **Figure 5.3**. The broad structureless band attributed to the MLCT is centred around 353 nm in the initial and control spectra. After photolysis the original band has divided into two bands; a blueshifted band at 331 nm and a redshifted band at 370 nm. The absorption spectra of sample B was recorded and found to be identical to that of the initial spectrum of sample A. It was therefore inferred that the chemical changes that changed the UV-vis absorption profile of sample A did not occur to **3Br** when kept in the dark.

The emission spectrum of sample A post photolysis had also significantly changed over the course of the experiment as shown in **Figure 5.3**. The original emission maximum was centred at 500 nm and over the course of the 99 scans the intensity of this emission maximum had decreased and a new red-shifted maximum had appeared at 583 nm.

This is very similar to the changes observed for *fac*-[Re(PyBzBu)(CO)<sub>3</sub>Br] (**74**) as discussed in **Section 5.2**. The experiment was repeated with the chloro analogue, **3Cl**, and analogous spectral changes to **3Br** were observed as shown in **Figure 5.4**.

The stability of **3Br** was further assessed at elevated temperatures to observe whether the spectral changes that were occurring in the photolysed sample could be caused by the heat of the UV lamp. A solution of **3Br** in deuterated acetonitrile was prepared and an initial <sup>1</sup>H NMR spectrum was collected. The NMR tube containing the solution was then heated at reflux temperature (82 °C) whilst protected from light for 2 hours.

After 2 hours, a second <sup>1</sup>H NMR spectrum was collected and compared to the initial spectrum as shown in **Figure 5.5**. There was no discernible difference between the two spectra indicating that the **3Br** was stable in acetonitrile solutions at reflux temperatures.

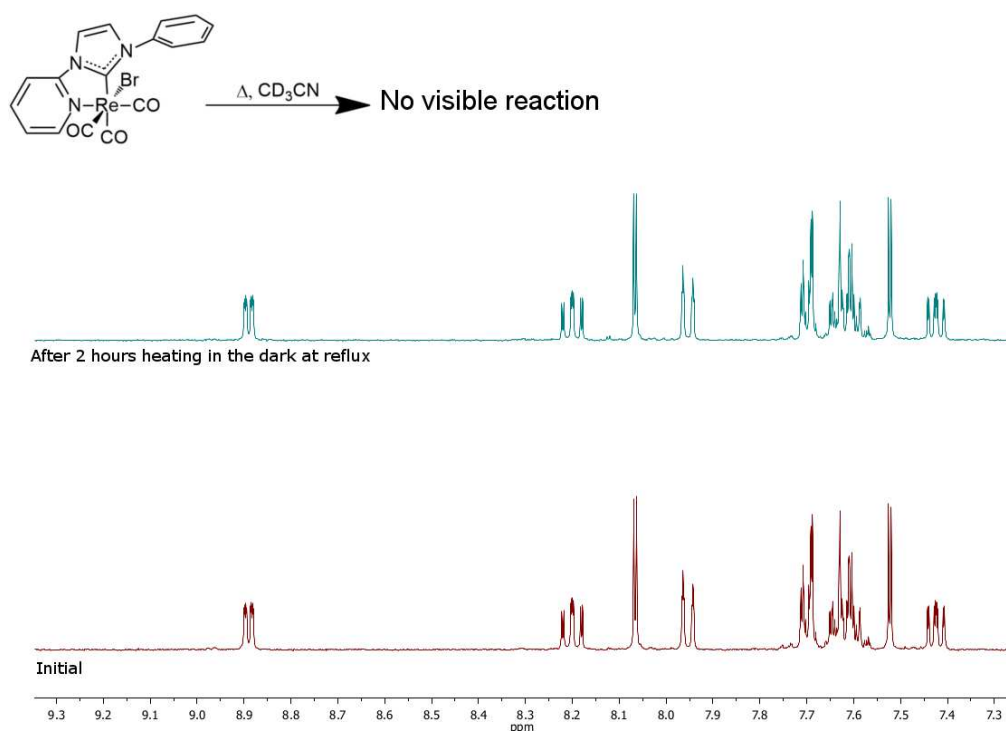


Figure 5.5: <sup>1</sup>H NMR spectra showing a CD<sub>3</sub>CN solution of **3Br** before (bottom in red) and after (top in blue) heating at reflux for 2 hours.

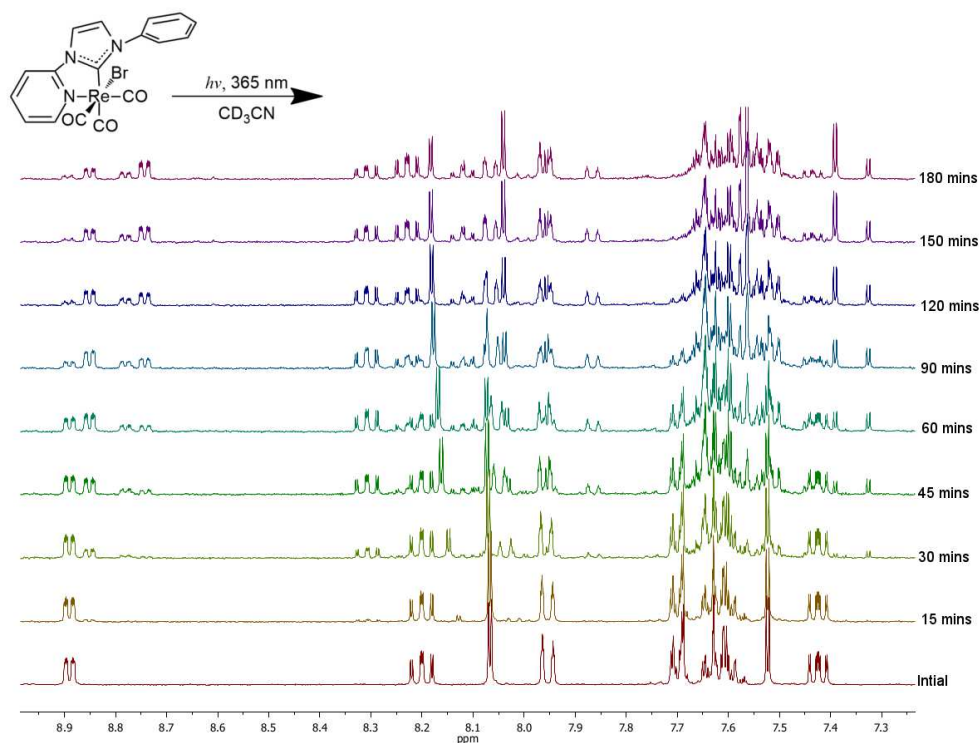


Figure 5.6: Successive  $^1\text{H}$  NMR spectra of **3Br** in  $\text{CD}_3\text{CN}$  showing the structural changes occurring during photolysis.

The  $^1\text{H}$  NMR experiment described in **Experimental Section 5.3.1** was adopted to observe structural changes occurring to **3Br** during photolysis at 365 nm. A solution of **3Br** in  $\text{CD}_3\text{CN}$  was prepared and an initial  $^1\text{H}$  NMR spectrum was collected as outlined in **Section 8.7.5**.

The clearest changes were those occurring to the downfield signal at 8.89 ppm belonging to the pyridyl-H6 proton. As this “doublet” (long range coupling and splitting have been omitted for simplicity) is the furthest downfield from the other signals, it is the easiest to observe for spectral changes due to lack of overlap with other signals as shown in **Figure 5.7**. Over the 3 hour photolysis period, the initial doublet belonging to the H6 proton, a, has significantly decreased in intensity as shown in **Figure 5.7**. Three new signals at 8.85 (b), 8.79 (c) and 8.75 (d) ppm have appeared upfield from the original doublet a. The approximate abundance ratios based on integration values show the most abundant compound is d, followed by b, c and finally a.

Infrared spectroscopy was then utilised to further probe the identity of the new photo-products. The IR spectrum of the reaction mixture post photolysis was obtained from the CD<sub>3</sub>CN solution and was compared to an initial IR spectrum of **3Br** as described in **Section 8.7.4**.

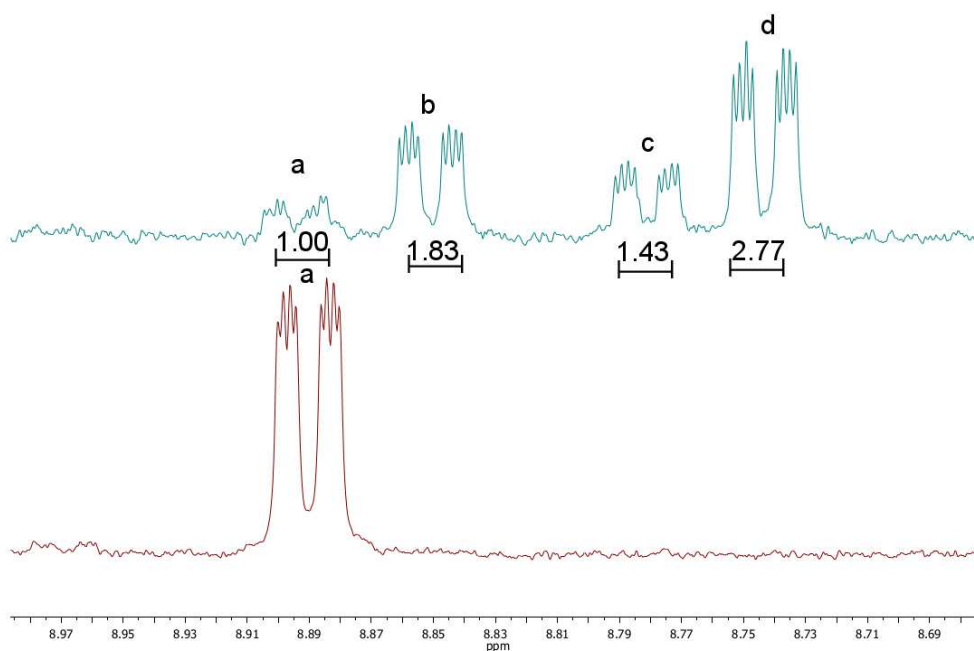


Figure 5.7: Expanded initial (bottom trace) and final (top trace) <sup>1</sup>H NMR spectrum of **3Br** in CD<sub>3</sub>CN showing the changes in the peak attributed to the H6 proton.

The two spectra were overlaid as shown in **Figure 5.8**. The region from 2050-1800 cm<sup>-1</sup> was specifically chosen as this region features the carbonyl stretches. Analysis of the IR spectrum of the photolysed sample indicates six distinguishable carbonyl stretches at 2036, 2021, 1938, 1918, 1863 and 1833 cm<sup>-1</sup> respectively. The stretch at 2036 cm<sup>-1</sup> is indicative of a cationic rhenium(I) complex.<sup>92</sup> The less intense stretch at 2021 cm<sup>-1</sup> is very similar to the starting material (in the solid state) and the decreased intensity indicates that there is less starting material present than photoproduct. This data is in accordance with <sup>1</sup>H NMR spectrum in **Figure 5.6** which depicted that the integration of the initial starting material had significantly decreased in intensity post photolysis.

Based on the intensity of the next four carbonyl stretches, two pairs of stretches become evident. The first pair consists of the peaks at 1938 and 1863  $\text{cm}^{-1}$ . The second pair consists of the small shoulder at 1918  $\text{cm}^{-1}$  and the peak at 1833  $\text{cm}^{-1}$ . These bands are occurring at lower wavenumbers than typically exhibited by the rhenium(I) tricarbonyl compounds as outlined in **Table 2.4**. Based on analysis of the  $^1\text{H}$  NMR data in conjunction with the IR data it would appear that four species are present in the reaction mixture post photolysis; remaining starting material, a cationic product and two more species both with two carbonyl stretches at lower wavenumbers.

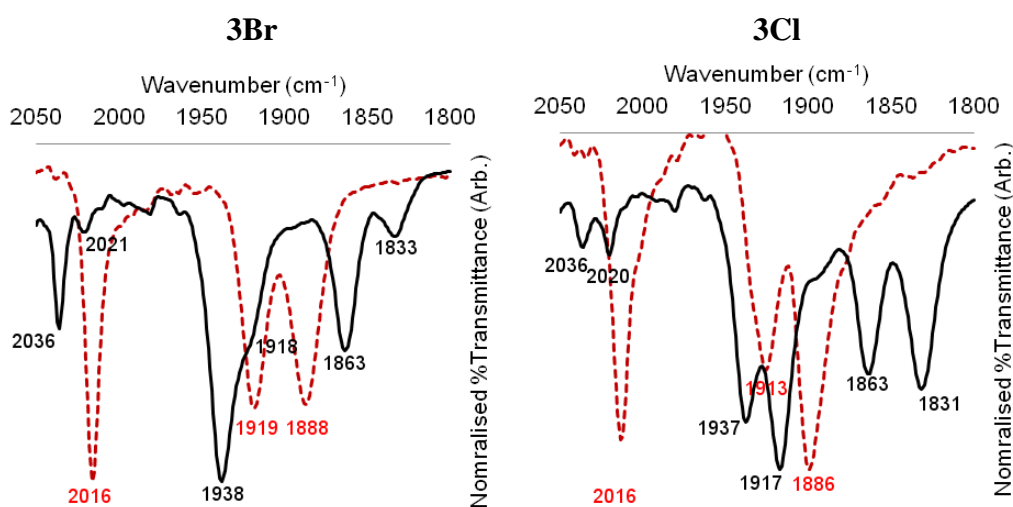


Figure 5.8: Infrared spectra of **3Br** and **3Cl** demonstrating the change in the stretching frequencies of the carbonyl bands before (red dashed line) and after (black bold line) photolysis.

It should also be noted that in all photolysed IR spectra of **3Br** there is a small band at 2293  $\text{cm}^{-1}$  which could be ascribed to the CN stretch of coordinated acetonitrile.<sup>93,94</sup> Therefore it can be concluded that the identity of the cationic species is most likely the acetonitrile solvate of **3Br**; *fac*-[Re(PyImPh)(CO)<sub>3</sub>(NCCH<sub>3</sub>)]<sup>+</sup>(**164**) and that the two remaining species correspond to dicarbonyl complexes.

The  $^1\text{H}$  NMR monitored experiment was repeated with **3Cl** and the results were comparable as shown in **Figure 5.9**. Unlike **3Br**, the three new sets of doublets appearing in the region shown in **Figure 5.7** are less defined and overlap slightly such that integration ratios could not be accurately determined. The trend however remains similar; as photolysis occurs the peaks belonging to the starting material, **3Cl**, decrease

in intensity whilst new, more upfield and hence more shielded peaks become more pronounced.

The IR spectrum of **3Cl** and its photoproducts in CD<sub>3</sub>CN are shown in **Figure 5.8**. The stretching frequencies for the carbonyl bands of **3Cl** are very similar to that of **3Br**, both pre and post photolysis. There are six distinguishable carbonyl stretches at 2036, 2020, 1937, 1917, 1863 and 1831 cm<sup>-1</sup>. In accordance with the IR spectrum of **3Br**, the signal at 2036 cm<sup>-1</sup> is attributed to a cationic species however the signal is not as intense as that observed for the photolysed sample of **3Br**. The small stretch at 2020 cm<sup>-1</sup> is again attributed to residual starting material.

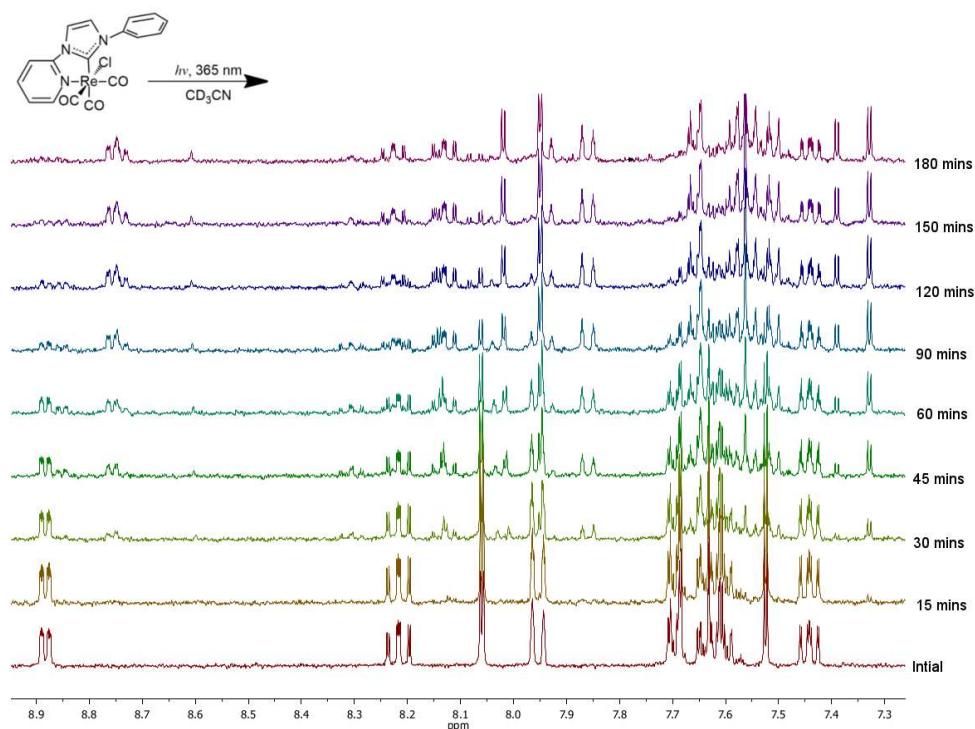


Figure 5.9: Successive <sup>1</sup>H NMR spectra of **3Cl** in CD<sub>3</sub>CN showing the structural changes occurring during photolysis.

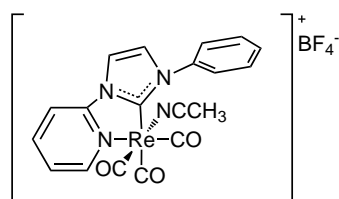
Similarly to **3Br**, there are two visible pairs of carbonyl bands with the first consisting of the stretches at 1937 and 1863 cm<sup>-1</sup> and the second consisting of the stretches at 1917 and 1831 cm<sup>-1</sup>. The wavenumbers of these stretches are analogous to those observed in the reaction mixture of **3Br** as shown in **Figure 5.8** however the relative ratio of the peaks is different which is in agreement with the previous NMR study of

**3Cl**. The second pair of stretches at 1917 and 1831  $\text{cm}^{-1}$  are higher in intensity in the photolysed reaction mixture of **3Cl** in comparison to the same pair of stretches in the photolysed reaction mixture **3Br**.

Based on analysis of the  $^1\text{H}$  NMR and IR spectra of photolysed acetonitrile solutions of **3Br** and **3Cl** it would seem that both tricarbonyl compounds are photoactive and form three distinct photoproducts. There is evidence of a cationic acetonitrile species and two separate dicarbonyl species in the IR spectrum of both **3Br** and **3Cl**.

### 5.3.2 Investigation of the Photochemical Properties of *fac*-[Re(PyImPh)(CO)<sub>3</sub>(NCCH<sub>3</sub>)]<sup>+</sup>

To confirm the identity of one of the photoproducts, *fac*-[Re(PyImPh)(CO)<sub>3</sub>(NCCH<sub>3</sub>)]<sup>+</sup> (**164**), was synthesised *via* a silver halide extraction as described in **Experimental Section 8.8.1** and analysed.



**164**

As this process involves removing the halide ligand and exchanging it for acetonitrile, the final product is the same whether the precursor used was **3Cl** or **3Br**. The  $^1\text{H}$  NMR of **164** was compared to that of the photolysed solution of **3Br** as shown in **Figure 5.10**.

Three of the signals (a', b' and c') in the  $^1\text{H}$  NMR spectrum of the photolysed reaction mixture of **3Br** align perfectly with the a, b and c signals in the  $^1\text{H}$  NMR spectrum of **164** as shown in **Figure 5.10**. This indicates that one of the photoproducts is either the acetonitrile solvate **164** itself or a compound with a very similar structure and electron density distribution. It should be noted that there is no corresponding shift for proton d and proton e in the photolysed spectrum and further evidence is required to confirm the identity of the photolysis product.

Analysis of the IR spectrum of **164** further implies that **164** is a likely photoproduct of the photolysis of **3Br**. The carbonyl band stretching region of **164** shows three strong

bands at 2036, 1937 and 1862  $\text{cm}^{-1}$  which are well aligned with the bands observed in IR spectrum of the photolysed reaction mixture of both **3Br** and **3Cl** as shown in **Figure 5.11**.

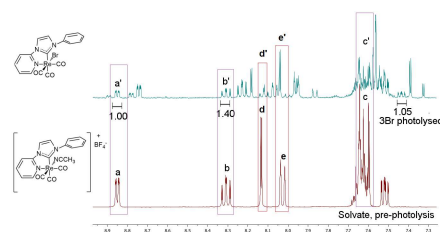


Figure 5.10: Comparison of the  $^1\text{H}$  NMR spectra of **164** and the photolysed MeCN solution of **3Br**.

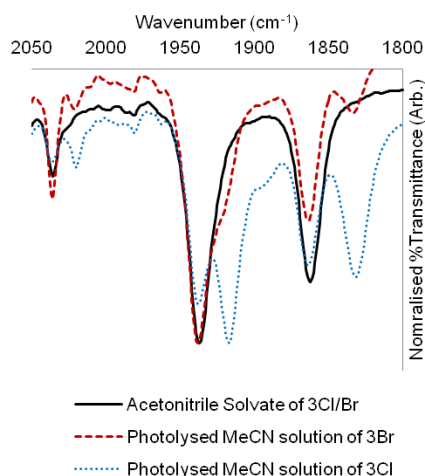


Figure 5.11: Comparison of IR spectra showing the solvato complex **164** present in the photolysis reaction mixture of both **3Br** and **3Cl**.

To assess whether **164** was photoactive itself a solution of **164** was prepared and photolysed under the same conditions as **3Br** and **3Cl** for 180 minutes. The  $^1\text{H}$  NMR progression in **Figure 5.12** clearly shows there are visible changes in the  $^1\text{H}$  NMR spectrum of the acetonitrile solvate **164** as it is photolysed with 365 nm light in  $\text{CD}_3\text{CN}$ . This indicates that not only is **3Br** photoactive and forms **164** upon photolysis, but additionally **164** itself is photoactive and forms further photoproducts.

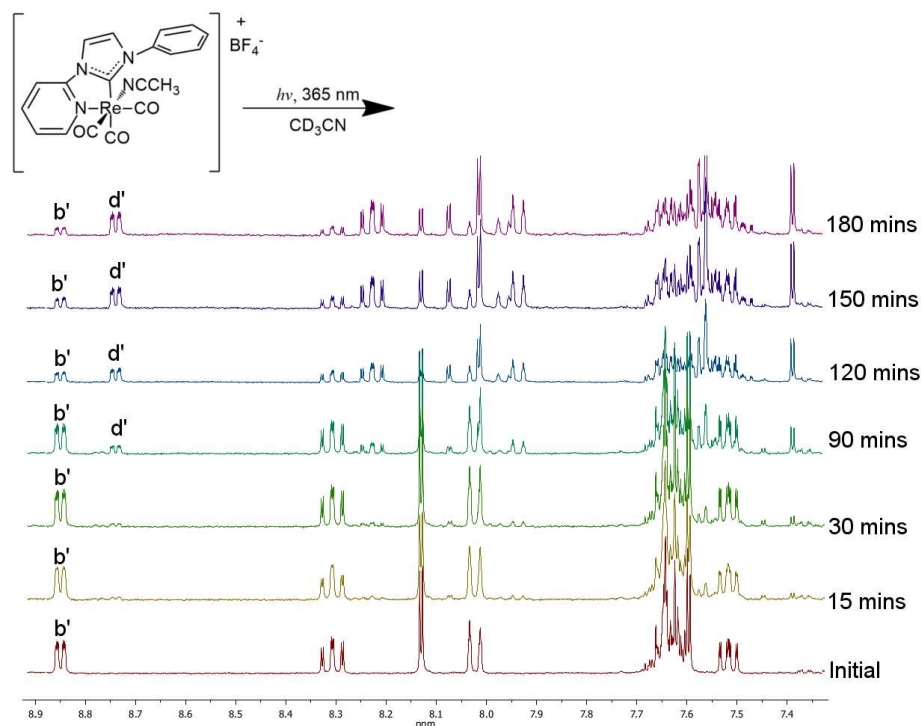


Figure 5.12: Successive  $^1\text{H}$  NMR spectra of **164** in  $\text{CD}_3\text{CN}$  showing the structural changes occurring during photolysis.

Comparison of the photolysed spectra of **164** to the photolysed reaction mixture of **3Br** shows some interesting similarities (**Figure 5.13**). As **3Br** is photolysed, it forms three photoproducts, *fac*- $[\text{Re}(\text{PyImPh})(\text{CO})_3(\text{NCCH}_3)]^+$  (**164**) indicated by the doublet *b'* in **Figure 5.13**, as well as two other photoproducts indicated by *c'* and *d'*. When a solution of **164** is photolysed as shown in **Figure 5.12**, the initial pyridyl-H6 resonance, *b'*, reduces in intensity and a new upfield peak which has the same chemical shift as the *d'* signal in photolysed NMR spectrum of **3Br** appears. Interestingly the peak labelled *c'* that is visible when **3Br** is photolysed *does not* appear when **164** is photolysed.

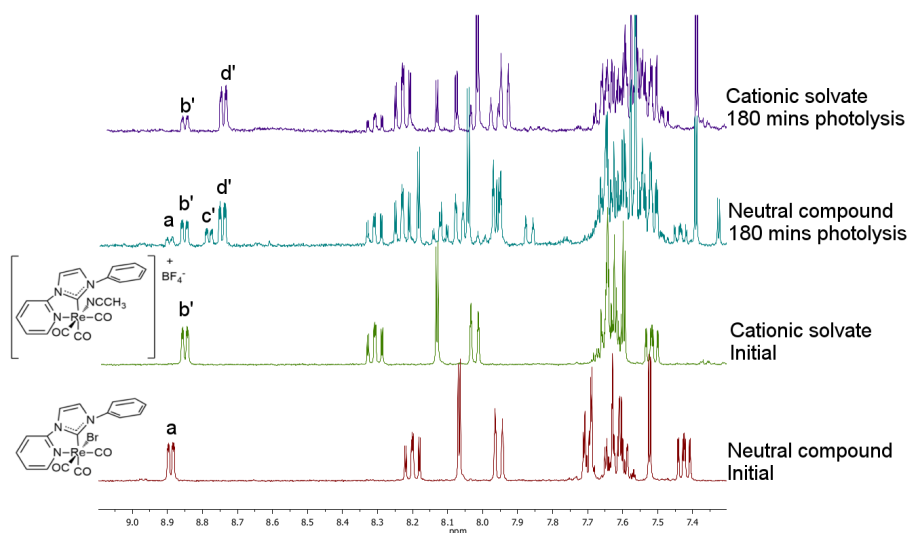


Figure 5.13: Comparison of the photoproducts produced by the photolysis of **3Br** to the photoproducts produced by the photolysis of **164**.

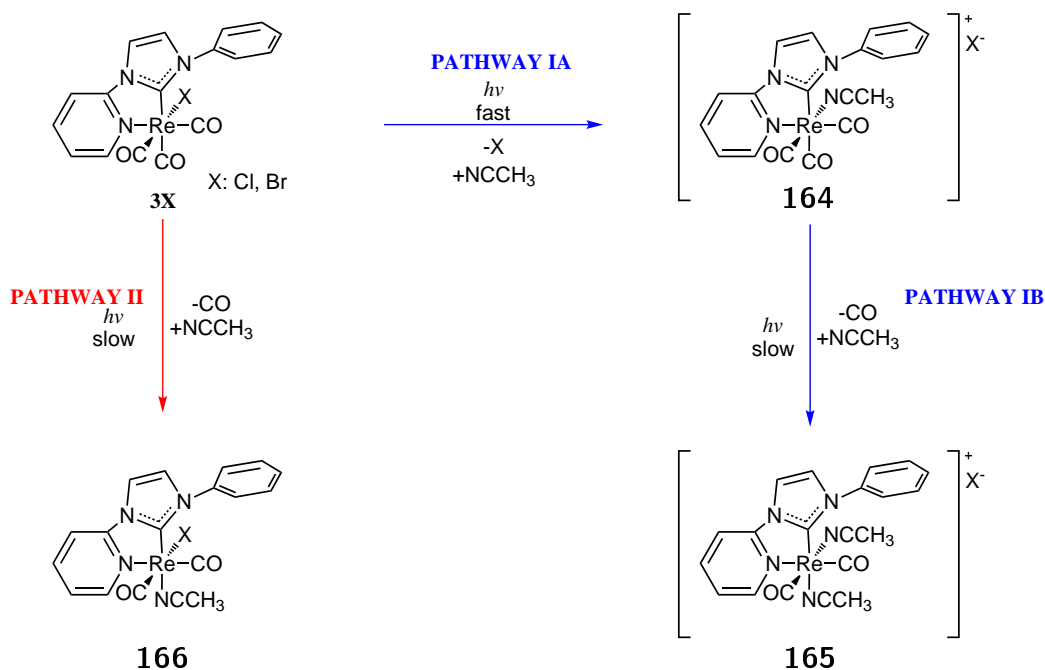
It should be noted that small scale column chromatography was utilised in an attempt to isolate various photoproducts but was not successful for this system.

### 5.3.3 Proposed Photochemical Mechanism

Based on this data a dual pathway photochemical mechanism starts to become apparent. When **3Br** is photolysed in acetonitrile it forms the acetonitrile solvate, *fac*-[Re(PyImPh)(CO)<sub>3</sub>(NCCH<sub>3</sub>)]<sup>+</sup> (**164**), *via* pathway IA (**Scheme 5.3**). The cationic species **164** then further reacts *via* pathway IB to form a third photoproduct indicated by the doublet in **Figure 5.10** labelled **d'**. The structure of this photoproduct is hypothesised to be a dicarbonyl species due to the two pairs of carbonyl stretches observed in **Figure 5.8**. The CO in *trans* to the NHC ligand is inferred to be the most labile carbonyl ligand as it should be experiencing a strong *trans* effect from the  $\sigma$  donating NHC ligand.

The labile carbonyl in *trans* to the NHC ligand can then be replaced by a neutral acetonitrile ligand to form the dicarbonyl species **165** as shown in **Scheme 5.3**.

The second reaction, pathway II, is the direct formation of a dicarbonyl product from



Scheme 5.3: Initial proposed photochemical mechanisms.

**3Br**. When **3Br** is photolysed in acetonitrile there is a NMR resonance labelled **c'** which is not seen during the photolysis of **164**.

The identity of this dicarbonyl photoproduct is therefore assigned to the structure of the dicarbonyl compound **166** as shown in **Scheme 5.3** due to the sets of carbonyl stretches in the photolysed IR spectrum of **3Br** (**Figure 5.8**), which indicated the existence of two dicarbonyl species. In the structure of **166** the CO in *trans* to the NHC ligand, the most labile CO due to the *trans* and effect of the NHC ligand, has been exchanged for a molecule of acetonitrile to form a neutral dicarbonyl species.

In order to confirm whether pathway IB was photochemically induced or due to the kinetic lability of the ligands, a  $^1\text{H}$  NMR experiment was developed where a  $\text{CD}_3\text{CN}$  solution of **3Br** was alternatively photolysed and heated in the dark for a 180 minute period. As shown by **Figure 5.14**, spectral changes only occurred after the photolysis sessions and the spectrum did not change upon heating. This indicates that for pathway IB to proceed it needs photoactivation just as step IA does.

In an attempt to isolate and confirm the identity of the photoproducts **165** and **166**, the photolysed reaction mixtures of **3Br** and **3Cl** were allowed to crystallise by slow evaporation of the solvent. Single crystals of X-ray quality mixed with amorphous solids grew from the reaction mixture of photolysed **3Cl**. Selected bond lengths and angles are detailed in **Table 5.1** and full X-ray crystallographic data and refinement

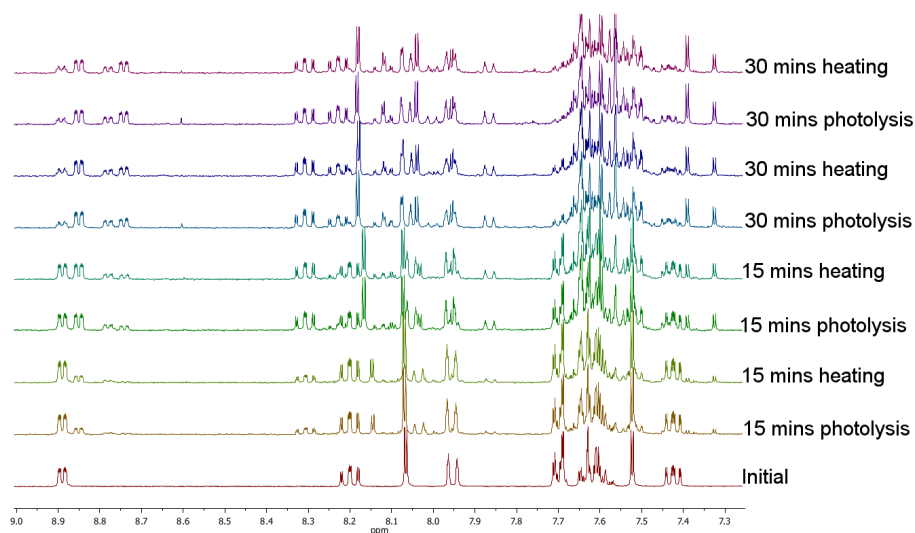


Figure 5.14:  $^1\text{H}$  NMR sequence of **3Br** in  $\text{CD}_3\text{CN}$  showing that spectral changes only occur after photolysis sessions and not during heating.

parameters are in **Appendix 9.1.11**. The chlorine atom and the carbonyl group *trans* to it are disordered between these two positions, with site occupancies refined to 0.756(6) and its complement. Geometries of the minor components were restrained to ideal values. Anisotropic displacement parameters were employed for the non-hydrogen atoms. All hydrogen atoms were added at calculated positions and refined by use of a riding model with isotropic displacement parameters based on those of the parent atom.

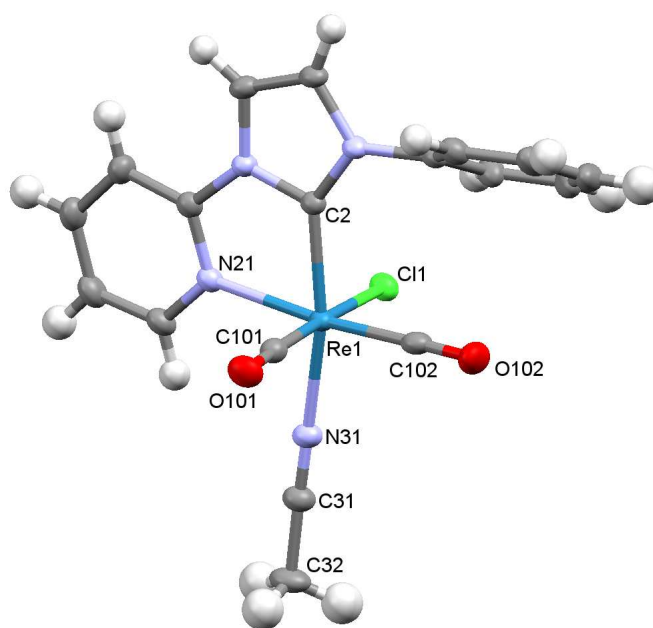


Figure 5.15: Crystal structure of *cis,cis*-[Re(PyImPh)(CO)<sub>2</sub>(NCCH<sub>3</sub>)Cl] (**166**) with ellipsoids drawn at the 50% probability level.

The structure of the isolated crystals was determined to be that of *cis,cis*-[Re(PyImPh)(CO)<sub>2</sub>(NCCH<sub>3</sub>)Cl] (**166**) where the carbonyl in *trans* to the carbon atom of the NHC ligand has been re-placed with a molecule acetonitrile as shown in **Figure 5.15**. The Re-CO bond lengths of the two remaining CO ligands are slightly shorter than they are in the tricarbonyl complex **3Br**. This appears to be characteristic of dicarbonyl complexes such as **110** where the Re-CO bond lengths were 1.895(5) and 1.931(5) Å.<sup>71</sup> The Re-C(2), Re-N(21) and Re-Cl(1/2) bond lengths are similar to those observed for the original com-pound **3Br**. The bite angle of the N<sup>^</sup>C ligand has not changed and the geometry of the complex is still distorted octahedron. The *trans* grouping are also still less than 180 ° further confirming the distorted octahedron geometry.

In this structure the rhenium metal centre would be experiencing an increase in electron density due the exchange of a carbonyl ligand for the MeCN ligand. This increased electron density could account for one pair of the lower wavenumber CO stretches observed in the IR of the reaction mixture of photolysed **3Br** (**Figure 5.8**).

Table 5.1: Selected bond lengths (Å) for *cis,cis*-[Re(PyImPh)(CO)<sub>2</sub>(NCCH<sub>3</sub>)Cl] (**166**).

Bond Length (Å)			
	Re-C(102) CO <i>trans</i> to N atom	Re-C(101/103) CO <i>trans</i> to chloro	Re-N(31) MeCN <i>trans</i> to the carbene
<b>166</b>	1.886(3)	1.888(5) and 1.937(14)	2.119(2)
<b>3Br</b>	1.923(4)	1.957(3)	1.917(4)

This result confirms that II is a plausible reaction pathway and that **166** is a confirmed photoproduct of the PLSR of **3Cl/Br**. This crystal structure not only confirms that **3Br** and **3Cl** are photochemically active but also demonstrates that the carbonyl ligand in *trans* to the NHC ligand is able to be dissociated and replaced by another ligand.

Table 5.2: Selected bond lengths (Å) and angles (°) for *cis,cis*-[Re(PyImPh)(CO)<sub>2</sub>(NCCH<sub>3</sub>)Cl] (**166**) continued.

Bond Length (Å)				Bond Angle (°)
	Re-C(2)	Re-N(21)	Re-X(1/2)	C(12)-Re- N(21); Bite angle of N <sup>^</sup> C ligand
<b>166</b>	2.062(2)	2.215(2)	2.416(4) and 2.4914(12)	74.71(8)
<b>3Br</b>	2.145(3)	2.210(3)	2.6255(4)	74.60(13)

Although no structural information was obtained to confirm the existence of **165** the previously discussed <sup>1</sup>H NMR and IR spectra of the photolysed reaction mixture support its formulation. It is plausible that the disolvated species is too unstable to be isolated *via* column chromatography or crystal growth experiments.

### 5.3.4 Solvent Dependence

Table 5.3: Summary of the spectral changes occurring in the  $^1\text{H}$  NMR spectrum of photolysed solutions of **3Cl** and **3Br** in a variety of solvents.

Compound	Solvent	Photolysis Time (minutes)	Observations of the $^1\text{H}$ NMR spectrum
<b>3Br</b>	acetone- $d_6$	180	Pyridyl-H6 proton unaffected
<b>3Cl</b>	acetone- $d_6$	180	Pyridyl-H6 proton unaffected
<b>3Br</b>	$\text{CDCl}_3$	180	No changes observed
<b>3Cl</b>	$\text{CDCl}_3$	180	No changes observed
<b>3Br</b>	pyridine- $d_5$	150*	Changes observed

\*Due to experimental restrictions the pyridine- $d_5$  solution could only be photolysed for a total of 150 minutes.

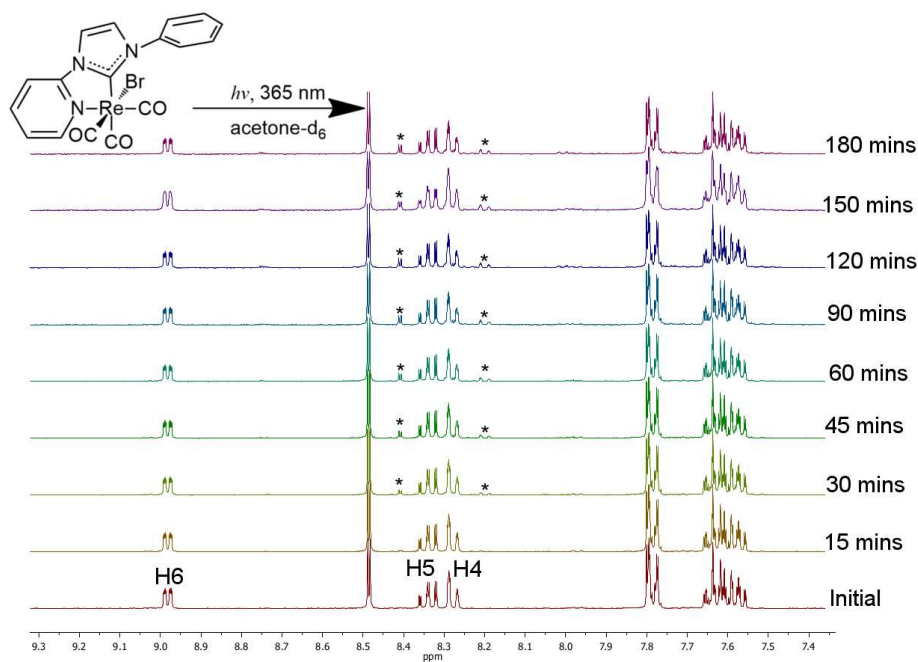


Figure 5.16:  $^1\text{H}$  NMR sequence of **3Br** photolysed in acetone- $d_6$  showing no major spectral changes occurring photolysis.

The next step in elucidating the mechanism of the PLSRs of **3Br** and **3Cl** was to assess if the reaction is solvent dependent. Solvent dependent reactions are more typical of associative mechanisms occurring from vibrationally hot MLCT states such as those

observed for *fac*-[Re(bpy)(CO)<sub>3</sub>Cl] (**117**) demonstrated by Sato and co-workers as previously shown in **Scheme 4.12**.<sup>90</sup>

The <sup>1</sup>H NMR monitored photolysis regime was repeated with both **3Br** and **3Cl** in a variety of coordinating and non-coordinating deuterated solvents; CDCl<sub>3</sub>, acetone-d<sub>6</sub> and pyridine-d<sub>5</sub>. The solutions were degassed before photolysis. The results are summarised in **Table 5.3** and the <sup>1</sup>H NMR progressions are depicted in **Figures 5.16, 5.17, 5.18, 5.19** and **5.20**.

Overall no major spectral changes were observed for any of the solvents systems except for pyridine-d<sub>5</sub>. For the acetone-d<sub>6</sub> solutions of **3Br** and **3Cl** there are small changes near the pyridyl-H5 and H4 protons shown by the asterisked regions in **Figures 5.16** and **5.17**. These changes occur at a considerably slower rate compared to the changes observed for acetonitrile and pyridine-d<sub>5</sub> solutions. Additionally the pyridyl-H6 proton is unaffected therefore **3Br** and **3Cl** are deemed photostable in acetone-d<sub>6</sub> solutions in the given time frame under the trialled photolysis conditions. If there is a photochemical ligand substitution reaction occurring it is very slow compared to that which was observed for CD<sub>3</sub>CN solutions.

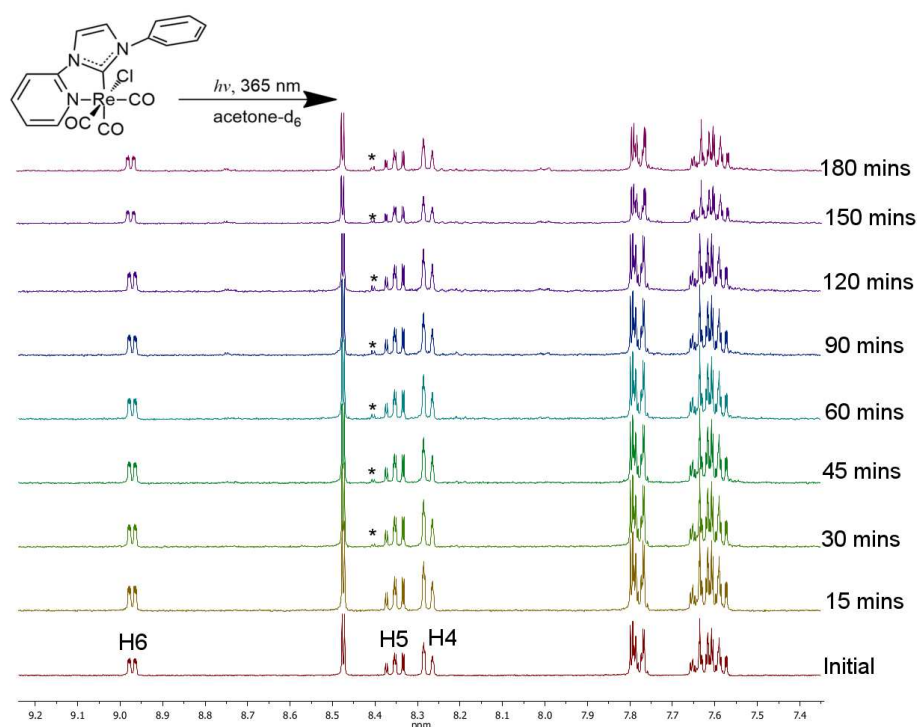
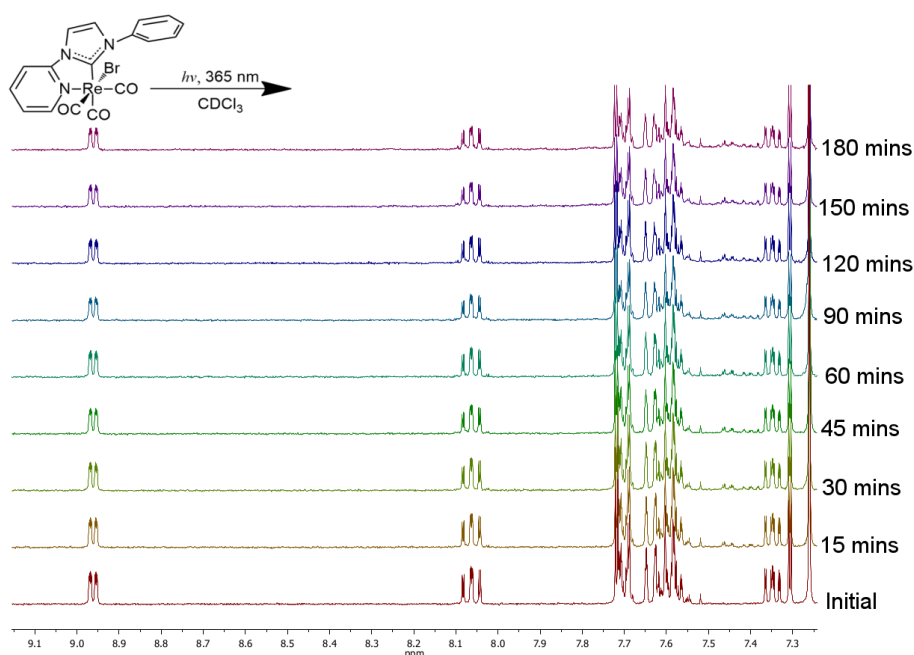


Figure 5.17: <sup>1</sup>H NMR sequence of **3Cl** photolysed in acetone-d<sub>6</sub> showing no major spectral changes occurring photolysis.

**Figure 5.20** shows the  $^1\text{H}$  NMR progression of the photolysis of **3Br** in pyridine- $d_5$  over 150 minutes. Several spectral changes are observed such as the formation of a new triplet in the asterisked region however the most well resolved changed is that occurring to the resonance of the pyridyl-H6 proton, a. As photolysis proceeds a new downfield doublet, i', appears adjacent to the original peak, a, after 30 minutes of photolysis.

A second small peak then starts to form after 90 minutes of photolysis. This peak, ii', seemingly shifts downfield until it overlaps with peak i' forming the multiplet seen at the 150 minute mark. Attempts to crystallise the photolysed solutions to provide further structural information proved unsuccessful. Overall these observations in different solvent systems demonstrate that the photochemical reaction is solvent dependent and suggests that the PLSRs might be occurring *via* an associative mechanism. An associative mechanism is dependent on the solvents ability to coordinate to the rhenium and possibly form a seven member intermediate such as compound **160** as seen in **Scheme 4.12** in **Chapter 4**.



**Figure 5.18:**  $^1\text{H}$  NMR sequence of **3Br** photolysed in  $\text{CDCl}_3$  showing no spectral changes occurring photolysis.

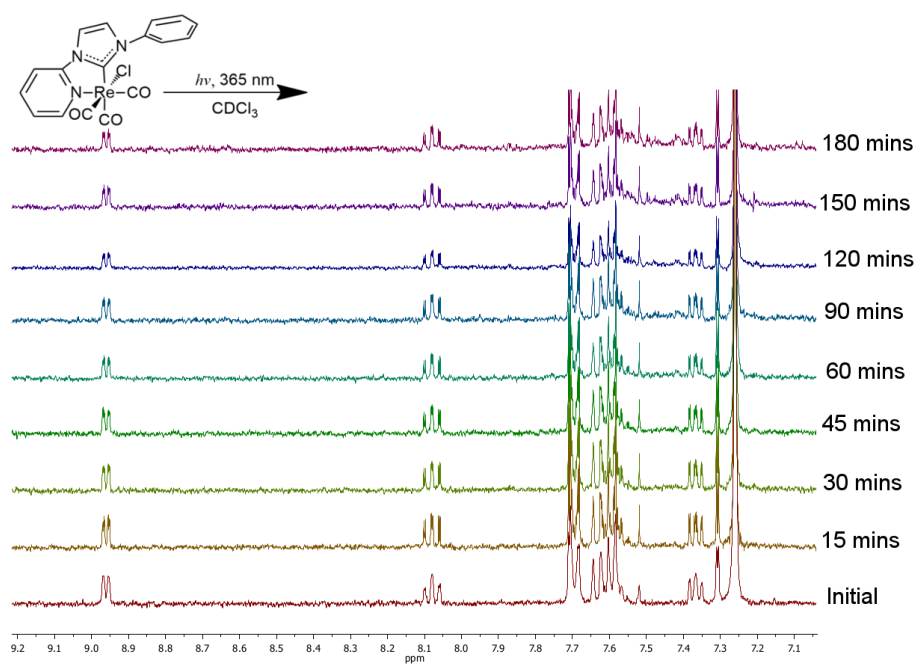


Figure 5.19:  $^1\text{H}$  NMR sequence of **3Cl** photolysed in  $\text{CDCl}_3$  showing no spectral changes occurring photolysis.

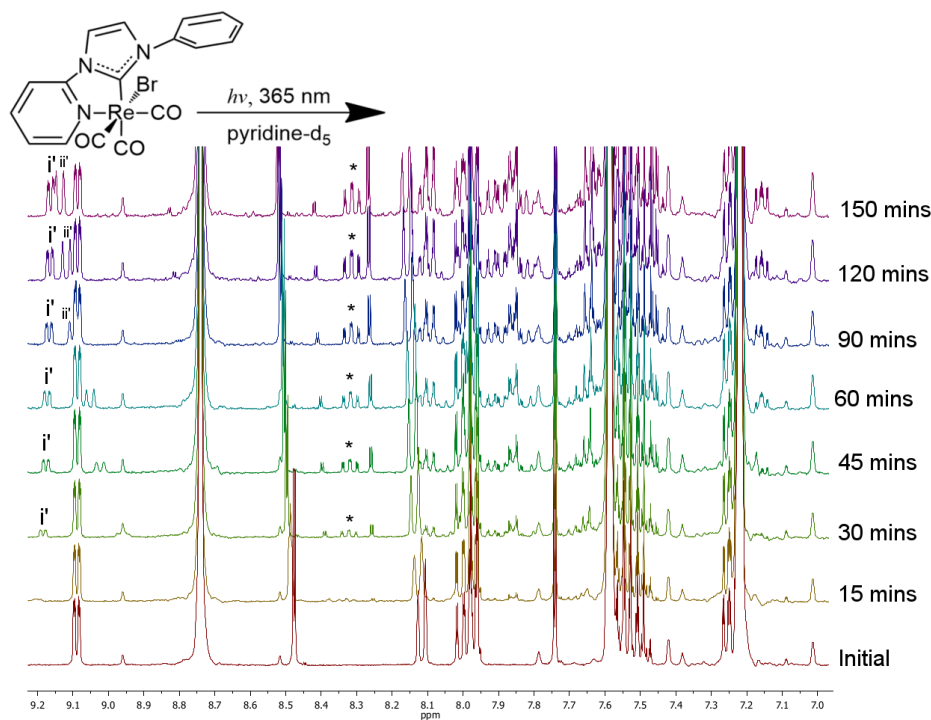


Figure 5.20:  $^1\text{H}$  NMR sequence of **3Br** photolysed in pyridine- $\text{d}_5$  showing major spectral changes occurring photolysis.

As the literature demonstrates that pyridine is known to readily participate in photochemical ligand substitution reactions with rhenium(I)-diimine compounds and is able to form stable photoproducts, it is not surprising that it participated in a PLSR with this rhenium(I)-NHC system.<sup>77,81,86</sup> This solvent dependence and associative mechanism further suggests that the photochemistry is occurring from vibrationally hot MLCT state rather than an thermally accessible LF state as the one depicted in **Figure 4.2**.<sup>70</sup>

## 5.4 The Photochemical Activity of the Remainder of the Pyridyl NHC Series

As compounds **3Br** and **3Cl** had been found to be photochemically active, the investigation was extended to the remainder of the 1-(2-pyridyl)-imidazol-2-ylidene series (**Figure 5.2**) to assess whether the functional group (R) had any effect on the photochemical properties. A qualitative approach was utilised without any rate measurements. Concentrated acetonitrile solutions of compounds **1-2Cl/Br** were photolysed

as per the procedure outlined in **Experimental Section 8.7.4**. The IR spectra of the carbonyl stretching region for each of the four compounds is shown in **Figure 5.21**.

The photolysed IR spectra of compounds **1-2Cl/Br** display similar spectral changes as those observed for **3Cl/Br**. Both the butyl and the mesityl series proved to be photoactive as the IR spectra of the photolysed reaction mixtures were visibly different to the spectra of the starting material. The compounds exhibited similar spectral changes to those observed for **3Br** and **3Cl** as previously shown in **Figure 5.8** indicating that manipulating the R group does not significantly alter the photochemical activity.

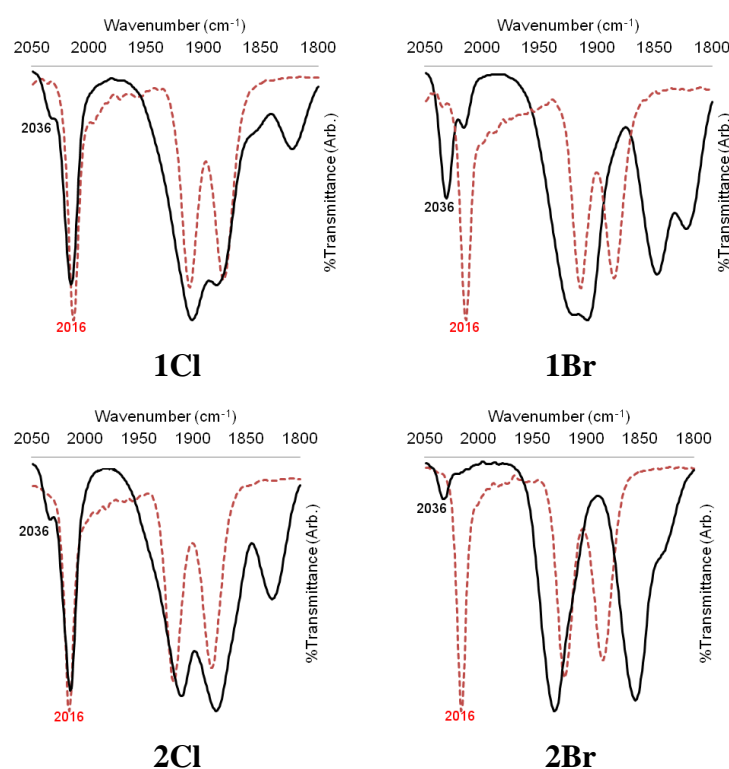


Figure 5.21: Infrared spectra of 1-(2-pyridyl)-imidazol-2-ylidene compounds **1-2Cl/Br** demonstrating the change in the stretching frequencies of the carbonyl bands before (red dashed line) and after (black bold line) photolysis.

For the bromo compounds, **1Br** and **2Br**, the initial band at  $2016\text{ cm}^{-1}$  has significantly decreased in intensity. In fact, in the case of **2Br** it seems to have disappeared completely and has been replaced by the higher energy band at  $2036\text{ cm}^{-1}$  indicative of the presence of the cationic acetonitrile solvated complex. On the other hand the  $2016\text{ cm}^{-1}$  band is still largely apparent in the spectra of the chloro compounds **1Cl**

and **2Cl** and the 2036  $\text{cm}^{-1}$  is only a small shoulder. This would suggest that the bromo compounds are more reactive towards forming the cationic acetonitrile complex than the chloro compounds.

## 5.5 Photochemical Investigation of the Pyrimidyl, Quinoyl and Quinoxyl NHC Compounds

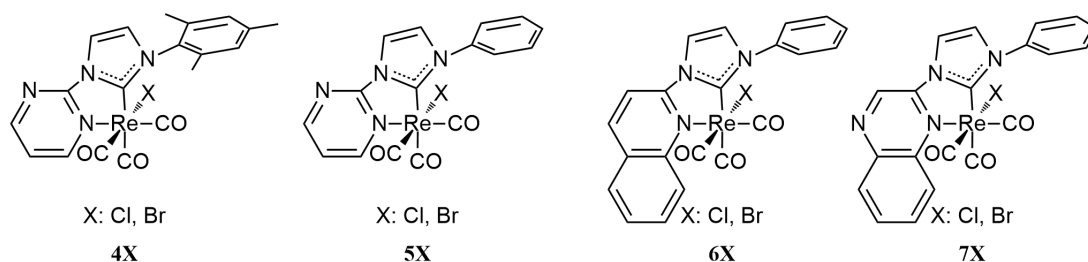


Figure 5.22: General structures for the 1-(2-pyrimidyl)-imidazol-2-ylidene, 1-(2-quinoyl)-imidazol-2-ylidene and 1-(2-quinoxyl)-imidazol-2-ylidene series.

The photochemical activity of the 1-(2-pyrimidyl)-imidazol-2-ylidene (**4-5Cl/Br**), 1-(2-quinoyl)-imidazol-2-ylidene (**6Cl/Br**) and 1-(2-quinoxyl)-imidazol-2-ylidene series (**7Cl/Br**) were investigated utilising the procedures previously outlined.

Table 5.4: Summary of the spectral changes occurring in the  $^1\text{H}$  NMR spectrum of photolysed solutions of **6Cl** and **6Br** in a variety of solvents.

Compound	Solvent	Photolysis Time (minutes)	Observations of the $^1\text{H}$ NMR spectrum
<b>6Cl</b>	$\text{CD}_3\text{CN}$	180	No changes observed
<b>6Br</b>	$\text{CD}_3\text{CN}$	180	No changes observed
<b>6Cl</b>	acetone- $\text{d}_6$	180	No changes observed
<b>6Br</b>	acetone- $\text{d}_6$	180	No changes observed
<b>6Cl</b>	$\text{CDCl}_3$	180	No changes observed
<b>6Br</b>	$\text{CDCl}_3$	180	No changes observed

The photochemical activity of **6Cl/Br** in deuterated acetonitrile, acetone and chloroform were examined using the experimental procedure outlined in **Experimental**

**Section 8.7.5** and the results are summarised in **Table 5.4**. The  $^1\text{H}$  NMR progressions are depicted in **Figures 5.23-5.28**. There are no observable spectral changes in any of the solvents for both **6Cl** and **6Br** indicating that the 1-(2-quinoyl)-imidazol-2-ylidene series is photostable and does not participate in PLSRs under these conditions. As a result of this analogous experiments in pyridine- $d_5$  were not performed to prioritise the limited amount of solvent for photoactive experiments.

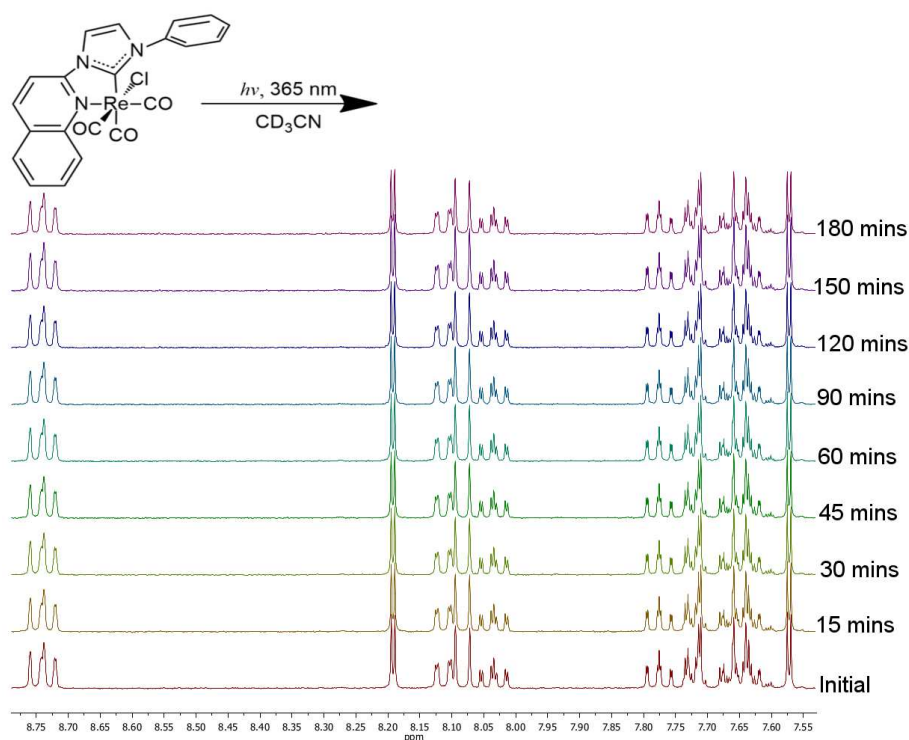


Figure 5.23:  $^1\text{H}$  NMR sequence of **6Cl** photolysed in  $\text{CD}_3\text{CN}$  showing no spectral changes occurring photolysis.

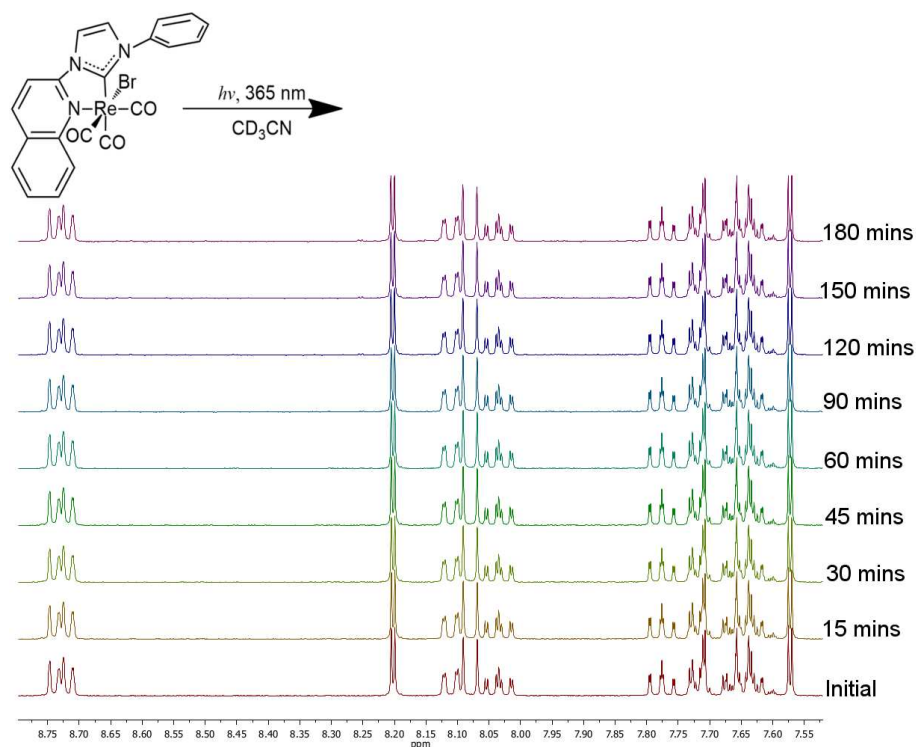


Figure 5.24:  $^1\text{H}$  NMR sequence of **6Br** photolysed in  $\text{CD}_3\text{CN}$  showing no spectral changes occurring photolysis.

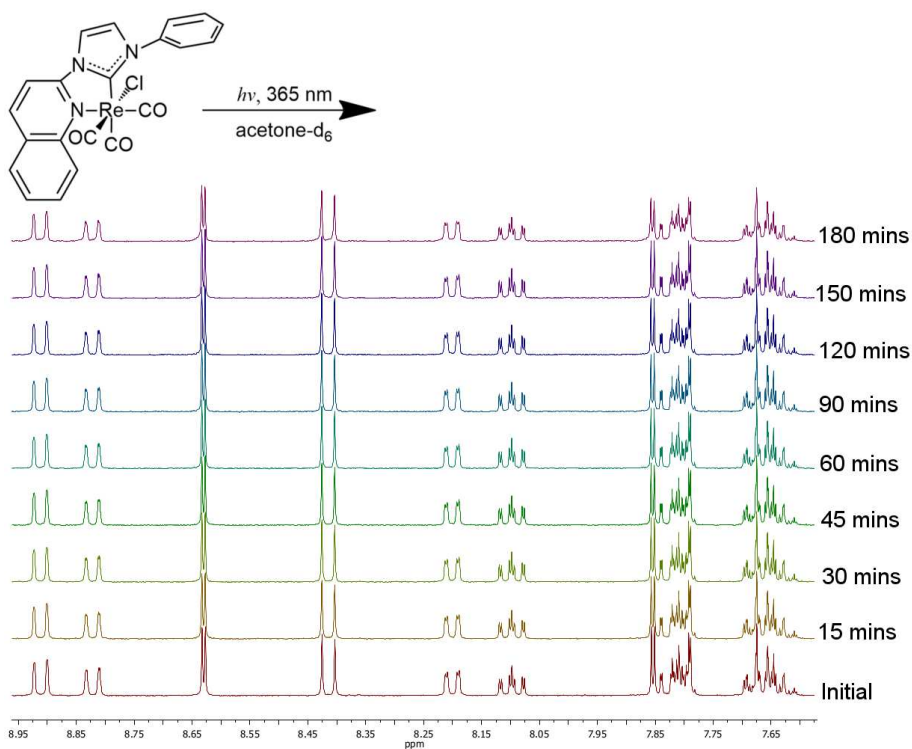


Figure 5.25:  $^1\text{H}$  NMR sequence of **6Cl** photolysed in  $\text{acetone-d}_6$  showing no spectral changes occurring photolysis.

The photochemical activity of the 1-(2-pyrimidyl)-imidazol-2-ylidene and 1-(2-quinoxyl)-imidazol-2-ylidene series was then assessed using the method outlined in **Experimental Section 8.7.4**. Acetonitrile solutions of each of the compounds, **4-5,7Cl/Br**, were photolysed and the infrared spectrum of the carbonyl stretching region was examined to see if any structural changes had occurred. As shown in **Figure 5.29** the stretching frequencies of the carbonyl bands for all the tested compounds are unaffected by the photolysis. There are small differences in the shape of the peaks which can be attributed to fact that the initial spectra are taken from DMSO solutions and the final spectra are from evaporated acetonitrile solutions.

The combined NMR and IR data indicates that the 1-(2-pyrimidyl)-imidazol-2-ylidene and 1-(2-quinoxyl)-imidazol-2-ylidene series are photochemically stable when excited to the MLCT manifold. Therefore, of the four new series of rhenium(I)-NHC tricarbonyl compounds, only 1-(2-pyridyl)-imidazol-2-ylidene series participates in photochemical ligand substitution reactions whilst the rest are photostable.

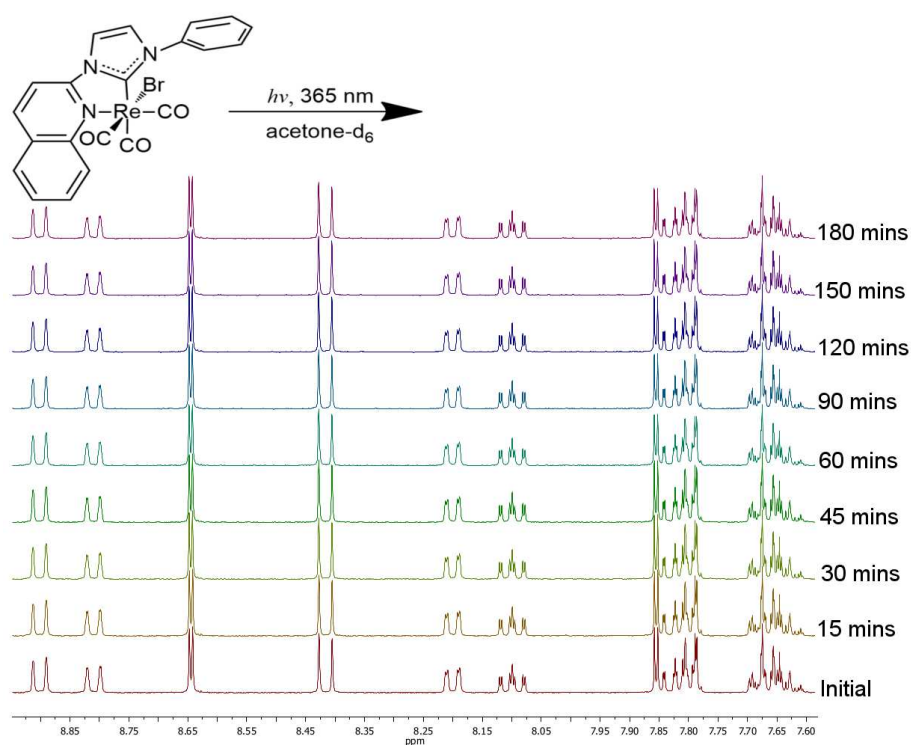


Figure 5.26:  $^1\text{H}$  NMR sequence of **6Br** photolysed in acetone- $\text{d}_6$  showing no spectral changes occurring photolysis.

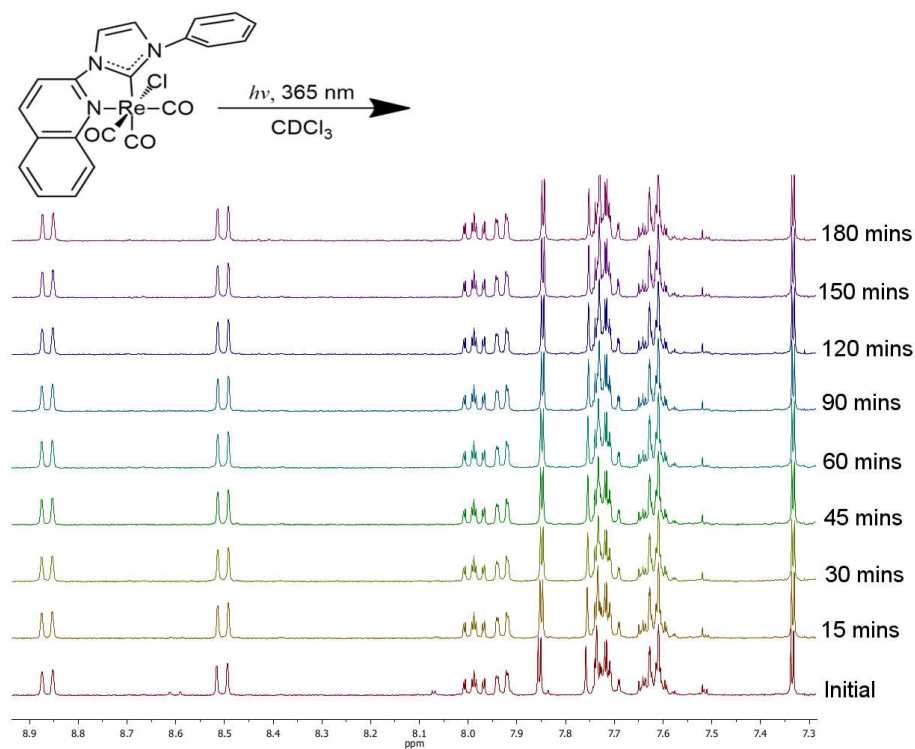


Figure 5.27:  $^1\text{H}$  NMR sequence of **6Cl** photolysed in  $\text{CDCl}_3$  showing no spectral changes occurring photolysis

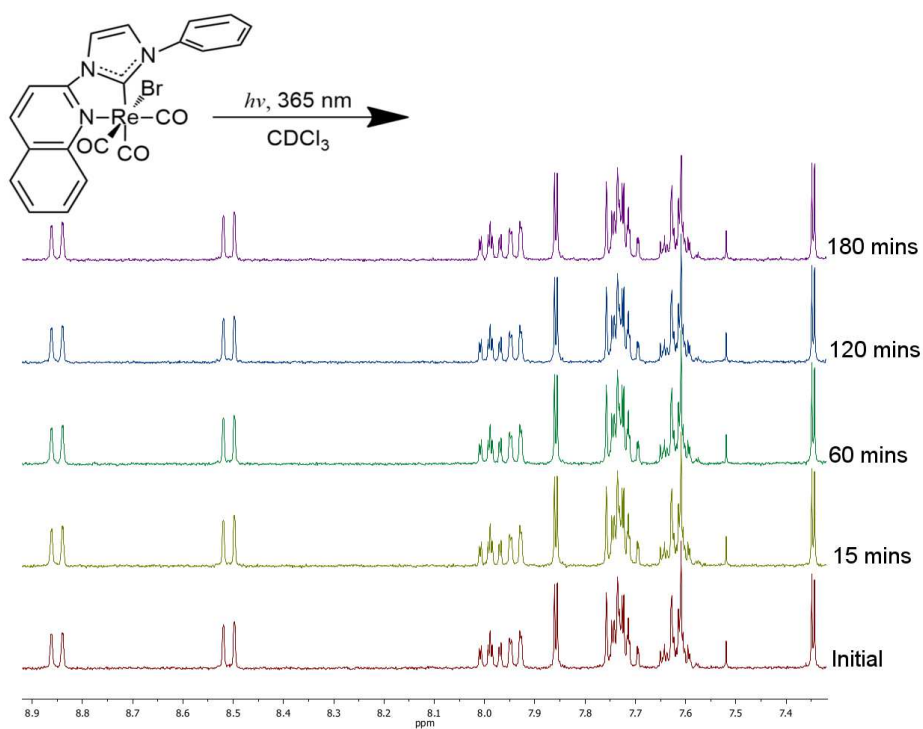


Figure 5.28:  $^1\text{H}$  NMR sequence of **6Br** photolysed in  $\text{CDCl}_3$  showing no spectral changes occurring photolysis. Due to experimental restrictions the  $^1\text{H}$  NMR spectra were collected at irregular periods to the those shown in **Figures 5.23-5.27** however the total photolysis time remains the same.

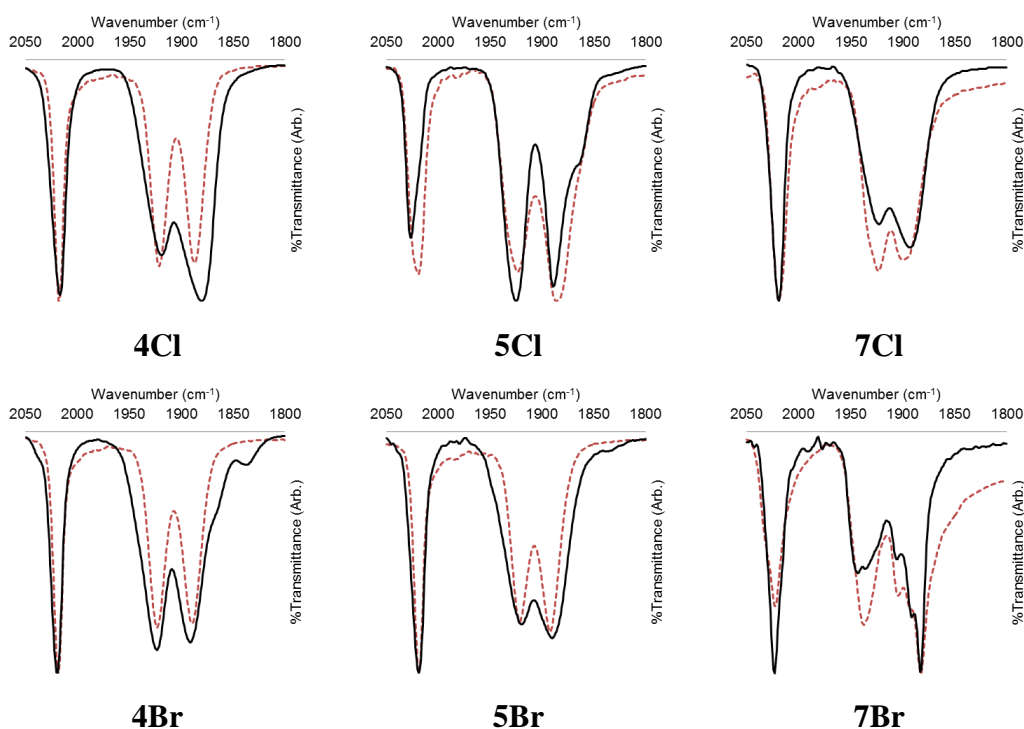


Figure 5.29: Infrared spectra of compounds **4**, **5** and **7Cl/Br** demonstrating no change in the stretching frequencies of the carbonyl bands before (red dashed line) and after (black bold line) photolysis.

## 5.6 Summary and Concluding Remarks

The photochemical activity of all fourteen rhenium(I)-NHC tricarbonyl compounds was assessed. Acetonitrile solutions of the 1-(2-pyridyl)-imidazol-2-ylidene compounds were found to be stable in the dark for up to 3 hours and stable up to 82 °C for 2 hours. When excited at the MLCT manifold (365-370 nm) the 1-(2-pyridyl)-imidazol-2-ylidene compounds were observed to undergo chemical transformations. On the other hand acetonitrile solutions of the 1-(2-pyrimidyl)-, 1-(2-quinoyl)- and 1-(2-quinoxyl)-imidazol-2-ylidene compounds were found to be stable when excited at the MLCT manifold.

The chemical transformations observed for 1-(2-pyridyl)-imidazol-2-ylidene compounds were characterised as photochemical ligand substitution reactions and were found to be solvent dependent. In acetonitrile solutions three photoproducts were observed and were identified as one cationic species and two dicarbonyl species. The cationic species was identified as the acetonitrile solvato species; *fac*-[Re(PyImPh)(CO)<sub>3</sub>(NCCH<sub>3</sub>)]<sup>+</sup> (**164**)

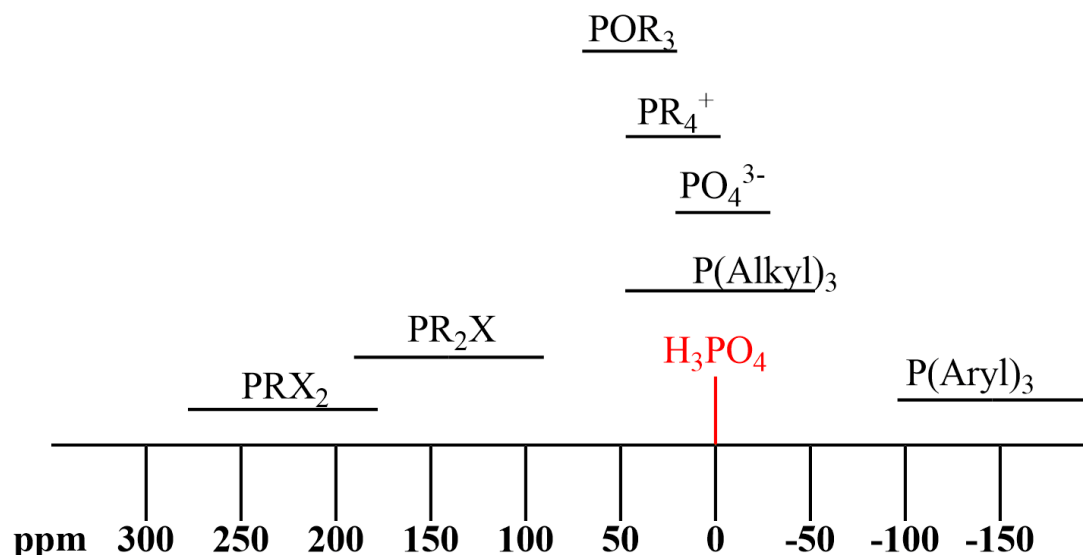
and one of the dicarbonyl species was confirmed as *cis,cis*-[Re(PyImPh)(CO)<sub>2</sub>(NCCH<sub>3</sub>)Cl] (**166**).

## Chapter 6

# Photochemical Investigation of Re(I)-NHC Tricarbonyl Compounds with Organophosphorous Ligands

### 6.1 Overview

Previous attempts to isolate *cis,cis*-[Re(PyImPh)(CO)<sub>2</sub>(NCCH<sub>3</sub>)Cl] (**165**), the proposed photoproduct in **Scheme 5.3**, had not been successful. The photolysis was therefore attempted in the presence of a stronger  $\sigma$  donating organophosphorous ligands with the aim of forming a more robust photoproduct. The use of organophosphorous ligands ( $L^P$ ) provides multiple benefits, the first being that [Re(diimine)( $L^P$ )<sub>x</sub>(CO)<sub>x</sub>] type compounds are known to induce photochemical ligand substitution reactions *via* a thermally accessible <sup>3</sup>LF state through a known dissociative mechanism. Therefore any photoactivity apparent for *fac*-[Re(NHC)(CO)<sub>3</sub>X] (X = Cl, Br) in conjunction with organophosphorous ( $L^P$ ) ligands can be compared directly to the known literature.<sup>70,84</sup> The use of organophosphorous ligands also allows for the use <sup>31</sup>P NMR spectroscopy which can be a useful tool for identifying coordinated and free organophosphorous ligands in solution.



X: Halogen

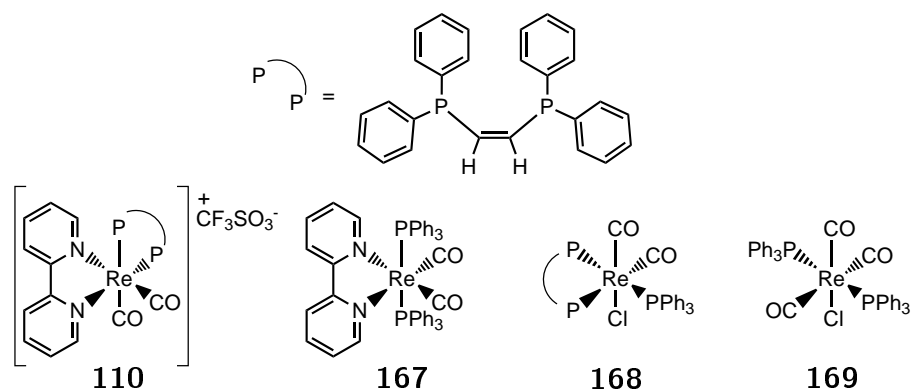
Figure 6.1: Typical chemical shifts for simple organophosphorous compounds (Adapted from Kuhl 2008).<sup>95</sup>

## 6.2 Characterisation of Rhenium(I) Complexes with $L^P$ Ligands by $^{31}\text{P}$ NMR

The use of organophosphorous ligands allows for the exploitation of  $^{31}\text{P}$  NMR to give additional information regarding the coordination state of the ligands.  $^{31}\text{P}$  resonances are well resolved and the measurements can be performed in non-deuterated solvents if necessary, however deuterated solvents are preferred for the NMR instrument to acquire a lock signal. The  $^{31}\text{P}$  resonances are observed as characteristic sharp line signals with predictable chemical shifts as shown in **Figure 6.1**.<sup>95</sup>

Standard  $^{31}\text{P}$  NMR experiments utilise proton decoupling to remove spin-spin coupling of the  $^{31}\text{P}$ - $^1\text{H}$  nuclei. Decoupling lessens signal broadening and causes the characteristic sharp line like resonances.<sup>95</sup> Coupling to other spin active nuclei such as  $^{19}\text{F}$ , other  $^{31}\text{P}$  nuclei and NMR active metals can be still be observed. However, coupling to  $^{13}\text{C}$  is not observed unless in a  $^{13}\text{C}$  enriched environment.<sup>95</sup> Alternatively, coupling of the  $^{31}\text{P}$ - $^{13}\text{C}$  nuclei can be observed in the  $^{13}\text{C}$  spectrum. As both of the abundant isotopes of rhenium ( $^{185}\text{Re}$ , 37.40% ;  $^{187}\text{Re}$ , 62.60%) have a spin of  $\frac{5}{2}$  both nuclei are considered

NMR inactive. Therefore coupling between rhenium and phosphorous can not occur due to the quadrupolar nature of the rhenium isotopes.



**110**<sup>1</sup>P{<sup>1</sup>H} (CD<sub>3</sub>CN):  $\delta = 52.2$  (d,  $J = 19$  Hz),  $42.2$  (d,  $J = 19$  Hz) ppm.

**167**<sup>1</sup>P{<sup>1</sup>H} (CD<sub>3</sub>CN):  $\delta = 24.6$  (s) ppm.

**168**<sup>1</sup>P{<sup>1</sup>H} (CDCl<sub>3</sub>):  $\delta = 49.6$  (dd,  $J = 186.5, 9.40$  Hz),  $29.8$  (dd,  $J = 21.01, 10.28$  Hz), and  $12.1$  (dd,  $J = 186.7, 21.38$  Hz) ppm.

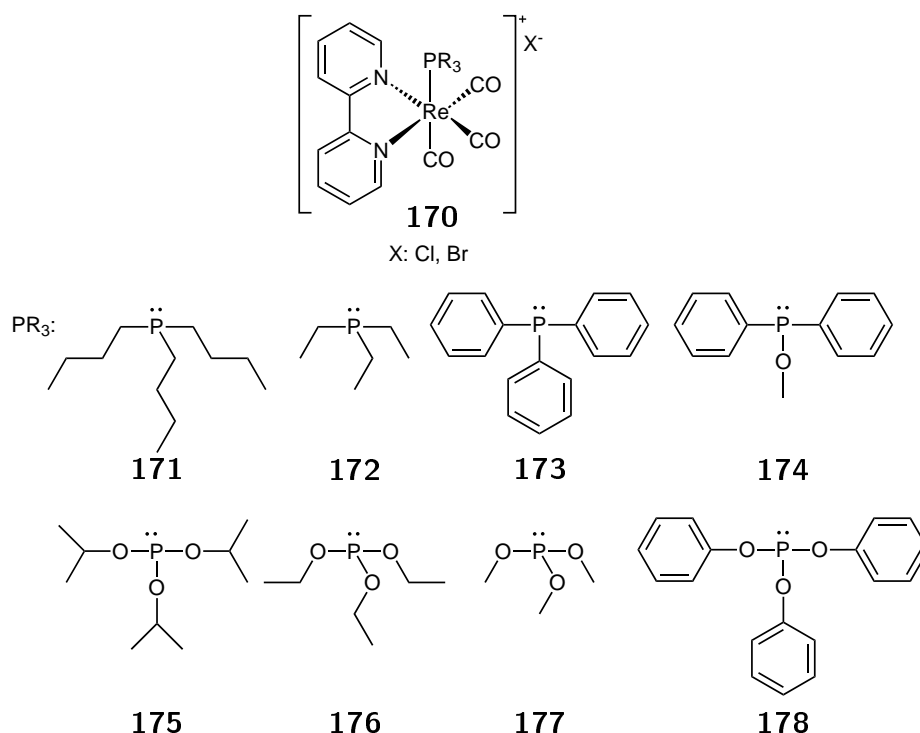
**169**<sup>1</sup>P{<sup>1</sup>H}:  $\delta = 10.04$  (s) ppm.

Scheme 6.1: Phosphorous NMR chemical shifts for various Re(I) compounds (Adapted from Smithback 2006).

<sup>31</sup>P-<sup>31</sup>P coupling of organophosphorous ligands through a metal centre can be observed if the ligands are in non-equivalent environments such as the two doublets exhibited by compound **110** in **Scheme 6.1**.<sup>71</sup> These coupling constants can be used to determine the geometry, such as *cis* and *trans*, of the ligands. For instance, Smithback stated for compound **168** the large coupling constant of ~186 Hz observed for the two doublet of doublets at 49.6 and 12.1 ppm, in their <sup>31</sup>P-<sup>1</sup>H coupled spectrum, was characteristic of a phosphine ligand in *trans* to a CO and *cis* to another phosphine.<sup>71</sup>

When identical L<sup>P</sup> ligands are in *trans* to one another, as in compound **167**, only one <sup>31</sup>P signal is observed as both ligands are in the same electronic environment due to the symmetry of the coordination compound.<sup>71</sup> The same phenomenon is observed for the two triphenylphosphine ligands in *trans* to one another in compound **169** even though the complex is in the *mer* configuration.<sup>71,96</sup>

The study by Hori demonstrated that the organophosphorous ligands, shown in **Scheme 6.2**, exhibited a change ( $\Delta\delta$ ) in their <sup>31</sup>P chemical shift upon coordination to rhenium(I) as outlined in **Table 6.1**.<sup>85</sup> Hori identified that the ligands which had lower Tolman's  $\chi$  constants, and were therefore poorer electron acceptors (**171**, **172**, and **173**), exhibited a positive  $\Delta\delta$  value upon coordination.



Scheme 6.2: Various phosphorous ligands investigated by Hori et al.<sup>85</sup>

Table 6.1:  $\delta^{31}\text{P}$  chemical shifts for coordinated and free organophosphorous ligands in  $\text{CDCl}_3$  (Adapted from Hori, 1997).<sup>85</sup>

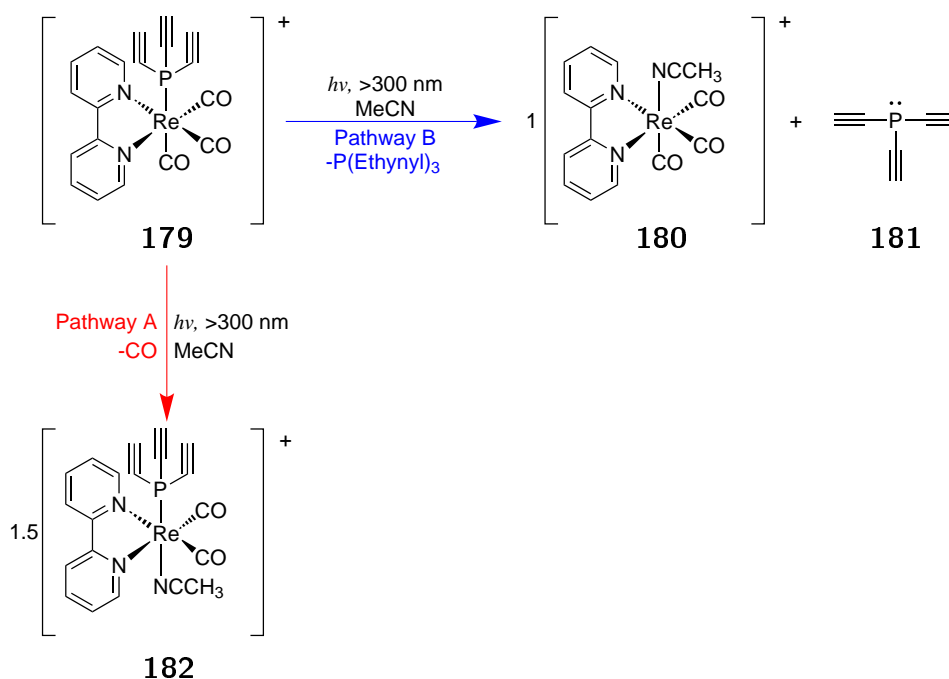
Ligand	$\delta^{31}\text{P}$ ligand	$\delta^{31}\text{P}$ complex <sup>a</sup>	$\Delta\delta^{31}\text{P}$ (complex - ligand)
<b>P(<sup>n</sup>Bu)<sub>3</sub> (171)</b>	-31.1 <sup>97</sup>	-12.7	18.4
<b>PEt<sub>3</sub> (172)</b>	-17.7 <sup>97</sup>	-6.9	10.8
<b>PPh<sub>3</sub> (173)</b>	-9.3	15.3	24.6
<b>P(OMe)Ph<sub>2</sub> (174)</b>	113.1	104.0	-9.1
<b>P(O<sup>i</sup>Pr)<sub>3</sub> (175)</b>	135.5	101.4	-34.1
<b>P(OEt)<sub>3</sub> (176)</b>	134.9	103.5	-31.4
<b>P(OMe)<sub>3</sub> (177)</b>	133.5 <sup>97</sup>	108.1	-25.4
<b>P(OPh)<sub>3</sub> (178)</b>	122.1 <sup>97</sup>	96.2	-25.9

85%  $\text{H}_3\text{PO}_4$  was used for the external standard.<sup>85</sup>

Accordingly, the stronger electron acceptors with higher Tolman's  $\chi$  constants; **174**, **175**, **176**, **177** and **178** exhibited negative  $\Delta\delta$  values. These characteristic changes in chemical shift can be utilised in this research to elucidate whether the  $\text{L}^{\text{P}}$  ligands are bound to the rhenium(I) or are free in solution.

### 6.3 Bifurcated Mechanistic Studies of Rhenium(I)-Diimine Tricarbonyl Compounds with $L^P$ Ligands

The photochemistry of rhenium(I)-diimine compounds bound to  $L^P$  ligands was reported by Koike who investigated the photochemical activity of  $fac$ -[Re(diimine)(CO)<sub>3</sub>( $L^P$ )]<sup>+</sup> type compounds with the following  $L^P$  ligands: triethylphosphite, tributylphosphine, triethylphosphine, triphenylphosphine, diphenylmethoxyphosphine, triisopropylphosphite and trimethylphosphite.<sup>70</sup> Koike classified the organophosphorous ligands into two categories; strong electron acceptors and weak electron acceptors. Koike established that photochemically induced carbonyl loss occurred for the  $fac$ -[Re(diimine)(CO)<sub>3</sub>( $L^P$ )]<sup>+</sup> compounds *via* population of a thermally accessible <sup>3</sup>LF state irrespective of the electron acceptor strength of the organophosphorous ligand.

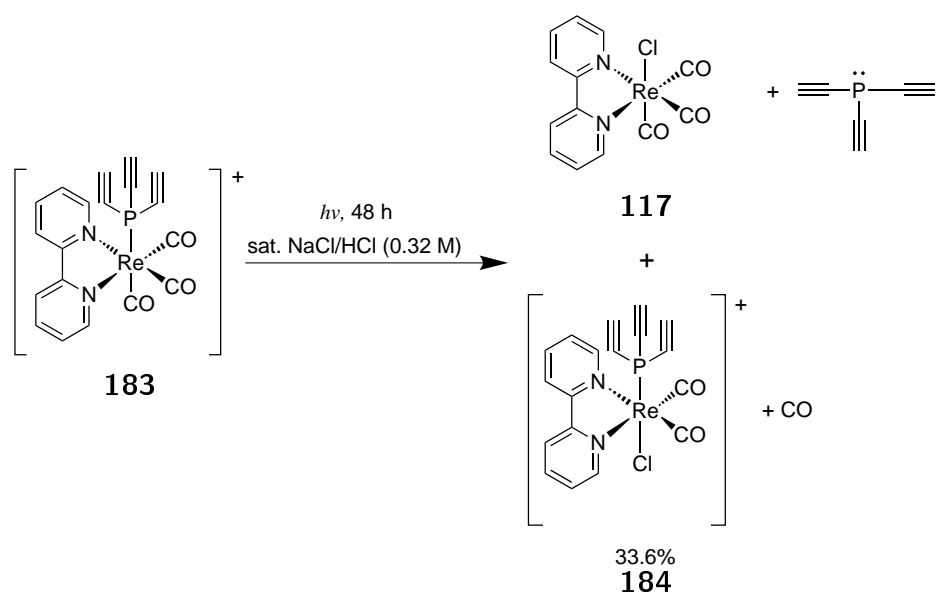


Scheme 6.3: Bifurcated photochemical mechanism of rhenium(I) with a triethynylphosphine ligand (Adapted from Hightower, 2005).<sup>98</sup>

After the initial studies by Hori and Koike, further investigations into the photoactivity of  $fac$ -[Re(bpy)(CO)<sub>3</sub>( $L^P$ )]<sup>+</sup> (**170**) type compounds was conducted by Hightower, who explored the photochemistry of  $fac$ -[Re(bpy)(CO)<sub>3</sub>(TEP)]<sup>+</sup> (**179**) where TEP was triethynylphosphine (**181**).<sup>98</sup>

Hightower discovered the photochemical ligand substitution reactions (PLSRs) of  $fac$ -[Re(bpy)(CO)<sub>3</sub>(TEP)]<sup>+</sup> (**179**) followed a bifurcated pathway with two competing pro-

cesses as detailed in **Scheme 6.3**.



Scheme 6.4: Bifurcated photochemical mechanism of rhenium(I) with a triethynylphosphine ligand in a saturated chloro environment (Adapted from Hightower, 2005).<sup>98</sup>

When *fac*-[Re(bpy)(CO)<sub>3</sub>(TEP)]<sup>+</sup> (**179**) was photolysed using high energy UV (specific  $\lambda$  not stated by authors) in an acetonitrile solution, the authors found that not only was the carbonyl in *trans* to the TEP ligand labile, as shown in Pathway A in **Scheme 6.3**, but so was the TEP ligand itself.

Hightower found that the TEP ligand could dissociate from the rhenium(I)-diimine compound and be replaced by a molecule of acetonitrile as shown by Pathway B in **Scheme 6.3**. The two pathways were thought to be in competition with one another with Pathway A, the loss of carbonyl pathway, favoured as after two hours of photolysis the ratio of photoproducts (**182:180**) was 1.5:1. Additionally, the authors found that in a rich chloride environment such as a saturated sodium chloride solution or hydrochloric acid (0.32 M) the substituent chloro ligand could displace either a molecule of TEP or CO as shown in **Scheme 6.4**, further substantiating the two pathways outlined in **Scheme 6.3**.

## 6.4 Stability of 3Br in the Presence of L<sup>P</sup> Ligands

As per **Chapter 5**, the stability of the rhenium(I)-NHC tricarbonyl compounds in the presence of organophosphorous ligands had to be addressed before a full photochemi-

cal investigation could commence. Hori used  $\text{CDCl}_3$  as the NMR solvent of choice for characterising their suite of  $\text{fac-}[\text{Re}(\text{bpy})(\text{CO})_3(\text{L}^P)]^+$  (**185**) compounds.<sup>85</sup> Due to the poor solubility of the  $\text{fac-}[\text{Re}(\text{PyImPh})(\text{CO})_3(\text{X})]$  (**3Br** and **3Cl**) compounds in  $\text{CDCl}_3$  a more polar solvent, acetone- $\text{d}_6$ , was utilised. Due to the increased polarity of the solvent, the  $^{31}\text{P}$  NMR resonances of the free organophosphorous ligands would be slightly different to those stated in **Table 6.1** which were recorded in  $\text{CDCl}_3$ . Nuclear magnetic resonance spectra were recorded using a Bruker Avance 400 spectrometer (400.1 MHz for  $^1\text{H}$ ; 100 MHz for  $^{13}\text{C}$ ; 162 MHz for  $^{31}\text{P}$ ).  $^{31}\text{P}$  NMR spectra were calibrated using an 85%  $\text{H}_3\text{PO}_4$  capillary external standard. All measurements were performed at room temperature, any heating was performed using a hotplate as described in **Experimental 8.7.2**.

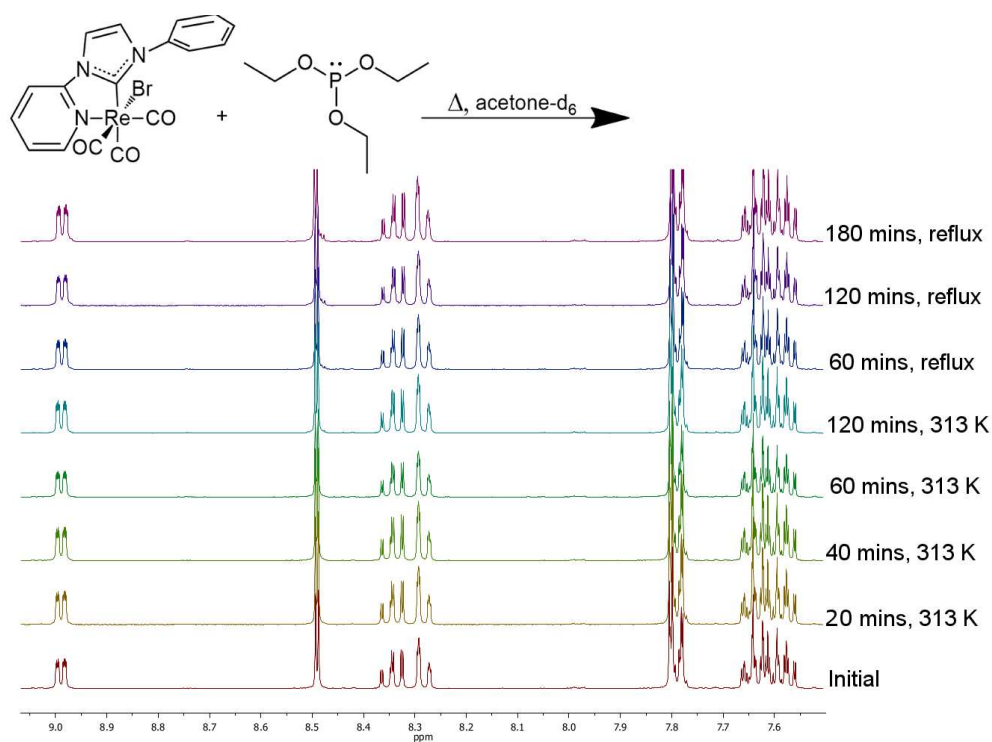


Figure 6.2:  $^1\text{H}$  NMR time series of **3Br** with triethylphosphite (3 molar equivalents) in acetone- $\text{d}_6$  showing no spectral changes during heating.

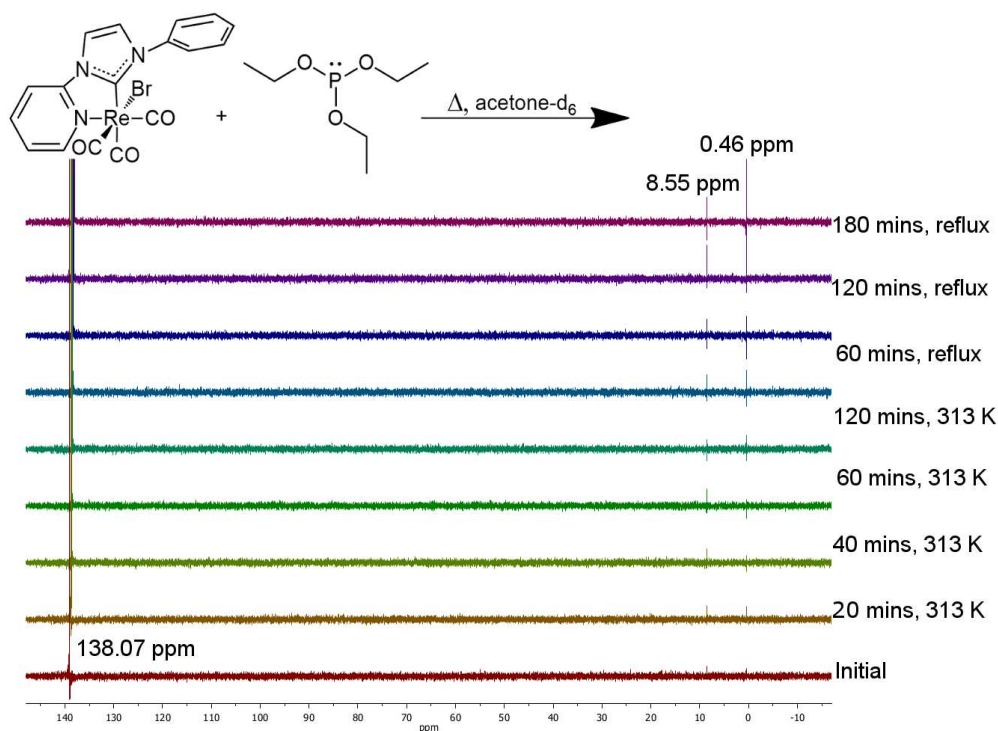
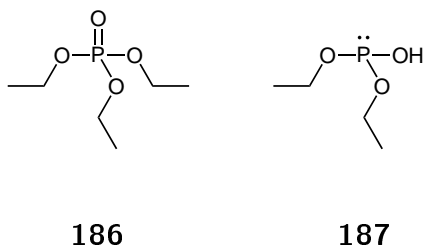


Figure 6.3:  $^{31}\text{P}$  NMR time series of **3Br** with triethylphosphite (3 molar equivalents) in acetone- $d_6$  showing minor changes during heating.

The ligand stability of **3Br** in the presence of triethylphosphite (3 molar equivalents) at 40 °C and at reflux temperatures in acetone- $d_6$  was monitored by both  $^1\text{H}$  and  $^{31}\text{P}$  NMR as per the method outlined in **Experimental Section 8.7.2**. The  $^1\text{H}$  NMR time series is shown in **Figure 6.2** and the  $^{31}\text{P}$  NMR time series is shown in **Figure 6.3**. The  $^1\text{H}$  NMR time series shows no change in the proton spectrum of the aromatic region of **3Br** over course of three hours of heating. This indicates that **3Br** and triethylphosphite do not engage in any thermally activated ligand substitutions under these reaction conditions. The  $^{31}\text{P}$  NMR time series shows a strong, high intensity singlet at 138.1 ppm which is similar to the literature value reported by Hori of 134.9 ppm for free triethylphosphite in  $\text{CDCl}_3$ .<sup>85</sup>

Additionally, there are two weak signals at 8.55 ppm and 0.46 ppm. The signal at 0.46 ppm is attributed to the oxidation product of triethylphosphite, triethylphosphate (**186**), which appears between -0.8 ppm -0.36 ppm in dichloromethane.<sup>99,100</sup> The signal at 8.55 ppm is attributed to hydrolysed triethylphosphite, diethyl phosphorous acid (**187**), which is a common by-product in the oxidation of triethylphosphite and appears at 7.97

ppm in dichloromethane.<sup>100</sup>



Scheme 6.5: Oxidation and hydrolysis products of triethylphosphite.

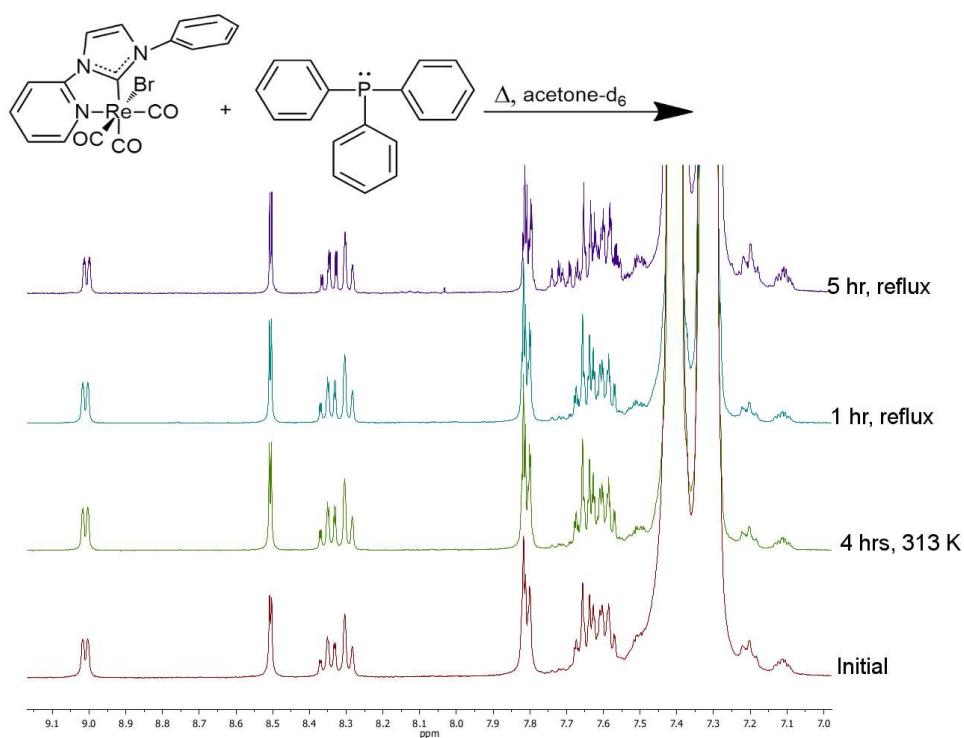


Figure 6.4:  $^{31}\text{P}$  NMR time series of **3Br** and triphenylphosphine (10 molar equivalents) in acetone- $d_6$  showing no spectral changes during heating.

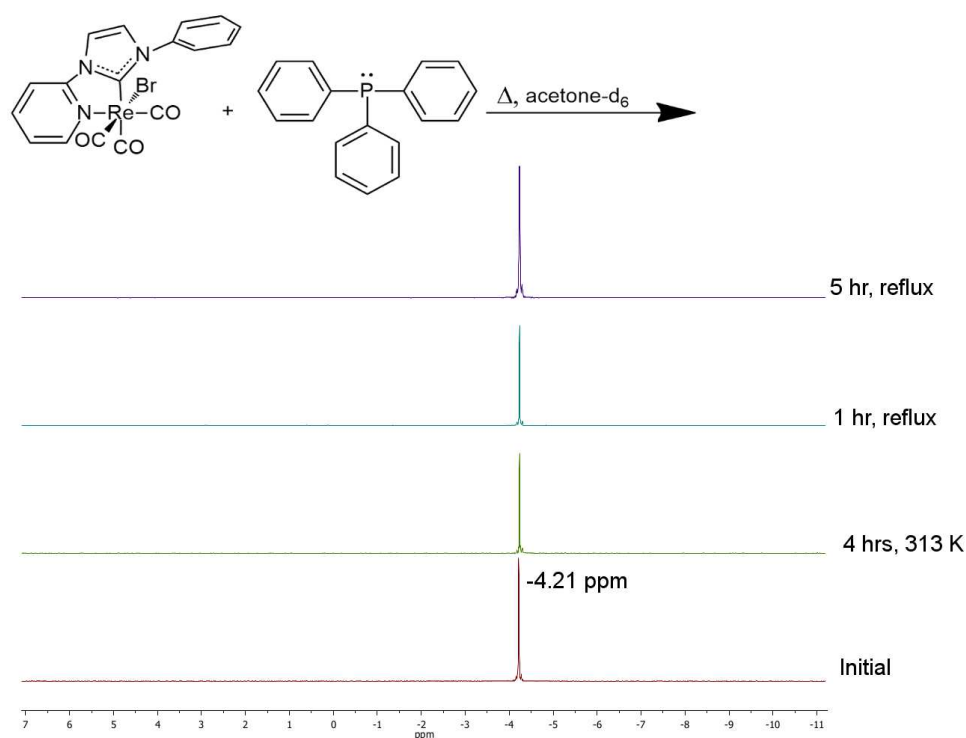


Figure 6.5: <sup>31</sup>P NMR time series of **3Br** and triphenylphosphine (10 molar equivalents) in acetone-d<sub>6</sub> showing no spectral changes during heating.

The thermal stability of **3Br** in the presence of triphenylphosphine (10 molar equivalents) in acetone-d<sub>6</sub> at 40°C and at reflux temperatures was monitored by both <sup>1</sup>H and <sup>31</sup>P NMR as per the method outlined in **Experimental Section 8.7.2**. The <sup>1</sup>H NMR time series is shown in **Figure 6.4** and the <sup>31</sup>P NMR time series is shown in **Figure 6.5**.

As per triethylphosphite, the <sup>1</sup>H NMR spectrum of **3Br** does not exhibit any spectral changes over the 9 hour heating process indicating that **3Br** does not undergo any thermally activated ligand substitution reactions with triphenylphosphine in acetone. The <sup>31</sup>P spectrum of triphenylphosphine shows one signal, a large singlet at -4.21 ppm which is very similar to the literature values of -4.84 ppm in CH<sub>2</sub>Cl<sub>2</sub> and -9.3 ppm in CDCl<sub>3</sub>.<sup>85,100</sup> The difference in the resonance compared to the literature value is attributed to the variability of <sup>31</sup>P NMR calibration method. For all measurements recorded by this investigation and external phosphoric acid standard was used.

## 6.5 Photochemical Activity of **3Br** with Triethylphosphite in Acetone

As **3Br** was found to be thermally stable with the organophosphorous ligands in acetone, a full photochemical investigation could be performed where any thermal contributions could be excluded. The UV-vis spectrum of a *ca.*  $10^{-5}$  M solution of **3Br** in acetone with 2.5 molar equivalents of triethylphosphite was collected as shown in **Figure 6.6**. The same solution, Sample A, was then photolysed by scanning at  $\lambda_{ex}=370$  nm. A total of 99 consecutive spectra, with no delay between replicates, were run per solution at a speed of  $240 \text{ nm min}^{-1}$  with the detector set to acquire a signal between 200 and 800 nm. Under these experimental conditions the solution was constantly irradiated for a period of approximately 4 hours as per the method outlined in **Experimental Section 8.7.3**. Whilst Sample A was photolysed, a second sample, Sample B, was kept in the dark for the same period of time at room temperature.

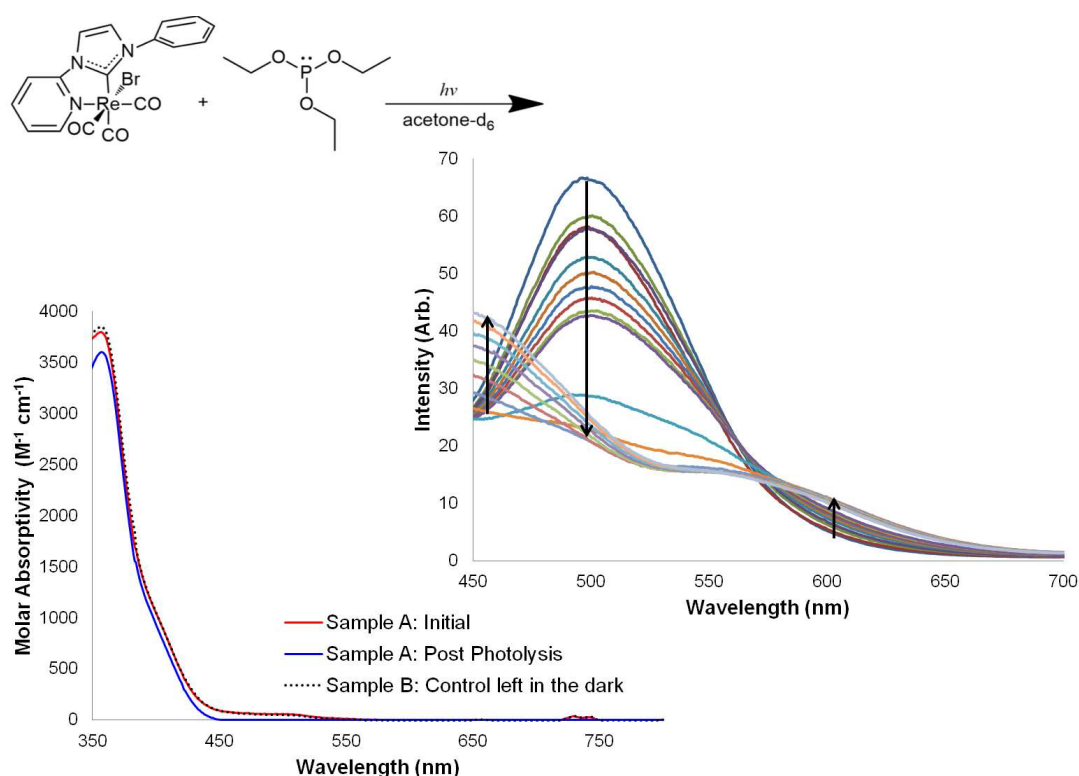


Figure 6.6: UV-Vis and emission spectrum displaying the spectral changes occurring to a *ca.*  $10^{-5}$  M solution of **3Br** and triethylphosphite (2.5 molar equivalents) in acetone when photolysed at  $\lambda_{ex} = 370$  nm for 99 consecutive scans.

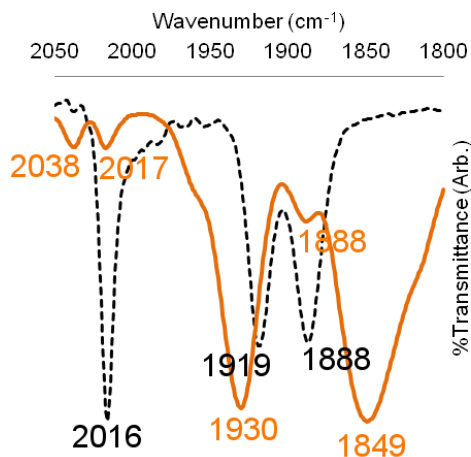


Figure 6.7: IR spectra of **3Br** (black dash) and the reaction mixture of **3Br** photolysed in acetone with triethylphosphite (2.5 molar equivalents) for seven hours photolysis at  $\lambda_{ex}$ : 365 nm (orange trace).

After photolysis, a second UV-vis spectrum of Sample A was collected and the three UV-vis spectra were overlaid in **Figure 6.6** to see if any spectral changes had occurred. The initial UV-vis spectrum of Sample A consists of one major band at 357 nm. The scan window has been reduced from 250-800 nm to 350-800 nm as acetone strongly absorbs wavelengths <330 nm.<sup>101</sup> After photolysis the maximum of the original band has not greatly shifted as shown by the blue trace in **Figure 6.6**. The UV-vis spectrum of control sample (B) left in the dark is superimposable with the initial UV-vis spectrum of Sample A indicating that **3Br** is stable in acetone in the presence of triethylphosphite under the dark conditions.

In the initial emission spectrum, the emission maximum is centred at 496 nm as shown in **Figure 6.6**. As the photolysis proceeds this maximum diminishes in intensity and a new blueshifted shoulder starts to appear at 450 nm. This blueshift is indicative of the presence of a cationic rhenium(I) species which are known to have a blueshifted maximum in comparison to their neutral analogues.<sup>102</sup> There is also a red-shifted shoulder of lower intensity centred around 600 nm that appears as the photolysis progresses. This band could indicate the formation of a dicarbonyl species. The existence of a cationic species implies that the anionic bromo ligand has been replaced by a neutral ligand. Previously in **Chapter 5** the formation of a cationic species was determined to be

an integral part of the photochemical mechanism of **3Br** in CD<sub>3</sub>CN.

Further analysis was performed on a solution of **3Br** with triphenylphosphine (2.5 molar equivalents) in acetone which was photolysed *via* a UV lamp for seven hours at 365 nm as per the method outlined in **Experimental Section 8.7.5**. The pale yellow solution turned orange over the course of the photolysis and an IR spectrum of the resultant solution was collected as per the method in **Experimental Section 8.7.4** and is shown in **Figure 6.7**. The photolysed spectrum appears to contain some starting material, as indicated by 2017 and 1888 cm<sup>-1</sup>, and a cationic species as indicated by the small stretch at 2038 cm<sup>-1</sup>. The pair of high intensity stretches at 1930 and 1849 cm<sup>-1</sup> could be indicative of a dicarbonyl species suggesting that the photolysis of **3Br** in acetone with triethylphosphite could result in similar photoproducts to those formed by the photolysis of **3Br** in acetonitrile solutions.<sup>71</sup>

To try and structurally identify the photoproducts being formed, an NMR monitored experiment was utilised. **3Br** was dissolved in acetone-d<sub>6</sub> and an initial <sup>1</sup>H NMR spectrum was collected. Triethylphosphite (2.5 equivalents) was then dissolved in the acetone-d<sub>6</sub> solution and the light yellow solution was photolysed according to the procedure outlined in **Experimental Section 8.7.5** for three hours. <sup>1</sup>H and <sup>31</sup>P NMR spectra were collected after the initial addition of the triethylphosphite ligand and at the end of the three hour photolysis.

Post photolysis, the pale yellow solution had turned orange in colour. Examination of the <sup>1</sup>H NMR spectrum post photolysis revealed spectral changes in the aromatic region as shown in **Figure 6.8**. The visible changes in the aromatic region were not as well resolved as those observed for the photolysis of **3Br** in CD<sub>3</sub>CN in **Chapter 5** however three new “H6” signals are visible in the photolysed spectrum. Two of the new signals are downfield of the original H6 proton at 9.78 ppm (H6a) and 9.64 ppm (H6b) and one signal is upfield of the original signal at 8.93 ppm (H6c). The integration ratios of the signals vary with H6a being the most abundant followed by H6c, H6b and finally the original signal, H6, is the least abundant. The two new downfield signals are indicative of the formation of a cationic complex based on the chemical shift of the H6-pyridyl proton observed for *fac*-[Re(PyImPh)(CO)<sub>3</sub>(NCCH<sub>3</sub>)]<sup>+</sup> (**164**) in **Section**

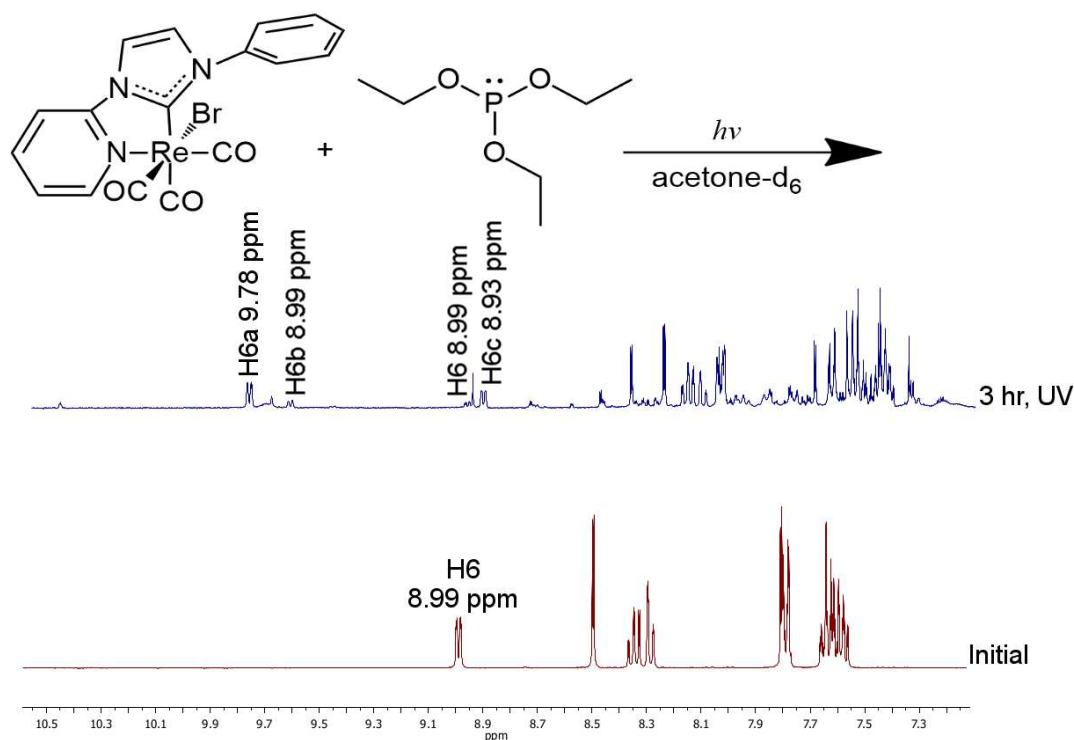


Figure 6.8:  $^1\text{H}$  NMR time series of the photolysis of **3Br** and triethylphosphite (2.5 molar equivalents) in acetone- $\text{d}_6$  at  $\lambda_{\text{ex}} = 365$  nm.

**5.3.2.** Additionally H6c could be indicative of a dicarbonyl complex as previously hypothesised in **Chapter 5**.

To try and identify what photoproducts were present, the orange solution was allowed to slowly evaporate in order to form X-ray quality crystals. Two types of crystals co-crystallised, yellow crystals and orange crystals. The crystals were structurally determined to be the *cis,trans*- and *cis,cis*- isomers of  $[\text{Re}(\text{PyImPh})(\text{CO})_2(\text{P}(\text{OEt})_3)\text{Br}]$  as shown in **Figure 6.9**. Both compounds are dicarbonyl species where one carbonyl ligand had been replaced by a phosphite ligand. Selected bond lengths and angles are detailed in **Tables 6.2-6.3** and full X-ray crystallographic data and refinement parameters are in **Appendix 9.1.11**.

Both structures exhibited the typical distorted octahedron geometry caused by the reduced bite angle of the  $\text{N}^{\wedge}\text{C}$  ligand. The *trans* groupings were also all less than  $180^\circ$ . As per the previously isolated photoproduct, *cis,cis*- $[\text{Re}(\text{PyImPh})(\text{CO})_2(\text{NCCH}_3)\text{Cl}]$  (**166**), the Re-CO bond lengths are slightly shorter compared to the parent tricarbonyl complex **3Br**. This is especially evident for **189**. The Re-C(2), Re-N(21) and Re-Br(1)

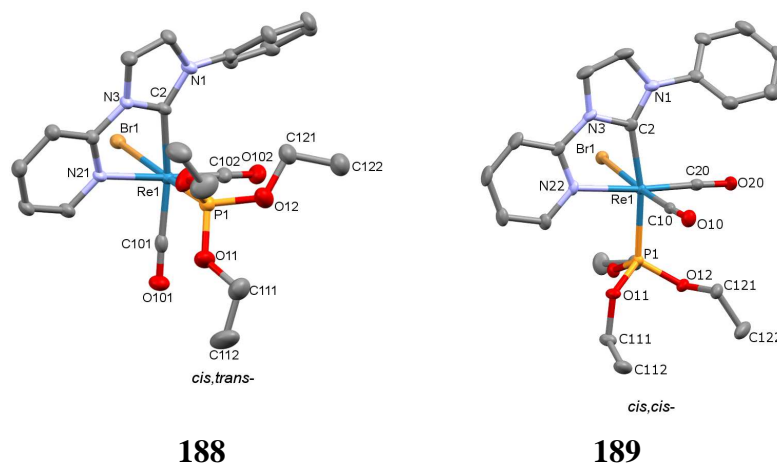


Figure 6.9: Crystal structures of *cis,trans*-[Re(PyImPh)(CO)<sub>2</sub>(P(OEt)<sub>3</sub>)Br] (**188**) and *cis,cis*-[Re(PyImPh)(CO)<sub>2</sub>(P(OEt)<sub>3</sub>)Br] (**189**) with ellipsoids drawn at the 50% probability level. Hydrogen atoms have been omitted for clarity.

bond lengths are relatively unchanged from those of the parent complex. The Re-P(1) bond lengths are on par with literature Re-P(1) bond lengths previously discussed in **Table 2.7**.<sup>47,71</sup>

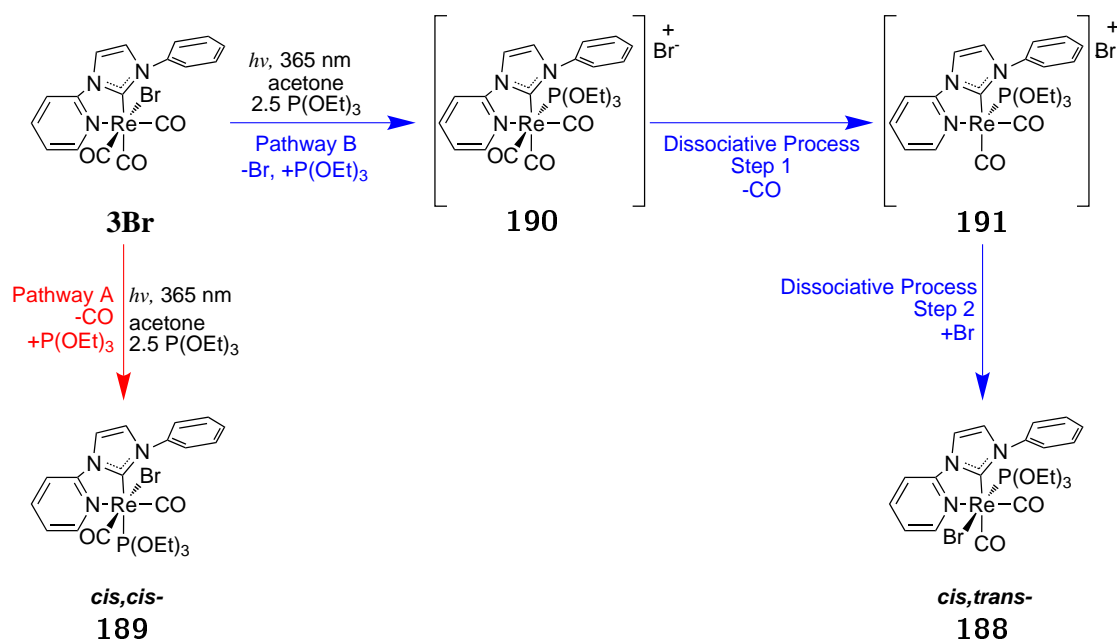
Table 6.2: Selected bond lengths (Å) and angles (°).

Bond Length (Å)				
	Re-C(102) CO <i>trans</i> to N atom	Re-C(101) CO	Re-P(1)	Re-C(2)
<b>188</b>	1.907(6)	1.927(6) ( <i>trans</i> to the carbene)	2.2793(16)	2.140(5)
<b>189</b>	1.890(4)	1.899(4) ( <i>trans</i> to the bromo)	2.3457(10)	2.117(4)
<b>3Br</b>	1.923(4)	1.957(3)	1.917(4)	2.145(3)

Table 6.3: Selected bond lengths (Å) and angles (°) continued.

	Bond Length (Å)		Bond Angle (°)
	Re-N(21)	Re-Br(1)	C(12)-Re-N(21); Bite angle of N^C ligand
<b>188</b>	2.209(5)	2.6602(6)	74.18(19)
<b>189</b>	2.236(3)	2.6557(4)	74.25(13)
<b>3Br</b>	2.210(3)	2.6255(4)	74.60(13)

### 6.5.1 Proposed Mechanism for the PLSRs of 3Br in the Presence of Triethylphosphite



Scheme 6.6: Proposed Bifurcated Photochemical Mechanism of a Rhenium(I)-NHC Tricarbonyl Compound with Triethylphosphite.

Based on the isolated photoproducts a bifurcated mechanism is proposed where the direct labilisation of the carbonyl in *trans* to the carbene *via* Pathway A in **Scheme 6.6** is in competition with a secondary pathway, Pathway B. The isolated structure for **189** gives credence to Pathway A of the proposed mechanism where the carbonyl in *trans* to the carbene highly labile due to the strong *trans* effect of the NHC ligand and

the strong *cis* effect of the bromo and is therefore readily labilised resulting in *cis,cis*-substituted photoproducts such as **189** and the previously observed acetonitrile solvate; *cis,cis*-[Re(PyImPh)(CO)<sub>2</sub>(NCCH<sub>3</sub>)Cl] (**166**).

Interestingly, in the *cis,trans*- isomer (**188**) structure the carbonyl in *trans* to the bromo ligand has been replaced. Direct labilisation of the CO ligand in *trans* to the bromo seems unlikely as the bromo has the weakest *trans* effect of the three ligands which would theoretically make the CO in *trans* to the bromo the most stable. Therefore it is hypothesised that this photoproduct is formed by a multi-step mechanism (Pathway B, **Scheme 6.6**) similar to that observed by Hightower in **Scheme 6.3**.<sup>98</sup> The first step is thought to be the exchange of the bromo ligand for P(OEt)<sub>3</sub> resulting in the cationic complex, *fac*-[Re(PyImPh)(P(OEt)<sub>3</sub>)(CO)<sub>3</sub>]Br (**190**). Formation of this cationic species in Pathway B of **Scheme 6.6** is akin to the formation of the cationic acetonitrile solvate, *fac*-[Re(PyImPh)(CO)<sub>3</sub>(NCCH<sub>3</sub>)]<sup>+</sup> (**164**) as discussed in **Chapter 5**. Whilst no cationic species is ever directly isolated from this system, the presence of such a species is suggested by the blueshifted band apparent in the emission spectrum of photolysed **3Br** as depicted in **Figure 6.6** and the two downfield signals in the <sup>1</sup>H NMR spectrum of photolysed **3Br** and triethylphosphite in acetone-d<sub>6</sub> as shown in **Figure 6.8**.

The strong *trans* effect of the phosphite ligand then labilises the CO ligand in *trans* to it which is released *via* a dissociative mechanism, observed for *fac*-[Re(bpy)(L<sup>P</sup>)(CO)<sub>3</sub>]<sup>+</sup> complexes by Koike and co-authors.<sup>70</sup> The vacant site is then reoccupied by the formerly labilised bromo ligand resulting in the isolated photoproduct

*cis,trans*-[Re(PyImPh)(CO)<sub>2</sub>(P(OEt)<sub>3</sub>)Br] (**188**). This type of photoproduct was not observed during the acetonitrile studies in **Chapter 5** and is attributed to the competitive *trans* effect of the triethylphosphite and NHC ligands. No photoproducts resembling *cis,cis*-[Re(PyImPh)(CO)<sub>2</sub>(NCCH<sub>3</sub>)<sub>2</sub>Br] (**165**) were isolated from the reaction mixture.

Based on the experimental data it would appear that when a phosphite ligand is present in solution in a 2.5 molar equivalents to the rhenium(I)-NHC tricarbonyl compound then the photochemical ligand substitution reaction proceeds *via* a similar bifurcated mechanism to that proposed in **Chapter 5** for the photochemistry of *fac*-[Re(PyImPh)(CO)<sub>3</sub>X] (X = Cl, Br) compounds in acetonitrile solutions. The triethylphosphite acts in a similar way to the acetonitrile solvent in the previous chapter whereby it facilitates the pho-

tochemical ligand substitution reaction by allowing for the formation of the cationic complex. Additionally when a phosphite ligand is added to the reaction mixture, CO dissociation can be achieved by both of the competing pathways of the bifurcated mechanism which was proposed to be possible in **Scheme 5.3** of **Section 5.3.2**

### 6.5.2 Characterisation of the *cis,trans*- and *cis,cis*- [Re(PyImPh)-(CO)<sub>2</sub>(P(OEt)<sub>3</sub>)Br] Photoproducts

Attempts were made to reproduce the photoproducts in order for them to be fully characterised. Efforts to isolate the *cis,cis*-isomer, **189**, proved futile however a pure sample of the *cis,trans*-isomer, **188**, was successfully eluted from a column and was characterised by elemental analysis, crystal X-ray analysis and <sup>1</sup>H and <sup>31</sup>P NMR spectroscopy as described in the **Experimental Section 8.8.3**. There was not enough sample to produce a well resolved <sup>13</sup>C NMR spectrum.

The <sup>1</sup>H and <sup>31</sup>P NMR spectra of **188** are shown in **Figure 6.10**. The <sup>1</sup>H NMR spectrum shows the H6 proton off the pyridyl ring occurring at 8.9 ppm in acetone-d<sub>6</sub> which is the same shift as H6c observed in the photolysed reaction mixture previously shown in **Figure 6.8**. The <sup>31</sup>P resonance for the organophosphorous rhenium(I) coordination complex (**188**) occurs at 123.3 ppm in acetone-d<sub>6</sub>.

The signal at 123.3 ppm is a -14.8 ppm shift from non-coordinated triethylphosphite which occurs at 138.1 ppm in the same solvent. Hori observed a shift of -31.4 ppm for triethylphosphite upon coordination to rhenium in CDCl<sub>3</sub> solutions.<sup>85</sup> The magnitude of the Δδ shift value for this system is less than that observed by Hori and this is attributed to the resulting *cis,trans*-[Re(PyImPh)(CO)<sub>2</sub>(P(OEt)<sub>3</sub>)Br] complex being neutral and therefore not drawing as much electron density from the organophosphorous ligand. This is unlike Hori's system where the final *fac*-[Re(bpy)(CO)<sub>3</sub>(L<sup>P</sup>)]<sup>+</sup> compounds are cationic which increases the degree of electron donation from the triethylphosphite to the rhenium(I) and results in a larger -Δδ value. The direction of the Δδ shift for the this rhenium(I)-NHC system is the same as that observed for Hori's system rhenium(I)-diimine system for the same strongly electron accepting organophosphorous ligand, triethylphosphite. Both systems follow the same trend whereby the electron density of the <sup>31</sup>P atom of the triethylphosphite decreases upon

coordination resulting in the  $-\Delta\delta$  value.

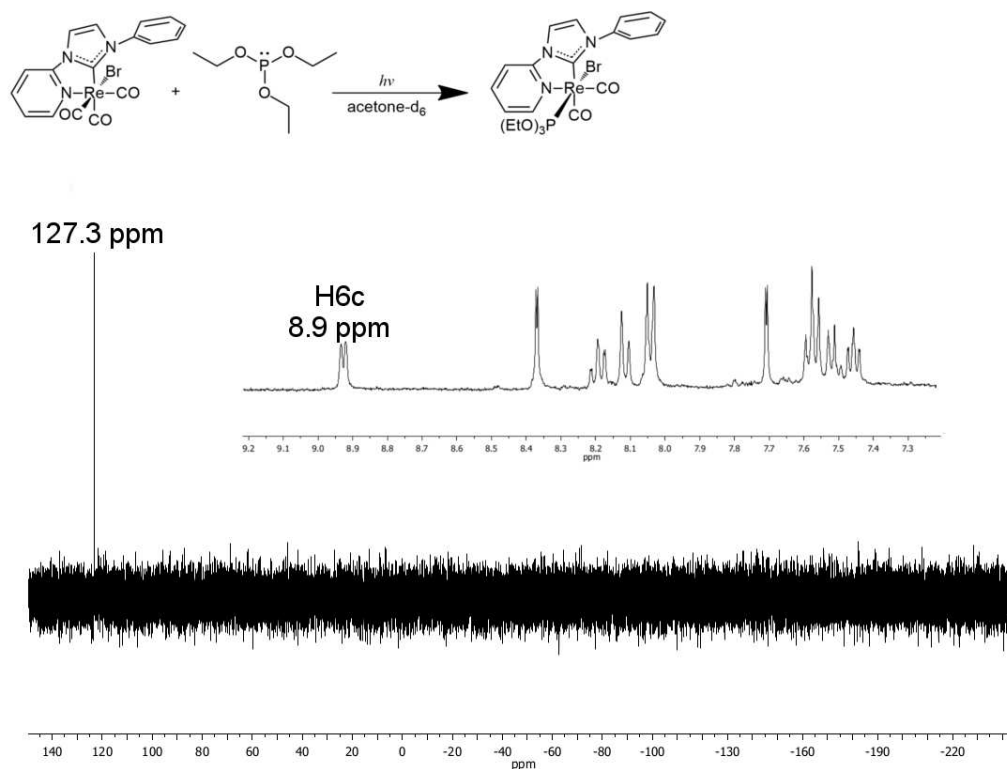


Figure 6.10: <sup>1</sup>H and <sup>31</sup>P NMR spectra of a pure sample of *cis,trans*-[Re(PyImPh)(CO)<sub>2</sub>(P(OEt)<sub>3</sub>)Br] (**188**) in acetone-d<sub>6</sub>.

## 6.6 Photochemical Activity of **3Br** with Triphenylphosphine

The triethylphosphite ligand seemed to have a competitive *trans* effect to that of the NHC ligand which resulted in the *cis,trans*-[Re(PyImPh)(CO)<sub>2</sub>(P(OEt)<sub>3</sub>)Br] (**188**) as the predominant photoproduct in the reaction mixture. Therefore a weaker  $\pi$  acceptor organophosphorous ligand, triphenylphosphine, was assessed to see what photoproducts would form and if a photoproduct resembling *cis,cis*-[Re(PyImPh)(CO)<sub>2</sub>(NCCH<sub>3</sub>)<sub>2</sub>Br] (**165**) (Scheme 5.3) could be isolated.

For an initial investigation a  $\sim 10^{-5}$  M solution of **3Br** with approximately 10 molar equivalents of triphenylphosphine was dissolved in dichloromethane. The solution was then photolysed as per the method outlined in **Experimental Section 8.7.3** with

the following amendments: there was a five minute interval between the collection of each consecutive spectrum and each spectrum is shown from 200-600 nm. The collated spectra are depicted in **Figure 6.11** and demonstrate similar changes to those observed for **3Br** in acetonitrile solutions are observed. As the photolysis proceeds the original maximum at 518 nm decreases in intensity and a new redshifted maximum develops.

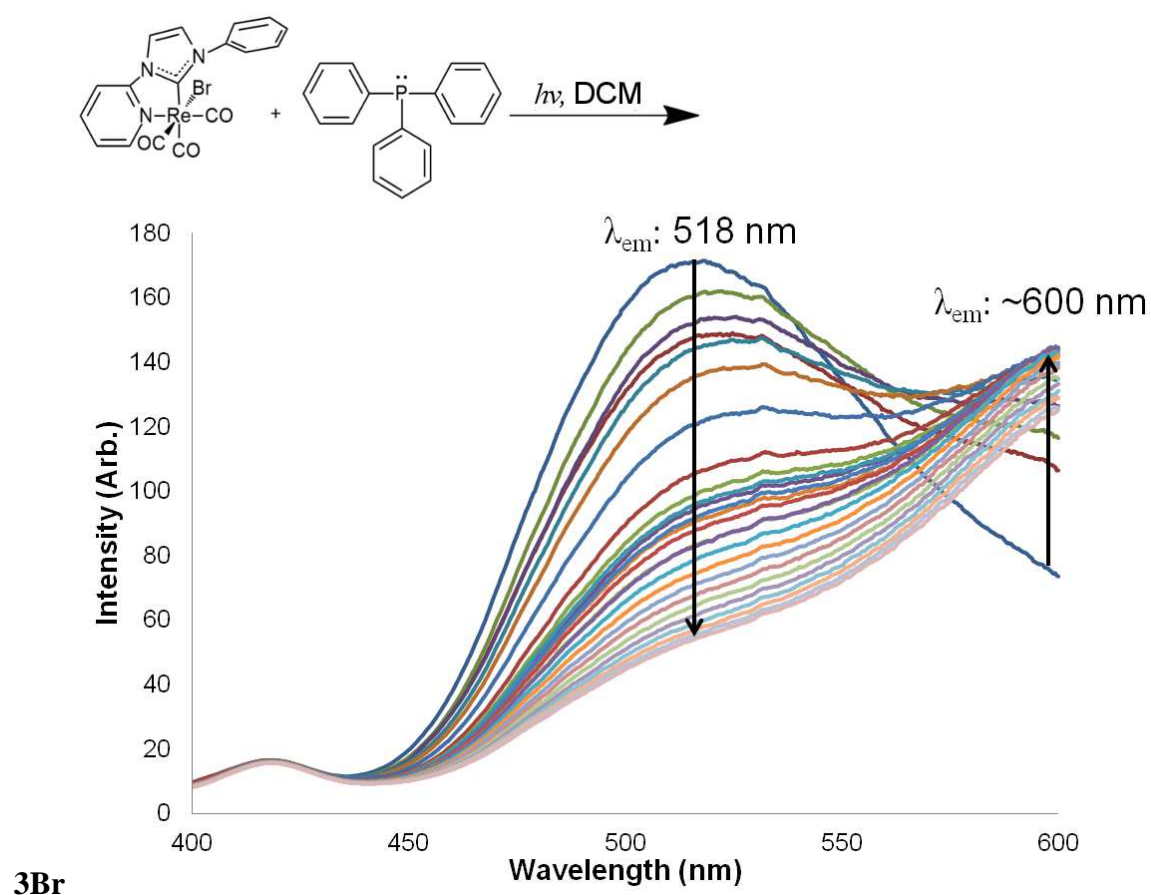


Figure 6.11: Emission spectrum displaying the spectral changes occurring to a *ca.*  $10^{-5}$  M solution of **3Br** and triphenylphosphine (10 molar equivalents) in dichloromethane when photolysed at  $\lambda_{\text{ex}} = 370 \text{ nm}$  every 5 minutes for 26 scans.

A qualitative analysis involving an NMR tube of an acetone solution of **3Br** with triphenylphosphine (3.4 molar equivalents) being photolysed in front of the UV lamp,  $\lambda_{\text{ex}} = 365 \text{ nm}$ , for five hours was then performed. After the five hour photolysis the initial light yellow solution had turned dark orange and small orange crystals had formed around the meniscus of the solution. The crystals were scraped away and an IR spectrum was collected as shown in **Figure 6.12**. The IR spectrum shows two distinct

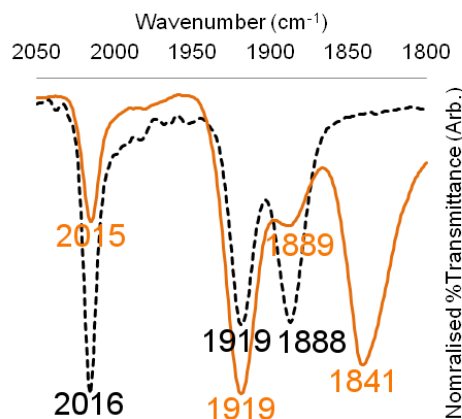


Figure 6.12: IR spectra of **3Br** (black dash) and the orange crystalline product (orange trace) formed after five hours photolysis at  $\lambda_{ex}$ : 365 nm with triphenylphosphine (3.4 molar equivalents) in acetone.

pair of overlapping bands; two high intensity stretches at 1919 and 1841  $\text{cm}^{-1}$  and two weaker stretches at 2015 and 1889  $\text{cm}^{-1}$ . The lower intensity stretches seem to resemble the starting material whilst the the strong, lower wavenumber stretches are reminiscent of the bands observed in the previous chapter which were attributed to a dicarbonyl product.

To further analyse the potential dicarbonyl product the experiment was repeated and the concentration of the triphenylphosphine was re-increased to 10 molar equivalents and deuterated acetone was used so the experiment could be monitored by NMR. Initial  $^1\text{H}$  and  $^{31}\text{P}$  spectra of the pale yellow solution of **3Br** and triphenylphosphine (10 molar equivalents) in acetone- $\text{d}_6$  were collected. The NMR tube was then clamped in front of the UV lamp as per the procedure outlined in **Experimental Section 8.7.5** and was photolysed for four hours after which a third set of  $^1\text{H}$  and  $^{31}\text{P}$  spectra were collected. At the end of the four hour photolysis the solution had turned a dark yellow and copious large, orange fluffy crystals had formed as shown in **Figure 6.13**.



Figure 6.13: Photograph of the reaction vessel post photolysis showing the formation of orange crystals.

The initial  $^{31}\text{P}$  NMR spectrum of triphenylphosphine showed a single singlet at -4.2 ppm which is similar to the literature value of -9.3 ppm in  $\text{CDCl}_3$  as reported by Hori and is therefore ascribed to free triphenylphosphine.<sup>85</sup> After the initial addition of **3Br** there is no change in the  $^{31}\text{P}$  spectrum. After the four hour photolysis period there are now two resonances present in the  $^{31}\text{P}$  spectrum, one at 26.3 ppm and one at -4.2 ppm.

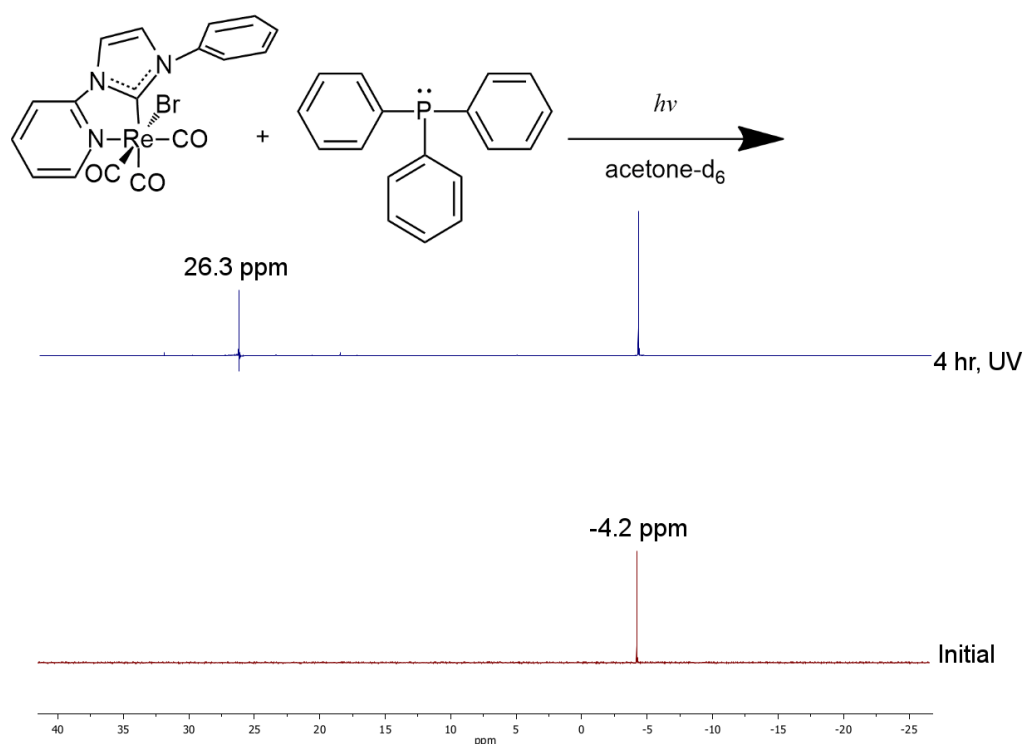


Figure 6.14:  $^{31}\text{P}$  NMR time series of the photolysis of **3Br** and triphenylphosphine (10 molar equivalents) in acetone- $d_6$  at  $\lambda_{ex}$ : 365 nm.

The new singlet at 26.3 ppm is similar in chemical shift to that of triphenylphosphine bound to rhenium(I) which is reported to be 15.3 ppm in CDCl<sub>3</sub>.<sup>85</sup> Based on this data there are two phosphorous environments present in the reaction mixture; free triphenylphosphine and either coordinated triphenylphosphine or oxidised triphenylphosphine.

Analysis of the <sup>1</sup>H NMR spectrum post photolysis is difficult as the high concentration of the triphenylphosphine effectively overwhelms the aromatic region of the proton spectrum of **3Br** and its resultant photoproducts as shown by the four hour trace in **Figure 6.15**. There are several downfield signals labeled **H6'** and **imidazolyl'** which are similar to peaks observed in previous studies in **Chapter 5** and are therefore tentatively assigned to the photoproducts of the reaction of **3Br** with triphenylphosphine.

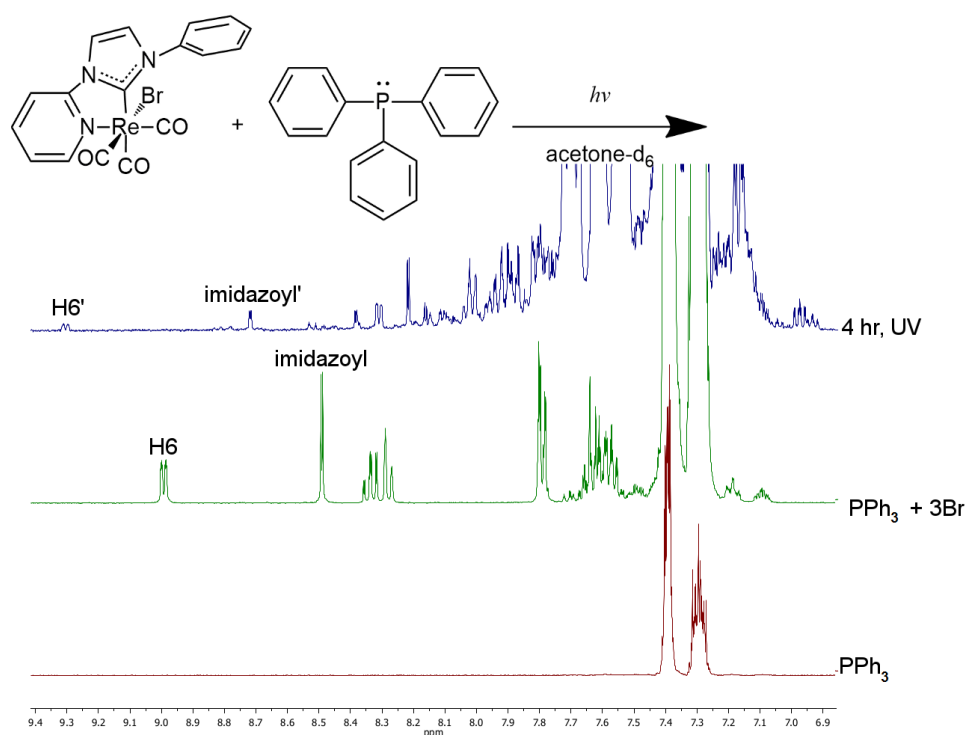


Figure 6.15: Magnified <sup>1</sup>H NMR time series of the photolysis of **3Br** and triphenylphosphine (10 molar equivalents) in acetone-d<sub>6</sub> at  $\lambda_{ex}$ : 365 nm.

Attempts were made to isolate the orange crystals and analyse them by NMR however they were found to be too insoluble to produce solutions concentrated enough for a

well resolved spectrum in all available NMR solvents (DMSO, acetone, acetonitrile and chloroform). An IR spectrum of the isolated crystals was collected and compared to the starting material, **3Br**, as shown in **Figure 6.16**. The IR spectrum of the orange crystalline photolysis product shows two broad bands (1927 and 1843  $\text{cm}^{-1}$ ), one small band (1980  $\text{cm}^{-1}$ ) and one small shoulder (1862  $\text{cm}^{-1}$ ) in the carbonyl stretching region.

Based on examination of this spectra it appears that increasing the concentration of the triphenylphosphine from 3.4 to 10 molar equivalents resulted in higher conversion of the starting material to the photoproduct. There are no stretches present indicative of the starting material. Interestingly there is no higher wavenumber band at around 2036  $\text{cm}^{-1}$  indicative of a cationic complex. Therefore it would appear that the orange crystalline photoproduct does not contain a cationic species or that the cationic species has fully reacted to form a secondary product and is no longer present. It is also possible that any cationic species present could be soluble in the acetone and is not visible in the IR of the precipitant.

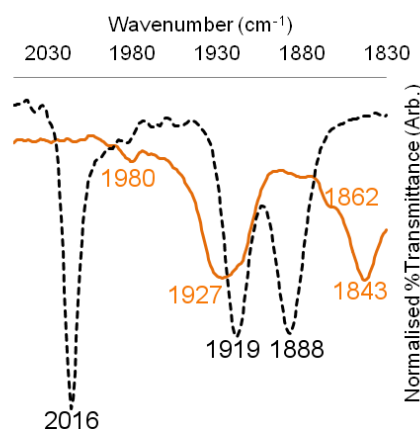


Figure 6.16: IR spectra of **3Br** (black dash) and the orange crystalline photoproduct (orange bold) formed after four hours photolysis at  $\lambda_{\text{ex}} = 365$  nm with triphenylphosphine (10 molar equivalents) in acetone- $\text{d}_6$ .

The UV-vis spectrum of a dilute dichloromethane solution of the orange crystalline product was obtained and compared to the starting material **3Br** as shown in **Figure 6.17**. The photoproduct has two major absorption bands, a broad band at 367 nm and a broad, lower energy band centred around 500 nm. Both of these bands are red-shifted

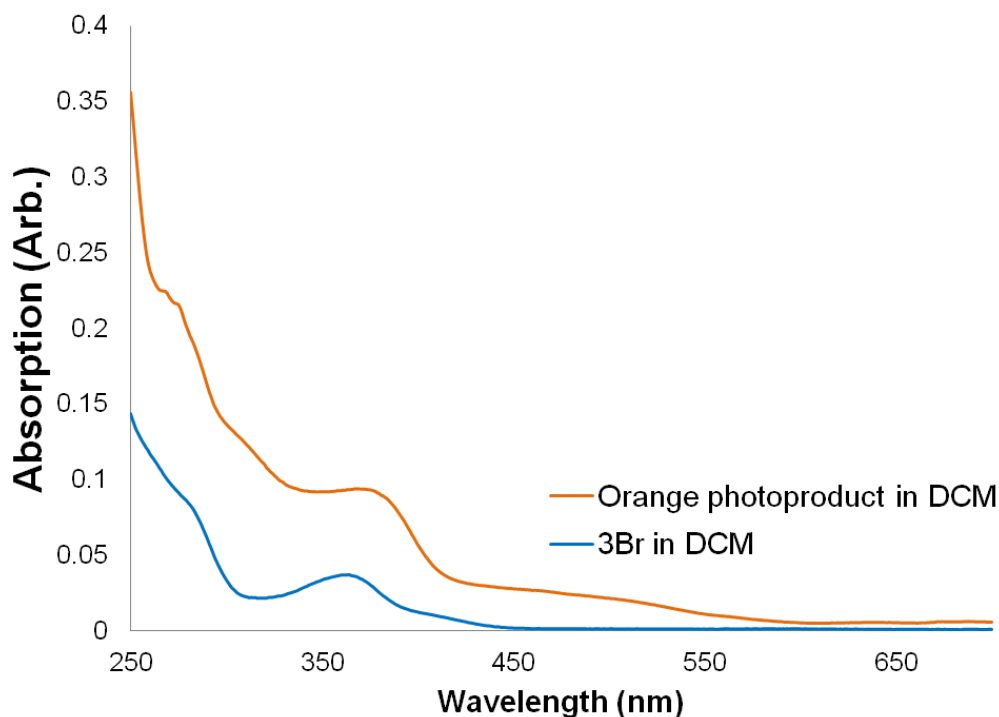


Figure 6.17: UV-Vis absorption spectra of the orange photoproduct diluted in DCM vs. **3Br** (*ca.*  $10^{-5}$  M) in DCM.

compared to absorption profile of the starting material **3Br**.

As the isolated orange crystals were insoluble in all available NMR solvents and as the crystals were not of X-ray diffraction quality the experiment was repeated to try and produce single crystals. The procedure was repeated utilising a solvent mixture of  $\text{CDCl}_3$ -acetone (9:1) as **3Br** was known to be photostable in chloroform. The solution was prepared as before with ten molar equivalents of phosphine to **3Br** and was photolysed for four hours according to the procedure outlined in **Experimental Section 8.7.5**. After photolysis the  $\text{CDCl}_3$ -acetone (9:1) solution had turned dark orange however no crystals had formed.

The  $^1\text{H}$  NMR of the  $\text{CDCl}_3$ -acetone reaction was not resolved and yielded no discernible information. Analysis of the  $^{31}\text{P}$  NMR presented more interpretable results as shown in **Figure 6.18**. In the reaction mixture before photolysis there is one singlet at -10.3 ppm indicative of free triphenylphosphine. After four hours of photolysis there are now two strong singlets, one at 31.9 and -5.1 ppm and two very small singlets at 24.9 and 22.1 ppm. The signals all exhibit a positive  $\Delta\delta$  in comparison to free

triphenylphosphine which is in accordance with Hori's findings for weaker  $\pi$  acidic organophosphorous ligands.<sup>85</sup> In general coordinated triphenylphosphine has a  $\Delta\delta$  of 21-44 ppm compared to the free ligand and Hori and co-authors observed  $\Delta\delta$  value of 24.6 for the coordination of triphenylphosphine to rhenium(I).<sup>85,95</sup> Therefore all four of the new signals are in the acceptable range to be considered coordinated triphenylphosphine.<sup>95</sup> The peak at 31.9 ppm could be indicative of oxidised triphenylphosphine which is known to appear at 30.1 ppm in  $\text{CH}_2\text{Cl}_2$  and 23.7 ppm in  $\text{CDCl}_3$ .<sup>100</sup> If a similar magnitude of  $\Delta\delta$  is occurring in this system it could be difficult to distinguish coordinated triphenylphosphine from the triphenylphosphine oxide.

The solvent was then allowed to slowly evaporate over night after which orange crystals formed in the reaction vessel. The crystals were isolated and were found to be slightly soluble in deuterated chloroform to produce a reasonable  $^{31}\text{P}$  NMR spectrum. The  $^{31}\text{P}$  spectrum of the isolated orange crystals show only one clear peak at 30.7 ppm.

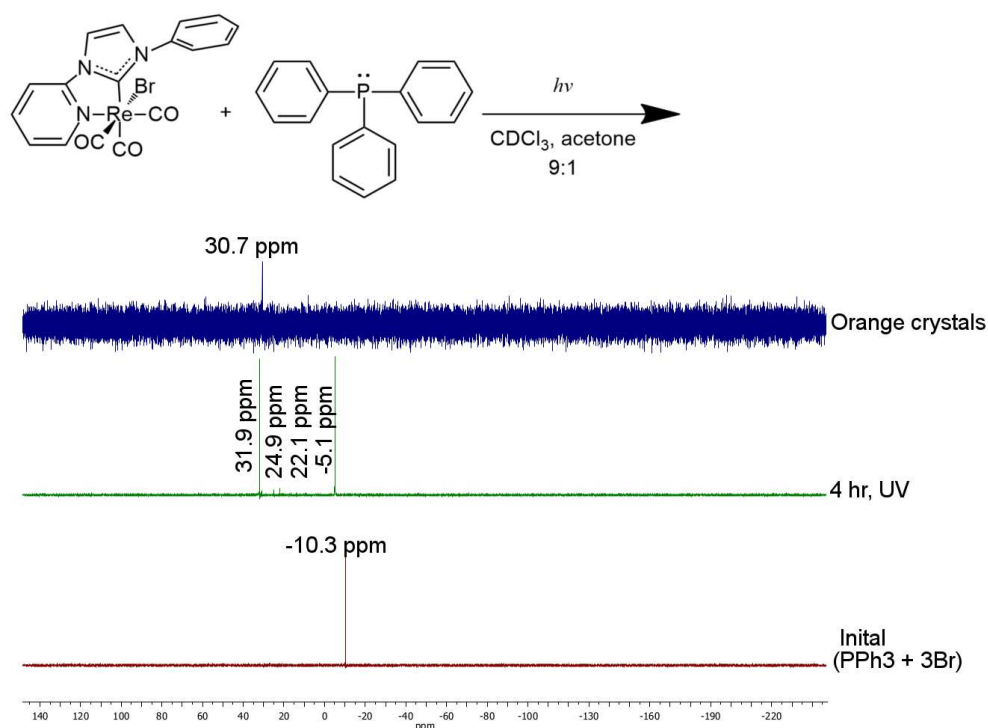


Figure 6.18:  $^{31}\text{P}$  NMR time series of the photolysis of **3Br** and triphenylphosphine (10 molar equivalents) in  $\text{CDCl}_3$  with acetone (9:1) at  $\lambda_{ex} = 365$  nm.

A selection of the crystals from the  $\text{CDCl}_3$  -acetone experiment were of suitable quality for X-ray diffraction analysis and the refined structure is shown in **Figure 6.19**.

The structure refinement is not of high quality however bond connectivity can still be observed. Unlike the two isomeric dicarbonyl species isolated from the triethylphosphite reaction mixture in **Section 6.5**, the crystal structure demonstrated the existence of a monocarbonyl species, *cis,trans*-[Re(PyImPh)(PPh<sub>3</sub>)<sub>2</sub>(CO)Cl/Br] (**192**). The two triphenylphosphine ligands are in *trans* to one another, the halide ligand is in *trans* to the NHC ligand and the sole carbonyl ligand is in *trans* to the pyridyl ring. Selected bond lengths and angles are detailed in **Table 6.2** and full X-ray crystallographic data and refinement parameters are in **Appendix 9.1.11**.

The coordinated halide atom was modelled as a mixture of both chloride and bromide with occupancies refined to 0.809(7), for Cl<sup>-</sup> and its complement for Br<sup>-</sup>. Similarly, the uncoordinated halide anion was modelled as part bromide (occupancy: 0.737(7)) and chloride (occupancy: 1-0.737(7)). The site occupancies of the chloroform solvent molecules were each refined to 0.854(3) after trial refinement showed no significant differences between the values for each. The remaining solvent was modelled as a diethyl ether molecule disordered about a crystallographic inversion centre, the geometries of which were restrained to ideal values. Anisotropic displacement parameters were employed for the non-hydrogen atoms. All hydrogen atoms were added at calculated positions and refined by use of a riding model with isotropic displacement parameters based on those of the parent atom.

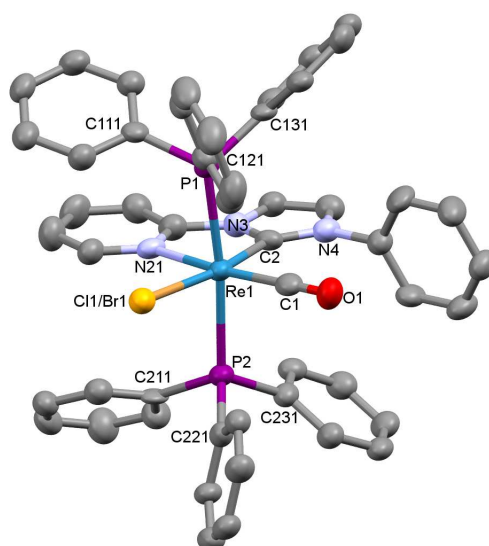
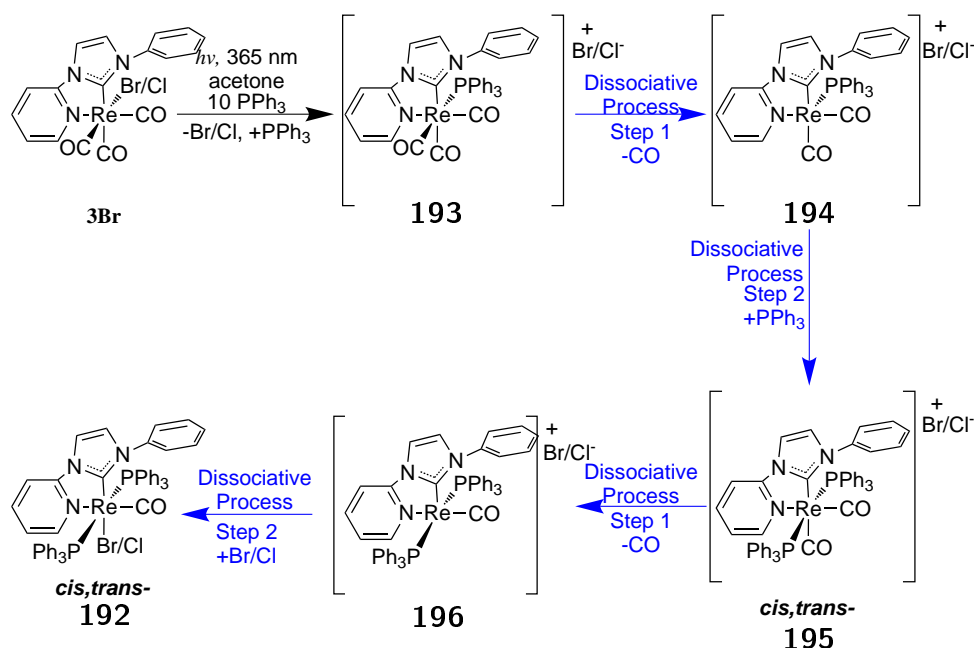


Figure 6.19: Crystal structure of *cis,trans*-[Re(PyImPh)(PPh<sub>3</sub>)<sub>2</sub>(CO)Cl/Br] (**192**) with ellipsoids drawn at the 50% probability level. The hydrogens, solvent molecules and counter anions have been omitted for clarity.

The isolated photoproduct, *cis,trans*-[Re(PyImPh)(PPh<sub>3</sub>)<sub>2</sub>COCl/Br] (**192**), is neutral and has a mixture of chloro/bromo ligands in a 0.26:0.74 ratio due to a chloro impurity in the starting material as previously discussed in **Section 2.3.1**. There is a secondary non-coordinated halide in the coordination sphere. There is a solvent molecule of chloroform present which is weakly hydrogen bonding to the free halide.

The structure proves that **3Br** can participate in CO dissociative, PLSRs with a weakly  $\pi$  acidic organophosphorous ligands. It is possible that the signal at 30.65 ppm in **Figure 6.18** is the photoproduct **192** as this compound would only exhibit one phosphorous singlet in a <sup>31</sup>P spectrum due to the coordination symmetry.<sup>71</sup>

### 6.6.1 Proposed Mechanism for the PLSRs of *fac*-[Re(PyImPh)(CO)<sub>3</sub>Br] (**3Br**) in the Presence of Triphenylphosphine



Scheme 6.7: Proposed Photochemical Mechanism of a Rhenium(I)-NHC Tricarbonyl Compound with Triphenylphosphine.

The proposed photochemical mechanism for **3Br** in acetone in the presence of triphenylphosphine is shown in **Scheme 6.7**. The first step involves the exchange of the labile halide ligand for a secondary ligand, triphenylphosphine. As no cationic compound is observed spectroscopically this first step is inferred based on the previous

studies with acetonitrile and triethylphosphite.

The next step is proposed to be the dissociation of the carbonyl in *trans* to the triphenylphosphine ligand to form a *cis,trans*- cationic dicarbonyl species (**195**). The presence of this species is inferred by the low wavenumber bands observed in the IR spectrum in **Figure 6.12** which are indicative of a dicarbonyl compound. Whether this step occurs *via* an associative or dissociative mechanism is unknown.

The final step is the loss of the carbonyl ligand in *trans* to the carbene, either by a dissociate or associative mechanism, and the re-inclusion of the bromo/chloro ligand into the coordination sphere to form the final isolated photoproduct *cis,trans*-[Re(PyImPh)(PPh<sub>3</sub>)<sub>2</sub>(CO)Cl/Br] (**192**). Whilst no photoproducts resembling *cis,cis*-[Re(PyImPh)(CO)<sub>2</sub>(NCCH<sub>3</sub>)<sub>2</sub>Br] (**165**) were isolated from this reaction mixture the isolation of **195** demonstrates the versatility of **3Br** as a photoactivated CO dissociative molecule.

## 6.7 Summary and Concluding Remarks

In summary, an acetone solution of **3Br** and triethylphosphite was found to be stable in the dark. Additionally acetone solutions of **3Br** with triethylphosphite/triphenylphosphine were found to be stable at elevated temperatures for prolonged periods of time. The inclusion of triethylphosphite in the photochemical reaction mixture of **3Br** and acetone was proposed to induce two competing photochemical pathways. The first proposed pathway involved CO loss in *trans* to the carbene ligand and resulting in the formation of *cis,cis*-[Re(PyImPh)(CO)<sub>2</sub>(P(OEt)<sub>3</sub>)Br] (**189**). The structure of **189** was confirmed by crystal X-ray analysis. The second pathway involves the exchange of the bromo ligand for triethylphosphite followed by CO dissociation in *trans* to the phosphite ligand to afford *cis,trans*-[Re(PyImPh)(CO)<sub>2</sub>(P(OEt)<sub>3</sub>)Br] (**188**), the structure of which was also confirmed by crystal X-ray analysis, elemental analysis and <sup>1</sup>H and <sup>31</sup>P NMR spectroscopy.

The introduction of triphenylphosphine to the reaction mixture of **3Br** in acetone elicited the formation of *cis,trans*-[Re(PyImPh)(PPh<sub>3</sub>)<sub>2</sub>(CO)Cl/Br] (**192**). Varying the concentration of the secondary ligand from 2.5 equivalents for the phosphite experiments to 10 equivalents for the phosphine experiments demonstrated that a variety of different substitution patterns are possible from the photochemically active, facial starting material **3Br**.



# Chapter 7

## Summary, Conclusions and Future Work

### 7.1 Summary and Conclusions

Whilst the field of optically active rhenium-diimine coordination complexes is vast, knowledge of rhenium coordination compounds utilising N-heterocyclic carbene ligands is lacking. In order to investigate the photophysical and photochemical properties of the latter compounds, NHC ligands were synthesised as azolium salts. Ten new azolium salts, in addition to four previously reported azolium salts, were synthesised and fully characterised by  $^1\text{H}$  and  $^{13}\text{C}$  NMR spectroscopy. The hexafluorophosphate salts, **QuImPhH.PF<sub>6</sub>** and **QxImPhH.PF<sub>6</sub>**, were used “as is” without further characterisation. The remaining novel azolium salts were found to pure by elemental analysis.

The chosen structural motif of the NHC ligands was based on the previously reported 1-(2-pyridyl)benzimidazolin-2-ylidene ligands which were successfully coordinated to rhenium(I) resulting in the first report of of a luminescent rhenium(I)-N-heterocyclic carbene complex where the carbene ligand acted as the major  $\pi^*$  acceptor in the lowest excited state.<sup>49</sup> In order to systematically assess the impact of structural modifications to the NHC ligand variations were applied at four site specific vectors; the N-heterocyclic carbene backbone, the N-donor ring on the N3 position of the NHC, the R substituent on the N1 position of the NHC and the ancillary ligand “X”. Each of this sites were modified in turn to assess the effect on the chemical characteristics

and photophysical properties of the final rhenium(I)-NHC tricarbonyl complex and to establish whether modification of these vectors could be used to “tune” the emission of the final rhenium(I)-NHC tricarbonyl complex.

The carbene vector was modified by changing the carbene backbone from the previously reported benzimidazolin-2-ylidene to an imidazolin-2-ylidene. This would reduce the conjugation of the carbene ligand. The N-donor ring vector was subsequently modified by changing the previously reported pyridyl moiety for the following N-donor rings; the pyrimidyl moiety, the quinoyl moiety and the quinoxyl moiety. The pyrimidyl ring is more electronegative than the pyridyl ring due to the additional nitrogen. The quinoyl ring is more conjugated than the original pyridyl ring whilst the quinoxyl ring is both more conjugated and more electronegative than the original pyridyl ring. The R substituent vector was varied by utilising three different R substituents; the butyl chain, the mesityl ring and the phenyl ring. The mesityl ring and the phenyl ring both increased the conjugation of the free ligand however when coordinated to the rhenium, the mesityl ring exhibited restricted rotation whilst the phenyl ring had free rotation. The ancillary ligand vector was varied by changing the anion of the azolium salt from chloro to bromo.

The salts were used to synthesise thirteen novel rhenium(I)-NHC tricarbonyl complexes (**1-3Cl/Br**, **4Br** and **5-7Cl/Br**) in addition to one previously reported compound (**4Cl**).<sup>51</sup> The rhenium compound *rac-fac*-chlorotricarbonyl[1-(2-pyridyl)-3-butyylimidazolin-2-ylidene]-rhenium(I) (**1Cl**) proved to be the most difficult to synthesise of the 14 compounds and could only be isolated using the silver transfer method. The remaining 13 complexes were successfully synthesised using the *in situ* method. As Wang and co-workers found the silver method to be favourable for the synthesis of their rhenium(I)-1-(2-pyrimidyl)-2-ylidene tricarbonyl compounds it would be worth trialling this method further in the future.<sup>51</sup>

The rhenium(I)-NHC tricarbonyl complexes were found to be pure by elemental analysis and were fully characterised by <sup>1</sup>H and <sup>13</sup>C NMR spectroscopy and infrared spectroscopy. <sup>1</sup>H NMR confirmed that the mesityl moieties of **2Cl/Br** and **4Cl/Br** were restricted in rotation compared to the freely rotating phenyl substituents of **3Cl/Br** and **5-7Cl/Br**. IR spectroscopy confirmed that the strength of the CO backbonding was similar for all fourteen complexes. Crystals of X-ray quality were obtained for ten

of the compounds which confirmed the *facial* configuration of the carbonyl ligands and established that the complexes exhibited a distorted octahedral geometry which is typical of NHC ligands with reduced bite angles.

The photophysical properties of fourteen rhenium(I)-NHC tricarbonyl compounds were investigated and they were found to perform as well as similar rhenium(I)-NHC systems. Compounds **1-6Cl/Br** were found to be emissive at room temperature in dichloromethane solutions from an <sup>3</sup>MLLCT state. The emission maximum was observed to red-shift as the N-donor ring was made more electron deficient and more conjugated i.e. from progressing from the pyridyl ring to the pyrimidyl, quinoyl and quinoxyl rings, proving the hypothesis that the optical output can be tuned by modifying the N-donor ring. Modifications to the halide ancillary ligand and R substituent vectors did not effect the optical output of the compounds.

The emission of **7Br** was extremely weak and the compound was considered non-emissive at room temperature for practical purposes. At ambient conditions the emission from **7Cl** was significantly blueshifted and the observed lifetime was extremely short indicating that the the triplet state is thermally suppressed. At 77 K in a frozen matrix the emission of **7Cl** was seen to red-shift indicating that emission from the triplet state was possible. **7Br** was also emissive from an apparent triplet state at 77 K. The observed excited state lifetime and quantum yield of the 1-(2-pyridyl)-imidazolin-2-ylidene compounds, **1-3Cl/Br**, were less than expected indicating that some non-radiative channels may be active in these compounds.

The photochemical activity of all fourteen rhenium(I)-NHC tricarbonyl compounds was assessed. Acetonitrile solutions of the 1-(2-pyridyl)-imidazolin-2-ylidene compounds were found to be stable in the dark for up to 3 hours and stable up to 82 °C for 2 hours. When excited at the MLCT manifold (365-370 nm) the 1-(2-pyridyl)-imidazolin-2-ylidene compounds were observed to undergo chemical transformations. On the other hand acetonitrile solutions of the 1-(2-pyrimidyl)-, 1-(2-quinoyl)- and 1-(2-quinoxyl)-imidazolin-2-ylidene compounds were found to be stable when excited at the MLCT manifold. A structure-activity relationship was therefore developed where the pyridyl compounds were photochemically active and the pyrimidyl, quinoyl and quinoxyl compounds were photochemically stable.

The chemical transformations observed for 1-(2-pyridyl)-imidazolin-2-ylidene com-

pounds were characterised as photochemical ligand substitution reactions and were found to be solvent dependent. In acetonitrile solutions three photoproducts were observed and were identified as one cationic species and two dicarbonyl species. The cationic species was identified as the acetonitrile solvato species; *fac*-[Re(PyImPh)(CO)<sub>3</sub>(NCCH<sub>3</sub>)]<sup>+</sup>(**164**) and one of the dicarbonyl species was confirmed as *cis,cis*-[Re(PyImPh)(CO)<sub>2</sub>(NCCH<sub>3</sub>)Cl] (**166**).

Further study to elucidate the photochemical mechanisms was attempted with the use of organophosphorous (L<sup>P</sup>) ligands in conjunction with the photochemically active *fac*-[Re(PyImPh)(CO)<sub>3</sub>X] (X: Cl,Br) compounds. An acetone solution of **3Br** and triethylphosphite was found to be stable in the dark. Additionally acetone solutions of **3Br** with triethylphosphite/triphenylphosphine were found to be stable at elevated temperatures for prolonged periods of time. The inclusion of triethylphosphite in the photochemical reaction mixture of **3Br** and acetone was proposed to induce two competing photochemical pathways. The first proposed pathway involved CO loss in *trans* to the carbene ligand and resulting in the formation of *cis,cis*-[Re(PyImPh)(CO)<sub>2</sub>(P(OEt)<sub>3</sub>)Br] (**189**). The structure of **189** was confirmed by crystal X-ray analysis. The second pathway involves the exchange of the bromo ligand for triethylphosphite followed by CO release in *trans* to the phosphite ligand to afford *cis,trans*-[Re(PyImPh)(CO)<sub>2</sub>(P(OEt)<sub>3</sub>)Br] (**188**), the structure of which was also confirmed by crystal X-ray analysis, elemental analysis and <sup>1</sup>H and <sup>31</sup>P NMR spectroscopy. The introduction of triphenylphosphine to the reaction mixture of **3Br** in acetone elicited the formation of *cis,trans*-[Re(PyImPh)(PPh<sub>3</sub>)<sub>2</sub>(CO)Cl/Br] (**192**). Varying the concentration of the secondary ligand from 2.5 equivalents for the phosphite experiments to 10 equivalents for the phosphine experiments demonstrated that a variety of different substitution patterns are possible from photochemically active, *facial* starting material **3Br**.

## 7.2 Future Work

Studies by Koike on photoactive *fac*-[Re(bpy)(CO)<sub>3</sub>(L<sup>P</sup>)]<sup>+</sup> type compounds demonstrate that when the photochemistry occurs from a thermally accessible reactive state, which was later identified by the authors as an <sup>3</sup>LF state, the quantum yield (Φ<sub>e</sub>) and observed lifetime (τ<sub>e</sub>) of the emissive state decrease upon increasing the tem-

perature.<sup>70</sup> In contrast, the quantum yield of the reaction ( $\Phi_r$ ) increases as the temperature increases. Below 280 K the quantum yield of the photochemical reaction ( $\Phi_r$ ) was observed to plateau to zero inferring that below this temperature the *fac*-[Re(bpy)(CO)<sub>3</sub>(L<sup>P</sup>)]<sup>+</sup> compounds were rendered photostable as the reactive state was no longer thermally accessible. It is recommended that the photochemistry of the photochemically active of the 1-(2-pyridyl)-imidazolin-2-ylidene series **1-3Cl/Br** be monitored at decreased temperatures in coordinating and non-coordinating solvents to confirm whether the photochemistry is occurring from a <sup>3</sup>LF state.

The photochemical mechanism of the photoactive compounds, specifically **2Br** and **3Br**, has demonstrated that the pyridyl series undergo ligand substitution reactions and release a carbonyl ligand when excited with ultraviolet light. A potential avenue for future investigation would be to explore harnessing the photochemical ligand substitution reactions of the pyridyl complexes and exploiting them as light activated CO emitters. Whilst carbon monoxide is known to be a toxic gas in large concentrations, research has shown that low molar concentrations can have therapeutic use for cardiovascular disorders and inflammation.<sup>103–107</sup> Controlled dosing can be performed by photo-CORMs which are photoactive CO releasing molecules. It is recommended that the photochemistry of the pyridyl series be trialled in biological medium to assess the viability of these compounds as photo-CORMs. If **2Br** and **3Br** are determined to not be suitable to application in biological medium, options to modify the existing NHC ligand motif with biologically relevant functional groups, such as simple sugars or amino acids, to increase solubility and specificity for various photo-CORM applications should be assessed.

It is recommended that the photochemically stable pyrimidyl and quinoyl compounds be further investigated for incorporation into light emitting devices such as those developed within the Massi research group using methylated Re(I) tetrazolato compounds.<sup>108</sup> The viability of the compounds as biological imaging agents such as the rhenium tetrazolato complexes coordinated to thioalkyl-functionalised phenanthroline ligands developed in the Massi research group should also be assessed.<sup>109</sup> As stated previously, if the compounds are determined to not be viable for biological imaging, options to modify the existing NHC ligand motif with biologically relevant functional groups or exchange the anionic ancillary ligand for a neutral ligand to result in charged, cationic complex could be assessed.



# Chapter 8

## Experimental

### 8.1 General Considerations

All reagents and solvents were purchased from Sigma Aldrich and Alfa Aesar and used as received without further purification. All procedures involving rhenium complexes were carried out under a nitrogen atmosphere using standard Schlenk techniques. Deactivated acidic alumina of Brockmann II activity was prepared by adding water to Brockmann I alumina at a ratio of 3% w/w, shaking until clumping stopped and leaving in a sealed container for two days.

The organophosphorous ligands ( $L^P$ ), triphenylphosphine and triethylphosphite, were purchased from Sigma Aldrich and used as received without any purification. The NMR solvents were purchased from Cambridge Isotopes and stored under  $N_2$  with 4 Å molecular sieves.

Nuclear magnetic resonance spectra were recorded using a Bruker Avance 400 spectrometer (400.1 MHz for  $^1H$ ; 100 MHz for  $^{13}C$ ; 162 MHz for  $^{31}P$ ) at 300 K. All the  $^1H$  and  $^{13}C$  NMR spectra were calibrated to residual solvent signals.  $^{31}P$  NMR spectra were calibrated to an 85%  $H_3PO_4$  capillary external standard. All NMR assignments were determined by COSY and HMBC 2D NMR.

Infrared spectra were recorded using an attenuated total reflectance Perkin Elmer Spectrometer 100 FT-IR with a diamond stage either by using solid state samples or by drop casting a concentrated solution on the stage. IR spectra were recorded from 4000 to  $650\text{ cm}^{-1}$ . The intensities of the IR bands are reported as strong (s), medium (m), or

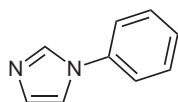
weak (w), with broad (br) bands also specified.

Melting points were determined using a BI Barnsted Electrothermal 9100 apparatus. Elemental analyses were obtained at the Central Science Laboratory, University of Tasmania, using a Thermo Finnigan EA 1112 Series Flash.

1-mesitylimidazole (**97**) was synthesised by previous Honours students utilising a literature procedure outlined below by Gardiner *et al.*<sup>54</sup>

## 8.2 Synthesis of N-Substituted Imidazoles

### 8.2.1 1-Phenylimidazole



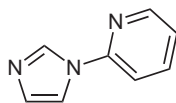
**99**

1-phenylimidazole was synthesised *via* the following literature procedure originally outlined by Xu *et al.*<sup>57</sup>

Imidazole (**86**) (1 g, 15 mmol), iodobenzene (**101**) (2.5 mL, 22 mmol), caesium carbonate (10.5 g, 30 mmol) and a catalytic amount of copper(II) acetate monohydrate (1 mol%) was stirred in dimethylformamide (50 mL) under nitrogen atmosphere at 110 °C for 3 days. The reaction was then cooled and diluted with water (100 mL). The green solution was extracted with ethyl acetate (2 x 100 mL) and the organic extract was back extracted with brine (1 x 100 mL). The organic layer was dried over anhydrous sodium sulphite and concentrated *in vacuo* to afford a brown oil. The oil was then dissolved in minimal amount of methanol and filtered over a plug of silica to remove any remaining starting material. The resulting filtrate was concentrated *in vacuo* and washed with ethyl acetate to remove any dissolved silica and afforded a yellow oil in good yield (1.97 g, 91%).

<sup>1</sup>H NMR (400 MHz, CDCl<sub>3</sub>): δ 7.88 (1H, s, NCHN), 7.50-7.47 (2H, m, 2 x *ortho* phenyl CH), 7.41-7.37 (3H, m, 2 x *meta* phenyl CH, *para* phenyl CH), 7.29 (1H, s, imidazolyl CH), 7.22 (1H, s, imidazolyl, CH) ppm.

## 8.2.2 1-(2-Pyridyl)imidazole



98

1-(2-pyridyl)imidazole was synthesised *via* the following literature procedure outlined by Yuan et al.<sup>55</sup>

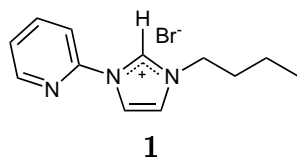
Imidazole (**86**) (516 mg, 7.6 mmol) and potassium hydroxide (608 mg, 10.8 mmol) were stirred in dimethyl sulfoxide (2 mL) at 110 °C for 1 hr. 2-Bromopyridine (870  $\mu$ L, 9.1 mmol) was then added and the reaction was stirred overnight at 110 °C under nitrogen atmosphere. The reaction mixture was then cooled and diluted with water (10 mL), and extracted with ethyl acetate (3 x 30 mL). The organic extract was dried over magnesium sulfate and concentrated *in vacuo* to afford a light brown oil which was purified by flash chromatography on silica with ethyl acetate as the eluent. The product was isolated as yellow oil from the second fraction. The oil slowly crystallised to afford yellow crystals in good yield (1.37 g, 72%). Mpt. 38-39 °C. [Literature: 38-40 °C].<sup>110</sup>

<sup>1</sup>H NMR (400 MHz, acetone-*d*<sub>6</sub>):  $\delta$  8.94 (1H, d,  $J$  = 4.8 Hz, pyridyl **H6**), 8.90 (1H, s, imidazolyl NCHN), 8.42 (1H, t,  $J$  = 8.0 Hz, pyridyl **CH**), 8.32 (1H, s, imidazolyl **CH**), 8.17 (1H, d,  $J$  = 8.4 Hz, pyridyl **H3**), 7.79 (1H, t,  $J$  = 6 Hz, pyridyl **CH**), 7.57 (1H, s, imidazolyl **CH**) ppm.

## 8.3 Synthesis of N-Heterocyclic Carbene Ligand Precursors

### 8.3.1 1-(2-Pyridyl)-3-butyliimidazolium Bromide (PyImBuH.Br)

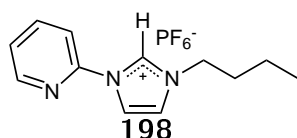
1-(2-Pyridyl)imidazole (**98**) (112 mg, 0.7 mmol) and 1-bromobutane (**197**) (1 mL, 9.3 mmol) were heated at reflux in acetonitrile (0.5 mL) under nitrogen atmosphere for 7



days. The reaction mixture was cooled and concentrated *in vacuo* to produce a light pink solid which was washed with diethyl ether to afford the desired product in good yield (176 mg, 81%). Mpt. 111-113 °C. [Literature: 68-70 °C] .<sup>61</sup>

<sup>1</sup>H NMR (400 MHz, CDCl<sub>3</sub>): δ 11.98 (1H, s, NCHN), 8.66 (1H, d, *J* = 8.0 Hz, pyridyl CH), 8.51 (1H, dd, *J*<sub>ab</sub> = 4.2 Hz, *J*<sub>ac</sub> = 2.0 Hz, pyridyl CH), 8.31 (1H, dd, , *J*<sub>ab</sub> = 3.6 Hz, *J*<sub>ac</sub> = 1.6 Hz, imidazolyl CH), 8.07 (1H, t, *J* = 7.4 Hz, pyridyl CH), 7.46 (1H, dd, *J*<sub>ab</sub> = 12.4 Hz, *J*<sub>ac</sub> = 6.4 Hz, pyridyl CH) , 7.37 (1H, dd, *J*<sub>ab</sub> = 3.6 Hz, *J*<sub>ac</sub> = 1.6 Hz, imidazolyl CH), 4.57 (2H, t, *J* = 7.2 Hz, CH<sub>2</sub>CH<sub>2</sub>CH<sub>2</sub>CH<sub>3</sub>), 2.04-1.98 (2H, m, CH<sub>2</sub>CH<sub>2</sub>CH<sub>2</sub>CH<sub>3</sub>), 1.50-1.44 (2H, m, CH<sub>2</sub>CH<sub>2</sub>CH<sub>2</sub>CH<sub>3</sub>), 1.01 (3H, t, *J* = 7.2 Hz, CH<sub>2</sub>CH<sub>2</sub>CH<sub>2</sub>CH<sub>3</sub>) ppm.

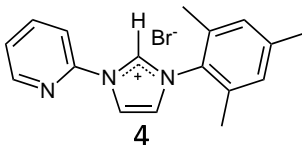
### 8.3.2 1-(2-Pyridyl)-3-butylimidazolium Hexafluorophosphate (PyImBuH.PF<sub>6</sub>)



A saturated aqueous solution of potassium hexafluorophosphate was added to an aqueous solution of PyImBuH.Br (**1**) (780 mg, 2.76 mmol) until precipitation of the fluffy white product ceased. The precipitate was collected and dried to afford an off white solid (506 mg, 53% yield). Mpt. 79-80 °C.

<sup>1</sup>H NMR (400 MHz, CDCl<sub>3</sub>): δ 9.44 (1H, s, NCHN), 8.56-8.55 (1H, m, pyridyl H<sub>6</sub>), 8.23 (1H, s, imidazolyl CH), 8.08-8.03 (1H, m, pyridyl CH), 7.95-7.92 (1H, m, pyridyl CH), 7.52-7.49 (1H, pyridyl CH), 7.44 (1H, s, imidazolyl CH), 4.38 (2H, t, *J* = 7.2 Hz, CH<sub>2</sub>CH<sub>2</sub>CH<sub>2</sub>CH<sub>3</sub>), 2.00-1.93 (2H, m, CH<sub>2</sub>CH<sub>2</sub>CH<sub>2</sub>CH<sub>3</sub>), 1.49-1.40 (2H, m, CH<sub>2</sub>CH<sub>2</sub>CH<sub>2</sub>CH<sub>3</sub>), 1.00 (3H, t, *J* = 4.6 Hz, CH<sub>2</sub>CH<sub>2</sub>CH<sub>2</sub>CH<sub>3</sub>) ppm.

### 8.3.3 1-(2-Pyridyl)-3-(2,4,6-trimethylphenyl)imidazolium Bromide (PyImMsH.Br)

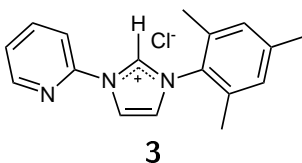


PyImMsH.Br (**4**) was synthesised *via* a literature procedure adapted from Gründemann et al.<sup>59</sup> The same procedure, described below, was used for the synthesis of the remainder of the halo-NHC precursor analogues.

A mixture of 2-bromopyridine (**100**) (230  $\mu$ L, 2.4 mmol) and 1-mesitylimidazole (**97**) (444 mg, 2.34 mmol) was heated in a sealed vessel at 170 °C for 4 days. On cooling to room temperature a brown solid formed, which was purified by repetitive re-precipitation from dichloromethane and tetrahydrofuran solutions, to afford a light brown solid (747 mg, 90% yield) . Mpt. 284-286 °C (dec.) [Literature: 280-282 °C]<sup>59</sup>.

<sup>1</sup>H NMR (400 MHz, DMSO-*d*<sub>6</sub>):  $\delta$  10.33 (1H, app t,  $J = 1.6$  Hz, NCHN), 8.81 (1H, app t,  $J = 1.6$  Hz, imidazolyl CH), 8.69 (1H, dd,  $J_{ab} = 4.8$  Hz,  $J_{ac} = 2.4$  Hz, pyridyl H**6**), 8.26 (1H, t,  $J = 6.8$  Hz, pyridyl CH), 8.19 (1H, app t,  $J = 1.6$  Hz, imidazolyl CH), 8.13 (1H, d, 8 Hz, pyridyl CH), 7.19 (2H, s, 2 x *meta* phenyl CH), 2.36 (3H, s, *para* CH<sub>3</sub>), 2.12 (6H, s, 2 x ortho CH<sub>3</sub>) ppm.

### 8.3.4 1-(2-Pyridyl)-3-(2,4,6-trimethylphenyl)imidazolium Chloride (PyImMsH.Cl)



PyImMsH.Cl (**3**) was synthesised utilising the same procedure as PyImMsH.Br (**4**) with the following modifications: 2-bromopyridine (**100**) was replaced with 2-chloropyridine

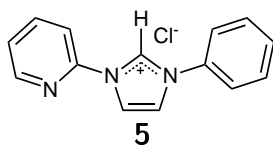
(**102**) to afford a light brown solid (550 mg, 85%). Mpt. 274 °C (dec.) [Literature: Not reported by authors].<sup>60</sup>

<sup>1</sup>H NMR (400 MHz, CDCl<sub>3</sub>): δ 11.81 (1H, s, NCHN), 9.30 (1H, d, *J* = 8.4 Hz, pyridyl CH), 8.88 (1H, s, imidazolyl CH), 8.50 (1H, m, *J* = 4.8 Hz, pyridyl CH), 8.09 (1H, m, *J* = 6.4 Hz, pyridyl CH), 7.46 (1H, m, *J* = 4.8 Hz, pyridyl CH), 7.33 (1H, s, imidazolyl CH), 7.02 (2H, s, *meta*-mesityl CH), 2.33 (3H, s, *para*-mesityl CH<sub>3</sub>), 2.18 (6H, s, *ortho*-mesityl CH<sub>3</sub>) ppm.

<sup>13</sup>C NMR (100 MHz, CDCl<sub>3</sub>): δ 148.7 (pyridyl CH), 146.2 (pyridyl quat. C), 141.6 (mesityl quat. C1), 141.1 (pyridyl CH), 137.2 (NCHN), 134.1 (mesityl quat. C2, C6), 130.8 (mesityl quat. C4), 130.1 (*meta*-mesityl CH), 125.5 (pyridyl CH), 123.8 (imidazolyl CH), 119.9 (imidazolyl CH), 116.6 (pyridyl CH), 21.2 (*para*-mesityl CH<sub>3</sub>), 17.9 (*ortho*-mesityl CH<sub>3</sub>) ppm.

ATR-IR: ν = 3116 w, 3077 w, 3011 m, 2951 m, 2803 w, 1704 w, 1597 m, 1538 m, 1488 w, 1474 m, 1437 m, 1382 w, 1330 w, 1308 w, 1276 w, 1240 m, 1172 w, 1149 w, 1119 w, 1092 w, 1066 w, 996 w, 965 w, 933 w, 913 w, 877 w, 855 w, 804 w, 795 w, 743 w, 728 w, 711 w, 672 w cm<sup>-1</sup>.

### 8.3.5 1-(2-Pyridyl)-3-phenylimidazolium Chloride (PyImPhH.Cl)



PyImPhH.Cl (**5**) was synthesised utilising the same procedure as PyImMsH.Br (**4**) with the following modifications: 2-bromopyridine (**100**) was replaced with 2-chloropyridine (**102**) and 1-mesitylimidazole (**97**) was replaced with 1-phenylimidazole (**99**) to afford a light brown solid (1.24 g, 48%). Mpt. 149-150 °C.

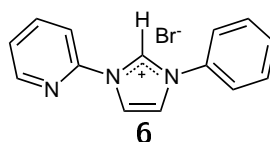
Anal. Calcd for (C<sub>14</sub>H<sub>12</sub>ClN<sub>3</sub>)·1.5H<sub>2</sub>O: C, 59.05; H, 5.31; N, 14.76. Found: C, 58.84; H, 5.28; N, 14.86.

$^1\text{H}$  NMR (DMSO- $d_6$ ):  $\delta$  = 10.79 (1H, s, imidazole NCHN), 8.77 (1H, app. t,  $J$  = 3.6 Hz, imidazole CH), 8.71 (1H, d,  $J$  = 4.8 Hz, pyridyl **H6**), 8.61 (1H, app. t,  $J$  = 3.6 Hz, imidazole CH), 8.32-8.25 (2H, m, pyridyl **H5**; pyridyl **H3**), 8.00 (2H, d,  $J$  = 5.4 Hz, phenyl *ortho*-H), 7.73-7.62 (4H, m, phenyl *meta*-H; phenyl *para*-H; pyridyl **H4**) ppm.

$^{13}\text{C}$  NMR (DMSO- $d_6$ ):  $\delta$  = 149.7 (pyridyl CH), 146.8 (pyridyl quat. C), 141.1 (pyridyl CH), 135.1 (phenyl quat. C), 134.8 (imidazole NCHN), 130.6 (pyridyl CH), 130.6 (phenyl CH), 125.9 (phenyl CH), 122.7 (imidazole CH), 122.6 (phenyl CH), 120.4 (imidazole CH), 115.4 (pyridyl CH) ppm.

ATR-IR:  $\nu$  = 3433 s, 3371 s, 3186 w, 3133 w, 3098 m, 3038 m, 3004 s, 1647 w, 1601 m, 1547 s, 1478 m, 1444 s, 1355 w, 1312 w, 1291 m, 1257 m, 1162 w, 1098 w, 1065 w, 997 w, 910 w, 780 w, 756 m, 720 w, 684 w  $\text{cm}^{-1}$ .

### 8.3.6 1-(2-Pyridyl)-3-phenylimidazolium Bromide (PyImPhH.Br)



PyImPhH.Br (**6**) was synthesised utilising the same procedure as PyImMsH.Br (**4**) with the following modifications: 1-mesitylimidazole (**97**) was replaced with 1-phenylimidazole (**99**) (2.39 g, 79%). Mpt. 222-223 °C.

Anal. Calcd for  $(\text{C}_{14}\text{H}_{12}\text{BrN}_3) \cdot 0.5\text{CH}_2\text{Cl}_2$ : C, 50.53; H, 3.80; N, 12.19. Found C, 50.45; H, 3.69; N, 12.14.

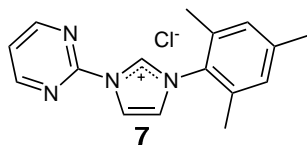
$^1\text{H}$  NMR (DMSO- $d_6$ ):  $\delta$  = 10.59 (1H, s, imidazole NCHN), 8.75 (1H, app. t,  $J$  = 3.6 Hz, imidazole CH), 8.71 (1H, d,  $J$  = 4.8 Hz, pyridyl **H6**), 8.57 (1H, app. t,  $J$  = 4.0 Hz, imidazole CH), 8.30-8.26 (1H, m, pyridyl **H5**), 8.16 (1H, d,  $J$  = 8.4 Hz, pyridyl **H3**), 7.94 (2H, d,  $J$  = 7.2 Hz, phenyl *ortho*-H), 7.74-7.63 (4H, m, phenyl *meta*-H; phenyl

*para*-H; pyridyl **H4**) ppm.

$^{13}\text{C}$  NMR (DMSO- $d_6$ ):  $\delta$  = 149.3 (pyridyl CH), 146.3 (pyridyl quat. C), 140.6 (pyridyl CH), 134.7 (phenyl quat. C), 134.3 (imidazole NCHN), 130.2 (pyridyl CH; phenyl CH), 125.5 (phenyl CH), 122.3 (imidazole CH; phenyl CH), 120.0 (imidazole CH), 114.8 (pyridyl CH) ppm.

ATR-IR:  $\nu$  = 3192 m, 3089 m, 3040 m, 2984 s, 1616 w, 1597 s, 1538 s, 1477 s, 1467 w, 1440 s, 1396 w, 1349 w, 1306 w, 1247 m, 1248 m, 1153 w, 1098 w, 1083 w, 1052 w, 993 w, 951 w, 906 w, 865 w, 793 w, 757 s, 717 w, 681 m  $\text{cm}^{-1}$ .

### 8.3.7 1-(2-Pyrimidyl)-3-(2,4,6-trimethylphenyl)-imidazolium Chloride (PmImMsH.Cl)



PmImMsH.Cl (**7**) was prepared *via* the same procedure as PyImMsH.Br (**4**) with the following modifications; 2-bromopyridine (**100**) was replaced with 2-chloropyrimidine (**103**) to afford a light brown solid (254 mg, 61%). Mpt. 272-275 °C.

Anal. Calcd for  $\text{C}_{16}\text{H}_{17}\text{ClN}_4 \cdot 1.2\text{H}_2\text{O}$ : C, 59.61; H, 6.07; N, 17.38. Found C, 59.34; H, 5.85; N, 17.88.

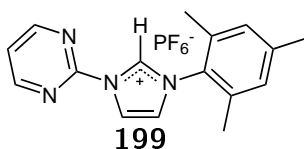
$^1\text{H}$  NMR (400 MHz, DMSO- $d_6$ ):  $\delta$  10.48 (1H, app. t,  $J$  = 1.6 and 1.2 Hz, NCHN), 9.10 (2H, d,  $J$  = 5.2 Hz, pyrimidyl **H4**, **H6**), 8.77 (1H, app. t,  $J$  = 2.0 Hz, imidazolyl), 8.19 (1H, app. t,  $J$  = 2 Hz, imidazolyl CH), 7.82 (1H, t,  $J$  = 4.8 Hz, pyrimidyl **H5**), 7.18 (2H, s, phenyl *meta*-H), 2.35 (3H, s,  $\text{CH}_3$ ), 2.11 (6H, s,  $\text{CH}_3$ ).

$^{13}\text{C}$  NMR (100 MHz, 100 MHz, DMSO- $d_6$ ):  $\delta$  160.0 (2 x pyrimidyl CH), 152.3 (pyrimidyl quat. C1), 140.4 (phenyl quat. C1), 137.2(NCHN), 134.3 (phenyl quat.

**C2, C6**), 131.2 (phenyl quat. **C4**), 129.2 (2 x phenyl CH), 125.3 (imidazolyl CH), 122.6 (pyrimidyl CH), 120.1 (imidazolyl CH), 20.6 (**CH**<sub>3</sub>), 17.0 (**CH**<sub>3</sub>), 16.9 (**CH**<sub>3</sub>).

ATR-IR:  $\nu = 3421$  w, 3363 w, 3255 w, 3189 w, 3160 m, 3122 m, 3049 m, 2978 m, 2918 s, 2753 w, 2324 w, 2287 w, 2193 w, 2162 w, 2152 w, 2103 w, 2067 w, 2050 w, 1823 w, 1628 w, 1605 w, 1584 s, 1561 w, 1521 s, 1489 w, 1450 w, 1412 s, 1377 m, 1344 w, 1327 w, 1307 w, 1291 w, 1248 w, 1191 w, 1120 w, 1101 w, 1073 w, 1051 w, 998 w, 971 w, 934 w, 902 w, 884 w, 852 w, 841 w, 790 w, 767 w, 738 w, 674 w  $\text{cm}^{-1}$ .

### 8.3.8 1-(2-Pyrimidyl)-3-(2,4,6-trimethylphenyl)-imidazolium Hexafluorophosphate (**PmImMsH.PF<sub>6</sub>**)



**PmImMsH.PF<sub>6</sub>** (**199**) was prepared *via* the same procedure as **PyImBuH.PF<sub>6</sub>** (**198**) with the following modifications; **PyImBuH.Br** (**1**) was replaced with **PmImMsH.Cl** (**7**) to afford a pale pink solid (201 mg, 71% yield). Mpt. 218 °C.

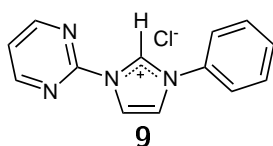
Anal. Calcd for **C<sub>16</sub>H<sub>17</sub>F<sub>6</sub>N<sub>4</sub>P**; C, 46.84; H, 4.18; N, 13.66. Found C, 46.61; H, 4.03; N, 13.00

<sup>1</sup>H NMR (400 MHz, DMSO-*d*<sub>6</sub>):  $\delta$  10.47 (1H, app. t,  $J = 1.6$  Hz, NCHN), 9.09 (2H, d,  $J = 5.2$  Hz, pyrimidyl **H4, H6**), 8.78 (1H, app. t,  $J = 1.6$  Hz, imidazolyl **H**), 8.18 (1H, app. t,  $J = 1.6$  Hz, imidazolyl **H**), 7.81 (1H, t,  $J = 4.8$  and 5.2 Hz, pyrimidyl **H5**), 7.18 (2H, s, phenyl **CH**), 2.36 (3H, s, **CH**<sub>3</sub>), 2.11 (6H, s, **CH**<sub>3</sub>).

<sup>13</sup>C NMR (100 MHz, DMSO-*d*<sub>6</sub>):  $\delta = 160.5$  (2 x pyrimidyl **CH**), 152.7 (pyrimidyl quat. **C1**), 141.2 (phenyl quat. **C1**), 137.3 (NCHN), 134.7 (phenyl quat. **C2, C6**), 131.4 (phenyl quat. **C4**), 129.8 (2 x phenyl **CH**), 125.7 (imidazolyl **CH**), 123.0 (pyrimidyl **CH**), 120.4 (imidazolyl **CH**), 21.0 (**CH**<sub>3</sub>), 17.4 (2 x **CH**<sub>3</sub>) ppm.

ATR-IR:  $\nu = 3676$  w,  $3177$  w,  $3143$  m,  $3097$  w,  $2988$  w,  $2974$  w,  $2902$  w,  $1644$   $1628$  w,  $1608$  w,  $1588$  m,  $1566$  w,  $1531$  m,  $1486$  w,  $1450$  w,  $1429$  w,  $1416$  s,  $1387$  w,  $1360$  w,  $1330$  w,  $1311$  w,  $1296$  w,  $1250$  m,  $1229$  w,  $1189$  w,  $1121$  w,  $1091$  w,  $1075$  w,  $1066$  w,  $1054$  w,  $999$  w,  $977$  w,  $969$  w,  $933$  w,  $901$  w,  $878$  w,  $865$  w,  $827$  s,  $819$   $\text{cm}^{-1}$ .

### 8.3.9 1-(2-Pyrimidyl)-3-phenylimidazolium Chloride (PmImPhH.Cl)



PmImPhH.Cl (**9**) was prepared *via* the same procedure as PyImMsH.Br (**4**) with the following modifications; 2-bromopyridine (**100**) was replaced with 2-chloropyrimidine (**103**) and 1-mesitylimidazole (**97**) was replaced with 1-phenylimidazole (**99**) to afford a light brown solid (622 mg, 66%). Mpt. 224-227 °C.

Anal. Calcd for  $\text{C}_{13}\text{H}_{11}\text{ClN}_4\text{H}_2\text{O}$ : C, 56.42; H, 4.74; N, 20.25. Found C, 56.29; H, 4.58; N, 20.56.

$^1\text{H}$  NMR (400 Hz,  $\text{DMSO-d}_6$ ):  $\delta = 10.70$  (1H, app. t,  $J_{ab} = 2$  Hz,  $J_{bc} = 1.6$  Hz, NCHN) 9.12 (2H, d,  $J = 4.8$  Hz, pyrimidyl **H4**, **H6**), 8.75 (1H, app. t,  $J_{ab} = 2$  Hz,  $J_{bc} = 1.6$  Hz, imidazolyl CH), 8.57 (1H, app. t,  $J_{ab} = 2$  Hz,  $J_{bc} = 1.6$  Hz, imidazolyl CH), 7.99-7.96 (2H, m, phenyl *ortho*-H), 7.84 (1H, t,  $J = 4.8$  Hz, pyrimidyl **H5**), 7.72-7.65 (3H, m, phenyl *meta*-H, *para*-H), ppm.

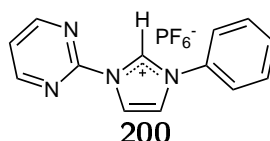
$^{13}\text{C}$  NMR (100 MHz,  $\text{DMSO-d}_6$ ):  $\delta = 160.2$  (2 x pyrimidyl CH), 152.2 (pyrimidyl quat. C), 135.0 (NCHN), 134.5 (phenyl quat. C), 130.4 (phenyl CH), 130.1 (2 x phenyl CH), 122.9 (imidazolyl CH), 122.8 (pyrimidyl CH), 122.6 (2 x phenyl CH), 120.0 (imidazolyl CH) ppm.

ATR-IR:  $\nu = 3140$  m,  $3015$  m,  $2324$  w,  $2163$  w,  $2105$  w,  $1660$  w,  $1587$  m,  $1561$  w,

1536 s, 1496 w, 1467 w, 1418 s, 1387 m, 1351 w, 1337 w, 1311 w, 1275 w, 1242 m, 1190 w, 1165 w, 1144 w, 1119 w, 1057 w, 1001 w, 977 w, 951 w, 914 w, 816 w, 788 w, 763 m, 737 w, 684 w cm<sup>-1</sup>.

### 8.3.10 1-(2-Pyrimidyl)-3-phenylimidazolium Hexafluorophosphate (PmImPhH.PF<sub>6</sub>)

PmImPhH.PF<sub>6</sub> (**200**) was prepared *via* the same procedure as PyImBuH.PF<sub>6</sub> (**198**) to



afford a pale pink solid (97 mg, 63% yield). Mpt. 217-218 °C.

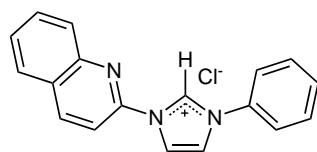
Anal. Calcd for 15C<sub>13</sub>H<sub>11</sub>F<sub>6</sub>N<sub>4</sub>P.C<sub>13</sub>H<sub>11</sub>ClN<sub>4</sub>\*: C, 43.21; H, 3.07; N, 15.50. Found C, 43.21; H, 2.90; N, 15.65. \*Note: 6% of the final product is thought to be the chloro precursor still present; this did not affect subsequent halogen purity.

<sup>1</sup>H NMR (400 Hz, DMSO-d<sub>6</sub>): δ = 10.69 (1H, app. t, *J* = 1.6 Hz, NCHN), 9.12 (2H, d, *J* = 5.2 Hz, pyrimidyl **H2**, **H4**), 8.75 (1H, app. t, *J* = 2 Hz, imidazolyl **CH**), 8.56 (1H, app. t, *J*<sub>ab</sub> = 2 Hz, *J*<sub>bc</sub> = 1.6 Hz, imidazolyl **CH**), 7.98-7.95 (2H, m, phenyl *ortho*-**H**), 7.83 (1H, t, *J* = 4.8 Hz, pyrimidyl **H3**), 7.72-7.63 (3H, m, phenyl *meta*-**H**, *para*-**H**) ppm.

<sup>13</sup>C NMR (100 MHz, DMSO-d<sub>6</sub>): δ = 160.3 (2 x pyrimidyl **CH**), 152.3 (pyrimidyl quat. **C**), 135.0 (NCHN), 134.6 (phenyl quat. **C**), 130.5 (phenyl **CH**), 130.3 (2 x phenyl **CH**), 123.0 (imidazolyl **CH**), 122.8 (2 x phenyl **CH**), 122.7 (pyrimidyl **CH**), 120.1 (imidazolyl **CH**) ppm.

ATR-IR: ν = 3641 w, 3407 w, 3199 w, 3174 w, 3151 w, 3009 w, 2929 w, 1669 w, 1599 w, 1588 m, 1566 w, 1534 m, 1500 w, 1467 w, 1450 w, 1423 w, 1395 w, 1361 w, 1349 w, 1334 w, 1267 w, 1238 w, 1196 w, 1135 w, 1107 w, 1076 w, 1056 w, 1000 w, 977 w, 919 w, 878 w, 820 s, 790 m, 766 m, 740 m, 688 w cm<sup>-1</sup>.

### 8.3.11 1-(2-Quinoyl)-3-phenylimidazolium Chloride (QuImPhH.Cl)



11

QuImPhH.Cl (**11**) was prepared *via* the same procedure as PyImMsH.Br (**4**) with the following modifications; 2-bromopyridine (**201**) was replaced with 2-chloroquinoline (**104**) and 1-mesitylimidazole (**97**) was replaced with 1-phenylimidazole (**99**) to afford a light brown solid (1.76 g, 68 %). Mpt. 203-204 °C.

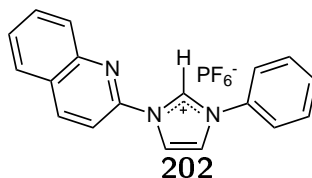
Anal. Calcd for (C<sub>18</sub>H<sub>14</sub>ClN<sub>3</sub>)·1.6 H<sub>2</sub>O: C, 64.23; H, 5.15; N, 12.49. Found C, 64.16; H, 4.87; N, 12.

<sup>1</sup>H NMR (DMSO-d<sub>6</sub>): δ = 10.87 (1H, s, imidazole NCHN), 8.93 (1H, app. t, *J* = 4.0 Hz, imidazole CH), 8.89 (1H, d, *J* = 8.8 Hz, quinoyl CH), 8.67 (1H, app. t, *J* = 4.0 Hz, imidazole CH), 8.39 (1H, d, *J* = 8.8 Hz, quinoyl CH), 8.19 (1H, d, *J* = 7.6 Hz, quinoyl CH), 8.14 (1H, d, *J* = 8.4 Hz, quinoyl CH), 8.03-7.95 (3H, m, phenyl *ortho*-H; quinoyl CH), 7.81-7.66 (4H, m, phenyl *meta*-H; phenyl *para*-H; quinoyl CH).

<sup>13</sup>C NMR (DMSO-d<sub>6</sub>): δ = 145.5 (quinoyl quat. C), 145.2 (quinoyl quat. C), 141.3 (quinoyl CH), 134.9 (imidazole NCHN), 134.6 (quinoyl quat. C), 131.8 (quinoyl CH), 130.2 (phenyl CH), 130.1 (phenyl CH), 128.4 (quinoyl CH), 128.3 (quinoyl CH), 128.1 (phenyl quat. C), 127.9 (quinoyl CH), 122.3 (imidazole CH), 122.2 (phenyl CH), 120.0 (imidazole CH), 113.0 (quinoyl CH).

ATR-IR: ν = 3341 s, 3091 m, 3037 w, 2959 m, 2825 w, 2161 w, 1646 w, 1617 w, 1594 w, 1580 w, 1547 m, 1501 m, 1463 w, 1434 w, 1390 w, 1309 w, 1292 w, 1283 w, 1267 w, 1255 w, 1239 w, 1201 w, 1133 w, 1118 w, 1066 w, 991 w, 934 w, 915 w, 871 w, 827 w, 779 w, 762 w, 753 w, 685 w cm<sup>-1</sup>.

### 8.3.12 1-(2-Quinoyl)-3-phenylimidazolium Hexafluorophosphate (QuImPhH.PF<sub>6</sub>)

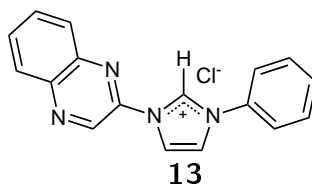


QuImPhH.PF<sub>6</sub> (**202**) was prepared *via* the same procedure as PyImBuH.PF<sub>6</sub> (**198**) to afford a light grey solid (1.23 g, 78%).

<sup>1</sup>H NMR (DMSO-d<sub>6</sub>): δ = 10.87 (1H, s, imidazole NCHN), 8.93 (1H, app. t, *J* = 4.0 Hz, imidazole CH), 8.89 (1H, d, *J* = 8.8 Hz, quinoyl CH), 8.67 (1H, app. t, *J* = 4.0 Hz, imidazole CH), 8.39 (1H, d, *J* = 8.8 Hz, quinoyl CH), 8.19 (1H, d, *J* = 7.6 Hz, quinoyl CH), 8.14 (1H, d, *J* = 8.4 Hz, quinoyl CH), 8.03-7.95 (3H, m, phenyl *ortho*-H; quinoyl CH), 7.81-7.66 (4H, m, phenyl *meta*-H; phenyl *para*-H; quinoyl CH).

<sup>13</sup>C NMR (DMSO-d<sub>6</sub>): δ = 145.5 (quinoyl quat. C), 145.2 (quinoyl quat. C), 141.3 (quinoyl CH), 134.9 (imidazole NCHN), 134.6 (quinoyl quat. C), 131.8 (quinoyl CH), 130.2 (phenyl CH), 130.1 (phenyl CH), 128.4 (quinoyl CH), 128.3 (quinoyl CH), 128.1 (phenyl quat. C), 127.9 (quinoyl CH), 122.3 (imidazole CH), 122.2 (phenyl CH), 120.0 (imidazole CH), 113.0 (quinoyl CH).

### 8.3.13 1-(2-Quinoxyl)-3-phenylimidazolium Chloride (QxImPhH.Cl)



QxImPhH.Cl (**13**) was prepared *via* the same procedure as PyImMsH.Br (**4**) with the following modifications; 2-bromopyridine (**100**) was replaced with 2-chloroquinoxaline

(**106**) and 1-mesitylimidazole (**97**) was replaced with 1-phenylimidazole (**99**) was substituted for to afford a black powder (589 mg, 95%). Mpt. 287 °C.

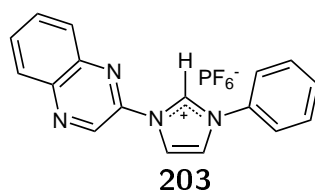
Anal. Calcd for C<sub>17</sub>H<sub>13</sub>N<sub>4</sub>Cl<sub>0.3</sub>H<sub>2</sub>O: C, 64.88; H, 4.38; N, 17.81. Found C, 64.90; H, 4.03; N, 17.70.

<sup>1</sup>H NMR (400 Hz, DMSO-d<sub>6</sub>): δ = 11.20 (1H, app. t, *J* = 1.6 Hz, NCHN), 9.93 (1H, s, quinoxyl CH), 8.96 (1H, app. t, *J* = 1.8 Hz, imidazolyl CH), 8.74 (1H, app. t, *J* = 1.8 Hz, imidazolyl CH), 8.30-8.19 (1H, m, quinoxyl CH), 8.22-8.19 (1H, m, quinoxyl CH), 8.09-8.01 (4H, m, 2 x phenyl CH, 2 x quinoxyl CH), 7.77-7.65 (3H, m, 3 x phenyl CH) ppm.

<sup>13</sup>C NMR (100 MHz, DMSO-d<sub>6</sub>): δ = 120.2 (imidazolyl CH), 121.9 (phenyl CH), 122.3 (imidazolyl CH), 128.6 (quinoxyl CH), 129.2 (quinoxyl CH), 130.0 (phenyl CH), 130.2 (phenyl CH), 130.4 (quat. phenyl C), 131.6 (quinoxyl CH), 132.4 (quinoxyl CH), 134.5 (quat. quinoxyl C), 135.5 (imidazolyl NCHN), 138.9 (quinoxyl C), 141.2 (quat. quinoxyl C), 141.8 (quat. quinoxyl C) ppm.

ATR-IR: ν = 3150 w, 3066 w, 3016 w, 2949 w, 2814 w, 1657 w, 1598 w, 1584 w, 1548 m, 1499 m, 1433 w, 1400 w, 1373 w, 1349 w, 1318 m, 1289 m, 1274 m, 1234 m, 1206 w, 1149 w, 1133 w, 1116 w, 1104 w, 1062 w, 1013 w, 1001 w, 959 w, 942 w, 895 w, 853 w, 771 w, 752 m, 677 m cm<sup>-1</sup>.

### 8.3.14 1-(2-Quinoxyl)-3-phenylimidazolium Hexafluorophosphate (QxImPhH.PF<sub>6</sub>)



QxImPhH.PF<sub>6</sub> (**203**) was prepared *via* the same procedure as PyImBuH.PF<sub>6</sub> (**198**) to afford a pale pink solid (459 mg, 78% yield%).

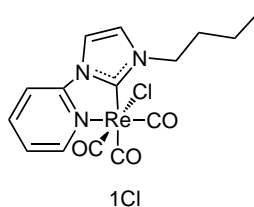
$^1\text{H}$  NMR (400 Hz,  $\text{DMSO-d}_6$ ):  $\delta$  = 10.74 (1H, s, NCHN), 8.89 (1H, d,  $J$  = 12 Hz, imidazolyl CH), 8.61 (1H, s, quinoxyl CH), 8.30 (1H, d,  $J$  = 12 imidazolyl CH), 8.19-8.13 (2H, m, quinoxyl CH), 7.99-7.95 (3H, m, 1 x phenyl CH, 1 x quinoxyl CH), 7.81-7.65 (4H, m, 4 x phenyl CH) ppm.

$^{31}\text{P}$  NMR (162 MHz,  $\text{DMSO-d}_6$ ):  $\delta$  = 130.7, 135.4, 139.1, 143.9, 148.1, 152.3 and 157.0.

## 8.4 Synthesis of Rhenium(I)-NHC Tricarbonyl Complexes

### 8.4.1 *rac-fac*-Chlorotricarbonyl[1-(2-pyridyl)-3-butylimidazol-2-ylidene]-rhenium(I) (1Cl)

A suspension of PyImBuH.Br (**1**) (408 mg, 1.45 mmol) and silver(I) oxide (375 mg,



1.62 mmol) in dichloromethane (20 mL) was stirred in darkness, at room temperature for 48 h after which pentacarbonylchloride rhenium(I) (346 mg, 0.95 mmol) was added and the reaction mixture was heated at reflux under inert atmosphere for 4 days. The resulting green solution was filtered through a short plug of deactivated acidic alumina and washed with dichloromethane (50 mL) followed by acetonitrile (50 mL). The combined fractions were concentrated in vacuo and washed with diethyl ether (50 mL) to afford a brown solid (178 mg, 37%). Crystals suitable for single X-ray diffraction study were grown by slow diffusion of diethyl ether into a solution of the compound in chloroform. Mpt. 198-199 °C (dec).

Anal. Calcd for  $\text{C}_{15}\text{ClH}_{15}\text{N}_3\text{O}_3\text{Re}$ : C, 35.54; H, 2.98; N, 8.29. Found: C, 35.19; H,

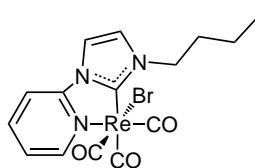
2.50; N, 7.90.

$^1\text{H}$  NMR (400 Hz DMSO- $d_6$ ):  $\delta$  = 8.83 (1H, d, 5.2 Hz, pyridyl **H6**), 8.45 (1H, d,  $J$  = 2, imidazolyl **CH**), 8.30 (2H, m, 2 x pyridyl **CH**), 7.74 (1H, d,  $J$  = 2.4, imidazolyl **CH**), 7.51 (1H, m, pyridyl **CH**), 4.23 (2H, t,  $J$  = 7.2, **NCH<sub>2</sub>**), 1.86 (2H, m, **CH<sub>2</sub>CH<sub>2</sub>CH<sub>3</sub>**), 1.38 (2H, m, **CH<sub>2</sub>CH<sub>3</sub>**), 0.93 (3H, t,  $J$  = 7.6 Hz **CH<sub>3</sub>**) ppm.

$^{13}\text{C}$  NMR (100 MHz, DMSO- $d_6$ )  $\delta$  = 198.9 (CO), 198.0 (CO) 190.0 (NCN), 189.2 (CO), 153.2 (pyridyl CH), 152.6 (pyridyl quat. C), 142.3 (pyridyl CH), 124.0 (pyridyl CH), 124.0 (imidazolyl CH), 117.5 (imidazolyl CH), 112.8 (pyridyl CH), 51.0 (**NCH<sub>2</sub>**), 32.7 (**CH<sub>2</sub>CH<sub>2</sub>CH<sub>3</sub>**), 19.1 (**CH<sub>2</sub>CH<sub>3</sub>**), 13.6 (**CH<sub>3</sub>**) ppm.

ATR-IR:  $\nu$  = 3937 w, 3775 w, 3164 w, 3114 w, 3092 w, 3060 w, 3030 w, 2964 w, 2935 w, 2864 w, 2017 s (CO), 1918 s (CO), 1871 s (CO), 1710 w, 1615 w, 1575 w, 1558 w, 1487 m, 1464 w, 1450 w, 1429 w, 1384 w, 1370 w, 1331 w, 1288 w, 1263 w, 1249 w, 1197 w, 1159 w, 1146 w, 1128 w, 1107 w, 1091  $\text{cm}^{-1}$ .

#### 8.4.2 *rac-fac*-Bromotricarbonyl[1-(2-pyridyl)-3-butyylimidazol-2-ylidene]-rhenium(I) (**1Br**)



**1Br**

A suspension of rhenium(I)pentacarbonylbromide (445 mg, 1.09 mmol), PyImBuH.Br (**1**) (305 mg, 1.08 mmol), and triethylamine (1.5 mL 10.8 mmol), in toluene (*ca.* 10 mL) was heated at reflux for 3 days. The resulting mixture was cooled to room temperature and water (*ca.* 5 mL) and hexanes (*ca.* 5 mL) were added and the hexanes layer was removed. The resulting brown solid was dissolved in dichloromethane, separated from the water layer and purified by flash column chromatography [deactivated acidic alumina, dichloromethane, first fraction]. The yellow eluent was concentrated *in vacuo*

and the yellow solid was collected and washed with hexanes (327 mg, 55%). Mpt. 192 °C (dec.).

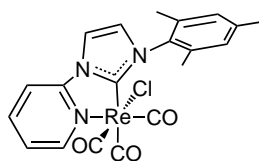
Anal. Calcd for  $C_{15}H_{15}N_3O_3ReBr \cdot H_2O$ : C, 31.63; H, 3.01; N, 7.38. Found C, 32.67; H, 2.74; N, 7.62.

$^1H$  NMR (400 MHz,  $CDCl_3$ ):  $\delta$  = 8.90 (1H, d,  $J$  = 5.6 Hz, pyridyl **H6**), 8.00 (1H, ddd,  $J$  = 8.4 Hz, pyridyl **CH**), 7.58-7.56 (2H, m, imidazolyl **CH**, pyridyl **CH**), 7.29 (1H, dd,  $J_{ab}$  = 6.8 Hz,  $J_{ac}$  = 1.6 Hz, pyridyl **CH**), 7.08 (1H, s, imidazolyl **CH**), 4.27 (2H, m,  $J$  = 7.2, **NCH<sub>2</sub>**), 1.97 (2H, m,  $J$  = 7.2, **NCH<sub>2</sub>CH<sub>2</sub>**), 1.49 (2H, m,  $J$  = 7.2, **CH<sub>2</sub>CH<sub>3</sub>**) 1.01 (3H, t,  $J$  = 7.2 Hz, **CH<sub>3</sub>**) ppm.

$^{13}C$  NMR (100 MHz,  $CDCl_3$ ):  $\delta$  197.3 (CO), 196.8 (CO), 193.0 (NCN), 188.0 (CO), 153.9 (pyridyl **CH**), 152.9 (pyridyl quat. **C**), 140.7 (pyridyl **CH**), 123.2 (pyridyl **CH**), 123.1 (imidazolyl **CH**), 115.8 (imidazolyl **CH**), 111.5 (pyridyl **CH**), 52.4 (**NCH<sub>2</sub>**), 33.0 (**NCH<sub>2</sub>CH<sub>2</sub>**), 19.8 (**CH<sub>2</sub>CH<sub>3</sub>**), 13.7 (**CH<sub>3</sub>**) ppm.

ATR-IR:  $\nu$  = 3905 w, 3748 w, 3164 w, 3118 w, 3095 w, 3067 w, 3039 w, 2964 w, 2942 w, 2867 w, 2014 s (CO), 1915 s (CO), 1887 s (CO), 1681 w, 1615 m, 1578 w, 1489 m, 1456 m, 1430 m, 1386 w, 1375 w, 1364 w, 1331 m, 1314 w, 1299 w, 1257 w, 1197 w, 1166 w, 1144 w, 1130 w, 1103 w, 1091 w, 1022 w, 1006 w, 958 w, 908 w, 892 w, 780 w, 747 w, 732 w, 704 w, 690 w  $cm^{-1}$ .

### 8.4.3 *rac-fac*-Chlorotricarbonyl[1-(2-pyridyl)-3-(2,4,6-trimethylphenyl)-imidazol-2-ylidene]rhenium(I) (2Cl)



2Cl

**2Cl** was prepared *via* the same procedure as **1Br** with the following modifications; Py-ImBuH.Br (**1**) was replaced with PyImMsH.Cl (**3**) to afford a yellow solid in moderate yield (32 mg, 49%). Crystals suitable for a single crystal X-ray diffraction study were grown by hot recrystallization from acetonitrile. Mpt. 235 °C (dec.)

Anal. Calcd for C<sub>20</sub>H<sub>17</sub>N<sub>3</sub>O<sub>3</sub>ReCl: C, 42.21; H, 3.01; N, 7.39. Found C, 42.03; H, 2.89; N, 7.21.

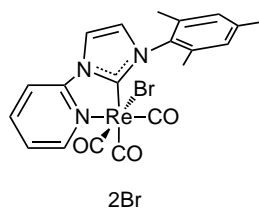
<sup>1</sup>H NMR (400 MHz, CDCl<sub>3</sub>): δ 8.92 (1H, d, *J* = 5.6 Hz, pyridyl CH), 8.06 (1H, m, *J* = 7.6 Hz, pyridyl CH), 7.78 (1H, d, *J* = 2.4 Hz, imidazolyl CH), 7.64 (1H, d, *J* = 8.4 Hz, pyridyl CH), 7.34 (1H, ddd, *J* = 5.6 Hz, pyridyl CH), 7.07 (1H, s, imidazolyl CH), 7.06 (2H, s, 2,5-mesityl CH), 2.37 (3H, s, 4-mesityl CH<sub>3</sub>), 2.25 (3H, s, 2,6-mesityl CH<sub>3</sub>) 2.13 (3H, s, 2,6-mesityl CH<sub>3</sub>) ppm.

<sup>13</sup>C NMR (100 MHz, CDCl<sub>3</sub>): δ 197.7 (CO), 196.8 (CO), 194.7 (CO), 188.7 (NCN), 154.2 (pyridyl CH), 153.3 (pyridyl quat. C), 140.8 (pyridyl CH), 140.3 (4-mesityl quat. C), 136.3 (2,6-mesityl quat. C), 135.2 (1-mesityl quat. C), 134.8 (2,6-mesityl quat. C), 129.8 (3,5-mesityl CH), 129.3 (3,5-mesityl CH), 124.3 (imidazolyl CH), 123.6 (pyridyl CH), 116.3 (imidazolyl CH), 111.7 (pyridyl CH), 21.3 (4-mesityl CH<sub>3</sub>), 18.5 (2,6-mesityl CH<sub>3</sub>), 17.8 (2,6-mesityl CH<sub>3</sub>) ppm.

ATR-IR: ν = 3089 w, 2924 w, 2010 s (CO), 1909 s (CO), 1867 s (CO), 1615 m, 1544 w, 1515 w, 1483 m, 1453 w, 1421 m, 1379 w, 1343 w, 1315 w, 1265 w, 1237 w, 1160 w, 1135 w, 1036 w, 910 w, 850 w, 771 w, 703 w cm<sup>-1</sup>.

#### 8.4.4 *rac-fac*-Bromotricarbonyl[1-(2-pyridyl)-3-(2,4,6-trimethyl-phenyl)-imidazol-2-ylidene]rhenium(I) (**2Br**)

**2Br** was prepared using the same procedure as for **1Br** with the following modifications: PyImBuH.Br (**1**) was replaced with PyImMsH.Br (**4**) to afford a yellow powder in moderate yield (199 mg, 66%). Crystals suitable for a single crystal X-ray diffrac-



tion study were grown by hot recrystallization from acetonitrile. Mpt. 243 °C (dec.).

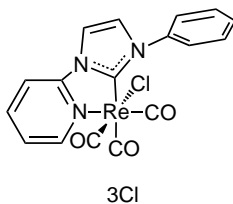
Anal. Calcd for  $C_{20}H_{17}N_3O_3ReBr$ : C, 39.16; H, 2.79; N, 6.85. Found: C, 39.22; H, 2.62; N, 6.79.

$^1H$  NMR (400 MHz,  $CDCl_3$ ):  $\delta$  8.92 (1H, d,  $J = 6.0$  Hz, pyridyl CH), 8.05 (1H, m, pyridyl CH), 7.77 (1H, d,  $J = 2.4$  Hz, imidazolyl CH), 7.64 (1H, d,  $J = 8.0$  Hz, pyridyl CH), 7.33 (1H, m,  $J = 6.6$  Hz, pyridyl CH), 7.07 (1H, d,  $J = 2.0$  Hz, imidazolyl CH), 7.06 (2H, s, 2,5-mesityl CH), 2.37 (3H, s, 4-mesityl  $CH_3$ ), 2.29 (3H, s, 2,6-mesityl  $CH_3$ ), 2.13 (3H, s, 2,6-mesityl  $CH_3$ ) ppm.

$^{13}C$  NMR (100 MHz,  $CDCl_3$ ):  $\delta$  196.9 (CO), 195.9 (CO), 194.2 (CO), 188.2 (NCN), 154.3 (pyridyl CH), 153.2 (pyridyl quat. C), 140.7 (pyridyl CH), 140.3 (4-mesityl C), 136.2 (2,6-mesityl C), 134.8 (2,6-mesityl C), 129.8 (2,5-mesityl CH), 129.3 (2,5-mesityl CH), 124.4 (imidazolyl CH), 123.5 (pyridyl CH), 116.3 (imidazolyl CH), 111.7 (pyridyl CH), 21.3 (4-mesityl  $CH_3$ ), 19.0 (2,6-mesityl  $CH_3$ ), 17.8 (2,6-mesityl  $CH_3$ ) ppm.

ATR-IR:  $\nu = 3919$  w, 3169 w, 3148 w, 3117 w, 3091 w, 3039 w, 2977 w, 2923 w, 2856 w, 2407 w, 2011 s (CO), 1918 s (CO), 1870 s (CO), 1616 m, 1575 w, 1558 w, 1484 m, 1453 w, 1439 w, 1419 w, 1378 w, 1342 w, 1314 w, 1266 w, 1159 w, 1135 w, 1111 w, 1093 w, 1083 w, 1038 w, 977 w, 953 w, 934 w, 872 w, 848 w, 768 w, 747 w, 720 w, 700 w  $cm^{-1}$ .

#### 8.4.5 *rac-fac*-Chlorotricarbonyl[1-(2-pyridyl)-3-(phenyl)imidazol-2-ylidene]rhenium(I) (**3Cl**)



**3Cl** was prepared using the same procedure as for **1Br** with the following modifications: PyImBuH.Br (**1**) was replaced with PyImPhH.Cl (**5**) to afford a yellow solid (60 mg, 45%). Crystals suitable for a single crystal X-ray diffraction study were grown from slow evaporation of an acetonitrile solution. Mpt. 243 °C.

Anal. Calcd for C<sub>17</sub>H<sub>11</sub>ClN<sub>3</sub>O<sub>3</sub>Re: C, 38.71; H, 1.96; N, 7.81. Found C, 38.75; H, 2.10; N, 7.00

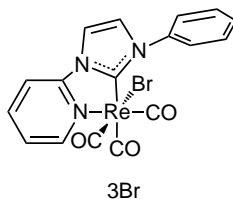
<sup>1</sup>H NMR (DMSO-d<sub>6</sub>): δ = 8.88 (1H, d, *J* = 5.2 Hz, pyridyl **H6**), 8.69 (1H, d, *J* = 2.0 Hz, imidazole **CH**), 8.39-8.37 (2H, m, 2 x pyridyl **CH**), 8.00 (1H, d, *J* = 2.0 Hz, imidazole **CH**), 7.71-7.55 (6H, m, 5 x phenyl **CH**; pyridyl **CH**).

<sup>13</sup>C NMR (DMSO-d<sub>6</sub>): δ = 197.9 (CO), 196.8 (CO), 190.9 (NCN), 189.2 (CO), 153.3 (pyridyl **CH**), 152.7 (pyridyl quat. C), 142.3 (pyridyl **CH**), 139.1 (phenyl quat. C), 129.6 (phenyl **CH**), 129.4 (phenyl **CH**), 126.1 (phenyl **CH**), 125.1 (imidazole **CH**), 124.3 (pyridyl **CH**), 118.1 (imidazole **CH**), 113.2 (pyridyl **CH**).

ATR-IR: ν = 3904 w, 3782 w, 3167 m, 3123 m, 3100 m, 2010 s (CO), 1921 s (CO), 1890 s (CO), 1613 m, 1595 m, 1578 m, 1485 s, 1456 m, 1424 m, 1385 w, 1345 m, 1324 m, 1309 m, 1294 m, 1272 m, 1175 w, 1161 w, 1136 w, 1094 w, 1076 w, 1028 w, 990 w, 964 w, 948 w, 929 w, 882 w, 780 m, 765 m, 749 m, 736 w, 700 m, 692 m cm<sup>-1</sup>.

IR (acetonitrile solution): ν = 2018 (CO), 1926 (CO), 1899 (CO) cm<sup>-1</sup>.

#### 8.4.6 *rac-fac*-Bromotricarbonyl[1-(2-pyridyl)-3-(phenyl)imidazol-2-ylidene]rhenium(I) (**3Br**)



**3Br** was prepared using the same procedure as for **1Br** with the following modifications: PyImBuH.Br (**1**) was replaced with PyImPhH.Br (**6**) to afford a yellow solid (100 mg, 72%). Crystals suitable for a single crystal X-ray diffraction study were grown from slow evaporation of an acetonitrile solution. Mpt. 255 °C.

Anal. Calcd for C<sub>17</sub>H<sub>11</sub>BrN<sub>3</sub>O<sub>3</sub>Re: C, 35.73; H, 1.94; N, 7.36. Found C, 35.73; H, 1.83; N, 7.00

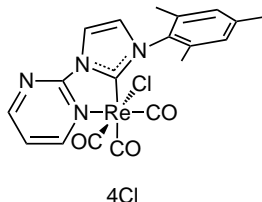
<sup>1</sup>H NMR (DMSO-d<sub>6</sub>): δ = 8.88 (1H, d, *J* = 4.4 Hz, pyridyl **H6**), 8.70 (1H, d, *J* = 2.4 Hz, imidazole **CH**), 8.38-8.34 (2H, m, 2 x pyridyl **CH**), 8.00 (1H, d, *J* = 2.4 Hz, imidazole **CH**), 7.71-7.53 (6H, m, 5 x phenyl **CH**; pyridyl **CH**).

<sup>13</sup>C NMR (DMSO-d<sub>6</sub>): δ = 197.3 (CO), 196.2 (CO), 190.0 (NCN), 188.7 (CO), 153.5 (pyridyl **CH**), 152.6 (pyridyl quat. C), 142.2 (pyridyl **CH**), 139.1 (phenyl quat. C), 129.6 (phenyl **CH**), 129.4 (phenyl **CH**), 126.1 (phenyl **CH**), 125.2 (imidazole **CH**), 124.2 (pyridyl **CH**), 118.1 (imidazole **CH**), 113.2 (pyridyl **CH**) ppm.

ATR-IR: ν = 3906 w, 3785 w, 3167 w, 3123 m, 3101 m, 2010 s (CO), 1923 s (CO), 1894 s (CO), 1614 m, 1595 m, 1578 m, 1485 s, 1456 m, 1423 m, 1383 m, 1344 m, 1324 m, 1308 m, 1293 m, 1272 m, 1175 w, 1161 m, 1136 m, 1123 w, 1093 m, 1076 m, 1028 w, 989 w, 963 w, 948 w, 929 w, 880 w, 779 m, 765 m, 747 m, 735 w, 700 m, 691 m cm<sup>-1</sup>.

IR (acetonitrile solution) ν = 2016 (CO), 1922 (CO), 1893 (CO) cm<sup>-1</sup>.

#### 8.4.7 *rac-fac*-Chlorotricarbonyl[1-(2-pyrimidyl)-3-mesitylimidazol-2-ylidene]rhenium(I) (**4Cl**)



**4Cl** was prepared via same procedure as **1Br** with the following modifications; PmImMsH.Cl was substituted for PyImBuH.Br to afford fine yellow powder (28 mg, 34%). Mpt. 240-255 °C (dec).

Anal. Calcd for  $C_{19}H_{16}ClN_4O_3Re \cdot 0.8CH_2Cl_2$ : C, 38.78; H, 2.78; N, 8.78. Found C, 38.72; H, 2.53; N, 8.54.

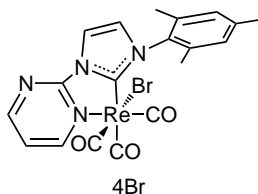
$^1H$  NMR (400 Hz, DMSO- $d_6$ ):  $\delta$  = 9.19 (2H, quart. d,  $J_{ab} = 2.0$  Hz,  $J_{ac} = 5.6$  Hz, 2 x pyrimidyl *meta*-H), 8.45 (1H, app. d,  $J = 2$  Hz, imidazolyl CH), 7.76 (1H, app. d,  $J = 2$  Hz, imidazolyl CH), 7.66 (1H, t,  $J = 5.2$  Hz, pyrimidyl *para*-H), 7.12 (2H, d,  $J = 12.8$  Hz, phenyl *meta*-H), 2.33 (3H, s,  $CH_3$ ), 2.12 (3H, s,  $CH_3$ ), 2.07 (3H, s,  $CH_3$ ) ppm.

$^{13}C$  NMR (100 MHz, DMSO- $d_6$ ):  $\delta$  = 197.6 (CO), 195.5 (CO), 192.4 (NCN), 188.6 (CO), 163.0 (pyrimidyl CH), 161.17 (pyrimidyl CH), 157.9 (pyrimidyl quat. C), 139.3 (phenyl quat. C), 135.4 (phenyl quat. C), 134.9 (phenyl quat. C), 134.5 (phenyl quat. C), 129.0 (phenyl CH), 128.9 (phenyl CH), 125.3 (imidazolyl CH), 121.0 (pyrimidyl *para*-CH), 118.6 (imidazolyl CH), 20.7 ( $CH_3$ ), 17.8 ( $CH_3$ ), 17.1 ( $CH_3$ ), ppm.

ATR-IR:  $\nu$  = 3922 w, 3335 w, 3171 w, 3139 w, 3099 w, 2985 w, 2924 w, 2745 w, 2654 w, 2403 w, 2014 s (CO), 1921 s (CO), 1889 s (CO), 1871 s (CO)\*, 1684 w, 1598 m, 1569 w, 1473 m, 1445 m, 180 m, 1348 m, 1311 w, 1275 w, 1258 w, 1199 w, 1143 w, 1101 w, 1077 w, 991 w, 936 w, 879 w, 847 w, 813 w, 789 w, 744 w, 703 w, 656 w  $cm^{-1}$ .

\*Due to solid state effects there is splitting of the CO stretches. This is not present in DMSO solution.

#### 8.4.8 *rac-fac*-Bromotricarbonyl[1-(2-pyrimidyl)-3-mesitylimidazol-2-ylidene]rhenium(I) (4Br)



**4Br** was prepared via same procedure as **1Br** with the following modifications; PmImMsH.PF<sub>6</sub> was substituted for PyImBuH.Br to afford fine yellow powder (46 mg, 58%). Mpt. 277-283 °C (dec).

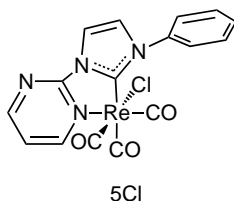
Anal. Calcd for C<sub>19</sub>H<sub>16</sub>BrN<sub>4</sub>O<sub>3</sub>Re: C, 37.14; H, 2.62; N, 9.12. Found C, 37.45; H, 2.66; N, 8.94.

<sup>1</sup>H NMR (400 Hz, DMSO-d<sub>6</sub>): δ = 9.18 (2H, quart. d, *J*<sub>ab</sub> = 2.0 Hz, *J*<sub>ac</sub> = 5.6 Hz, pyrimidyl *meta*-H), 8.45 (1H, app. d, *J* = 2 Hz, imidazolyl CH), 7.76 (1H, app. d, *J* = 2.4 Hz, imidazolyl CH), 7.64 (1H, t, *J* = 5.2 Hz, pyrimidyl *para*-H), 7.12 (2H, d, *J* = 12.8 Hz, phenyl *meta*-H), 2.33 (1H, s, CH<sub>3</sub>), 2.17 (1H, s, CH<sub>3</sub>), 2.07 (1H, s, CH<sub>3</sub>) ppm.

<sup>13</sup>C NMR (100 MHz, DMSO-d<sub>6</sub>): δ = 196.7 (CO), 194.9 (CO), 191.2 (NCN), 188.1 (CO), 163.1 (pyrimidyl CH), 161.0 (pyrimidyl CH), 157.7 (pyrimidyl quat. C), 139.2 (phenyl quat. C), 135.3 (phenyl quat. C), 134.8 (phenyl quat. C), 134.4 (phenyl quat. C), 129.0 (phenyl CH), 128.8 (phenyl CH), 125.4 (imidazolyl CH), 120.8 (pyrimidyl *para*-CH), 118.6 (imidazolyl CH), 20.7 (CH<sub>3</sub>), 18.1 (CH<sub>3</sub>), 17.1 (CH<sub>3</sub>) ppm.

ATR-IR: ν = 3926 w, 3685 w, 3676 w, 3182 w, 2988 m, 2973 m, 2912 m, 2902 m, 2747 w, 2410 w, 2324 w, 2489 w, 2012 s (CO), 1921 s (CO), 1891 s (CO), 1874 s (CO),\* 1595 m, 1568 w, 1557 w, 1512, 1470 m, 1449 m, 1411 w, 1394 w, 1379 w, 1343 w, 1306 w, 1257 w, 1197 w, 1168 w, 1139 w, 1058 w, 1028 w, 978 w, 963 w, 934 w, 848 w, 809 w, 788 w, 744 w, 699 w, 655 w cm<sup>-1</sup>. \*Due to solid state effects there is splitting of the CO stretches. This is not present in DMSO solution.

#### 8.4.9 *rac-fac*-Chlorotricarbonyl[1-(2-pyrimidyl)-3-phenylimidazol-2-ylidene]rhenium(I) (**5Cl**)



**5Cl** was prepared via the same procedure as **1Br** with the following modifications; PmImPhH.Cl was substituted for PyImBuH.Br to afford fine yellow powder (43 mg, 58%). Crystals suitable for single X-ray diffraction study were grown by slow evaporation of a solution of the compound in acetonitrile. Mpt. 249-251 °C (dec).

Anal. Calcd for C<sub>16</sub>H<sub>10</sub>ClN<sub>4</sub>O<sub>3</sub>Re: C, 36.40; H, 1.91; N, 10.61. Found C, 36.47; H, 2.17; N, 10.03.

<sup>1</sup>H NMR (400 Hz, DMSO-d<sub>6</sub>): δ = 9.21 (2H, quart. d, *J*<sub>ab</sub> = 2.0 Hz, *J*<sub>ac</sub> = 3.2 Hz, pyrimidyl *meta*-H), 8.42 (1H, app. d, *J* = 2.0 Hz, imidazolyl CH), 8.01 (1H, app. d, *J* = 2.0 Hz, imidazolyl CH), 7.71-7.61 (6H, m, pyrimidyl *para*-H, phenyl *ortho*-H, *meta*-H, *para*-H) ppm.

<sup>13</sup>C NMR (100 MHz, DMSO-d<sub>6</sub>): δ = 197.3 (CO), 196.5 (CO), 190.4 (NCN), 188.6 (CO), 162.8 (pyrimidyl CH), 161.2 (pyrimidyl CH), 157.7 (pyrimidyl quat. C), 138.6 (phenyl quat. C), 129.7 (phenyl CH), 129.6 (2 x phenyl CH), 126.0 (2 x phenyl CH), 125.4 (imidazolyl CH), 121.0 (pyrimidyl CH), 118.3 (imidazolyl CH) ppm.

ATR-IR: ν = 3175 w, 3145 w, 3067 w, 2020 s (CO), 1913 s (CO), 1882 s (CO), 1847 s (CO)\*, 1596 m, 1568 m, 1500 w, 1470 m, 1446 m, 1416 m, 1378 m, 1346 m, 1320 m, 1301 w, 1263 m, 1199 w, 1144 w, 1097 w, 1070 w, 1022 w, 979 w, 951 w, 817 w, 787 w, 761 w, 746 m, 690 m, 633 w, 618 w, 527 w cm<sup>-1</sup>. \*Due to solid state effects there is splitting of the CO stretches. This is not present in DMSO solution.

#### 8.4.10 *rac-fac*-Bromotricarbonyl[1-(2-pyrimidyl)-3-phenylimidazol-2-ylidene]rhenium(I) (5Br)



5Br

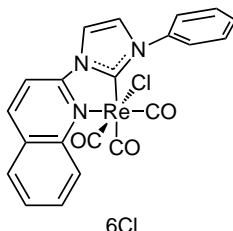
**5Br** was prepared *via* the same procedure as **1Br** with the following modifications; PmImPhH.PF<sub>6</sub> was substituted for PyImBuH.Br to afford fine yellow powder (28 mg, 35%). Crystals suitable for single X-ray diffraction study were grown by slow evaporation of a solution of the compound in acetonitrile. Mpt. 200-220 °C (dec). Anal. Calcd for C<sub>16</sub>H<sub>10</sub>BrN<sub>4</sub>O<sub>3</sub>Re.0.44CH<sub>2</sub>Cl<sub>2</sub>: C, 32.37; H, 1.80; N, 9.18. Found C, 32.73; H, 1.80; N, 8.77.

<sup>1</sup>H NMR (400 Hz, DMSO-d<sub>6</sub>): δ = 9.21 (2H, quart. d, *J*<sub>ab</sub> = 2.0 Hz, *J*<sub>ac</sub> = 2.4 Hz, pyrimidyl *meta*-H), 8.43 (1H, app. d, *J* = 2.4 Hz, imidazolyl CH), 8.00 (1H, app. d, *J* = 2.0 Hz, imidazolyl CH), 7.72-7.59 (6H, m, pyrimidyl *para*-H, phenyl *ortho*-H, *meta*-H, *para*-H) ppm.

<sup>13</sup>C NMR (100 MHz, DMSO-d<sub>6</sub>): δ = 196.6 (CO), 195.9 (CO), 189.4 (NCN), 188.1 (CO), 163.0 (pyrimidyl CH), 161.2 (pyrimidyl CH), 157.7 (pyrimidyl quat. C), 138.6 (phenyl quat. C), 129.7 (phenyl CH), 129.6 (2 x phenyl CH), 126.1 (2 x phenyl CH), 125.5 (imidazolyl CH), 120.9 (pyrimidyl CH), 118.4 (imidazolyl CH) ppm.

ATR-IR: ν = 3146 w, 2014 s (CO), 1913 s (CO), 1873 s (CO) 1847 s (CO)\*, 1594 m, 1566 m, 1498 w, 1469 m, 1423 m, 1381 m, 1345 m, 1303 w, 1263 w, 1142 w, 1074 w, 978 w, 952 w, 816 w, 788 w, 768 w, 744, 691 w, 634 w cm<sup>-1</sup>. \*Due to solid state effects there is splitting of the CO stretches. This is not present in DMSO solution.

#### 8.4.11 *rac-fac*-Chlorotricarbonyl[1-(2-quinolinyl)-3-phenylimidazol-2-ylidene]rhenium(I) (6Cl)



**6Cl** was prepared via the same procedure as **1Br** with the following modifications; QuImPhH.Cl was substituted for PyImBuH.Br to afford fine yellow powder (219 mg, 55%). Mpt. 290 °C. Crystals suitable for a single crystal X-ray diffraction study were grown from slow evaporation of an acetonitrile solution.

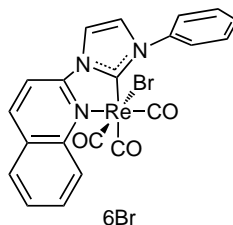
Anal. Calcd for C<sub>21</sub>H<sub>13</sub>ClN<sub>3</sub>O<sub>3</sub>Re: C, 43.71; H, 2.27; N, 7.28. Found C, 43.50; H, 2.06; N, 6.00

<sup>1</sup>H NMR (DMSO-d<sub>6</sub>): δ = 9.01 (1H, d, *J* = 8.8 Hz, quinoyl CH), 8.40 (1H, d, *J* = 2.0 Hz, imidazole CH), 8.61 (1H, d, *J* = 8.0 Hz, quinoyl CH), 8.53 (1H, d, *J* = 8.8 Hz, quinoyl CH), 8.23 (1H, d, *J* = 8.0 Hz, quinoyl CH), 8.10 (1H, dd, *J*<sub>ab</sub> = 7.6 Hz, *J*<sub>ac</sub> = 8.0 Hz, quinoyl CH), 7.85 (1H, d, *J* = 2.4 Hz, imidazole CH), 7.83 (1H, dd, *J*<sub>ab</sub> = 7.2 Hz, *J*<sub>ac</sub> = 7.8 Hz, quinoyl CH), 7.73-7.63 (5H, m, phenyl CH).

<sup>13</sup>C NMR (DMSO-d<sub>6</sub>): δ = 198.4 (CO), 195.2 (CO), 192.8 (NCN), 189.5 (CO), 154.2 (quinoyl quat. C), 145.5 (quinoyl quat. C), 143.7 (quinoyl CH), 139.1 (quinoyl quat. C), 132.9 (quinoyl CH), 129.7 (phenyl CH), 129.6 (phenyl CH), 129.4 (quinoyl CH), 128.7 (quinoyl CH), 127.7 (phenyl quat. C), 126.8 (quinoyl CH), 126.2 (phenyl CH), 125.4 (imidazole CH), 118.9 (imidazole CH), 112.0 (quinoyl CH).

IR: ν = 3097 w, 2010 s (CO), 1910 (CO) s, 1876 (CO) s, 1852 (CO) s, 1599 m, 1513 m, 1499 m, 1474 w, 1428 m, 1371 w, 1331 m, 1310 w, 1276 w, 1251 w, 1168 w, 1149 w, 1108 m, 1099 w, 990 w, 961 w, 944 w, 865 w, 844 w, 821 m, 773 m, 749 s, 696 s, 677 m cm<sup>-1</sup>.

#### 8.4.12 *rac-fac*-Bromotricarbonyl[1-(2-quinolinyl)-3-phenylimidazol-2-ylidene]rhenium(I) (6Br)



**6Br** was prepared via the same procedure as **1Br** with the following modifications; QuImPhH.PF<sub>6</sub> was substituted for PyImBuH.Br to afford fine yellow powder (188 mg, 59%). Crystals suitable for a single crystal X-ray diffraction study were grown from slow evaporation of an acetonitrile solution. Mpt. 295 °C.

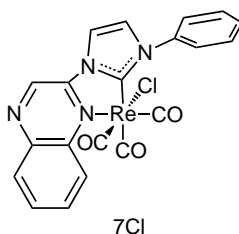
Anal. Calcd for C<sub>21</sub>H<sub>13</sub>BrN<sub>3</sub>O<sub>3</sub>Re: C, 40.50; H, 2.09; N, 6.76. Found C, 40.47; H, 1.91; N, 6.55.

<sup>1</sup>H NMR (DMSO-d<sub>6</sub>): δ = 9.00 (1H, d, *J* = 8.8 Hz, quinoyl CH), 8.85 (1H, d, *J* = 2.0 Hz, imidazole CH), 8.60 (1H, d, *J* = 8.8 Hz, quinoyl CH), 8.53 (1H, d, *J* = 8.8 Hz, quinoyl CH), 8.23 (1H, d, *J* = 8.0 Hz, quinoyl CH), 8.10 (1H, dd, *J*<sub>ab</sub> = 7.6 Hz, *J*<sub>ac</sub> = 8.0 Hz, quinoyl CH), 8.06 (1H, d, *J* = 2.0 Hz, imidazole CH), 7.83 (1H, dd, *J*<sub>ab</sub> = 7.6 Hz, *J*<sub>ac</sub> = 7.8 Hz, quinoyl CH), 7.73-7.64 (5H, m, phenyl CH).

<sup>13</sup>C NMR (DMSO-d<sub>6</sub>): δ = 197.7 (CO), 194.6 (CO), 191.8 (NCN), 188.9 (CO), 154.3 (quinoyl quat. C), 145.7 (quinoyl quat. C), 143.6 (quinoyl CH), 139.1 (quinoyl quat. C), 132.8 (quinoyl CH), 129.7 (phenyl CH), 129.6 (phenyl CH), 129.5 (quinoyl CH), 128.8 (quinoyl CH), 127.7 (phenyl quat. C), 126.8 (quinoyl CH), 126.3 (phenyl CH), 125.6 (imidazole CH), 118.9 (imidazole CH), 112.0 (quinoyl CH).

IR: ν = 3169 m, 3097 m, 2011 s (CO), 1912 s (CO), 1880 s (CO), 1857 s (CO), 3169 w, 3097 w, 1616 w, 1599 w, 1514 w, 1499 w, 1474 w, 1427 w, 1393 w, 1371 w, 1332 w, 1309 w, 1276 w, 1250 w, 1214 w, 1168 w, 1149 w, 1122 w, 1027 w, 991 w, 961 w, 944 w, 864 w, 821 w, 778 w, 745 w, 695 w cm<sup>-1</sup>.

### 8.4.13 *rac-fac*-Chlorotricarbonyl[1-(2-quinoxaliny)-3-phenylimidazol-2-ylidene]rhenium(I) (7Cl)



**7Cl** was prepared *via* the same procedure as **1Br** with the following modifications: QxImPh.Cl was substituted for PyImBuH.Br to afford a dark yellow solid (176 mg, 65%). Mpt. 247 °C (dec.).

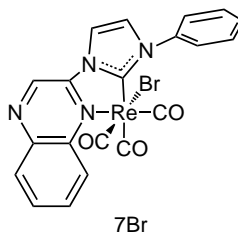
Anal. Calcd for C<sub>20</sub>H<sub>12</sub>ClN<sub>4</sub>O<sub>3</sub>Re: C, 41.40; H, 2.07; N, 9.65. Found C, 41.72; H, 1.91; N, 9.49.

<sup>1</sup>H NMR (400 Hz, DMSO-d<sub>6</sub>): δ = 9.99 (1H, s, quinoxyl *ortho*-CH), 9.01 (1H, d, *J* = 2.4 Hz, imidazolyl CH), 8.55 (1H, d, *J* = 8.0 Hz, 2,5-quinoxyl CH), 8.35 (1H, dd, *J*<sub>ab</sub> = 1.2 Hz, *J*<sub>ac</sub> = 8.2 Hz, 2,5-quinoxyl CH), 8.20 (1H, t, *J* = 7.2 Hz, 3,4-quinoxyl CH), 8.13 (1H, d, *J* = 2.4 Hz, imidazolyl CH), 8.05 (1H, t, *J* = 7.6 Hz, 3,4-quinoxyl CH), 7.73-7.64 (5H, m, phenyl CH) ppm.

<sup>13</sup>C NMR (100 MHz, DMSO-d<sub>6</sub>): δ = 197.9 (CO) 194.9 (CO), 194.0 (NCN), 188.1 (CO), 148.6 (quat. quinoxyl C), 141.0 (quat. quinoxyl C), 138.9 (quat. quinoxyl C), 138.4 (quinoxyl CH), 133.3 (quinoxyl CH), 130.8 (quinoxyl CH), 130.3 (quinoxyl CH), 129.8 (phenyl CH), 128.1 (quinoxyl CH), 126.2 (phenyl CH), 125.7 (imidazolyl CH), 119.1 (imidazolyl CH) ppm.

ATR-IR: ν = 3164 w, 3114 w, 3024 w, 2013 (CO) s, 1915 (CO) s, 1902 (CO) s, 1851 m, 1675 w, 1597 w, 1569 w, 1544 w, 1497 m, 1478 w, 1442 m, 1428 m, 1392 w, 1359 m, 1327 w, 1293 m, 1261 w, 1234 w, 1219 w, 1173 w, 1157 w, 1137 w, 1115 w, 1101 w, 1023 w, 994 w, 964 w, 944 w, 931 w, 874 w, 855 w, 840 w, 774 w, 759 w, 734 w, 701 w, 688 w, 677 w cm<sup>-1</sup>.

#### 8.4.14 *rac-fac*-Bromotricarbonyl[1-(2-quinoxaliny)-3-phenylimidazol-2-ylidene]rhenium(I) (**7Br**)



**7Br** was prepared *via* same procedure as **1Br** with the following modifications: Qx-ImPh.PF<sub>6</sub> was substituted for PyImBuH.Br to afford an orange solid (15 mg, 45%). Mpt. 250 °C (dec.).

Anal. Calcd for: C<sub>20</sub>H<sub>12</sub>BrN<sub>4</sub>O<sub>3</sub>Re: C, 38.60; H, 1.93; N, 9.00. Found C, 38.44; H, 1.73; N, 8.71.

<sup>1</sup>H NMR (CDCl<sub>3</sub>): 9.31 (1H, s, ortho-quinoxyl CH) 8.76 (1H, dd,  $J_{ab} = 0.8$  Hz,  $J_{ac} = 8.8$  Hz, 2,5-quinoxyl CH), 8.28 (1H, dd,  $J_{ab} = 1.2$  Hz,  $J_{ac} = 8.4$  Hz, 2,5-quinoxyl CH) 8.08-8.03 (2H, m, 3,4-quinoxyl CH, imidazolyl CH) (1H, ddd,  $J_{ab} = 1.2$  Hz,  $J_{ac} = 7.6$  Hz, 3,4-quinoxyl CH) 7.73-7.62 (5H, m, phenyl CH) 7.41 (1H, d,  $J = 2.0$  Hz, imidazolyl CH) ppm.

<sup>13</sup>C NMR (CDCl<sub>3</sub>):  $\delta = 197.2$  (CO), 196.4 (CO), 193.2 (NCN), 186.8 (CO), 147.7 (quat. quinoxyl C), 142.1 (quat. quinoxyl C), 140.3 (quat. quinoxyl C), 139.1 (quat phenyl C), 134.7 (quinoxyl CH), 134.0 (quinoxyl CH), 131.2 (quinoxyl CH), 130.7 (quinoxyl CH), 130.5 (phenyl CH), 130.2 (2 x phenyl CH), 129.7 (quinoxyl CH), 126.8 (2 x phenyl CH), 125.6 (imidazolyl CH), 116.5 (imidazolyl CH) ppm.

ATR-IR:  $\nu = 3083$  w, 2023 s (CO), 1938 s (CO), 1904 s (CO), 1883 s (CO)\*, 1596 w, 1542 w, 1495 m, 1475 w, 1438 m, 1421 w, 1359 w, 1333 w, 1300 w, 1231 w, 1212

w, 1154 w, 1119 w, 1023 w, 996 w, 964 w, 944 w, 919 w, 893 w, 856 w, 764 w, 690 w cm<sup>-1</sup>. \*Due to solid state effects there is splitting of the CO stretches. This is not present in DMSO solution.

## 8.5 Photophysical Measurements

Absorption spectra were recorded at room temperature using a Perkin-Elmer Lambda 35 UV-vis spectrometer. Uncorrected steady-state emission and excitation spectra were recorded on an Edinburgh FLSP980 spectrometer equipped with a 450 W xenon arc lamp, double-excitation and double-emission monochromators, and a Peltier cooled Hamamatsu R928P photomultiplier tube (185-850 nm). Emission and excitation spectra were corrected for source intensity (lamp and grating) and emission spectral response (detector and grating) by a calibration curve supplied with the instrument. According to the approach described by Demas and Crosby<sup>111</sup>, luminescence quantum yields ( $\Phi$ ) were measured in optically dilute solutions (OD < 0.1 at excitation wavelength) obtained from absorption spectra on a wavelength scale [nm] and compared to the reference emitter by the following equation<sup>36</sup>:

$$\Phi_x = \Phi_r \left[ \frac{A_r(\lambda_r)}{A_x(\lambda_x)} \right] \left[ \frac{I_r(\lambda_r)}{I_x(\lambda_x)} \right] \left[ \frac{n_x^2}{n_r^2} \right] \left[ \frac{D_x}{D_r} \right]$$

where  $A$  is the absorbance at the excitation wavelength ( $\lambda$ ),  $I$  is the intensity of the excitation light at the excitation wavelength ( $\lambda$ ),  $n$  is the refractive index of the solvent,  $D$  is the integrated intensity of the luminescence, and  $\Phi$  is the quantum yield. The subscripts r and x refer to the reference and the sample, respectively.

The quantum yield determinations were performed at identical excitation wavelengths for the sample and the reference, therefore cancelling the  $I(\lambda_r)/I(\lambda_x)$  term in the equation. All of the complexes were measured against an air equilibrated aqueous solution of [Ru(bpy)<sub>3</sub>]Cl<sub>2</sub> used as reference ( $\Phi = 0.028$ ), with the exception of **1Cl** and **2Cl**, which were measured against an air equilibrated ethanol solution of rhodamine 101 ( $\Phi = 1.0$ ).<sup>33,36</sup>

Emission lifetimes  $\tau$  were determined with the time correlated single photon counting technique (TCSPC) with the same Edinburgh FLSP980 spectrometer using a pulsed

picosecond diode laser (EPL 375, fwhm < 800 ps) as the excitation source, with repetition rates between 10 kHz and 1 MHz, and the aforementioned R928P PMT as detector. The goodness of fit was assessed by minimising the reduced  $\chi^2$  function and by visual inspection of the weighted residuals. To record the 77 K luminescence spectra, the samples were put in quartz tubes (2 mm diameter) and inserted in a special quartz Dewar filled with liquid nitrogen.

The dichloromethane and acetonitrile solvents used in the preparation of the solutions for the photophysical investigations were of spectrometric grade. Degassed samples were prepared by the bubbling N<sub>2</sub> gas through the solution for 10 minutes.

Temperature dependent lifetime measurements were obtained with an Edinburgh FLS980-stm spectrometer equipped with a temperature-controlled cuvette holder, for measurements between 293 and 333 K, or a liquid nitrogen cooled Oxford Instrument OptiscanDN cryostat, for measurements below room temperature. Experimental uncertainties are estimated to be  $\pm 8\%$  for lifetime determinations,  $\pm 20\%$  for quantum yields, and  $\pm 2$  for absorption and emission peaks.

## 8.6 Computational Calculations

Time-dependent density functional theory (TDDFT) calculations were performed by Dr Paolo Raiteri and Mr Phillip Wright at Curtin University and the results were given to the author for interpretation and discussion. The calculations were performed using GAUSSIAN 09 in order to calculate the absorption spectra for synthesised complexes.<sup>74</sup> Prior to these calculations, the structures were relaxed at the B3LYP level of theory in the presence of an implicit solvent (dichloromethane). The Re atoms were treated with the Stuttgart–Dresden (SDD) effective core potential;<sup>75</sup> the Pople 6-311++G\*\* basis set was used for C, H, N, O, Cl, and Br atoms, and in all calculations the effect of the solvent was mimicked with the PCM solvation model,<sup>76</sup> with parameters adequate for dichloromethane. The low-lying singlet–singlet excitation energies were calculated at the same level of theory, and the spectra were reproduced as the superposition of functions with heights proportional to calculated intensities and a variance of 11 nm.

## 8.7 Photochemistry Experimental Details

### 8.7.1 Thermal Stability Measurements with CD<sub>3</sub>CN

The *fac*-[Re(NHC)(CO)<sub>3</sub>X] (X = Cl, Br) compound of interest (~5 mg) was dissolved in CD<sub>3</sub>CN (1.5 mL) and an initial <sup>1</sup>H NMR spectrum was acquired. The NMR tube was then wrapped in aluminium foil to be kept in the dark and heated in an oil bath on a Heidolph magnetically stirred hotplate equipped with a temperature probe. Anti-bumping granules were added to the NMR tube and the sample was heated at 355 K for 2 hours after which a second <sup>1</sup>H NMR spectrum was acquired.

### 8.7.2 Thermal Stability Measurements with L<sup>P</sup> Ligands

The *fac*-[Re(NHC)(CO)<sub>3</sub>X] (X = Cl, Br) compound of interest (~5 mg) was dissolved in acetone-d<sub>6</sub> (1.5 mL) and an initial <sup>1</sup>H NMR spectrum was acquired. The organophosphorous ligand (L<sup>P</sup>) of interest (2.5 molar equivalents of triethylphosphite or 10 molar equivalents of triphenylphosphine) was added to the solution and a second <sup>1</sup>H NMR and initial <sup>31</sup>P NMR were acquired. The NMR tube was then completely wrapped in aluminium foil and heated in an oil bath on a Heidolph magnetically stirred hotplate equipped with a temperature probe. The sample was heated to 60 °C and <sup>1</sup>H and <sup>31</sup>P NMR spectra were acquired at set intervals.

### 8.7.3 Photolysis Monitored by Absorption and Emission Spectroscopy

A ~10<sup>-5</sup> M solution of the *fac*-[Re(NHC)(CO)<sub>3</sub>X] (X = Cl, Br) compound of interest was made up in a volumetric flask and immediately covered in aluminium foil to protect it from light. An aliquot of the bulk solution was taken and an initial absorption spectrum was collected on a Perkin-Elmer Lambda 35 UV/Vis spectrometer. The cuvette was then irradiated at λ<sub>ex</sub> = 370 nm on a Hitachi F-7000 spectrofluorimeter with the excitation slit set to 20 nm and emission slit to 5 nm.

A total of 99 consecutive spectra, with no delay between replicates, were run per solution at a speed of 240 nm min<sup>-1</sup> with the detector set to acquire a signal between

200 and 800 nm. Under these experimental conditions the solution was constantly irradiated for a period of approximately 4 hours. The spectra were recorded uncorrected for the detector response. At the end of the 4 hours, the absorption spectrum of the photolysed solution was re-run followed by the absorption spectrum of a fresh aliquot of the bulk solution which had been kept in dark.

#### 8.7.4 Photolysis Monitored by $^1\text{H}$ NMR and Infrared Spectroscopy

The *fac*-[Re(NHC)(CO)<sub>3</sub>X] (X = Cl, Br) compound of interest (~5 mg) was dissolved in CD<sub>3</sub>CN (1.5 mL) and an initial  $^1\text{H}$  NMR spectrum was acquired. The solution was then transferred to a quartz cuvette and was irradiated at  $\lambda_{\text{ex}} = 370$  nm as per the procedure outline in **Section 8.7.3**.

At the end of the 4 hours of photolysis a second  $^1\text{H}$  NMR spectrum was acquired. An IR spectrum was then collected by slow addition of small droplets of the solution onto the diamond stage of the Perkin-Elmer Spectrum 100 FT-IR spectrometer. The solution was allowed to evaporate and the dropping procedure was repeated until the sample was concentrated enough for the carbonyl bands to be visible. The IR spectrum of the photolysed sample was overlaid with the IR spectrum of the same rhenium(I)-NHC tricarbonyl compound in DMSO, as the low solubility of the starting material in acetonitrile produced poor quality spectra.

#### 8.7.5 Lamp Photolysis

Lamp photolysis experiments were carried out using a UVP Blak-Ray B-100AP High Intensity UV lamp with a 100 W bulb at a single wavelength output of 365 nm. The reaction vessel consisted of either a glass NMR tube, containing a degassed deuterated solvent solution of the *fac*-[Re(NHC)(CO)<sub>3</sub>X] (X = Cl, Br) compound of interest, or a glass Schlenk tube containing a degassed and dry solution of the compound maintained under a nitrogen atmosphere. The reaction vessel was clamped 5 cm away from the lamp and was positioned so the middle of the solution was in line with the centre of the lamp as shown in **Figure 8.1**.

Each sample was clamped at the same distance and a mercury thermometer was clamped alongside the reaction vessel to monitor the ambient temperature of the UV lamp. In

each case, degassing was performed by bubbling a gentle stream of gaseous  $N_2$  for a minimum of 5 minutes *via* a Pasteur pipette immersed in the solution of the complex. The experiments were performed in a fume hood protected from external light.

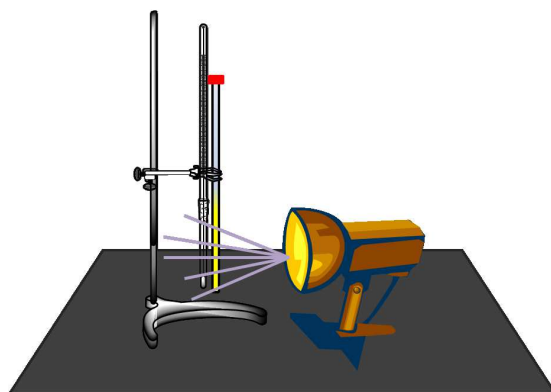


Figure 8.1: Diagram illustrating the experimental set-up for the lamp photolysis experiments.

The method above was used for bulk photolysis and for  $^1H$  NMR monitored photolysis. For  $^1H$  NMR monitored sequences, an initial  $^1H$  NMR spectrum of the freshly dissolved sample in the deuterated solvent was collected. The tube was then clamped as shown in **Figure 8.1** and, after 15 minutes, the lamp was turned off and a second  $^1H$  NMR spectrum was collected. The solution was then re-clamped in front of the lamp and photolysed for a further 15 minutes. This was repeated twice more at 15 minute intervals and then 4 more times with the photolysis time elongated to 30 minutes. In total, the sample was photolysed for 180 minutes and 9  $^1H$  NMR spectra were collected.

### 8.7.6 Photostable Control

To ensure that any spectral changes observed for the *fac*-[Re(NHC)(CO)<sub>3</sub>X] (X = Cl, Br) compounds were predominantly induced by the photochemical process, a known photostable control was analysed. A  $CD_3CN$  solution of *fac*-[Re(phen)(CO)<sub>3</sub>Br] (**114**) was photolysed under the conditions outlined in **Section 8.7.5**.

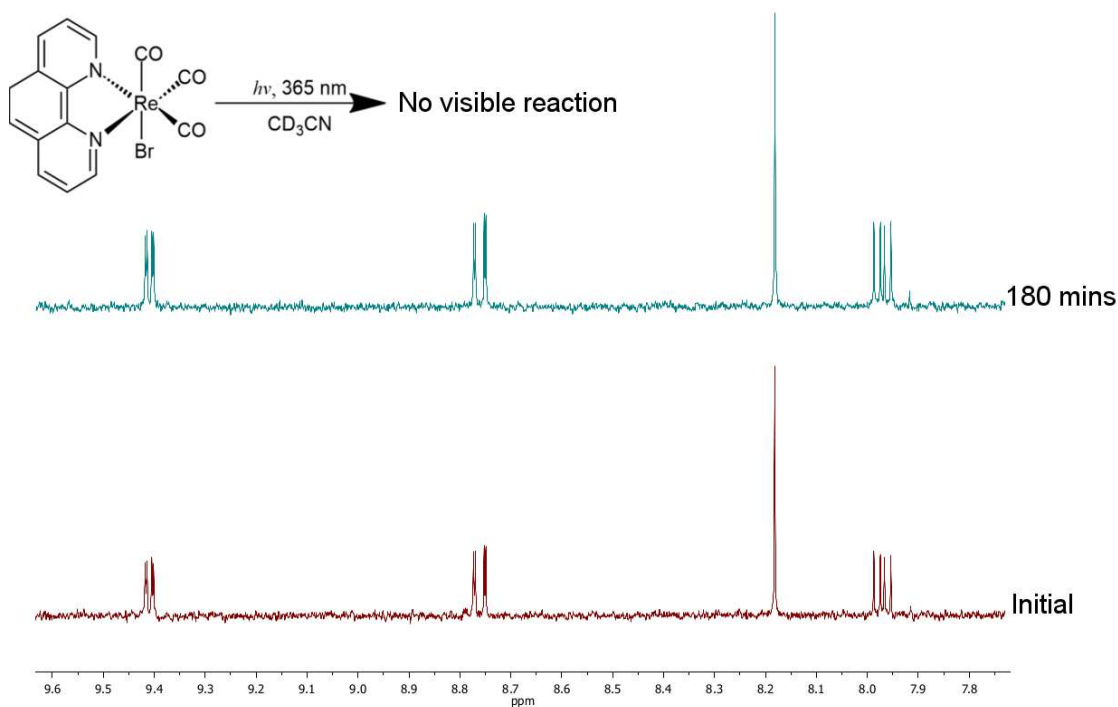


Figure 8.2: <sup>1</sup>H NMR sequence demonstrating the photochemical stability of *fac*-[Re(phen)(CO)<sub>3</sub>Br] (**114**) in CD<sub>3</sub>CN.

As shown in **Figure 8.2**, no spectral changes were observed for *fac*-[Re(phen)(CO)<sub>3</sub>Br] (**114**) which is what was expected at this excitation wavelength ( $\lambda_{ex}$ : 365 nm).<sup>8,88,90</sup>

### 8.7.7 Temperature Controlled Photolysis

Temperature-dependent photolysis studies were performed on an Edinburgh FLSP980-stm spectrometer equipped with a liquid nitrogen cooled Oxford Instrument OptiscanDN cryostat. The acetonitrile solution of the *fac*-[Re(NHC)(CO)<sub>3</sub>X] (X = Cl, Br) compound in question (*ca.* 10<sup>-5</sup> M) was degassed by bubbling nitrogen through the cuvette for 10 minutes. The atmosphere of the cryostat was purged with nitrogen gas to remove any air and moisture for 10 minutes. The cuvette was then placed in the cryostat, the temperature was set and the cuvette allowed to equilibrate for 10 minutes before photolysis. Once the temperature had equilibrated the emission profile of the compound was scanned as per the following parameters;  $\lambda_{ex}$ : 370 nm, sweep window: 450-800 nm, dwell time: 0.2 s, step: 2 nm, excitation slit width: 3 nm and emission slit width: 3 nm, for 25-30 replicates. The scan number *vs.* wavelength *vs.* intensity values were plotted to form a 3D emission map. A fresh sample was used at the beginning of every experiment.

### 8.7.8 Temperature Controlled Excited State Lifetime Measurements

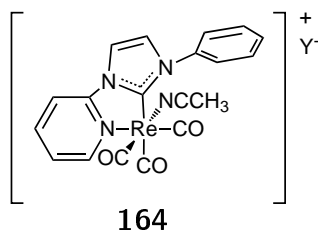
Temperature-dependent excited state lifetime studies were performed on an Edinburgh FLSP980-stm spectrometer equipped with a temperature-controlled cuvette holder, for measurements between 293 and 333 K, or a liquid nitrogen cooled Oxford Instrument OptiscanDN cryostat, for measurements below room temperature. Excited state lifetimes  $\tau$  were determined with the time correlated single photon counting technique (TCSPC) with the same Edinburgh FLSP980 spectrometer using a pulsed picosecond diode laser (EPL 375, fwhm < 800 ps) as the excitation source, with repetition rates between 10 kHz and 1 MHz, and the aforementioned R928P PMT as detector. The goodness of fit was assessed by minimising the reduced  $\chi^2$  function and by visual inspection of the weighted residuals.

The solution of the *fac*-[Re(NHC)(CO)<sub>3</sub>X] (X = Cl, Br) compound in question (*ca.* 10<sup>-5</sup> M in either acetonitrile or dichloromethane) was degassed by bubbling nitrogen through the cuvette for 10 minutes. The atmosphere of the cryostat was purged with nitrogen gas to remove any air and moisture for 10 minutes. The cuvette was then placed in the cryostat, the temperature was set and the cuvette allowed to equilibrate for 10 minutes before photolysis. The observed lifetime values were then used to construct Arrhenius-type plots. Experimental uncertainties are estimated to be  $\pm 8\%$  for lifetime determinations.

## 8.8 Synthesis and Characterisation of Solvates and Photochemical Products

### 8.8.1 Acetonitrile Solvate *fac*-[Re(PyImPh)(CO)<sub>3</sub>(NCCH<sub>3</sub>)]<sup>+</sup>

Silver tetrafluoroborate or silver trifluoromethanesulfonate (1.1 molar equivalents) was weighed out into a light protected vial and added to a suspension of **3Br** or **3Cl** (1 molar equivalent) in acetonitrile (~20 mL). The reaction vessel was protected from light

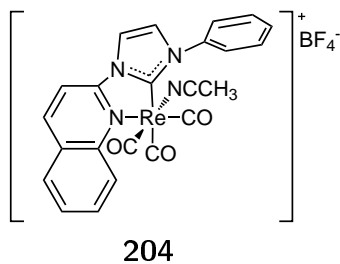


and was heated at reflux for 24 hours under a nitrogen atmosphere. The reaction mixture was allowed to cool to room temperature, filtered through a short plug of celite and washed with additional acetonitrile (10 mL). The solvent was then removed *in vacuo* on a Schlenk line to afford a colourless glassy solid, *fac*-[Re(PyImPh)(CO)<sub>3</sub>(NCCH<sub>3</sub>)]<sup>+</sup> (**164**). The compound was typically redissolved in acetonitrile (or acetonitrile-*d*<sub>3</sub>) and used immediately. The product was not characterised beyond <sup>1</sup>H NMR and IR due to its reactivity. A sample of *fac*-[Re(PyImPh)(CO)<sub>3</sub>(NCCH<sub>3</sub>)]<sup>+</sup> where silver tetrafluoroborate was used was further characterised below.

<sup>1</sup>H NMR (CD<sub>3</sub>CN): δ = 8.85 (1H, d, *J* = 8.0 Hz, pyridyl **H6**), 8.31 (1H, t, *J* = 8.4 Hz, pyridyl **H5**), 8.13 (1H, d, *J* = 2.0 Hz, imidazolyl **CH**), 8.03 (1H, d, *J* = 8.4 Hz, pyridyl **H3**), 7.66-7.59 (6H, m, 1 x imidazolyl **CH**, 5 x phenyl **CH**), 7.52 (1H, t, *J* = 6.6 Hz, pyridyl **H4**), 2.12 (3H, s, NCCH<sub>3</sub>) ppm.

ATR-IR: ν = 3628 (br), 2262 (w), 2116 (w), 2035 (m), 1937 (s), 1862 (s), 1062 (s) and 833 (m) cm<sup>-1</sup>.

### 8.8.2 Acetonitrile Solvate; *fac*-[Re(QuImPh)(CO)<sub>3</sub>(NCCH<sub>3</sub>)]<sup>+</sup> tetrafluoroborate



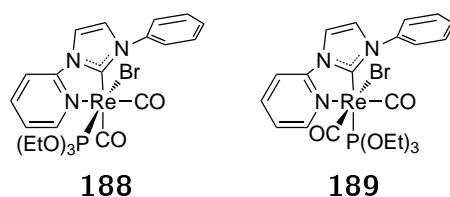
*fac*-[Re(QuImPh)(CO)<sub>3</sub>(NCCH<sub>3</sub>)]<sup>+</sup> (**204**) was synthesised as per the procedure outlined in **Section 8.8.1** with the following amendments; **6Br** was used in place of

**3Cl/3Br** and silver tetrafluoroborate was the silver source used to afford the product as yellow solid. The solvate was dissolved in CD<sub>3</sub>CN and used immediately. The product was not characterised beyond <sup>1</sup>H NMR and IR due to its reactivity.

<sup>1</sup>H NMR (CD<sub>3</sub>CN): δ = 8.86 (1H, d, *J* = 8.8 Hz, quinoyl CH), 8.63 (1H, d, *J* = 9.2 Hz, quinoyl CH), 8.27 (1H, d, *J* = 2.0 Hz, imidazolyl CH), 8.16 (2H, t, *J* = 9.2 Hz, quinoyl CH), 8.08 (2H, t, *J* = 6.8 Hz, quinoyl CH), 7.83 (1H, t, *J* = 7.6 Hz, quinoyl CH), 7.68 (5H, s, phenyl CH), 7.65 (1H, d, *J* = 2.4 Hz, imidazolyl CH), 2.09 (3H, s, NCCH<sub>3</sub>) ppm.

ATR-IR: ν = 3550 (br), 2307 (w), 2282 (w), 2119 (w), 2030 (s), 1916 (s), 1600 (m), 1520 (m), 1433 (m), 1056 (s) and 1020 (s) cm<sup>-1</sup>.

### 8.8.3 *cis,trans*- and *cis,cis*-[Re(CO)<sub>2</sub>(PyImPh)(P(OEt)<sub>3</sub>)Br]



A light yellow solution of **3Br** (4.6 mg, 0.01 mmol) and triethylphosphite (3 μL, 0.03 mmol) in acetone (2 mL) was irradiated with UV light (365 nm) for 3 hr while being vigorously stirred. The resulting dark orange solution was left undisturbed to slowly evaporate and formed a mixture of yellow and orange crystals amidst some yellow amorphous solid. The crystals were separated by hand-picking. The yellow crystals were determined to be the *cis,cis*-[Re(CO)<sub>2</sub>(PyImPh)(P(OEt)<sub>3</sub>)Br] whilst the orange crystals were determined to be the *cis,trans*-[Re(CO)<sub>2</sub>(PyImPh)(P(OEt)<sub>3</sub>)Br]. The IR spectrum indicated evidence of starting material still present.

ATR-IR (from acetone solution): ν = 2016 m (CO), 1927 s (CO), 1905 s (CO), 1860 s (CO), 1838 s (CO) cm<sup>-1</sup>.

In an attempt to isolate a pure product, a light yellow solution of **3Cl** (47.3 mg, 0.08 mmol) and triethylphosphite (36 μL, 0.20 mmol) in acetone (15 mL) was irradiated

with UV light (365 nm) for 5.5 hr while being vigorously stirred. The resulting dark orange solution was concentrated *in vacuo* and separated *via* column chromatography on deactivated alumina. The first four fractions were eluted by gradually increasing the polarity of the eluent, from pure diethyl ether to pure ethyl acetate, and contained several unidentified species. IR data suggested the presence of starting **3Cl** in these fractions. The fifth fraction was eluted with pure acetonitrile and was further purified with a second column, again on deactivated alumina as stationary phase, using ethyl acetate as eluent. The combined fractions were concentrated *in vacuo* to afford a yellow powder (5 mg, 8%).

Elemental Analysis for isolated fraction. Chemical formula based on [Re(CO)<sub>2</sub>(PyImPh)(P(OEt)<sub>3</sub>)Br]. Anal. Calcd: (C<sub>22</sub>H<sub>26</sub>ClN<sub>3</sub>O<sub>5</sub>PRE)4CH<sub>3</sub>CO<sub>2</sub>CH<sub>2</sub>CH<sub>3</sub>: C, 43.04; H, 4.57; N, 5.02. Found: C, 42.83; H, 4.97; N, 5.04.

<sup>1</sup>H NMR (acetone-d<sub>6</sub>): δ = 8.93 (1H, d, *J* = 5.6 Hz, pyridyl **H6**), 8.37 (1H, d, *J* = 2.4 Hz, imidazole **CH**), 8.22-8.17 (1H, dd, *J*<sub>ab</sub> = 8.4 Hz, *J*<sub>ac</sub> = 7.2 Hz, pyridyl **H4**), 8.13-8.11 (1H, m, pyridyl **H3**), 8.10-8.03 (2H, m, phenyl *ortho*-**H**), 7.71 (1H, d, *J* = 2.4 Hz, imidazole **CH**), 7.60-7.44 (4H, m, phenyl *meta*-**H**; phenyl *para*-**H**; pyridyl **H5**) ppm. The NMR spectrum also showed the presence of ethyl acetate in a ratio consistent with the obtained elemental analysis.

<sup>31</sup>P (162 MHz, acetone-d<sub>6</sub>): δ = 123.2 ppm.

A complete <sup>13</sup>C-NMR could not be obtained due to the low concentration of the solution.



# Chapter 9

## Appendix

### 9.1 Selected Bond Lengths and Angles Tables

#### 9.1.1 X-Ray Crystallographic Data for 1Cl

The crystal data for **1Cl** is summarized in **Table A1.1**. Selected coordination geometries are listed in **Table A1.2**. Crystallographic data for the structures were collected at 150(2) K on an Oxford Diffraction Gemini diffractometer fitted with Mo K $\alpha$  radiation. Following analytical absorption corrections and solution by direct methods, the structure was refined against  $F^2$  with full-matrix least-squares using the program SHELXL-97.<sup>112</sup>

The two terminal atoms of the butyl chain are disordered over two sets of sites with occupancies constrained to 0.5 after trial refinement. Anisotropic displacement parameters were employed for the non-hydrogen atoms. All H-atoms were added at calculated positions and refined by use of a riding model with isotropic displacement parameters based on those of the parent atom.

Table A1.1: Crystal data and structure refinement for **1CI**

<b>Empirical formula</b>	$C_{15}H_{15}ClN_3O_3Re$
<b>Formula weight</b>	506.95
<b>Temperature</b>	150(2) K
<b>Wavelength</b>	0.71073 Å
<b>Crystal system</b>	Monoclinic
<b>Space group</b>	$P2_1/c$
<b>Unit cell dimensions</b>	a = 18.0965(4) Å b = 10.2473(2) Å c = 9.2381(2) Å $\beta = 90.810(2)^\circ$
<b>Volume</b>	1712.94(6) Å <sup>3</sup>
<b>Z</b>	4
<b>Density (calculated)</b>	1.966 Mg/m <sup>3</sup>
<b>Absorption coefficient</b>	7.266 mm <sup>-1</sup>
<b>Crystal size</b>	0.26 x 0.17 x 0.05 mm <sup>3</sup>
<b><math>\theta</math> range for data collection</b>	3.71 to 38.00°
<b>Index ranges</b>	-30 ≤ h ≤ 31, -17 ≤ k ≤ 17, -16 ≤ l ≤ 16
<b>Reflections collected</b>	66202
<b>Independent reflections</b>	9297 [R(int) = 0.0471]
<b>Completeness to <math>\theta = 38.00^\circ</math></b>	99.9 %
<b>Absorption correction</b>	Analytical
<b>Max. and min. transmission</b>	0.704 and 0.362
<b>Refinement method</b>	Full-matrix least-squares on $F^2$
<b>Data / restraints / parameters</b>	9297 / 24 / 228
<b>Goodness-of-fit on <math>F^2</math></b>	1.092
<b>Final R indices [<math>I &gt; 2\sigma(I)</math>]</b>	R1 = 0.0309, wR2 = 0.0569
<b>R indices (all data)</b>	R1 = 0.0453, wR2 = 0.0603
<b>Largest diff. peak and hole</b>	2.619 and -1.293 e.Å <sup>-3</sup>

Table A1.2: Selected bond lengths (Å) and angles (°) for **1Cl**

Bond Lengths (Å)		Bond Angles (°)	
Re(1)-C(20)	1.910(3)	C(20)-Re(1)-C(30)	89.33(12)
Re(1)-C(30)	1.913(3)	C(20)-Re(1)-C(10)	88.40(11)
Re(1)-C(10)	1.957(2)	C(30)-Re(1)-C(10)	91.34(10)
Re(1)-C(12)	2.133(2)	C(20)-Re(1)-C(12)	98.71(9)
Re(1)-N(21)	2.2083(19)	C(30)-Re(1)-C(12)	91.51(9)
Re(1)-Cl(1)	2.5080(6)	C(10)-Re(1)-C(12)	172.36(10)
		C(20)-Re(1)-N(21)	172.61(9)
		C(30)-Re(1)-N(21)	93.51(10)
		C(10)-Re(1)-N(21)	98.34(9)
		C(12)-Re(1)-N(21)	74.41(7)
		C(20)-Re(1)-Cl(1)	94.55(8)
		C(30)-Re(1)-Cl(1)	176.02(9)
		C(10)-Re(1)-Cl(1)	87.85(8)
		C(12)-Re(1)-Cl(1)	88.82(6)
		N(21)-Re(1)-Cl(1)	82.75(5)

### 9.1.2 X-Ray Crystallographic Data for **2Cl**

The crystal data for **2Cl** is summarized in **Table A1.3**. Selected coordination geometries are listed in **Table A1.4**. Diffraction data were collected at 100(2) K on an Oxford Diffraction Xcalibur diffractometer fitted with Mo K $\alpha$  radiation. Following analytical absorption corrections and solution by direct methods, the structure was refined against  $F^2$  with full-matrix least-squares using the program SHELXL-97.<sup>112</sup>

The Cl atom is positionally disordered with the carbonyl group in the trans position with site occupancies refined to 0.689(9) and its complement. The geometries of the disordered carbonyl groups were restrained to ideal values. All non-hydrogen atoms were refined with anisotropic displacement parameters. All hydrogen atoms were added at calculated positions and refined by use of a riding model with isotropic displacement parameters based on those of the parent atoms.

Table A1.3: Crystal data and structure refinement for **2Cl**

<b>Empirical formula</b>	$C_{20}H_{17}ClN_3O_3Re$
<b>Formula weight</b>	569.02
<b>Temperature</b>	100(2) K
<b>Wavelength</b>	0.71073 Å
<b>Crystal system</b>	Monoclinic
<b>Space group</b>	$P2_1/n$
<b>Unit cell dimensions</b>	a = 8.1644(7) Å b = 17.6255(17) Å c = 13.6343(15) Å $\beta = 97.645(9)^\circ$
<b>Volume</b>	1944.6(3) Å <sup>3</sup>
<b>Z</b>	4
<b>Density (calculated)</b>	1.944 Mg/m <sup>3</sup>
<b>Absorption coefficient</b>	6.413 mm <sup>-1</sup>
<b>F(000)</b>	1096
<b>Crystal size</b>	0.12 x 0.08 x 0.07 mm <sup>3</sup>
<b><math>\theta</math> range for data collection</b>	2.76 to 31.96°
<b>Index ranges</b>	-11 ≤ h ≤ 11, -25 ≤ k ≤ 25, -19 ≤ l ≤ 19
<b>Reflections collected</b>	21725
<b>Independent reflections</b>	6310 [R(int) = 0.0690]
<b>Completeness to <math>\theta = 30.00^\circ</math></b>	99.9 %
<b>Absorption correction</b>	Analytical
<b>Max. and min. transmission</b>	0.694 and 0.604
<b>Refinement method</b>	Full-matrix least-squares on $F^2$
<b>Data / restraints / parameters</b>	6310 / 18 / 272
<b>Goodness-of-fit on <math>F^2</math></b>	1.147
<b>Final R indices [I &gt; 2σ(I)]</b>	R1 = 0.0565, wR2 = 0.0786
<b>R indices (all data)</b>	R1 = 0.0813, wR2 = 0.0849
<b>Largest diff. peak and hole</b>	1.733 and -1.723 e.Å <sup>-3</sup>

Table A1.4: Selected bond lengths (Å) and angles (°) for **2Cl**

Bond Lengths (Å)		Bond Angles (°)	
Re(1)-C(2)	1.917(6)	C(2)-Re(1)-C(1)	91.1(2)
Re(1)-C(1)	1.942(5)	C(2)-Re(1)-C(3)	88.7(6)
Re(1)-C(3)	1.953(9)	C(1)-Re(1)-C(3)	89.3(7)
Re(1)-C(4)	2.08(4)	C(2)-Re(1)-C(4)	90.7(13)
Re(1)-C(12)	2.123(5)	C(1)-Re(1)-C(4)	89.4(13)
Re(1)-N(21)	2.199(4)	C(2)-Re(1)-C(12)	99.1(2)
Re(1)-Cl(3)	2.321(6)	C(1)-Re(1)-C(12)	169.9(2)
Re(1)-Cl(4)	2.434(3)	C(3)-Re(1)-C(12)	90.4(6)
		C(4)-Re(1)-C(12)	91.0(12)
		C(2)-Re(1)-N(21)	173.65(19)
		C(1)-Re(1)-N(21)	95.21(19)
		C(3)-Re(1)-N(21)	92.4(6)
		C(4)-Re(1)-N(21)	88.4(12)
		C(12)-Re(1)-N(21)	74.67(17)
		C(2)-Re(1)-Cl(3)	94.1(3)
		C(1)-Re(1)-Cl(3)	88.4(3)
		C(4)-Re(1)-Cl(3)	174.8(13)
		C(12)-Re(1)-Cl(3)	90.3(3)
		N(21)-Re(1)-Cl(3)	87.1(2)
		C(2)-Re(1)-Cl(4)	93.66(18)

### 9.1.3 X-Ray Crystallographic Data for **2Br**

The crystal data for **2Br** is summarized in **Table A1.5**. Selected coordination geometries are listed in **Table A1.6**. Diffraction data were collected at 100(2) K on an Oxford Diffraction Gemini diffractometer fitted with Mo K $\alpha$  radiation. Following analytical absorption corrections and solution by direct methods, the structure was refined against  $F^2$  with full-matrix least-squares using the program SHELXL-97.<sup>112</sup>

The Br atom in **2Br** is positionally disordered with the carbonyl group in the trans position with site occupancies refined to 0.595(2) and its complement. The geometries of the disordered carbonyl groups were restrained to ideal values. All non-hydrogen atoms were refined with anisotropic displacement parameters. All hydrogen atoms were added at calculated positions and refined by use of a riding model with isotropic displacement parameters based on those of the parent atoms.

Table A1.5: Crystal data and structure refinement for **2Br**

<b>Empirical formula</b>	C <sub>20</sub> H <sub>17</sub> BrN <sub>3</sub> O <sub>3</sub> Re
<b>Formula weight</b>	613.48
<b>Temperature</b>	100(2) K
<b>Wavelength</b>	0.71073 Å
<b>Crystal system</b>	Monoclinic
<b>Space group</b>	<i>P</i> 2 <sub>1</sub> / <i>n</i>
<b>Unit cell dimensions</b>	a = 8.2661(2) Å b = 17.5306(3) Å c = 13.6552(4) Å β = 97.690(2)°
<b>Volume</b>	1960.97(8) Å <sup>3</sup>
<b>Z</b>	4
<b>Density (calculated)</b>	2.078 Mg/m <sup>3</sup>
<b>Absorption coefficient</b>	8.261 mm <sup>-1</sup>
<b>F(000)</b>	1168
<b>Crystal size</b>	0.29 x 0.21 x 0.15 mm <sup>3</sup>
<b>θ range for data collection</b>	3.59 to 36.42°
<b>Index ranges</b>	-13 ≤ h ≤ 13, -28 ≤ k ≤ 29, -22 ≤ l ≤ 22
<b>Reflections collected</b>	48086
<b>Independent reflections</b>	9217 [R(int) = 0.0405]
<b>Completeness to θ = 35.50°</b>	99.6 %
<b>Absorption correction</b>	Analytical
<b>Max. and min. transmission</b>	0.341 and 0.166
<b>Refinement method</b>	Full-matrix least-squares on <i>F</i> <sup>2</sup>
<b>Data / restraints / parameters</b>	9217 / 6 / 272
<b>Goodness-of-fit on <i>F</i><sup>2</sup></b>	1.129
<b>Final R indices [I &gt; 2σ(I)]</b>	R1 = 0.0484, wR2 = 0.0764
<b>R indices (all data)</b>	R1 = 0.0761, wR2 = 0.0807
<b>Largest diff. peak and hole</b>	3.912 and -6.113 e.Å <sup>-3</sup>

Table A1.6: Selected bond lengths (Å) and angles (°) for **2Br**

Bond Lengths (Å)		Bond Angles (°)	
Re(1)-C(2)	1.921(4)	C(2)-Re(1)-C(1)	91.27(17)
Re(1)-C(1)	1.952(4)	C(2)-Re(1)-C(3)	88.7(4)
Re(1)-C(3)	2.002(8)	C(1)-Re(1)-C(3)	90.4(3)
Re(1)-C(4)	2.113(15)	C(2)-Re(1)-C(4)	88.2(4)
Re(1)-C(12)	2.125(4)	C(1)-Re(1)-C(4)	89.0(4)
Re(1)-N(21)	2.197(3)	C(3)-Re(1)-C(4)	176.8(5)
Re(1)-Br(3)	2.4097(13)	C(2)-Re(1)-C(12)	99.08(15)
Re(1)-Br(4)	2.5102(9)	C(1)-Re(1)-C(12)	169.65(15)
		C(3)-Re(1)-C(12)	89.7(3)
		C(4)-Re(1)-C(12)	91.4(4)
		C(2)-Re(1)-N(21)	173.54(15)
		C(1)-Re(1)-N(21)	95.05(15)
		C(3)-Re(1)-N(21)	92.6(3)
		C(4)-Re(1)-N(21)	90.6(4)
		C(12)-Re(1)-N(21)	74.60(13)
		C(2)-Re(1)-Br(3)	94.01(15)
		C(1)-Re(1)-Br(3)	88.59(14)
		C(4)-Re(1)-Br(3)	176.8(4)
		C(12)-Re(1)-Br(3)	90.52(11)
		N(21)-Re(1)-Br(3)	87.46(10)
		C(2)-Re(1)-Br(4)	93.27(15)
		C(1)-Re(1)-Br(4)	88.61(14)
		C(12)-Re(1)-Br(4)	90.94(10)
		N(21)-Re(1)-Br(4)	85.60(10)

### 9.1.4 X-Ray Crystallographic Data for **3Cl**

The crystal data for **3Cl** is summarized in **Table A1.7**. Selected coordination geometries are listed in **Table A1.8**. Crystallographic data for the structures were collected at 100(2) K on an Oxford Diffraction Gemini diffractometer fitted with Mo K $\alpha$  radiation. Following analytical absorption corrections and solution by direct methods, the structure was refined against  $F^2$  with full-matrix least-squares using the program SHELXL-97.<sup>112</sup>

Anisotropic displacement parameters were employed for the non-hydrogen atoms. All H-atoms were added at calculated positions and refined by use of a riding model with isotropic displacement parameters based on those of the parent atom.

Table A1.7: Crystal data and structure refinement for **3CI**

<b>Empirical formula</b>	$C_{17}H_{11}ClN_3O_3Re$
<b>Formula weight</b>	526.94
<b>Temperature</b>	100(2) K
<b>Wavelength</b>	0.71073 Å
<b>Crystal system</b>	Monoclinic
<b>Space group</b>	$P2_1/n$
<b>Unit cell dimensions</b>	a = 11.55800(10) Å b = 8.39400(10) Å c = 16.9605(2) Å $\beta = 96.2870(10)^\circ$
<b>Volume</b>	1635.57(3) Å <sup>3</sup>
<b>Z</b>	4
<b>Density (calculated)</b>	2.140 Mg/m <sup>3</sup>
<b>Absorption coefficient</b>	7.615 mm <sup>-1</sup>
<b>F(000)</b>	1000
<b>Crystal size</b>	0.46 x 0.15 x 0.056 mm <sup>3</sup>
<b><math>\theta</math> range for data collection</b>	3.86 to 45.71°
<b>Index ranges</b>	-23 ≤ h ≤ 23, -16 ≤ k ≤ 16, -34 ≤ l ≤ 34
<b>Reflections collected</b>	96088
<b>Independent reflections</b>	13943 [R(int) = 0.0389]
<b>Completeness to <math>\theta = 45.71^\circ</math></b>	99.7 %
<b>Absorption correction</b>	Analytical
<b>Max.min. transmission</b>	0.656/0.128
<b>Refinement method</b>	Full-matrix least-squares on $F^2$
<b>Data / restraints / parameters</b>	13943 / 0 / 226
<b>Goodness-of-fit on <math>F^2</math></b>	0.883
<b>Final R indices [I &gt; 2σ(I)]</b>	R1 = 0.0174, wR2 = 0.0321
<b>R indices (all data)</b>	R1 = 0.0285, wR2 = 0.0329
<b>Largest diff. peak and hole</b>	1.657 and -0.834 e.Å <sup>-3</sup>

Table A1.8: Selected bond lengths (Å) and angles (°) for **3Cl**

Bond Lengths (Å)		Bond Angles (°)	
Re(1)-C(3)	1.9123(10)	C(3)-Re(1)-C(2)	88.78(5)
Re(1)-C(2)	1.9169(11)	C(3)-Re(1)-C(1)	91.37(4)
Re(1)-C(1)	1.9552(11)	C(2)-Re(1)-C(1)	87.66(4)
Re(1)-C(12)	2.1488(10)	C(3)-Re(1)-C(12)	95.71(4)
Re(1)-N(21)	2.2117(8)	C(2)-Re(1)-C(12)	99.91(4)
Re(1)-Cl(4)	2.4956(2)	C(1)-Re(1)-C(12)	169.71(4)
		C(3)-Re(1)-N(21)	93.78(4)
		C(2)-Re(1)-N(21)	173.94(4)
		C(1)-Re(1)-N(21)	97.76(4)
		C(12)-Re(1)-N(21)	74.38(3)
		C(3)-Re(1)-Cl(4)	178.13(3)
		C(2)-Re(1)-Cl(4)	92.98(3)
		C(1)-Re(1)-Cl(4)	88.06(3)
		C(12)-Re(1)-Cl(4)	84.62(3)
		N(21)-Re(1)-Cl(4)	84.53(2)

### 9.1.5 X-Ray Crystallographic Data for **3Br**

The crystal data for **3Br** is summarized in **Table A1.9**. Selected coordination geometries are given in **Table A1.10**. Crystallographic data for the structures were collected at 100(2) K on an Oxford Diffraction Xcalibur diffractometer fitted with Mo K $\alpha$  radiation. Following analytical absorption corrections and solution by direct methods, the structure was refined against  $F^2$  with full-matrix least-squares using the program SHELXL-97.<sup>112</sup>

Anisotropic displacement parameters were employed for the non-hydrogen atoms. All H-atoms were added at calculated positions and refined by use of a riding model with isotropic displacement parameters based on those of the parent atom.

Table A1.9: Crystal data and structure refinement for **3Br**

<b>Empirical formula</b>	C <sub>17</sub> H <sub>11</sub> BrN <sub>3</sub> O <sub>3</sub> Re
<b>Formula weight</b>	571.40
<b>Temperature</b>	100(2) K
<b>Wavelength</b>	0.71073 Å
<b>Crystal system</b>	Monoclinic
<b>Space group</b>	<i>P</i> 2 <sub>1</sub> / <i>n</i>
<b>Unit cell dimensions</b>	a = 11.7834(3) Å b = 8.4832(3) Å c = 17.0208(6) Å β = 96.719(3)°
<b>Volume</b>	1689.73(9) Å <sup>3</sup>
<b>Z</b>	4
<b>Density (calculated)</b>	2.246 Mg/m <sup>3</sup>
<b>Absorption coefficient</b>	9.578 mm <sup>-1</sup>
<b>Crystal size</b>	0.19 x 0.08 x 0.02 mm <sup>3</sup>
<b>θ range for data collection</b>	2.97 to 32.00°
<b>Index ranges</b>	-16 ≤ h ≤ 17, -12 ≤ k ≤ 12, -24 ≤ l ≤ 25
<b>Reflections collected</b>	26852
<b>Independent reflections</b>	5877 [R(int) = 0.0619]
<b>Completeness to θ = 32.00°</b>	99.9 %
<b>Absorption correction</b>	Analytical
<b>Max. and min. transmission</b>	0.813 and 0.268
<b>Refinement method</b>	Full-matrix least-squares on <i>F</i> <sup>2</sup>
<b>Data / restraints / parameters</b>	5877 / 0 / 226
<b>Goodness-of-fit on <i>F</i><sup>2</sup></b>	1.046
<b>Final R indices [I &gt; 2σ(I)]</b>	R1 = 0.0323, wR2 = 0.0591
<b>R indices (all data)</b>	R1 = 0.0409, wR2 = 0.0617
<b>Largest diff. peak and hole</b>	2.138 and -1.513 e.Å <sup>-3</sup>

Table A1.10: Selected bond lengths (Å) and angles (°) for **3Br**

Bond Lengths (Å)		Bond Angles (°)	
Re(1)-C(3)	1.917(4)	C(3)-Re(1)-C(2)	89.42(15)
Re(1)-C(2)	1.923(4)	C(3)-Re(1)-C(1)	92.06(14)
Re(1)-C(1)	1.957(3)	C(2)-Re(1)-C(1)	87.94(14)
Re(1)-C(12)	2.145(3)	C(3)-Re(1)-C(12)	96.25(13)
Re(1)-N(21)	2.210(3)	C(2)-Re(1)-C(12)	100.14(13)
Re(1)-Br(4)	2.6255(4)	C(1)-Re(1)-C(12)	168.43(14)
		C(3)-Re(1)-N(21)	93.24(13)
		C(2)-Re(1)-N(21)	174.42(12)
		C(1)-Re(1)-N(21)	96.86(12)
		C(12)-Re(1)-N(21)	74.70(12)
		C(3)-Re(1)-Br(4)	177.81(11)
		C(2)-Re(1)-Br(4)	92.66(11)
		C(1)-Re(1)-Br(4)	87.32(10)
		C(12)-Re(1)-Br(4)	84.07(9)
		N(21)-Re(1)-Br(4)	84.75(7)

### 9.1.6 X-Ray Crystallographic Data for **5Cl**

The crystal data for **5Cl** is summarized in **Table A1.11**. Selected coordination geometries are given in **Table A1.12**. Crystallographic data for the structures were collected at 100(2) K on an Oxford Diffraction Xcalibur diffractometer fitted with Mo K $\alpha$  radiation. Following analytical absorption corrections and solution by direct methods, the structure was refined against  $F^2$  with full-matrix least-squares using the program SHELXL-97.<sup>112</sup>

All hydrogen atoms were added at calculated positions and refined by use of a riding model with isotropic displacement parameters based on those of the parent atom.

Table A1.11: Crystal data and structure refinement for **5Cl**

<b>Empirical formula</b>	$C_{18}H_{13}ClN_5O_3Re$
<b>Formula weight</b>	568.98
<b>Temperature</b>	100(2) K
<b>Wavelength</b>	0.71073 Å
<b>Crystal system</b>	Triclinic
<b>Space group</b>	
<b>Unit cell dimensions</b>	a = 6.6905(4) Å b = 10.8368(7) Å c = 13.3444(11) Å $\alpha = 101.192(6)^\circ$ $\beta = 90.789(6)^\circ$ $\gamma = 98.036(5)^\circ$
<b>Volume</b>	938.96(11) Å <sup>3</sup>
<b>Z</b>	2
<b>Density (calculated)</b>	2.012 Mg/m <sup>3</sup>
$\mu$	6.643 mm <sup>-1</sup>
<b>Crystal size</b>	0.13 x 0.10 x 0.07 mm <sup>3</sup>
<b><math>\theta</math> range for data collection</b>	3.08 to 27.50°
<b>Index ranges</b>	-8 ≤ h ≤ 8, -14 ≤ k ≤ 13, -17 ≤ l ≤ 17
<b>Reflections collected</b>	10669
<b>Independent reflections</b>	4308 [R(int) = 0.0539]
<b>Completeness to <math>\theta = 27.50^\circ</math></b>	99.9 %
<b>Absorption correction</b>	Analytical
<b>Max. and min. transmission</b>	0.664 and 0.517
<b>Refinement method</b>	Full-matrix least-squares on $F^2$
<b>Data / restraints / parameters</b>	4308 / 0 / 255
<b>Goodness-of-fit on <math>F^2</math></b>	1.119
<b>Final R indices [I &gt; 2σ(I)]</b>	R1 = 0.0661, wR2 = 0.1575
<b>R indices (all data)</b>	R1 = 0.0734, wR2 = 0.1614
<b>Largest diff. peak and hole</b>	10.633 and -1.768 e.Å <sup>-3</sup>

Table A1.12: Selected bond lengths (Å) and angles (°) for **5Cl**

Bond Lengths (Å)		Bond Angles (°)	
Re(1)-C(201)	1.907(10)	C(201)-Re(1)-C(101)	88.7(4)
Re(1)-C(101)	1.946(10)	C(201)-Re(1)-C(301)	87.5(4)
Re(1)-C(301)	1.969(14)	C(101)-Re(1)-C(301)	89.7(5)
Re(1)-C(2)	2.136(9)	C(201)-Re(1)-C(2)	98.8(4)
Re(1)-N(21)	2.211(8)	C(101)-Re(1)-C(2)	172.4(4)
Re(1)-Cl(1)	2.494(3)	C(301)-Re(1)-C(2)	90.8(4)
		C(201)-Re(1)-N(21)	172.3(4)
		C(101)-Re(1)-N(21)	98.9(4)
		C(301)-Re(1)-N(21)	91.7(4)
		C(2)-Re(1)-N(21)	73.5(3)
		C(201)-Re(1)-Cl(1)	95.4(3)
		C(101)-Re(1)-Cl(1)	92.2(4)
		C(301)-Re(1)-Cl(1)	176.6(3)
		C(2)-Re(1)-Cl(1)	86.9(3)
		N(21)-Re(1)-Cl(1)	85.2(2)

### 9.1.7 X-Ray Crystallographic Data for **5Br**

The crystal data for **5Br** is summarized in **Table A1.13**. Selected coordination geometries are given in **Table A1.14**. Crystallographic data for the structures were collected at 100(2) K on an Oxford Diffraction Xcalibur diffractometer fitted with Mo K $\alpha$  radiation. Following analytical absorption corrections and solution by direct methods, the structure was refined against  $F^2$  with full-matrix least-squares using the program SHELXL-97.<sup>112</sup>

The data could support anisotropic refinement of the Re and Br atoms only. All hydrogen atoms were added at calculated positions and refined by use of a riding model with isotropic displacement parameters based on those of the parent atom.

Table A1.13: Crystal data and structure refinement for **5Br**

<b>Empirical formula</b>	$C_{16}H_{10}BrN_4O_3Re$
<b>Formula weight</b>	572.39
<b>Temperature</b>	100(2) K
<b>Wavelength</b>	0.71073 Å
<b>Crystal system</b>	Triclinic
<b>Space group</b>	
<b>Unit cell dimensions</b>	$a = 6.7096(14)$ Å $b = 10.825(2)$ Å $c = 12.490(3)$ Å $\alpha = 68.04(2)^\circ$ $\beta = 88.674(19)^\circ$ $\gamma = 81.954(16)^\circ$
<b>Volume</b>	$832.6(3)$ Å <sup>3</sup>
<b>Z</b>	2
<b>Density (calculated)</b>	2.283 Mg/m <sup>3</sup>
$\mu$	9.721 mm <sup>-1</sup>
<b>Crystal size</b>	0.35 x 0.14 x 0.03 mm <sup>3</sup>
<b><math>\theta</math> range for data collection</b>	3.07 to 26.50°
<b>Index ranges</b>	$-8 \leq h \leq 7, -13 \leq k \leq 13, -14 \leq l \leq 15$
<b>Reflections collected</b>	5860
<b>Independent reflections</b>	3444 [R(int) = 0.1222]
<b>Completeness to <math>\theta = 26.50^\circ</math></b>	99.4 %
<b>Absorption correction</b>	Analytical
<b>Max. and min. transmission</b>	0.753 and 0.239
<b>Refinement method</b>	Full-matrix least-squares on $F^2$
<b>Data / restraints / parameters</b>	3444 / 1 / 111
<b>Goodness-of-fit on <math>F^2</math></b>	1.091
<b>Final R indices [I &gt; 2<math>\sigma</math>(I)]</b>	$R1 = 0.1267, wR2 = 0.2083$
<b>R indices (all data)</b>	$R1 = 0.1956, wR2 = 0.2411$
<b>Largest diff. peak and hole</b>	4.951 and -2.888 e.Å <sup>-3</sup>

Table A1.14: Selected bond lengths (Å) and angles (°) for **5Br**

Bond Lengths (Å)		Bond Angles (°)	
Re(1)-C(2)	1.77(3)	C(2)-Re(1)-C(1)	88.8(12)
Re(1)-C(1)	1.92(2)	C(2)-Re(1)-C(3)	87.6(12)
Re(1)-C(3)	1.99(3)	C(1)-Re(1)-C(3)	91.6(10)
Re(1)-C(12)	2.19(2)	C(2)-Re(1)-C(12)	100.9(12)
Re(1)-N(21)	2.20(2)	C(1)-Re(1)-C(12)	170.1(11)
Re(1)-Br(1)	2.621(3)	C(3)-Re(1)-C(12)	87.2(9)
		C(2)-Re(1)-N(21)	176.7(11)
		C(1)-Re(1)-N(21)	94.5(9)
		C(3)-Re(1)-N(21)	92.7(9)
		C(12)-Re(1)-N(21)	75.8(8)
		C(2)-Re(1)-Br(1)	95.8(10)
		C(1)-Re(1)-Br(1)	92.4(8)
		C(3)-Re(1)-Br(1)	174.8(6)
		C(12)-Re(1)-Br(1)	88.3(7)
		N(21)-Re(1)-Br(1)	83.7(5)

### 9.1.8 X-Ray Crystallographic Data for **6Cl**

The crystal data for **6Cl** is summarized in **Table A1.15**. Selected coordination geometries are given in **Table A1.16**. Crystallographic data for the structures were collected at 100(2) K on an Oxford Diffraction Xcalibur diffractometer fitted with Mo K $\alpha$  radiation. Following analytical absorption corrections and solution by direct methods, the structure was refined against  $F^2$  with full-matrix least-squares using the program SHELXL-97.<sup>112</sup>

The phenyl ring was modelled as being disordered over two sets of sites with occupancies refined to 0.688(13) and its complement. Geometries and displacement parameters of the minor component were restrained to reasonable values. Anisotropic displacement parameters were employed for the non-hydrogen atoms. All hydrogen atoms were added at calculated positions and refined by use of a riding model with isotropic displacement parameters based on those of the parent atom.

Table A1.15: Crystal data and structure refinement for **6Cl**

<b>Empirical formula</b>	$C_{21}H_{13}ClN_3O_3Re$
<b>Formula weight</b>	576.99
<b>Temperature</b>	100(2) K
<b>Wavelength</b>	0.71073 Å
<b>Crystal system</b>	Monoclinic
<b>Space group</b>	$C_2/c$
<b>Unit cell dimensions</b>	a = 10.6269(3) Å b = 11.7796(3) Å c = 30.7456(5) Å $\beta = 90.507(2)^\circ$
<b>Volume</b>	3848.60(16) Å <sup>3</sup>
<b>Z</b>	8
<b>Density (calculated)</b>	1.992 Mg/m <sup>3</sup>
$\mu$	6.482 mm <sup>-1</sup>
<b>Crystal size</b>	0.15 x 0.12 x 0.08 mm <sup>3</sup>
<b><math>\theta</math> range for data collection</b>	2.89 to 31.45°
<b>Index ranges</b>	-15 ≤ h ≤ 15, -16 ≤ k ≤ 16, -44 ≤ l ≤ 44
<b>Reflections collected</b>	25394
<b>Independent reflections</b>	6146 [R(int) = 0.0479]
<b>Completeness to <math>\theta = 31.00^\circ</math></b>	99.1 %
<b>Absorption correction</b>	Analytical
<b>Max. and min. transmission</b>	0.723 and 0.496
<b>Refinement method</b>	Full-matrix least-squares on $F^2$
<b>Data / restraints / parameters</b>	6146 / 78 / 311
<b>Goodness-of-fit on <math>F^2</math></b>	1.129
<b>Final R indices [<math>I &gt; 2\sigma(I)</math>]</b>	R1 = 0.0415, wR2 = 0.0694
<b>R indices (all data)</b>	R1 = 0.0522, wR2 = 0.0725
<b>Largest diff. peak and hole</b>	1.643 and -0.794 e.Å <sup>-3</sup>

Table A1.16: Selected bond lengths (Å) and angles (°) for **6Cl**

Bond Lengths (Å)		Bond Angles (°)	
Re(1)-C(201)	1.908(4)	C(201)-Re(1)-C(101)	85.75(18)
Re(1)-C(101)	1.949(5)	C(201)-Re(1)-C(301)	91.65(19)
Re(1)-C(301)	1.977(6)	C(101)-Re(1)-C(301)	88.6(2)
Re(1)-C(2)	2.119(4)	C(201)-Re(1)-C(2)	95.88(17)
Re(1)-N(21)	2.277(3)	C(101)-Re(1)-C(2)	177.60(18)
Re(1)-Cl(1)	2.4799(13)	C(301)-Re(1)-C(2)	89.60(19)
		C(201)-Re(1)-N(21)	168.61(17)
		C(101)-Re(1)-N(21)	104.68(15)
		C(301)-Re(1)-N(21)	93.14(16)
		C(2)-Re(1)-N(21)	73.84(14)
		C(201)-Re(1)-Cl(1)	92.14(16)
		C(101)-Re(1)-Cl(1)	93.60(14)
		C(301)-Re(1)-Cl(1)	175.74(13)
		C(2)-Re(1)-Cl(1)	88.09(13)
		N(21)-Re(1)-Cl(1)	82.78(10)

### 9.1.9 X-Ray Crystallographic Data for **6Br**

The crystal data for **6Br** is summarized in **Table A1.17**. Selected coordination geometries are given in **Table A1.18**. Crystallographic data for the structures were collected at 100(2) K on an Oxford Diffraction Xcalibur diffractometer fitted with Mo K $\alpha$  radiation. Following analytical absorption corrections and solution by direct methods, the structure was refined against  $F^2$  with full-matrix least-squares using the program SHELXL-97.<sup>112</sup>

The phenyl ring was modelled as being disordered over two sets of sites with occupancies refined to 0.639(9) and its complement. Geometries of the minor component were restrained to ideal values. Anisotropic displacement parameters were employed for the non-hydrogen atoms. All hydrogen atoms were added at calculated positions and refined by use of a riding model with isotropic displacement parameters based on those of the parent atom.

Table A1.17: Crystal data and structure refinement for **6Br**

<b>Empirical formula</b>	$C_{21}H_{13}BrN_3O_3Re$
<b>Formula weight</b>	621.45
<b>Temperature</b>	100(2) K
<b>Wavelength</b>	0.71073 Å
<b>Crystal system</b>	Monoclinic
<b>Space group</b>	$C_2/c$
<b>Unit cell dimensions</b>	a = 10.6245(2) Å b = 11.8726(2) Å c = 30.9574(4) Å $\beta = 90.701(2)^\circ$
<b>Volume</b>	3904.69(11) Å <sup>3</sup>
<b>Z</b>	8
<b>Density (calculated)</b>	2.114 Mg/m <sup>3</sup>
$\mu$	8.299 mm <sup>-1</sup>
<b>Crystal size</b>	0.30 x 0.25 x 0.06 mm <sup>3</sup>
<b><math>\theta</math> range for data collection</b>	2.88 to 35.00°
<b>Index ranges</b>	-17 ≤ h ≤ 17, -19 ≤ k ≤ 19, -49 ≤ l ≤ 49
<b>Reflections collected</b>	56772
<b>Independent reflections</b>	8586 [R(int) = 0.0546]
<b>Completeness to <math>\theta = 35.00^\circ</math></b>	99.9 %
<b>Absorption correction</b>	Analytical
<b>Max. and min. transmission</b>	0.653 and 0.169
<b>Refinement method</b>	Full-matrix least-squares on $F^2$
<b>Data / restraints / parameters</b>	8586 / 90 / 317
<b>Goodness-of-fit on <math>F^2</math></b>	1.087
<b>Final R indices [<math>I &gt; 2\sigma(I)</math>]</b>	R1 = 0.0375, wR2 = 0.0850
<b>R indices (all data)</b>	R1 = 0.0453, wR2 = 0.0884
<b>Largest diff. peak and hole</b>	2.478 and -1.996 e.Å <sup>-3</sup>

Table A1.18: Selected bond lengths (Å) and angles (°) for **6Br**

Bond Lengths (Å)		Bond Angles (°)	
Re(1)-C(201)	1.913(4)	C(201)-Re(1)-C(101)	85.28(15)
Re(1)-C(101)	1.955(4)	C(201)-Re(1)-C(301)	92.03(18)
Re(1)-C(301)	2.058(5)	C(101)-Re(1)-C(301)	88.77(17)
Re(1)-C(2)	2.114(4)	C(201)-Re(1)-C(2)	95.91(14)
Re(1)-N(21)	2.275(3)	C(101)-Re(1)-C(2)	178.61(15)
Re(1)-Br(1)	2.6243(5)	C(301)-Re(1)-C(2)	90.46(17)
		C(201)-Re(1)-N(21)	168.85(14)
		C(101)-Re(1)-N(21)	104.79(13)
		C(301)-Re(1)-N(21)	92.97(13)
		C(2)-Re(1)-N(21)	74.10(11)
		C(201)-Re(1)-Br(1)	91.74(14)
		C(101)-Re(1)-Br(1)	94.00(12)
		C(301)-Re(1)-Br(1)	175.50(11)
		C(2)-Re(1)-Br(1)	86.70(12)
		N(21)-Re(1)-Br(1)	82.90(8)

### 9.1.10 X-Ray Crystallographic Data for **7Br**

The crystal data for **7Br** is summarized in **Table A1.19**. Selected coordination geometries are given in **Table A1.20**. Crystallographic data for the structures were collected at 100(2) K on an Oxford Diffraction Gemini diffractometer fitted with Cu K $\alpha$  radiation. Following analytical absorption corrections and solution by direct methods, the structure was refined against  $F^2$  with full-matrix least-squares using the program SHELXL-97.<sup>112</sup>

Anisotropic displacement parameters were employed for the non-hydrogen atoms. All hydrogen atoms were added at calculated positions and refined by use of a riding model with isotropic displacement parameters based on those of the parent atom.

Table A1.19: Crystal data and structure refinement for **7Br**

<b>Empirical formula</b>	C <sub>20</sub> H <sub>12</sub> BrN <sub>4</sub> O <sub>3</sub> Re
<b>Formula weight</b>	622.45
<b>Temperature</b>	100(2) K
<b>Wavelength</b>	1.54178 Å
<b>Crystal system</b>	Monoclinic
<b>Space group</b>	<i>P</i> 2 <sub>1</sub> / <i>c</i>
<b>Unit cell dimensions</b>	a = 7.1179(9) Å b = 46.0879(5) Å c = 34.7382(5) Å β = 90.3160(10)°
<b>Volume</b>	11395.7(15) Å <sup>3</sup>
<b>Z</b>	24
<b>Density (calculated)</b>	2.177 Mg/m <sup>3</sup>
<b>μ</b>	15.250 mm <sup>-1</sup>
<b>Crystal size</b>	0.48 x 0.03 x 0.02 mm <sup>3</sup>
<b>θ range for data collection</b>	3.15 to 67.49°
<b>Index ranges</b>	-8 ≤ h ≤ 7, -53 ≤ k ≤ 55, -39 ≤ l ≤ 41
<b>Reflections collected</b>	146805
<b>Independent reflections</b>	20461 [R(int) = 0.0495]
<b>Completeness to θ = 67.00°</b>	99.9 %
<b>Absorption correction</b>	Analytical
<b>Max. and min. transmission</b>	0.762 and 0.286
<b>Refinement method</b>	Full-matrix least-squares on <i>F</i> <sup>2</sup>
<b>Data / restraints / parameters</b>	20461 / 18 / 1567
<b>Goodness-of-fit on <i>F</i><sup>2</sup></b>	1.217
<b>Final R indices [I &gt; 2σ(I)]</b>	R1 = 0.0375, wR2 = 0.0802
<b>R indices (all data)</b>	R1 = 0.0412, wR2 = 0.0817
<b>Largest diff. peak and hole</b>	1.393 and -0.970 e.Å <sup>-3</sup>

Table A1.20: Selected bond lengths (Å) and angles (°) for **7Br**

Bond Lengths (Å)		Bond Angles (°)	
Re(1)-C(102)	1.906(6)	C(102)-Re(1)-C(101)	87.0(3)
Re(1)-C(101)	1.964(6)	C(102)-Re(1)-C(103)	92.9(3)
Re(1)-C(103)	2.000(7)	C(101)-Re(1)-C(103)	93.1(3)
Re(1)-C(12)	2.112(6)	C(102)-Re(1)-C(12)	96.7(3)
Re(1)-N(121)	2.227(5)	C(101)-Re(1)-C(12)	172.3(2)
Re(1)-Br(1)	2.6272(7)	C(103)-Re(1)-C(12)	93.5(2)
Re(2)-C(203)	1.907(7)	C(102)-Re(1)-N(121)	169.0(2)
Re(2)-C(202)	1.931(6)	C(101)-Re(1)-N(121)	100.7(2)
Re(2)-C(201)	1.966(6)	C(103)-Re(1)-N(121)	94.5(2)
Re(2)-C(22)	2.104(6)	C(12)-Re(1)-N(121)	74.8(2)
Re(2)-N(221)	2.225(5)	C(102)-Re(1)-Br(1)	87.8(2)
Re(2)-Br(2)	2.6457(7)	C(101)-Re(1)-Br(1)	88.08(19)
Re(3)-C(302)	1.897(6)	C(103)-Re(1)-Br(1)	178.65(18)
Re(3)-C(301)	1.965(7)	C(12)-Re(1)-Br(1)	85.28(16)
Re(3)-C(303)	1.984(7)	N(121)-Re(1)-Br(1)	84.67(13)
Re(3)-C(32)	2.129(6)	C(203)-Re(2)-C(202)	91.3(2)
Re(3)-N(321)	2.216(5)	C(203)-Re(2)-C(201)	89.9(2)
Re(3)-Br(3)	2.6270(7)	C(202)-Re(2)-C(201)	90.3(2)
Re(4)-C(403)	1.919(7)	C(203)-Re(2)-C(22)	96.9(2)
Re(4)-C(402)	1.933(6)	C(202)-Re(2)-C(22)	95.3(2)
Re(4)-C(401)	1.961(6)	C(201)-Re(2)-C(22)	171.1(2)
Re(4)-C(42)	2.116(6)	C(203)-Re(2)-N(221)	95.8(2)
Re(4)-N(421)	2.235(5)	C(202)-Re(2)-N(221)	167.5(2)
Re(4)-Br(4)	2.6443(7)	C(201)-Re(2)-N(221)	99.9(2)
Re(5)-C(502)	1.902(7)	C(22)-Re(2)-N(221)	73.6(2)
Re(5)-C(501)	1.966(7)	C(203)-Re(2)-Br(2)	179.12(18)
Re(5)-C(503)	1.977(7)	C(202)-Re(2)-Br(2)	88.10(16)
Re(5)-C(52)	2.114(6)	C(201)-Re(2)-Br(2)	89.46(17)
Re(5)-N(521)	2.226(5)	C(22)-Re(2)-Br(2)	83.83(16)
Re(5)-Br(5)	2.6296(7)	N(221)-Re(2)-Br(2)	84.84(12)
Re(6)-C(603)	1.903(6)	C(302)-Re(3)-C(301)	86.9(3)
Re(6)-C(602)	1.930(6)	C(302)-Re(3)-C(303)	92.1(3)
Re(6)-C(601)	1.963(6)	C(301)-Re(3)-C(303)	90.6(2)
Re(6)-C(62)	2.114(6)	C(302)-Re(3)-C(32)	96.9(3)
Re(6)-N(621)	2.228(5)	C(301)-Re(3)-C(32)	172.5(2)
Re(6)-Br(6)	2.6431(7)	C(303)-Re(3)-C(32)	95.6(2)

Selected bond lengths (Å) and angles (°) for **7Br** continued

<b>Bond Angles (°)</b>	
C(302)-Re(3)-N(321)	167.7(2)
C(301)-Re(3)-N(321)	100.7(2)
C(303)-Re(3)-N(321)	97.4(2)
C(32)-Re(3)-N(321)	74.5(2)
C(302)-Re(3)-Br(3)	87.9(2)
C(301)-Re(3)-Br(3)	88.09(17)
C(303)-Re(3)-Br(3)	178.73(19)
C(32)-Re(3)-Br(3)	85.66(16)
N(321)-Re(3)-Br(3)	82.83(13)
C(403)-Re(4)-C(402)	90.9(2)
C(403)-Re(4)-C(401)	89.8(3)
C(402)-Re(4)-C(401)	89.0(2)
C(403)-Re(4)-C(42)	96.5(2)
C(402)-Re(4)-C(42)	95.6(2)
C(401)-Re(4)-C(42)	172.2(2)
C(403)-Re(4)-N(421)	96.2(2)
C(402)-Re(4)-N(421)	167.8(2)
C(401)-Re(4)-N(421)	101.0(2)
C(42)-Re(4)-N(421)	73.8(2)
C(403)-Re(4)-Br(4)	179.02(17)
C(402)-Re(4)-Br(4)	88.21(17)
C(401)-Re(4)-Br(4)	89.90(18)
C(42)-Re(4)-Br(4)	83.87(16)
N(421)-Re(4)-Br(4)	84.78(12)
C(502)-Re(5)-C(501)	88.5(3)
C(502)-Re(5)-C(503)	92.2(3)
C(501)-Re(5)-C(503)	90.9(3)

### 9.1.11 X-Ray Crystallographic Data for *cis,cis*-[Re(PyImPh)(CO)<sub>2</sub>(NCCH<sub>3</sub>)Cl]

The crystal data for *cis,cis*-[Re(PyImPh)(CO)<sub>2</sub>(NCCH<sub>3</sub>)Cl] is summarized in **Table A1.21**. Selected coordination geometries are given in Table A1.22. Crystallographic data for the structures were collected at 100(2) K on an Oxford Diffraction Xcalibur diffractometer fitted with Mo K $\alpha$  radiation. Following analytical absorption corrections and solution by direct methods, the structure was refined against  $F^2$  with full-matrix least-squares using the program SHELXL-97.<sup>112</sup>

The chlorine atom and the carbonyl group trans to it are disordered between these two

positions, with site occupancies refined to 0.756(6) and its complement. Geometries of the minor components were restrained to ideal values. Anisotropic displacement parameters were employed for the non-hydrogen atoms. All hydrogen atoms were added at calculated positions and refined by use of a riding model with isotropic displacement parameters based on those of the parent atom.

Table A1.21: Crystal data and structure refinement for *cis,cis*-[Re(PyImPh)(CO)<sub>2</sub>(NCCH<sub>3</sub>)Cl]

<b>Empirical formula</b>	C <sub>20</sub> H <sub>17</sub> ClN <sub>5</sub> O <sub>2</sub> Re
<b>Formula weight</b>	581.04
<b>Temperature</b>	100(2) K
<b>Wavelength</b>	0.71073 Å
<b>Crystal system</b>	Monoclinic
<b>Space group</b>	<i>P</i> 2 <sub>1</sub> / <i>n</i>
<b>Unit cell dimensions</b>	a = 13.1652(2) Å b = 10.76130(10) Å c = 15.3184(2) Å β = 110.527(2)°
<b>Volume</b>	2032.43(4) Å <sup>3</sup>
<b>Z</b>	4
<b>Density (calculated)</b>	1.899 Mg/m <sup>3</sup>
<b>μ</b>	6.137 mm <sup>-1</sup>
<b>Crystal size</b>	0.22 x 0.14 x 0.05 mm <sup>3</sup>
<b>θ range for data collection</b>	3.16 to 34.00°
<b>Index ranges</b>	-20 ≤ h ≤ 20, -16 ≤ k ≤ 16, -24 ≤ l ≤ 22
<b>Reflections collected</b>	55709
<b>Independent reflections</b>	8283 [R(int) = 0.0376]
<b>Completeness to θ = 34.00°</b>	99.9 %
<b>Absorption correction</b>	Analytical
<b>Max. and min. transmission</b>	0.717 and 0.404
<b>Refinement method</b>	Full-matrix least-squares on <i>F</i> <sup>2</sup>
<b>Data / restraints / parameters</b>	8283 / 2 / 292
<b>Goodness-of-fit on <i>F</i><sup>2</sup></b>	1.106
<b>Final R indices [I &gt; 2σ(I)]</b>	R1 = 0.0273, wR2 = 0.0570
<b>R indices (all data)</b>	R1 = 0.0335, wR2 = 0.0588
<b>Largest diff. peak and hole</b>	2.079 and -0.738 e.Å <sup>-3</sup>

Table A1.22: Selected bond lengths (Å) and angles (°) for *cis,cis*-[Re(PyImPh)(CO)<sub>2</sub>(NCCH<sub>3</sub>)Cl]

Bond Lengths (Å)		Bond Angles (°)	
Re(1)-C(102)	1.886(3)	C(102)-Re(1)-C(101)	84.83(15)
Re(1)-C(101)	1.888(5)	C(102)-Re(1)-C(103)	90.8(5)
Re(1)-C(103)	1.937(14)	C(102)-Re(1)-C(2)	98.38(9)
Re(1)-C(2)	2.062(2)	C(101)-Re(1)-C(2)	91.70(14)
Re(1)-N(31)	2.119(2)	C(103)-Re(1)-C(2)	90.5(4)
Re(1)-N(21)	2.215(2)	C(102)-Re(1)-N(31)	94.10(9)
Re(1)-Cl(2)	2.416(4)	C(101)-Re(1)-N(31)	90.06(14)
Re(1)-Cl(1)	2.4914(12)	C(103)-Re(1)-N(31)	88.7(4)
		C(2)-Re(1)-N(31)	167.50(9)
		C(102)-Re(1)-N(21)	172.96(9)
		C(101)-Re(1)-N(21)	93.89(14)
		C(103)-Re(1)-N(21)	90.7(5)
		C(2)-Re(1)-N(21)	74.71(8)
		N(31)-Re(1)-N(21)	92.83(8)
		C(102)-Re(1)-Cl(2)	91.26(13)
		C(103)-Re(1)-Cl(2)	177.4(4)
		C(2)-Re(1)-Cl(2)	90.87(11)
		N(31)-Re(1)-Cl(2)	89.49(10)
		N(21)-Re(1)-Cl(2)	87.52(12)
		C(102)-Re(1)-Cl(1)	95.12(8)
		C(101)-Re(1)-Cl(1)	177.13(13)
		C(2)-Re(1)-Cl(1)	91.15(7)
		N(31)-Re(1)-Cl(1)	87.08(6)
		N(21)-Re(1)-Cl(1)	86.51(6)

### 9.1.12 X-Ray Crystallographic Data for *cis,cis*-[Re(PyImPh)(CO)<sub>2</sub>(P(OEt)<sub>3</sub>)Br]

The crystal data for *cis,cis*-[Re(PyImPh)(CO)<sub>2</sub>(P(OEt)<sub>3</sub>)Br] is summarized in **Table A1.23**. Selected coordination geometries are given in **Table A1.24**. Crystallographic data for the structures were collected at 100(2) K on an Oxford Diffraction Xcalibur diffractometer fitted with Mo K $\alpha$  radiation. Following analytical absorption corrections and solution by direct methods, the structure was refined against  $F^2$  with full-matrix least-squares using the program SHELXL-97.<sup>112</sup>

The solvent diethyl ether molecule is disordered about a crystallographic inversion centre. Geometries were restrained to ideal values. Anisotropic displacement param-

eters were employed for the non-hydrogen atoms. All hydrogen atoms were added at calculated positions and refined by use of a riding model with isotropic displacement parameters based on those of the parent atom.

Table A1.23: Crystal data and structure refinement for *cis,cis*-[Re(PyImPh)(CO)<sub>2</sub>(P(OEt)<sub>3</sub>)Br]

<b>Empirical formula</b>	C <sub>24</sub> H <sub>31</sub> BrN <sub>3</sub> O <sub>5.50</sub> Re
<b>Formula weight</b>	746.60
<b>Temperature</b>	100(2) K
<b>Wavelength</b>	0.71073 Å
<b>Crystal system</b>	Monoclinic
<b>Space group</b>	<i>P</i> 2 <sub>1</sub> / <i>c</i>
<b>Unit cell dimensions</b>	a = 16.3806(5) Å b = 12.9573(10) Å c = 12.8904(10) Å β = 100.172(4)°
<b>Volume</b>	2693.0(3) Å <sup>3</sup>
<b>Z</b>	4
<b>Density (calculated)</b>	1.841 Mg/m <sup>3</sup>
<b>μ</b>	6.096 mm <sup>-1</sup>
<b>Crystal size</b>	0.22 x 0.16 x 0.11 mm <sup>3</sup>
<b>θ range for data collection</b>	2.71 to 29.00°.
<b>Index ranges</b>	-22 ≤ h ≤ 21, -17 ≤ k ≤ 17, -17 ≤ l ≤ 17
<b>Reflections collected</b>	40569
<b>Independent reflections</b>	7154 [R(int) = 0.057]
<b>Completeness to θ = 29.00°</b>	99.9 %
<b>Absorption correction</b>	Analytical
<b>Max. and min. transmission</b>	0.562 and 0.335
<b>Refinement method</b>	Full-matrix least-squares on <i>F</i> <sup>2</sup>
<b>Data / restraints / parameters</b>	7154 / 7 / 348
<b>Goodness-of-fit on <i>F</i><sup>2</sup></b>	1.072
<b>Final R indices [I &gt; 2σ(I)]</b>	R1 = 0.0316, wR2 = 0.0753
<b>R indices (all data)</b>	R1 = 0.0378, wR2 = 0.0783
<b>Largest diff. peak and hole</b>	2.381 and -1.833 e.Å <sup>-3</sup>

Table A1.24: Selected bond lengths (Å) and angles (°) for *cis,cis*-[Re(PyImPh)(CO)<sub>2</sub>(P(OEt)<sub>3</sub>)Br]

Bond Lengths (Å)		Bond Angles (°)	
Re(1)-C(20)	1.890(4)	C(20)-Re(1)-C(10)	87.45(16)
Re(1)-C(10)	1.899(4)	C(20)-Re(1)-C(2)	101.57(15)
Re(1)-C(2)	2.117(4)	C(10)-Re(1)-C(2)	94.62(15)
Re(1)-N(22)	2.236(3)	C(20)-Re(1)-N(22)	174.12(14)
Re(1)-P(1)	2.3457(10)	C(10)-Re(1)-N(22)	96.94(14)
Re(1)-Br(1)	2.6557(4)	C(2)-Re(1)-N(22)	74.25(13)
		C(20)-Re(1)-P(1)	87.15(12)
		C(10)-Re(1)-P(1)	91.45(11)
		C(2)-Re(1)-P(1)	169.56(10)
		N(22)-Re(1)-P(1)	96.61(9)
		C(20)-Re(1)-Br(1)	91.50(12)
		C(10)-Re(1)-Br(1)	176.42(11)
		C(2)-Re(1)-Br(1)	82.23(10)
		N(22)-Re(1)-Br(1)	83.88(8)
		P(1)-Re(1)-Br(1)	91.92(2)

### 9.1.13 X-Ray Crystallographic Data for *cis,trans*-[Re(PyImPh)-(CO)<sub>2</sub>(P(OEt)<sub>3</sub>)Br]

The crystal data for *cis,trans*-[Re(PyImPh)(CO)<sub>2</sub>(P(OEt)<sub>3</sub>)Br] is summarized in **Table A1.25**. Selected coordination geometries are given in **Table A1.26**. Crystallographic data for the structures were collected at 100(2) K on an Oxford Diffraction Gemini diffractometer fitted with Mo K $\alpha$  radiation. Following analytical absorption corrections and solution by direct methods, the structure was refined against  $F^2$  with full-matrix least-squares using the program SHELXL-97.<sup>112</sup>

Anisotropic displacement parameters were employed for the non-hydrogen atoms. All hydrogen atoms were added at calculated positions and refined by use of a riding model with isotropic displacement parameters based on those of the parent atom.

Table A1.25: Crystal data and structure refinement for *cis,trans*-[Re(PyImPh)(CO)<sub>2</sub>(P(OEt)<sub>3</sub>)Br]

<b>Empirical formula</b>	C <sub>22</sub> H <sub>26</sub> BrN <sub>3</sub> O <sub>5</sub> PRe
<b>Formula weight</b>	709.54
<b>Temperature</b>	100(2) K
<b>Wavelength</b>	0.71073 Å
<b>Crystal system</b>	Triclinic
<b>Space group</b>	
<b>Unit cell dimensions</b>	a = 8.4078(5) Å b = 11.7586(6) Å c = 12.8983(7) Å α = 98.323(4)° β = 102.735(5)° γ = 93.632(4)°
<b>Volume</b>	1224.70(12) Å <sup>3</sup>
<b>Z</b>	1
<b>Density (calculated)</b>	1.924 Mg/m <sup>3</sup>
<b>μ</b>	6.696 mm <sup>-1</sup>
<b>Crystal size</b>	0.17 x 0.11 x 0.04 mm <sup>3</sup>
<b>θ range for data collection</b>	3.52 to 29.00°
<b>Index ranges</b>	-11 ≤ h ≤ 11, -16 ≤ k ≤ 16, -17 ≤ l ≤ 17
<b>Reflections collected</b>	21461
<b>Independent reflections</b>	6495 [R(int) = 0.0811]
<b>Completeness to θ = 29.00°</b>	99.8 %
<b>Absorption correction</b>	Analytical
<b>Max. and min. transmission</b>	0.755 and 0.479
<b>Refinement method</b>	Full-matrix least-squares on F <sup>2</sup>
<b>Data / restraints / parameters</b>	6495 / 0 / 301
<b>Goodness-of-fit on F<sup>2</sup></b>	1.041
<b>Final R indices [I &gt; 2σ(I)]</b>	R1 = 0.0492, wR2 = 0.1083
<b>R indices (all data)</b>	R1 = 0.0606, wR2 = 0.1129
<b>Largest diff. peak and hole</b>	4.302 and -1.685 e.Å <sup>-3</sup>

Table A1.26: Selected bond lengths (Å) and angles (°) for *cis,trans*-[Re(PyImPh)(CO)<sub>2</sub>(P(OEt)<sub>3</sub>)Br]

Bond Lengths (Å)		Bond Angles (°)	
Re(1)-C(102)	1.907(6)	C(102)-Re(1)-C(101)	88.2(2)
Re(1)-C(101)	1.927(6)	C(102)-Re(1)-C(2)	103.7(2)
Re(1)-C(2)	2.140(5)	C(101)-Re(1)-C(2)	167.3(2)
Re(1)-N(21)	2.209(5)	C(102)-Re(1)-N(21)	176.0(2)
Re(1)-P(1)	2.2793(16)	C(101)-Re(1)-N(21)	94.3(2)
Re(1)-Br(1)	2.6602(6)	C(2)-Re(1)-N(21)	74.18(19)
		C(102)-Re(1)-P(1)	91.89(18)
		C(101)-Re(1)-P(1)	86.38(17)
		C(2)-Re(1)-P(1)	88.61(15)
		N(21)-Re(1)-P(1)	91.49(12)
		C(102)-Re(1)-Br(1)	90.97(18)
		C(101)-Re(1)-Br(1)	97.39(16)
		C(2)-Re(1)-Br(1)	87.14(14)
		N(21)-Re(1)-Br(1)	85.52(12)
		P(1)-Re(1)-Br(1)	175.34(4)

### 9.1.14 X-Ray Crystallographic Data for *cis,trans*-[Re(PyImPh)(PPh<sub>3</sub>)<sub>2</sub>(CO)Cl/Br]

The crystal data for *cis,trans*-[Re(PyImPh)(PPh<sub>3</sub>)<sub>2</sub>(CO)Cl/Br] is summarized in **Table 1** with the structure depicted in **Figs. 1-2** where ellipsoids have been drawn at the 50% probability level and also in **Figs. 3-4**. Selected coordination geometries are given in **Table 2**. Crystallographic data for the structures were collected at 100(2) K on an Oxford Diffraction Gemini diffractometer fitted with Cu K $\alpha$  radiation. Following analytical absorption corrections and solution by direct methods, the structure was refined against  $F^2$  with full-matrix least-squares using the program SHELXL-97.<sup>112</sup>

The coordinated halide atom was modelled as a mixture of both chloride and bromide with occupancies refined to 0.809(7), for Cl- and its complement for Br-. Similarly, the uncoordinated halide anion was modelled as part bromide (occupancy: 0.737(7)) and chloride (occupancy: 1-0.737(7)). The site occupancies of the chloroform solvent molecules were each refined to 0.854(3) after trial refinement showed no significant differences between the values for each. The remaining solvent was modelled as a diethyl ether molecule disordered about a crystallographic inversion centre, the geometries of which were restrained to ideal values. Anisotropic displacement param-

eters were employed for the non-hydrogen atoms. All hydrogen atoms were added at calculated positions and refined by use of a riding model with isotropic displacement parameters based on those of the parent atom.

Table A1.27: Hydrogen bonds for *cis,trans*-[Re(**PyImPh**)(PPh<sub>3</sub>)<sub>2</sub>(CO)Cl/Br] (Å and °)

<b>Empirical formula</b>	C <sub>55.5</sub> H <sub>48.56</sub> Br <sub>0.93</sub> Cl <sub>8.75</sub> N <sub>3</sub> O <sub>1.50</sub> P <sub>2</sub> Re
<b>Formula weight</b>	1414.90
<b>Temperature</b>	100(2) K
<b>Wavelength</b>	1.54178 Å
<b>Crystal system</b>	Triclinic
<b>Space group</b>	
<b>Unit cell dimensions</b>	a = 12.0367(7) Å b = 14.9844(11) Å c = 17.1380(11) Å α = 99.150(6)° β = 105.028(5)° γ = 92.586(5)°
<b>Volume</b>	2935.2(3) Å <sup>3</sup>
<b>Z</b>	2
<b>Density (calculated)</b>	1.601 Mg/m <sup>3</sup>
<b>Absorption coefficient</b>	9.303 mm <sup>-1</sup>
<b>Crystal size</b>	0.14 x 0.06 x 0.02 mm <sup>3</sup>
<b>θ range for data collection</b>	3.67 to 67.00°
<b>Index ranges</b>	-14 ≤ h ≤ 11, -17 ≤ k ≤ 17, -20 ≤ l ≤ 20
<b>Reflections collected</b>	26651
<b>Independent reflections</b>	10397 [R(int) = 0.0779]
<b>Completeness to θ = 66.75°</b>	99.5 %
<b>Absorption correction</b>	Analytical
<b>Max. and min. transmission</b>	0.810 and 0.480
<b>Refinement method</b>	Full-matrix least-squares on F <sup>2</sup>
<b>Data / restraints / parameters</b>	10397 / 43 / 688
<b>Goodness-of-fit on F<sup>2</sup></b>	1.012
<b>Final R indices [I &gt; 2σ(I)]</b>	R1 = 0.0563, wR2 = 0.1302
<b>R indices (all data)</b>	R1 = 0.0874, wR2 = 0.1420
<b>Largest diff. peak and hole</b>	2.887 and -0.851 e.Å <sup>-3</sup>

Table A1.28: Selected bond lengths (Å) and angles (°) for *cis,trans*-[Re(PyImPh)(PPh<sub>3</sub>)<sub>2</sub>(CO)Cl/Br]

Bond Lengths (Å)		Bond Angles (°)	
Re(1)-C(1)	1.928(8)	C(1)-Re(1)-C(2)	96.2(3)
Re(1)-C(2)	2.067(7)	C(1)-Re(1)-N(21)	171.7(3)
Re(1)-N(21)	2.218(6)	C(2)-Re(1)-N(21)	75.5(3)
Re(1)-P(2)	2.4659(18)	C(1)-Re(1)-P(2)	91.7(2)
Re(1)-P(1)	2.4776(18)	C(2)-Re(1)-P(2)	92.3(2)
Re(1)-Cl(1)	2.4840(16)	N(21)-Re(1)-P(2)	89.30(15)
		C(1)-Re(1)-P(1)	92.2(2)
		C(2)-Re(1)-P(1)	92.43(19)
		N(21)-Re(1)-P(1)	87.57(15)
		P(2)-Re(1)-P(1)	173.48(6)
		C(1)-Re(1)-Cl(1)	96.5(2)
		C(2)-Re(1)-Cl(1)	167.3(2)
		N(21)-Re(1)-Cl(1)	91.83(17)
		P(2)-Re(1)-Cl(1)	87.92(6)
		P(1)-Re(1)-Cl(1)	86.46(6)

Table A1.29: Selected hydrogen bond lengths (Å) and angles (°) for *cis,trans*-[Re(PyImPh)(PPh<sub>3</sub>)<sub>2</sub>(CO)Cl/Br]

D-H...A	d(D-H)	d(H...A)	d(D...A)	<(DHA)
C(10)-H(10)...Br(2)	1.00	2.62	3.540(10)	153.1
C(20)-H(20)...Br(2)	1.00	2.53	3.464(10)	155.8
C(30)-H(30)...Br(2)	1.00	2.57	3.517(12)	158.8

## 9.2 Emission and Excitation Spectra

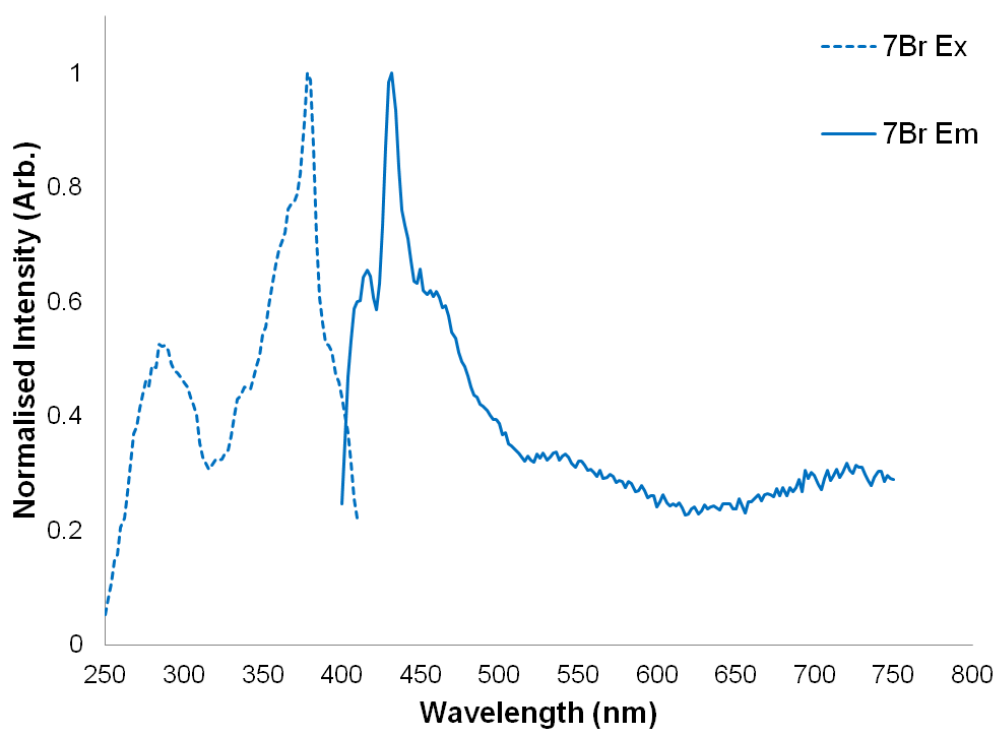


Figure A1.1: Normalised excitation and emission spectra for **7Br** in dichloromethane

### 9.3 Predicted Absorption Profiles

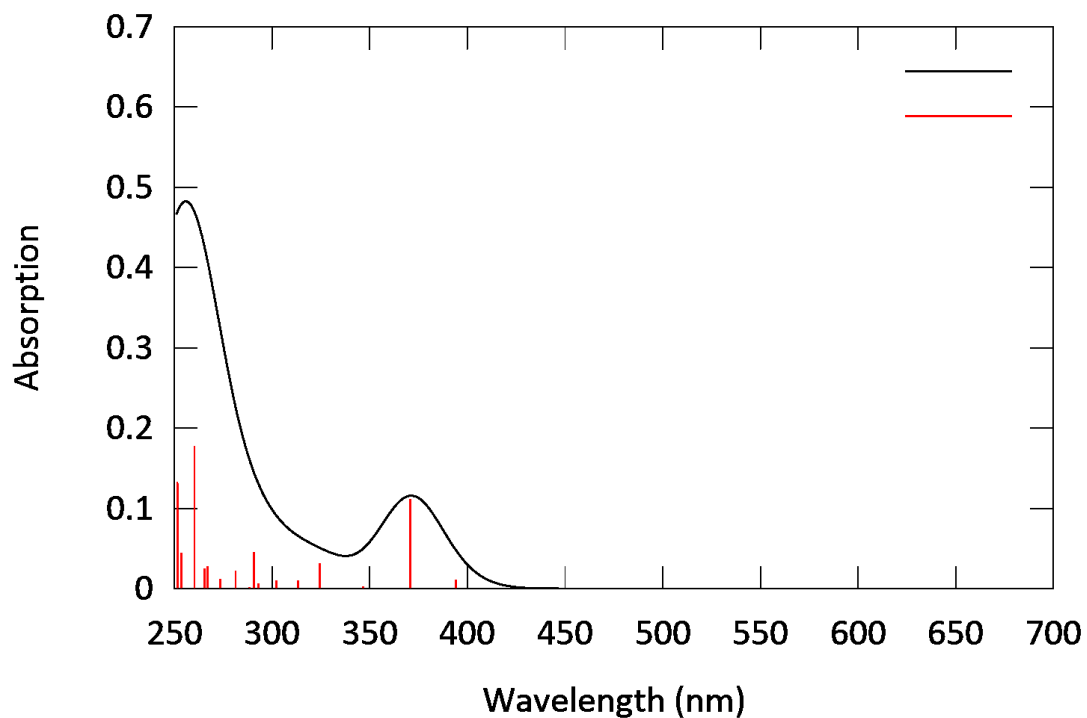


Figure A1.2: Predicted absorption profile of **1Cl**.

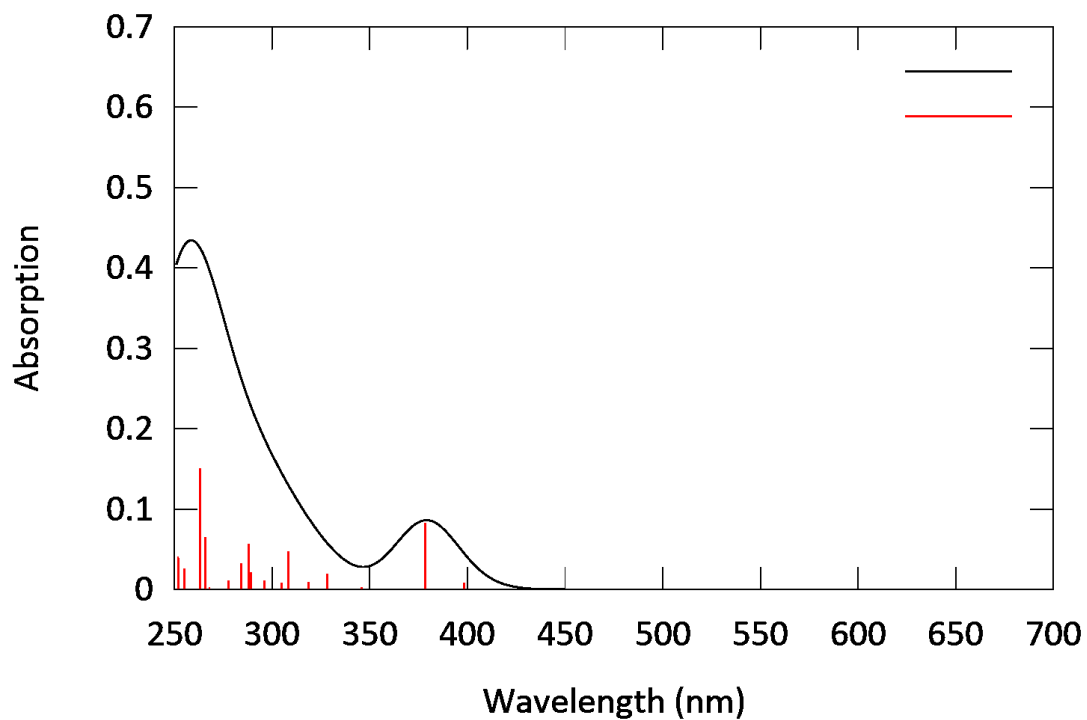


Figure A1.3: Predicted absorption profile of **1Br**.

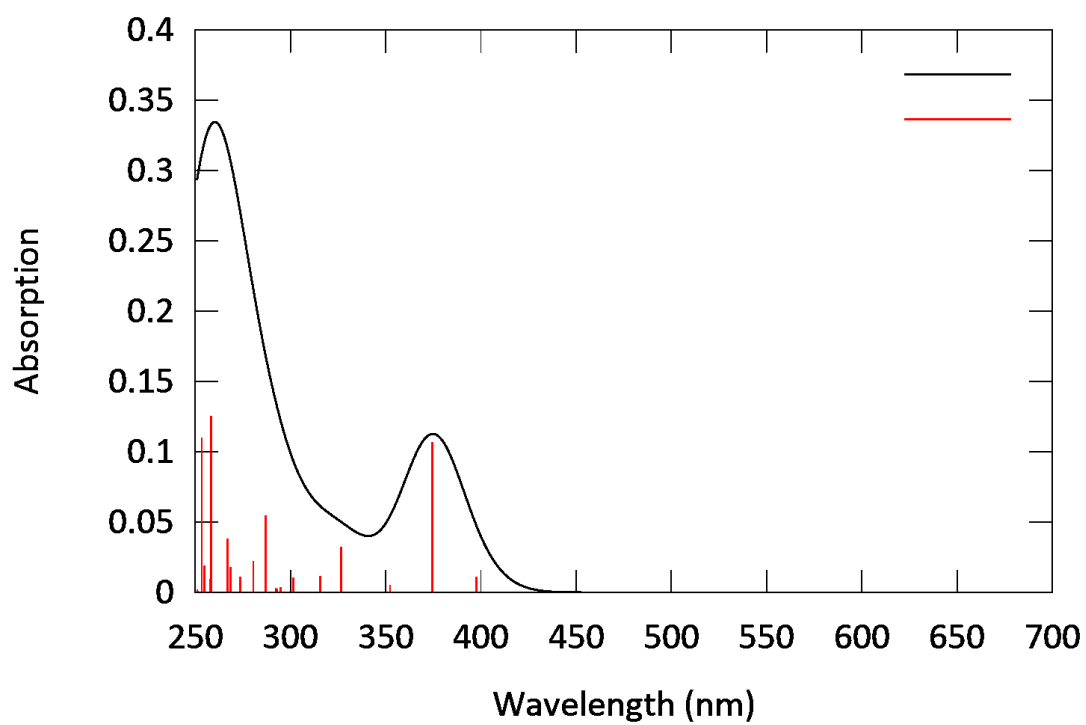


Figure A1.4: Predicted absorption profile of **2Cl**.

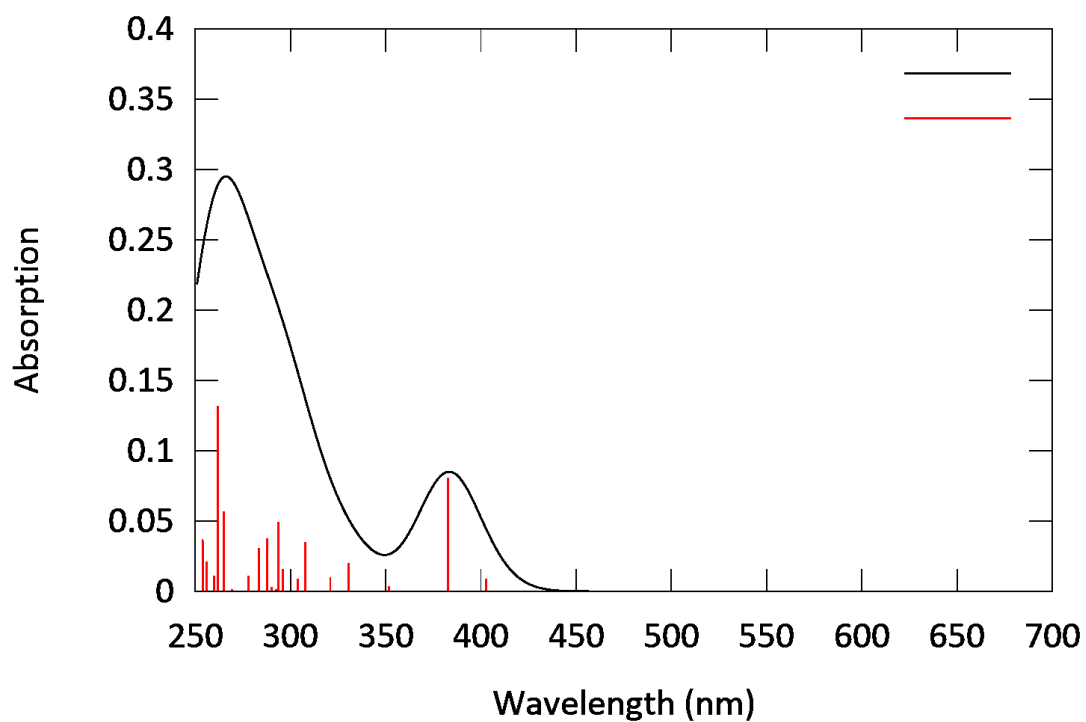


Figure A1.5: Predicted absorption profile of **2Br**.

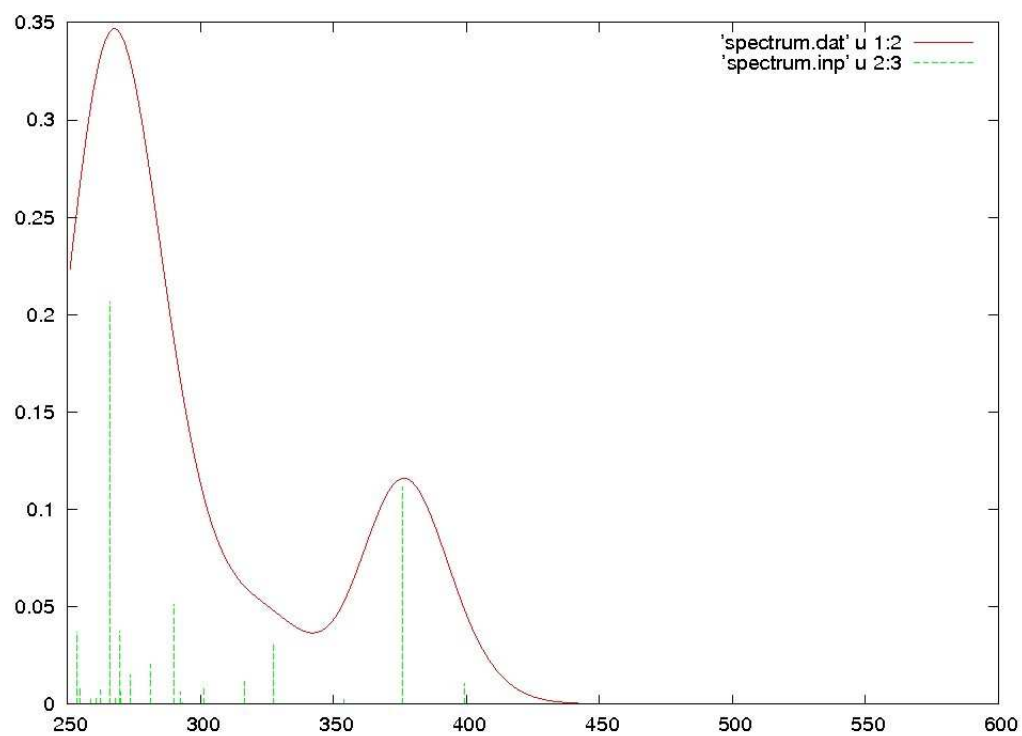


Figure A1.6: Predicted absorption profile of **3Cl**.

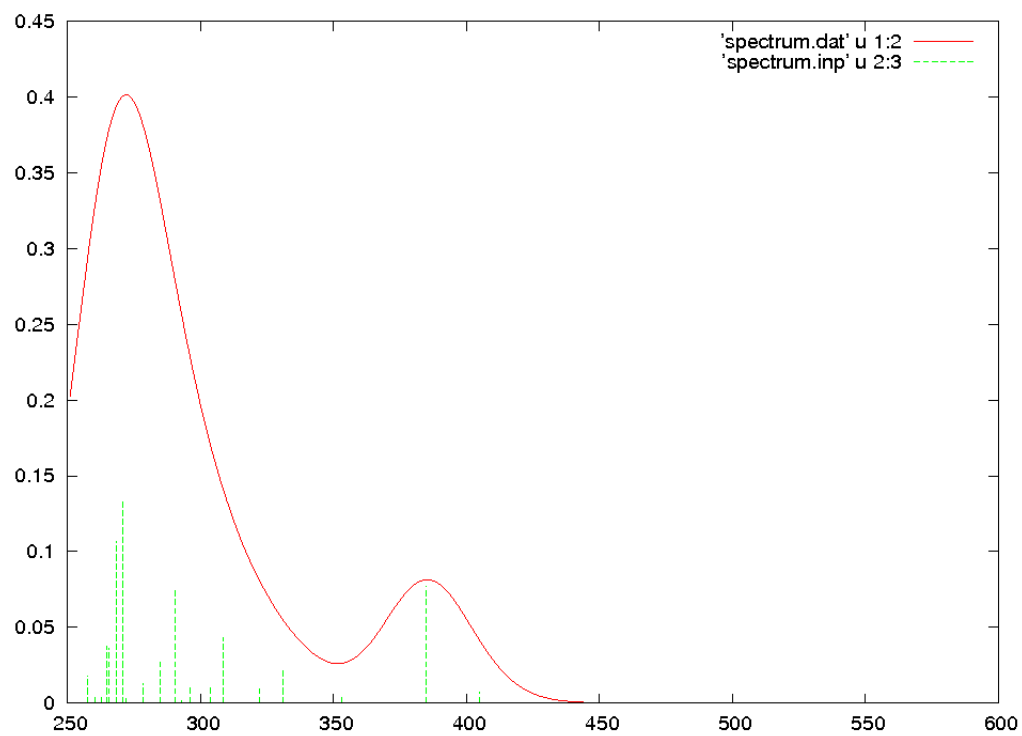


Figure A1.7: Predicted absorption profile of **3Br**.

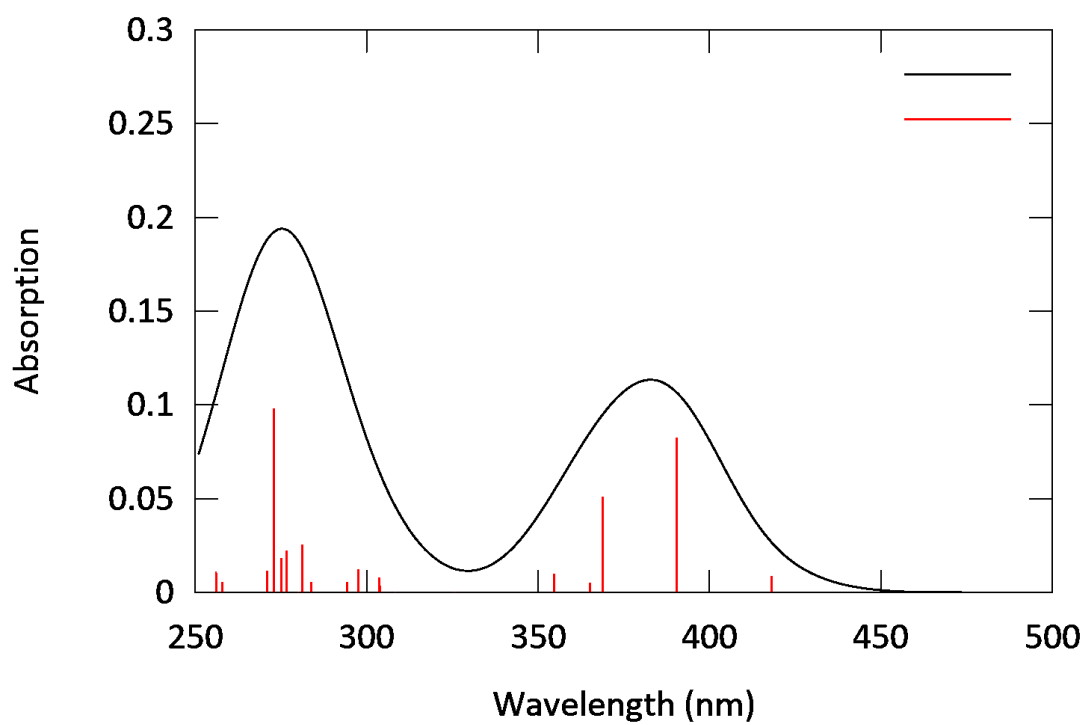


Figure A1.8: Predicted absorption profile of **4Cl**.

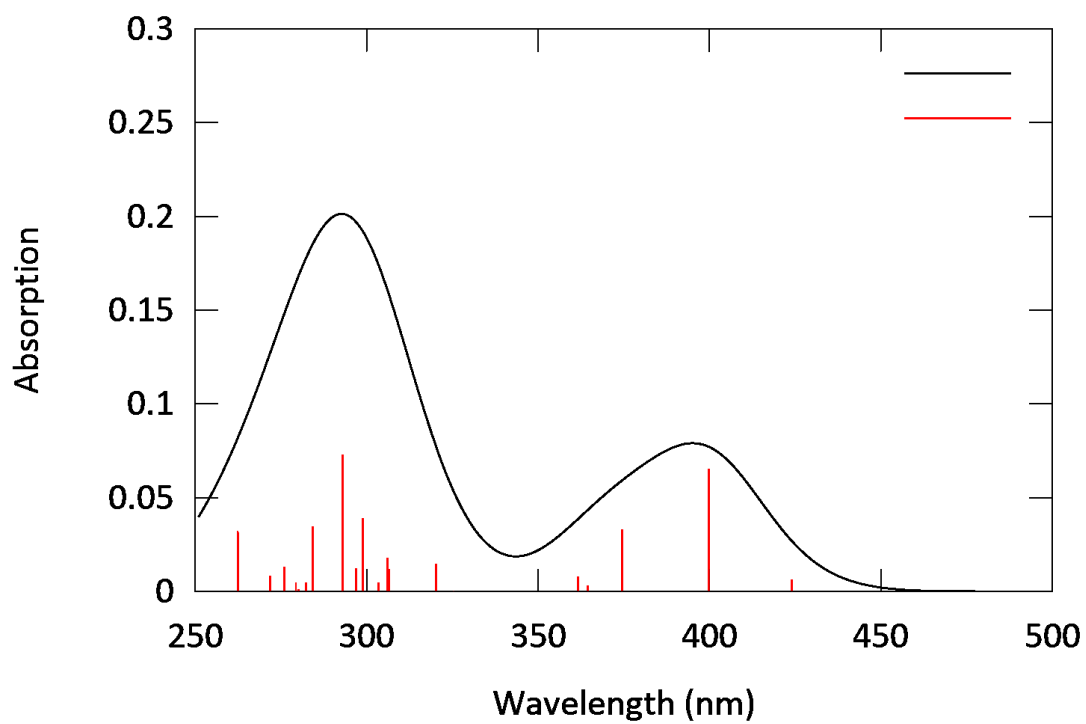


Figure A1.9: Predicted absorption profile of **4Br**.

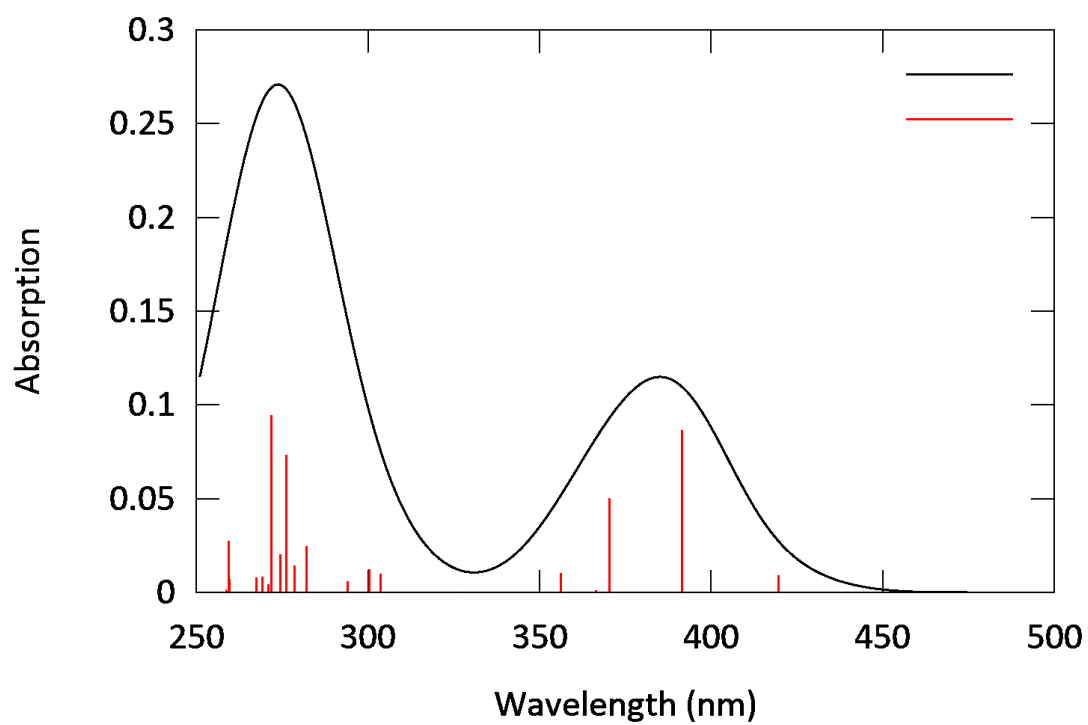


Figure A1.10: Predicted absorption profile of **5Cl**.

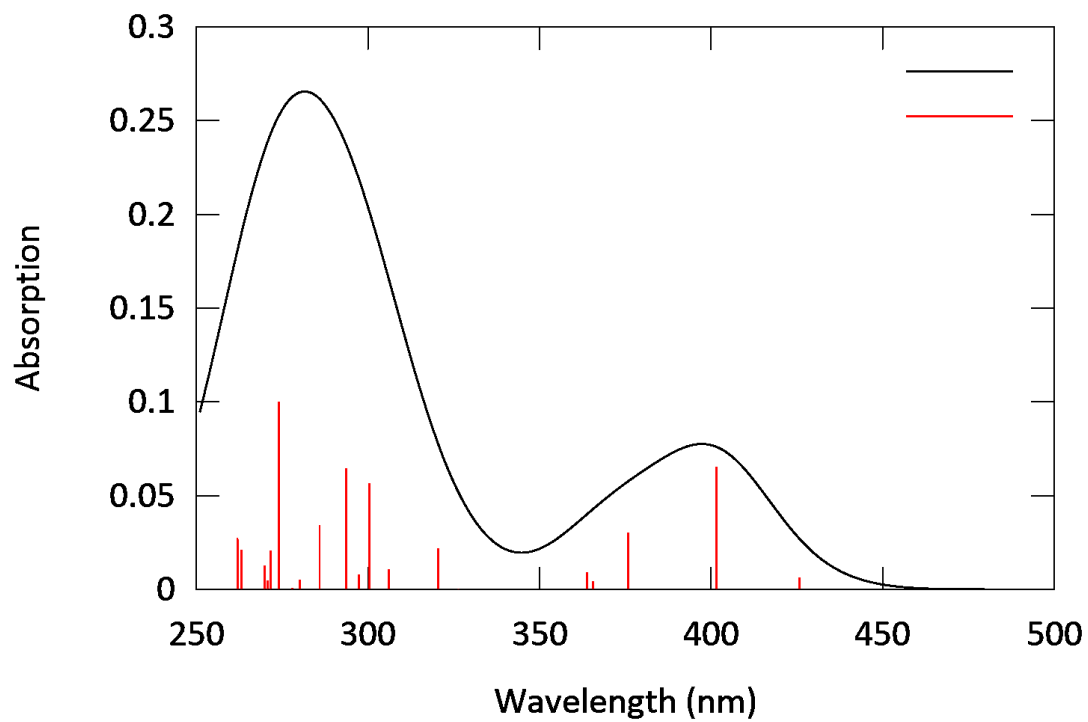


Figure A1.11: Predicted absorption profile of **5Br**.

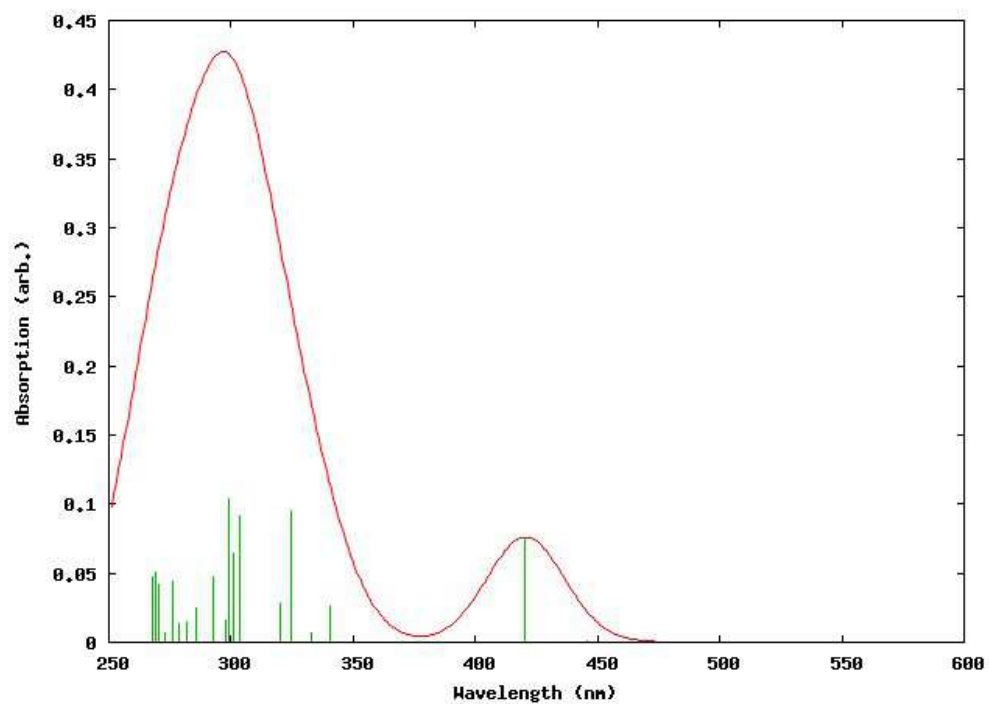


Figure A1.12: Predicted absorption profile of **6Br**.

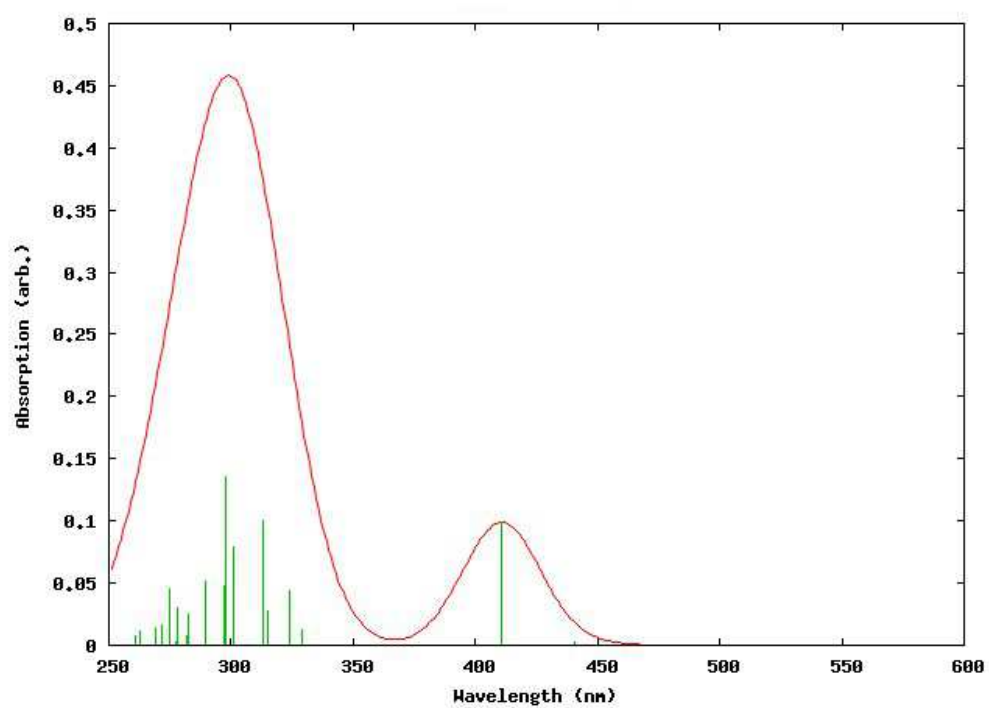


Figure A1.13: Predicted absorption profile of **6Cl**.

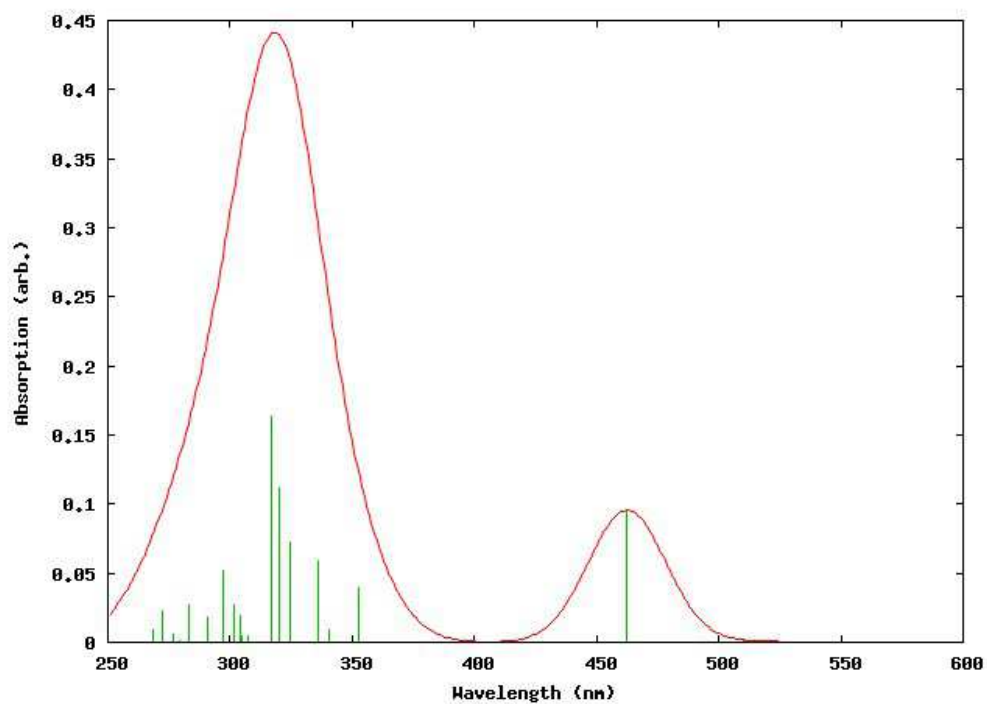


Figure A1.14: Predicted absorption profile of **7Cl**.

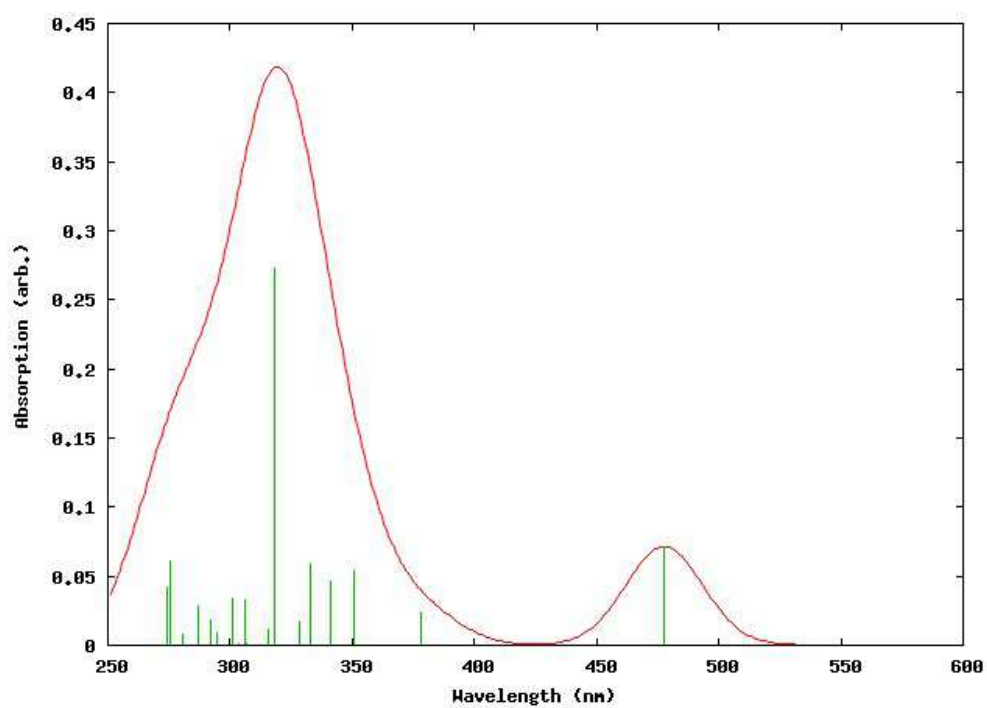


Figure A1.15: Predicted absorption profile of **7Br**.



## 9.4 Calculated Transitions

Table A1.30: Calculated transitions for **1Cl**

Wavelength	Intensity	Levels	Character
394.07 nm	0.0104	HOMO -> LUMO	96.6 %
370.78 nm	0.1111	HOMO-1 -> LUMO	95.2 %
346.58 nm	0.0021	HOMO-2 -> LUMO	96.1 %
324.52 nm	0.0309	HOMO -> LUMO+1	95.9 %
		HOMO -> LUMO+2	2.3 %
313.25 nm	0.0101	HOMO-1 -> LUMO+1	94.8 %
302.16 nm	0.0094	HOMO -> LUMO+1	2.2 %
		HOMO -> LUMO+2	83.5 %
		HOMO -> LUMO+3	8.2 %
292.94 nm	0.0059	HOMO-3 -> LUMO	5.7 %
		HOMO-2 -> LUMO+2	2.2 %
		HOMO-1 -> LUMO+2	58.8 %
		HOMO-1 -> LUMO+3	8.0 %
		HOMO -> LUMO+2	3.9 %
290.67 nm	0.0453	HOMO-3 -> LUMO	90.8 %
		HOMO -> LUMO+3	3.2 %
288.55 nm	0.0010	HOMO-2 -> LUMO+1	92.0 %
		HOMO-2 -> LUMO+2	3.3 %
281.28 nm	0.0216	HOMO-2 -> LUMO+2	3.3 %
		HOMO-2 -> LUMO+3	3.1 %
		HOMO-1 -> LUMO+2	10.0 %
		HOMO-1 -> LUMO+3	20.7 %
		HOMO -> LUMO+3	52.7 %
273.27 nm	0.0119	HOMO-1 -> LUMO+2	18.7 %
		HOMO-1 -> LUMO+3	65.5 %
		HOMO -> LUMO+3	4.8 %
266.81 nm	0.0271	HOMO-5 -> LUMO	19.3 %
		HOMO-4 -> LUMO	19.1 %
		HOMO-2 -> LUMO+1	3.5 %
		HOMO-2 -> LUMO+2	44.9 %
		HOMO-2 -> LUMO+3	3.5 %
		HOMO -> LUMO+3	2.0 %
265.48 nm	0.0247	HOMO-5 -> LUMO	11.1 %
		HOMO-4 -> LUMO	48.7 %
		HOMO-2 -> LUMO+2	27.2 %
		HOMO-2 -> LUMO+3	5.5 %
260.23 nm	0.1771	HOMO-5 -> LUMO	51.8 %
		HOMO-4 -> LUMO	27.0 %
		HOMO-3 -> LUMO+1	5.4 %
		HOMO-2 -> LUMO+3	5.9 %

Calculated transitions for **1Cl** continued

Wavelength	Intensity	Levels	Character
253.39 nm	0.0445	HOMO-5 -> LUMO	2.1 %
		HOMO-3 -> LUMO+1	2.3 %
		HOMO-2 -> LUMO+3	50.3 %
		HOMO-1 -> LUMO+4	2.9 %
		HOMO -> LUMO+3	2.1 %
		HOMO -> LUMO+5	13.5 %
		HOMO -> LUMO+6	3.3 %
251.51 nm	0.1319	HOMO-5 -> LUMO	7.0 %
		HOMO-3 -> LUMO+1	88.4 %
245.46 nm	0.0818	HOMO-6 -> LUMO	3.7 %
		HOMO-2 -> LUMO+3	2.8 %
		HOMO-1 -> LUMO+5	2.7 %
		HOMO -> LUMO+2	2.0 %
		HOMO -> LUMO+3	3.0 %
		HOMO -> LUMO+4	24.2 %
		HOMO -> LUMO+5	31.4 %
		HOMO -> LUMO+6	9.1 %
		HOMO -> LUMO+7	6.9 %
		242.51 nm	0.0056
HOMO-4 -> LUMO+1	3.0 %		
HOMO-1 -> LUMO+4	3.0 %		
HOMO-1 -> LUMO+5	4.5 %		
HOMO -> LUMO+6	6.7 %		
HOMO -> LUMO+7	2.1 %		
238.83 nm	0.0198	HOMO-6 -> LUMO	13.8 %
		HOMO-2 -> LUMO+3	7.0 %
		HOMO-2 -> LUMO+4	5.2 %
		HOMO-2 -> LUMO+5	8.6 %
		HOMO-2 -> LUMO+6	4.6 %
		HOMO-1 -> LUMO+4	5.6 %
		HOMO-1 -> LUMO+5	7.9 %
		HOMO-1 -> LUMO+6	4.8 %
		HOMO-1 -> LUMO+7	3.6 %
		HOMO -> LUMO+4	4.9 %
		HOMO -> LUMO+5	2.4 %
		HOMO -> LUMO+6	16.6 %
236.18 nm	0.0028	HOMO -> LUMO+7	2.2 %
		HOMO-2 -> LUMO+4	3.8 %
		HOMO-2 -> LUMO+5	9.3 %
		HOMO-1 -> LUMO+5	6.1 %
		HOMO-1 -> LUMO+6	59.6 %
		HOMO-1 -> LUMO+7	4.4 %
		HOMO-1 -> LUMO+13	2.1 %

Table A1.31: Calculated transitions for **1Br**

Wavelength	Intensity	Levels	Character
398.30 nm	0.0078	HOMO -> LUMO	96.7 %
378.37 nm	0.0821	HOMO-1 -> LUMO	95.8 %
345.78 nm	0.0024	HOMO-2 -> LUMO	96.0 %
328.19 nm	0.0194	HOMO -> LUMO+1	96.0 %
		HOMO -> LUMO+2	2.0 %
318.47 nm	0.0089	HOMO-1 -> LUMO+1	94.9 %
308.16 nm	0.0470	HOMO-3 -> LUMO	96.1 %
304.91 nm	0.0079	HOMO -> LUMO+2	84.1 %
		HOMO -> LUMO+3	7.7 %
295.99 nm	0.0106	HOMO-2 -> LUMO+2	2.1 %
		HOMO-1 -> LUMO+2	60.3 %
		HOMO-1 -> LUMO+3	6.9 %
		HOMO -> LUMO+2	4.3%
		HOMO -> LUMO+3	16.9 %
289.00 nm	0.0211	HOMO-4 -> LUMO	26.9 %
		HOMO-2 -> LUMO+1	63.6 %
		HOMO-2 -> LUMO+2	4.1 %
288.02 nm	0.0564	HOMO-4 -> LUMO	64.7 %
		HOMO-2 -> LUMO+1	28.4 %
284.07 nm	0.0320	HOMO-4 -> LUMO	2.5 %
		HOMO-2 -> LUMO+2	2.0 %
		HOMO-2 -> LUMO+3	2.2 %
		HOMO-1 -> LUMO+2	9.2 %
		HOMO-1 -> LUMO+3	17.8 %
		HOMO -> LUMO+3	56.2 %
277.60 nm	0.0109	HOMO-1 -> LUMO+2	16.8 %
		HOMO-1 -> LUMO+3	68.7 %
		HOMO -> LUMO+3	5.4 %
267.87	0.0023	HOMO-5 -> LUMO	9.1 %
		HOMO-3 -> LUMO+1	4.8 %
		HOMO-2 -> LUMO+1	4.7 %
		HOMO-2 -> LUMO+2	66.0 %
		HOMO-2 -> LUMO+3	4.0 %
265.90 nm	0.0645	HOMO-5 -> LUMO	4.5 %
		HOMO-3 -> LUMO+1	80.5 %
		HOMO-2 -> LUMO+2	6.1 %
		HOMO-2 -> LUMO+3	3.2 %
262.99 nm	0.1501	HOMO-5 -> LUMO	66.9 %
		HOMO-4 -> LUMO+1	10.0 %
		HOMO-3 -> LUMO+1	11.6 %
		HOMO-2 -> LUMO+2	3.2 %
		HOMO-2 -> LUMO+3	3.1 %

Calculated transitions for **1Br** continued

Wavelength	Intensity	Levels	Character
254.99	0.0254	HOMO-4 -> LUMO+1	4.5 %
		HOMO-2 -> LUMO+3	55.0 %
		HOMO-1 -> LUMO+4	2.2 %
		HOMO-1 -> LUMO+5	5.5 %
		HOMO -> LUMO+4	3.8 %
		HOMO -> LUMO+5	9.9 %
		HOMO -> LUMO+6	3.8 %
251.88 nm	0.0393	HOMO-6 -> LUMO	48.2 %
		HOMO-5 -> LUMO	3.0 %
		HOMO-4 -> LUMO+1	31.5 %
		HOMO -> LUMO+4	3.5 %
		HOMO -> LUMO+5	5.9 %
248.23	0.1258	HOMO-6 -> LUMO	41.2 %
		HOMO-5 -> LUMO	6.7 %
		HOMO-4 -> LUMO+1	44.7 %
		HOMO-3 -> LUMO+2	2.3 %
247.96 nm	0.0418	HOMO-6 -> LUMO	2.2 %
		HOMO-5 -> LUMO	2.8 %
		HOMO-4 -> LUMO+1	2.8 %
		HOMO-3 -> LUMO+2	5.8 %
		HOMO-2 -> LUMO+3	2.7 %
		HOMO-1 -> LUMO+5	2.4 %
		HOMO -> LUMO+4	25.4 %
		HOMO -> LUMO+5	27.3 %
		HOMO -> LUMO+6	7.1 %
		HOMO -> LUMO+7	5.8 %
242.32 nm	0.0106	HOMO-7 -> LUMO	7.6 %
		HOMO-6 -> LUMO	2.4 %
		HOMO-3 -> LUMO+2	13.8 %
		HOMO-2 -> LUMO+3	3.7 %
		HOMO-2 -> LUMO+5	2.6 %
		HOMO-1 -> LUMO+4	8.2 %
		HOMO-1 -> LUMO+5	10.1 %
		HOMO-1 -> LUMO+6	4.6 %
		HOMO-1 -> LUMO+7	2.6 %
		HOMO -> LUMO+6	24.5 %
		HOMO -> LUMO+7	3.2 %
		HOMO -> LUMO+7	3.2 %

Table A1.32: Calculated transitions for **2Cl**

Wavelength	Intensity	Levels	Character
397.54 nm	0.0109	HOMO-1 -> LUMO	2.2 %
		HOMO -> LUMO	96.2 %
374.46 nm	0.1068	HOMO-1 -> LUMO	94.3 %
		HOMO -> LUMO	2.3 %
352.33 nm	0.0049	HOMO-2 -> LUMO	95.5 %
326.49 nm	0.0320	HOMO -> LUMO+1	96.4 %
315.46 nm	0.0114	HOMO-1 -> LUMO+1	95.5 %
301.42 nm	0.0104	HOMO -> LUMO+2	84.1 %
		HOMO -> LUMO+3	2.5 %
		HOMO -> LUMO+4	5.1 %
294.96 nm	0.0037	HOMO-5 -> LUMO	7.2 %
		HOMO-4 -> LUMO	5.6 %
		HOMO-3 -> LUMO	80.6 %
		HOMO-1 -> LUMO+2	2.6 %
292.98 nm	0.0024	HOMO-3 -> LUMO	4.1 %
		HOMO-2 -> LUMO+1	19.7 %
		HOMO-2 -> LUMO+2	3.6 %
		HOMO-1 -> LUMO+2	45.8 %
		HOMO-1 -> LUMO+3	2.6 %
		HOMO-1 -> LUMO+4	3.5 %
		HOMO -> LUMO+3	9.2 %
		HOMO -> LUMO+4	3.6 %
292.29 nm	0.0032	HOMO-2 -> LUMO+1	72.0 %
		HOMO-1 -> LUMO+2	13.8 %
		HOMO -> LUMO+3	2.7 %
290.45 nm	0.0004	HOMO-4 -> LUMO	89.9 %
		HOMO-3 -> LUMO	7.2 %
287.12 nm	0.0547	HOMO-5 -> LUMO	88.5 %
		HOMO-2 -> LUMO+2	6.1 %
280.54 nm	0.0219	HOMO-1 -> LUMO+2	3.9 %
		HOMO-1 -> LUMO+3	9.8 %
		HOMO-1 -> LUMO+4	13.5 %
		HOMO -> LUMO+3	5.4 %
		HOMO -> LUMO+4	41.3 %
273.74 nm	0.0108	HOMO-1 -> LUMO+2	12.0 %
		HOMO-1 -> LUMO+3	17.3 %
		HOMO-1 -> LUMO+4	51.5 %
		HOMO -> LUMO+3	16.1 %
		HOMO-7 -> LUMO	4.1 %

Calculated transitions for **2Cl** continued

<b>Wavelength</b>	<b>Intensity</b>	<b>Levels</b>	<b>Character</b>		
268.66 nm	0.0176	HOMO-6 -> LUMO	4.7 %		
		HOMO-2 -> LUMO+1	16.0 %		
		HOMO-2 -> LUMO+2	3.8 %		
		HOMO-2 -> LUMO+3	57.6 %		
		HOMO -> LUMO+3	6.4 %		
		HOMO-7 -> LUMO	2.4 %		
266.84 nm	0.0379	HOMO-6 -> LUMO	2.6 %		
		HOMO-2 -> LUMO+2	73.7 %		
		HOMO-2 -> LUMO+3	14.4 %		
258.49 nm	0.1255	HOMO-7 -> LUMO	3.4 %		
		HOMO-6 -> LUMO	63.7 %		
		HOMO-6 -> LUMO+1	6.5 %		
		HOMO-5 -> LUMO+1	2.3 %		
		HOMO-3 -> LUMO+1	4.6 %		
		HOMO-2 -> LUMO+3	3.0 %		
		HOMO-2 -> LUMO+4	7.5 %		
		257.79 nm	0.0092	HOMO-7 -> LUMO	2.9 %
				HOMO -> LUMO+3	2.0 %
HOMO -> LUMO+4	25.4 %				
HOMO-7 -> LUMO	63.3 %				
254.67 nm	0.0190	HOMO-5 -> LUMO+1	3.3 %		
		HOMO-3 -> LUMO+1	3.6 %		
		HOMO-7 -> LUMO	85.8 %		
253.46 nm	0.1100	HOMO-2 -> LUMO+2	8.0 %		
		HOMO-2 -> LUMO+3	2.5 %		
		HOMO-2 -> LUMO+4	27.9 %		
		HOMO-2 -> LUMO+8	12.9 %		
		HOMO-1 -> LUMO+4	2.1 %		
		HOMO-1 -> LUMO+7	4.1 %		
		HOMO-1 -> LUMO+8	5.2 %		
		HOMO -> LUMO+4	2.8 %		
		HOMO -> LUMO+7	7.0 %		
		HOMO -> LUMO+ 8	6.1 %		
		HOMO-4 -> LUMO+1	6.9 %		
251.30 nm	0.0012	HOMO-3 -> LUMO+1	94.1 %		
		HOMO-3 -> LUMO+1	3.1 %		

Table A1.33: Calculated transitions for **2Br**

Wavelength	Intensity	Levels	Character
402.59 nm	0.0086	HOMO-1 -> LUMO	2.3 %
		HOMO -> LUMO	96.1 %
382.62 nm	0.0805	HOMO-1 -> LUMO	94.9 %
		HOMO -> LUMO	2.5 %
351.74 nm	0.0037	HOMO-2 -> LUMO	95.9 %
330.55 nm	0.0202	HOMO -> LUMO+1	96.7 %
320.92 nm	0.0100	HOMO-1 -> LUMO+1	95.7 %
307.87 nm	0.0349	HOMO-5 -> LUMO	23.8 %
		HOMO-4 -> LUMO	17.7 %
		HOMO-3 -> LUMO	54.4 %
304.01 nm	0.0089	HOMO -> LUMO+2	85.5 %
		HOMO -> LUMO+3	3.4 %
		HOMO -> LUMO+4	3.5 %
296.06 nm	0.0157	HOMO-6 -> LUMO	3.9 %
		HOMO-1 -> LUMO+2	56.9 %
		HOMO-1 -> LUMO+3	3.8 %
		HOMO-1 -> LUMO+4	2.9 %
		HOMO -> LUMO+2	2.3 %
		HOMO -> LUMO+3	13.0 %
293.83 nm	0.0490	HOMO -> LUMO+4	3.9 %
		HOMO-6 -> LUMO	18.0 %
		HOMO-5 -> LUMO	38.1 %
		HOMO-4 -> LUMO	7.4 %
		HOMO-3 -> LUMO	27.7 %
292.40 nm	0.0013	HOMO-1 -> LUMO+2	5.4 %
		HOMO-2 -> LUMO+1	91.8 %
		HOMO-2 -> LUMO+2	2.8 %
290.07 nm	0.0027	HOMO-5 -> LUMO	24.1 %
		HOMO-4 -> LUMO	70.7 %
		HOMO-3 -> LUMO	2.7 %
287.81 nm	0.0377	HOMO-6 -> LUMO	72.4 %
		HOMO-5 -> LUMO	9.3 %
		HOMO-3 -> LUMO	12.9 %
283.29 nm	0.0306	HOMO-2 -> LUMO+2	2.5 %
		HOMO-1 -> LUMO+2	9.4 %
		HOMO-1 -> LUMO+3	13.4 %
		HOMO-1 -> LUMO+4	3.8 %
		HOMO -> LUMO+3	46.8 %
278.13 nm	0.0108	HOMO -> LUMO+4	10.3 %
		HOMO-1 -> LUMO+2	16.3 %
		HOMO-1 -> LUMO+3	56.1 %
		HOMO-1 -> LUMO+4	13.7 %
		HOMO -> LUMO+3	4.8 %

Calculated transitions for **2Br** continued

Wavelength	Intensity	Levels	Character
269.27 nm	0.0011	HOMO-7 -> LUMO	4.1 %
		HOMO-2 -> LUMO+1	4.3 %
		HOMO-2 -> LUMO+2	72.3 %
265.15 nm	0.0567	HOMO-2 -> LUMO+3	5.9 %
		HOMO-7 -> LUMO	5.6 %
		HOMO-5 -> LUMO+1	21.0 %
		HOMO-4 -> LUMO+1	15.7 %
		HOMO-3 -> LUMO+1	47.3 %
		HOMO-2 -> LUMO+2	2.1 %
		HOMO-2 -> LUMO+3	2.2 %
261.83 nm	0.1319	HOMO-7 -> LUMO	65.5 %
		HOMO-6 -> LUMO+1	11.7 %
		HOMO-5 -> LUMO+1	5.6 %
		HOMO-4 -> LUMO+1	2.8 %
		HOMO-3 -> LUMO+1	3.6 %
		HOMO-2 -> LUMO+3	3.1 %
259.75 nm	0.0109	HOMO-2 -> LUMO+3	2.5 %
		HOMO -> LUMO+3	21.9 %
		HOMO -> LUMO+4	69.3 %
255.86 nm	0.0210	HOMO-6 -> LUMO+1	10.6 %
		HOMO-5 -> LUMO+1	2.8 %
		HOMO-3 -> LUMO+1	6.8 %
		HOMO-2 -> LUMO+3	32.7 %
		HOMO-2 -> LUMO+4	11.1 %
		HOMO-1 -> LUMO+4	2.6 %
		HOMO-1 -> LUMO+7	3.3 %
		HOMO -> LUMO+4	5.7 %
		HOMO -> LUMO+8	4.7 %
254.20 nm	0.0365	HOMO-8 -> LUMO	2.8 %
		HOMO-7 -> LUMO	5.7 %
		HOMO-6 -> LUMO+1	6.8 %
		HOMO-5 -> LUMO+1	24.2 %
		HOMO-4 -> LUMO+1	10.3 %
		HOMO-3 -> LUMO+1	26.1 %
		HOMO-2 -> LUMO+3	4.5 %
		HOMO-1 -> LUMO+4	5.4 %
		HOMO-1 -> LUMO+4	5.4 %

Table A1.34: Calculated transitions for **3Cl**

<b>Wavelength</b>	<b>Intensity</b>	<b>Levels</b>	<b>Character</b>
399.47 nm	0.0107	HOMO -> LUMO	96.5 %
376.08 nm	0.1112	HOMO-1 -> LUMO	95.0 %
354.04 nm	0.0021	HOMO-2 -> LUMO	96.4 %
327.41 nm	0.0309	HOMO -> LUMO+1	96.6 %
316.59 nm	0.0116	HOMO-1 -> LUMO+1	95.8 %
301.27 nm	0.0085	HOMO -> LUMO+2	83.5 %
293.46 nm	0.0007	HOMO-2 -> LUMO+1	73.7 %
		HOMO-1 -> LUMO+2	12.8 %
292.70 nm	0.0063	HOMO-2 -> LUMO+1	19.8 %
		HOMO-1 -> LUMO+2	48.7 %
290.22 nm	0.0512	HOMO-3 -> LUMO	91.6 %
281.10 nm	0.0204	HOMO-1 -> LUMO+2	10.6 %
273.68 nm	0.0147	HOMO-1 -> LUMO+2	13.8 %
270.05 nm	0.0061	HOMO -> LUMO+3	75.1 %
269.74 nm	0.0377	HOMO-6 -> LUMO	59.4 %
		HOMO-2 -> LUMO+2	11.2 %
267.92 nm	0.0047	HOMO-6 -> LUMO	13.8 %
		HOMO-2 -> LUMO+2	52.4 %
265.94 nm	0.2067	HOMO-4 -> LUMO	77.7 %
262.54 nm	0.0082	HOMO-1 -> LUMO+3	82.4 %
260.99 nm	0.0041	HOMO-6 -> LUMO	11.7 %
258.93 nm	0.0021	HOMO-5 -> LUMO	84.3 %
254.76 nm	0.0079	HOMO-7 -> LUMO	31.1 %
253.60 nm	0.0370	HOMO-3 -> LUMO+1	20.8 %

Table A1.35: Calculated transitions for **3Br**

Wavelength	Intensity	Levels	Character
404.80 nm	0.0073	HOMO -> LUMO	97.1 %
384.74 nm	0.0774	HOMO-1 -> LUMO	96.1 %
353.09 nm	0.0050	HOMO-2 -> LUMO	96.6 %
331.18 nm	0.0212	HOMO -> LUMO+1	97.2 %
322.04 nm	0.0108	HOMO-1 -> LUMO+1	96.4 %
308.51 nm	0.0434	HOMO-3 -> LUMO	96.1 %
303.88 nm	0.0100	HOMO -> LUMO+2	72.4 %
		HOMO -> LUMO+3	6.9 %
		HOMO -> LUMO+5	12.9 %
296.23 nm	0.0106	HOMO-4 -> LUMO	2.4 %
		HOMO-1 -> LUMO+2	50.9 %
		HOMO-1 -> LUMO+3	4.5 %
		HOMO-1 -> LUMO+5	10.5 %
		HOMO -> LUMO+2	3.0 %
		HOMO -> LUMO+4	15.8 %
		HOMO -> LUMO+5	3.1 %
292.96 nm	0.0014	HOMO-2 -> LUMO+1	92.3 %
		HOMO-2 -> LUMO+4	2.2 %
290.74 nm	0.0742	HOMO-4 -> LUMO	89.7 %
		HOMO-2 -> LUMO+1	2.1 %
		HOMO-1 -> LUMO+2	2.6 %
285.01 nm	0.0269	HOMO-2 -> LUMO+2	2.1 %
		HOMO-1 -> LUMO+2	11.4 %
		HOMO-1 -> LUMO+4	8.6 %
		HOMO-1 -> LUMO+5	6.3 %
		HOMO -> LUMO+3	3.3 %
		HOMO -> LUMO+4	45.2 %
		HOMO -> LUMO+5	10.1 %
278.51 nm	0.0126	HOMO-1 -> LUMO+2	14.3 %
		HOMO-1 -> LUMO+3	5.3 %
		HOMO-1 -> LUMO+4	55.4 %
		HOMO-1 -> LUMO+5	11.5 %
		HOMO -> LUMO+4	3.3 %
272.19 nm	0.0029	HOMO-5 -> LUMO	6.4 %
		HOMO -> LUMO+2	9.9 %
		HOMO -> LUMO+3	73.0 %
		HOMO -> LUMO+4	5.6 %
270.80 nm	0.1328	HOMO-7 -> LUMO	3.9 %
		HOMO-5 -> LUMO	53.1 %
		HOMO-3 -> LUMO+1	2.4 %
		HOMO-2 -> LUMO+2	15.8 %
		HOMO-2 -> LUMO+4	4.5 %
		HOMO -> LUMO+3	7.0 %
		HOMO -> LUMO+4	2.4 %

Calculated transitions for **3Br** continued

Wavelength	Intensity	Levels	Character
268.38 nm	0.1069	HOMO-5 -> LUMO	24.1 %
		HOMO-2 -> LUMO+1	2.6 %
		HOMO-2 -> LUMO+2	40.2 %
		HOMO-2 -> LUMO+4	19.5 %
265.43 nm	0.0361	HOMO-3 -> LUMO+1	72.6 %
		HOMO-2 -> LUMO+4	2.2 %
		HOMO-1 -> LUMO+3	15.7 %
		HOMO-1 -> LUMO+4	3.4 %
264.89 nm	0.0372	HOMO-3 -> LUMO+1	20.3 %
		HOMO-1 -> LUMO+2	4.5 %
		HOMO-1 -> LUMO+3	60.0 %
		HOMO-1 -> LUMO+4	7.4 %
262.87 nm	0.0048	HOMO -> LUMO+2	8.6 %
		HOMO -> LUMO+3	7.0 %
		HOMO -> LUMO+4	12.2 %
		HOMO -> LUMO+5	66.3 %
260.39 nm	0.0052	HOMO-6 -> LUMO	91.9 %
257.63 nm	0.0176	HOMO-7 -> LUMO	35.8 %
		HOMO-6 -> LUMO	2.2 %
		HOMO-5 -> LUMO	5.3 %
		HOMO-4 -> LUMO+1	3.6 %
		HOMO-2 -> LUMO+4	9.7 %
		HOMO-2 -> LUMO+5	4.2 %
		HOMO-1 -> LUMO+3	2.9 %
		HOMO-1 -> LUMO+4	6.0 %
		HOMO-1 -> LUMO+5	16.4 %

Table A1.36: Calculated transitions for **4Cl**

Wavelength	Intensity	Levels	Character
418.09 nm	0.0084	HOMO -> LUMO	96.5 %
390.44 nm	0.0825	HOMO-1 -> LUMO	91.3 %
		HOMO-1 -> LUMO+1	2.2 %
		HOMO -> LUMO+1	3.2 %
368.89 nm	0.0508	HOMO-1 -> LUMO	3.5 %
365.21 nm	0.0052	HOMO-2 -> LUMO	93.0 %
		HOMO-2 -> LUMO+1	3.5 %
354.70 nm	0.0096	HOMO-1 -> LUMO	2.4 %
		HOMO-1 -> LUMO+1	96.5 %
325.61 nm	0.0003	HOMO-2 -> LUMO	4.2 %
		HOMO-2 -> LUMO+1	93.5 %
308.36 nm	0.0003	HOMO-5 -> LUMO	3.4 %
		HOMO-4 -> LUMO	3.9 %
		HOMO-3 -> LUMO	88.1 %
		HOMO-3 -> LUMO+1	3.4 %
303.91 nm	0.0034	HOMO-4 -> LUMO	53.6 %
		HOMO-4 -> LUMO+1	2.8 %
		HOMO-3 -> LUMO	3.0 %
		HOMO -> LUMO+2	34.3 %
303.64 nm	0.0076	HOMO-4 -> LUMO	35.5 %
		HOMO -> LUMO+2	53.3 %
		HOMO -> LUMO+3	2.1 %
297.61 nm	0.0122	HOMO-5 -> LUMO	93.6 %
		HOMO-3 -> LUMO	2.8 %
294.23 nm	0.0056	HOMO-1 -> LUMO+2	63.1 %
		HOMO-1 -> LUMO+3	4.6 %
		HOMO-1 -> LUMO+4	2.3 %
		HOMO -> LUMO+3	18.2 %
		HOMO -> LUMO+4	3.1 %
283.88 nm	0.0053	HOMO-5 -> LUMO+1	2.4 %
		HOMO-4 -> LUMO+1	3.0 %
		HOMO-3 -> LUMO	3.8 %
		HOMO-3 -> LUMO+1	89.7 %
281.33 nm	0.0252	HOMO-2 -> LUMO+2	4.6 %
		HOMO-2 -> LUMO+3	2.4 %
		HOMO-1 -> LUMO+2	13.7 %
		HOMO-1 -> LUMO+3	12.1 %
		HOMO -> LUMO+3	47.3 %
		HOMO -> LUMO+4	5.7 %
280.13 nm	0.0004	HOMO-4 -> LUMO	5.0 %
		HOMO-4 -> LUMO+1	89.6 %
		HOMO-3 -> LUMO+1	3.5 %
276.60 nm	0.022	HOMO-6 -> LUMO	75.3 %
		HOMO-5 -> LUMO+1	15.6 %

Calculated transitions for **4Cl** continued

<b>Wavelength</b>	<b>Intensity</b>	<b>Levels</b>	<b>Character</b>
275.06	0.0182	HOMO-6 -> LUMO	2.6 %
		HOMO-5 -> LUMO+1	7.5 %
		HOMO-1 -> LUMO+2	12.8 %
		HOMO-1 -> LUMO+3	58.0 %
		HOMO-1 -> LUMO+4	7.9 %
		HOMO -> LUMO+3	3.7 %
273.00 nm	0.0980	HOMO-6 -> LUMO	12.4 %
		HOMO-5 -> LUMO+1	72.0 %
		HOMO-1 -> LUMO+3	7.6 %
270.93 nm	0.0114	HOMO-2 -> LUMO+2	75.6 %
		HOMO-2 -> LUMO+3	10.7 %
257.96 nm	0.0053	HOMO-10 -> LUMO	8.9 %
		HOMO-8 -> LUMO	2.2 %
		HOMO-7 -> LUMO	10.8 %
		HOMO-6 -> LUMO+1	71.4 %
256.25 nm	0.0104	HOMO-10 -> LUMO	29.7 %
		HOMO-7 -> LUMO	31.3 %
		HOMO-6 -> LUMO	2.2 %
		HOMO-2 -> LUMO+3	11.8 %
		HOMO-2 -> LUMO+4	2.2 %
		HOMO -> LUMO+3	4.5 %
		HOMO -> LUMO+4	7.8 %
		HOMO -> LUMO+4	7.8 %

Table A1.37: Calculated transitions for **4Br**

Wavelength	Intensity	Levels	Character
418.09 nm	0.0084	HOMO -> LUMO	96.5 %
390.44 nm	0.0825	HOMO-1 -> LUMO	91.3 %
		HOMO-1 -> LUMO+1	2.2 %
		HOMO -> LUMO+1	3.2 %
368.89 nm	0.0508	HOMO-1 -> LUMO	3.5 %
		HOMO -> LUMO+1	93.9 %
365.21 nm	0.0052	HOMO-2 -> LUMO	93.0 %
		HOMO-2 -> LUMO+1	3.5 %
354.70 nm	0.0096	HOMO-1 -> LUMO	2.4 %
		HOMO-1 -> LUMO+1	96.5 %
325.61 nm	0.0003	HOMO-2 -> LUMO	4.2 %
		HOMO-2 -> LUMO+1	93.5 %
308.36 nm	0.0003	HOMO-5 -> LUMO	3.4 %
		HOMO-4 -> LUMO	3.9 %
		HOMO-3 -> LUMO	88.1 %
		HOMO-3 -> LUMO+1	3.4 %
303.91 nm	0.0034	HOMO-4 -> LUMO	53.6 %
		HOMO-4 -> LUMO+1	2.8 %
		HOMO-3 -> LUMO	3.0 %
		HOMO -> LUMO+2	34.3 %
303.64 nm	0.0076	HOMO-4 -> LUMO	35.5 %
		HOMO -> LUMO+2	53.3 %
		HOMO -> LUMO+3	2.1 %
297.61 nm	0.0122	HOMO-5 -> LUMO	93.6 %
		HOMO-3 -> LUMO	2.8 %
294.23 nm	0.0056	HOMO-1 -> LUMO+2	63.1 %
		HOMO-1 -> LUMO+3	4.6 %
		HOMO-1 -> LUMO+4	2.3 %
		HOMO -> LUMO+3	18.2 %
		HOMO -> LUMO+4	3.1 %
283.88 nm	0.0053	HOMO-5 -> LUMO+1	2.4 %
		HOMO-4 -> LUMO+1	3.0 %
		HOMO-3 -> LUMO	3.8 %
		HOMO-3 -> LUMO+1	89.7 %
281.33 nm	0.0252	HOMO-2 -> LUMO+2	4.6 %
		HOMO-2 -> LUMO+3	2.4 %
		HOMO-1 -> LUMO+2	13.7 %
		HOMO-1 -> LUMO+3	12.1 %
		HOMO -> LUMO+3	47.3 %
		HOMO -> LUMO+4	5.7 %
280.13 nm	0.0004	HOMO-4 -> LUMO	5.0 %
		HOMO-4 -> LUMO+1	89.6 %
		HOMO-3 -> LUMO+1	3.5 %
276.60 nm	0.022	HOMO-6 -> LUMO	75.3 %
		HOMO-5 -> LUMO+1	15.6 %

Calculated transitions for **4Br** continued

<b>Wavelength</b>	<b>Intensity</b>	<b>Levels</b>	<b>Character</b>
275.06	0.0182	HOMO-6 -> LUMO	2.6 %
		HOMO-5 -> LUMO+1	7.5 %
		HOMO-1 -> LUMO+2	12.8 %
		HOMO-1 -> LUMO+3	58.0 %
		HOMO-1 -> LUMO+4	7.9 %
		HOMO -> LUMO+3	3.7 %
273.00 nm	0.0980	HOMO-6 -> LUMO	12.4 %
		HOMO-5 -> LUMO+1	72.0 %
		HOMO-1 -> LUMO+3	7.6 %
270.93 nm	0.0114	HOMO-2 -> LUMO+2	75.6 %
		HOMO-2 -> LUMO+3	10.7 %
257.96 nm	0.0053	HOMO-10 -> LUMO	8.9 %
		HOMO-8 -> LUMO	2.2 %
		HOMO-7 -> LUMO	10.8 %
		HOMO-6 -> LUMO+1	71.4 %
256.25 nm	0.0104	HOMO-10 -> LUMO	29.7 %
		HOMO-7 -> LUMO	31.3 %
		HOMO-6 -> LUMO	2.2 %
		HOMO-2 -> LUMO+3	11.8 %
		HOMO-2 -> LUMO+4	2.2 %
		HOMO -> LUMO+3	4.5 %
		HOMO -> LUMO+4	7.8 %
		HOMO -> LUMO+4	7.8 %

Table A1.38: Calculated transitions for 5Cl

Wavelength	Intensity	Levels	Character
419.65 nm	0.0090	HOMO -> LUMO	96.6 %
391.58 nm	0.0863	HOMO-1 -> LUMO	91.6 %
		HOMO-1 -> LUMO+1	2.2 %
		HOMO -> LUMO+1	3.3 %
370.33 nm	0.0500	HOMO-1 -> LUMO	3.8 %
		HOMO -> LUMO+1	94.0 %
366.53 nm	0.0010	HOMO-2 -> LUMO	94.4 %
		HOMO-2 -> LUMO+1	3.5 %
356.22 nm	0.0102	HOMO-1 -> LUMO	2.4 %
		HOMO-1 -> LUMO+1	96.6 %
326.67 nm	0.0003	HOMO-2 -> LUMO	4.0 %
		HOMO-2 -> LUMO+1	94.4 %
303.73 nm	0.0099	HOMO -> LUMO+2	84.3 %
		HOMO -> LUMO+3	5.1 %
		HOMO -> LUMO+5	2.9 %
300.44 nm	0.0122	HOMO-5 -> LUMO	2.4 %
		HOMO-3 -> LUMO	94.3 %
294.12 nm	0.0059	HOMO-1 -> LUMO+2	61.4 %
		HOMO-1 -> LUMO+3	4.6 %
		HOMO-1 -> LUMO+5	3.5 %
		HOMO -> LUMO+3	3.2 %
		HOMO -> LUMO+4	8.1 %
		HOMO -> LUMO+5	10.2 %
282.04 nm	0.0245	HOMO-6 -> LUMO	2.2 %
		HOMO-2 -> LUMO+2	3.7 %
		HOMO-1 -> LUMO+2	13.5 %
		HOMO-1 -> LUMO+3	4.4 %
		HOMO-1 -> LUMO+4	3.6 %
		HOMO-1 -> LUMO+5	5.2 %
278.62 nm	0.0142	HOMO-6 -> LUMO	56.4 %
		HOMO-5 -> LUMO	14.1 %
		HOMO-5 -> LUMO+1	2.2 %
		HOMO-3 -> LUMO+1	19.6 %
276.26 nm	0.0732	HOMO-6 -> LUMO	9.9 %
		HOMO-5 -> LUMO	7.6 %
		HOMO-3 -> LUMO+1	60.9 %
		HOMO-1 -> LUMO+2	2.8 %
		HOMO-1 -> LUMO+3	3.3 %
		HOMO-1 -> LUMO+4	4.5 %
		HOMO-1 -> LUMO+5	4.4 %
274.54 nm	0.0203	HOMO-3 -> LUMO+1	14.2 %
		HOMO-1 -> LUMO+2	12.6 %
		HOMO-1 -> LUMO+3	15.0 %
		HOMO-1 -> LUMO+4	23.4 %
		HOMO-1 -> LUMO+5	24.5 %

Calculated transitions for 5Cl continued

Wavelength	Intensity	Levels	Character
271.84 nm	0.0943	HOMO-6 -> LUMO	9.8 %
		HOMO-5 -> LUMO	23.9 %
		HOMO-4 -> LUMO	51.5 %
		HOMO-4 -> LUMO+1	2.1 %
		HOMO-2 -> LUMO+2	3.3 %
271.04 nm	0.0043	HOMO-4 -> LUMO	4.0 %
		HOMO-2 -> LUMO+2	72.9 %
		HOMO-2 -> LUMO+4	6.1 %
		HOMO-2 -> LUMO+5	3.8 %
269.24 nm	0.0081	HOMO-6 -> LUMO	12.8 %
		HOMO-5 -> LUMO	43.1 %
		HOMO-4 -> LUMO	36.2 %
267.55 nm	0.0078	HOMO -> LUMO+2	2.1 %
		HOMO -> LUMO+3	63.6 %
		HOMO -> LUMO+4	27.1 %
		HOMO -> LUMO+5	2.6 %
		HOMO -> LUMO+3	17.1 %
		HOMO -> LUMO+4	20.6 %
		HOMO -> LUMO+5	17.2 %
259.58 nm	0.0070	HOMO-6 -> LUMO+1	2.6 %
		HOMO-1 -> LUMO+3	56.7 %
		HOMO-1 -> LUMO+4	23.0 %
		HOMO-1 -> LUMO+5	2.9 %
		HOMO -> LUMO+4	4.3 %
		HOMO -> LUMO+5	3.5 %
259.37 nm	0.0272	HOMO-10 -> LUMO	6.4 %
		HOMO-7 -> LUMO	2.7 %
		HOMO-6 -> LUMO+1	47.4 %
		HOMO-5 -> LUMO+1	16.7 %
		HOMO -> LUMO+4	7.2 %
		HOMO -> LUMO+5	8.0 %
258.72 nm	0.0012	HOMO-10 -> LUMO	3.2 %
		HOMO-6 -> LUMO+1	11.2 %
		HOMO-5 -> LUMO+1	3.3 %
		HOMO-2 -> LUMO+4	2.8 %
		HOMO-2 -> LUMO+5	3.1 %
		HOMO-1 -> LUMO+3	9.2 %
		HOMO-1 -> LUMO+4	3.5 %
		HOMO -> LUMO+3	3.5 %
		HOMO -> LUMO+4	24.1 %
		HOMO -> LUMO+5	29.3 %
HOMO -> LUMO+5	29.3 %		

Table A1.39: Calculated transitions for **5Br**

Wavelength	Intensity	Levels	Character
425.72 nm	0.0064	HOMO -> LUMO	96.9 %
401.64 nm	0.0651	HOMO-1 -> LUMO	94.3 %
		HOMO-1 -> LUMO+1	2.1 %
375.89 nm	0.0302	HOMO -> LUMO+1	96.0 %
365.56 nm	0.0042	HOMO-2 -> LUMO	92.8 %
		HOMO-2 -> LUMO+1	3.3 %
363.83 nm	0.0090	HOMO-1 -> LUMO+1	95.3 %
326.35 nm	0.0004	HOMO-2 -> LUMO	3.9 %
		HOMO-2 -> LUMO+1	94.7 %
320.53 nm	0.0216	HOMO-3 -> LUMO	96.6 %
306.06 nm	0.0106	HOMO -> LUMO+2	79.1 %
		HOMO -> LUMO+3	5.7 %
		HOMO -> LUMO+5	9.1 %
300.40 nm	0.0566	HOMO-4 -> LUMO	82.3 %
		HOMO-4 -> LUMO+1	2.1 %
		HOMO-3 -> LUMO+1	3.3 %
		HOMO-1 -> LUMO+2	3.9 %
297.40 nm	0.0076	HOMO-4 -> LUMO	6.2 %
		HOMO-3 -> LUMO+1	3.7 %
		HOMO-1 -> LUMO+2	51.2 %
		HOMO-1 -> LUMO+3	3.9 %
		HOMO-1 -> LUMO+5	6.5 %
		HOMO -> LUMO+3	2.9 %
		HOMO -> LUMO+4	16.0 %
293.61 nm	0.0645	HOMO-4 -> LUMO	5.6 %
		HOMO-3 -> LUMO+1	89.8 %
285.93 nm	0.0342	HOMO-1 -> LUMO+2	16.6 %
		HOMO-1 -> LUMO+3	2.9 %
		HOMO-1 -> LUMO+4	6.4 %
		HOMO-1 -> LUMO+5	3.1 %
		HOMO -> LUMO+3	11.9 %
		HOMO -> LUMO+4	41.2 %
		HOMO -> LUMO+5	4.7 %
280.18 nm	0.0052	HOMO-1 -> LUMO+2	12.7 %
		HOMO-1 -> LUMO+3	16.6 %
		HOMO-1 -> LUMO+4	55.4 %
		HOMO-1 -> LUMO+5	6.4 %
277.87 nm	0.0008	HOMO-6 -> LUMO	2.9 %
		HOMO-5 -> LUMO	6.7 %
		HOMO-4 -> LUMO	2.4 %
		HOMO-4 -> LUMO+1	81.9 %
273.97 nm	0.0998	HOMO-6 -> LUMO	19.9 %
		HOMO-5 -> LUMO	60.4 %
		HOMO-5 -> LUMO+1	2.9 %
		HOMO-4 -> LUMO+1	12.1 %

Calculated transitions for **5Br** continued

<b>Wavelength</b>	<b>Intensity</b>	<b>Levels</b>	<b>Character</b>
271.58 nm	0.0204	HOMO-6 -> LUMO	10.4 %
		HOMO-2 -> LUMO+2	59.5 %
		HOMO-2 -> LUMO+4	17.9 %
270.68 nm	0.0045	HOMO-6 -> LUMO	56.8 %
		HOMO-5 -> LUMO	24.1 %
		HOMO-2 -> LUMO+2	6.5 %
		HOMO-2 -> LUMO+4	2.6 %
		HOMO -> LUMO+3	2.0 %
		HOMO -> LUMO+3	2.0 %
269.81 nm	0.0124	HOMO-6 -> LUMO	2.1 %
		HOMO -> LUMO+2	6.8 %
		HOMO -> LUMO+3	64.8 %
		HOMO -> LUMO+4	20.6 %
263.13 nm	0.0208	HOMO-7 -> LUMO	66.3 %
		HOMO-1 -> LUMO+3	18.2 %
		HOMO-1 -> LUMO+4	5.4 %
262.10 nm	0.0269	HOMO-7 -> LUMO	20.9 %
		HOMO-2 -> LUMO+4	3.3 %
		HOMO-1 -> LUMO+3	44.8 %
		HOMO-1 -> LUMO+4	19.7 %
		HOMO-1 -> LUMO+4	19.7 %

Table A1.40: Calculated transitions for **6Cl**

Wavelength	Intensity	Levels	Character
440.48 nm	0.0021	HOMO -> LUMO	97.8 %
410.61 nm	0.0984	HOMO-1 -> LUMO	97.5 %
382.95 nm	0.0003	HOMO-2 -> LUMO	97.3 %
328.79 nm	0.0131	HOMO-3 -> LUMO	4.8 %
		HOMO -> LUMO+1	81.0 %
		HOMO -> LUMO+2	7.6 %
323.64 nm	0.0434	HOMO-4 -> LUMO	6.6 %
		HOMO-3 -> LUMO	82.1 %
		HOMO-1 -> LUMO+1	5.3 %
		HOMO -> LUMO+1	2.7 %
314.94 nm	0.0277	HOMO-5 -> LUMO	2.3 %
		HOMO-3 -> LUMO	4.2 %
		HOMO-1 -> LUMO+1	81.0 %
		HOMO-1 -> LUMO+2	5.4 %
313.08 nm	0.1007	HOMO-5 -> LUMO	5.0 %
		HOMO-4 -> LUMO	83.9 %
		HOMO-3 -> LUMO	5.5 %
301.11 nm	0.0795	HOMO-7 -> LUMO	3.5 %
		HOMO-5 -> LUMO	38.4 %
		HOMO-4 -> LUMO	5.2 %
		HOMO-3 -> LUMO+1	2.5 %
		HOMO-2 -> LUMO+1	7.5 %
		HOMO-1 -> LUMO+2	2.3 %
		HOMO -> LUMO+1	5.4 %
		HOMO -> LUMO+2	24.1 %
		HOMO -> LUMO+3	2.7 %
298.08 nm	0.1358	HOMO-5 -> LUMO	28.3 %
		HOMO-3 -> LUMO+1	2.6 %
		HOMO-2 -> LUMO+1	33.3 %
		HOMO-2 -> LUMO+2	8.7 %
		HOMO -> LUMO+1	2.3 %
		HOMO -> LUMO+2	6.7 %
		HOMO -> LUMO+4	4.2 %
		HOMO -> LUMO+5	2.2 %
297.15 nm	0.0477	HOMO-5 -> LUMO	0.1 %
		HOMO-2 -> LUMO+1	36.4 %
		HOMO-2 -> LUMO+2	5.6 %
		HOMO -> LUMO+1	3.9 %
		HOMO -> LUMO+2	27.1 %
		HOMO -> LUMO+3	3.9 %
		HOMO -> LUMO+4	7.7 %
		HOMO -> LUMO+5	3.0 %

Calculated transitions for <b>6Cl</b> continued			
Wavelength	Intensity	Levels	Character
289.66 nm	0.0516	HOMO-5 -> LUMO	4.8 %
		HOMO-1 -> LUMO+1	7.0 %
		HOMO-1 -> LUMO+2	18.4 %
		HOMO-1 -> LUMO+3	3.1 %
		HOMO-1 -> LUMO+4	12.1 %
		HOMO-1 -> LUMO+5	6.1 %
		HOMO -> LUMO+2	7.6 %
		HOMO -> LUMO+4	19.8 %
		HOMO -> LUMO+5	13.0 %
		HOMO -> LUMO+6	2.5 %
282.62 nm	0.0247	HOMO-1 -> LUMO+2	25.8 %
		HOMO-1 -> LUMO+3	2.5 %
		HOMO-1 -> LUMO+4	8.7 %
		HOMO-1 -> LUMO+5	3.2 %
		HOMO -> LUMO+2	10.2 %
		HOMO -> LUMO+4	24.8 %
281.97 nm	0.0078	HOMO-8 -> LUMO	78.7 %
		HOMO-6 -> LUMO	14.3 %
278.23 nm	0.0298	HOMO-7 -> LUMO	9.8 %
		HOMO-5 -> LUMO	3.9 %
		HOMO-1 -> LUMO+2	24.3 %
		HOMO-1 -> LUMO+4	31.3 %
		HOMO-1 -> LUMO+5	19.8 %
277.18 nm	0.0031	HOMO-1 -> LUMO+6	5.6 %
		HOMO-8 -> LUMO	12.0 %
		HOMO-7 -> LUMO	4.9 %
		HOMO-6 -> LUMO	79.3 %
274.89 nm	0.0446	HOMO-8 -> LUMO	3.0 %
		HOMO-7 -> LUMO	55.7 %
		HOMO-6 -> LUMO	3.4 %
		HOMO-5 -> LUMO	6.8 %
		HOMO-3 -> LUMO+1	9.4 %
		HOMO-1 -> LUMO+2	6.4 %
		HOMO-1 -> LUMO+4	3.4 %
		HOMO-1 -> LUMO+5	2.4 %
271.52 nm	0.0166	HOMO -> LUMO+2	7.8 %
		HOMO -> LUMO+3	83.9 %
		HOMO -> LUMO+4	2.6 %
269.30 nm	0.0144	HOMO-2 -> LUMO+1	18.5 %
		HOMO-2 -> LUMO+2	64.7 %
		HOMO-2 -> LUMO+3	6.2 %

Calculated transitions for **6Cl** continued

<b>Wavelength</b>	<b>Intensity</b>	<b>Levels</b>	<b>Character</b>
262.55 nm	0.0110	HOMO-1 -> LUMO+2	5.8 %
		HOMO-1 -> LUMO+3	84.2 %
260.78 nm	0.0076	HOMO-9 -> LUMO	11.0 %
		HOMO-3 -> LUMO+1	6.9 %
		HOMO-2 -> LUMO+4	6.6 %
		HOMO-2 -> LUMO+5	3.7 %
		HOMO-1 -> LUMO+3	2.4 %
		HOMO -> LUMO+4	24.2 %
		HOMO -> LUMO+5	37.1 %
		HOMO -> LUMO+5	37.1 %

Table A1.41: Calculated transitions for **6Br**

Wavelength	Intensity	Levels	Character
445.85 nm	0.0012	HOMO -> LUMO	98.0 %
420.40 nm	0.0758	HOMO-1 -> LUMO	97.8 %
382.29 nm	0.0002	HOMO-2 -> LUMO	97.3 %
340.23 nm	0.0258	HOMO-4 -> LUMO	4.5 %
		HOMO-3 -> LUMO	93.4 %
332.70 nm	0.0065	HOMO-4 -> LUMO	7.7 %
		HOMO -> LUMO+1	78.8 %
		HOMO -> LUMO+2	7.6 %
324.35 nm	0.0950	HOMO-4 -> LUMO	79.7 %
		HOMO-3 -> LUMO	3.3 %
		HOMO-1 -> LUMO+1	5.6 %
		HOMO -> LUMO+1	6.3 %
320.36 nm	0.0281	HOMO-5 -> LUMO	2.6 %
		HOMO-4 -> LUMO	3.3 %
		HOMO-1 -> LUMO+1	82.9 %
		HOMO-1 -> LUMO+2	4.9 %
303.78 nm	0.0916	HOMO-8 -> LUMO	2.8 %
		HOMO-6 -> LUMO	3.6 %
		HOMO-5 -> LUMO	48.2 %
		HOMO-4 -> LUMO+1	2.4 %
		HOMO-1 -> LUMO+2	2.4 %
		HOMO -> LUMO+1	4.0 %
		HOMO -> LUMO+2	24.6 %
		HOMO -> LUMO+3	2.3 %
301.32 nm	0.0648	HOMO-6 -> LUMO	22.0 %
		HOMO-5 -> LUMO	17.0 %
		HOMO-2 -> LUMO+1	2.7 %
		HOMO -> LUMO+1	6.1 %
		HOMO -> LUMO+2	31.1 %
		HOMO -> LUMO+3	4.3 %
		HOMO -> LUMO+4	4.8 %
		HOMO -> LUMO+5	2.5 %
298.90 nm	0.1038	HOMO-8 -> LUMO	2.0 %
		HOMO-6 -> LUMO	49.9 %
		HOMO-5 -> LUMO	7.7 %
		HOMO-2 -> LUMO+1	9.9 %
		HOMO-1 -> LUMO+2	4.4 %
		HOMO -> LUMO+2	6.1 %
		HOMO -> LUMO+3	2.1 %
		HOMO -> LUMO+4	3.8 %
		HOMO -> LUMO+5	2.1 %
297.86 nm	0.0163	HOMO-6 -> LUMO	12.5 %
		HOMO-2 -> LUMO+1	62.5 %
		HOMO-2 -> LUMO+2	14.1 %

Calculated transitions for **6Br** continued

Wavelength	Intensity	Levels	Character
292.75 nm	0.0471	HOMO-6 -> LUMO	3.0 %
		HOMO-5 -> LUMO	4.5 %
		HOMO-1 -> LUMO+1	6.4 %
		HOMO-1 -> LUMO+2	24.9 %
		HOMO-1 -> LUMO+3	5.3 %
		HOMO-1 -> LUMO+4	10.8 %
		HOMO-1 -> LUMO+5	6.1 %
		HOMO -> LUMO+2	6.3 %
		HOMO -> LUMO+4	13.6 %
		HOMO -> LUMO+5	10.0 %
285.79 nm	0.0245	HOMO-1 -> LUMO+2	29.7 %
		HOMO-1 -> LUMO+3	2.1 %
		HOMO-1 -> LUMO+4	2.2 %
		HOMO -> LUMO+2	10.1 %
		HOMO -> LUMO+3	6.7 %
		HOMO -> LUMO+4	25.1 %
281.71 nm	0.0147	HOMO -> LUMO+5	12.7 %
		HOMO-1 -> LUMO+2	22.6 %
		HOMO-1 -> LUMO+3	4.9 %
		HOMO-1 -> LUMO+4	34.6 %
		HOMO-1 -> LUMO+5	23.4 %
278.84 nm	0.0134	HOMO-1 -> LUMO+6	5.5 %
		HOMO-9 -> LUMO	5.3 %
		HOMO-8 -> LUMO	23.4 %
		HOMO-7 -> LUMO	59.1 %
276.03 nm	0.0441	HOMO-6 -> LUMO	4.1 %
		HOMO-8 -> LUMO	47.4 %
		HOMO-7 -> LUMO	32.8 %
		HOMO-5 -> LUMO	7.2 %
		HOMO-4 -> LUMO+1	2.6 %
272.94 nm	0.0066	HOMO-3 -> LUMO+1	4.3 %
		HOMO -> LUMO+2	3.4 %
		HOMO -> LUMO+3	77.8 %
		HOMO -> LUMO+4	12.5 %
270.26 nm	0.0412	HOMO-9 -> LUMO	2.1 %
		HOMO-8 -> LUMO	3.4 %
		HOMO-3 -> LUMO+1	6.3 %
		HOMO-2 -> LUMO+1	18.0 %
		HOMO-2 -> LUMO+2	59.1 %
		HOMO-2 -> LUMO+3	3.7 %

Calculated transitions for **6Br** continued

<b>Wavelength</b>	<b>Intensity</b>	<b>Levels</b>	<b>Character</b>
269.25 nm	0.0511	HOMO-9 -> LUMO	76.7 %
		HOMO-7 -> LUMO	2.2 %
		HOMO-4 -> LUMO+1	7.7 %
		HOMO-3 -> LUMO+1	3.2 %
267.70 nm	0.0471	HOMO-8 -> LUMO	5.4 %
		HOMO-4 -> LUMO+1	4.2 %
		HOMO-3 -> LUMO+1	73.9 %
		HOMO-2 -> LUMO+2	7.9 %
		HOMO-2 -> LUMO+2	7.9 %

Table A1.42: Calculated transitions for 7Cl

Wavelength	Intensity	Levels	Character
510.00 nm	0.0008	HOMO -> LUMO	98.7 %
462.54 nm	0.0955	HOMO-1 -> LUMO	98.4 %
429.36 nm	0.0002	HOMO-2 -> LUMO	98.7 %
352.93 nm	0.0397	HOMO-4 -> LUMO	2.4 %
		HOMO-3 -> LUMO	95.1 %
340.25 nm	0.0089	HOMO-5 -> LUMO	6.5 %
		HOMO-4 -> LUMO	47.4 %
		HOMO -> LUMO+1	39.9 %
		HOMO -> LUMO+2	2.7 %
336.15 nm	0.0590	HOMO-5 -> LUMO	5.0 %
		HOMO-4 -> LUMO	35.5 %
		HOMO-1 -> LUMO+1	2.0 %
		HOMO -> LUMO+1	48.9 %
		HOMO -> LUMO+2	3.0 %
324.66 nm	0.0721	HOMO-7 -> LUMO	3.0 %
		HOMO-5 -> LUMO	28.2 %
		HOMO-1 -> LUMO+1	58.3 %
320.22 nm	0.1113	HOMO-10 -> LUMO	21.5 %
		HOMO-9 -> LUMO	6.0 %
		HOMO-8 -> LUMO	12.8 %
		HOMO-5 -> LUMO	25.8 %
		HOMO-4 -> LUMO	4.2 %
		HOMO-1 -> LUMO+1	23.8 %
317.15 nm	0.1637	HOMO-10 -> LUMO	25.6 %
		HOMO-9 -> LUMO	7.5 %
		HOMO-8 -> LUMO	11.4 %
		HOMO-7 -> LUMO	11.3 %
		HOMO-5 -> LUMO	23.5 %
		HOMO-4 -> LUMO	5.4 %
		HOMO-1 -> LUMO+1	7.0 %
307.55 nm	0.0043	HOMO-10 -> LUMO	8.5 %
		HOMO-8 -> LUMO	16.6 %
		HOMO-7 -> LUMO	3.9 %
		HOMO-6 -> LUMO	68.0 %
304.70 nm	0.0046	HOMO-8 -> LUMO	17.8 %
		HOMO-6 -> LUMO	11.7 %
		HOMO-2 -> LUMO+1	36.8 %
		HOMO-2 -> LUMO+2	6.5 %
		HOMO -> LUMO+2	14.2 %

Calculated transitions for 7Cl continued			
Wavelength	Intensity	Levels	Character
304.01 nm	0.0190	HOMO-10 -> LUMO	6.4 %
		HOMO-8 -> LUMO	34.8 %
		HOMO-7 -> LUMO	2.5 %
		HOMO-6 -> LUMO	16.1 %
		HOMO-2 -> LUMO+1	27.2 %
		HOMO-2 -> LUMO+2	5.6 %
301.81 nm	0.0276	HOMO-8 -> LUMO	2.8 %
		HOMO-2 -> LUMO+1	18.2 %
		HOMO -> LUMO+1	4.9 %
		HOMO -> LUMO+2	51.8 %
		HOMO -> LUMO+3	6.3 %
		HOMO -> LUMO+4	4.4 %
297.07 nm	0.0517	HOMO-10 -> LUMO	7.9 %
		HOMO-9 -> LUMO	7.5 %
		HOMO-7 -> LUMO	64.6 %
		HOMO-5 -> LUMO	5.5 %
		HOMO-1 -> LUMO+2	2.8 %
290.60 nm	0.0186	HOMO-7 -> LUMO	3.1 %
		HOMO-1 -> LUMO+1	5.2 %
		HOMO-1 -> LUMO+2	32.7 %
		HOMO-1 -> LUMO+3	5.8 %
		HOMO-1 -> LUMO+4	7.0 %
		HOMO-1 -> LUMO+5	2.6 %
		HOMO -> LUMO+2	3.9 %
		HOMO -> LUMO+3	4.0 %
		HOMO -> LUMO+4	18.3 %
		HOMO -> LUMO+5	8.3 %
		HOMO -> LUMO+6	4.0 %
		283.19 nm	0.0269
HOMO-1 -> LUMO+3	2.3 %		
HOMO -> LUMO+2	9.0 %		
HOMO -> LUMO+3	10.1 %		
HOMO -> LUMO+4	24.1 %		
HOMO -> LUMO+5	8.5 %		
HOMO -> LUMO+10	3.3 %		
279.25 nm	0.0013	HOMO-10 -> LUMO	22.5 %
		HOMO-9 -> LUMO	69.4 %

Calculated transitions for 7Cl continued

Wavelength	Intensity	Levels	Character
276.55 nm	0.0061	HOMO-9 -> LUMO	2.1 %
		HOMO-1 -> LUMO+2	17.2 %
		HOMO-1 -> LUMO+3	11.0 %
		HOMO-1 -> LUMO+4	38.6 %
		HOMO-1 -> LUMO+5	15.9 %
		HOMO-1 -> LUMO+6	9.4 %
272.28 nm	0.0221	HOMO-2 -> LUMO+1	15.1 %
		HOMO-2 -> LUMO+2	75.3 %
		HOMO-2 -> LUMO+3	3.2 %
268.51 nm	0.0088	HOMO -> LUMO+2	2.8 %
		HOMO -> LUMO+3	70.8 %
		HOMO -> LUMO+4	20.5 %
		HOMO -> LUMO+4	20.5 %

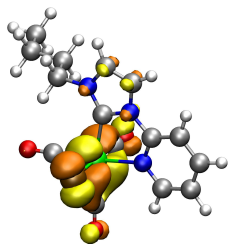
Table A1.43: Calculated transitions for **7Br**

Wavelength	Intensity	Levels	Character
518.14 nm	0.0005	HOMO -> LUMO	98.8 %
477.66 nm	0.0714	HOMO-1 -> LUMO	98.7 %
428.72 nm	0.0003	HOMO-2 -> LUMO	98.7 %
378.39 nm	0.0239	HOMO-3 -> LUMO	98.8 %
350.56 nm	0.0540	HOMO-5 -> LUMO	2.9 %
		HOMO-4 -> LUMO	5.5 %
		HOMO -> LUMO+1	8.8 %
340.99 nm	0.0463	HOMO-4 -> LUMO	8.8 %
		HOMO -> LUMO+1	81.4 %
		HOMO -> LUMO+2	5.3 %
332.56 nm	0.0583	HOMO-10 -> LUMO	2.4 %
		HOMO-7 -> LUMO	18.4 %
		HOMO-6 -> LUMO	2.5 %
		HOMO-5 -> LUMO	51.0 %
		HOMO-1 -> LUMO+1	21.1 %
328.60 nm	0.0173	HOMO-7 -> LUMO	12.8 %
		HOMO-6 -> LUMO	4.2 %
		HOMO-5 -> LUMO	7.0 %
		HOMO-1 -> LUMO+1	66.9 %
		HOMO-1 -> LUMO+2	3.2 %
318.47 nm	0.2730	HOMO-8 -> LUMO	9.3 %
		HOMO-7 -> LUMO	28.3 %
		HOMO-6 -> LUMO	24.8 %
		HOMO-5 -> LUMO	25.6 %
		HOMO-1 -> LUMO+1	3.6 %
315.50 nm	0.0113	HOMO-11 -> LUMO	2.6 %
		HOMO-10 -> LUMO	76.8 %
		HOMO-8 -> LUMO	11.2 %
		HOMO-6 -> LUMO	3.8 %
306.93 nm	0.0010	HOMO-10 -> LUMO	2.3 %
		HOMO-9 -> LUMO	3.2 %
		HOMO-8 -> LUMO	2.6 %
		HOMO-7 -> LUMO	29.2 %
		HOMO-6 -> LUMO	58.9 %
305.93 nm	0.0324	HOMO-2 -> LUMO+1	12.3 %
		HOMO-2 -> LUMO+2	3.3 %
		HOMO -> LUMO+1	6.4 %
		HOMO -> LUMO+2	59.1 %
		HOMO -> LUMO+3	6.6 %
		HOMO -> LUMO+4	3.3 %
303.50 nm	0.0011	HOMO-8 -> LUMO	4.5 %
		HOMO-2 -> LUMO+1	64.5 %
		HOMO-2 -> LUMO+2	10.0 %
		HOMO -> LUMO+2	11.0 %

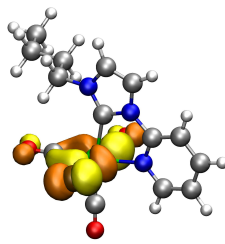
Calculated transitions for **7Br**

Wavelength	Intensity	Levels	Character
300.88 nm	0.0340	HOMO-10 -> LUMO	7.0 %
		HOMO-9 -> LUMO	10.6 %
		HOMO-8 -> LUMO	55.0 %
		HOMO-7 -> LUMO	6.8 %
		HOMO-5 -> LUMO	7.1 %
		HOMO-2 -> LUMO+1	4.7 %
294.54 nm	0.0093	HOMO-9 -> LUMO	2.8 %
		HOMO-1 -> LUMO+1	4.2 %
		HOMO-1 -> LUMO+2	44.6 %
		HOMO-1 -> LUMO+3	6.2 %
		HOMO-1 -> LUMO+4	5.5 %
		HOMO-1 -> LUMO+5	2.0 %
		HOMO -> LUMO+2	2.5 %
		HOMO -> LUMO+3	5.2 %
		HOMO -> LUMO+4	12.5 %
		HOMO -> LUMO+5	6.2 %
		HOMO -> LUMO+6	3.1 %
		291.77 nm	0.0182
HOMO-9 -> LUMO	77.3 %		
HOMO-8 -> LUMO	7.3 %		
HOMO-6 -> LUMO	2.0 %		
HOMO-4 -> LUMO+1	2.2 %		
286.76 nm	0.0280	HOMO-1 -> LUMO+2	29.4 %
		HOMO -> LUMO+2	8.2 %
		HOMO -> LUMO+3	16.9 %
		HOMO -> LUMO+4	24.5 %
		HOMO -> LUMO+5	9.3 %
280.65 nm	0.0079	HOMO-1 -> LUMO+2	11.3 %
		HOMO-1 -> LUMO+3	20.2 %
		HOMO-1 -> LUMO+4	36.6 %
		HOMO-1 -> LUMO+5	15.7 %
		HOMO-1 -> LUMO+6	7.8 %
		HOMO-11 -> LUMO	47.7 %
275.56 nm	0.0614	HOMO-3 -> LUMO+1	40.3 %
		HOMO-2 -> LUMO+2	2.9 %
		HOMO-2 -> LUMO+2	7.3 %
274.47 nm	0.0422	HOMO-11 -> LUMO	44.0 %
		HOMO-3 -> LUMO+1	39.5 %
		HOMO-2 -> LUMO+1	2.1 %
		HOMO-2 -> LUMO+2	7.3 %
		HOMO-2 -> LUMO+2	7.3 %

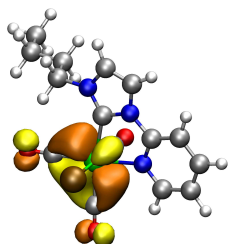
## 9.5 Calculated Orbital Contours



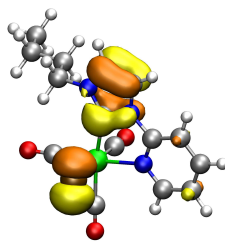
HOMO



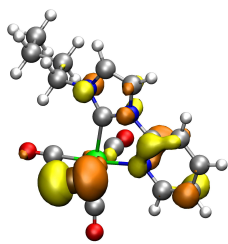
HOMO-1



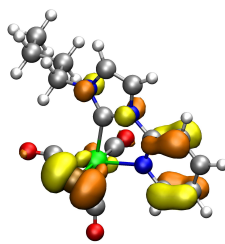
HOMO-2



HOMO-3

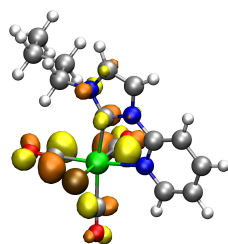


HOMO-4

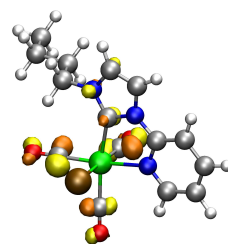


HOMO-5

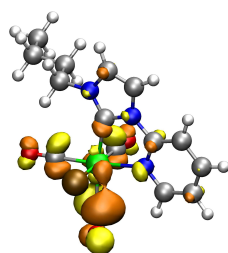
Figure A1.16: Selected occupied orbitals contours of **1Cl**.



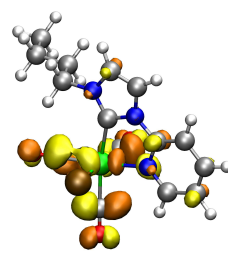
LUMO+5



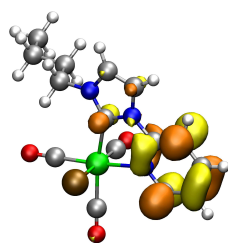
LUMO+4



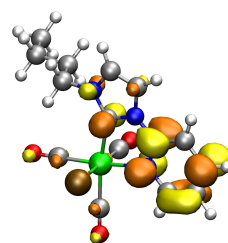
LUMO+3



LUMO+2

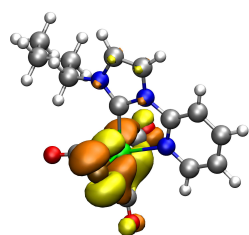


LUMO+1

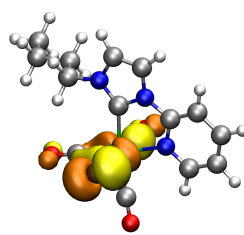


LUMO

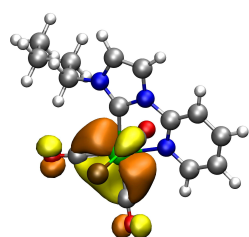
Figure A1.17: Selected unoccupied orbitals contours of **1Cl**.



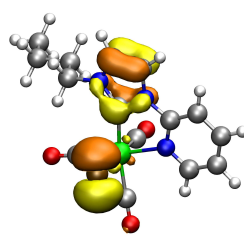
HOMO



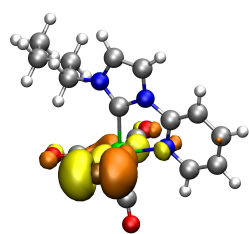
HOMO-1



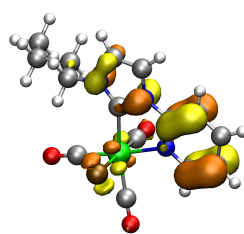
HOMO-2



HOMO-3

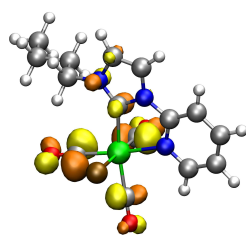


HOMO-4

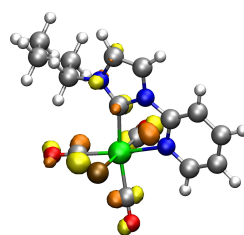


HOMO-5

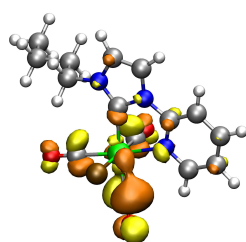
Figure A1.18: Selected occupied orbitals contours of **1Br**.



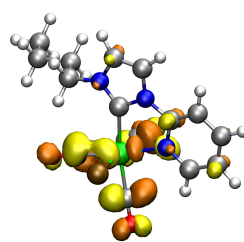
LUMO+5



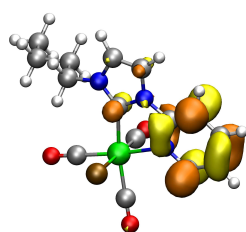
LUMO+4



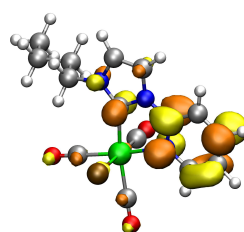
LUMO+3



LUMO+2

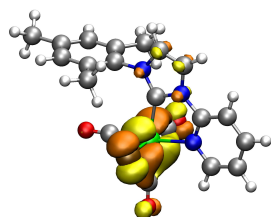


LUMO+1

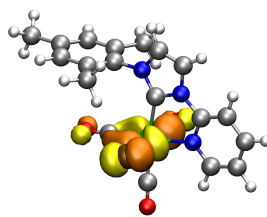


LUMO

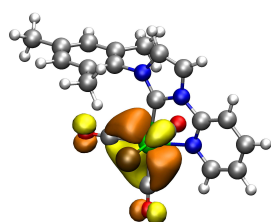
Figure A1.19: Selected unoccupied orbitals contours of **1Br**.



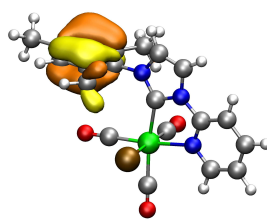
HOMO



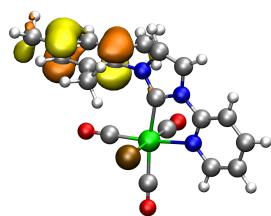
HOMO-1



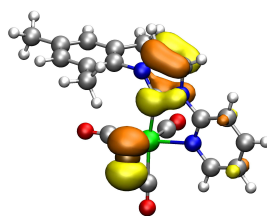
HOMO-2



HOMO-3

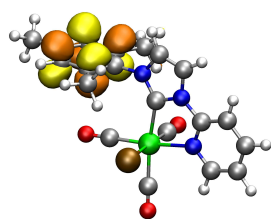


HOMO-4

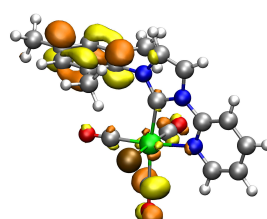


HOMO-5

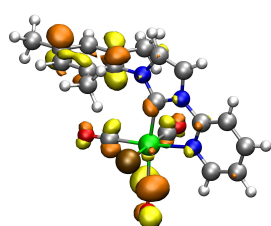
Figure A1.20: Selected occupied orbitals contours of **2Cl**.



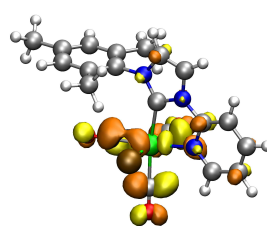
LUMO+5



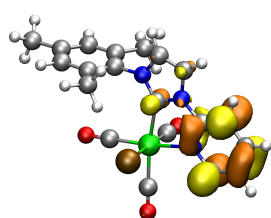
LUMO+4



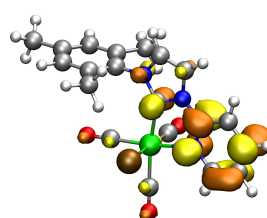
LUMO+3



LUMO+2

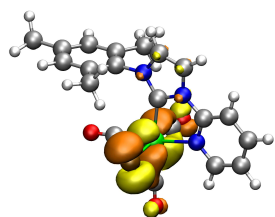


LUMO+1

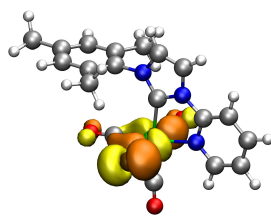


LUMO

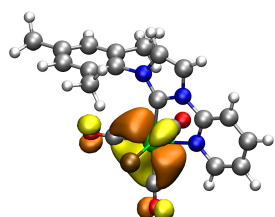
Figure A1.21: Selected unoccupied orbitals contours of **2Cl**.



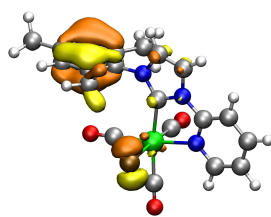
HOMO



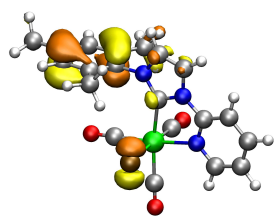
HOMO-1



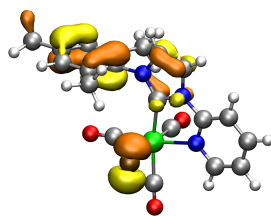
HOMO-2



HOMO-3

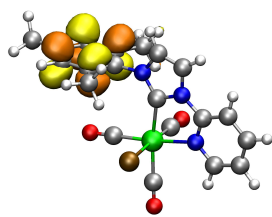


HOMO-4

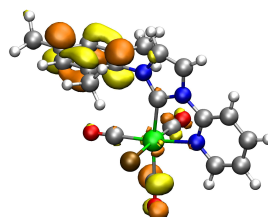


HOMO-5

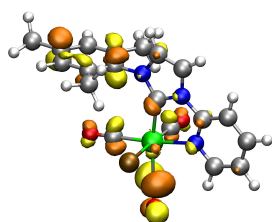
Figure A1.22: Selected occupied orbitals contours of **2Br**.



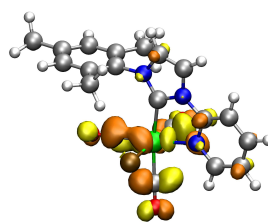
LUMO+5



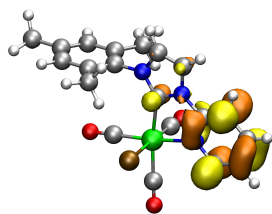
LUMO+4



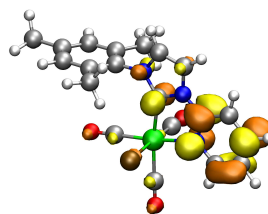
LUMO+3



LUMO+2

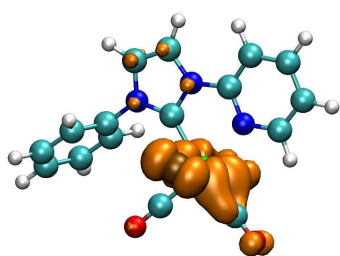


LUMO+1

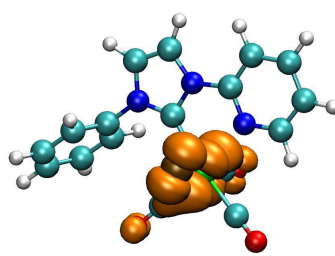


LUMO

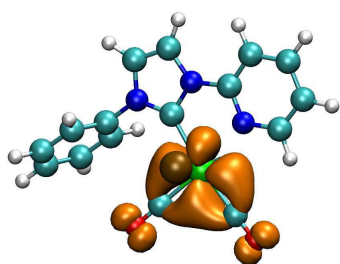
Figure A1.23: Selected unoccupied orbitals contours of **2Br**.



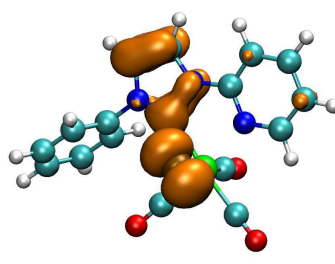
HOMO



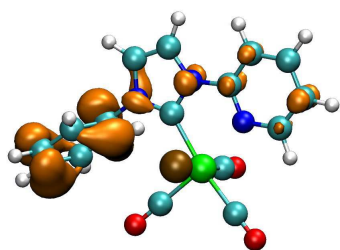
HOMO-1



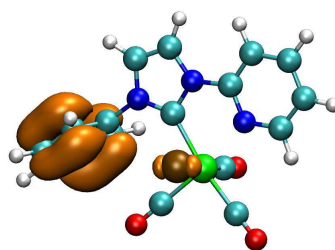
HOMO-2



HOMO-3

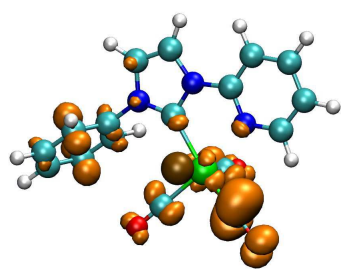


HOMO-4

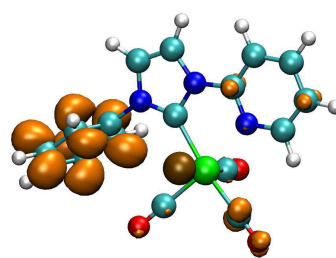


HOMO-5

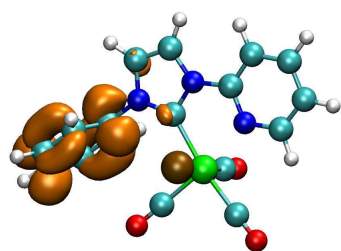
Figure A1.24: Selected occupied orbitals contours of **3Cl**.



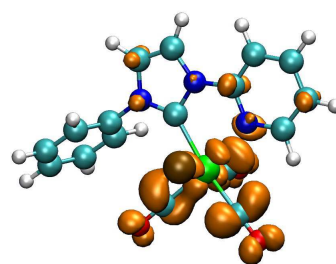
LUMO+5



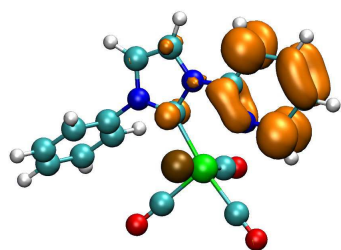
LUMO+4



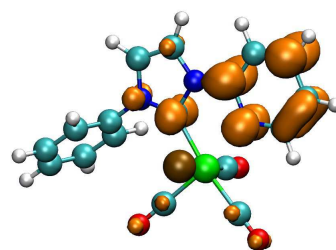
LUMO+3



LUMO+2

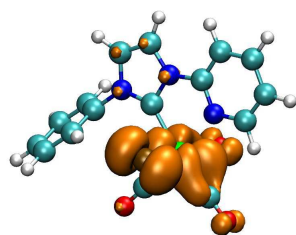


LUMO+1

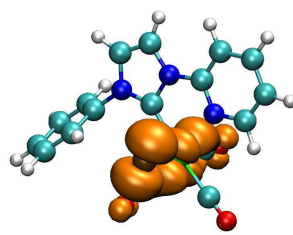


LUMO

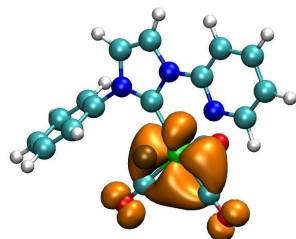
Figure A1.25: Selected unoccupied orbitals contours of **3Cl**.



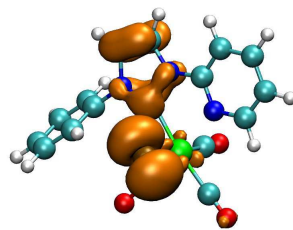
HOMO



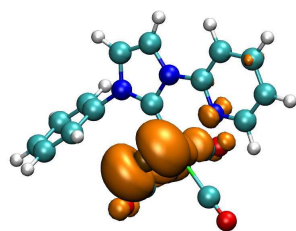
HOMO-1



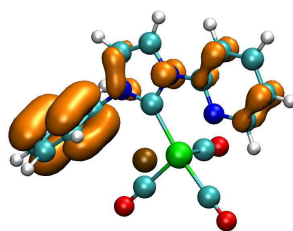
HOMO-2



HOMO-3

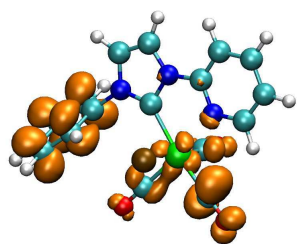


HOMO-4

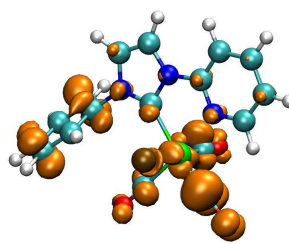


HOMO-5

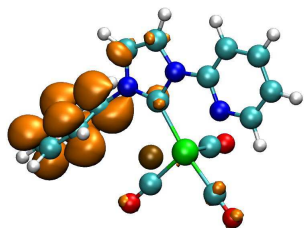
Figure A1.26: Selected occupied orbitals contours of **3Br**.



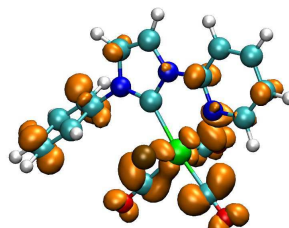
LUMO+5



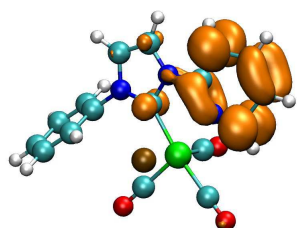
LUMO+4



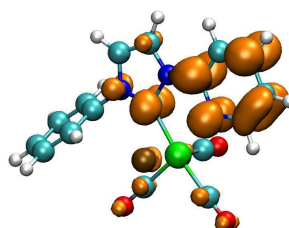
LUMO+3



LUMO+2

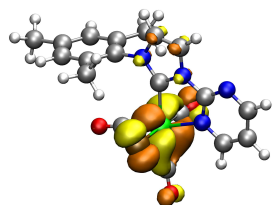


LUMO+1

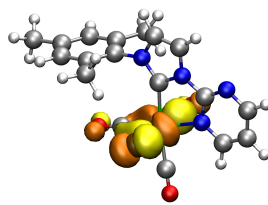


LUMO

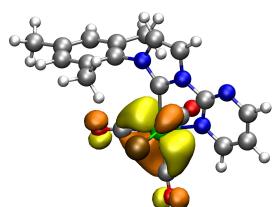
Figure A1.27: Selected unoccupied orbitals contours of **3Br**.



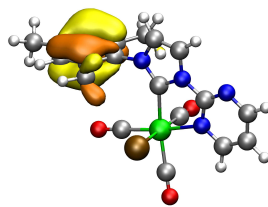
HOMO



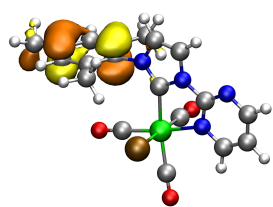
HOMO-1



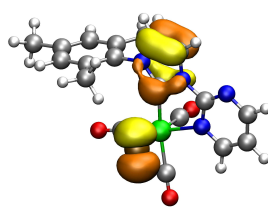
HOMO-2



HOMO-3

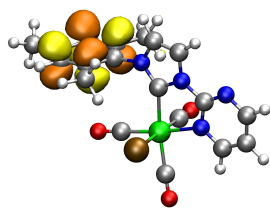


HOMO-4

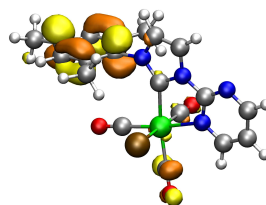


HOMO-5

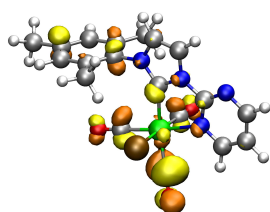
Figure A1.28: Selected occupied orbitals contours of **4Cl**.



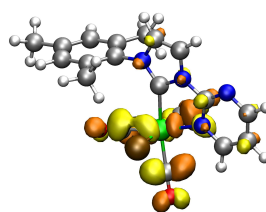
LUMO+5



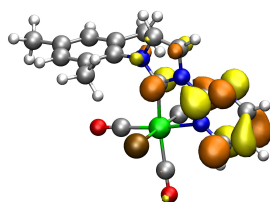
LUMO+4



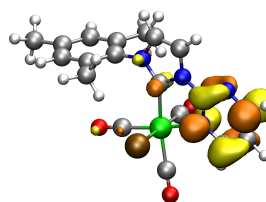
LUMO+3



LUMO+2

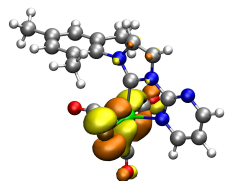


LUMO+1

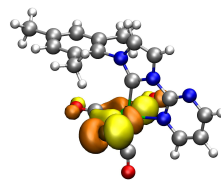


LUMO

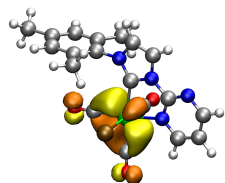
Figure A1.29: Selected unoccupied orbitals contours of **4Cl**.



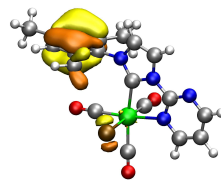
HOMO



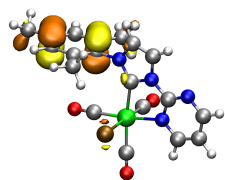
HOMO-1



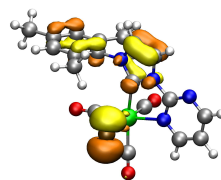
HOMO-2



HOMO-3

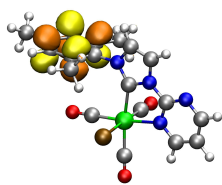


HOMO-4

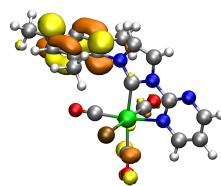


HOMO-5

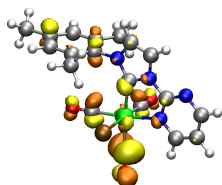
Figure A1.30: Selected occupied orbitals contours of **4Br**.



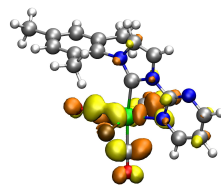
LUMO+5



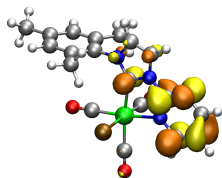
LUMO+4



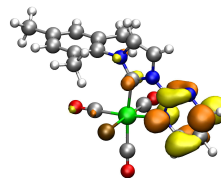
LUMO+3



LUMO+2

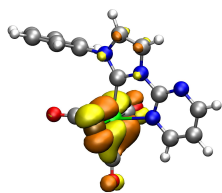


LUMO+1

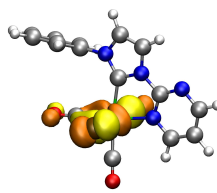


LUMO

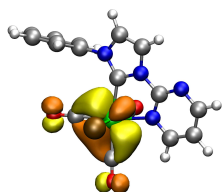
Figure A1.31: Selected unoccupied orbitals contours of **4Br**.



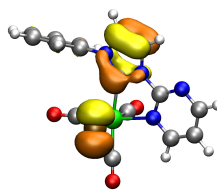
HOMO



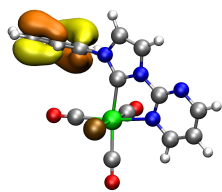
HOMO-1



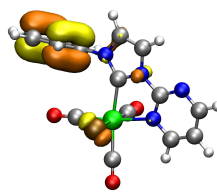
HOMO-2



HOMO-3

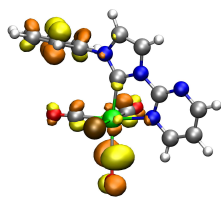


HOMO-4

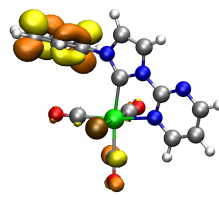


HOMO-5

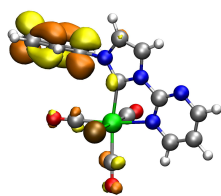
Figure A1.32: Selected occupied orbitals contours of **5Cl**.



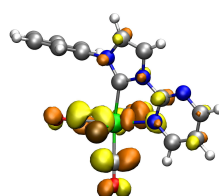
LUMO+5



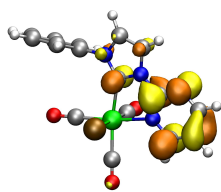
LUMO+4



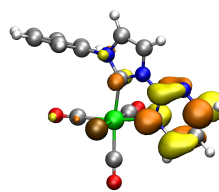
LUMO+3



LUMO+2

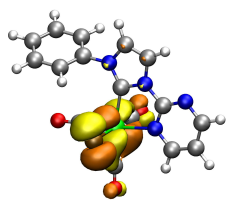


LUMO+1

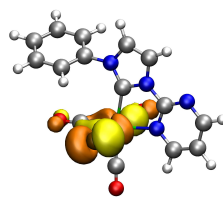


LUMO

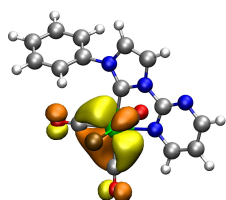
Figure A1.33: Selected unoccupied orbitals contours of **5Cl**.



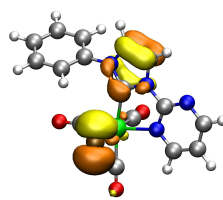
HOMO



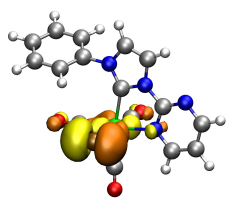
HOMO-1



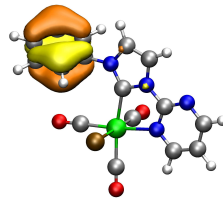
HOMO-2



HOMO-3

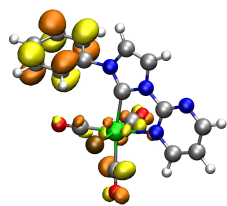


HOMO-4

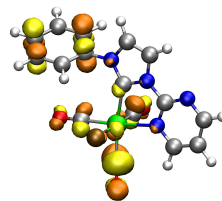


HOMO-5

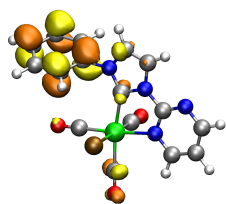
Figure A1.34: Selected occupied orbitals contours of **5Br**.



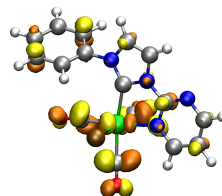
LUMO+5



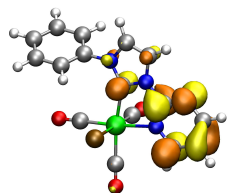
LUMO+4



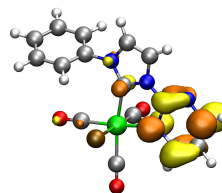
LUMO+3



LUMO+2



LUMO+1



LUMO

Figure A1.35: Selected unoccupied orbitals contours of **5Br**.

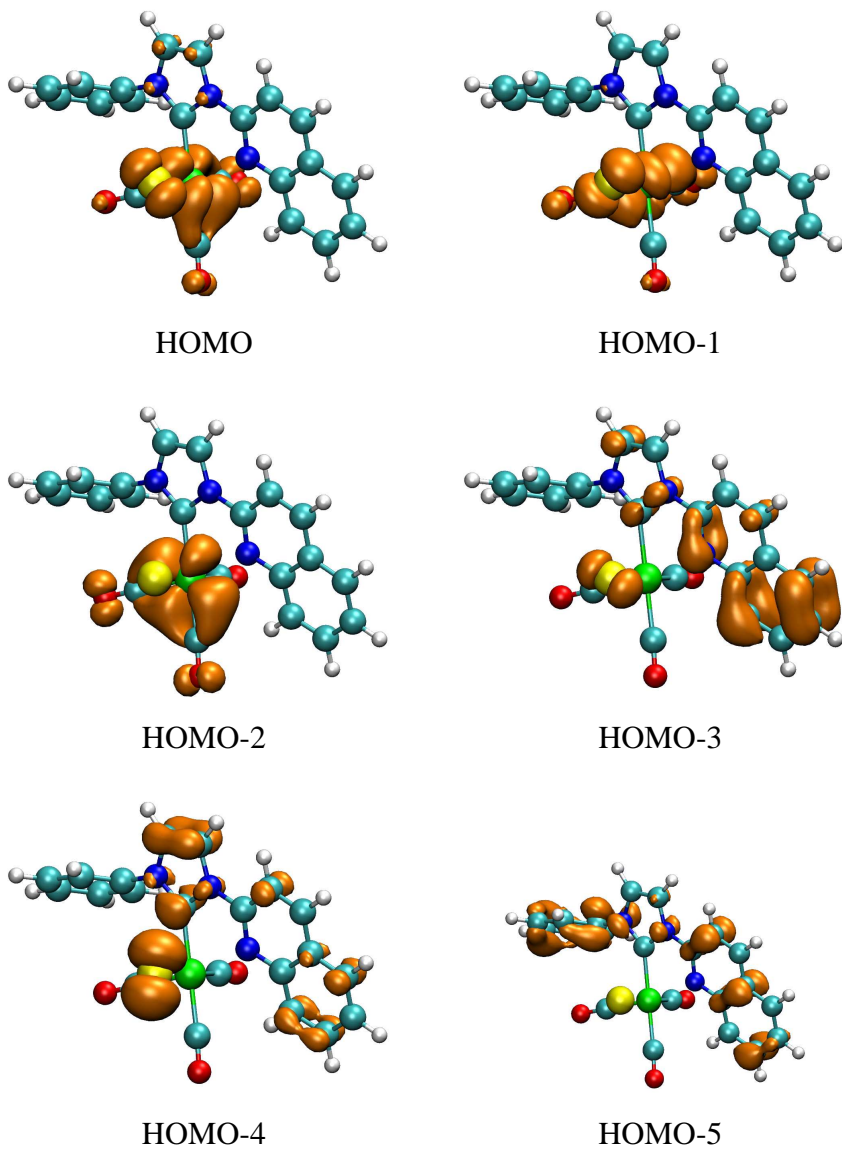


Figure A1.36: Selected occupied orbitals contours of **6Cl**.

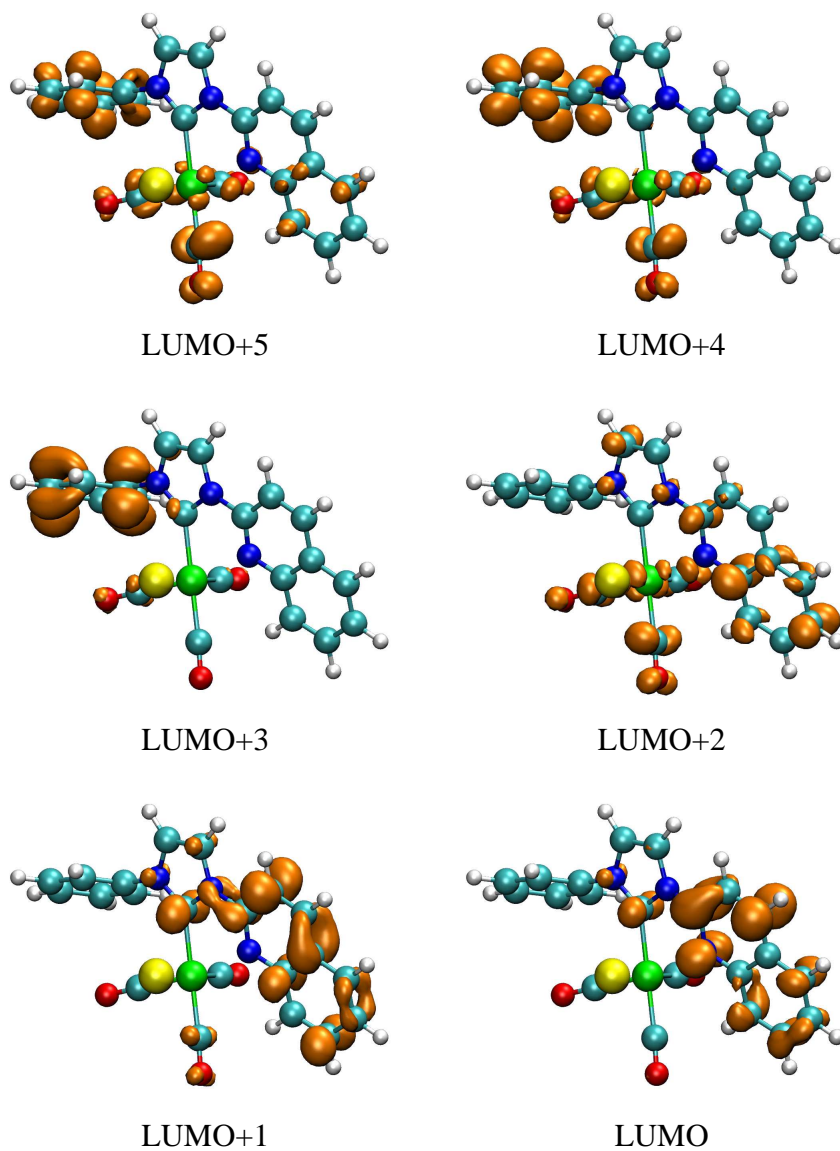
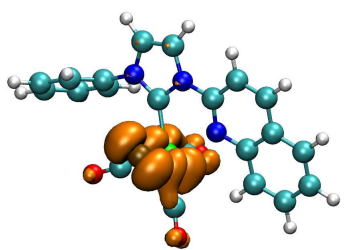
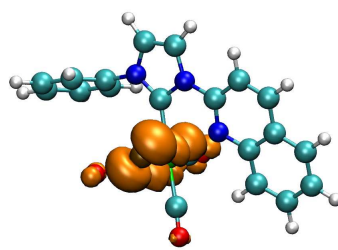


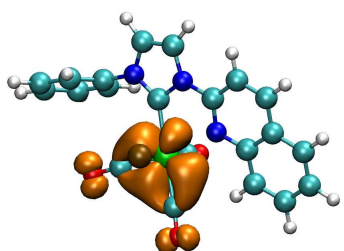
Figure A1.37: Selected unoccupied orbitals contours of **6Cl**.



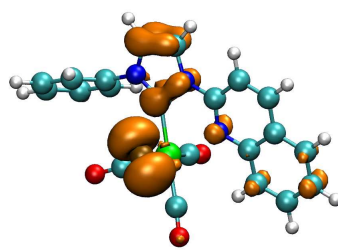
HOMO



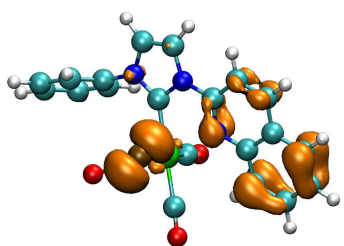
HOMO-1



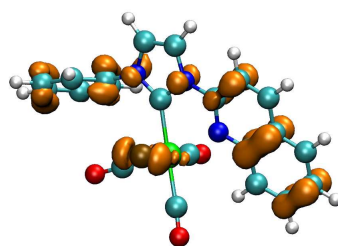
HOMO-2



HOMO-3

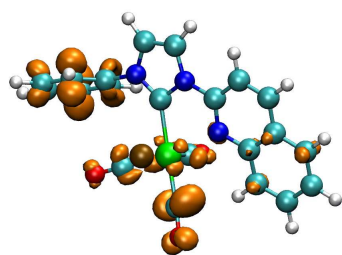


HOMO-4

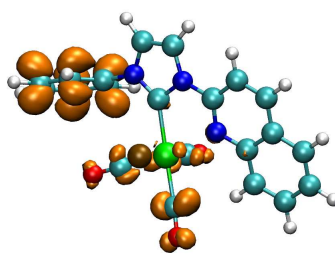


HOMO-5

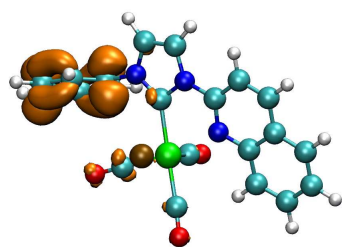
Figure A1.38: Selected occupied orbitals contours of **6Br**.



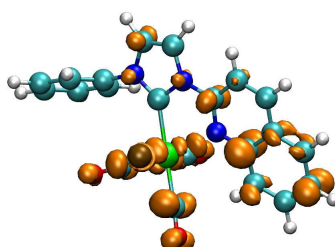
LUMO+5



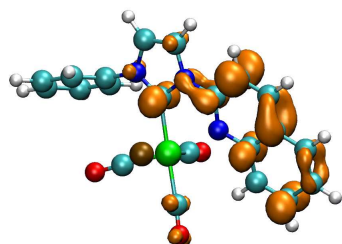
LUMO+4



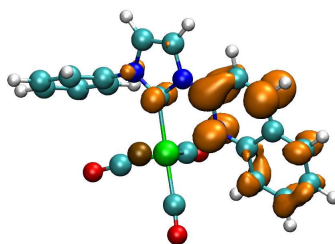
LUMO+3



LUMO+2

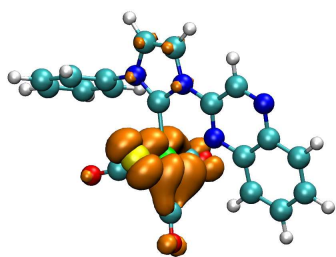


LUMO+1

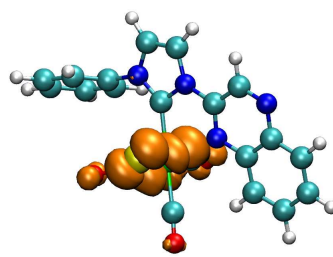


LUMO

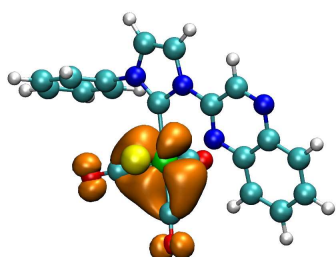
Figure A1.39: Selected unoccupied orbitals contours of **6Br**.



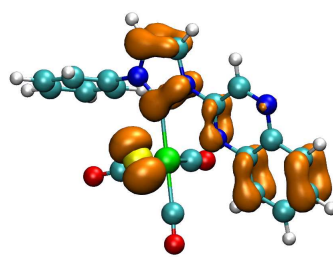
HOMO



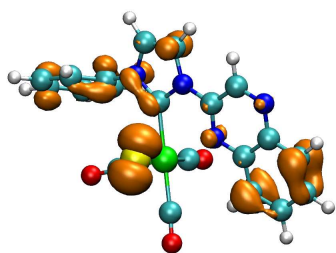
HOMO-1



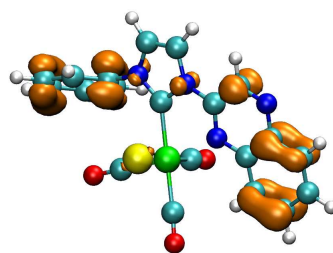
HOMO-2



HOMO-3

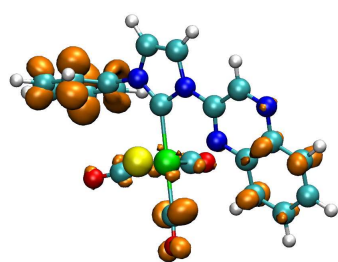


HOMO-4

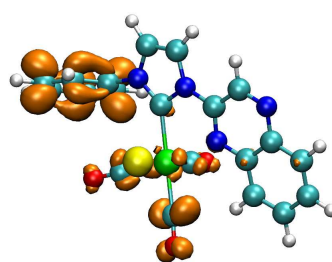


HOMO-5

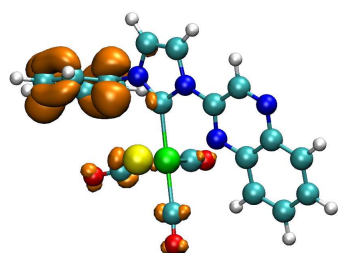
Figure A1.40: Selected occupied orbitals contours of **7Cl**.



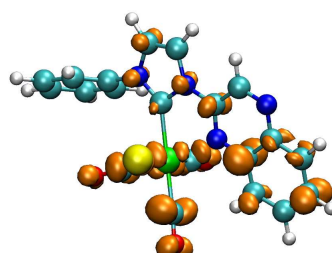
LUMO+5



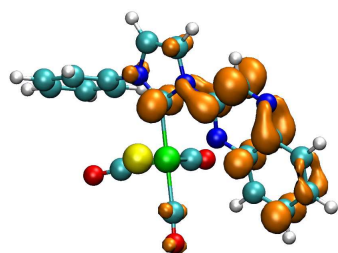
LUMO+4



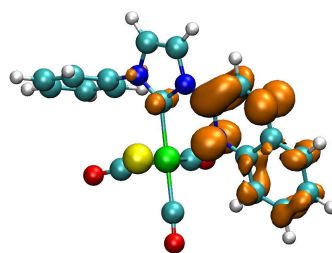
LUMO+3



LUMO+2

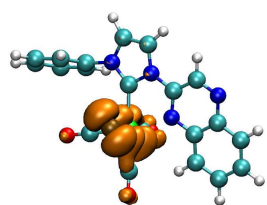


LUMO+1

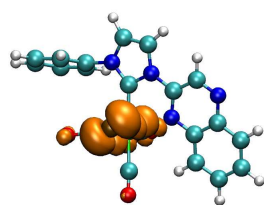


LUMO

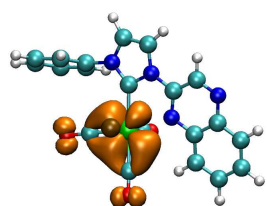
Figure A1.41: Selected unoccupied orbitals contours of **7Cl**.



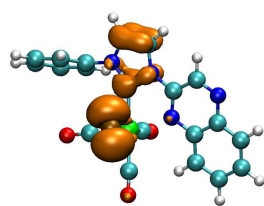
HOMO



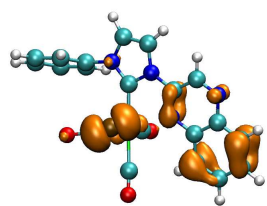
HOMO-1



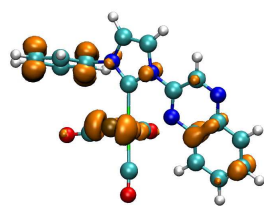
HOMO-2



HOMO-3

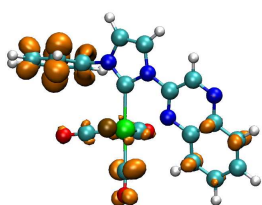


HOMO-4

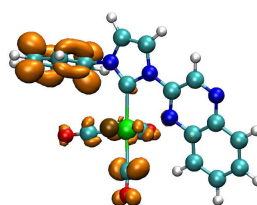


HOMO-5

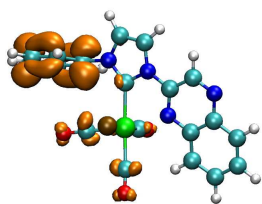
Figure A1.42: Selected occupied orbitals contours of **7Br**.



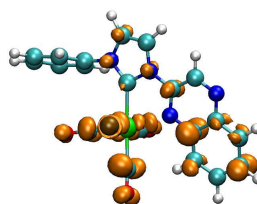
LUMO+5



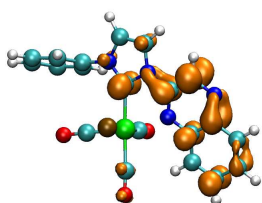
LUMO+4



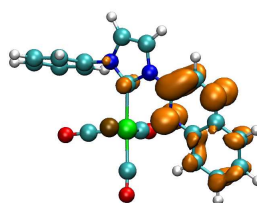
LUMO+3



LUMO+2



LUMO+1



LUMO

Figure A1.43: Selected unoccupied orbitals contours of **7Br**.



# References

- [1] Noddack, W.; Tacke, I.; Berg, O. *Naturwissenschaften* **1925**, *13*, 567–574.
- [2] Braband, H.; Kückmann, T. I.; Abram, U. *Journal of Organometallic Chemistry* **2005**, *690*, 5421–5429.
- [3] Hock, S. J.; Schaper, L.-A.; Herrmann, W. A.; Kühn, F. E. *Chemical Society Reviews* **2013**, *42*, 5073–5089.
- [4] Chan, C. Y.; Pellegrini, P. A.; Greguric, I.; Barnard, P. J. *Inorganic Chemistry* **2014**, *53*, 10862–10873.
- [5] Hayes, T. R.; Kasten, B. B.; Barnes, C. L.; Benny, P. D. *Dalton Transactions* **2014**, *43*, 6998–7001.
- [6] Abram, U. In *Comprehensive Coordination Chemistry II*; McCleverty, J. A., Meyer, T. J., Eds.; Elsevier: Amsterdam, 2003; pp 271–402.
- [7] Wrighton, M.; Morse, D. L. *Journal of the American Chemical Society* **1974**, *23*, 998–1003.
- [8] Kirgan, R. A.; Sullivan, B. P.; Rillema, D. P. *Photochemistry and Photophysics of Coordination Compounds II*; 2007; Vol. 281.
- [9] Vites, J. C.; Lynam, M. M. *Coordination Chemistry Reviews* **1994**, *131*, 127–152.
- [10] Bertrand, G. *Carbene Chemistry : From Fleeting Intermediates to Powerful Reagents*; Marcel Dekker Inc.: New York, 2002; p 301.
- [11] Wanzlick, H. W.; Schönherr, H.-J. *Angewandte Chemie International Edition* **1968**, *7*, 141–142.

- [12] Arduengo, A. J.; Harlow, R. L.; Kline, M. *Journal of the American Chemical Society* **1991**, *113*, 361–363.
- [13] Herrmann, W. A.; Köcher, C. *Angewandte Chemie International Edition* **1997**, *36*, 2162–2187.
- [14] Hahn, F. E.; Jahnke, M. C. *Angewandte Chemie International Edition* **2008**, *47*, 3122–3172.
- [15] de Frémont, P.; Marion, N.; Nolan, S. P. *Coordination Chemistry Reviews* **2009**, *253*, 862–892.
- [16] Hindi, K. M.; Panzner, M. J.; Tessier, C. A.; Cannon, C. L.; Youngs, W. J. *Chemical Reviews* **2009**, *109*, 3859–3884.
- [17] Jacobsen, H.; Correa, A.; Poater, A.; Costabile, C.; Cavallo, L. *Coordination Chemistry Reviews* **2009**, *253*, 687–703.
- [18] Poyatos, M.; Mata, J. A.; Peris, E. *Chemical Reviews* **2009**, *109*, 3677–3707.
- [19] Mercks, L.; Albrecht, M. *Chemical Society Reviews* **2010**, *39*, 1903–1912.
- [20] Oehninger, L.; Rubbiani, R.; Ott, I. *Dalton Transactions* **2013**, *42*, 3269–3284.
- [21] Visbal, R.; Gimeno, M. C. *Chemical Society Reviews* **2014**, *43*, 3551–3574.
- [22] Chen, C.; Qiu, H.; Chen, W.; Wang, D. *Journal of Organometallic Chemistry* **2008**, *693*, 3273–3280.
- [23] Hillier, A. C.; Grasa, G. A.; Viciu, M. S.; Lee, H. M.; Yang, C.; Nolan, S. P. *Journal of Organometallic Chemistry* **2002**, *653*, 69–82.
- [24] Nolan, S. P. *Accounts of Chemical Research* **2011**, *44*, 91–100.
- [25] Brown, D. H.; Nealon, G. L.; Simpson, P. V.; Skelton, B. W.; Wang, Z. *Organometallics* **2009**, *28*, 1965–1968.
- [26] Fischer, E. O.; Ofhaus, E.; Muller, J.; Dietrich, N. *Chemische Berichte* **1972**, *105*, 3027–3035.

- [27] Herrmann, W. A.; Mihalios, D.; Kiprof, P. *Chemische Berichte* **1992**, *3*, 1795–1799.
- [28] Chen, L.-c.; Chen, M.-y.; Chen, J.-h.; Wen, Y.-s.; Lu, K.-l. *Journal of Organometallic Chemistry* **1992**, *425*, 99–111.
- [29] Liu, C.-Y.; Chen, D.-Y.; Lee, G.-H.; Peng, S.-M.; Liu, S.-T. *Organometallics* **1996**, *15*, 1055–1061.
- [30] Chen, C.-H.; Liu, Y.-H.; Peng, S.-M.; Chen, J.-T.; Liu, S.-T. *Dalton Transactions* **2012**, *41*, 2747–54.
- [31] Hahn, F. E.; Wittenbecher, L.; Boese, R.; Bläser, D. *Chemistry - A European Journal* **1999**, *5*, 1931–1935.
- [32] Tafipolsky, M.; Scherer, W.; Ofele, K.; Artus, G.; Pedersen, B. r.; Herrmann, W. a.; McGrady, G. S. *Journal of the American Chemical Society* **2002**, *124*, 5865–5880.
- [33] Lakowicz, J. R. *Principles of Fluorescence Spectroscopy*, third edit ed.; Springer, 2006; p 960.
- [34] Montalti, M.; Credi, A.; Prodi, L.; Gandolfi, M. T. *Handbook of Photochemistry*; Taylor & Francis, 2006.
- [35] Atkins, P.; Overton, T.; Rourke, J.; Weller, M.; Armstrong, F. *Shriver and Atkins Inorganic Chemistry*, 4th ed.; Oxford University Press, 2006.
- [36] Eaton, D. F. *Pure and Applied Chemistry* **1988**, *60*, 1107–1114.
- [37] Bixon, M.; Jortner, J. *The Journal of Chemical Physics* **1968**, *48*, 715–726.
- [38] Caspar, J. V.; Meyer, T. J. *The Journal of Physical Chemistry* **1983**, *87*, 952–957.
- [39] Caspar, J. V.; Kober, E. M.; Sullivan, B. P.; Meyer, T. J. *Journal of the American Chemical Society* **1982**, *104*, 630–632.
- [40] Stolik, S.; Delgado, J. a.; Pérez, A.; Anasagasti, L. *Journal of Photochemistry and Photobiology. B, Biology* **2000**, *57*, 90–3.

- [41] Fernández-Suárez, M.; Ting, A. *Nature Reviews Molecular Cell Biology* **9**, 929–943.
- [42] D'Andrade, B. W.; Forrest, S. R. *Advanced Materials* **2004**, *16*, 1585–1595.
- [43] Baldo, M. A.; O'Brien, D. F.; You, Y.; Shoustikov, A.; Sibley, S.; Thompson, M. E.; Forrest, S. R. *Nature* **1998**, *395*, 151–154.
- [44] Sacksteder, L.; Zipp, A. P.; Brown, E. A.; Streich, J.; Demas, J. N.; Degraff, B. A. *Inorganic Chemistry* **1990**, *29*, 4335–4340.
- [45] Itokazu, M. K.; Polo, A. S.; Iha, N. Y. M. *Journal of Photochemistry and Photobiology A: Chemistry* **2003**, *160*, 27–32.
- [46] Ogilby, P. R. *Photochemical & Photobiological Sciences* **2010**, *9*, 1543–60.
- [47] Xue, W.-M.; Chan, M. C.-W.; Su, Z.-M.; Cheung, K.-K.; Liu, S.-T.; Che, C.-M. *Organometallics* **1998**, *17*, 1622–1630.
- [48] Lai, S.-w.; Cheung, K.-k.; Chi-wang, M.; Che, C.-m. *Angewandte Chemie International Edition* **1998**, *37*, 182–184.
- [49] Casson, L. A.; Muzzioli, S.; Raiteri, P.; Skelton, B. W.; Stagni, S.; Massi, M.; Brown, D. H. *Dalton Transactions* **2011**, *40*, 11960–11967.
- [50] Ko, C.-C.; Ng, C.-O.; Yiu, S.-M. *Organometallics* **2012**, *31*, 7074–7084.
- [51] Wang, G.-F.; Liu, Y.-Z.; Chen, X.-T.; Zheng, Y.-X.; Xue, Z.-L. *Inorganica Chimica Acta* **2013**, *394*, 488–493.
- [52] Fernandez-Moreira, V.; Thorp-Greenwood, F. L.; Coogan, M. P. *Chemical Communications* **2010**, *46*, 186–202.
- [53] Parker, D. *Australian Journal of Chemistry* **2011**, *64*, 239–243.
- [54] Gardiner, M. G.; Herrmann, W. A.; Reisinger, C.-p.; Spiegler, M. *Journal of Organometallic Chemistry* **1999**, *572*, 239–247.
- [55] Yuan, Y.; Thomé, I.; Kim, S. H.; Chen, D.; Beyer, A.; Bonnamour, J.; Zuidema, E.; Chang, S.; Bolm, C. *Advanced Synthesis & Catalysis* **2010**, *352*, 2892–2898.

- [56] Sperotto, E.; Klink, G. P. M. V.; Koten, G. V.; Vries, J. G. D. *Dalton Transactions* **2010**, *39*, 10338–10351.
- [57] Xu, Z.-L.; Li, H.-X.; Ren, Z.-G.; Du, W.-Y.; Xu, W.-C.; Lang, J.-P. *Tetrahedron* **2011**, *67*, 5282–5288.
- [58] Huang, Y.-Z.; Miao, H.; Zhang, Q.-H.; Chen, C.; Xu, J. *Catalysis Letters* **2008**, *122*, 344–348.
- [59] Gründemann, S.; Albrecht, M.; Kovacevic, A.; Faller, J. W.; Crabtree, R. H. *Dalton Transactions* **2002**, 2163–2167.
- [60] Kaufhold, O.; Hahn, F. E.; Pape, T.; Hepp, A. *Journal of Organometallic Chemistry* **2008**, *693*, 3435–3440.
- [61] Loch, J. A.; Albrecht, M.; Peris, E.; Mata, J.; Faller, J. W.; Crabtree, R. H. *Organometallics* **2002**, *21*, 700–706.
- [62] Reid, B. L. Synthesis and Photophysical Investigation of N-Heterocyclic Carbene-Rhenium(I) Complexes. Chemistry Honours Dissertation, Curtin University, 2011.
- [63] Meyer, D.; Taige, M. A.; Zeller, A.; Hohlfeld, K.; Ahrens, S.; Strassner, T. *Organometallics* **2009**, 2142–2149.
- [64] Avent, A. G.; Chaloner, P. A.; Day, M. P.; Seddon, K. R.; Welton, T. *Journal of the Chemical Society Dalton Transactions* **1994**, 3405–3413.
- [65] Moyer, B. A.; Singh, R. P. *Fundamentals and Applications of Anion Separations*; Kluwer Academic/Plenum Publications: New York, 2004.
- [66] Wang, H. M. J.; Lin, I. J. B. *Organometallics* **1998**, *17*, 972–975.
- [67] Taube, H. *Chemical Reviews* **1952**, *50*, 69–126.
- [68] Ramchandani, S. Modulation of the Photochemical Properties in Re(I)-NHC Complexes. Chemistry Honours Dissertation, Curtin University, 2012.
- [69] Li, X.-W.; Li, H.-Y.; Wang, G.-f.; Chen, F.; Li, Y.-Z.; Chen, X.-T.; Zheng, Y.-X.; Xue, Z.-L. *Organometallics* **2012**, *31*, 3829–3835.

- [70] Koike, K.; Okoshi, N.; Hori, H.; Takeuchi, K.; Ishitani, O.; Tsubaki, H.; Clark, I. P.; George, M. W.; Johnson, F. P. A.; Turner, J. J. *Journal of the American Chemical Society* **2002**, *124*, 11448–11455.
- [71] Smithback, J. L.; Helms, J. B.; Schutte, E.; Woessner, S. M.; Sullivan, B. P. *Inorganic Chemistry* **2006**, *45*, 2163–2174.
- [72] Albert, A. *Heterocyclic Chemistry*, 2nd ed.; The Athlone Press, University of London: London, 1968; p 547.
- [73] Kalyanasundaram, K. *Journal of the Chemical Society, Faraday Transactions 2* **1986**, *82*, 2401.
- [74] Frisch, M. J. et al. Gaussian 09, Revision B.01. 2009.
- [75] Andrae, D.; Haeussermann, U.; Dolg, M.; Stoll, H.; Preuss, H. *Theoretica Chimica Acta* **1990**, 123–141.
- [76] Tomasi, J.; Mennucci, B.; Cammi, R. *Chemical Reviews* **2005**, *105*, 2999–3093.
- [77] Wrighton, M. S.; Morse, D. L.; Gray, H. B.; Ottesen, D. K. *Journal of the American Chemical Society* **1976**, *98*, 1111–1119.
- [78] Treichel, P. M.; Willams, J. P. *Journal of Organometallic Chemistry* **1977**, *135*, 39–51.
- [79] Sullivan, B. P.; Bolinger, C. M.; Conrad, D.; Vining, W. J.; Meyer, T. J. *Journal of the Chemical Society, Chemical Communications* **1985**, 1414–1416.
- [80] Fredericks, S. M.; Wrighton, M. S. *Journal of the American Chemical Society* **1980**, *102*, 6168–6169.
- [81] Summers, D. P.; Luong, J. C.; Wrighton, M. S. *Journal of the American Chemical Society* **1981**, *103*, 5238–5241.
- [82] Fredericks, S. M.; Luong, J. C.; Wrighton, M. S. *Journal of the American Chemical Society* **1979**, *101*, 7415–7417.
- [83] Pac, C.; Kaseda, S.; Yanagida, S. *Journal of the Chemical Society, Chemical Communications* **1991**, 787–788.

- [84] Koike, K.; Tanabe, J.; Toyama, S.; Tsubaki, H.; Sakamoto, K.; Westwell, J. R.; Johnson, F. P. A.; Hori, H.; Saitoh, H.; Ishitani, O. *Inorganic Chemistry* **2000**, *39*, 2777–2783.
- [85] Hori, H.; Koike, K.; Ishizuka, M.; Takeuchi, K.; Ibusuki, T.; Ishitani, O. *Journal of Organometallic Chemistry* **1997**, *530*, 169–176.
- [86] Ko, C.-C.; Lo, L. T.-L.; Ng, C.-O.; Yiu, S.-M. *Chemistry - A European Journal* **2010**, *16*, 13773–82.
- [87] Ko, C.-C.; Cheung, A. W.-Y.; Lo, L. T.-L.; Siu, J. W.-K.; Ng, C.-O.; Yiu, S.-M. *Coordination Chemistry Reviews* **2012**, *256*, 1546–1555.
- [88] Sato, S.; Sekine, A.; Ohashi, Y.; Ishitani, O.; Blanco-Rodríguez, A. M.; Vlcek, A.; Unno, T.; Koike, K. *Inorganic Chemistry* **2007**, *46*, 3531–40.
- [89] Sato, S.; Morimoto, T.; Ishitani, O. *Inorganic Chemistry* **2007**, *46*, 9051–3.
- [90] Sato, S.; Matubara, Y.; Koike, K.; Falkenström, M.; Katayama, T.; Ishibashi, Y.; Miyasaka, H.; Taniguchi, S.; Chosrowjan, H.; Mataga, N.; Fukazawa, N.; Koshihara, S.; Onda, K.; Ishitani, O. *Chemistry - A European Journal* **2012**, *18*, 15722–15734.
- [91] Albani, B. a.; Durr, C. B.; Turro, C. *The Journal of Physical Chemistry. A* **2013**, *117*, 13885–92.
- [92] Bullock, J. P.; Carter, E.; Johnson, R.; Kennedy, A. T.; Key, S. E.; Kraft, B. J.; Saxon, D.; Underwood, P. *Inorganic Chemistry* **2008**, *47*, 7880–7.
- [93] Palazzi, A.; Sabatino, P.; Stagni, S.; Bordoni, S.; Albano, V. G.; Castellari, C. *Journal of Organometallic Chemistry* **2004**, *689*, 2324–2337.
- [94] Wright, P. J.; Muzzioli, S.; Werrett, M. V.; Raiteri, P.; Skelton, B. W.; Silvester, D. S.; Stagni, S.; Massi, M. *Organometallics* **2012**, *31*, 7566–7578.
- [95] Kuhl, O. *Phosphorus-31 NMR Spectroscopy : A Concise Introduction for the Synthetic Organic and Organometallic Chemist*; Springer: Berlin, 2008; p 138.

- [96] Bond, A. M.; Colton, R.; McDonald, M. E. *Inorganic Chemistry* **1978**, *17*, 2842–2847.
- [97] Inoue, H.; Nakagome, T.; Kuroiwa, T.; Shirai, T.; Fluck, E. *Zeitschrift Fur Naturforschung Section B - A Journal Of Chemical Sciences* **1987**, *42*, 573–578.
- [98] Hightower, S. E.; Corcoran, R. C.; Sullivan, B. P. *Inorganic Chemistry* **2005**, *44*, 9601–9603.
- [99] Peng, W.; Shreeve, J. M. *Journal of Fluorine Chemistry* **2005**, *126*, 1054–1056.
- [100] Wozniak, L. A.; Stec, W. J. *Tetrahedron Letters* **1999**, *40*, 2637–2640.
- [101] Pavia, D.; Lampman, G.; Kriz, G. *Introduction to Spectroscopy*, 3rd ed.; Saunders College Division, 2001.
- [102] Werrett, M. V.; Muzzioli, S.; Wright, P. J.; Palazzi, A.; Raiteri, P.; Zacchini, S.; Massi, M.; Stagni, S. *Inorganic Chemistry* **2014**, *53*, 229–43.
- [103] Huber, W.; Linder, R.; Niesel, J.; Schatzschneider, U.; Spingler, B.; Kunz, P. C. *European Journal of Inorganic Chemistry* **2012**, *2012*, 3140–3146.
- [104] Pierri, A. E.; Pallaoro, A.; Wu, G.; Ford, P. C. *Journal of the American Chemical Society* **2012**, *134*, 18197–18200.
- [105] Rimmer, R. D.; Pierri, A. E.; Ford, P. C. *Coordination Chemistry Reviews* **2012**, *256*, 1509–1519.
- [106] Bischof, C.; Joshi, T.; Dimri, A.; Spiccia, L.; Schatzschneider, U. *Inorganic Chemistry* **2013**, *52*, 9297–308.
- [107] Pai, S.; Hafftlang, M.; Atongo, G.; Nagel, C.; Niesel, J.; Botov, S.; Schmalz, H.-G.; Yard, B.; Schatzschneider, U. *Dalton Transactions* **2014**, 32–35.
- [108] Werrett, M. V.; Huff, G. S.; Muzzioli, S.; Fiorini, V.; Zacchini, S.; Skelton, B. W.; Maggiore, A.; Malicka, J. M.; Cocchi, M.; Gordon, K. C.; Stagni, S.; Massi, M. *Dalton Transactions* **2015**, *44*, 8379–93.

- [109] Werrett, M. V.; Wright, P. J.; Simpson, P. V.; Raiteri, P.; Skelton, B. W.; Stagni, S.; Buckley, A. G.; Rigby, J.; Massi, M. *Dalton Transactions* **2015**, 20636–20647.
- [110] Lv, X.; Wang, Z.; Bao, W. *Tetrahedron* **2006**, *62*, 4756–4761.
- [111] Demas, J. N.; Crosby, G. A. *The Journal of Physical Chemistry* **1971**, *75*, 991–1024.
- [112] Sheldrick, G. M. *Acta Crystallographica. Section A, Foundations of Crystallography* **2008**, *64*, 112–122.

Every reasonable effort has been made to acknowledge the owners of copyright material. I would be pleased to hear from any copyright owner who has been omitted or incorrectly acknowledged.